ASME
SETTING THE STANDARD

Transactions of the ASME, Journal of Turbomachinery (ISSN 0889-504X) is published quarterly (Jan., Apr., July, Oct.) by The American Society of Mechanical Engineers, Three Park Avenue, New York, NY 10016. Periodicals postage paid at New York, NY and additional mailing offices.
POSTMASTER: Send address changes to Transactions of the ASME, Journal of Turbomachinery, c/o THE AMERICAN SOCIETY OF MECHANICAL ENGINEERS, 22 Law Drive, Box 2300, Fairfield, NJ 07007-2300.
CHANGES OF ADDRESS must be received at Society headquarters seven weeks before they are to be effective. Please send old label and new address.
STATEMENT from By-Laws. The Society shall not be responsible for statements or opinions advanced in papers or ... printed in its publications (B7.1, Par. 3).

Journal of Turbomachinery

Published Quarterly by ASME

VOLUME 130 • NUMBER 3 • JULY 2008

RESEARCH PAPERS

(Contents continued on inside back cover)

This journal is printed on acid-free paper, which exceeds the ANSI Z39.48-1992 specification for permanence of paper and library materials. ♾™
♻ 85% recycled content, including 10% post-consumer fibers.

Journal of Turbomachinery Volume 130, Number 3 JULY 2008

TECHNICAL BRIEFS

The ASME Journal of Turbomachinery is abstracted and indexed in the following:

Aluminum Industry Abstracts, Aquatic Science and Fisheries Abstracts, Ceramics Abstracts, Chemical Abstracts, Civil Engineering Abstracts, Compendex (The electronic equivalent of Engineering Index), Corrosion Abstracts, Current Contents, Ei EncompassLit, Electronics & Communications Abstracts, Energy Information Abstracts, Engineered Materials Abstracts, Engineering Index, Environmental Science and Pollution Management, Excerpta Medica, Fluidex, Fuel and Energy Abstracts, INSPEC, Index to Scientific Reviews, Materials Science Citation Index, Mechanical & Transportation Engineering Abstracts, Mechanical Engineering Abstracts, METADEX (The electronic equivalent of Metals Abstracts and Alloys Index), Metals Abstracts, Oceanic Abstracts, Pollution Abstracts, Referativnyi Zhurnal, Shock & Vibration Digest, Steels Alert

Calculation of the Time-Averaged Flow in Squirrel-Cage Blowers by Substituting Blades With Equivalent Forces

Markus Tremmel
Neurosurgery Department,
University at Buffalo,
437 Biomedical Research Building,
Buffalo, NY 14214
e-mail: mtremmel@buffalo.edu

Dale B. Taulbee
MAE Department,
University at Buffalo,
315 Jarvis Hall,
Buffalo, NY 14260
e-mail: trldale@eng.buffalo.edu

Radial fans of the squirrel-cage type are used in various industrial applications. The analysis of such fans via computational fluid mechanics can provide the overall fan performance coefficients, as well as give insights into the detailed flow field. However, a transient simulation of a 3D machine using a sliding grid for the rotating blades still requires prohibitively large computational resources, with CPU run times in the order of months. To avoid such long simulation times, a faster method is developed in this paper. Instead of solving the transient Navier–Stokes equations, they are first averaged over one impeller rotation, and then solved for the mean flow since only this flow is of practical interest. Due to the averaging process, the blades disappear as solid boundaries, but additional equation terms arise, which represent the blade forces on the fluid. An innovative closure model for these terms is developed by calculating forces in 2D blade rows with the same blade geometry as the 3D machine for a range of flow parameters. These forces are then applied in the 3D machine, and the resulting 3D time-averaged flow field and performance coefficients are calculated. The 3D flow field showed several characteristic features of squirrel-cage blowers, such as a cross-flow pattern through the fan at low flow coefficients, and a vortexlike flow pattern at the fan outlet. The 3D fan performance coefficients showed an excellent agreement with experimental data. Since the 3D simulation solves for the mean flow, it can be run as a steady-state problem with a comparatively coarse grid in the blade region, reducing CPU times by a factor of about 10 when compared to a transient simulation with a sliding grid. It is hoped that these savings in computational cost will encourage other researchers and industrial companies to adopt the new method presented here. [DOI: 10.1115/1.2775483]

Keywords: radial turbomachinery, automobile fan, squirrel-cage blower, drum-impeller fan, sirocco fan, circumferential fan, time-averaged flow, deterministic stresses, blade forces, momentum sources, flow averaging, mean flow, averaged Navier–Stokes equations, computational fluid dynamics, STAR-CD

Introduction

Due to their compact size, radial or circumferential fans are in widespread use for industrial applications. For small air-handling equipment, the so-called "squirrel-cage fan" (also "drum-impeller fan" or "sirocco fan") with forward-curved blades is the most extensively used type since it produces very low noise at medium pressure heads and occupies an extremely small space for a given capacity. The impeller typically has 30 to 60 untwisted blades (constant chord), which are placed vertically around the circumference and stiffened by a plate or liner at the impeller top. The volute typically has a constant horizontal cross section and provides little guidance for the flow as it passes through the impeller.

Fan performance is measured in terms of global fan coefficients for flow rate, torque, and pressure, but these cannot be predicted by empirical formulas for a new fan geometry. Experiments can provide these coefficients, but they are costly and require the building of numerous blower models for design optimization. In addition, it is desirable to know details about the flow field in order to identify sources of losses or noise and to gain a better understanding about the fluid mechanics in such machines. Only with considerable effort can such details be obtained from experimental measurements.

Consequently, papers presenting experimental data on squirrel-cage fans are rare. Experimental studies were performed by Roth [1], who ran tests for a number of fans with varying geometry, and by Kind and Tobin [2], who measured pressure and velocity distributions at several azimuthal stations before and behind the blades. Other experimental publications limit their measurements to the regions directly downstream of the impeller (Raj and Swim [3] and Velarde-Suárez et al. [4]) or are of more special interest, like the inlet clearance gap study by Wright [5] or the acoustic study by Velarde-Suárez et al. [6]

With the advent of the digital computer, computational fluid dynamics (CFD) has become an important tool to investigate the flow through squirrel-cage blowers due to its potential to quickly obtain very detailed flow field data and to allow fast geometrical changes for fan design optimization. At first, researchers considered the volute and the impeller separately in their CFD studies. The flow through volutes was investigated by Nursen and Ayder [7], Dilin et al. [8], Chen et al. [9], and Ayder and Van den Braembussche [10], while the flow through isolated impellers was researched by Guzy [11], Tanger [12], and Wright et al. [13]. However, it was soon realized that a realistic picture of the whole flow field (and, with it, a realistic prediction of blower performance) can only be achieved by a full 3D machine simulation, encompassing both impeller and volute.

The most straightforward way for such a simulation would be to perform a transient analysis with a sliding grid for the rotating blades, but the computational cost for such an analysis is still

Contributed by the Turbomachinery Division of ASME for publication in the JOURNAL OF TURBOMACHINERY. Manuscript received May 16, 2006; final manuscript received April 8, 2007; published online April 1, 2008. Review conducted by Michael Casey.

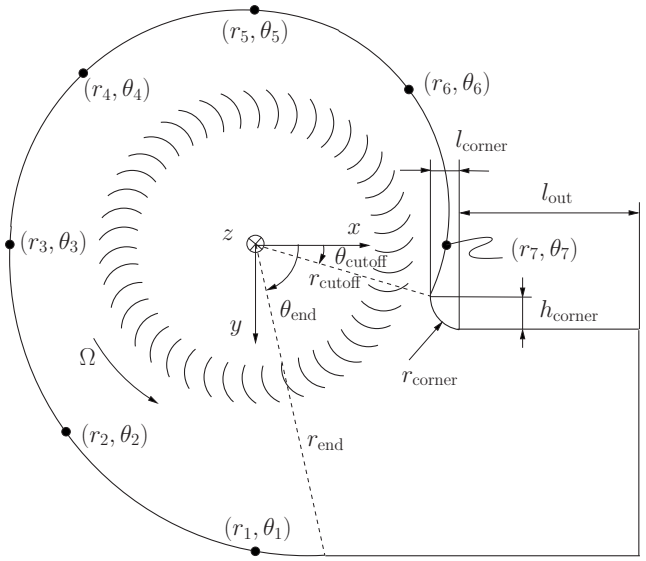

Fig. 1 Horizontal cross section of g-car fan (schematic)

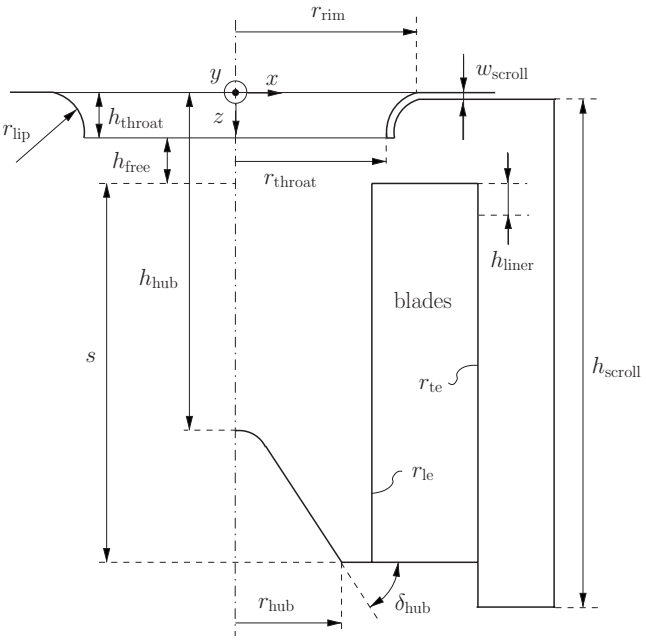

Fig. 2 Vertical cross section of g-car fan (schematic)

prohibitively high. Two researchers who have tried this approach are Sun [14] and Gilotte [15], but their success has been mixed. Sun only compared the velocity at the outlet with experimental data (not a stringent test for numerical accuracy because continuity is easily satisfied in CFD), while Gilotte reported calculated torque values that are 60% lower than measured ones. Moreover, CPU times for such transient simulations range in the order of 6–12 months (run times cited by Turunen-Saaresti [16] and Cobe Cardiovasuclar [17]), and it is obvious that a more economical method is needed.

A possible solution to the problem of computational cost is offered by a groundbreaking idea first advanced by Sehra [18] and Adamczyk [19], who proposed to *not* solve the transient Navier–Stokes equations but to solve their time-averaged forms instead since only the mean flow is of practical interest. In such an approach, the analysis becomes steady state, and the blades are replaced by equivalent mean forces, which eliminates the need to grid the blade region in great detail. This way, computational cost can be dramatically reduced. However, the blade forces are unknown and must be modeled (closure problem).

In his paper, Adamczyk derived an "average-passage" equation system, which yields a flow field that is periodic from blade passage to blade passage. It has been used to successfully predict periodic flow fields in rotating turbomachinery without volutes (Celestina et al. [20], Mulac et al. [21], and Heidmann and Beach [22]) and multistage compressors (Rhie et al. [23], Hall [24], and Kirtley et al. [25]). However, it is not directly applicable to an inherently aperiodic machine, such as a squirrel-cage radial blower with its asymmetric volute, and has, to our knowledge, never been applied to such a case. In the present paper, appropriate equations for this case are derived using Adamczyk's methodology, an innovative closure model for the force terms is developed, and the model is tested on an automobile fan for which experimental data was provided by Delphi-Harrison Thermal Systems, Lockport, NY.

Blower Geometry

The blower was a squirrel-cage automobile cooling fan with $N=43$ blades and a spiral volute. It will subsequently be referred to as the "g-car" fan. Horizontal and vertical cross sections are shown schematically in Figs. 1 and 2, and the blade geometry is defined in Fig. 3. The blade centerline starts at r_{le} as a radial line and remains straight until r_{curve}. Then, the blade continues as a circular arc until it reaches r_{te} and has a blade angle of γ_{te}. The shape $z=z(r)$ of the fan hub was approximated by the function $z = \sqrt{r^2 \tan^2 \delta_{hub} + \tilde{b}^2} + h_{hub} - \tilde{b}$, where $\tilde{b} = (r_{hub}^2 \tan^2 \delta_{hub} - \tilde{a}^2)/(2\tilde{a})$, where $\tilde{a} = (h_{throat} + h_{free} + s - h_{hub})$. The scroll spiral shape $r = r(\theta)$ was interpolated between the given points. (For a list of all symbols used in Figs. 1–3 and their respective values, please refer to Table 1).

Governing Equations

The Navier–Stokes equations in cylindrical coordinates for a Newtonian fluid with a constant density ϱ (incompressible flow) were averaged over one rotation of the impeller rotating at a constant angular rate Ω. It was assumed that the time-averaged flow is steady and that the flow field is perfectly periodic with period $2\pi/(\Omega N)$ at any point in the blade region. The blade thickness of 1.5 mm was neglected here for simplicity, but its effect on overall machine coefficients was considered in a later section of this paper. Following Adamczyk's notation, the time average of any quantity f was defined as

$$\bar{f} = \frac{\Omega}{2\pi} \int_{t_1}^{t_1 + 2\pi/\Omega} f(t)\, dt \tag{1}$$

and the momentary deviation from the average as

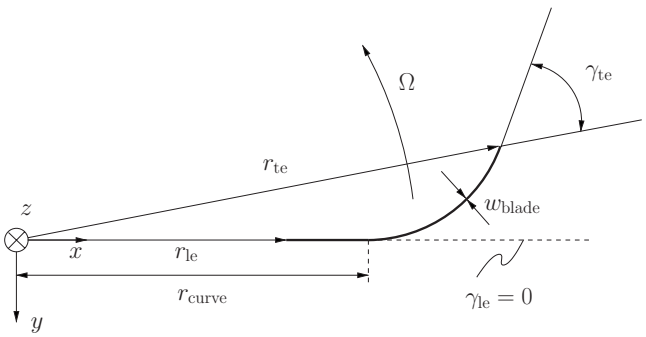

Fig. 3 Blade geometry of g-car fan, top view (schematic)

Table 1 Geometry values for g-car fan

Used symbol	Value	Used symbol	Value
N	43	r_{corner}	11 mm
Ω	6000π rad/min	l_{corner}	10.8 mm
r_{end}	136.2 mm	h_{corner}	13.4 mm
θ_{end}	83 deg	l_{out}	70 mm
r_1	135 mm	r_{le}	64 mm
θ_1	90 deg	γ_{le}	0 deg
r_2	127.2 mm	r_{curve}	67.5 mm
θ_2	135 deg	r_{te}	75 mm
r_3	119.5 mm	γ_{te}	60 deg
θ_3	180 deg	w_{blade}	1.5 mm
r_4	111.5 mm	r_{rim}	72 mm
θ_4	225 deg	r_{throat}	65 mm
r_5	103.7 mm	h_{throat}	8 mm
θ_5	270 deg	h_{free}	7.5 mm
r_6	95.85 mm	r_{lip}	8.1 mm
θ_6	315 deg	w_{scroll}	1.75 mm
r_7	88.1 mm	h_{scroll}	89 mm
θ_7	360 deg	h_{hub}	25 mm
r_{cutoff}	85.4 mm	r_{hub}	57 mm
θ_{cutoff}	15.5 deg	δ_{hub}	47 deg
s	66.5 mm	h_{liner}	6.05 mm

$$\hat{f}(t) = f(t) - \overline{f} \tag{2}$$

Applying this averaging operator and using the fact that blades in squirrel-cage blowers have a constant chord length along the (vertical) span, the Navier–Stokes equations take the following form: continuity equation,

$$\frac{\partial}{\partial r}r\overline{V_r} + \frac{\partial}{\partial \theta}\overline{V_\theta} + \frac{\partial}{\partial z}r\overline{V_z} = 0 \tag{3}$$

r-momentum equation,

$$\frac{1}{r}\frac{\partial}{\partial r}\varrho r\overline{V_r}\,\overline{V_r} + \frac{1}{r}\frac{\partial}{\partial \theta}\varrho\overline{V_\theta}\,\overline{V_r} + \frac{\partial}{\partial z}\varrho\overline{V_z}\,\overline{V_r} - \frac{1}{r}\varrho\overline{V_\theta}\,\overline{V_\theta}$$
$$= -\frac{\partial}{\partial r}\overline{p} + \frac{1}{r}\frac{\partial}{\partial r}r\overline{\tau_{rr}} + \frac{1}{r}\frac{\partial}{\partial \theta}\overline{\tau_{\theta r}} + \frac{\partial}{\partial z}\overline{\tau_{zr}} - \frac{1}{r}\overline{\tau_{\theta\theta}} + \underbrace{F_{flu}^{(r)} + F_{inv}^{(r)} + F_{vis}^{(r)}}_{F_{tot}^{(r)}}$$

$$F_{flu}^{(r)} = \frac{1}{r}\frac{\partial}{\partial r}r(-\varrho\overline{\hat{V}_r\hat{V}_r}) + \frac{1}{r}\frac{\partial}{\partial \theta}(-\varrho\overline{\hat{V}_\theta\hat{V}_r}) + \frac{\partial}{\partial z}(-\varrho\overline{\hat{V}_z\hat{V}_r}) - \frac{1}{r}(-\varrho\overline{\hat{V}_\theta\hat{V}_\theta})$$

$$F_{inv}^{(r)} = -\frac{N}{2\pi}(p|_{aft} - p|_{front})\frac{\partial \theta_B}{\partial r}$$

$$F_{vis}^{(r)} = \frac{N}{2\pi}\left[(\tau_{rr}|_{aft} - \tau_{rr}|_{front})\frac{\partial \theta_B}{\partial r} - \frac{1}{r}(\tau_{\theta r}|_{aft} - \tau_{\theta r}|_{front})\right] \tag{4}$$

θ-momentum equation,

$$\frac{1}{r}\frac{\partial}{\partial r}\varrho r\overline{V_r}\,\overline{V_\theta} + \frac{1}{r}\frac{\partial}{\partial \theta}\varrho\overline{V_\theta}\,\overline{V_\theta} + \frac{\partial}{\partial z}\varrho\overline{V_z}\,\overline{V_\theta} + \frac{1}{r}\varrho\overline{V_r}\,\overline{V_\theta}$$
$$= -\frac{1}{r}\frac{\partial}{\partial \theta}\overline{p} + \frac{1}{r}\frac{\partial}{\partial r}r\overline{\tau_{r\theta}} + \frac{1}{r}\frac{\partial}{\partial \theta}\overline{\tau_{\theta\theta}} + \frac{\partial}{\partial z}\overline{\tau_{z\theta}} + \frac{1}{r}\overline{\tau_{r\theta}} + \underbrace{F_{flu}^{(\theta)} + F_{inv}^{(\theta)} + F_{vis}^{(\theta)}}_{F_{tot}^{(\theta)}}$$

$$F_{flu}^{(\theta)} = \frac{1}{r}\frac{\partial}{\partial r}r(-\varrho\overline{\hat{V}_r\hat{V}_\theta}) + \frac{1}{r}\frac{\partial}{\partial \theta}(-\varrho\overline{\hat{V}_\theta\hat{V}_\theta}) + \frac{\partial}{\partial z}(-\varrho\overline{\hat{V}_z\hat{V}_\theta}) + \frac{1}{r}(-\varrho\overline{\hat{V}_r\hat{V}_\theta})$$

$$F_{inv}^{(\theta)} = \frac{1}{r}\frac{N}{2\pi}(p|_{aft} - p|_{front})$$

$$F_{vis}^{(\theta)} = \frac{N}{2\pi}\left[(\tau_{r\theta}|_{aft} - \tau_{r\theta}|_{front})\frac{\partial \theta_B}{\partial r} - \frac{1}{r}(\tau_{\theta\theta}|_{aft} - \tau_{\theta\theta}|_{front})\right] \tag{5}$$

z-momentum equation,

$$\frac{1}{r}\frac{\partial}{\partial r}\varrho r\overline{V_r}\,\overline{V_z} + \frac{1}{r}\frac{\partial}{\partial \theta}\varrho\overline{V_\theta}\,\overline{V_z} + \frac{\partial}{\partial z}\varrho\overline{V_z}\,\overline{V_z}$$
$$= -\frac{\partial}{\partial z}\overline{p} + \frac{1}{r}\frac{\partial}{\partial r}r\overline{\tau_{rz}} + \frac{1}{r}\frac{\partial}{\partial \theta}\overline{\tau_{\theta z}} + \frac{\partial}{\partial z}\overline{\tau_{zz}} + \underbrace{F_{flu}^{(z)} + F_{inv}^{(z)} + F_{vis}^{(z)}}_{F_{tot}^{(z)}}$$

$$F_{flu}^{(z)} = \frac{1}{r}\frac{\partial}{\partial r}r(-\varrho\overline{\hat{V}_r\hat{V}_z}) + \frac{1}{r}\frac{\partial}{\partial \theta}(-\varrho\overline{\hat{V}_\theta\hat{V}_z}) + \frac{\partial}{\partial z}(-\varrho\overline{\hat{V}_z\hat{V}_z})$$

$$F_{inv}^{(z)} = 0$$

$$F_{vis}^{(z)} = \frac{N}{2\pi}\left[(\tau_{rz}|_{aft} - \tau_{rz}|_{front})\frac{\partial \theta_B}{\partial r} - \frac{1}{r}(\tau_{\theta z}|_{aft} - \tau_{\theta z}|_{front})\right] \tag{6}$$

viscous stress averages,

$$\frac{\overline{\tau_{rr}}}{2\mu} = \frac{\overline{\partial V_r}}{\partial r} = \frac{\partial \overline{V_r}}{\partial r} \qquad \frac{\overline{\tau_{\theta\theta}}}{2\mu} = \frac{\overline{1}}{r}\frac{\overline{\partial V_\theta}}{\partial \theta} + \frac{\overline{1}}{r}\overline{V_r} = \frac{1}{r}\frac{\partial \overline{V_\theta}}{\partial \theta} + \frac{1}{r}\overline{V_r}$$

$$\frac{\overline{\tau_{zz}}}{2\mu} = \frac{\overline{\partial V_z}}{\partial z} = \frac{\partial \overline{V_z}}{\partial z}$$

$$\frac{\overline{\tau_{r\theta}}}{\mu} = \frac{\overline{\tau_{\theta r}}}{\mu} = r\overline{\frac{\partial}{\partial r}\frac{V_\theta}{r}} + \overline{\frac{1}{r}\frac{\partial V_r}{\partial \theta}} = r\frac{\partial}{\partial r}\frac{\overline{V_\theta}}{r} + \frac{1}{r}\frac{\partial \overline{V_r}}{\partial \theta}$$

$$\frac{\overline{\tau_{rz}}}{\mu} = \frac{\overline{\tau_{zr}}}{\mu} = \frac{\overline{\partial V_r}}{\partial z} + \frac{\overline{\partial V_z}}{\partial r} = \frac{\partial \overline{V_r}}{\partial z} + \frac{\partial \overline{V_z}}{\partial r}$$

$$\frac{\overline{\tau_{\theta z}}}{\mu} = \frac{\overline{\tau_{z\theta}}}{\mu} = \overline{\frac{1}{r}\frac{\partial V_z}{\partial \theta}} + \frac{\overline{\partial V_\theta}}{\partial z} = \frac{1}{r}\frac{\partial \overline{V_z}}{\partial \theta} + \frac{\partial \overline{V_\theta}}{\partial z} \tag{7}$$

In the above equations, the subscript "front" denotes the blade side that first reaches a point in the blade region, and "aft" the opposite side on the blade. If flow enters the blades radially in the nonrotating frame, the front side corresponds to the conventional pressure surface and the aft side to the conventional suction surface. The term $\partial\theta_B/\partial r$ denotes the slope of the blade line. For brevity, only the final forms of Eqs. (3)–(7) are presented here. For a more detailed description, including their general forms without neglecting blade thickness, please refer to Tremmel [26].

It will be noted that the mean Navier–Stokes equations are identical to (the steady-state case of) the ordinary Navier–Stokes equations in cylindrical coordinates, plus additional source terms in the momentum equations. These additional terms are fluctuation forces (mixing stresses) $\mathbf{F}_{flu}$ due to velocity unsteadiness, inviscid blade forces $\mathbf{F}_{inv}$ due to pressures on the blade surfaces, and viscous blade forces $\mathbf{F}_{vis}$ due to viscous stresses on blade surfaces. The latter two forces are zero outside the blade region. Once all source terms have been modeled, the above equations can be solved with any available Navier–Stokes solver that allows for sources in the momentum equations. In this work, the com-

mercially available code STAR-CD has been used.

Equations (3)–(7) have the same form, no matter if the flow is actually laminar or turbulent. However, in the experimental test data for the g-car fan, the average blade passage Reynolds number

$$\mathrm{Re}_b = \frac{\varrho V^*_{r_{\mathrm{te}}} L_{\mathrm{te}}}{\mu} = \frac{\varrho (Q/\pi D s)(\pi D/N)}{\mu} \tag{8}$$

which characterizes the flow through the blades ranged between 500 and 3500, suggesting a predominantly laminar flow through the blades. Since the blade region is most important for the ultimate blower performance and is the location of energy transfer to the fluid, laminar flow has been assumed throughout in the following.

The overall blower performance is characterized by the flow coefficient

$$\phi = \frac{2Q}{\pi \Omega D^3} \tag{9}$$

the torque coefficient

$$\vartheta = \vartheta(\phi) = \frac{16T}{\pi \varrho \Omega^2 D^5} = \frac{16a}{\pi \varrho \Omega^2 D^5} \tag{10}$$

and the static and total (gauge) pressure coefficients

$$\psi = \psi(\phi) = \frac{8\Delta p}{\varrho \Omega^2 D^2} = \frac{8(p_{\mathrm{out}} - p_\infty)}{\varrho \Omega^2 D^2} = \frac{8(p_{\mathrm{out}} - p_{t_{\mathrm{rim}}})}{\varrho \Omega^2 D^2} \tag{11}$$

$$\psi_t = \psi_t(\phi) = \frac{8\Delta p_t}{\varrho \Omega^2 D^2} = \frac{8(p_{t_{\mathrm{out}}} - p_\infty)}{\varrho \Omega^2 D^2} = \frac{8(p_{t_{\mathrm{out}}} - p_{t_{\mathrm{rim}}})}{\varrho \Omega^2 D^2} \tag{12}$$

In general, torque and pressure coefficients are also dependent on the rotational Reynolds number

$$\mathrm{Re}_\Omega = \frac{\varrho \Omega D^2}{\mu} \tag{13}$$

but this dependence becomes negligible if Re_Ω is high. This was the case in the experimental tests for the g-car fan, where rotational frequencies ranged between 2000 rpm and 3000 rpm and measured blower performance curves did not vary with Re_Ω. Thus, a fixed rotation rate of 3000 rpm was chosen in the numerical simulations, and fan performance was plotted as a function of flow coefficient only.

Force Model

We introduce a horizontal cut through the time-averaged 3D machine in Fig. 4. For each radial line (constant θ), the forces in the z plane that are exerted by the blades on the fluid will depend on the *average flow rate per unit span* passing radially through the blade region and the *preswirl* of the fluid (i.e., the fluid's tangential velocity just before the blades as a percentage of blade edge velocity). These can be expressed as

$$q'_{\mathrm{av}}(\theta, z) = \int_{r_{\mathrm{le}}}^{r_{te}} q' \, dr \tag{14}$$

$$w_{\mathrm{ch}}(\theta, z) = \begin{cases} w(r^-_{\mathrm{le}}, \theta, z) & \text{if } q'_{\mathrm{av}} \geq 0 \\ w(r^+_{\mathrm{te}}, \theta, z) & \text{if } q'_{\mathrm{av}} < 0 \end{cases} \tag{15}$$

where local flow rate per unit span and local swirl are defined in the blower as

$$q'(r, \theta, z) \equiv 2\pi r \overline{V_r} \tag{16}$$

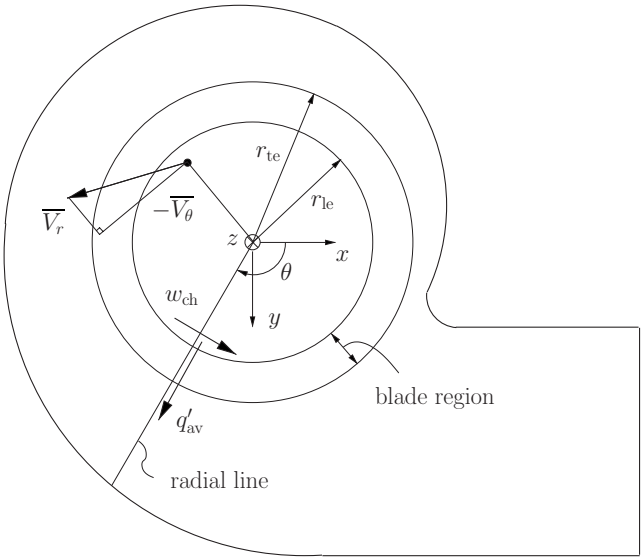

Fig. 4 Cut in z plane through time-averaged 3D blower, top view (schematic)

$$w(r, \theta, z) \equiv \begin{cases} \dfrac{(-\overline{V_\theta})(r/r_{\mathrm{le}})}{\Omega r_{\mathrm{le}}} 100\% & \text{for } r < r_{\mathrm{le}} \\ \dfrac{(-\overline{V_\theta})(r/r_{\mathrm{te}})}{\Omega r_{\mathrm{te}}} 100\% & \text{for } r > r_{\mathrm{te}} \end{cases} \tag{17}$$

Note that the local swirl, which is not defined inside the blade region, equals the percentage of blade edge speed if the local tangential velocity is extrapolated hyperbolically to the closest blade edge, assuming an ideal vortex flow.

We now stipulate that the r, θ forces exerted by the blades on the fluid as it passes through the blade region at position θ in Fig. 4 can be approximated by the forces exerted on fluid that passes through a 2D periodic blade row at the same q'_{av} and w_{ch}. This concept is illustrated in Fig. 5. From such a 2D rotating blade channel solution, the r, θ forces as a function of radius can be exactly calculated from the force definitions in Eqs. (4)–(6). Repeating this for all radial lines in the 3D machine, the complete 3D force field can be determined. However, only regions of positive q'_{av} in the 3D machine need to be considered for forces in this way since in backflow regions the fluid (which has traveled through the blades at an earlier time) will have a tangential velocity comparable to blade speed and will pass through the blades without receiving any significant acceleration. Therefore, zero forces can be assumed in backflow regions. It will be noted that forces in the z direction and terms with $\partial/\partial\theta$ and $\partial/\partial z$ in the fluctuation forces are neglected in the above force model. This was deemed acceptable since the inviscid blade force in the z direction is zero, and fluctuation forces only have a small net effect on the flow through the blades (see Tremmel [26]).

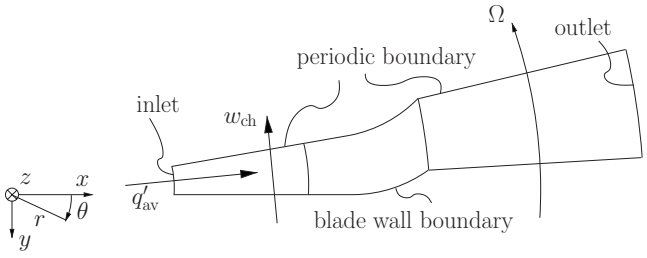

Fig. 5 Equivalent 2D periodic machine (rotating domain, schematic)

The solution strategy can therefore be summarized as follows.

1. Run a number of 2D periodic channel solutions for a range of q'_{av} and w_{ch} that cover all q'_{av} (≥ 0) and w_{ch} to be expected in the 3D machine. In this 2D simulation, use a rotating blade channel domain, as shown in Fig. 5. For each separate case, extract the r, θ forces as a function of radius from the velocity and pressure fields, thus creating a force database that depends on q'_{av} and w_{ch}.
2. Model the 3D blower, assuming a steady flow with velocities and pressures representing time-averaged values. Blades are *not* modeled, which greatly simplifies the grid generation in the force region. Make sure to create radial cell rows in the blade region that allow an easy calculation of q'_{av} and w_{ch} for a given velocity field. Then specify an initial flow field in the 3D blower.
3. For each radial line (radial cell row) through the blade region in the 3D blower, calculate the current q'_{av} and w_{ch}, and if q'_{av} is positive, interpolate the appropriate entry from the force database. If q'_{av} is negative (backflow), assume that the blade force is zero.
4. Apply the forces in the 3D machine as momentum sources, and find the new flow field that these forces produce.
5. Go back to step 3 and repeat until the flow field is consistent with the force field. This is the converged final solution.

2D Model and Results

The 2D domain shown in Fig. 5 was meshed with a structured grid consisting of $I_m=76$ cells in the radial direction, $J_m=20$ cells in the azimuthal direction, and one cell in the axial direction ($K_m=1$). The left grid boundary was specified to be at $r_{left}=0.5r_{le}$ and the right grid boundary to be at $r_{right}=r_{te}+5(r_{te}-r_{le})$, i.e., five chord lengths behind the trailing edge. The grid was then imported into STAR-CD, and boundaries were specified in accordance with Fig. 5. The (x,y) planes at the top and bottom were set as symmetry boundaries to achieve a 2D solution. The flow is steady in the relative frame, but the 2D grid itself rotates anticlockwise at a constant rotation rate of $\bar{n}=3000$ rpm in the absolute frame. The fluid density and viscosity were set to $\varrho=1.204\ \mathrm{kg/m^3}$ and $\mu=1.82\times10^{-5}\ \mathrm{kg/(m\,s)}$. For a given q'_{av} and w_{ch} in the 3D machine, the corresponding conditions at the 2D inlet are given by $q'_{in}=q'_{av}$ and $w_{in}=w_{ch}$, with the resulting inlet velocities

$$\bar{V}_{r,in}=q'_{av}[2\pi r_{left}(\sin\beta)/\beta]^{-1} \tag{18}$$

$$\bar{V}_{\theta,in}=-\Omega r_{le}[r_{left}/r_{le}]^{-1}w_{ch}/100\% \tag{19}$$

where $\beta=\Delta\theta/(2J_m)$ is the half-width of one cell in the 2D grid.

A total of 81 runs were performed for the 2D model for flow rates of $q'_{av}=0\ \mathrm{m^2/s}$ to $q'_{av}=9.6\ \mathrm{m^2/s}$ in steps of $1.2\ \mathrm{m^2/s}$ and inlet swirls of $w_{ch}=-100\%$ to $w_{ch}=300\%$ in steps of 50%, which covered all flow conditions in the 3D machine. The chosen step sizes were small enough for step size independence, as was verified in a refinement study (Tremmel [26]). Then, the total blade force $F^{(r)}_{tot}(r)$ and $F^{(\theta)}_{tot}(r)$ for each run was calculated from the (in the absolute frame) unsteady 2D flow field using the force definitions in Eqs. (4)–(6) and stored in a force database. Because of the small 2D grid, the 81 runs were completed in a total CPU time of approximately 2.7 h.

As an example, the STAR-CD solutions for the 2D blade channel at an inlet flow rate per unit span of $q'_{in}=4.2\ \mathrm{m^2/s}$ and three inlet swirls of 0%, 100%, and 200% are shown in Figs. 6, 7, and 8. Velocities are plotted in the rotating coordinate system for clarity. In the case of zero swirl, the blades need to accelerate the flow strongly in the tangential direction, leading to high pressures on the front blade side and a separation bubble with low pressures on the aft side. In the case of 100% swirl, the flow enters the blades radially, and it passes through the blades without receiving much tangential acceleration. In the case of 200% swirl, the flow at the leading edge has a tangential speed twice the speed of the blades themselves. Thus, the blades need to tangentially brake the flow, causing high pressures on the aft side and a separation bubble with low pressures on the front side. It is interesting to note that total pressure (not shown) rises strongly across the blades in the case of 0% swirl, changes only little in the case of 100% swirl, and actually decreases in the case of 200% swirl.

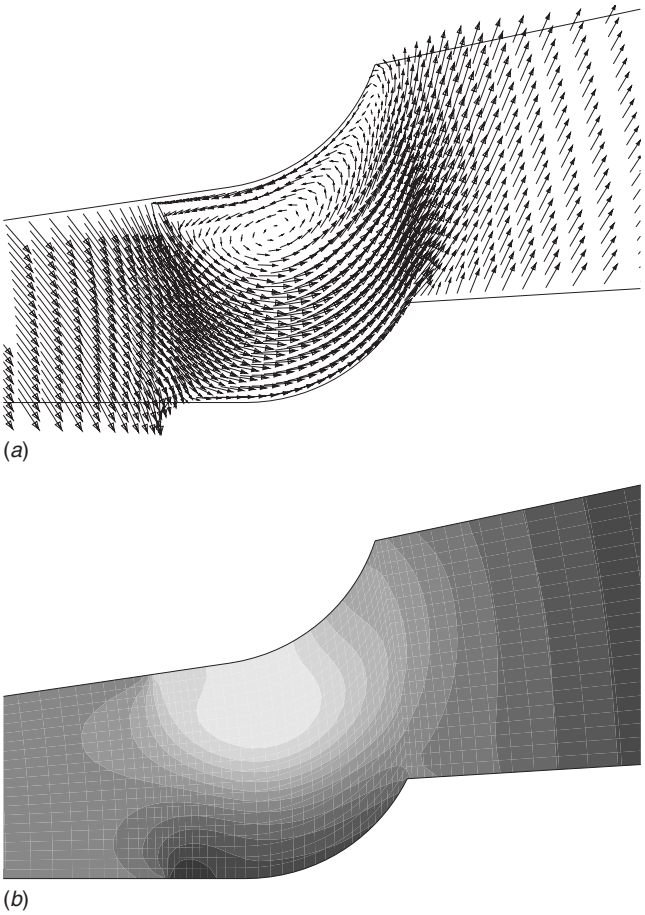

Fig. 6 2D channel flow field, $q'_{in}=4.2\ \mathrm{m^2/s}$, $w_{in}=0\%$; (*a*) Relative velocity $\vec{V}$, (*b*) static pressure p

The forces for these three solutions as calculated by Eqs. (4)–(6) are shown in Figs. 9 and 10. Only inviscid and fluctuation forces are shown here since the viscous force was about two orders of magnitude smaller and is therefore negligible for practical purposes. Because of the forward curvature of the blades, the inviscid radial force is always opposed to the flow direction. The inviscid tangential force at the leading edge acts in the direction of blade rotation for zero swirl, becomes small for 100% swirl since the fluid passes straight through the blades in this case, and reverses its sign for 200% swirl because now the fluid needs to be braked tangentially by the blades. Fluctuation forces generally assume complicated shapes and have magnitudes comparable to the inviscid forces. They are not confined to the blade region but extend slighly outward of the blades. For 100% swirl, fluctuation forces are small because of the missing separation bubble in this case. Finally, Fig. 11 shows the total force, which is the sum of the individual forces and describes the total effect of the blades on the fluid.

It should be pointed out that the grid used for the 2D force database was not designed to resolve the shear stresses in the boundary layer in detail because the viscous force is small and

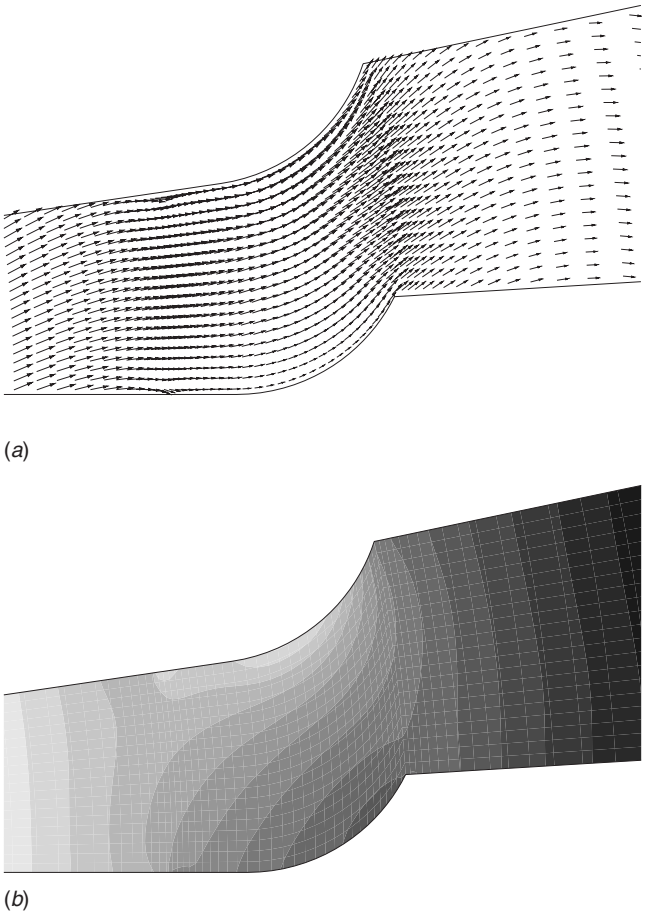

(*a*)

(*b*)

Fig. 7 2D channel flow field, $q'_{in}=4.2\ m^2/s$, $w_{in}=100\%$; (*a*) Relative velocity $\vec{V}$, (*b*) static pressure *p*

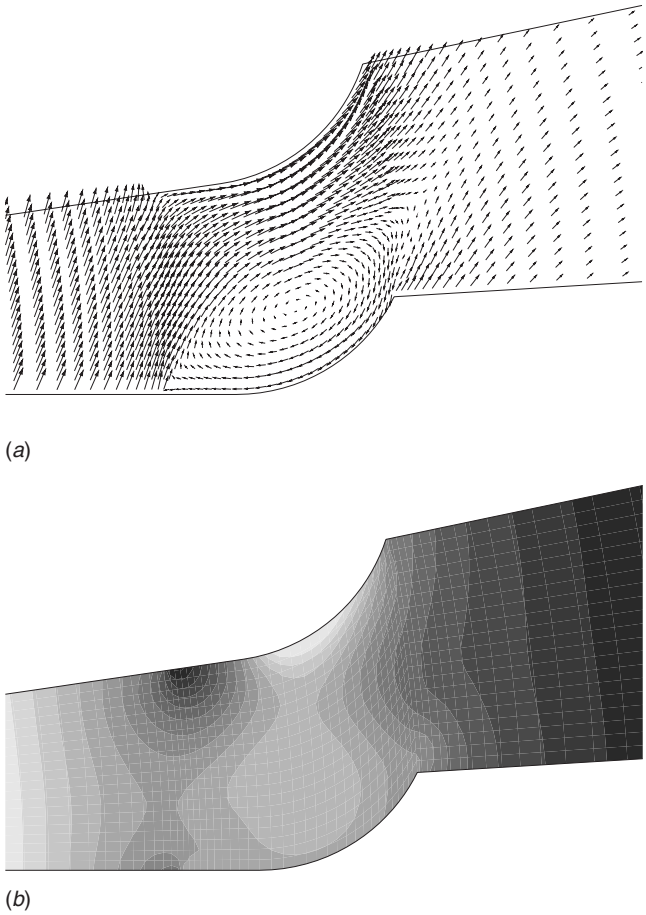

(*a*)

(*b*)

Fig. 8 2D channel flow field, $q'_{in}=4.2\ m^2/s$, $w_{in}=200\%$; (*a*) Relative velocity $\vec{V}$, (*b*) static pressure *p*

their exact value is of little importance. This way, a relatively coarse grid could be used and the CFD solutions could be achieved in minimum CPU time. To verify that viscous forces indeed remain small for all grid densities, we performed a grid refinement study for $q'_{in}=4.2\ m^2/s$ at inlet swirls $w_{in}=0\%$ and $w_{in}=100\%$, which is the most important swirl range in the 3D machine. We doubled the original grid density in both directions, and then further subdivided the cells closest to the blades until their angular width was 1/32 of the original grid cells. For all grids, the average viscous force along the blade never exceeded 2.9% of the inviscid force, confirming that the original grid was adequate.

Influence of Blade Thickness. In the derivation of the governing equations, the blade thickness was neglected to keep the theoretical framework as simple as possible. This limits the additional equation terms (due to the averaging procedure) to momentum sources that can be easily implemented in widely available commercial solvers, such as STAR-CD, thus increasing the potential user base who can benefit from the method presented here. However, it should be pointed out that the omission of blade thickness is a rather large simplification. For the g-car fan, the thickness of 1.5 mm is equivalent to an angular blockage of 16.0% at the leading edge and 13.6% at the trailing edge. Therefore, we will now estimate the global effect of blade thickness on machine performance for the g-car fan.

In order to estimate the influence of the blade thickness on overall machine coefficients, we first note that the 2D solutions with zero inlet swirl can serve as a crude model for the whole machine if one imagines the 2D domain extended in z by the span s. Only the case $w_{in}=0\%$ can serve as such a model since in the 3D case, the fluid originally also has zero swirl as it enters the blower from the ambient surroundings. The flow rate for this fictitious machine is then $Q=sq'_{in}$, the blade torque is $T=sT'$, and the total pressure rise across the blades is $\Delta p_t=\bar{p}_{t,B}-\bar{p}_{t,A}$, where the total pressure before (A) and behind (B) the blades should be taken at radial stations just outside of the force region. Overall machine coefficients can then be readily calculated according to their definitions in Eqs. (9)–(12).

To get an estimate of blade thickness influence, we created two separate 2D channel grids identical to the 2D grid used for the force database runs except for a finer cell spacing of $I_m=115$, $J_m=25$, and $K_m=1$. The first of these two grids was kept unchanged, while in the second the two outermost cell rows in the blade region were deleted, resulting in a finite blade thickness of 1.496 mm at the leading edge. Then, cases of $w_{in}=0\%$ were run for a range of q'_{in} analogous to the 2D database runs, and performance curves $\vartheta(\phi)$ and $\psi_t(\phi)$ were calculated. Stations A and B for the total pressure values were located 0.3 chord lengths in front of the leading edge and 0.74 chord lengths behind the trailing edge, thus ensuring that the stations were outside of the range of blade influence. The resulting coefficients are plotted in Figs. 12 and 13. Generally, finite blade thickness has the effect of lowering the torque and total pressure coefficients. It should be noted that the loss in total pressure for the case of finite blade thickness is really a loss in static pressure since the velocities (before and) behind the blades are about the same for thin or thick blades at a given flow coefficient ϕ. In the 3D machine, similar losses can be expected, and the curves $\vartheta(\phi)$ and $\psi(\phi)$ will be adjusted downward accordingly.

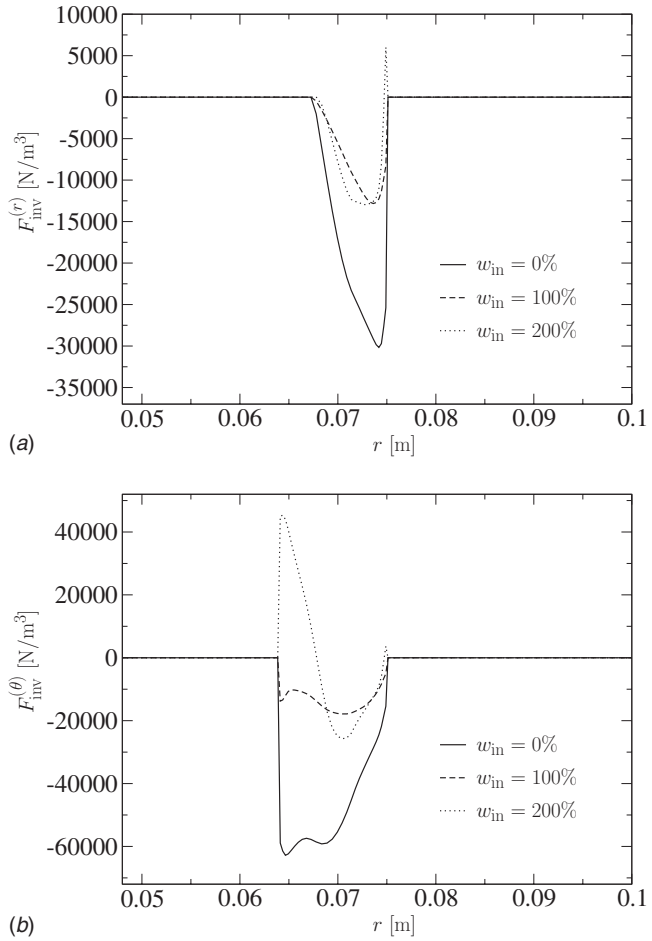

Fig. 9 Inviscid force distribution in 2D channel at q'_{in} = 4.2 m^2/s; (*a*) Radial component $F_{\mathrm{inv}}^{(r)}$, (*b*) tangential component $F_{\mathrm{inv}}^{(\theta)}$

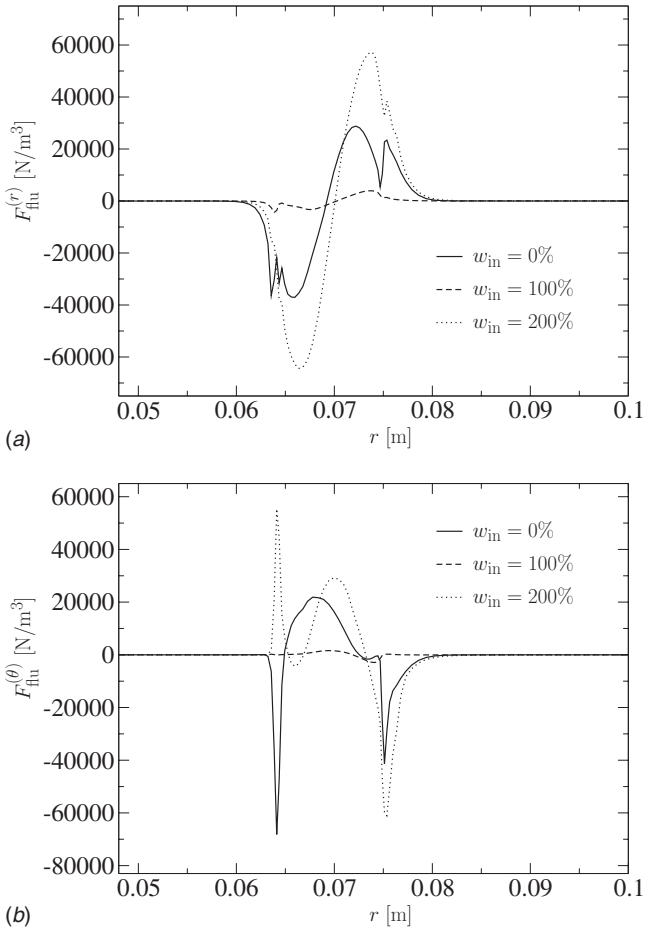

Fig. 10 Fluctuation force distribution in 2D channel at q'_{in} = 4.2 m^2/s; (*a*) Radial component $F_{\mathrm{flu}}^{(r)}$, (*b*) tangential component $F_{\mathrm{flu}}^{(\theta)}$

3D Model

The grid for the 3D machine consisted of 12 separate structured grid blocks, which were generated by customized FORTRAN codes, imported into STAR-CD, and joined at the interfaces by integral and arbitrary coupling, as shown in Fig. 14. The grid had a total of about 460,000 hexahedral cells, which collapsed into triangular prisms at the axis of rotation. The liner at the top of the blade trailing edge was modeled by impenetrable baffles. Because of the two-dimensional nature of the force model, the top of the blade region was left impenetrable to flow, so that swirls entering from above did not remain unaccounted for (leading to excessive forces). To assure a plausible incoming flow profile at the rim, a cylindrical inflow channel with a radius r_{in}=120 mm and a height h_{in}=70 mm was placed on top of the rim (not shown in Fig. 14). To get a grid-independent solution, there were 440 cells around the circumference of the blade region. All walls were stationary no-slip walls, except for the outer wall of the inlet cylinder, which was a wall with slip, and for the bottom of the impeller, which was taken to rotate at 3000 rpm in the negative θ direction. The inlet velocity is purely axial (z direction) and, for a desired flow coefficient ϕ, assumes the value

$$V_{\mathrm{in}} = \frac{Q}{A_{\mathrm{in}}} = \frac{(\pi/2)\Omega D^3 \phi}{r_{\mathrm{in}}^2 n_c \sin(\pi/n_c)\cos(\pi/n_c)}, \tag{20}$$

where n_c is the number of azimuthal cell divisions at the inlet top. At the blower outlet, a traction-free outflow boundary condition (zero gradients along flow direction) was imposed.

The STAR-CD solution was run for a series of flow coefficients, with forces implemented according to steps 2–5 of the solution procedure outlined earlier. The values q'_{av} and w_{ch} for each radial cell row through the blade region were calculated every ten iterations, updated with a relaxation factor of 0.1, and then used for linear force interpolation from the database. Since the force value space is not smooth, a too short update interval or too high relaxation factor will lead to fluctuations in the numerical solution and should be avoided. For the g-car fan, the above settings for update interval and relaxation factor yielded a stable solution and may serve as a starting point for other researchers. Convergence with these settings was typically achieved within 3000 iterations. All runs were executed on a single 400 MHz processor of an SGI Origin 2000 computer at the CCR of the University at Buffalo.[1] The typical CPU time required for one run (one flow coefficient) was 2–3 d.

3D Results

After the runs were completed, flow coefficient, torque coefficient and static pressure coefficient were calculated based on the last terms of Eqs. (9)–(11), respectively. For the angular momentum flow a, the value at the 0.29 chord lengths behind the trailing edge was used since this was the local maximum behind the blade region. In Figs. 15 and 16, the coefficients are shown together with experimental data. To account for blade thickness, the curves

[1]Center for Computational Research, University at Buffalo, 701 Ellicott St., Buffalo, New York, 14203.

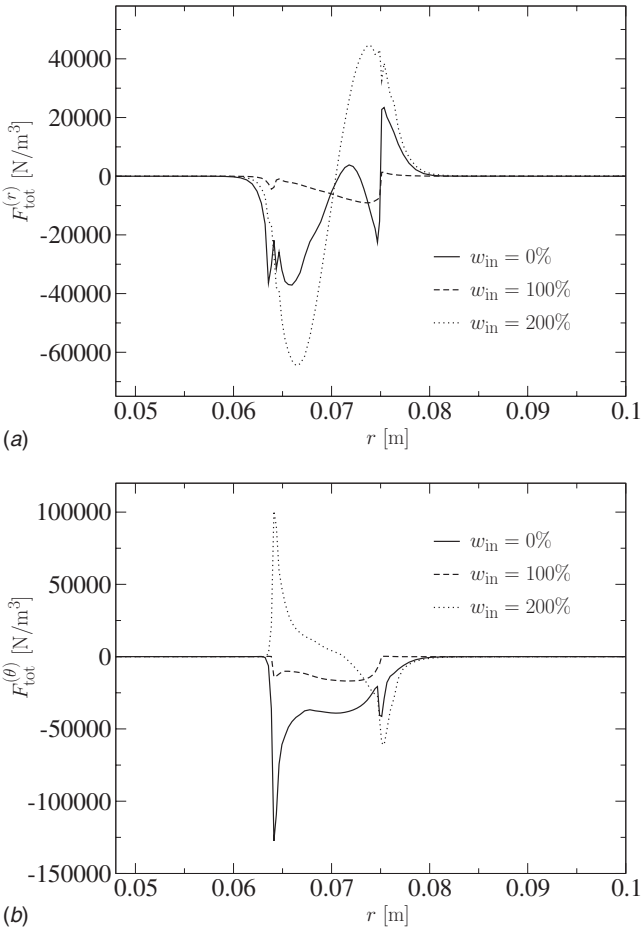

Fig. 11 Total force distribution in 2D channel at q'_{in}=4.2 m^2/s; (*a*) Radial component $F_{tot}^{(r)}$, (*b*) tangential component $F_{tot}^{(\theta)}$

have been lowered by the amount determined from Figs. 12 and 13. Generally, a good agreement with experimental values is observed. The calculated torque coefficient curve lies somewhat below the experimental data, which is most likely due to bearing friction included in the experimental torque measurements. The calculated pressure coefficient curve lies slightly above the experimental values at both ends of the flow coefficient range, which is probably due to the simplifications inherent in the two-dimensional force model. It should be noted that for very low flow coefficients (less than $\phi \approx 0.02$, not shown), the solution became unstable and convergence could not be achieved. This is caused by a pronounced backflow at the blower exit at such low flow coefficients, which is incompatible with the traction-free outlet boundary condition used in the numerical model.

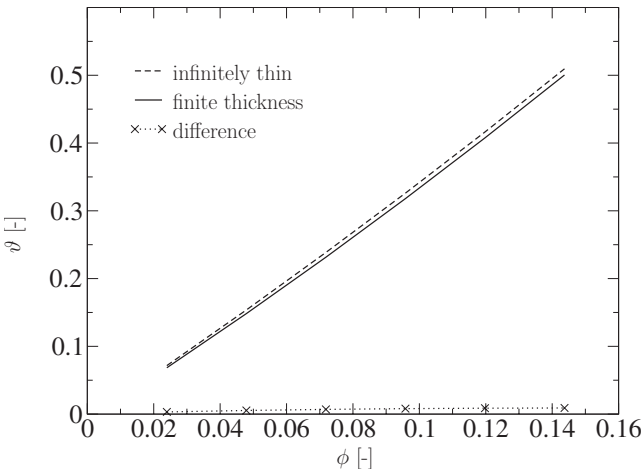

Fig. 12 Torque coefficient from 2D channel, effect of blade thickness

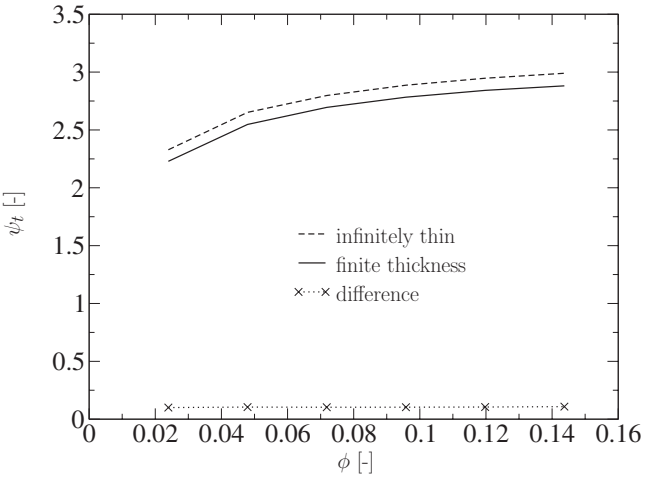

Fig. 13 Total pressure coefficient from 2D channel, effect of blade thickness

To get a better picture of the flow field in the blower operating range, detailed field plots are provided in Figs. 17 and 18 for a high flow coefficient of ϕ=0.122 (V_{in}=4.5 m/s) and in Figs. 19 and 20 for a low flow coefficient of ϕ=0.0407 (V_{in}=1.5 m/s).

For the *high flow coefficient case*, the velocity vectors in a horizontal plane at midspan (z=0.04875 m), viewed from the origin, are shown in Fig. 17(*a*). We see that the flow enters the blade region radially around the circumference and that there are no backflow regions. Since preswirls are close to zero everywhere, the region of the largest radial throughflow is also the region of the strongest forces. This happens at $\theta \approx 70$ deg, where the large forces lead to high tangential velocities. The total pressure distribution is shown in Fig. 17(*b*) and illustrates how energy is transferred to the fluid across the blades. In the inner blower regions, total pressures are low (light shades), while behind the blades,

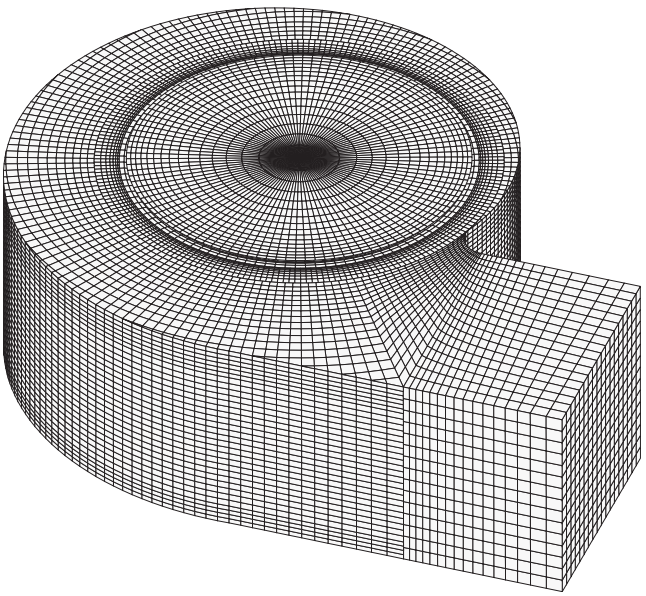

Fig. 14 Grid for g-car fan (inlet region not shown)

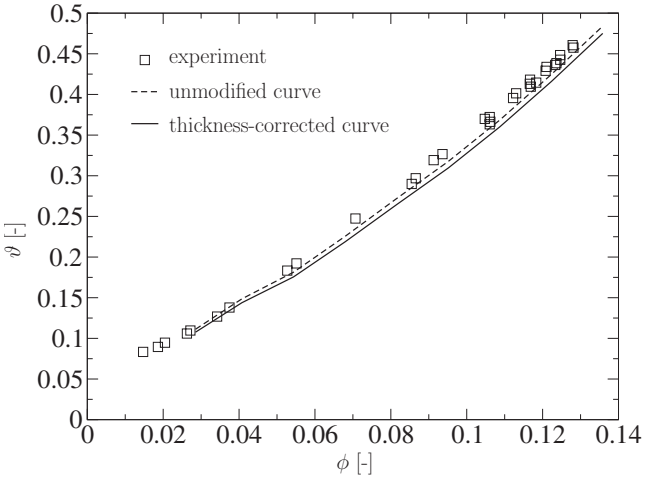

Fig. 15 Torque coefficient results

they have risen to high values (dark shades). The velocity field in a vertical cut in the *yz* plane, viewed from the positive *x* direction, is shown in Fig. 18(*a*). Here, the cylindrical inflow region above the rim is also shown, and it can be seen how it successfully creates a plausible entrance-flow profile at the blower rim. Behind the blades on the left side of the figure, the flow assumes a circular motion because after exiting the blades, the air impacts on the outer scroll wall and has no other option but to go up and around in a circle. This three-dimensional rotation pattern is carried downstream as one single vortex all the way to the fan outlet and has been observed by other researchers [1,7,8]. It causes a reduction in the static outlet pressure because some flow energy is contained as a dynamic pressure in the vortex. Reducing this pattern (for example, by vanes in the scroll) will therefore lead to a higher static pressure at the outlet and should be considered in the design of future blowers. The static pressure in the *yz* plane is shown in Fig. 18(*b*). It corresponds loosely with the velocity field, with low pressures at regions of high velocities and vice versa. However, the static pressure generally increases in the outward direction and is highest at the outer blower walls, where the flow is forced to change direction by the scroll.

For the *low flow coefficient case*, the velocity vectors in the horizontal plane at midspan are shown in Fig. 19(*a*). Now, there is a significant backflow in the vicinity of the cutoff point, causing the outer flow to return to the inside of the blower and reexit at $\theta \approx -45$ deg. It is interesting to note that this cross-flow pattern is

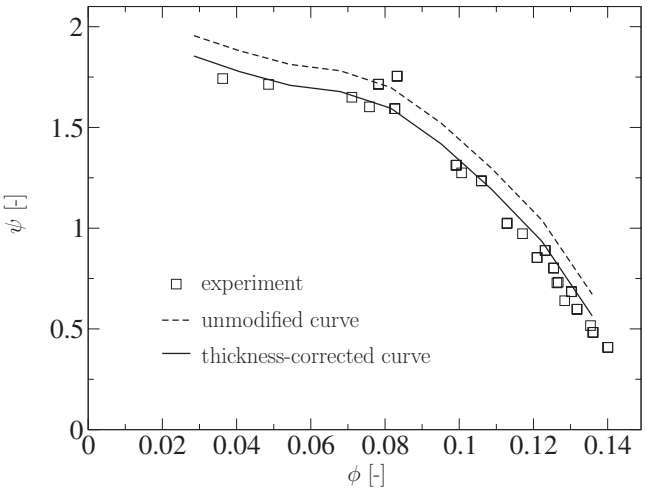

Fig. 16 Pressure coefficient results

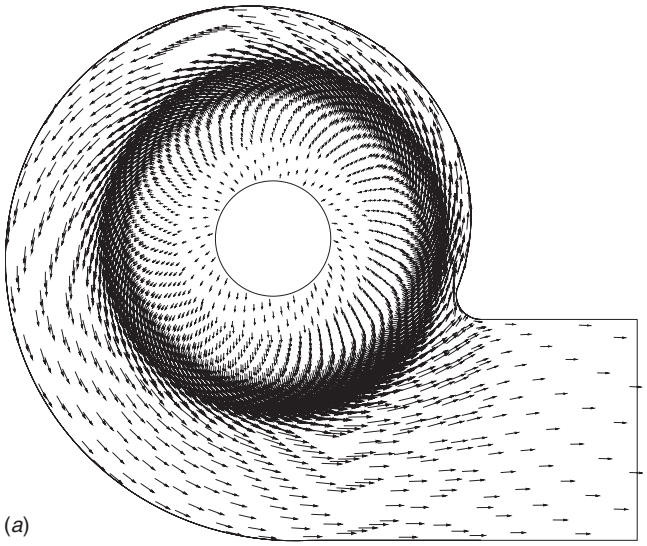

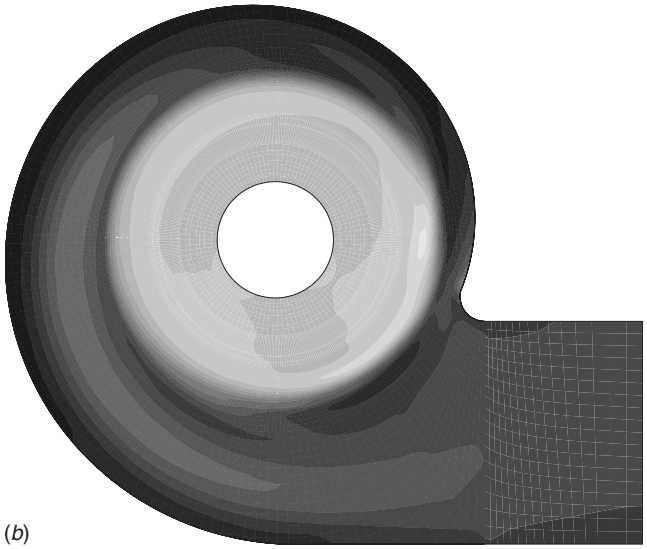

Fig. 17 V_{in}=4.5 m/s, flow field in the midspan plane; (*a*) Velocity $\vec{V}$, (*b*) total pressure $\overline{p_t}$

typical for squirrel-cage centrifugal blowers at low flow coefficients and has been observed by other researchers (see Kind and Tobin [2]). Now, the highest velocities occur on the blower side opposite to the outlet. It should be noted that upon reexiting, the cross flow is associated with low forces in spite of its high values of q'_{av} because it also brings high preswirls with it that lower the force. The corresponding distribution of the total pressure is shown in Fig. 19(*b*). From the total pressure plot, it is clearly seen how the cross flow carries the high energy level of the outer flow regions back through the interior of the blower. Figure 20(*a*) shows the velocities in the *yz* plane. This time, two separate vortices exist behind the blades on the left side of the figure, in contrast to the single vortex in the case of high flow coefficient. The two vortices are carried downstream to the fan outlet and reduce the static pressure head of the fan. The static pressure distribution in the *yz* plane is plotted in Fig. 20(*b*). As in the case of high flow coefficient, the static pressure rises in the outward direction and assumes its highest values at the outer scroll wall.

Conclusion

In this paper, a new method for a fast and cost-effective numerical analysis of circumferential fans of the squirrel-cage type was

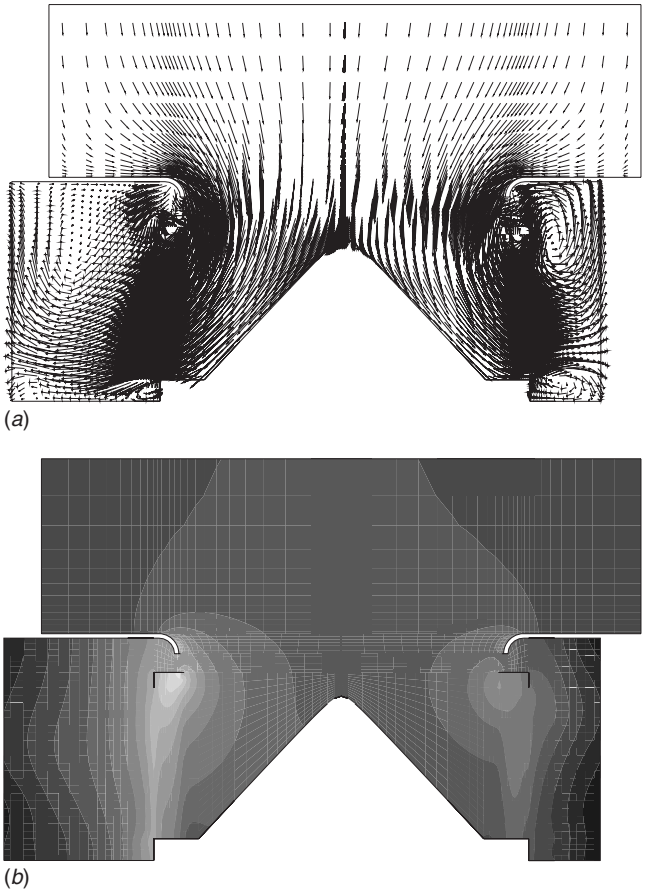

Fig. 18 V_{in}=4.5 m/s, flow field in the *yz* plane; (*a*) Velocity $\vec{\bar{V}}$, (*b*) static pressure $\bar{p}$

developed and tested on a fan for which experimental data existed from Delphi-Harrison at Lockport, NY. The quantitatively good agreement with experimental data as well as the presence of physically correct 3D flow features, such as cross flow and outlet vortex, are quite remarkable and underline the method's usefulness. Compared to lengthy sliding-grid approaches with run times in the order of months, the newly developed method requires only a few days of CPU time, which makes it both economical and practical, particularly in an industry setting where short run times are essential for a competitive design and optimization process. The applicability of the method with *any* CFD Navier–Stokes solver that allows for momentum sources and unstructured grids is an additional benefit in industrial settings where a large variety of commercial CFD codes is available for companies to choose from. In the present paper, the program STAR-CD has been used.

To our knowledge, the method developed here is the first to provide *both* a detailed 3D average flow field for squirrel-cage fans and short CPU times, thus filling a real gap in the current state of research on the subject. Moreover, the 2D force model with its calculation of the true 2D blade forces has, to our knowledge, not been presented before in the literature, and could result in a new branch of research on the analysis of radial turbomachinery.

A caveat to keep in mind, however, is that a number of approximations were made in the theoretical development of the method, particularly when defining the flow parameters in the 3D machine to be used for the force interpolation (preswirl and average flow rate per unit span). Therefore, the presented method should always be viewed as an approximation to the real blower flow field, not as an exact solution. Additionally, the method can currently only be used for squirrel-cage blowers with untwisted blades and ideally

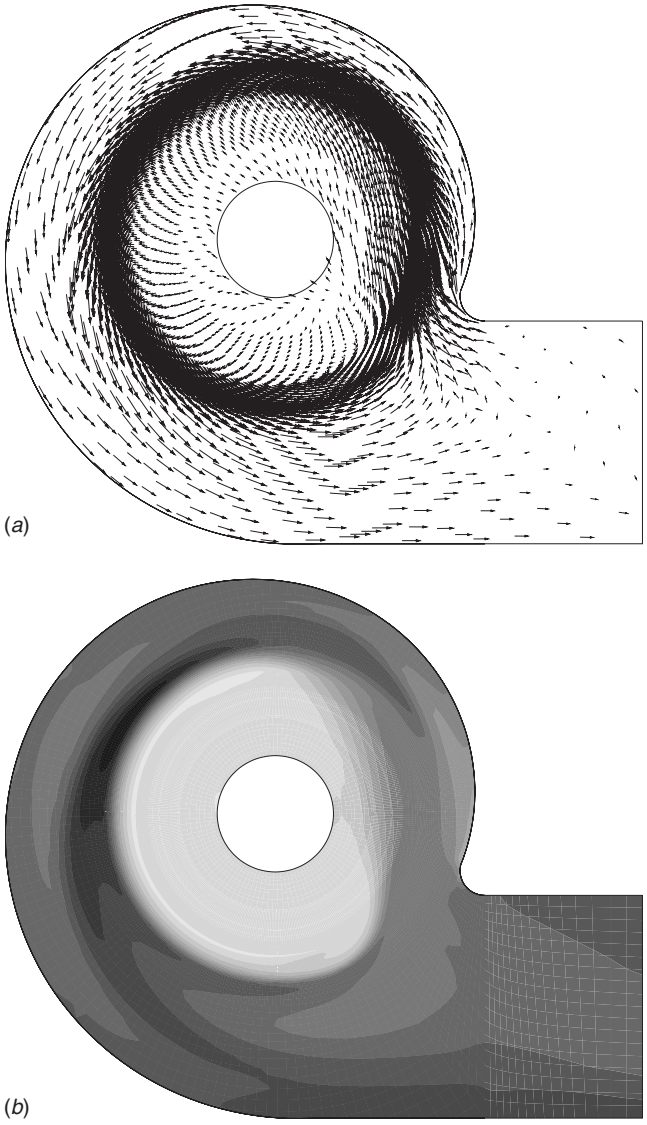

Fig. 19 V_{in}=1.5 m/s, flow field in the midspan plane; (*a*) Velocity $\vec{\bar{V}}$, (*b*) total pressure $\overline{p_t}$

with a closed blade region top due to the 2D nature of the force model. Further research should be aimed at investigating these limitations and possibly expanding the method to other types of radial turbomachinery.

Nomenclature

Latin Symbols and Units

a = angular momentum flow behind the blades (N m)

$\tilde{a}$, $\tilde{b}$ = constants in hub shape function (m)

aft = denotes blade side that first touches point in blade region

A_{in} = inlet area of cylindrical entrance domain above rim (m^2)

D = outer impeller diameter (m)

f = placeholder for any variable

$\bar{f}$ = time average (over one shaft revolution) of variable f

$\hat{f}$ = fluctuation of variable f (note: $\hat{f}=f-\bar{f}$)

$F_{flu}^{(r)}$, $F_{flu}^{(\theta)}$, $F_{flu}^{(z)}$ = components of fluctuation force $\mathbf{F}_{flu}$ (N/m^3)

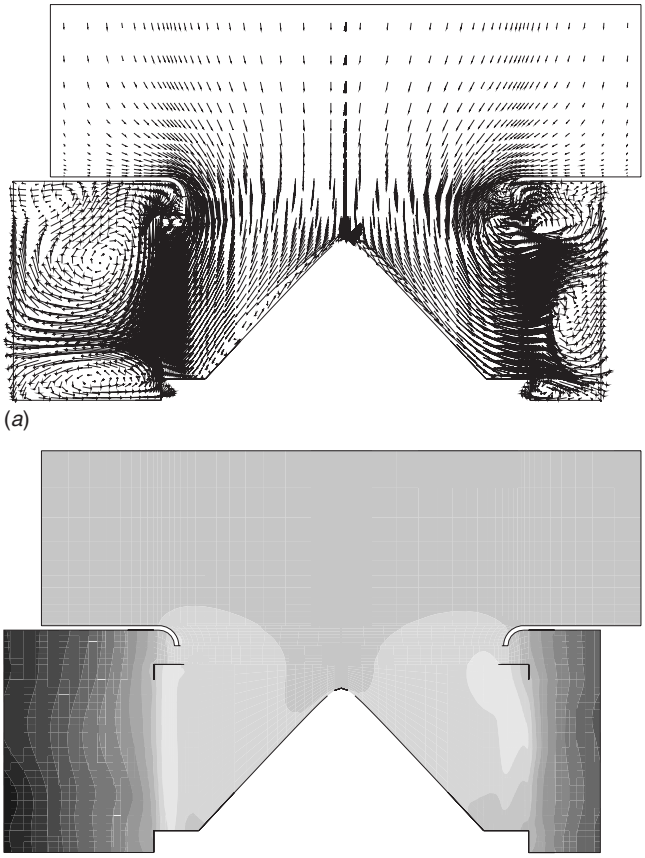

Fig. 20 V_{in}=1.5 m/s, flow field in the *yz* plane; (*a*) Velocity $\vec{\bar{V}}$, (*b*) static pressure $\bar{p}$

$F_{inv}^{(r)}, F_{inv}^{(\theta)}, F_{inv}^{(z)}$ = components of inviscid force $\mathbf{F}_{inv}$ (N/m^3)
$F_{tot}^{(r)}, F_{tot}^{(\theta)}, F_{tot}^{(z)}$ = components of total force $\mathbf{F}_{tot}$ (N/m^3)
$F_{vis}^{(r)}, F_{vis}^{(\theta)}, F_{vis}^{(z)}$ = components of viscous force $\mathbf{F}_{vis}$ (N/m^3)
front = denotes blade side that last touches point in blade region
h_{corner} = height of cutoff corner (m)
h_{free} = distance throat to blade top (m)
h_{hub} = distance from rim to hub (m)
h_{in} = domain inlet height (m)
h_{liner} = height of liner at blade top trailing edge (m)
h_{scroll} = inside height of scroll (m)
h_{throat} = throat height (m)
I_m, J_m, K_m = maximum cell indices for 2D blade channel grid
l_{corner} = length of cutoff corner (m)
l_{out} = straight outlet section length (m)
L_{te} = channel width between (thin) blades at trailing edge (m)
$\tilde{n}$ = impeller rotational frequency (1/s)
n_c = number of azimuthal cell divisions at 3D blower inlet
N = total number of blades
p, p_t = static/total pressure (N/m^2)
$\bar{p}, \bar{p}_t$ = time-averaged static/total pressure (N/m^2)
p_{aft}, p_{front} = static pressure at blade aft/front side (N/m^2)
$p_{out}, p_{t_{out}}$ = static/total pressure at fan outlet (N/m^2)
$\Delta p, \Delta p_t$ = static/total gauge pressure at fan outlet (N/m^2)
$p_{t_{rim}}$ = total pressure across the blower rim (N/m^2)
$\bar{p}_{t,A}, \bar{p}_{t,B}$ = value of $\bar{p}_t$ before (A) and after (B) 2D channel blades (N/m^2)
p_∞ = ambient (stagnation) pressure (N/m^2)
q' = local flow rate per unit span (m^2/s)
q'_{av} = average of q' over blade region (m^2/s)
q'_{in} = value of q' at the inlet of 2D blade channel (m^2/s)
Q = volumetric flow rate (m^3/s)
r, θ, z = cylindrical coordinates (m, rad, m)
r_{1-7} = coordinate of scroll spiral (m)
r_{corner} = radius of cutoff corner (m)
r_{curve} = radius to start of curved blade part (m)
r_{cutoff} = radius to cutoff point (m)
r_{end} = radius to end point of spiral (m)
r_{hub} = radius to end of hub curve (m)
r_{in} = domain inlet radius (m)
r_{le}, r_{te} = leading/trailing edge radius (m)
r_{le}^-, r_{te}^+ = position directly before/after the leading/trailing edge (m)
r_{left}, r_{right} = left and right boundary radii of 2D channel grid (m)
r_{lip} = throat lip radius (m)
r_{rim}, r_{throat} = rim and throat radius (m)
$r(\theta)$ = scroll spiral shape function (m)
Re_b = average blade passage Reynolds number
Re_Ω = rotational Reynolds number
s = blade span (m)
t = time (s)
t_1 = starting time for time-averaging operation (s)
T = torque (N m)
T' = torque per unit span (N)
V_{in} = axial inlet velocity into 3D blower at domain inlet (m/s)
V_r, V_θ, V_z = velocity components (m/s)
$\bar{V}_r, \bar{V}_\theta, \bar{V}_z$ = time-averaged velocity components (m/s)
$\hat{V}_r, \hat{V}_\theta, \hat{V}_z$ = fluctuations of velocity components (m/s)
$\overline{\hat{V}_r\hat{V}_r}, \overline{\hat{V}_r\hat{V}_\theta}, \ldots$ = time averages of velocity fluctuation products (m^2/s^2)
$\bar{V}_{r,in}, \bar{V}_{\theta,in}$ = 2D blade channel inlet velocity (m/s)
$V^*_{r_{te}}$ = average (from Q/s) radial velocity at trailing edge (m/s)
w = local swirl (%)
w_{ch} = preswirl of fluid as it enters the blade region (%)
w_{blade} = blade thickness (m)
w_{in} = value of w at the inlet of 2D blade channel (%)
w_{scroll} = scroll thickness (m)
x, y, z = Cartesian coordinates (m)
$z(r)$ = fan hub shape function (m)

Greek Symbols and Units

β = half azimuthal width of 2D blade channel cells (rad)
γ_{le}, γ_{te} = leading/trailing edge blade angle (rad)
δ_{hub} = angle of hub slope (rad)
θ_{1-7} = coordinate of scroll spiral (rad)
θ_B = blade line for infinitely thin blades (rad)
θ_{cutoff} = angle to cutoff point (rad)
θ_{end} = angle to end point of spiral (rad)
$\Delta\theta$ = azimuthal width of 2D channel (rad)
ϑ = torque coefficient
μ = dynamic viscosity (N/(m s))
ϱ = density (kg/m^3)
$\tau_{rr}, \tau_{r\theta}, \ldots$ = viscous stress components (N/m^2)

$\overline{\tau_{rr}}, \overline{\tau_{r\theta}}, \cdots$ = time average of viscous stress components (N/m^2)
ϕ = flow coefficient
ψ = pressure coefficient
ψ_t = total pressure coefficient
Ω = angular rate of rotation (rad/s)

References

[1] Roth, H. W., 1981, "Optimierung von Trommelläufer-Ventilatoren," Strömungsmechanik und Strömungsmaschinen: Mitteilungen des Instituts für Strömungslehre und Strömungsmaschinen der Universität Karlsruhe, **29**, pp. 1–45.

[2] Kind, R. J., and Tobin, M. G., 1990, "Flow in a Centrifugal Fan of the Squirrel-Cage Type," ASME J. Turbomach., **112**, pp. 84–90.

[3] Raj, D., and Swim, W. B., 1981, "Measurements of the Mean Flow Velocity and Velocity Fluctuations at the Exit of an FC Centrifugal Fan Rotor," ASME J. Eng. Power, **103**, pp. 393–399.

[4] Velarde-Suárez, S., Ballesteros-Tajadura, R., Santolaria-Morros, C., and González-Pérez, J., 2001, "Unsteady Flow Pattern Characteristics Downstream of a Forward-Curved Blades Centrifugal Fan," ASME J. Fluids Eng., **123**, pp. 265–270.

[5] Wright, T., 1984, "Centrifugal Fan Performance With Inlet Clearance," ASME J. Eng. Gas Turbines Power, **106**, pp. 906–912.

[6] Velarde-Suárez, S., Santolaria-Morros, C., and Ballesteros-Tajadura, R., 1999, "Experimental Study on the Aeroacoustic Behavior of a Forward-Curved Blades Centrifugal Fan," ASME J. Fluids Eng., **121**, pp. 276–281.

[7] Nursen, C. E., and Ayder, E., 2002, "Numerical Calculation of the Three-Dimensional Swirling Flow Inside the Centrifugal Pump Volutes," *The Ninth International Symposium on Transport Phenomena and Dynamics of Rotating Machinery*, Honolulu, HI, pp. 1–7.

[8] Dilin, P., Sakai, T., Wilson, M., and Whitfield, A., 1998, "A Computational and Experimental Evaluation of the Performance of a Centrifugal Fan Volute," Proc. Inst. Mech. Eng., Part A, **212**, pp. 235–246.

[9] Chen, S.-R., Lee, S. S., and Huang, Y. M., 1986, "A Mathematical Model for the Analysis of Fluid Flow in a Scroll," ASME J. Fluids Eng., **108**, pp. 6–11.

[10] Ayder, E., and Van den Braembussche, R., 1994, "Numerical Analysis of the Three-Dimensional Swirling Flow in Centrifugal Compressor Volutes," ASME J. Turbomach., **116**, pp. 462–468.

[11] Guzy, S. C., 1995, "Centrifugal Fan Blade Design Using a Two-Dimensional Blade Passage Analysis Program," MS thesis, Department of Mechanical and Aerospace Engineering, University at Buffalo.

[12] Tanger, M., 1997, "Investigation of Computational Models to Predict and Optimize Centrifugal Blower Performance," MS project, Department of Mechanical and Aerospace Engineering, University at Buffalo.

[13] Wright, T., Tzou, K. T. S., and Madhavan, S., 1984, "Flow in a Centrifugal Fan Impeller at Off-Design Conditions," ASME J. Eng. Gas Turbines Power, **106**, pp. 913–919.

[14] Sun, Q., 2000, "Numerical Analysis and Application of an Air Conditioning Centrifugal Fan System," Adapco-Online User Articles, http://www.adapco-online.com

[15] Gilotte, P., 2000, "Blower Analysis and Design With CFD," *Star-CD Users Conference*, CD-Adapco, Paris.

[16] Turunen-Saaresti, T., Reunanen, A., and Larjola, J., 2002, "The Time-Accurate Numerical Simulation of a Centrifugal Compressor," ASME Paper No. GT-2002-30385.

[17] Cobe Cardiovascular, 2000, "Flow Analysis Through COBE Cardiovascular's Centrifugal Blood Pump, the Revolution™," Adapco-Online Website, User Articles, http://www.adapco-online.com

[18] Sehra, A. K., 1979, "Boundary Layer and Wake Modifications to Compressor Design Systems: The Effect of Blade-to-Blade Flow Variations on the Mean Flow Field of a Tansonic Rotor," Gas Turbine and Plasma Dynamics Laboratory, Massachusetts Institute of Technology, Cambridge, MA, Report No. GT/PDL-144, pp. 1–224.

[19] Adamczyk, J. J., 1985, "Model Equation for Simulating Flows in Multistage Turbomachinery," ASME Paper No. 85-GT-226.

[20] Celestina, M. L., Mulac, R. A., and Adamczyk, J. J., 1986, "A Numerical Simulation of the Inviscid Flow Through a Counterrotating Propeller," ASME J. Turbomach., **108**, pp. 187–193.

[21] Mulac, R. A., Celestina, M. L., Adamczyk, J. J., Misegades, K. P., and Dawson, J. M., 1987, "The Utilization of Parallel Processing in Solving the Inviscid Form of the Average-Passage Equation System for Multistage Turbomachinery," *AIAA Eighth Computational Fluid Dynamics Conference*, Honolulu, HI, pp. 70–80.

[22] Heidmann, J. D., and Beach, T. A., 1990, "An Analysis of the Viscous Flow Through a Compact Radial Turbine by the Average Passage Approach," NASA Technical Memorandum No. 102471.

[23] Rhie, C. M., Gleixner, A. J., Spear, D. A., Fischberg, C. J., and Zacharias, R. M., 1995, "Development and Application of a Multistage Navier-Stokes Solver. Part I: Multistage Modeling Using Bodyforces and Deterministic Stresses," ASME Paper No. 95-GT-342.

[24] Hall, E. J., 1997, "Aerodynamic Modeling of Multistage Compressor Flowfields. Part 2: Modeling Deterministic Stresses," ASME Paper No. 97-GT-345.

[25] Kirtley, K. R., Turner, M. G., and Saeidi, S., 1999, "An Average Passage Closure Model for General Meshes," ASME Paper No. 99-GT-77.

[26] Tremmel, M., 2004, "Application of the Time-Averaged Navier-Stokes Equations to an Asymmetric Fan Geometry," Ph.D. thesis, Department of Mechanical and Aerospace Engineering, University at Buffalo, Buffalo, pp. 2–29 and 109.

Clearance Effects on the Onset of Instability in a Centrifugal Compressor

Matthias Schleer[1]
Turbomachinery Laboratory,
Swiss Federal Institute of Technology Zurich,
8092 Zurich, Switzerland

Seung Jin Song
School of Mechanical and Aerospace Engineering,
Seoul National University,
151-742 Seoul, Korea

Reza S. Abhari
Turbomachinery Laboratory,
Swiss Federal Institute of Technology Zurich,
8092 Zurich, Switzerland

This report intends to shed an insight into the effect of large relative tip clearances on the onset of instability in a highly loaded centrifugal compressor. Time-resolved pressure measurements have been performed along the casing of a scaled-up model of a small compressor for two clearances at a wide range of operating conditions. Based on these time-resolved measurements, the pressure distribution along the meridional length and the blade loading distribution are calculated for each operating condition. In addition, the phase locked pressure fluctuation and its deviation are computed. The results show the behavior of each subcomponent of the compressor at different flow conditions and explain the role of the relative tip clearance on the onset of instability. For high mass-flow rates, the steady pressure distribution along the casing reveals that the inducer acts as an accelerating nozzle. Pressure is only built up in the radial part due to the centrifugal forces and in the subsequent diffuser due to area change. For off-design conditions, incidence effects are seen in the blade loading distribution at the leading edge while the inducer is unloaded. A region of high pressure deviation originates at the leading edge of the main blade and convects downstream. This feature is interpreted as the trajectory of the leakage vortex. The trajectory of these vortices is strongly affected by the mass-flow coefficient. If the mass-flow rate is sufficiently small, the trajectory of the leakage vortex becomes perpendicular to the axis of rotation, the leakage vortex interacts with the adjacent blade, and inlet tip recirculation is triggered. If the flow rate is further reduced, the leakage vortex vanishes and rotating stall is initiated in the diffuser. For larger clearances, stronger vortices are formed, stall is triggered at higher flow rates, and the overall compressor performance deteriorates. [DOI: 10.1115/1.2776956]

Introduction

Small-scale centrifugal compressors are widely used in high volume applications such as automotive turbocharging or in distributed power applications. For these applications, typically unshrouded impellers with splitter blades are used. The blades are designed using ruled surfaces and show little rake or lean. The performance of such blading is hampered by the pressure loss over the tip gap and the formation of secondary flows. In addition, the effect of the tip clearance flows is very strong as the manufacturing accuracy determines a minimum clearance and thus the relative tip clearance ratio is large.

Only little work has been done in centrifugal compressors on the interaction of the tip clearance flow with the passage flow and its influence on the stability. Based on measurements in several centrifugal impellers, Senoo and Ishida [1] described the deterioration of the compressor performance due to tip clearance. For all compressors, an increased tip clearance width results in increased leakage ratios and higher losses. A general description of the flow interaction within a centrifugal compressor was presented by Eckardt [2]. In his work, Eckardt presented a schematic model of the secondary flow pattern, which included effects due to tip clearance flows. Hong et al. [3] showed experimental results on the influence of the relative tip clearance on the flow structure and efficiency in radial compressors. A complete and generalized overview on the stability of compressing systems is given by Denton [4]. The stability of the present compressor system was discussed based on the information gained at the inlet of the diffuser (Schleer et al. [5,6]). It was found that for increased tip clearance ratio, stall occurs at higher flow coefficients while the stage pressure ratio was substantially reduced. In an accompanying paper by the authors [7], the influence of the tip clearance ratio on the evolution and mixing of the flow in the diffuser is studied in detail.

In the current work, the influence of the relative tip clearance width on the onset of instability is studied by analyzing time-resolved measurements of the static pressures along the casing for a wide range of flow coefficients. A dense array of flush-mounted pressure sensors is used along the flow path to measure the static pressure fluctuation and its deviation in order to detect clearance vortices and stall precursors. The method is similar to the method used by Yoon et al. [8] in axial compressors. Based on these measurements, the blade loading distribution and its sensitivity to clearance ratio and operating condition are examined. Further, the sequence of events leading to rotating stall in the diffuser is investigated. Measurements at different clearance ratios show a relation between the strength of the interaction of the leakage jet and the passage flow and the compressor performance.

Experimental Setup and Data Evaluation

The experimental investigations have been performed on the "Rigi" research facility in the Turbomachinery Laboratory of the Swiss Federal Institute of Technology in Zurich, Switzerland. The compressor facility is a scaled-up model of a one-stage centrifugal compressor used in small-scale distributed power generation or automotive turbocharging. It was designed to match the main design criteria and nondimensional parameters typical for these small devices and a comparable stability and operational behavior were achieved.

[1]Present address: ABB Turbosystems Ltd., 5401 Baden, Switzerland.

Contributed by the International Gas Turbine Institute of ASME for publication in the JOURNAL OF TURBOMACHINERY. Manuscript received November 23, 2006; final manuscript received December 10, 2006; published onlineApril 1, 2008. Review conducted by David Wisler. Paper presented at the ASME Turbo Expo 2006: Land, Sea and Air (GT2006), Barcelona, Spain, May 8–11, 2006, Paper No. GT2006-90084.

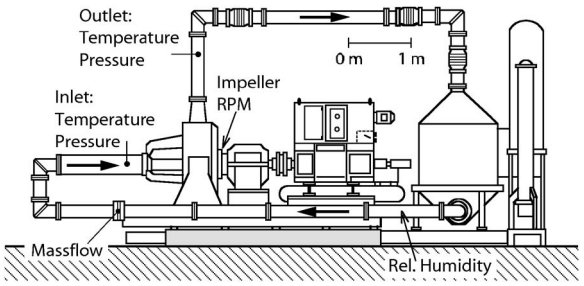

Fig. 1 "Rigi" research facility

The Rigi facility consists of a single stage, vaneless centrifugal compressor system operating in a closed loop, as shown in Fig. 1. It is designed for air and delivers a design volume flow rate of $\dot{V}=3.5\ \mathrm{m}^3/\mathrm{s}$ at a design pressure ratio of $\pi=2.8$. The centrifugal impeller has an outer diameter $D_2=400$ mm and is designed with seven full and splitter blades. At impeller exit, the blades are swept 30 deg backward from the radial directions while the rake and lean angle are nearly 0 deg, respectively. The rotor is followed by a parallel vaneless diffuser with an exit diameter of $D_5=580$ mm. A flow straightener mounted in the suction pipe ensures axial flow at the stage inlet. A large toroidal collecting chamber follows the radial diffuser. This arrangement ensures a virtually uniform circumferential pressure distribution at the impeller exit under all through-flow conditions.

A 440 kW dc motor coupled to a two-stage gearbox drives the facility. As the facility is a closed loop type, the compressed air has to be cooled by a counterflow air-water heat exchanger. The mass flow is measured in the backflow duct with a standard orifice assuming steady state. The system inlet pressure can be varied between 16 kPa and 125 kPa. The impeller load can be varied with a throttle downstream of the cooler. The pressure is reduced back to inlet conditions by the throttle and controlled by a pressure regulation system. The closed loop arrangement facilitates measurements under repeatable and constant conditions without depending on the atmospheric conditions.

Experiments have been conducted at two different relative clearances. The base line tip clearance ratio at impeller exit was set to a value of CR=12.7%. This very large tip clearance ratio is common for small-scale applications as the axial displacement in the bearing is large compared to the diffuser width. In the Rigi facility, it is possible to reduce the tip clearance width to 0.7 mm by changing shim plates between the inlet assembly and the casing. The reduced gap configuration corresponds to a clearance ratio of CR=4.5% and is equivalent to a well-designed industrial scale compressor. The actual tip gap configuration is sketched for both cases in Fig. 2.

In Fig. 3, a comparison of the operating maps and stability behavior of the compressor is shown for the base line and reduced clearance cases. The stability of the compressor system is determined by investigating the pressure fluctuation in the inlet of the diffuser (Schleer and Abhari [6]).

The operating mode of the compressor is assessed by analyzing the frequency content of a pressure reading using a fast Fourier transformation (FFT). To determine if stall or surge are present, the relative magnitude of the dominant instability frequency is compared to the magnitude related to the blade passing frequency. Rotating stall shows a rather wide and modulated peak at more than one frequency in the FFT spectrum. The frequency of rotating stall depends on the rotational speed of the shaft, the number of stall cells, the direction, and the speed of propagation. Surge is seen in the FFT as a distinct frequency, which depends only on the geometry of the compression system and the arrangement of the piping and is thus not affected by impeller speed. Classic surge is seen in the FFT as a coupled mode where the rotating stall signature is superimposed and modulated by the surge frequency.

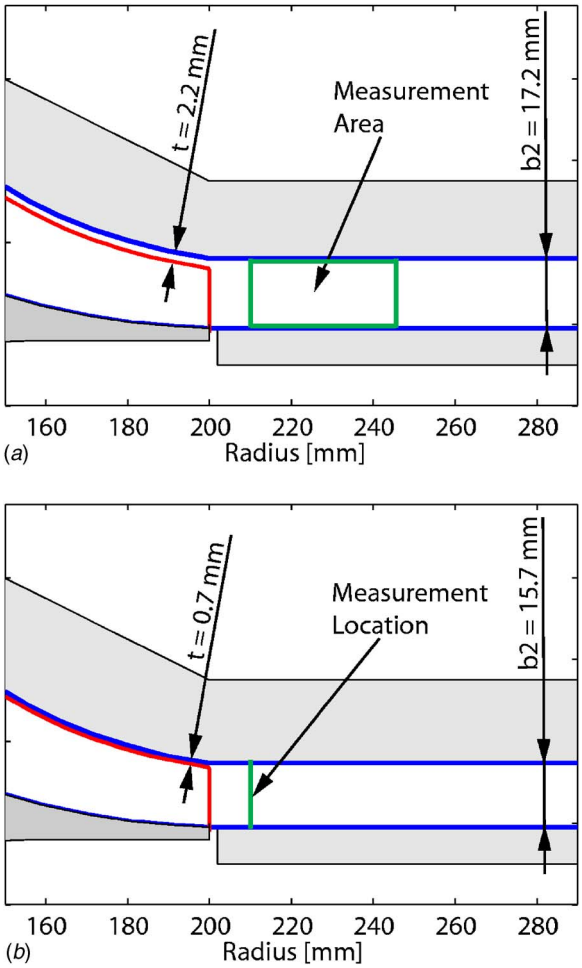

Fig. 2 Investigated clearance configurations

In the comparison, an improved characteristic is seen for the reduced clearance case. The pressure ratio is improved by 6% for the same impeller speed. The choke and the system resistance limit remain unchanged. Toward low mass-flow rates, the stability limit is not affected for high impeller speeds. For part speed, an improvement is found for the reduced tip clearance case. At high impeller speed, the surge margin remains unchanged as surge depends mainly on the overall setup of the compression system and is not affected by changes of the local flow pattern at impeller exit due to tip gap variations. The gain in stability margin for the reduced clearance case at part speed is due to a shift of the onset of rotating stall inception toward lower mass flows. It is postulated that flow features, which depend on the tip clearance, affect the onset of rotating stall. In this work, the detailed measurements show the mechanism how the onset of rotating stall is affected by the tip clearance flow.

Investigated Operating Conditions

To understand the influence of the relative tip clearance on the onset of stability, an experimental investigation was performed with two relative tip clearances for a rotational speed of Mu =0.6 (9949 rpm). In Fig. 4, the investigated operating conditions are shown in terms of isentropic head and flow coefficients for both tip clearance ratios.

The letters in Fig. 4 mark the operating conditions where detailed pressure measurements have been obtained by a combination of static wall pressure taps and time-resolved high frequency response pressure plugs along the casing. The onset of instability is marked for each tip clearance case by a black line. The shift of

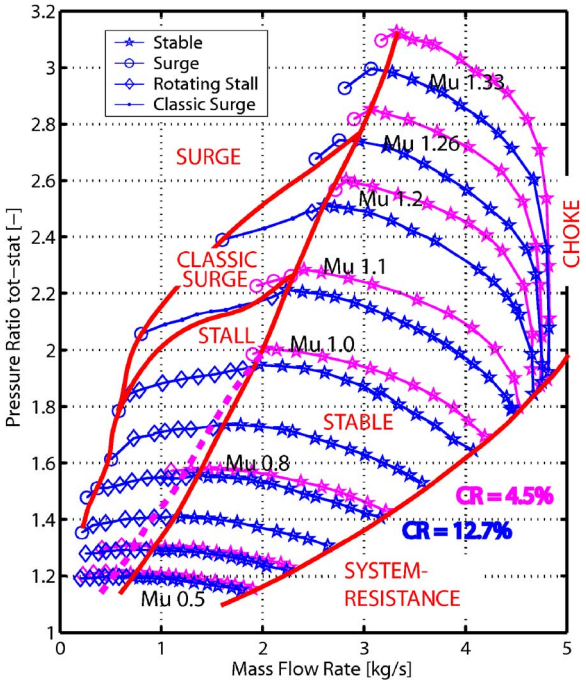

Fig. 3 Comparison of the operating map at base line and reduced clearance

the instability line toward lower mass flow described above is also seen in Fig. 4. With increasing tip clearance, pressure rise is reduced and stall inception is shifted toward higher mass flows. This shift of the stall limit at different clearances agrees with previous findings in axial and radial compressors.

Data Acquisition

The unsteady pressure fluctuations have been measured using flush-mounted pressure sensors with a high temporal resolution. The time-resolved pressure plugs were developed in-house and successfully applied in the present study. The inserts are assembled using a 1 bar differential piezoresistive pressure transducer. The reference pressure side of the transducer can be connected to static pressure taps along the flow path. The signals are amplified with an amplifier with a cutoff frequency of 25 kHz and are sampled at 100 kHz using a multichannel analog-to-digital (AD) data acquisition system. The complete measurement chain is calibrated for offset and gain before the measurements and is estimated to be accurate within 100 Pa.

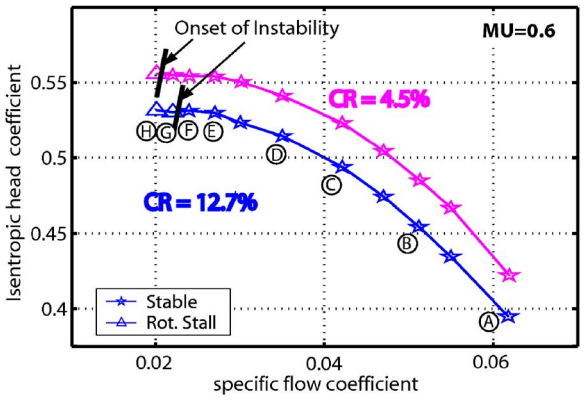

Fig. 4 Investigated operating conditions

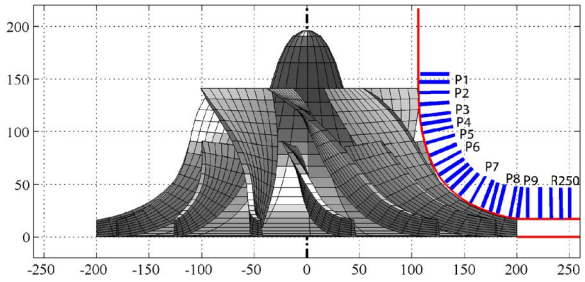

Fig. 5 Location of the pressure transducer (mm)

A total of 30 high frequency response sensors is located in the inlet pipe, along the shroud wall, and the diffuser. Figure 5 shows the locations of the pressure sensors. For each measurement location, a time series of 300,000 pressure readings has been obtained at a sampling rate of 100 kHz. The steady reference pressure for each sensor and the steady pressure along the casing are acquired with a multichannel pressure scanner system at 32 locations along the meridional flow path. The accuracy of the PSI 9016 pressure scanner is given with $\pm 0.05\%$ of the full scale range of 1 bar.

Using this experimental setup, the time history of the static wall pressure can be reconstructed as the sum of the steady pressure $\bar{p}$, the periodic pressure fluctuation $\tilde{p}$, and the random pressure p':

$$p_{(t)} = \bar{p} + \tilde{p}_{(t)} + p'_{(t)} \tag{1}$$

The steady pressure $\bar{p}$ is acquired by the steady pressure measurement system. The time related pressure fluctuation $\tilde{p}_{(t)} + p'_{(t)}$ is given by the time-resolved measurements. By performing an ensemble average on the time-resolved pressure reading, the periodic fluctuation $\tilde{p}_{(t)}$ due to the blade passing can be separated from the random part $p'_{(t)}$. The ensemble averaging is performed based on the impeller position delivered by a pickup on the shaft, and all seven full-blade channels are treated similarly. By calculating for each sensor the phase locked periodic pressure fluctuation $\tilde{p}_{(t)}$ relative to the position of the blades, the blade loading distribution throughout the flow path is obtained. One full-blade passage is discretized into 103 equal parts representing an angular discretization of 0.5 deg. In each of these discrete angular positions or so-called "boxes," more than 2500 samples are acquired and averaged to obtain a good statistical accuracy.

To allow for a better comparability of different measurements, the pressure values are normalized with the inlet static pressure p_0 and the normalized phase locked pressure coefficient is obtained:

$$\tilde{C}_{p(\text{box})} = \frac{\tilde{p}_{(\text{box})}}{p_0} \tag{2}$$

The randomness of the pressure fluctuation $p'_{(t)}$ is described by the root-mean-square (rms) or standard deviation of the pressure samples in each individual angular box. The phase locked deviation is computed as

$$\sigma_{(\text{box})} = \sqrt{\frac{1}{N}\sum_{i=1}^{N} (p_{i(\text{box})} - \bar{p} - \tilde{p}_{(\text{box})})^2} \tag{3}$$

where N is the number of samples and $p_{i(\text{box})}$ are the individual pressure values. The local value of the pressure deviation is interpreted as the level of unsteadiness of the flow due to vortices and separation at this location. It can be used to resolve the trajectory of tip vortices or the extent of separated zones.

Steady Pressure Distribution

In Fig. 6, the steady wall pressure distribution along the meridional length is plotted for the base line tip clearance case "STR

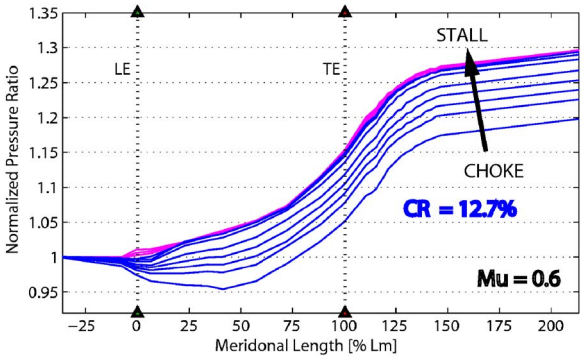

Fig. 6 Measured steady wall pressure distribution for the base line clearance ratio (CR=12.7%), normalized by the inlet static pressure

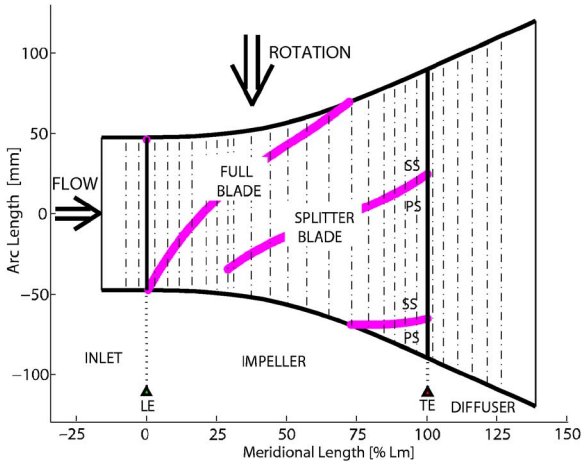

Fig. 7 Representation used for plotting the periodic pressure fluctuation and deviation

17.2." The measured pressure has been normalized using the inlet static pressure. Each individual line in the plots represents a different mass-flow condition between the choke and the stall limit. Stalled conditions are displayed in magenta, while stable conditions are plotted in blue.

The overall pressure rise in the machine is mostly dependent on the pressure rise within the radial section of the impeller. A similar pressure rise in the radial section of the impeller and the diffuser is observed for all mass-flow conditions. The slope of the pressure rise in the diffuser is nearly independent of the flow rate. For high mass-flow conditions, a decompression takes place in the inducer section of the impeller before pressure is built up in the radial section and the diffuser. At these conditions, the inducer behaves as an accelerating nozzle providing the inflow condition into the radial section. Unlike axial compressors, the pressure rise in the radial section is mostly due to the centrifuge effect instead of turning by the blades. The pressure rise in the diffuser is mainly due to diffusion as a consequence of the increase in flow area.

Toward stall, no decompression is observed in the inducer and the pressure is monotonously rising throughout the machine. For unstable operating conditions, a deterioration of the diffuser performance is seen. The deterioration occurs due to the increased blockage in the diffuser by the rotating stall pattern. For stalled operating conditions, a pressure rise in front of the leading edge is encountered. This pressure rise is a sign that energy has been imparted into the fluid. Since this is seen before the impeller leading edge, it indicates the occurrence of a local flow recirculation, which transports energy upstream of the impeller. Gyarmathy et al. [9] concluded from their similar measurements that a ring-shaped separation bubble exits at the impeller leading edge in which fluid is driven around the annulus at blade speed. In this separated zone, energized fluid is able to migrate upstream and is seen as raised pressure in front of the impeller.

Blade Passing Related Periodic Pressure Fluctuation

The normalized local periodic pressure fluctuation $\tilde{C}_{p(\mathrm{box})}$ caused by the blades and the deviation $\tilde{\sigma}_{(\mathrm{box})}$ of the periodic pressure fluctuation are calculated for each sensor along the flow path. The results are plotted in the representation shown in Fig. 7. Displayed is an unwrapped development of the casing surface for one blade pitch. The arclength and the meridional length are plotted on the ordinate and abscissa, respectively. The inlet, impeller, and diffuser sections are labeled. The positions of the full and splitter blade tips are marked, and the dotted lines give the positions of the individual pressure sensors. The normalized phase locked pressure coefficient $\tilde{C}_{p(\mathrm{box})}$ and the phase locked deviation $\tilde{\sigma}_{(\mathrm{box})}$ are interpolated along the blade line and are plotted as a color surface on top of this representation.

In Fig. 8, the phase locked pressure coefficient $\tilde{C}_p$ is shown at four mass-flow conditions for the base line tip clearance case STR 17.2. The color scale is identical for all operating conditions and the specific flow coefficient is labeled in each subplot. Positive values of the phase locked pressure coefficient are seen on the pressure side, while negative values are found on the suction side. The difference across the blade can be interpreted as blade loading. The integral value of the blade loading is related to the overall power consumption of the compressor. As the mass-flow rate is much higher for the case near choke (a), the power consumption is also higher even though the pressure rise is lower. Therefore, despite the lower pressure ratio, the highest variations of the pres-

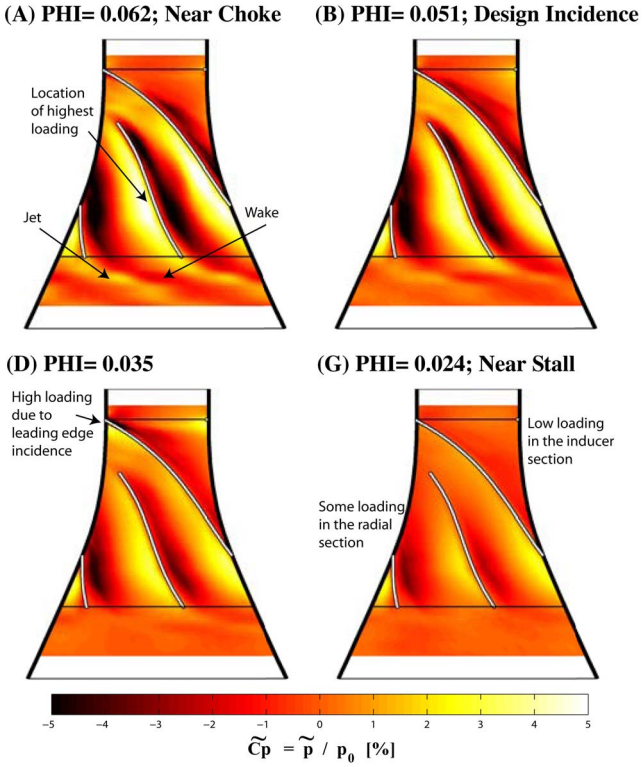

Fig. 8 Measured periodic pressure coefficient for the base line clearance case (CR=12.7%) at different mass-flow rates

sure coefficient $\tilde{C}_p$ are seen near choke conditions while the smallest variation of the pressure coefficient is seen for the operating condition near stall (g).

In the high mass-flow cases ((a) and (b)), the pressure difference across the blades is maintained in the diffuser. These pressure traces can be interpreted as the trajectory of the jet-wake flow leaving the impeller. If the mass-flow rate is throttled, the jet-wake pattern becomes weaker and the trajectory moves toward the tangential direction. At near stall condition (g), the flow in the diffuser is disturbed and no clear jet-wake pattern can be identified in the diffuser. At all mass-flow rates, the highest variation of the phase locked pressure coefficient $\tilde{C}_p$ is seen at about 70% of the meridional length in the radial section of the impeller. For the near stall condition (g), the axial inducer section is barely loaded while in the design incidence condition (b), a more even distribution of the blade loading along the meridional blade length is obtained. The unloading in the inducer section is consistent with the inlet tip recirculation postulated above for low mass-flow conditions. In condition (d), a locally high loading is seen at the main blade leading edge. This locally high loading at the leading edge is caused by positive incidence at part load.

A more quantitative description of the flow can be given if the blade loading along the meridional length of the blade is calculated. The blade loading is determined for each meridional location as the difference between the periodic pressure fluctuation value at the pressure and suction sides. The local pressure values are interpolated at circumferential positions, which are shifted by 3 deg from the blade chamber line. These locations for the interpolation of the blade loading value are marked in the left subplot of Fig. 9 by thin lines beside the positions of the blades. The resultant blade loading coefficient

$$\tilde{C}_p = \tilde{p}/p_1 \tag{4}$$

is plotted in the right subfigure. The loading on the full blade is shown by solid lines while the loading of the splitter blade is plotted using dashed lines.

In Fig. 10, the normalized blade loading distribution is plotted for the base line clearance case (CR=12.7%) at four operating conditions. The small perturbations of the curves are due to the limited meridional resolution of the pressure measurements as only 30 sensors have been placed along the flow path.

For all conditions, the blade loading is the highest at 70–80% of the meridional length, which agrees with the location of the highest loading calculated in the design phase. Due to the higher mass-flow rate, the absolute blade loading is elevated at near choke condition (a). In the design incidence case (b), a steady distribution of the blade loading is seen. In the case near choke, a negative loading is seen as a result of the negative incidence at the leading edge of the full blade. The opposite trend is seen in case (d) where due to positive incidence, a locally high loading is seen at the leading edge. In the case near stall, only little loading is seen due to the recirculation pattern and no incidence effects can be identified in the inducer section.

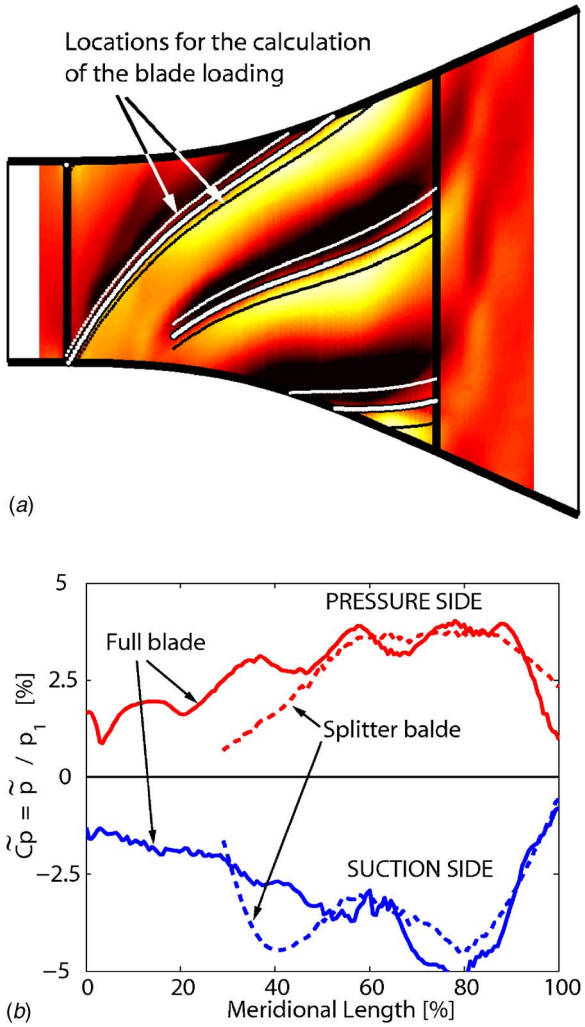

Fig. 9 Designation of the local blade loading

Random Pressure Fluctuation

More insight into the stability behavior and the sequence of the events is gained if the deviation of the phase locked pressure fluctuation is investigated. The deviation is calculated from the periodic pressure fluctuation using Eq. (3). High values of the pressure deviation indicate regions where the temporal fluctuations for the phase locked pressure value are large and thus indicate regions of high unsteadiness. For example, high unsteadiness can result if a vortex is shed at a frequency different from the blade passing frequency or if a stall cell is present in the diffuser. In Fig. 11, the plots of the deviation are given for eight mass-flow conditions at a clearance ratio of CR=12.7% (STR 17.2). Subplot (a) is acquired at a mass-flow rate close to the system resistance line, while subplot (h) represents a condition within rotating stall. As a dominant feature, a strong pressure deviation is found at the location of the blades. The highest values of the phase locked deviation are found for the highest mass flow, as in this condition, the pressure difference between the pressure and the suction sides is the largest (Fig. 8). For lower mass-flow coefficients, the pressure deviation across the blades in the inducer section is diminished.

The clearance flows are seen as high levels of flow unsteadiness beside the blades. Toward low flow coefficients, the pattern is dominated by the unsteady phenomena such as rotating stall and inlet tip recirculation. In subplots (a)–(e) of Fig. 11, a pattern with high levels of random pressure deviation is seen departing at the leading edge of the main blade. This pattern of high pressure deviation is marked by a dashed line and is interpreted as the trajectory of the leakage vortex. The vortex is caused by the interaction and collision of the tip clearance jet and the passage flow. Under the action of the pressure difference across the blade, a leakage jet is formed and penetrates into the passage. After a certain distance, the leakage jet is stopped by the main flow, which separates the jet from the wall, turns it backward, and leads to the formation of the tip leakage vortex (Song and Martinez-Sanchez [10]). The leakage vortex trajectory starts in all cases at the leading edge tip of the full blade and convects with the flow. For smaller mass-flow rates, the leakage vortex trajectory moves

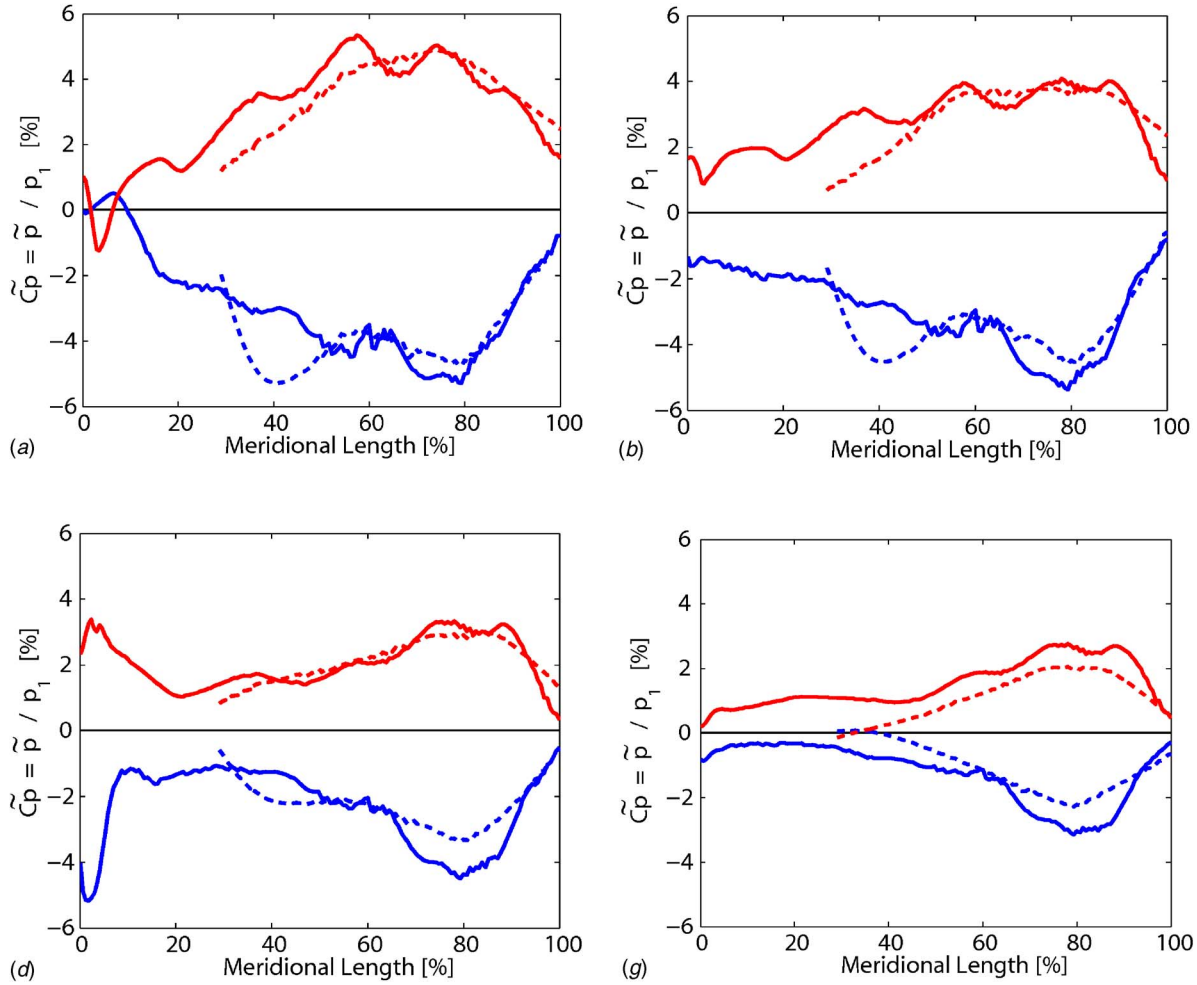

Fig. 10 Measured blade loading distribution for the base line clearance case (CR=12.7%)

away from the suction side and migrates toward the adjacent pressure side. A similar behavior of the leakage vortex is observed in axial compressors. In axial compressors, Inoue et al. [11] and Yoon et al. [8] found a strengthening and upward movement of the leakage vortex at smaller mass-flow coefficients. This was also postulated theoretically by Chen et al. [12] who linked the upward migration of the vortex at decreasing mass-flow rates with a strengthened leakage jet and longer convection times.

At design incidence, the leakage vortex of the previous full blade interacts with the splitter blade leading edge resulting in a lift-off of the splitter leakage vortex. If the flow is throttled further, the leakage vortex hits the leading edge of the adjacent blade (Figs. 11(*e*) and 11(*f*)) and a strong increase of the pressure deviation in the inlet region of the compressor is seen.

This sudden increase of the pressure deviation at the inlet occurs at the mass-flow condition where the steady wall pressure distribution shows an inlet tip recirculation zone. From this coincidence, it is concluded that inlet tip recirculation is triggered as soon as the leakage vortex trajectory becomes perpendicular to the machine axis and approaches the leading edge of the adjacent blade. Due to the inlet tip recirculation, the overall level of pressure unsteadiness increases in the entire impeller passage. If the compressor is throttled further to a flow coefficient below phi =0.022, rotating stall is initiated in the vaneless diffuser (Figs. 11(*g*) and 11(*h*)). As a result of the rotating pattern, large pressure deviations are recorded in the diffuser section. During rotating stall, the inlet tip recirculation zone recovers and low levels of pressure deviations are seen in the inlet. Thus, rotating stall becomes the dominant feature and suppresses the tip recirculation in the inducer of the impeller.

Near the suction side of the splitter blade, a strong feature can be identified in subplots (*A*)–(*D*) of Fig. 11. The feature is the strongest and closest to the suction side for the highest flow coefficient and weakens at smaller mass-flow rates. For smaller mass-flow rates, it lifts off the blade surface while at choked condition, it appears directly at the suction side. The feature could not be observed for operating conditions in the unstable regime (subplots (*F*)–(*H*)). This structure is associated with the leakage vortex forming at the leading edge of the splitter blade. In the measurements, a strong, but localized, interaction is seen at the splitter leading edge. However, the downstream convection of the splitter blade leakage vortex is not clear. This is a result of the different interaction mechanisms of the splitter blade leakage vortex. In the case of the main blade, the leakage vortex interacts with the nonrotational freestream approaching the compressor. Behind the splitter blade, the vortex interacts with a skewed and rotating channel flow. As no downstream convection of the leakage vortex is seen, it is postulated that due to the interaction with the skewed channel flow, the leakage vortex is entrained in the channel and lifted off the casing. This hypothesis is supported by the time-resolved flow measurements presented in an accompanying paper by the authors [7] where the area, which is affected by the clearance flows across the splitter blade, shifts toward the midheight of the diffuser channel.

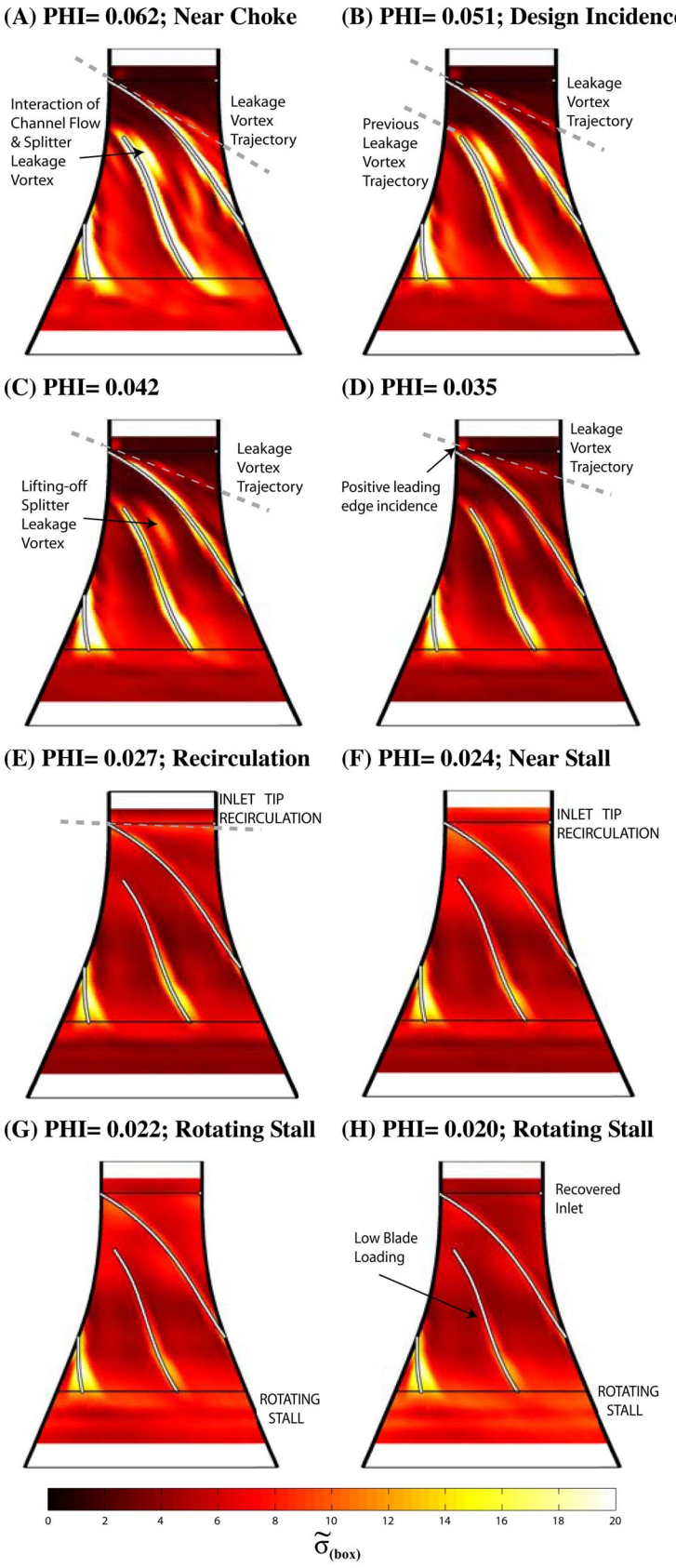

Fig. 11 Deviation of the measured periodic pressure fluctuation for the base line clearance case (CR=12.7%) at different mass-flow rates

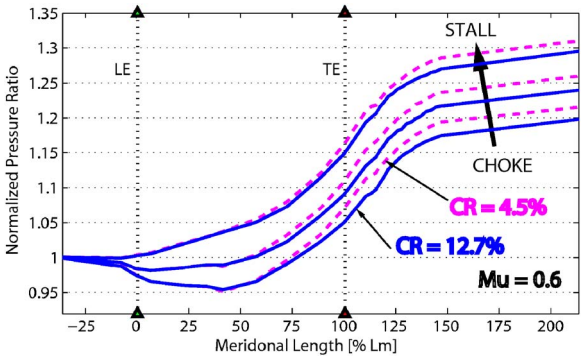

Fig. 12 Measured steady wall pressure distribution for base line clearance ratio (CR=12.7%) and the reduced clearance ratio (CR=4.5%); normalized by the Impeller inlet static pressure

Effect of Reduced Clearance on Steady Pressure Distribution and Blade Loading

In Fig. 12, the normalized steady wall pressure along the meridional length is plotted for the base line tip clearance case CR =12.7% and the reduced clearance case CR=4.5%. The measured pressures are normalized with the inlet static pressure. For each configuration, three mass-flow rates between choke and the stall limit have been plotted. The measurements in the base line configuration are displayed using a solid line, while the reduced clearance case is plotted using a dashed line. For all mass-flow rates, no differences in the steady wall pressure distributions are seen for the inlet and the inducer section. In the radial part of the impeller, a significantly better performance is seen for the reduced clearance case. The improved performance persists throughout the diffuser and is seen as an improved pressure ratio at the stage exit (Fig. 3).

In Fig. 13, the normalized blade loading distributions on the main blade and the splitter blade are plotted for the reduced clearance case (CR=4.5%). The mass-flow rates are the same as shown in Fig. 10 for the base line case.

At similar mass-flow rates, the blade loading is higher for the reduced clearance case. This is consistent with the increased pressure rise for the reduced clearance case seen in Figs. 3 and 12. As in the base line clearance case, a slightly smaller loading is seen on the splitter blade for small mass-flow rates while toward choke, a high loading of the splitter leading edge is found. The same incidence effect is seen for both clearance cases. Due to the positive incidence in the midrange condition (*d*), a high loading is seen on the main blade leading edge while near choke (*a*), the negative incidence causes a negative loading. Also, for the condition near stall (*b*), a very low loading is seen for both clearance cases in the inducer section while the radial section is still loaded.

Comparison of the Pressure Deviation at Base Line and Reduced Clearance

In Fig. 14, the deviation of the periodic pressure is plotted for the reduced clearance case. In all stable operating conditions, a comparison with Fig. 11 reveals generally lower levels of pressure deviations for the reduced clearance case. Especially in the radial

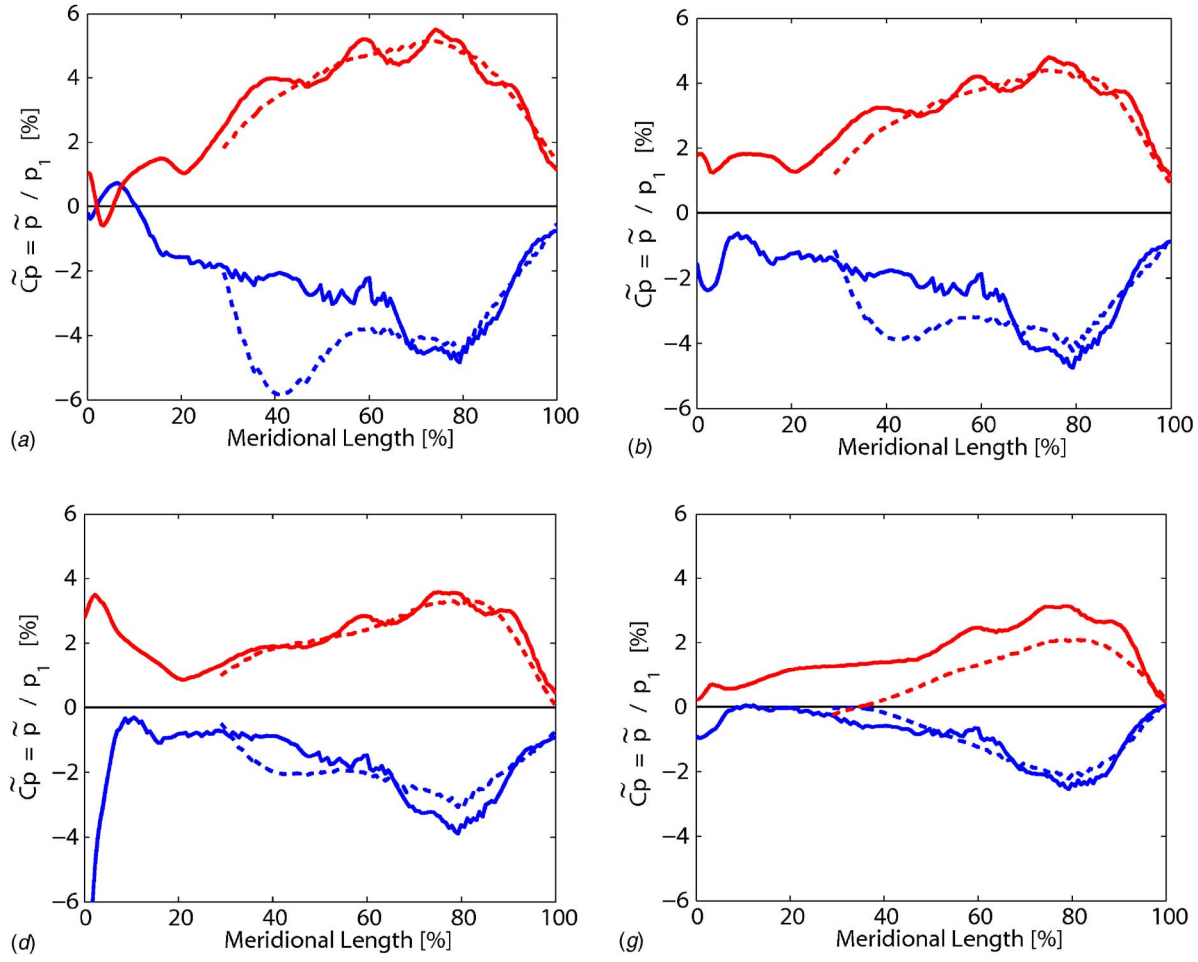

Fig. 13 Measured blade loading distribution for the reduced clearance case (CR=4.5%) at different mass-flow rates

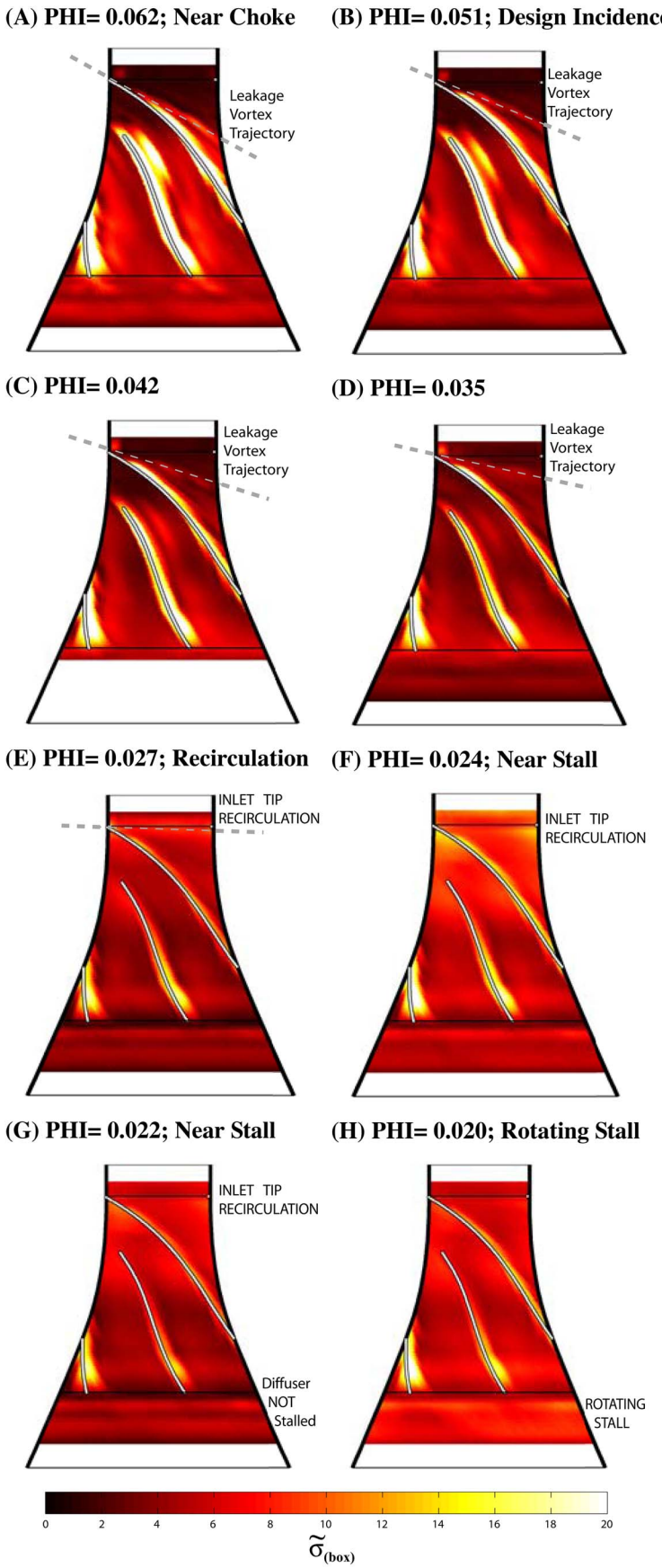

Fig. 14 Deviation of the measured periodic pressure fluctuation for the reduced clearance case (CR=4.5%) at different mass-flow rates

section, where the tip clearance has been changed the most by the shim, the deviation of the phase locked pressure fluctuations is strongly elevated for the larger clearance case. This indicates a stronger interaction and disturbance of the passage flow by the tip clearance flows for the wide clearance case. This increased flow interaction would lead to increased mixing losses and a deteriorated compressor performance.

In the inlet region, a similar migration and trajectory of the leakage vortex are found for both clearance cases. For reduced tip clearance, the leakage vortex core appears weaker than in the base line configuration. A similar upstream movement of the main blade leakage vortex trajectory is found for both clearance cases. Inlet tip recirculation is provoked for both clearance cases as soon as the leakage vortex becomes perpendicular and approaches the adjacent blade leading edge (Fig. 14(*e*)). The splitter blade leakage vortex behaves similarly in both cases but is weaker for the reduced clearance case. A similar lift-off from the splitter blade suction side is observed for positive incidence conditions. Differences are seen in the operating condition at phi=0.022 (Fig. 14(*f*)) where rotating stall in the diffuser is present for the larger base line clearance case while for the reduced clearance configuration, only little deviations are found in the diffuser. This complies with the stability analysis shown in Fig. 4. A shift of the stall inception point toward lower mass-flow rates was found for the reduced clearance case. In the condition at phi=0.020 (Fig. 14(*h*)), rotating stall is present for both clearances and no differences in the stability behavior are found. For the enlarged tip clearance, stronger interactions of the leakage and passage flows are concluded. This complies with the observed reduction in stall margin and pressure rise for the increased tip clearance configuration.

Conclusion

The influence of the relative tip clearance width on the onset of instability has been studied by analyzing time-resolved measurements of the static pressures along the shroud casing of a centrifugal compressor. The distribution of steady pressure along the casing shows that for high mass-flow rates, the inducer acts as an accelerating nozzle, which sets the in-flow condition for the radial section. In the radial section, pressure is built up due to centrifugal forces. In the subsequent diffuser, the pressure rise is due to area change and recovery of the dynamic pressure.

Based on the experimental results, the mechanism leading to rotating stall and deterioration of stage performance can be summarized. For highest mass-flow condition, and evenly distributed blade loading dominates the flow pattern. Highest values are found as predicted by the design calculations at around 75% meridional length of the impeller. At off-design conditions, the effects of incidence are seen as high loading at the full-blade leading edge. In the deviation of the phase locked pressure fluctuation, the trajectory of the clearance vortex could be identified on the main blade. This clearance vortex is caused by the interaction of the leakage jet and the passage flow. The passage flow stops the leakage jet, separates it from the wall, and turns it backward. This leads to the formation of the tip leakage vortex next to the suction side of the main blade. On the splitter blade, an immediate interaction between the leakage flow and the skewed channel flow is seen but no trajectory of the leakage vortex could be identified.

Measurements at different clearance ratios reveal a close relation between the strength of the leakage jet and the compressor performance. Even though no significant differences have been found in the blade loading distribution for large and reduced relative tip clearance, a significant deterioration of the steady pressure rise is seen in the radial section. For larger clearance, the level of the random pressure deviations reveals higher flow disturbances. The increased levels of pressure disturbance are caused by the increased intensity of the secondary flows and result in increased losses.

The sequence of events leading to rotating stall in the diffuser is seen in the measured random pressure fluctuation: For high mass-flow rates, a leakage vortex is formed as a result of the interaction between the flow through the clearance space and the passage flow. Starting on the leading edge, the leakage vortex convects with the flow and migrates toward the adjacent pressure side. Similar to axial compressors, the trajectory of the tip leakage vortex is related to the mass-flow coefficient. If the flow coefficient is reduced, the apparent stagger angle of the leakage vortex increases and the leakage vortex trajectory moves upstream. If the mass-flow rate is sufficiently small, the leakage vortex trajectory becomes perpendicular to the axis of the machine and interacts with the adjacent leading edge. A stability analysis revealed that at this condition where the leakage vortex approaches the adjacent blade, inlet tip recirculation is triggered. This leads to a sudden increase of random pressure fluctuation in the inducer section and a change in the loading distribution. If the flow is throttled further, rotating stall is initiated in the diffuser while the inlet recovers. For increased tip clearance, the onset of rotating stall is shifted to higher mass flows while the onset of tip recirculation is not affected by a change in tip clearance width.

Acknowledgment

The authors would like to acknowledge the dedicated support by the Swiss Federal Institute of Technology, Zurich, and its permission to publish the paper. The assistance of the workshop staff at the Turbomachinery Laboratory, both in the mechanical and electronic laboratories, has been very much appreciated at all times.

Nomenclature

b = axial diffuser width (m)
D = diameter (m)
L_m = meridional length (m)
p = pressure (kPa)
t = tip gap width (m)
U = circumferential speed (m/s)
$\dot{V}$ = volume flow rate (m^3/s)
ρ = density (kg/m^3)
σ = pressure deviation (kPa)
Δh_{ts} = total-static enthalpy rise (kJ/kg)

Dimensionless Numbers

$\phi = V_0/D_2^2U_2$ = specific flow coefficient (phi)
$\psi = \Delta h_{ts}/U$ = isentropic head coefficient
Mu
$= U_2/\sqrt{\kappa R}$ = impeller tip Mach number
$\pi = p_{2s}/p_0$ = total-static pressure ratio
$C_p = p/p_0$ = normalized pressure coefficient
CR$= t/b$ = tip clearance ratio

Subscripts

0 = stage inlet
1 = impeller inlet
2 = impeller outlet
5 = diffuser outlet

References

[1] Senoo, Y., and Ishida, M., 1987, "Deterioration of Compressor Performance Due to Tip Clearance of Centrifugal Impellers," ASME J. Turbomach., **109**(1), pp. 55–61.
[2] Eckardt, D., 1975, "Instantaneous Measurements in Jet-Wake Discharge Flow of a Centrifugal Compressor Impeller," ASME J. Eng. Power, **97**(3), pp. 337–346.
[3] Hong, S.-S., Schleer, M., and Abhari, R. S., "Effect of Tip Clearance on the Flow and Performance of a Centrifugal Compressor," *FEDSM'03, Fourth ASME/JSME Joint Fluids Engineering Conference*, Honolulu, HI.
[4] Denton, J. D., 1993, "The 1993 IGTI Scholar Lecture-Loss Mechanisms in Turbomachines," ASME J. Turbomach., **115**(4), pp. 621–656.
[5] Schleer, M., Mokulys, T., and Abhari, R. S., 2003, "Design of a High Pressure-Ratio Centrifugal Compressor for Studying Reynolds Number Effects," *International Conference on Compressors and Their Systems*, pp. 391–404.
[6] Schleer, M., and Abhari, R. S., 2005, "Influence of Geometric Scaling on the

Stability and Range of a Turbo-Charger Centrifugal Compressor," ASME Paper No. GT 2005-68713.
[7] Schleer, M., and Abhari, R. S., 2006, "Evolution of the Flow in the Vaneless Diffuser of a Centrifugal Compressor at Part Load Condition," ASME Paper No. GT 2006-90083.
[8] Yoon, Y., Song, S., and Shin, H. W., 2005, "Influence of Tip Clearance, Stagger Angle and Flow Coefficient on Tip Vortex in Axial Compressors," ASME J. Fluids Eng., to be published.
[9] Gyarmathy, G., Hunziker, R., Ribi, B., and Spirig, M., 1991, "On the Change of Impeller Flow Non-Uniformities With Flow Rate in a Centrifugal Compressor," IMechE, **C423/054**, pp. 143–154.
[10] Song, S. J., and Martinez-Sanchez, M., 1997, "Rotordynamic Forces Due to Turbine Tip Leakage: Part I: Blade Scale Effects," ASME J. Turbomach., **119**(3), pp. 695–703.
[11] Inoue, M., Kuroumaru, M., Iwamoto, T., and Ando, Y., 1991, "Detection of a Rotating Stall Precursor in Isolated Axial-Flow Compressor Rotors," ASME J. Turbomach., **113**(2), pp. 281–289.
[12] Chen, G. T., Greitzer, E. M., Tan, C. S., and Marble, F. E., 1991, "Similarity Analysis of Compressor Tip Clearance Flow Structure," ASME J. Turbomach., **113**(2), pp. 260–271.

Causes of Acoustic Resonance in a High-Speed Axial Compressor

Bernd Hellmich
Kerntech GmbH,
Am Forsthaus 8,
DE-30890 Barsinghausen, Germany
e-mail: hellmich@kerntech.de

Joerg R. Seume
Institute of Turbomachinery and Fluid Dynamic,
University of Hannover, Appelstrasse 9,
DE-30167 Hannover, Germany
e-mail: seume@tfd.uni-hannover.de

Nonharmonic acoustic resonance was detected in the static pressure and sound signals in a four-stage high-speed axial compressor when the compressor was operating close to the surge limit. Based on prior research reported in the literature and measurements of the resonance frequency, Mach number of the mean flow, and the axial and circumferential phase shifts of the pressure signal during resonance, it is shown that the acoustic resonance is an axial standing wave of a spinning acoustic mode with three periods around the circumference of the compressor. This phenomenon occurs only if the aerodynamic load in the compressor is high, because the mode needs a high circumferential Mach number for resonance conditions. Mathematics of existing analyses of acoustic resonances in turbomachinery complex and have therefore rarely resulted in published examples of good agreement with real engine data. The present paper provides suitable, physically based simplifications of the existing mathematical models which are applicable for modes with circumferential wavelengths of more than two blade pitches and resonance frequencies considerably higher than the rotor speed.
[DOI: 10.1115/1.2775487]

Keywords: axial compressor, acoustic resonance, mode trapping, cut-off frequency, transmission, reflection, rotating stall, rotating instability

Introduction

Besides the well known phenomenon of rotating stall and surge, the latest literature reports other phenomena of flow distortion or even flow instability in compressors, called rotating instabilities (März et al. [1], Weidenfeller and Lawerenz [2], Mailach et al. [3], Kameier and Neise [4], and Baumgartner et al. [5]), tip-clearance noise (Kameier and Neise [4]), and acoustic resonance (AR).

While rotating stall is a rotating blockage propagating by flow separation in neighboring channels due to an incidence caused by the blocked channel, rotating instabilities are interpreted as periodic flow separations on the rotor without blockage. They appear as wide flat peaks in the frequency spectra of pressure signals of pneumatic probes or wall-mounted pressure transducers at a frequency higher than the rotor speed. The tip-clearance noise looks similar, but it is caused by reversed flow at the rotor tips and is strongly dependent on the tip-clearance gap. Compared to these effects, acoustic resonances cause a high and narrow peak in the pressure signal spectrum at a certain resonance frequency.

Unlike the effects mentioned before, acoustic resonances themselves must be explained by an acoustic approach. A simple example of an acoustic resonator is an organ whistle where the tube is a resonator driven by broadband noise caused by shear layers in the flow. The driving forces of a resonance could be aerodynamic effects, such as vortex shedding, rotor-stator interaction, shear layers in the flow, etc. In turbomachinery, the resonance conditions are typically satisfied only at specific flow conditions.

The relevance of these effects in modern turbomachinery is still under discussion as shown below.

Acoustic Resonances in Compressors and Cascades: A Literature Review

Due to the wide use of jet engines in civil aircraft, noise reduction is necessary. After the noise emissions of the nozzles have been reduced through higher bypass ratios, compressor and fan noise emissions have become more relevant. Blade passing frequencies and rotor-stator interaction have been found to be major noise sources of fans and compressor stages. Pioneering work in this field has been done by Tyler and Sofrin [6] and Lighthill [7].

These papers deal with jet noise and rotor-stator interaction which always occurs at blade-passage frequency or an integer multiple of it with a phase velocity that is a multiple of the rotor speed. By contrast, acoustic resonances are characterized by discrete frequencies which are not, in general, an integer multiple of rotor speed. Pioneering work in this field has been done by Parker and co-workers [8–13]. With plates in a wind tunnel, Parker shows that the resonance occurs slightly above the air speed for which the natural shedding frequency equals the resonance frequency. The frequency has also been predicted by solving the acoustic wave equations for the wind tunnel and the plate. The resonances Parker found are standing waves within the blade pitch or between blades and the tunnel wall.

In a similar experiment, Cumpsty and Whitehead [14] found that the presence of the acoustic field correlates the eddy shedding by the plate over the whole span of the plate, while it is correlated over short length scales at off-resonance conditions only.

Compared to the wind tunnel, the conditions in a turbomachine are far more complicated. So, the transfer of Parker's results to a real machine faces two major problems: Firstly, the acoustic modes of an annular duct with nonuniform swirl flow, varying cross section of the duct, and blade rows in the duct are rather complicated as will be shown below. Secondly, the blades in turbomachines are heavily loaded at off-design conditions and the flow speed is high compared to those in Parker's experiments. So, both the acoustics and aerodynamics are more complicated. Nevertheless, this does not mean that acoustic resonances could not exist in turbomachinery; it is just hard to predict them in advance for a given machine. However, if a machine exhibits resonant behavior under certain flow conditions, it is sometimes possible to simplify the problem and to show that the anomalous behavior fits an acoustic resonance.

Before different mathematical approaches for sound propagation through ducts and blade rows will be discussed, the existence of acoustic resonance in real machines or test rigs reported in the literature should be reviewed.

Contributed by the International Gas Turbine Institute of ASME for publication in the JOURNAL OF TURBOMACHINERY. Manuscript received July 18, 2006; final manuscript received March 18, 2007; published online May 2, 2008. Review conducted by David Wisler. Paper presented at the ASME Turbo Expo 2006: Land, Sea and Air (GT2006), Barcelona, Spain, May 8–11, 2006. Paper No. GT2006-90947.

In his early papers, Parker mentioned Rizk and Seymour [15] who reported an acoustic resonance driven by vortex shedding in a gas circulator at Hinkley Point Nuclear Power Station in the UK.

After Parker published his results, some experimental and theoretical papers about acoustic resonances in turbomachines followed in the 1970s and 1980s. The next acoustic resonance reported in the literature the present authors know is mentioned by Von Heesen [16] who was facing the problem that the same type of blowers was noisy in some street tunnels, while it was not in others. He found out that the noisy ones were running at a different operating point with a different axial velocity of the flow so that the frequency of a helical acoustic mode in the duct fits the vortex shedding frequency of the blades. They suppressed this mode by extending a few stator vanes in the axial direction, so that the propagation of helical modes in circumferential direction was suppressed.

Later, Ulbricht [17] found an acoustic mode in a ring cascade. The circumferential phase velocity of the acoustic field she measured was above the speed of sound. This was interpreted as a contradiction to acoustic laws, but it is typical for helical modes as explained in [20].

In a similar ring cascade, Weidenfeller and Lawerenz [2] found a helical acoustic mode at a Mach number of 0.482. They showed that the acoustic field was present at the hub and tip of the blades and measured significant mechanical blade stresses at the frequency of the acoustic mode.

During testing of the Rolls Royce BR710 and BR715 aircraft engines, some unexpected unsteady pressure fluctuations were measured, as reported by Kameier [18].

Camp [19] carried out some experiments on the C106 low-speed high-pressure axial compressor. He also found a helical acoustic mode quite similar to the acoustic resonance that is the subject of this and previous papers of the present authors (Hellmich and Seume [20]). Camp also assumed vortex shedding of the blades as the excitation mechanism. He found Strouhal numbers around 0.8 based on the blade thickness at the trailing edge. He argued that this is far above the usual value of 0.21 for vortex shedding by a cylinder because the blades were highly loaded, so that the effective aerodynamic thickness of the blades is more than the geometric thickness.

Ziada et al. [21] reported an acoustic resonance in the inlet of a 35 MW Sulzer multistage radial compressor in a natural gas storage station in Canada. The resonance leads to mechanical vibration levels of the whole compressor so that the measured vibration at the compressor casing is above the specified limit of vibration for this class of machines. The resonance was driven by vortex shedding struts and could be eliminated by a modification of the struts' trailing edges. This effect is also well known for tube bundles in heat exchangers, too.

Kielb [22] found in the work supported by GE nonsynchronous vibrations in a high-speed multistage axial compressor. The size of the compressor was not specified in the paper, but the resonance frequency he and his co-workers found was in the same range as those measured at the present rig.

Vignau-Tuquet and Girardeau [23] measured nonengine order pressure fluctuations with discrete frequencies between rotor speed and blade passing frequency (BPF) in a three-stage high-speed compressor test rig. Because they measured in the fixed and rotating frame, they were able to make a clear estimation of the circumferential modes of the pressure fluctuation. The order numbers and rotating speed of the modes fit an acoustic resonance.

A recent paper by Cyrus et al. [24] deals with a phenomenon that might be an acoustic resonance. They faced the problem of stator vane damage in the rear stages of an Alstom gas turbine compressor. With pneumatic pressure probes, they found out that a nonsynchronous pressure oscillation with a frequency close to a natural frequency of the damaged blades existed in the rear stages of the compressor. From the measurements and numerical calculations, it turned out that "stalled flow on vane surfaces with vortex flow shedding" [24] was responsible for the flow pulsations.

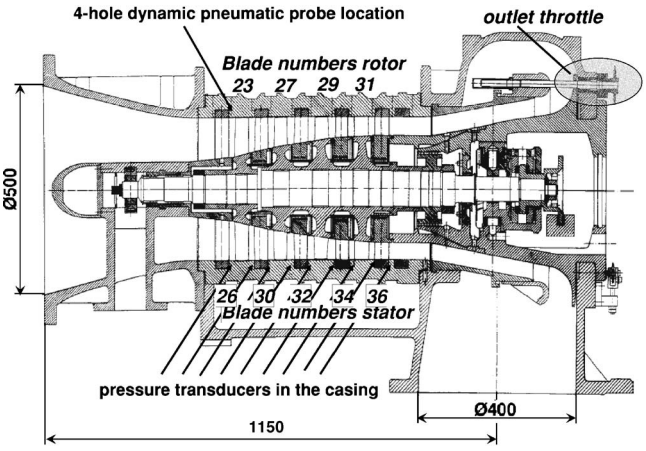

Fig. 1 Turbomachinery laboratory four-stage high-speed axial compressor

All these cases can be summarized by the following features.

- Acoustic resonances occur in real machines and cascades inside an annulus.
- They occur as nonsynchronous pressure fluctuations at discrete frequencies.
- The acoustic field in most cases has a helical structure.
- In most cases, vortex shedding was assumed to be the excitation of the resonance.

Acoustic Resonance of Hannover Test Rig

The acoustic resonance of the Hannover four-stage high-speed axial compressor has already been discussed in Ref. [20]. For a better understanding, the results will be summarized below.

Test Rig. A detailed description of the test rig with performance map is given by Fischer and Seume [25], Walkenhorst and Riess [26], and Braun and Seume [27].[1] The measurements provided here are measured with the configuration that is called "reference" configuration in their work.

Phenomenon. The nonharmonic acoustic resonances were detected in static pressure signals of transducers in the compressor casing and the signals of an unsteady pneumatic flow probe, when the compressor was operating close to the stall limit. The static pressure transducer is placed behind the stator and rotor rows in three lines, with each line at different circumferential position as shown on the sketch of the test rig in Fig. 1. Originally, the experiments were carried out for an examination of rotating stall inception in the compressor. The acoustic phenomenon had been noticed during earlier experiments, but most of the several research teams analyzing the Hannover near-stall data did not devote attention to the acoustics because their work mainly focused on rotating stall inception (see, e.g., Ref. [28]). Levy and Pismenny were the first to investigate the phenomenon as a problem of nonlinear pressure oscillations and published several papers of which Ref. [29], to the knowledge of the authors, is the latest. A difference from the present work is that Levy and Pismenny use a nonlinear aerodynamical explanation that links the phenomenon to rotating stall, while the present authors propose a linear acoustics approach. In addition, the data base used for the analysis by Levy and Pismenny used data acquired with a system that allows only short samples of a few seconds. During the experiments, the throttle of the compressor was therefore closed very fast. The

[1] See also Table 1.

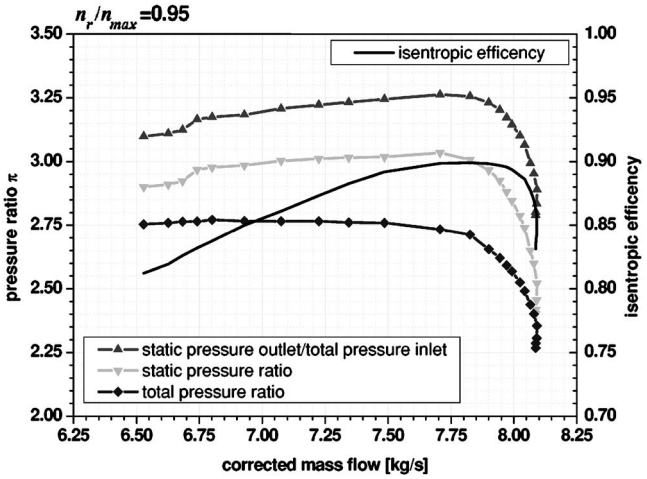

Fig. 2 Operating map for $n_r/n_{max}=0.95$

present work is based on long term measurements with very slow closing of the throttle, over a duration more than 20 times longer. Therefore, the changing of the flow regime and of the conditions for acoustic resonance could be resolved in more detail and the difference between acoustic resonance and rotating stall could be resolved out more clearly. With respect to their physical origin, acoustic resonance and rotating stall are different phenomena. The interaction of acoustic resonance and rotating stall is not subject of the present paper. The data acquisition system for the present work was originally also optimized for stall detection but it turns out that the results are still useful for an acoustic analysis because the measured sound level at resonance is comparatively high.

Based on the measured resonance frequency, Mach number of the mean flow, and the axial and circumferential phase shifts of the pressure signals during resonance, it was shown that the acoustic resonance is a spinning acoustic mode with three periods around the circumference of the compressor [30].

By throttling the compressor with a ring throttle at its outlet and keeping the rotor speed constant, the operating point of the compressor is shifted to lower mass flows on the speed line in Fig. 2. The pressure amplitude of a transducer in the casing in front of the compressor, between inlet guided vanes (IGV) and first rotor, is plotted against frequency and throttle position in Fig. 3. The colors in Fig. 3 and the spectra in Fig. 4 show that close to the stability limit the pressure level of the acoustic resonance exceeds the level of the usually dominated blade passing frequency. Additionally, Fig. 4 shows that the resonance occurs all over the compressor at one single frequency. At a throttle position of 89.9%, the pressure level at the resonance frequency in the middle of the compressor is over 180 dB (Fig. 5).

In the last milliseconds before the compressor stalls, the decreasing Mach number of the mean flow is shifting the resonance frequency and phase velocity to a rotor harmonic frequency, such that the high-pressure areas of the acoustic wave are blocking certain channels in the rotor, which leads to a rotating stall in the highly loaded compressor [20].

Because the measured circumferential mode of the acoustic resonance at design speed was three and the frequency was over five times the rotor speed, a multicell mild stall that would not be unusual for heavily loaded multistage machines could be excluded as the reason for the pressure fluctuations.

To prove that the measured pressure fluctuations are an acoustic resonance, it needs to be shown how the compressor annulus with the embedded cascades operates as a resonator. In general, this is a difficult task because there is more than one mechanism working in a turbo compressor that can lead to acoustic resonances. In the present case, this task is less complicated because it is sufficed that the conditions for one of all the possible mechanisms that lead to acoustic resonances are satisfied in the compressor when the resonance occurs.

Theoretical Prediction of Resonant Modes

Up to now, unsteady computational fluid dynamics (CFD) calculations of two or even more complete stages in the required

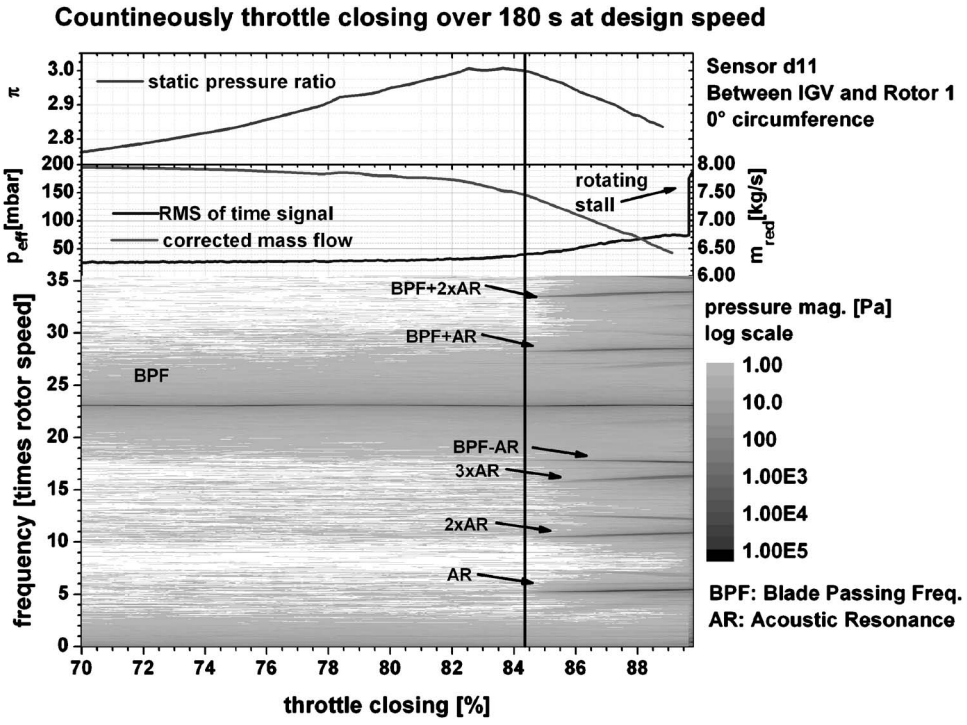

Fig. 3 Contour plot of static wall pressure

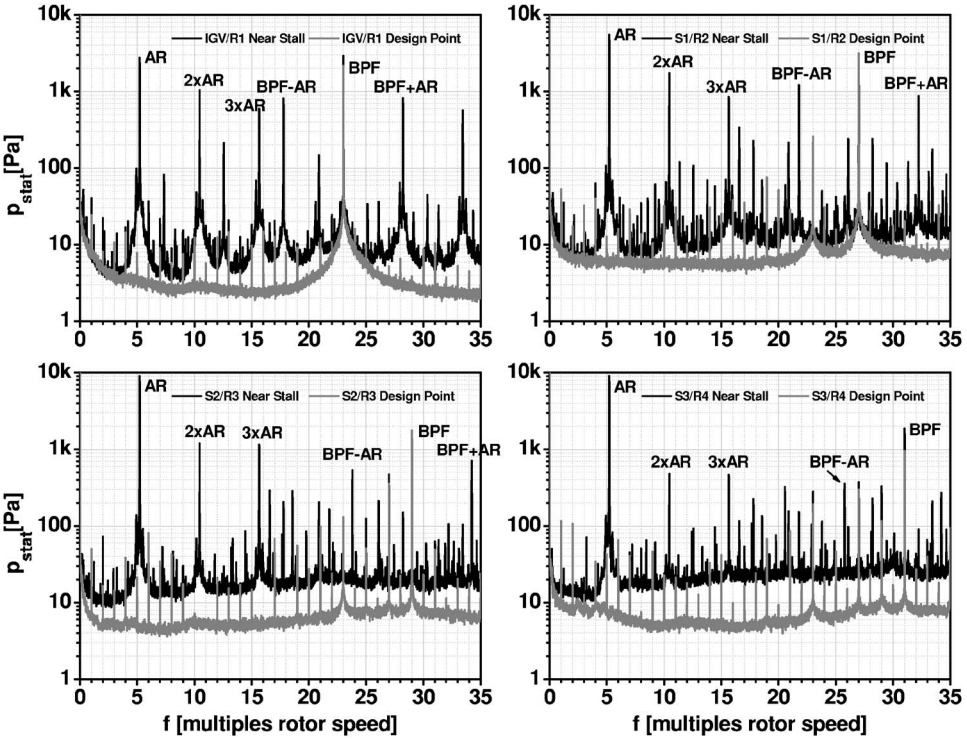

Fig. 4 Power spectra of wall pressure signals

time resolution are pushing even state of the art computer systems to their limits. So in most cases, the fact that the influence of the flow on the acoustic field is stronger is used and the problem is broken down into two tasks. The mean flow is measured or calculated with steady CFD and the results are used as boundary condition for an acoustic analysis.

If the mean flow is known, the major problems for the prediction of resonant modes of a compressor are as follows. They must take into account, firstly, the reflection and transmission of the acoustic waves at the blade rows, and secondly, the nonuniform flow, especially the swirl. If those problems are solved, the prediction of the noise sources is still unsolved. Therefore, the interaction of the resonant field with the source remains an unsolved problem.

Effect of Blade Rows. For acoustic waves with wavelengths of the same order as the dimension of the compressor, resonances can occur and the transmission and reflection of acoustic waves

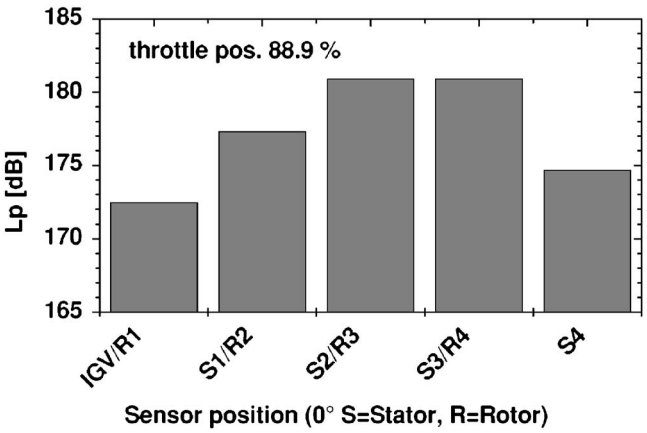

Fig. 5 Acoustic pressure level close to stability limit

are strongly dependent on frequency.

Since the 1960s, several researchers have attempted to solve these problems theoretically. The following short and incomplete review of this work focuses on results which are useful for the explanation of the acoustic resonance in the Hannover compressor.

After Tyler and Sofrin [6] showed that acoustic modes can propagate in a compressor due to rotor-stator interaction, the question of how these modes propagate through a blade row became important. Mani and Horvay [31] used the Wiener-Hopf technique with simplified unloaded blades for the solution of this problem. Kaji and Okazaki [32] used an even simpler actuator disk approach to determine the transmission and reflection coefficients of helical modes. Because this method delivers no information about the effect of different blade spacing, they provide a sophisticated theory in the second part of their paper. They showed that under certain conditions, a compressor becomes "super resonant." The transmission and reflection coefficients of a blade row depend on the incidence angle of the incident waves (this is not the incidence angle of the flow, see Fig. 6). The authors show that under a certain incidence angle and blade spacing, the incident and reflected acoustic fields form a new resonant acoustic mode. It is one important result that, in general, this mode has a different number of lobes around the circumference compared to incident wave (mode scattering). This is important because the number of lobes together with the frequency determines whether the mode can propagate in the compressor or not (cut-off effect).

All authors used a model comparable to Fig. 6. This means that they used plane plates as model for the blades and a mean flow in the direction of the blades. The blade loading is unaccounted as well. From the model in Fig. 6, they found that if the incidence angle of the waves is high, the wave is totally reflected (Zones 1 and 3 in Fig. 7). In Zone 2, transmission and reflection are possible. At the border between Zones 2 and 3, the acoustic wave fronts are normal to the blades and so they can penetrate the cascade without any resistance. At the border between Zones 1 and 2, an observer moving with the mean flow would see the

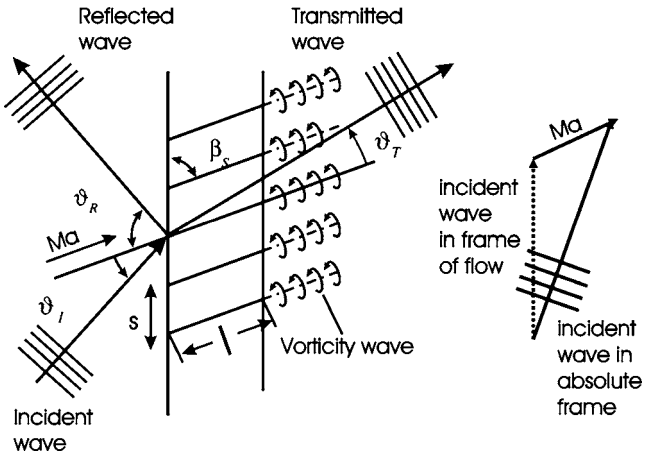

Fig. 6 Scheme of wave scattering at a blade row with nonzero mean flow [36]

wave fronts moving circumferentially. Therefore, they do not hit the cascade (see the left sketch in Fig. 6). This is the area where modes could be trapped in between the blades and super resonance occurs. This is not shown in Fig. 7. It should be noticed that in Zone 2, absorption processes take place, so that the acoustic energy is not preserved. With increasing Mach number, the border 1/2 moves to the right and the transmission coefficient in Zone 2 decreases.

Effect of Nonuniform Flow and Geometry. From simple three-dimensional acoustics of ducts, it is known that the mode shape of an acoustic field depends on the hub ratio. This will be explained later in more detail. In addition to this effect, Tam [33] found in an early paper that helical acoustic modes are significantly scattered back in a throat behind a cylindrical duct, if the flow Mach number exceeds 0.4.

While the above researchers have limited their work to nonswirling flow, Kerrebrock [34] has shown that for swirling flow, where vortices, pressure, and entropy fields are not independent anymore, the influence of the swirling base flow on high frequency pressure oscillations is weak. This means that for modes with frequencies far above the rotor speed, only the general condition of acoustic cut-off needs to be considered.

The first approach for the calculation of sound transmission

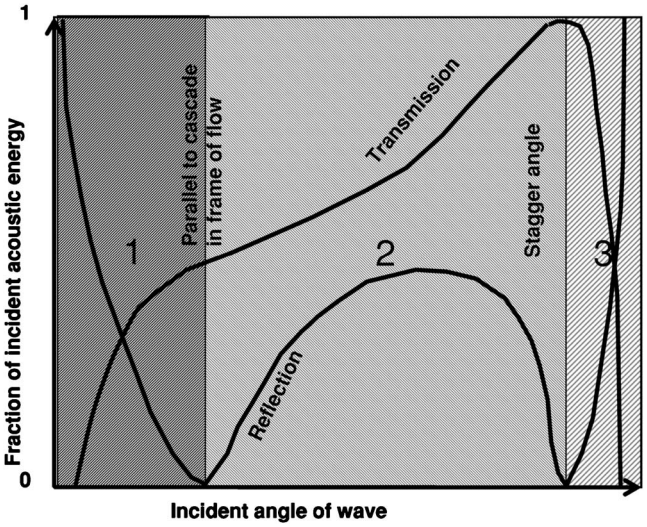

Fig. 7 Example of transmission and reflection coefficients for Ma=0.5 and β_s=60 deg [32]

through a duct with swirling flow and blade rows was suggested by Heinig [35] in conjunction with a calculation method for the reflection and transmission of the blades provided by Koch [36] who enhanced the model of Mani and Horvay [31]. Heinig divided the annulus in small disks in the axial direction and assumed a constant flow and constant hub-to-tip ratio in each disk. Mathematically, each disk is presented by a simple four-pole matrix. Then, propagation of sound in the whole machine is estimated by a simple matrix multiplication. A limitation of this model is that mode scattering is unaccounted for. However, Heinig showed that mode scattering mainly occurs for waves with circumferential wavelengths of two blade pitches or less. For larger wavelengths, his model is valid. Vortex waves are ignored by the model.

The most advanced model for acoustic resonances in turbomachinery to the authors' knowledge was presented by Peake and co-workers in a set of papers during the last years. In Ref. [37], Cooper and Peake show for an aeroengine intake that turning points of acoustic modes can be caused by the varying duct cross section as well as by the blade rows. They showed that a third cause for turning points of a mode is the change from cut-on to cut-off condition due to the swirl. This has also been shown by Rienstra [38] and Ovenden et al. [39]. They show that the phase of the reflected mode is shifted by $\pi/2$.

As shown in the next section, Eq. (1) describes the acoustic field in an annulus. Under certain conditions, the axial wave number k_z becomes a complex number with a nonvanishing imaginary part. Then, the pressure field decays exponentially in the axial direction. This effect is called cut-off. If k_z is a real number, the wave is not damped in the axial direction and the mode is cut-on. This condition is also called regular propagation.

Summary. With a focus on the explanation of the acoustic resonance in the Hannover test rig, this literature review can be summarized as follows.

- Blade rows work as reflectors for acoustic waves when the incident wave hits the blade under a high positive or negative incidence angle.
- Modes with wavelengths of the magnitude of the blade pitch could be trapped if the wave fronts are parallel to the blades (super-resonance).
- For high frequencies, the swirl has to be considered only for cut-off conditions.
- Mode scattering takes place mainly for wavelengths of the magnitude of the blade pitch.
- The swirl of the flow will only be considered for the estimation of cut-on/off condition.
- Change from cut-on to cut-off turns the waves with a phase shift of $\pi/2$.
- Variation in the duct cross section can also lead to turning points.

Application to Measurement

Based on the results of the last section, a simple mathematical model will explain the acoustic resonance of the compressor. This is possible because the number of lobes of the pressure field is much lower than the number of blades. Therefore, mode scattering will not occur. Mode trapping between the blades (Parker resonances) can be neglected from our model for the same reason. Because the frequency is five times higher than the rotor speed, the swirl will be considered only for the estimation of cut-on/off conditions. The variation of the cross section will be considered in the model only for the estimation of the cut-on/off condition as well. The flow is assumed to be uniform in the radial direction.

Simplified Model. For a hard-walled annulus with constant inner and outer diameters along the z axis, the pressure field is given by Eq. (1) which is taken from Ghiladi [40]. The equation is stated in cylindrical coordinates with radius r, circumferential angle φ,

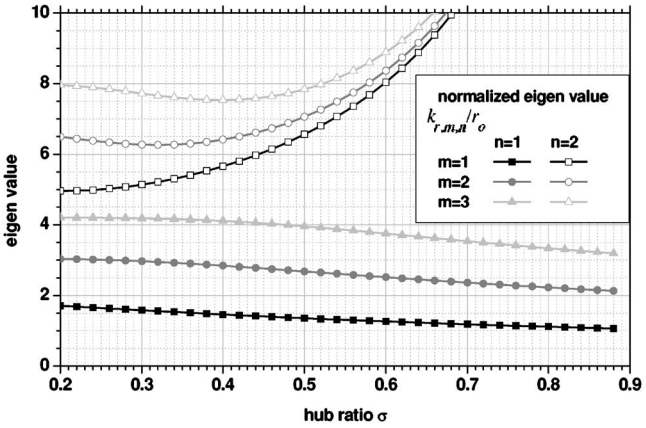

Fig. 8 Calculated eigenvalues $k_{r,m,n}$ normalized to outer radius over hub ratio

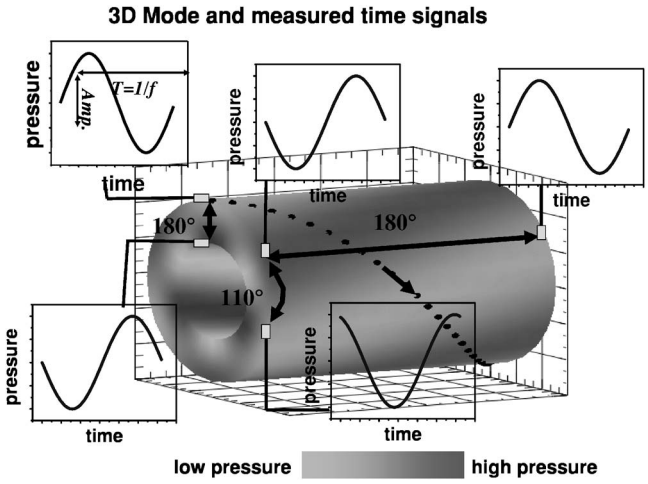

Fig. 9 Example of a (3,1) helical acoustic mode with time series of pressure signals

and z as axial coordinate. The constants B are scaling factors, ω is the angular frequency, and k is the wave number. The function f contains the pressure distribution in the r-φ plane.

$$p_{m,n}(r,\varphi,z,t) = f(k_{r,m,n}r)[B_1 \exp(im\varphi) + B_2 \exp(im\varphi)]\exp[i(k_z z - \omega t)] \quad (1)$$

Even without knowing f in Eq. (1), the harmonic function indicates that the sound field has a helical structure which spins in the annulus. The axial wave number k_z depends on the flow in the annulus and the eigenvalue $k_{r,m,n}$. For the assumption that the mean flow could be treated as rigid body, k_z is given by Lohmann [41]:

$$k_{\pm z} = \frac{\mp \mathrm{Ma}_z(k \pm \mathrm{Ma}_\varphi k_{r,m,n}) + \sqrt{(k \pm \mathrm{Ma}_\varphi k_{r,m,n})^2 - (1 - \mathrm{Ma}_z^2)k_{r,m,n}^2}}{1 - \mathrm{Ma}_z^2} \quad (2)$$

Ma_z and Ma_φ are the axial and circumferential Mach numbers of the flow and $k = 2\pi/\lambda = 2\pi f/a$ is the wave number of a free acoustic wave. The sign in front of the circumferential Mach number Ma_φ depends on the direction of the spin. Positive means the mode spins with the flow and negative means against it. The sign in the index of k_z is always opposite to the sign in front of Ma_z. Positive index of k_z means propagation in the direction of the axial flow and negative against the flow. The eigenvalues $k_{r,m,n}$ depend on the hub ratio $\sigma = r_i/r_o$ of inner to outer radius of the annulus and the (m,n) mode which is defined by the numbers m and n of lobes around the circumference (m) and along the radius (n). $k_{r,m,n}$ could be calculated numerically from Bessel functions [20]. Because $k_{r,m,n}$ depends on the hub ratio, the axial wave number changes with the annulus cross-sectional area, as shown in Fig. 8. If the hub ratio of an annulus is increasing along its axis, like it is in a compressor, a mode with a given frequency can change from cut-on to cut-off and vice versa at a certain point in the compressor.

The frequency where the root in Eq. (2) becomes zero is called cut-off frequency and is given by Eq. (3).

$$f_{m,n}^{\mathrm{cut}} = \frac{a k_{r,m,n}}{2\pi}(\sqrt{1 - \mathrm{Ma}_z^2} \mp \mathrm{Ma}_\varphi) \quad (3)$$

$$\delta = \arctan\left(\frac{\lambda_z}{\lambda_\varphi}\right) = \arctan\left(\frac{m}{r_o k_z}\right) \quad (4)$$

For a duct without any flow, the cut-off condition is given by $k = k_{r,m,n}$. In this case, k_z vanishes and the acoustic field becomes uniform in the z direction. The wave fronts of the field are spinning parallel to the duct axis and no acoustic energy is transported in the z direction. This is the physical meaning of cut-off. The same applies to a mode in a duct with flow, but the acoustic field in the fixed frame of reference is not uniform in the z direction anymore.

In Fig. 9, the acoustic field of a (3,1) mode with three lobes around the circumference and one in radial direction is shown. The sketches of time series in Fig. 9 show the signal of virtual pressure transducers in the acoustic field. The field has high (red) and low (green) pressure areas that form wave fronts with a helix structure and a slope angle δ. These wave fronts are moving perpendicular to the helix as shown by the black arrow in Fig. 9. δ is given by Eq. (4).

Experimental Data. The pressure signals of a four-hole pneumatic probe were measured simultaneously with the pressure signals from the casing. The probe was inserted behind the first rotor at midspan. From the pressure signals, the direction of the flow field behind the first rotor was computed. With the axial and circumferential Mach numbers and the eigenvalue of the duct at the sensor position, it is possible to calculate the cut-off frequency of each mode. The presence of flow in the duct leads to four different wave numbers k_z for each duct mode, depending on the direction of propagation (with or against the flow in circumferential and axial directions), but the cut-off frequency depends only on the sense of rotation of the mode, not on the axial direction of propagation (see Eq. (3)). Waves traveling against the flow in circumferential direction are cut-off at higher frequencies than those traveling with the flow.

Due to the varying cross section, the eigenvalue $k_{r,m,n}$ is different for each stage of the compressor and so is the cut-off frequency. On the other hand, the fluid temperature increases during compression and so does the speed of sound a. Also, the axial and circumferential Mach numbers are different for each stage. Table 2 contains the results of a flow field measurement for each compressor stage performed with a pneumatic probe at an operating point near stall (Braun and Seume [42]). The values in Table 2 are measured from 88% (Rotor 1) to 77% (Rotor 4) channel height. The results show that even though the flow field and duct cross section vary from stage to stage, the resulting cut-off frequency in the tip region of each stage is nearly identical. This probably leads to a lock-in effect of the acoustic resonance of the individual stages and thus to the common resonance frequency observed for the entire test rig.

If the compressor is slowly throttled at a constant rotor speed, the axial flow velocity decreases and the circumferential flow velocity increases and so does the cut-off frequency. The measurements show that the frequency of the resonant acoustic mode fol-

Table 2 Cut-off frequencies near stall for each stage (R=160 mm, N=0.95/$\dot{m}_{corr}$=7.07 kg s^{-1}) (Braun and Seume [42])

Behind rotor	$k_{r,m,n}$ (1/m)	a (m/s^2)	Ma$_z$	Ma$_\varphi$	f^{cut} (Hz)
1	23.28	349	0.405	0.387	1681
2	21.82	365	0.380	0.390	1665
3	21.07	381	0.350	0.367	1665
4	20.34	397	0.315	0.332	1645

lows the change of the computed cut-off frequency of the (3,0) mode in discrete steps with a constant offset of approximately −185 Hz (Fig. 10). Because the offset is constant while the flow field changes and the speed of sound is known precisely, the error must be in the evaluation of the eigenvalue $k_{r,m,n}$. The true eigenvalue $k_{r,m,n}$ of the compressor duct is only 88.5% of the computed value probably because the effective acoustic cross section of the duct is smaller than the geometric cross section due to the boundary layers at the duct wall and flow separation. Also, the assumption of a homogeneous flow field at each axial location made in the analytical model is not strictly true and the true acoustic impedance of the wall might be slightly different from the model used (totally reflecting walls without phase shift) for the same reason.

From previous authors, it is known that acoustic waves at cut-off conditions are reflected with a phase shift of $\pi/2$. In this compressor, this happens for every mode at a certain frequency. Figure 10 shows that the compressor is not in resonance all the time. For the excitation of the resonance in the compressor, additional conditions must be satisfied.

There must be either a strong noise source to excite the resonance which suddenly appears at a certain flow regime or an additional mechanism that traps the broadband noise at a specific frequency and mode shape within the compressor. A combination of both options might be possible as well. Often, it is assumed that vortex shedding of the blades is the major driving force of acoustic resonances in compressors. It is known that the effective aerodynamic thickness of the trailing edge of loaded blades is different from their physical thickness. In our case, with a Strouhal number St=0.21, this would lead to an effective blade thickness at the trailing edge x of 20–25 mm (St=0.21=$f(x/c)$). This is about half the blade pitch. Even for heavily loaded blades, this value seems to be too high.

Therefore, an additional trapping mechanism is needed that forms a resonator together with the mode trapping due to cut-off. It is known from literature that a cross-section variation of the annulus can work as reflector. Because the cross section in the compressor is changing continuously all along the compressor axis, no discrete turning points are created. This leaves us with the role of the blade rows which has not been considered so far. If wave fronts are reflected at blade rows and no mode scattering occurs, the reflected wave fronts have a direction to the flow different from that of the incident waves. To build a resonator, all waves of a mode, whatever their direction to the mean flow is, must be trapped in a certain area of the compressor.

All waves of mode (3,0) running against the swirl are known to be reflected due to cut-off conditions behind the rotor rows where the swirl is maximal.

It remains to be shown that the waves running with the swirl of the flow are reflected, e.g., by the blade rows. It has been shown by previous authors [32] that this is the case when the incident waves are starting to hit the blades from the suction side instead of hitting them from the pressure side, because then they are entering Zone 3 in Fig. 7 where the transmission coefficient of the blade rows vanishes. Therefore, the sketch in Fig. 11 shows how the wave fronts running with the swirl are hitting the blade rows. The downstream mode is represented by the red wave fronts and the upstream mode by the orange ones. Both modes are discussed separately in the next two sections.

Downstream Mode in the Direction of Swirl. In Fig. 12, the crossing of the red (flow angle) and green (incidence angle) lines indicates that the incident waves are starting to hit the blades from the suction side instead of hitting them from the pressure side, i.e., the acoustic boundary condition moves from Zone 2 to Zone 3 in Fig. 7. In Zone 3, the transmission coefficient of the blade rows drops and the reflection coefficient increases, which is exactly what happens to the downstream mode at a stator row immediately prior to the onset of the acoustic resonance in the compressor, denoted as resonant area in Fig. 12. Note that the green line is completely computed from the measured mean flow, i.e., it is

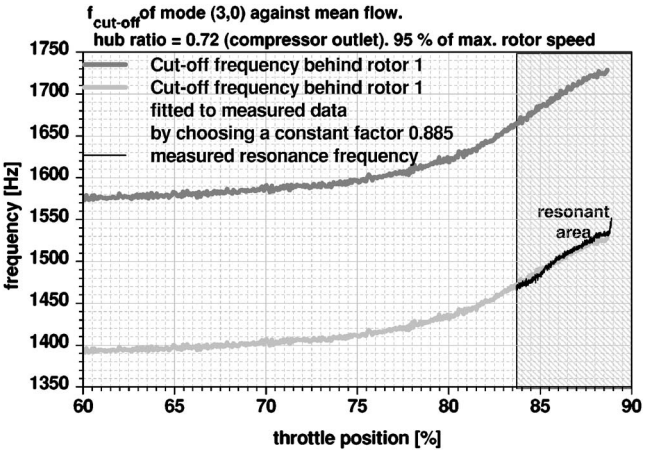

Fig. 10 Computed cut-off frequency and measured resonance frequency

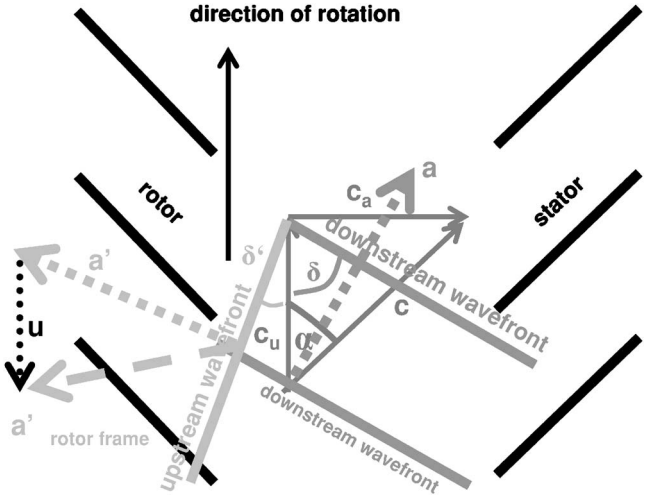

Fig. 11 Flow angle and incidence angle of helical wave fronts

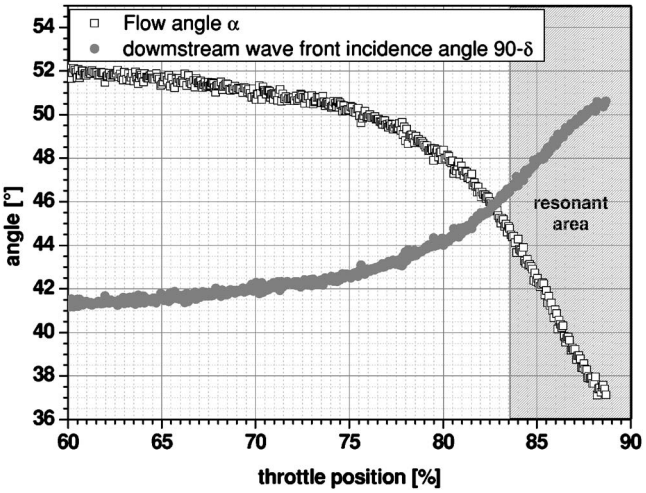

Fig. 12 Helix slope angle of resonant (3,0) mode and flow angle

derived solely from mean flow data without results of dynamic measurements. The only additional assumption, namely, that the frequency of the (3,0) mode is the cut-off frequency of (3,0) mode waves traveling against the swirl, is also based on mean flow data, i.e. the axial and circumferential Mach numbers in Eq. (3).

Upstream Mode in the Direction of Swirl. The upstream mode hits the rotor rows with a nearly constant incidence angle 90 deg $-\delta$ of approximately 21 deg. At 290 Hz rotor speed, this is an incidence angle of 120 deg in the rotor frame (see Figs. 11 and 13). This is also in Zone 3 of Fig. 7.

Summary of Mode Trapping in the Test Rig. This means that all (3,0) modes are trapped between the rotor and stator rows. Other modes with less or more lobes and a frequency close to their cut-off frequency are not trapped, because due to their different eigenvalue $k_{r,m,n}$ they have a different angle of incidence.

This result still leaves the question of the driving force. So far, we assumed that the acoustic field is fed by the broadband noise of the compressor.

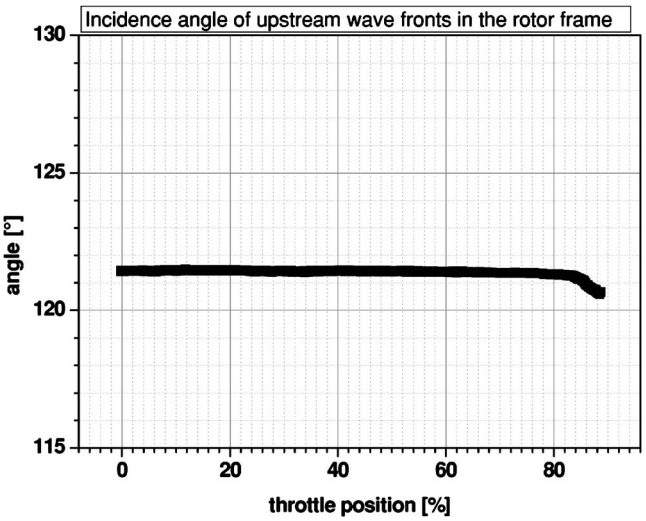

Fig. 13 Incidence angle of upstream wave fronts on the rotor

Summary

An acoustic resonance in an axial four-stage high-speed compressor has been explained with a simplified model for helical acoustic modes. It has been shown that for this concrete case, mode scattering, vortex waves, and mode trapping within the blade pitch need not be considered. The accordingly simplified mathematical model considers the flow field in the compressor a rigid body. The swirl is considered for the calculation of cut-off conditions. From the resonance frequency and mode shape, it turns out that wave fronts of the measured mode running against the swirl of the mean flow are close to cut-off. This means that they are trapped or reflected at axial positions where the swirl in the compressor is maximal, i.e., behind the rotor rows. The waves traveling with the swirl can propagate through the compressor over wide parts of the operating map. However, at a certain point of low mass flow, the waves cannot pass the stator rows anymore because their incidence angle is changing due to changing flow conditions in such a way that the waves hit the stator vanes from the suction side instead of hitting them from the pressure side. As shown by previous work, this means that they are reflected by the blade rows and consequently all waves of the mode are trapped between the rotor and stator rows.

The present paper thus shows that a suitable, physically based simplification of mathematical models from the literature yields both the correct condition and the correct modes and approximate frequencies for acoustic resonance in this compressor.

Nomenclature

a = speed of sound (m/s)
c = mean flow velocity (m/s)
c_u = swirl velocity of mean flow (m/s)
c_a = axial velocity of mean flow (m/s)
d = diameter of the compressor annulus (m)
f = absolute frequency (Hz)
k = wave number (1/m)
l = chord length (m)
Ma = Mach number of the mean flow
$\dot{m}_{\mathrm{corr}}$ = corrected mass flow (kg/s)
m = circumferential mode number
n = physical rotor speed, radial mode number (Hz)
n_R = reduced rotor speed (Hz)
p = pressure (Pa)
r = radius (m)
s = blade pitch (m)
t = time (s)
z = axial coordinate (m)
α = flow angle (deg)
β_S = stagger angle of the blade row (deg)
δ = slope angle of helical wave fronts (deg)
λ = wavelength (m)
θ_I = incidence angle of wave in Heinigs model (deg)
θ_R = reflection angle of wave in Heinigs model (deg)
θ_T = transmission angle of wave in Heinigs model (deg)
π = total pressure ratio
σ = hub ratio (r_i/r_o)
φ = azimuthal coordinate (deg)
ω = angular frequency (1/s)

References

[1] März, J., Hah, C., and Neise, W., 2002, "An Experimental and Numerical Investigation Into the Mechanisms of Rotating Instability," ASME J. Turbomach., **124**, pp. 367–374.
[2] Weidenfeller, J., and Lawerenz, M., 2002, "Time Resolved Measurements in an Annular Compressor Cascade With High Aerodynamic Loading," ASME Paper No. GT2002-30439.

[3] Mailach, R., Lehmann, I., and Vogeler, K., 2001, "Rotating Instability in an Axial Compressor Originating From the Fluctuating Blade Tip Vortex," ASME J. Turbomach., **123**, pp. 453–460.
[4] Kameier, F., and Neise, W., 1997, "Experimental Study of Tip Clearance Losses and Noise in Axial Turbomachines and Their Reduction," ASME J. Turbomach., **119**, pp. 460–471.
[5] Baumgartner, M., Kameier, F., and Hourmouziadis, J., 1995, "Non-Engine Order Blade Vibration in a High Pressure Compressor," ISABE, 12th International Symposium on Airbreathing Engines, Melbourne, Australia.
[6] Tyler, J. M., and Sofrin, T. G., 1962, "Axial Flow Compressor Noise Studies," SAE, pp. 309–332.
[7] Lighthill, M. J., 1997, "Collected Papers of Sir James Lighthill," *Proceedings of the Royal Society*, Vol. III, Oxford Univ. Press, New York.
[8] Legerton, M. L., Stoneman, S. A. T., and Parker, R., 1991, "An Experimental Investigation Into Flow Induced Acoustic Resonances in an Annular Cascade," ImechE Paper No. C416/060.
[9] Parker, R., and Stoneman, S. A. T., 1989, "The Excitation and Consequences of Acoustic Resonances in Enclosed Fluid Flow Around Solid Bodies," *Proceedings of the Institution of Mechanical Engineers*, Vol. 203.
[10] Parker, R., and Stoneman, S. A. T., 1987, "An Experimental Investigation of the Generation and Consequences of Acoustic Waves in an Axial-Flow Compressor: The Effect of Variations in the Axial Spacing Between Blade Rows," J. Sound Vib., **116**(3), pp. 509–525.
[11] Parker, R., 1984, "Acoustic Resonances and Blade Vibration in Axial Flow Compressors," J. Sound Vib., **92**(4), pp. 529–539.
[12] Parker, R., 1967, "Resonance Effects in Wake Shedding From Parallel Plates: Calculation of Resonant Frequencies," J. Sound Vib., **5**(2), pp. 330–343.
[13] Parker, R., 1966, "Resonance Effects in Wake Shedding From Parallel Plates: Some Experimental Observations," J. Sound Vib., **4**(1), pp. 62–72.
[14] Cumpsty, N. A., and Whitehead, D. S., 1971, "The Excitation of Acoustic Resonances by Vortex Shedding," J. Sound Vib., **18**(3), pp. 353–369.
[15] Rizk, W., and Seymour, D. F., 1964, "Investigations Into the Failure of Gas Circulators and Circuit Components at Hinkley Point Nuclear Power Station," Proc. Inst. Mech. Eng., **179**(1), pp. 627–703.
[16] Von Heesen, W., 1997, "Experimentelle Untersuchungen Nicht-Drehklangbezogener Tonaler und Breitbandig-Rauschartiger Störgeräusche Bei Radial- und Axialventilatoren," Abschlußbericht zum Forschungsvorhaben AiF 10047.
[17] Ulbricht, I., 2001, "Stabilität Des Stehenden Ringgitters," dissertation, TU Berlin, Arbeitskreis Industrielle Forschung, Germany, http://edocs.tu-berlin.de/diss/2001/ulbricht_iris.pdf
[18] Kameier, F., 2001, "Experimentelle Untersuchungen StröMungserregter Schaufelschwingungen Bei Axialverdichtern," Abschlußbericht AIF FKZ 1700599.
[19] Camp, T. R., 1999, "A Study of Acoustic Resonance in a Low-Speed Multistage Compressor," ASME J. Turbomach., **121**, pp. 36–43.
[20] Hellmich, B., and Seume, J. R., 2004, "Acoustic Resonance in a Four-Stage High-Speed Axial Compressor," ISROMAC, Honolulu, Mar. 8–11, Paper No. ISROMAC10-2004-004.
[21] Ziada, S., Oengören, A., and Vogel, A., 2002, "Acoustic Resonance in the Inlet Scroll of a Turbo-Compressor," J. Fluids Struct., **16**(3), pp. 361–373.
[22] Kielb, R. E., 2003, "Blade Excitation by Aerodynamic Instabilities—A Compressor Blade Study," ASME Paper No. GT2003–38634.
[23] Vignau-Tuquet, F., and Girardeau, D., 2005, "Aerodynamic Rotating Vortex Instability in a Multi-Stage Axial Compressor," 17th ISABE, Munich, Germany.
[24] Cyrus, V., Rehak, K., and Polansky, J., 2005, "Aerodynamic Causes of Stator Vanes Damage of the Alstom Gas Turbine Compressor in the Gasification Combined Cycle Using Brown Coal," Sixth Conference on Turbomachinery, Fluid Dynamics and Thermodynamics, Lille, France, Paper No. OPE-094_03/15.
[25] Fischer, A., and Seume, J., 2003, "Performance of Strongly Bowed Stators in a 4-Stage High Speed Compressor," Atlanta, Paper No. GT2003–38392.
[26] Walkenhorst, J., and Riess, W., 2000, "Experimentelle Unter-Suchung Von Wandkonurierung in Einem Vierstufigen Axialverdichter," Abschlußbericht zum Vorhaben 1.121 der Arbeitsgemeinschaft Hochtemperatur Gasturbine, http://edok01.tib.uni-hannover.de/edoks/e001/313061823.pdf.
[27] Braun, M., and Seume, J. R., 2006, "Forward Sweep in a Four-Stage High-Speed Axial Compressor," ASME Paper No. GT2006–90218.
[28] Stoff, H., and Methling, F.-O., 2002, "Aktive Stabilitätsverbesserung am Verdichter-Analyseverfahren. Abschlußbericht," Ruhr-Universität Bochum, Bochum, Germany.
[29] Levy, Y., and Pismenny, J., 2005, "High-Frequency Pressure Oscillations of Rotating Stall Type," Int. J. Turbo Jet Engines, **22**, pp. 59–87.
[30] Hellmich, B., Braun, M., Fischer, A., and Seume, J., 2003, "Observations on the Causal Relationship Between Blade Count and Developing Rotating Stall in a Four Stage Axial Compressor," Fifth European Conference on Turbomachinery, Prag, Czech Republic.
[31] Mani, R., and Horvay, G., 1970, "Sound Transmission Through Blade Rows," J. Sound Vib., **12**(1), pp. 59–83.
[32] Kaji, S., and Okazaki, T., 1970, "Propagation of Sound Waves Through a Blade Row. I. Analysis Based on Semi Actuator Disk Theory, II. Analysis Based on the Acceleration Potential Method," J. Sound Vib., **11**(3), pp. 339–375.
[33] Tam, C. K. W., 1971, "Transmission of Spinning Acoustic Modes in a Slightly Nonuniform Duct," J. Sound Vib., **18**(3), pp. 339–351.
[34] Kerrebrock, J. L., 1977, "Small Disturbances in Turbo-Machine Annuli with Swirl," AIAA J., **15**(6), pp. 794–803.
[35] Heinig, K. E., 1983, "Sound Propagation in Multistage Axial Flow Turbomachines," AIAA J., **21**(1), pp. 98–105.
[36] Koch, W., 1971, "On Transmission of Sound Waves Through a Blade Row," J. Sound Vib., **18**(1), pp. 111–128.
[37] Cooper, A. J., and Peake, N., 2000, "Trapped Acoustic Modes in Aeroengine Intakes With Swirling Flow," J. Fluid Mech., **419**, pp. 151–175.
[38] Rienstra, S. W., 1999, "Sound Transmission in Slowly Varying Circular and Annular Lined Ducts With Flow," J. Fluid Mech., **380**, pp. 279–296.
[39] Ovenden, N. C., Eversman, W., and Rienstra, S. W., 2004, "Cut-On Cut-Off Transition in Flow Ducts: Comparing Multiple-Scales and Finite-Element Solutions," AIAA Paper No. 2004-2945.
[40] Ghiladi, A., 1981, "Drehklangentstehung in Axialen Turbomaschinen und Ausbreitung in Angeschlossenen Rohrleitungen," dissertation, RWTH Aachen, Germany.
[41] Lohmann, D., 1978, "Zur Schallausbreitung in Zylinder-Kanälen Mit Helikalen Einbauten," DFVLR-FB 78-30, Germany.
[42] Braun, M., and Seume, J., 2005, "Experimentelle Untersuchung Einer Vorwärtsgepfeilten Beschaufelung in Einem Mehrstufigen Axialverdichter," FVV., Abschlussbericht, Heft 800, Frankfurt, Germany.

Internal Cooling Near Trailing Edge of a Gas Turbine Airfoil With Cooling Airflow Through Blockages With Holes

S. C. Lau

J. Cervantes

J. C. Han

Department of Mechanical Engineering,
Texas A&M University,
College Station, TX 77843-3123

R. J. Rudolph
Siemens Power Group,
1680 S. Central Boulevard,
Jupiter, FL 33458

Naphthalene sublimation experiments were conducted to study heat transfer for flow through blockages with holes in an internal cooling passage near the trailing edge of a gas turbine airfoil. The cooling passage was modeled as two rectangular channels whose heights decreased along the main flow direction. The air made a right-angled turn before passing through two blockages with staggered holes in each channel and left the channel through an exit that was partially blocked by periodic lands with rounded leading edges. There were ten holes along each blockage and all of the holes had rounded edges. Local heat (mass) transfer was measured and overall heat (mass) transfer results were obtained, on the exposed surfaces of one of the walls downstream of the two blockages, for Reynolds numbers (based on the hydraulic diameter of the channel at the upstream surface of the first blockage) between 5000 and 36,000. The results showed that the blockages with the larger hole-to-channel cross-sectional area ratio in one of the two test sections enhanced the heat (mass) transfer downstream of the blockages more than the blockages with the smaller open area ratio in the second test section. For the geometric configurations and flow conditions studied, the average heat (mass) transfer was higher downstream of the second blockage than downstream of the first blockage. The configurations of the inlet channel and the exit slots considered in this study did not significantly affect the local heat (mass) transfer distributions or the average heat (mass) transfer downstream of the blockages. [DOI: 10.1115/1.2775489]

Keywords: turbine blade trailing edge cooling, naphthalene sublimation, mass transfer, blockages with holes

Introduction

In a recent design concept for cooling the pressure and suction walls near the trailing edge of an airfoil, cooling air is forced to flow through parallel blockages with staggered holes before it exits the airfoil through the trailing edge slots. Each of these blockages has the same cross section as the flow cross section between the pressure and suction walls near the airfoil trailing edge. After passing through the holes along a blockage, the cooling air impinges onto the next blockage and is deflected toward the suction and pressure walls of the airfoil before it finally passes through the staggered holes along the next blockage.

In this experimental study, we examined the heat transfer characteristics of flows through these blockages with staggered holes. The tail region of an airfoil with these blockages was modeled as two tapered (or converging) rectangular channels, in which air flowed through elongated holes with rounded edges in two blockages. In each channel, the two blockages had the same cross section as the channel. Downstream of the second blockage, the air exited through slots separated by lands with rounded leading edges. We conducted naphthalene sublimation experiments to determine the overall mass transfer coefficients and the distributions of the local mass transfer coefficient on the walls between the two blockages and between the second blockage and the exit slots, for airflow rates corresponding to Reynolds numbers of up to 36,000. We used the analogy between heat transfer and mass transfer to relate the experimentally determined mass transfer enhancement to heat transfer enhancement.

Detailed surveys of published studies on internal cooling of gas turbine airfoils have been presented in Han et al. [1]. Many researchers have studied heat transfer enhancement in channels with turbulence promoters, pin fins, and impinging jets, with and without rotation. There have been a number of studies of heat transfer for turbulent flows through channels with perforated ribs or ribs with various openings for flows to pass through, such as Kukreja and Lau [2], Hwang et al. [3], Liou and Chen [4], and Buchlin [5].

Moon and Lau [6] conducted experiments with thermochromic liquid crystals to study heat transfer between two blockages with holes and pressure drops across the blockages, for turbulent airflow in a rectangular channel. They obtained the average heat transfer coefficients and the local heat transfer distributions on one of the channel walls between two blockages, and the overall pressure drops across the blockages, for nine different staggered arrays of holes in the blockages and two Reynolds numbers. For the hole configurations studied, the blockages enhanced heat transfer by about five to eight times, but significantly increased the pressure drop. Smaller holes in the blockages caused higher heat transfer enhancement but larger increase of the pressure drop than larger holes. Because of the large pressure drop, the heat transfer per unit pumping power was lower with the blockages than without them. The local heat transfer was the lowest immediately downstream of the holes in the upstream blockage, the highest upstream of the downstream blockage, and also relatively high in regions of reattachment of the jets leaving the upstream holes. The local heat transfer distribution was strongly dependent on the configuration of the hole array in the blockages.

Contributed by the International Gas Turbine Institute of ASME for publication in the JOURNAL OF TURBOMACHINERY. Manuscript received July 24, 2006. final manuscript received March 13, 2007; published online May 2, 2008. Review conducted by David Wisler. Paper presented at the ASME Turbo Expo 2006: Land, Sea and Air (GT2006), 2006, Barcelona, Spain, May 8–11, 2006. Paper No. GT2006-91230.

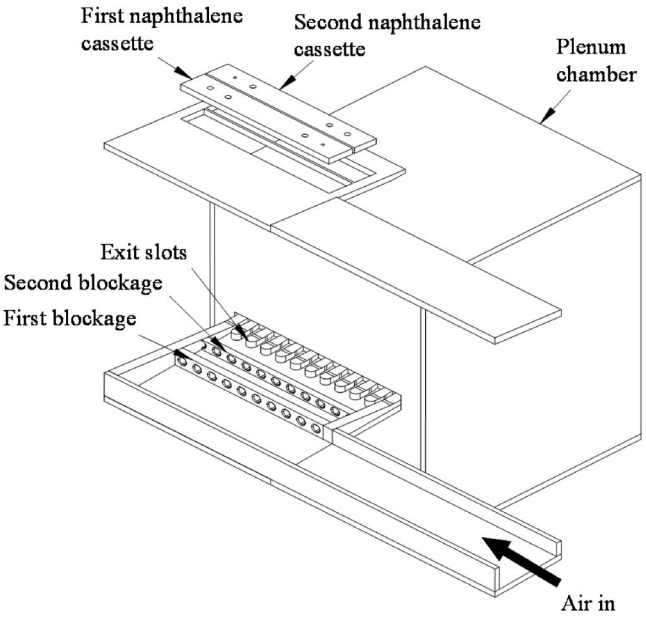

Fig. 1 Schematic of one of the two test sections

Lau et al. [7] conducted naphthalene sublimation experiments to study heat (mass) transfer enhancement by blockages with staggered round and square holes for turbulent airflows through a wide rectangular channel. The blockages and the channel had the same cross section. The results showed that the blockages enhanced the average heat (mass) transfer on the channel walls by 4.7–6.3 times that for fully developed turbulent flow through a smooth channel. The blockages with round holes enhanced more heat (mass) transfer on the channel walls but caused larger pressure drops than the blockages with square holes, which had a 27% larger flow cross-sectional area.

Experimental Apparatus and Instrumentation

The test apparatus for this study was an open flow loop in an air-conditioned laboratory. The main components of the open flow loop were one of two acrylic test sections, a plenum chamber, a calibrated orifice flow meter, a gate valve, and a blower. During an experiment, air at about 22°C was drawn through the test section. Upon exiting the flow loop, the air was ducted to the outside of the laboratory.

Figure 1 shows a schematic of one of the two test sections with its top wall displaced to expose the interior of the test section. During an experiment, the air that was drawn through an entrance section turned to pass through staggered holes along two parallel blockages and slots between lands before exiting into a settling chamber. The schematic also shows two removable naphthalene cassettes that were installed on the top wall of the test section to facilitate the measurements of the local and average mass transfer coefficients downstream of the two blockages with holes.

Experiments were conducted with two test sections. Figure 2 gives the top view of the first test section. Results were obtained with the first test section for two exit conditions: with the exit slots aligned with the holes along the second blockage and with the exit slots staggered with respect to the holes along the second blockage. Figure 3 shows the top view of the second test section. Results were obtained with the second test section for two inlet conditions: with the outer wall of the entrance channel parallel to the first blockage and with the outer wall of the entrance channel at an angle with respect to the first blockage.

The key dimensions of the two test sections are given in Table 1. These dimensions are given relative to the widths of the two test sections, which are the same. Note that the second test section

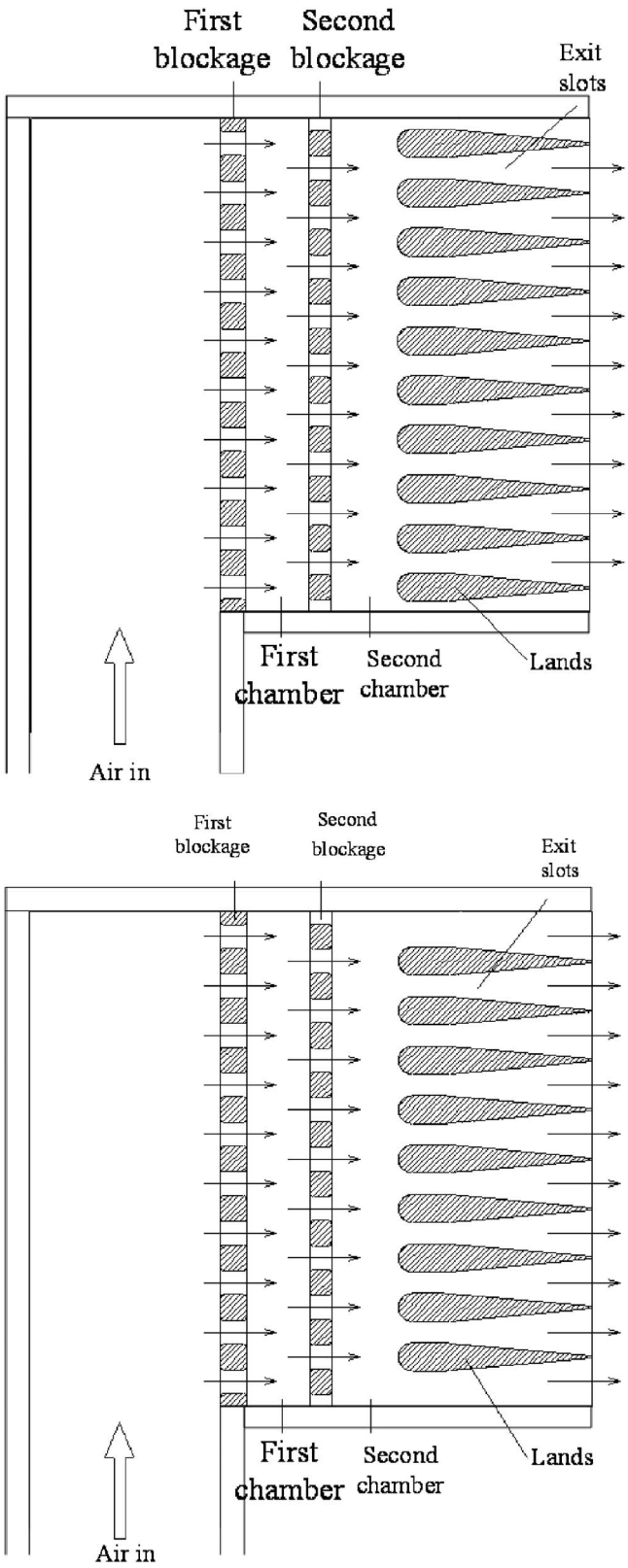

Fig. 2 Top view of first test section: with aligned exit slots and with staggered exit slots

was taller than the first test section at the entrance and had smaller holes along the two blockages. The ratios of the total flow cross-sectional area for the ten holes to the cross-sectional area at the upstream surface of the first blockage were 0.19 and 0.10, respec-

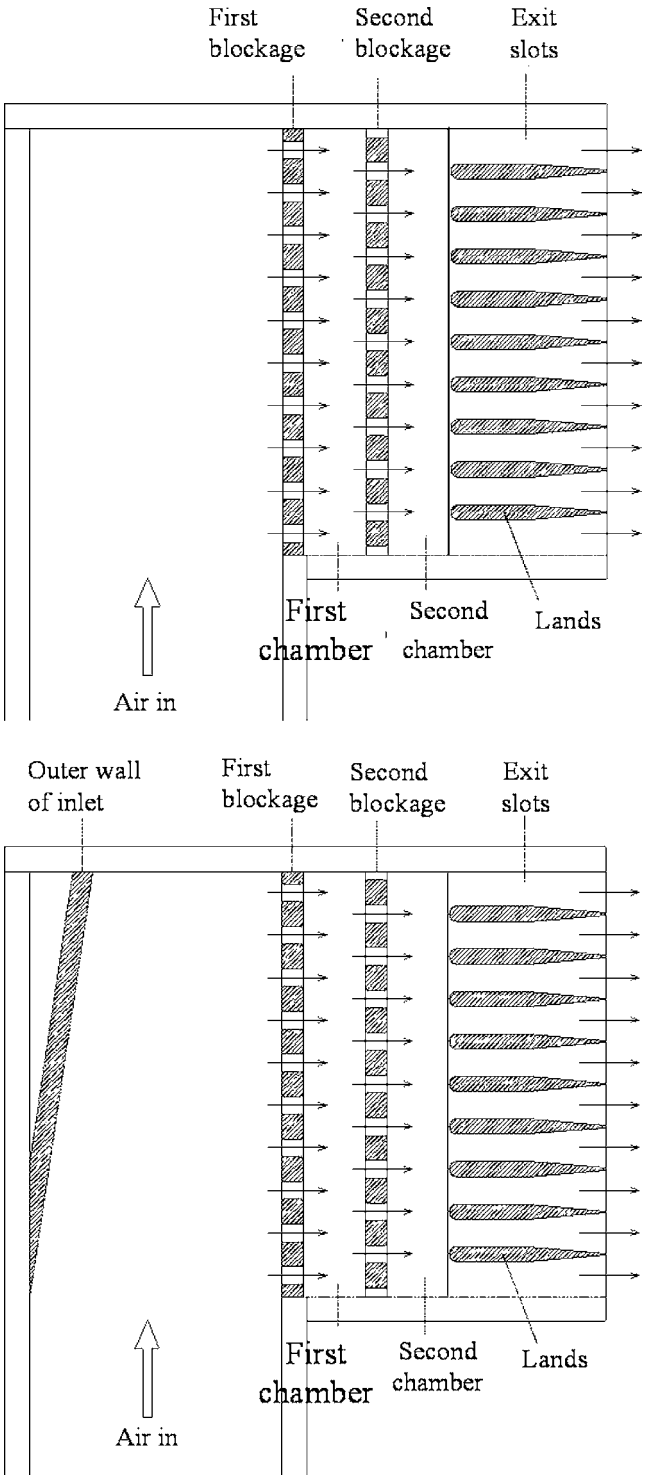

Fig. 3 Top view of second test section with two different inlet conditions

tively, for the two test sections. For the second test section, there were also a step on the inner surface of each of the two primary walls, just upstream of the leading edges of the lands (see Fig. 3), such that the height of the test section is further reduced at the entrance of the exit slots. In addition, for one set of experiments conducted with the second test section, an acrylic strip was added to the inlet channel such that the outer wall of the entrance channel was displaced by an angle of 8.3deg with respect to the blockages with holes (see Fig. 3).

To facilitate measurements of the local and overall mass transfer coefficients on the exposed surfaces of one of the principal walls, two aluminum cassettes were inserted into slots in the top wall (see Fig. 1). The cavity was filled with naphthalene during a casting process, exposing a smooth flat naphthalene surface. The rim of each cassette rested on top of the blockages and the sidewalls so that the entire surface of the top wall between two blockages was a naphthalene surface. Also, the cassettes were designed such that they could be quickly inserted into the slots in the top wall or removed for measurements. Adhesive tape was used to prevent air leakage between the cassettes and the channel walls during an experiment.

The mass flow rate of air through the test section and the flow loop was controlled with the gate valve. The pressure drops across the orifice and the pressure upstream of the orifice were measured with an inclined manometer and a U-tube manometer, respectively. The pressures at the orifice flow meter were needed to calculate the air mass flow rate. The temperature of the air was measured with two thermocouples, whose junctions were located at the entrance of the test section, and a digital multichannel thermometer with a resolution of 0.1 °C. The thermocouples and the digital thermometer were calibrated with a constant temperature bath and a NIST calibrated mercury thermometer. The duration of an experiment was measured with a digital stopwatch that had a resolution of 0.01 s.

To obtain the average mass transfer coefficients, the naphthalene cassettes were weighed one at a time with a Sartorius electronic balance before and after each test run. The electronic balance had a range of 0.0–160.0 g and a resolution of 0.1 mg. To determine the local mass transfer distributions, the elevations at a grid of points with a spacing of 1.6 mm on the naphthalene surface and on the top surface of the rim of each cassette were measured with a Starrett electronic depth gauge before and after each test run. The depth gauge had a lever-type LVDT head, a range of ± 0.2 mm, and a resolution of 0.0002 mm. The elevation measurements on the top surface of the rim were needed to determine the location of the reference plane of the naphthalene surface in the calculations of the elevation changes at the grid points on the naphthalene surface.

Because the test procedure in this study was similar to that in Lau et al. [7], readers are referred to that paper for the detailed descriptions of the instrumentation, the preparation of the naphthalene cassettes, the weighing of the cassettes, and the measurements of the local elevations at a grid of points on the surfaces of the naphthalene cassettes.

Supplementary experiments were conducted to determine the corrections for the mass transfer from the naphthalene surfaces during blower motor startup and shutdown and due to natural convection, while the naphthalene cassettes were weighed or the local elevations on the naphthalene surfaces were measured. Heat transfer experiments were also conducted with the first of the two test sections by replacing the aluminum naphthalene cassettes with two copper blocks and by using electric heaters attached to the outer surfaces of the blocks and thermocouples with their junctions installed inside the blocks (Cervantes [8]). Balsa wood strips insulated the copper blocks from the acrylic test section and fiber glass insulation prevented extraneous heat losses. Average heat transfer results from these experiments were used to ensure the accuracy of the average results from the naphthalene sublimation experiments. In addition, the transient liquid crystal method was used to determine the local distributions of the heat transfer coefficient in two acrylic test sections that are geometrically identical to the two test sections in this study (Choi [9]). These heat transfer results, along with pressure measurement results, will be presented in a separate paper.

Data Reduction

The Reynolds number was based on the hydraulic diameter of the test channel at the upstream surface of the first blockage, D_h,

Table 1 Dimensions of the two test sections in this study relative to the width of the two test sections

Dimensions relative to width of test section	First test section	Second test section
Height of upstream surface of first blockage	0.075	0.109
Thickness of first blockage	0.052	0.056
Thickness of second blockage	0.043	0.056
Distance separating two blockages	0.129	0.148
Distance separating second blockage and leading edge of lands	0.117	0.151
Dimensions of holes along both first and second blockages (height and width)	0.036 and 0.048	0.031 and 0.042
Total hole-to-channel cross-sectional area ratio (all ten holes and at upstream surface of first blockage)	0.19	0.10
Tapered angles, top and bottom walls of test section	3.3 deg and 3.6 deg	7.9 deg and 0.0 deg
Width of leading edge of lands	0.057	0.037
Length and width of entrance section	1.57 and 0.386	1.63 and 0.624

and was expressed in terms of the air mass flow rate $\dot{m}$, the dynamic viscosity of air μ, and the perimeter of the test channel, P, at the upstream surface of the first blockage.

$$\mathrm{Re} = \frac{\rho \bar{V} D_h}{\mu} = \frac{4\dot{m}}{\mu P} \tag{1}$$

The overall and local mass transfer coefficients were defined, respectively, as

$$\bar{h}_m = \frac{\Delta M_n / \Delta t}{A_s(\rho_{v,w} - \bar{\rho}_{v,b})} \tag{2}$$

$$h_m = \frac{\dot{M}_n''}{\rho_{v,w} - \rho_{v,b}} = \frac{\rho_s \Delta z / \Delta t}{\rho_{v,w} - \rho_{v,b}} \tag{3}$$

where ΔM_n was the total mass transfer from a naphthalene surface to the air, Δt was the duration of the experiment, $\dot{M}_n''$ was the local naphthalene mass flux, ρ_s Z was the density of solid naphthalene, and Δz was the local change of elevation on the naphthalene surface. In the above equations, $\rho_{v,w}$ was the local vapor density of naphthalene at the wall and was evaluated using the ideal gas law.

$$\rho_{v,w} = \frac{p_{v,w}}{R T_w} \tag{4}$$

In Eq. (4), the vapor pressure $p_{v,w}$ was determined using the vapor pressure–temperature correlation for naphthalene by Ambrose et al. [10].

$$T_w \log(p_{v,w}) = \frac{a_0}{2} + \sum_{s=1}^{3} a_s E_s(x)$$

with

$$E_1(x) = x, E_2(x) = 2x^2 - 1 \tag{5}$$

and

$$E_3(x) = 4x^3 - 3x$$

where $a_0 = 301.6247$, $a_1 = 791.4937$, $a_2 = -8.2536$, $a_3 = 0.4043$, and $x = (2T_w - 574)/114$. In Eq. (5), T_w was in Kelvin and $p_{v,w}$ was in $\mathrm{N/m^2}$.

The average bulk vapor density of naphthalene in Eq. (2) was the average of the vapor densities at the upstream and downstream edges of the naphthalene surface being considered and was calculated as

$$\bar{\rho}_{v,b} = \frac{1}{2}\left[\left(\frac{\dot{M}_n}{\dot{V}}\right)_{\text{upstream}} + \left(\frac{\dot{M}_n}{\dot{V}}\right)_{\text{downstream}}\right] \tag{6}$$

where $\dot{M}_n$ was the rate of total mass transfer from the upstream naphthalene surfaces and $\dot{V}$ was the volumetric flow rate of air. The bulk vapor density was zero upstream of the first blockage since there was no naphthalene vapor in the air at the test channel inlet. Similarly, the local bulk vapor density $\rho_{v,b}$ in Eq. (3) for determining the local mass transfer coefficient at a grid point was the rate of total mass transfer from naphthalene surfaces upstream of the grid point divided by the air volumetric flow rate.

The average and local Sherwood numbers were defined, respectively, as

$$\overline{\mathrm{Sh}} = \frac{\bar{h}_m D_h}{\sigma} \tag{7}$$

$$\mathrm{Sh} = \frac{h_m D_h}{\sigma} \tag{8}$$

where σ was the mass diffusion coefficient for naphthalene vapor in the air. A correlation given by Goldstein and Cho [11] was used to determine the mass diffusion coefficient.

$$\sigma = 0.0681\left(\frac{T}{298.16}\right)^{1.93}\left(\frac{1.013 \times 10^5}{p}\right) \times 10^{-4} \tag{9}$$

where σ was in $\mathrm{m^2/s}$, T was in Kelvin, and p was in $\mathrm{N/m^2}$. According to the analogy between heat transfer and mass transfer described by Eckert [12],

$$\frac{\overline{\mathrm{Nu}}}{\mathrm{Nu}_0} = \frac{\overline{\mathrm{Sh}}}{\mathrm{Sh}_0} \tag{10}$$

$$\frac{\mathrm{Nu}}{\mathrm{Nu}_0} = \frac{\mathrm{Sh}}{\mathrm{Sh}_0} \tag{11}$$

where the reference Nusselt number and Sherwood number were based on the Dittus–Boelter correlations (Incropera and DeWitt [13]) for a fully developed turbulent flow at the same Reynolds number through a smooth channel with the same hydraulic diameter as the test channel.

$$\mathrm{Nu}_0 = 0.023\,\mathrm{Re}^{0.8}\,\mathrm{Pr}^{0.4} \tag{12}$$

$$\mathrm{Sh}_0 = 0.023\,\mathrm{Re}^{0.8}\,\mathrm{Sc}^{0.4} \tag{13}$$

In Eqs. (12) and (13), Pr was the Prandtl number and Sc was the Schmidt number.

The estimation of uncertainty values was based on a confidence level of 95% (or 20:1 odds) and the relative uncertainty analysis method of Coleman and Steele [14]. Also, in all uncertainty calculations, uncertainty values of $\pm 1.0\%$ for all properties of air and ± 0.25 mm for all physical dimensions were used.

The maximum uncertainty of the calculated Reynolds number was $\pm 3.1\%$. The uncertainty of the local mass transfer coefficient was estimated to be $\pm 6.3\%$, and the uncertainty of the average mass transfer coefficient was estimated to be $\pm 5.1\%$. According

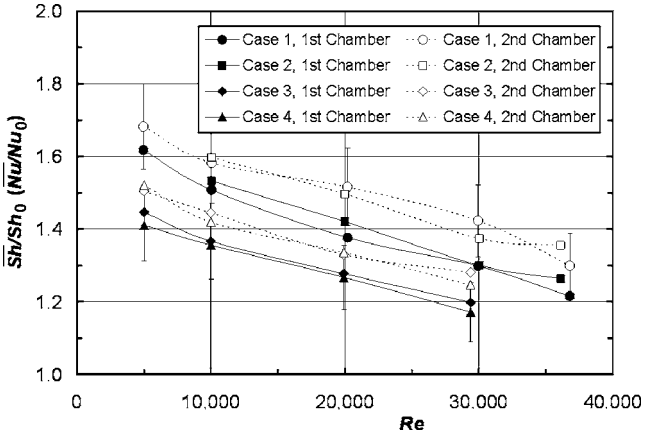

Fig. 4 Overall heat (mass) transfer enhancement downstream of blockages with holes in two test sections with different inlet and exit conditions

to Goldstein and Cho [11], the diffusion coefficient of naphthalene vapor in air had an uncertainty of about ±5.0%. With this value, the calculated values of the relative uncertainties for the local and average Sherwood numbers were ±8.2% and ±7.3%, respectively.

Presentation and Discussion of Results

Average Heat (Mass) Transfer. In this section, results of the average heat (mass) transfer coefficients are given. Figure 4 gives $\overline{Sh}/Sh_0$ (or $\overline{Nu}/Nu_0$) as a function of Re, for air flows through holes along two blockages and exit slots downstream of the second blockage in the two test sections. In Cases 1 and 2, air flows through the first test section with exit slots aligned and staggered, respectively, with respect to the holes along the second blockage (see Fig. 2). In Cases 3 and 4, air flows through the second test section with two different entrance channel geometries (see Fig. 3). In Fig. 4, solid symbols are for the exposed surface of the top channel wall between the two blockages ("first chamber"), while open symbols are for the exposed surface of the top channel wall downstream of the second blockage ("second chamber"). Error bars are shown for two sets of results (the highest and the lowest) to indicate the calculated uncertainty for $\overline{Sh}$ of 7.3%.

In the figure, values of $\overline{Sh}/Sh_0$ are based on overall measurements, although local elevation measurements also give similar values of $\overline{Sh}/Sh_0$, with an average variation of 2.8%. Since local Sherwood numbers were not determined over the regions near the two sidewalls, the averages of the measured Sh/Sh_0 values were expected to be slightly different from corresponding values from average measurements—results show a maximum variation between −4.2% and +9.3%. The values of $\overline{Sh}/Sh_0$ based on overall measurements were also comparable to corresponding values of $\overline{Nu}/Nu_0$ based on overall heat transfer measurements with two copper blocks, electric heaters, and thermocouples (Cervantes [8])—with variations between −1.4% and −7.9%.

The results in Fig. 4 show that $\overline{Sh}/Sh_0$ decreases with increasing Re, that is, heat (mass) transfer enhancement is lower at a higher Reynolds number. The blockages enhance heat (mass) transfer on the exposed surfaces of the top channel wall downstream of the two blockages by about 20–70%. The results clearly show that heat (mass) transfer is enhanced more in the second chamber than in the first chamber in all four cases. The higher heat (mass) transfer enhancement in the second chamber is believed to be the result of the higher turbulence intensities and better mixing of the flow in the second chamber than in the first chamber and the higher flow velocities in the second chamber because of the converging channel geometries. Also, the jets of air from the holes along the first blockage tend to impinge onto the upstream surface of the second blockage and cause the heat (mass) transfer to be high immediately upstream of the second blockage. However, the heat (mass) transfer is quite low immediately downstream of the first blockage. Indeed, when the spanwise-averaged value of Sh/Sh_0 is plotted versus distance in the main flow direction, the results show a larger variation of the spanwise-averaged Sh/Sh_0 value in the first chamber than in the second chamber. After the airflow passes through the first blockage, it tends to leave the holes along the second blockage as jets that spread wider toward the walls in the second chamber, causing a smaller streamwise variation of the Sh/Sh_0 value and slightly higher overall $\overline{Sh}/Sh_0$ values in the second chamber. It will be seen shortly that local distribution data show relatively large values of Sh/Sh_0 in the second chamber immediately downstream of the holes along the second blockage.

Figure 4 also shows that the blockages in the first test section cause higher heat (mass) transfer enhancement (in Cases 1 and 2) than in the second test section (in Cases 3 and 4), and that the overall heat (mass) transfer is not significantly affected by the aligned or staggered exit slots, nor the inlet channel with a parallel outer wall or a converging outer wall. Note that the holes along the two blockages are smaller in the second test section than in the first test section, and that the second test section is taller than the first test section—a height at the upstream face of the first blockage that is 0.109 times the width of the test section versus 0.075 times (Table 1).

The local distributions of Sh/Sh_0 will indicate that the local heat (mass) transfer on the channel walls is very high immediately upstream of a blockage, as a result of the deflection of the airflow toward the channel walls after it impinges onto the upstream face of the blockage. Thus, for the cooling of the trailing edge region of a gas turbine blade, although the average results show heat transfer enhancement on the walls of only 20–70%, the heat transfer may be much higher on the upstream face of a blockage than on the walls. Since the surface area of the upstream face of a blockage is a significant fraction of the exposed surface area of the walls and a substantial amount of heat may be conducted from the walls to the blockage, the overall heat transfer may be much higher than the heat transfer from the exposed surface of the walls only.

Local Heat (Mass) Transfer Distribution. Attention is now focused on the local heat (mass) transfer results. Local heat (mass) transfer coefficients were determined at a regular grid of points with a spacing of 1.6 mm (up to 1785 (21×85) points) on each of the two naphthalene surfaces between the two blockages and between the second blockage and exit slots. Local heat (mass) transfer coefficients were obtained over the middle region on each of the two naphthalene surfaces downstream of up to eight of the ten holes along a blockage in Cases 1 and 2, and downstream of up to seven of the ten holes along a blockage in Cases 3 and 4. Local heat (mass) transfer coefficients were not obtained over the regions of each surface near the two sidewalls. Local elevations were measured at these points for the same Reynolds numbers between 5000 and 36,000 as for the overall mass transfer measurements.

In Figs. 5 and 6, the local heat (mass) transfer results are presented, for Cases 1 and 2, respectively, as contours of the local heat transfer coefficient h in W/m^2K. The local heat transfer coefficient is calculated from the local mass transfer coefficient h_m using Eqs. (11)–(13), and Pr=0.7 for air and Sc=2.28 for naphthalene vapor in air. In these figures, the arrows indicate the direction of the flow through the holes along the blockages and the exit slots—they also indicate the locations of the holes and exit slots. In Case 1, the exit slots are aligned with the holes along the second blockage (Fig. 5), while, in Case 2, the exit slots are staggered with respect to the holes along the second blockage (Fig. 6).

As shown in Figs. 5 and 6, the distributions of the heat transfer

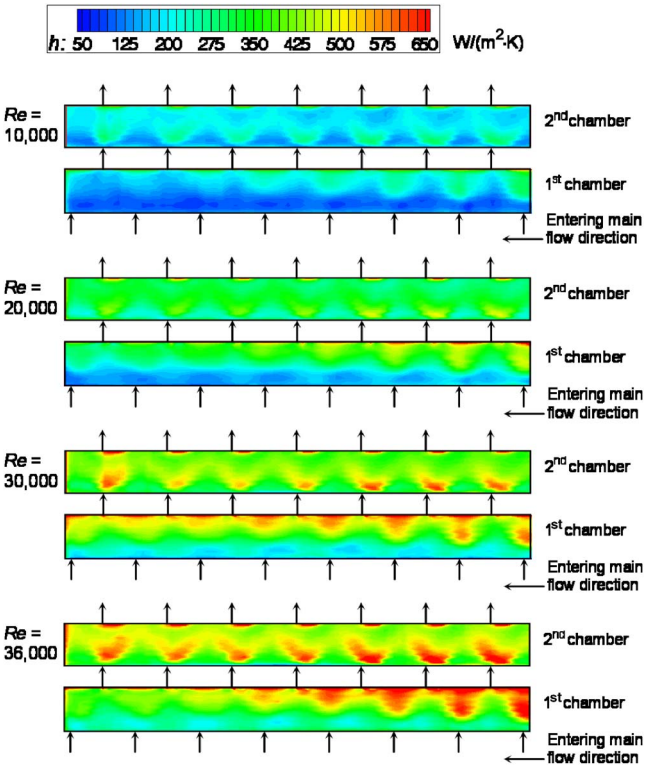

Fig. 5 Distributions of local heat transfer coefficient in Case 1: first test section with aligned exit slots

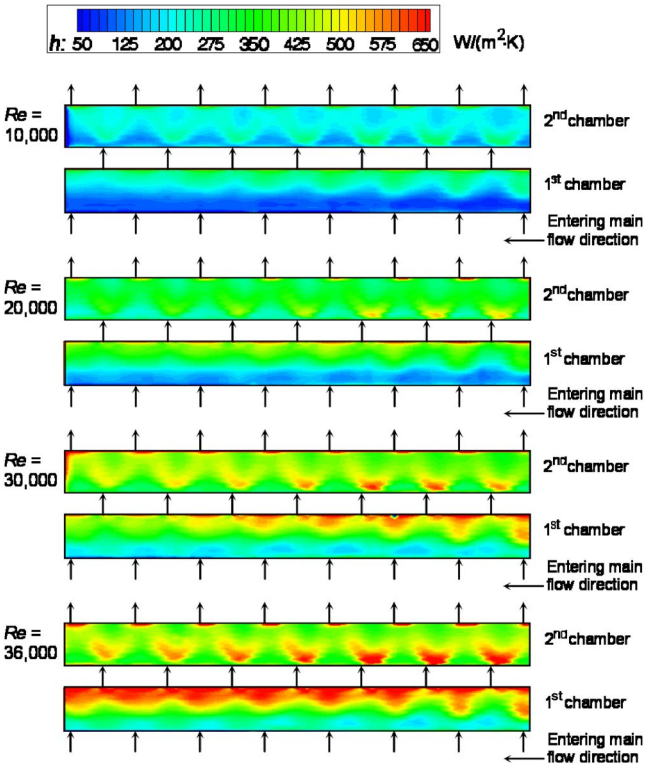

Fig. 6 Distributions of local heat transfer coefficient in Case 2: first test section with staggered exit slots

coefficient are higher for higher Reynolds numbers, with values of up to about 600 $W/m^2 K$. The range of the heat transfer coefficient is comparable to that obtained in corresponding liquid crystal experiments (Choi [9]). There are periodic spanwise variations of the heat transfer coefficient because of the holes along the blockages and the exit slots. In addition, there are spanwise variations as a result of the flow making a right-angled turn in the entrance channel before entering the test section.

In the first chamber, between the two blockages, the value of the heat transfer coefficient is small immediately downstream of the first blockage and is very large upstream of the second blockage, especially at locations where the jets of air are deflected toward the walls after impinging onto the upstream face of the second blockage between two adjacent holes. The high heat (mass) transfer region is larger nearer the inlet of the entrance channel (located on the right side of each figure)—the higher pressure forces more air through the holes.

The airflow through the staggered holes along the two blockages causes a periodic spanwise distribution, with wavy contours and higher values immediately upstream of a blockage between two holes than upstream of a hole. The spanwise variation of h is small compared with the streamwise variation between the two blockages. The aforementioned deflected airflow toward the channel wall upstream of a blockage between two holes may turn to either side along the wall. The air may then turn away from the wall before escaping through one of the two holes.

In the second chamber, the streamwise variation of the heat transfer coefficient is not monotonic, as in the first chamber. The heat transfer coefficient is high in periodic horseshoe-shaped regions immediately downstream of the holes along the second blockage, as the air that passes through these holes appears to spread much wider than the jets of air passing through the holes in the first blockage. The flow field over these high heat transfer regions may be the result of both the airflow passing through the holes, with rounded edges, along the second blockages after making possibly multiple turns in the first chamber and the rounded leading edge geometry of the lands that divide the exit into slots. Upstream of the exit slots, there are relatively small high heat transfer regions where the flow is deflected from the leading edges of the lands toward the wall. These high heat transfer regions are not located immediately upstream of the lands, possibly because the air enters the test section at a right angle and the air mass flow rates through all the holes may not be the same. The streamwise variation of the heat transfer coefficient is smaller in the second chamber than in the first chamber.

For Cases 3 and 4, the second test section is taller and has a slightly larger converging angle than the first test section in Cases 1 and 2. Also, both the height and the width of the holes along the blockages are smaller in the second test section than in the first test section. In addition, in the second test section, there is a step on the wall where the local heat (mass) transfer distributions are determined, just downstream of the measurement region in the second chamber and upstream of the leading edges of the lands. As a result of the difference in the geometries of the two test sections, the distributions of the local heat (mass) transfer coefficient in Cases 3 and 4 are very different from those in Cases 1 and 2. As shown in Figs. 7 and 8, the streamwise variation of the heat (mass) transfer coefficient is monotonic, continually increasing value in the main flow direction, with relatively small spanwise variations. In Figs. 7 and 8, the heat (mass) transfer distributions are given as distributions of Sh/Sh_0, and arrows indicate the locations of the holes along the two blockages and the exit slots. The distributions in Fig. 7 are for airflow entering the second test section from an entrance channel with the outer wall parallel to the blockages (Case 3), while those in Fig. 8 are for airflow entering the second test section from a converging entrance channel (Case 4).

The Sh/Sh_0 distributions in Figs. 7 and 8 show that the blockages cause higher heat (mass) transfer enhancement when the flow rate is lower. The geometry of the entrance channel does not appear to affect the Sh/Sh_0 distribution at all. In the first chamber, the jets of air impinging onto the upstream face of the second

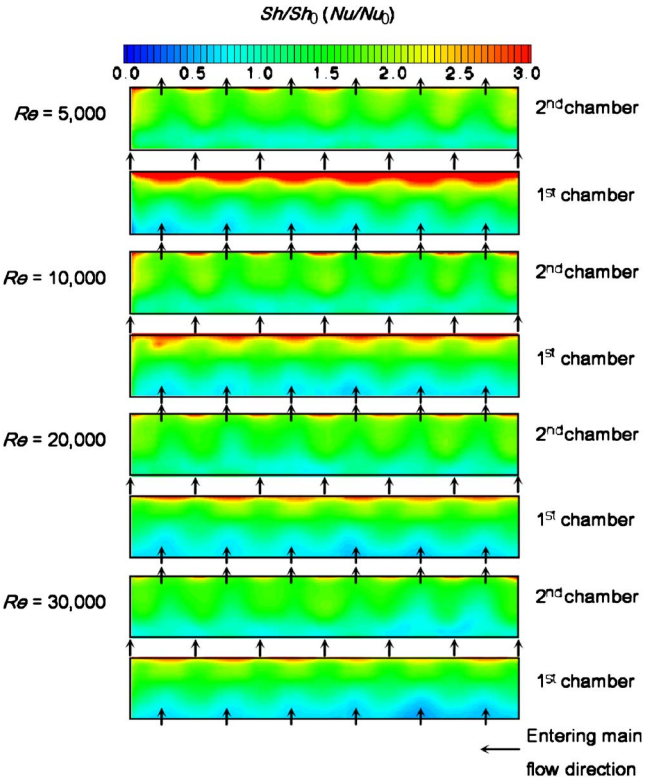

Fig. 7 Distributions of local Sherwood number ratio in Case 3: second test section, inlet channel with parallel sidewalls

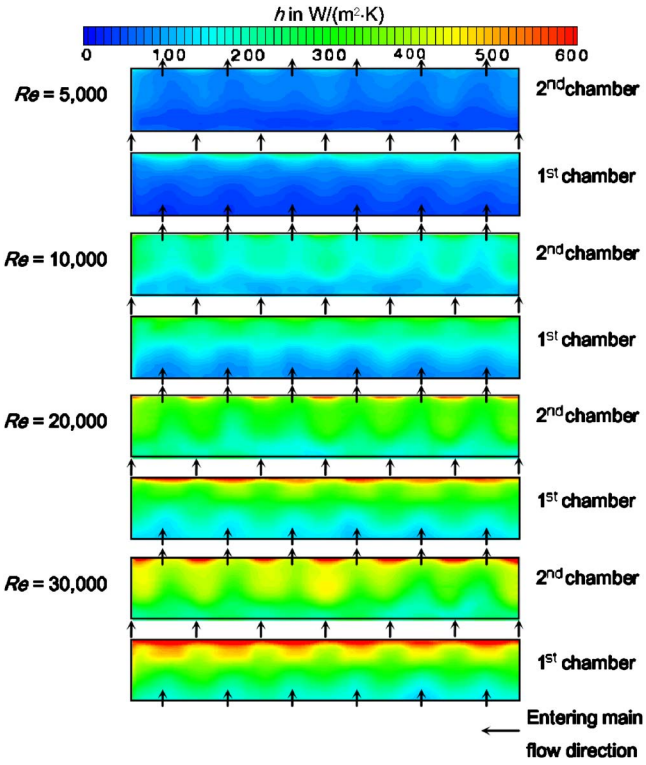

Fig. 9 Distributions of local heat transfer coefficient in Case 3: second test section, inlet channel with parallel sidewalls

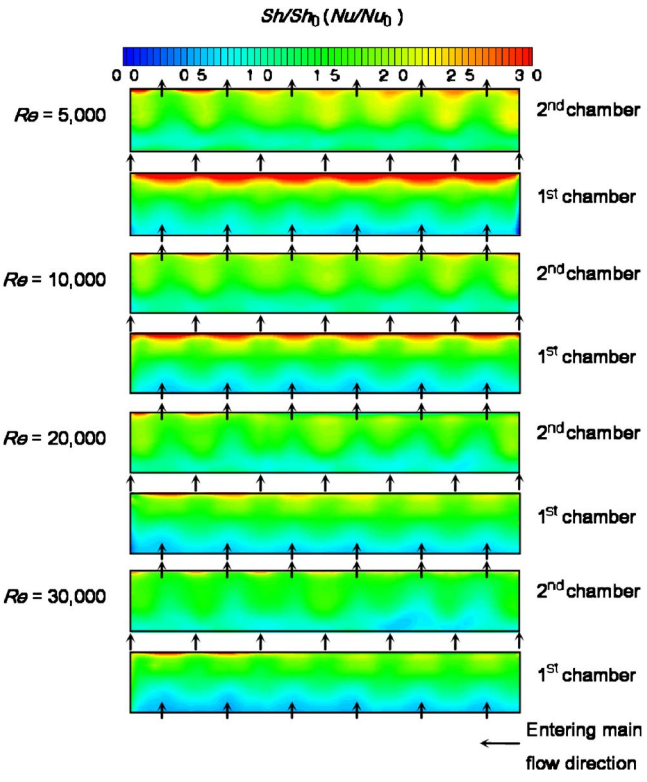

Fig. 8 Distributions of local Sherwood number ratio in Case 4: second test section, inlet channel with converging sidewalls

blockage are deflected toward the walls and toward the holes along the second blockage. The Sh/Sh_0 values are high upstream of the second blockage, especially in regions between two holes along the second blockage. Because the holes along the two blockages in the second test section are small relative to the height of the blockage, the heat (mass) transfer is low immediately downstream of the holes along the first blockage.

The monotonic increasing trend of Sh/Sh_0 in the streamwise direction, along with small spanwise variation of Sh/Sh_0, in the first chamber, is the same regardless of the air mass flow rate (or Reynolds number). The Sh/Sh_0 distributions in the second chamber are also very similar to those in the first chamber. The heat (mass) transfer is high just upstream of the step on the wall at the semicircular leading edges of the lands at the exit in the second chamber. The main difference between the Sh/Sh_0 distributions in the first and second chambers in Cases 3 and 4 is the smaller streamwise variation in the second chamber than in the first chamber, which is more evident in the lower Reynolds number cases.

In Figs. 9 and 10, the local heat (mass) transfer results for Cases 3 and 4, respectively, are presented as contours of the local heat transfer coefficient h in W/m^2 K. The local heat transfer coefficient is calculated from the local mass transfer coefficient h_m using Eqs. (11)–(13), and Pr=0.7 for air and Sc=2.28 for naphthalene vapor in air. Comparing the distributions of the heat transfer coefficient for Cases 3 and 4 with those for Cases 1 and 2 (Figs. 5 and 6), it may be shown that the heat transfer coefficient distributions are consistently lower on the average in Cases 3 and 4 than in Cases 1 and 2. The geometry of the second test section—with smaller holes and taller blockages—causes lower heat (mass) transfer enhancement than the geometry of the first test section. With the expected higher pressure drops across the two blockages in the second test section because of the smaller hole-to-channel cross-sectional area ratio, the first test section should give higher thermal performance than the second test section. That is, for a

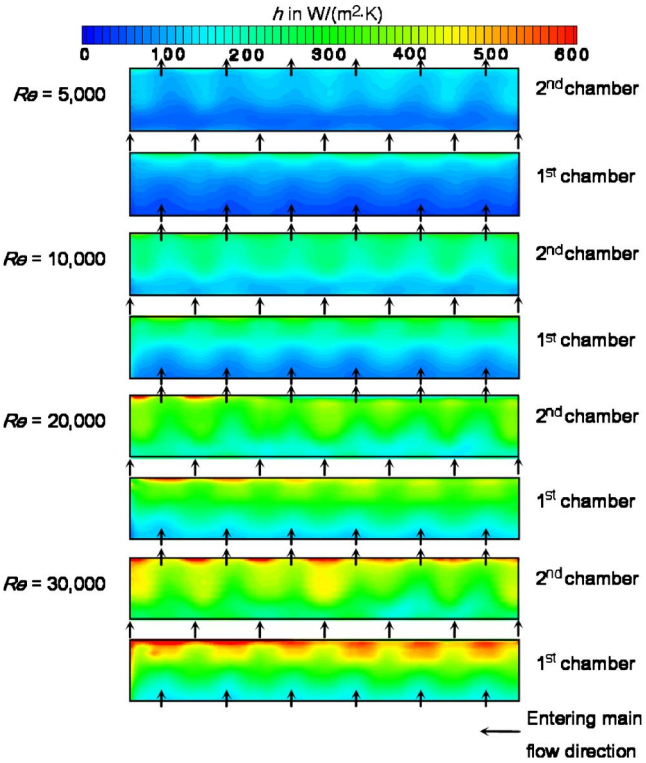

Fig. 10 Distributions of local heat transfer coefficient in Case 4: second test section, inlet channel with converging sidewalls

given pumping power, the blockages in the first test section should cause even higher heat (mass) transfer enhancement than the blockages in the second test section.

Concluding Remarks

Naphthalene sublimation experiments were conducted to study heat (mass) transfer enhancement by blockages with elongated holes in two test sections that modeled the trailing edge region of an internally cooled gas turbine blade. Average and local heat (mass) transfer results were obtained with the two test sections, for two inlet and two exit geometries, and Reynolds numbers up to 36,000. For the conditions under which the experiments were conducted and the geometries of the two test sections that were studied, the results are summarized below.

- Blockages with holes enhance heat (mass) transfer on the walls downstream of the blockages. For the two test sections in this study, the blockages with holes enhance heat (mass) transfer by 20–70%. For internal cooling of gas turbine blades, heat transfer is further enhanced as heat is conducted from the walls to the blockages whose upstream surfaces are subjected to cooling by the jets of air from the holes along the upstream blockages.
- For the two test sections considered in this study, the blockages in the first test section with larger hole-to-channel cross-sectional area ratio cause higher heat (mass) transfer enhancement.
- In both test sections, the average heat (mass) transfer is higher in the second chamber between the second blockage and the exit slots than in the first chamber between the two blockages. There is less streamwise heat (mass) transfer variation in the second chamber than in the first chamber.
- The overall heat (mass) transfer enhancement is lower when the Reynolds number is larger.
- Neither the average heat (mass) transfer nor the distribution of the local heat (mass) transfer is significantly affected by the geometries of the entrance channel and the exit slots considered in this study.

Acknowledgment

Siemens Power Group sponsored this research.

Nomenclature

A_s = surface area, m^2
D_h = hydraulic diameter of test channel at upstream surface of the first blockage, m
h = local heat transfer coefficient, $W/m^2\,K$
h_m = local mass transfer coefficient, m/s
$\bar{h}_m$ = average mass transfer coefficient, m/s
$\dot{m}$ = air mass flow rate, kg/s
$\dot{M}_n$ = rate of total mass transfer from upstream naphthalene surfaces, kg/s
$\dot{M}''_n$ = local naphthalene mass flux, $kg/m^2\,s$
$\underline{\mathrm{Nu}}$ = local Nusselt number
$\overline{\mathrm{Nu}}$ = average Nusselt number
Nu_0 = reference Nusselt number for fully developed turbulent flow in smooth channel
$p_{v,w}$ = vapor pressure on naphthalene surface, N/m^2
P = perimeter of test channel at upstream surface of the first blockage, m
Pr = Prandtl number
R = gas constant of naphthalene vapor, kJ/kg K
Re = Reynolds number
Sc = Schmidt number
$\underline{\mathrm{Sh}}$ = local Sherwood number
$\overline{\mathrm{Sh}}$ = average Sherwood number
Sh_0 = reference Sherwood number for fully developed turbulent flow in smooth channel
T_w = surface temperature, K
$\dot{V}$ = volumetric flow rate of air, m^3/s
$\bar{V}$ = average velocity, m/s

Greek Symbols

ΔM_n = total mass transfer from naphthalene surface to air, kg
Δt = duration of experiment, s
Δz = local change of elevation on naphthalene surface, m
μ = dynamic viscosity of air, $N\,s/m^2$
ρ = density of air, kg/m^3
$\rho_{v,b}$ = local bulk vapor density of naphthalene, kg/m^3
$\bar{\rho}_{v,b}$ = average bulk vapor density of naphthalene, kg/m^3
ρ_s = density of solid naphthalene, kg/m^3
$\rho_{v,w}$ = vapor density of naphthalene on naphthalene surface, kg/m^3
σ = mass diffusion coefficient of naphthalene vapor in air, m^2/s

References

[1] Han, J. C., Dutta, S., and Ekkad, S. V., 2000, *Gas Turbine Heat Transfer and Cooling Technology*, Taylor & Francis, New York.
[2] Kukreja, R. T., and Lau, S. C., 1998, "Distributions of Local Heat Transfer Coefficient on Surfaces With Solid and Perforated Ribs," J. Enhanced Heat Transfer, **5**(1), pp. 9–21.
[3] Hwang, J. J., Lia, T. Y., and Liou, T. M., 1998, "Effect of Fence Thickness on Pressure Drop and Heat Transfer in a Perforated-Fenced Channel," Int. J. Heat Mass Transfer, **41**(4–5), pp. 811–816.
[4] Liou, T. M., and Chen, S. H., 1998, "Turbulent Heat and Fluid Flow in a Passage Distributed by Detached Perforated Ribs of Different Heights," Int. J. Heat Mass Transfer, **41**(12), pp. 1795–1806.
[5] Buchlin, J. M., 2002, "Convective Heat Transfer in a Channel With Perforated Ribs," Int. J. Therm. Sci., **41**, pp. 332–340.
[6] Moon, S. W., and Lau, S. C., 2003, "Heat Transfer Between Blockages With

Holes in a Rectangular Channel," ASME J. Heat Transfer, **125**, pp. 587–594.
[7] Lau, S. C., Cervantes, J., Han, J. C., Rudolph, R. J., and Flannery, K., 2003, "Measurements of Wall Heat (Mass) Transfer for Flow Through Blockages With Round and Square Holes in a Wide Rectangular Channel," Int. J. Heat Mass Transfer, **46**, pp. 3991–4001.
[8] Cervantes, J., 2002, "Measurements of Wall Heat (Mass) Transfer for Flow Through Blockages With Round and Square Holes in a Wide Rectangular Channel," M.S. thesis, Texas A&M University, College Station, TX.
[9] Choi, J., 2004, "An Experimental Investigation of Turbine Blade Heat Transfer and Turbine Blade Trailing Edge Cooling," dissertation, Texas A&M University, College Station, TX.
[10] Ambrose, D., Lawrenson, I. J., and Sprake, C. H. S., 1975, "The Vapor Pressure of Naphthalene," J. Chem. Thermodyn., **7**, pp. 1172–1176.
[11] Goldstein, R. J., and Cho, H. H., 1995, "A Review of Mass Transfer Measurements Using Naphthalene Sublimation," Exp. Therm. Fluid Sci., **10**, pp. 416–434.
[12] Eckert, E. R. G., 1976, "Analogies to Heat Transfer Processes," *Measurements in Heat Transfer*, E. R. G. Eckert and R. J. Goldstein eds., Hemisphere, New York, 397–423.
[13] Incropera, F. P., and DeWitt, D. P., 2002, *Fundamentals of Heat and Mass Transfer*, 5th ed., Wiley, New York.
[14] Coleman, H. W., and Steele, W. G., 1989, *Experimentation and Uncertainty Analysis for Engineers*, Wiley, New York.

Experimental Flow Structure Investigation of Compound Angled Film Cooling

Vipluv Aga

Martin Rose

Reza S. Abhari
e-mail: rabhari@ethz.ch

Institute for Energy Technologies,
Department of Mechanical and Process Engineering,
ETH Zurich,
CH-8092, Zurich, Switzerland

The experimental investigation of film-cooling flow structure provides reliable data for calibrating and validating a 3D feature based computational fluid dynamics (CFD) model being developed synchronously at the ETH Zurich. This paper reports on the flow structure of a film-cooling jet emanating from one hole in a row of holes angled 20 deg to the surface of a flat plate having a 45 deg lateral angle to the freestream flow in a steady flow, flat plate wind tunnel. This facility simulates a film-cooling row typically found on a turbine blade, giving engine representative nondimensionals in terms of geometry and operating conditions. The main flow is heated and the injected coolant is cooled strongly to obtain the requisite density ratio. All three velocity components were measured using a nonintrusive stereoscopic particle image velocimetry (PIV) system. The blowing ratio and density ratio are varied for a single compound angled geometry, and the complex three dimensional flow is investigated with special regard to vortical structure. [DOI: 10.1115/1.2775491]

Introduction

Film cooling of gas turbine stator and rotor airfoil surfaces has played a major role in preserving the structural integrity of these hot-section components at operating temperatures in excess of the melting temperatures of the constituent alloys. Additionally, a judicious choice of film cooling strategies can be instrumental in substantially improving engine efficiency, thus making a strong case for a cogent understanding of its flow and thermal structure. Film cooling basically comprises the use of relatively cool air extracted from the latter stages of a high pressure compressor and ejected over the airfoil to be cooled into the hot flow path through small holes in the airfoil surface. The geometry and orientation of the holes have a direct influence on the film uniformity, adiabatic effectiveness, and heat transfer coefficient of the surface.

Previous film-cooling studies have primarily concentrated on surface heat transfer and adiabatic effectiveness measurements using various methods such as thin-film gauges and thermocouples (e.g., Refs. [1–4], etc.), liquid crystals (e.g., Refs. [5–7]), and infrared cameras (e.g., Ref. [8]). Such studies have primarily concerned themselves with surface heat transfer information rather than the flow structure per se. These studies also took into account the effects of geometry and orientation on the surface results apart from the various flow conditions.

Compound angles are implemented in modern film-cooling designs to improve the spreading rate of the coolant and, thus, to provide a more uniform coverage. With respect to compound angled holes, some past studies, namely, Refs. [9,10], have shown almost contradictory surface results for adiabatic effectiveness (η) and heat transfer coefficient (h). In order to combine the two results to determine the ultimate effect on film-cooling performance, a heat flux reduction ratio (heat flux for a film-cooled surface normalized by that for a surface under a simple boundary layer flow) was used. Some studies, such as Refs. [3,4,11] reported temperature distributions within the emanating cooling jet and also provided surface measurements for η. It was noted that the need to understand the flow structure, which ultimately governs the surface results, is of paramount importance for future designs.

Some numerical studies for different hole geometries compare and contrast the flow physics among streamwise injection [12], compound angled holes [13], shaped holes [14], and compound angled shaped holes [15]. Specifically, with respect to compound angled cylindrical holes, these studies showed some characteristic aspects of a lateral jet in a cross flow, manifested by an increase in the asymmetry (with increasing lateral angle) of the erstwhile symmetric counter-rotating vortex pair (CVP) encountered in streamwise injection and an increase in the lateral uniformity of the adiabatic effectiveness.

The film-cooling problem is primarily governed by the Mach number M, blowing ratio (BR), density ratio (DR), and momentum flux ratio (IR) in addition to the geometry parameters such as the length-to-diameter ratio L/D of the cooling holes, the relevant surface angle β, and the lateral angle ϕ, as shown in Fig. 1. The freestream turbulence intensity Tu and the momentum thickness θ of the boundary layer also have some effect. The effect of freestream turbulence intensity on cooling effectiveness on streamwise injection was studied in Ref. [16], and it was concluded that greater Tu leads to some increase in film effectiveness at higher BRs. The variation of DR has been accomplished in previous studies by using different gases like in Ref. [7] or by actually creating a change in temperature between the two streams [17,18]. The increase in jet penetration and thinning of the boundary layer with increasing IR was shown by Ref. [17].

Current film-cooling research efforts at ETH Zurich have been centered around the strategy of developing a computationally efficient model based on flow structure data for a wide variety of geometries and flow conditions. The computational fluid dynamics (CFD) model uses experimental data for calibration and validation. The salient features of this model are found in Refs. [19,20], and the experimental data used for calibration for streamwise injection are documented in Ref. [17]. The current study builds up on the streamwise injection experimental database of Ref. [17] by examining the dominant flow physics of compound angled injection for a single compound angled case.

The film-cooling jet is basically a simple jet in a cross flow, which is inclined to the surface. There have been some visualization studies for a simple jet in a cross flow. A smoke visualization experiment in Ref. [21] demonstrated the generation of vortices

Contributed by the Turbomachinery Division of ASME for publication in the JOURNAL OF TURBOMACHINERY. Manuscript received July 27, 2006; final manuscript received April 3, 2007; published online May 2, 2008. Review conducted by Karen A. Thole.

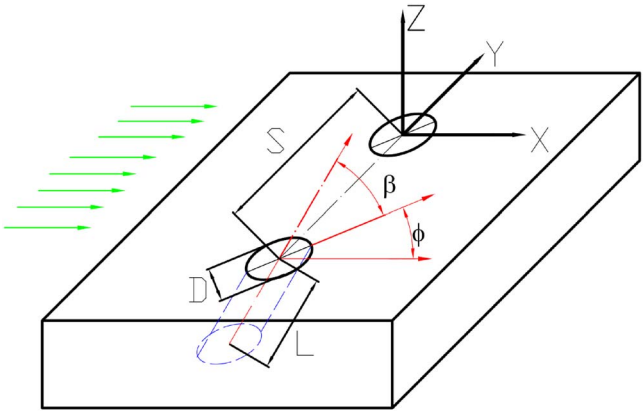

Fig. 1 Definition of coordinate system and geometrical parameters

from the shear between the cross flow and a round jet, causing wake vortices. It was also pointed out that, unlike many modeling strategies, the wake of a jet in a cross flow was fundamentally different from that due to a solid body, as the wake vorticity comes from the boundary layer on the wall from which the jet issues. Other experimental studies on jets in cross flow, using methods such as dye or smoke visualization like that in Refs. [22,23], also qualitatively document the kaleidoscopic vortical phenomena that contribute to the mixing and transfer of mass and momentum between the jet and the surroundings.

Quantitative full field velocity measurements are tenable these days due to the extensive use of noninvasive techniques such as particle image velocimetry (PIV) [24]. Stereoscopic 3D PIV allows a complete flow field investigation. It consists of imaging small particles following a flow with high speed cameras to determine their positions between two snapshots. Perspective is used for 3D velocimetry by positioning two cameras at slightly different angles. Practical aspects of this technique are documented in Ref. [25]. The current study uses stereo PIV to obtain the three velocity components in the region of investigation and subsequent processing to obtain vorticity information.

A film-cooling hole row consisting of seven holes of diameter $d=5$ mm, with a separation of $S=4d$, is placed in a flat plate cooling configuration with zero pressure gradient. The angle that a hole makes with the surface is, $\beta=20$ deg, and the lateral angle through which the hole is turned from the streamwise direction is $\phi=45$ deg. The length-to-diameter ratio is $L/D=2.8$. This coordinate system is illustrated in Fig. 1. Only one such representative geometry is studied under varying BR and DR. The variable parameters BR and DR encompassed the values BR=1,2,3 and DR=1,1.55. The velocities at spanwise slices are plotted, and the secondary flow structures thereof are discussed for the varying parameters. The primary vortex core issuing from the hole is plotted next to the velocity streamlines. The behavior of normal vortices and the wall flow due to entrainment is also commented upon.

Experimental Setup and Procedure

A schematic of the test facility is shown in Fig. 2. It is the same as the one detailed in Ref. [17] and situated in ETH Zurich. The film-cooling test rig is powered by a centrifugal compressor that, through insulated piping, leads to a heat exchanger wherein the freestream flow can be heated to about 120°C. This heat exchanger is fed by 7 bar saturated steam from the house heating system. A water-cooled heat exchanger extracts heat from the freestream downstream from the test section. Various pressure and temperature probes at different points within the loop allow a real-time monitoring and measurement of the conditions within the rig.

The boundary layer thickness of the main flow is controlled by a suction arrangement. A centrifugal blower drives the boundary layer suction, extracting through 327 discrete holes of 1.2 mm diameter stacked over an area of 60×180 mm^2. The extracted air is fed back into the loop far downstream of the cooler.

The secondary or the cooling flow is delivered by a shop air system with a maximum of 75 g/s mass flow rate. First, a drier lowers the dew point of the air to −70°C. Solid water-absorbing particles then alternatively dry the air and recuperate within the drier. The dried air can then be cooled to about −60°C by a single cycle cooler for ejecting into the test section after being seeded by oil droplets from a Laskin nozzle for PIV seeding.

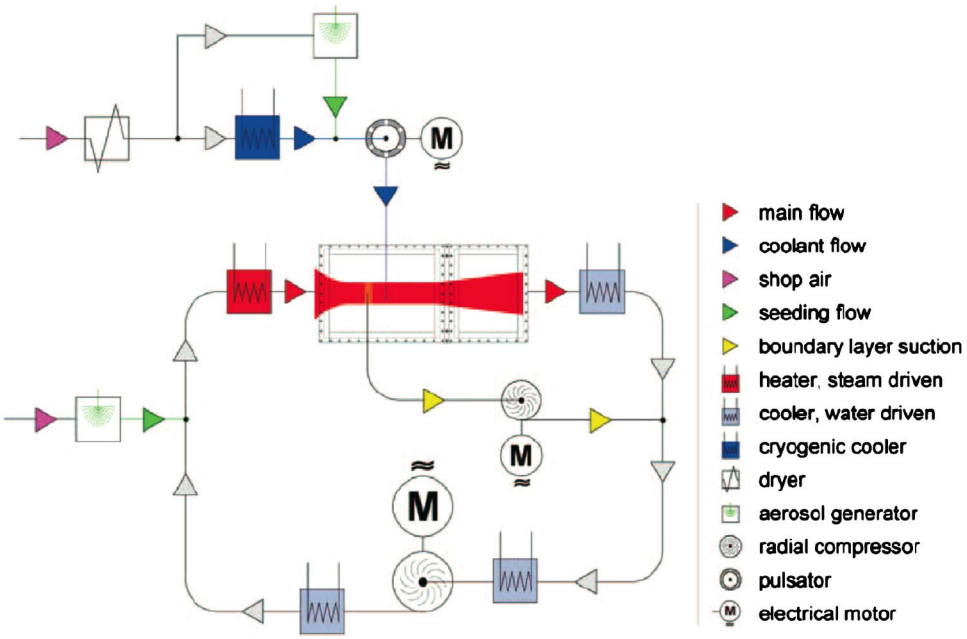

Fig. 2 Schematic of the test rig

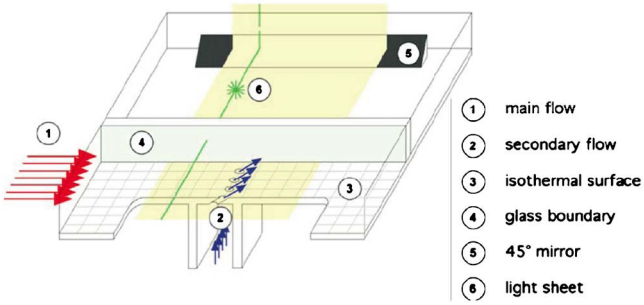

Fig. 3 Schematic of the injection arrangement

The test section consists of a rectangular flow path of 40 $\times$ 181 mm^2 cross section. The area of main interest is near the injection site of the secondary flow until the 35*d* downstream of the origin of coordinates. The 15 mm glass walls on three sides provide optical access. The top and bottom walls allow access for the light sheet. The laser light sheet is introduced into the system from the front and deflected by 90 deg, as shown in Fig. 3.

Particle Image Velocimetry System. The PIV system used in this project is a commercially available stereo PIV system. Two charge coupled device (CCD) cameras with a resolution of 1280 $\times$ 1024 pixels and a dynamic range of 12 bits are mounted on a two-axis high accuracy traverse system, as shown in Fig. 4. A double-pulsed Nd:YAG (yttrium aluminum garnet) laser with 120 mJ of energy per pulse is mounted on an additional traverse

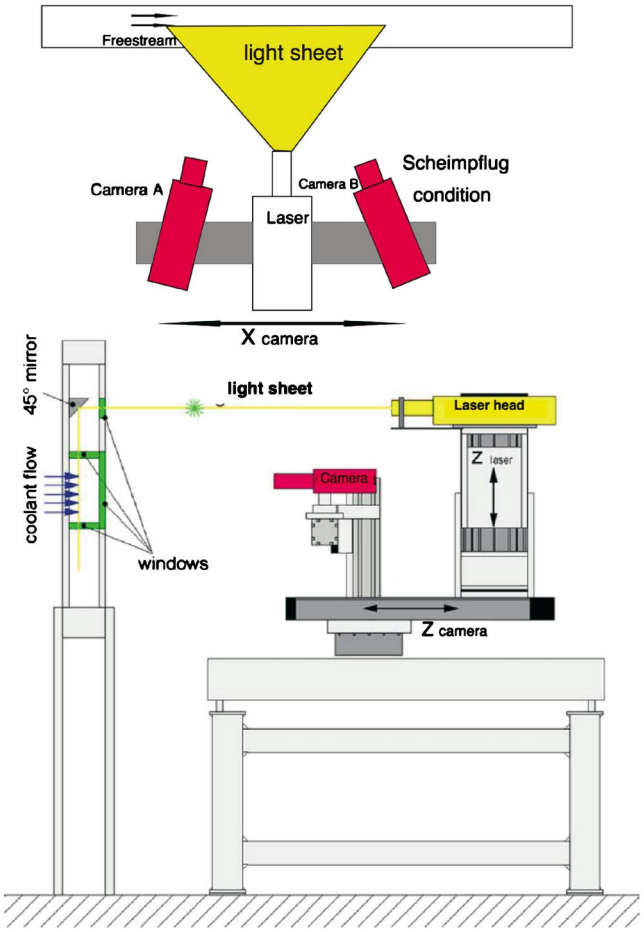

Fig. 4 Schematic and diagram of the stereoscopic PIV Mounting

axis. The light sheet optics create a light sheet with *XY* orientation and variable thickness. Simultaneous traversing of the laser in the vertical direction while traversing the cameras in the horizontal direction allows the scanning of the flow volume in the *Z* direction without the need for recalibration at every light sheet position.

The system also consists of two linked computers. The first computer is a specialized device containing the frame-grabber cards and the unit to synchronize the cameras and the laser. It also functions as a data buffer between the second computer and the cameras. The second computer is a standard PC for storage of images and their subsequent postprocessing.

Measurement Procedure. First, the flow parameters are adjusted with the aid of the real-time monitoring system. Forty primary data channels (pressure, temperature, frequency, and mass flow) are acquired directly from their corresponding sensors. These are written to file together with ten derived flow parameters. The most relevant parameters such as main flow Mach number, BR, and DR are shown online, thus allowing their fast and accurate adjustment.

The measurement of PIV data starts off with a camera calibration procedure, error assessment, and, finally, the actual measurement and postprocessing. The PIV system is used with two cameras at different angles to the test surface. Double pictures separated by a time step of 2.5 μs are taken for all experiments. The field of view of a camera is around 45 $\times$ 36 mm^2. The corresponding displacement between the two frames of a seeding particle traveling with the freestream main flow velocity of 110 m/s is close to eight pixels. The cameras are adjusted so that they look at the same area of the flow. Then, they are focused according to the Scheimpflug condition, and the light sheet is adjusted to be parallel to the *XY* coordinates of the flow and to have a defined thickness of 1 mm. The three traverse axes are adjusted to be parallel to the *X*, *Y*, and *Z* axes (described in Fig. 1).

The calibration is performed with the aid of a single layer calibration target, consisting of a flat black plate with white points. The coordinate system nomenclature is shown in Fig. 1. The target is placed into the test section parallel to the *XY* plane. The points are arranged in a 2D array of constant spacing and have three different sizes. The difference in size defines the center of the target and the orientation. Both cameras take pictures of that target in five defined distances orthogonal to the target. The PIV software detects the points and determines a linear transformation matrix for each camera. This matrix allows the transformation of the pictures taken in the respective orientation of each camera into the flow coordinate system. Furthermore, the two matrices allow the transformation of the two 2D vector fields, derived from each camera, into one vector field in the *XY* plane with 3D flow vectors.

Validation is carried out using sandpaper as the target and traversing the cameras in such a way so as to create a virtual velocity field of 100 m/s in one direction and 0 m/s in the other directions. The results show that the error for the *U* and *V* components is of the order of 1% of the virtual freestream velocity (U = 100 m/s), while the error for the *W* component is about 5%. These errors incorporate the complete error in the measurement system including the random error, processing errors, etc.

Each velocity vector is created by averaging 50 double frames for each condition. The mean of these images is then subtracted from every raw image to negate background reflection. The subtracted images are subjected to the cross-correlation procedure described hence. The velocity vectors so obtained are themselves subsequently averaged, and using the 3D transformation matrix from the calibration procedure, a 3D vector map for that plane is obtained.

The final cross correlation on every single frame is performed with 32 $\times$ 32 pixel interrogation windows to obtain a vector field. Further features used in the correlation are 50% overlap of the

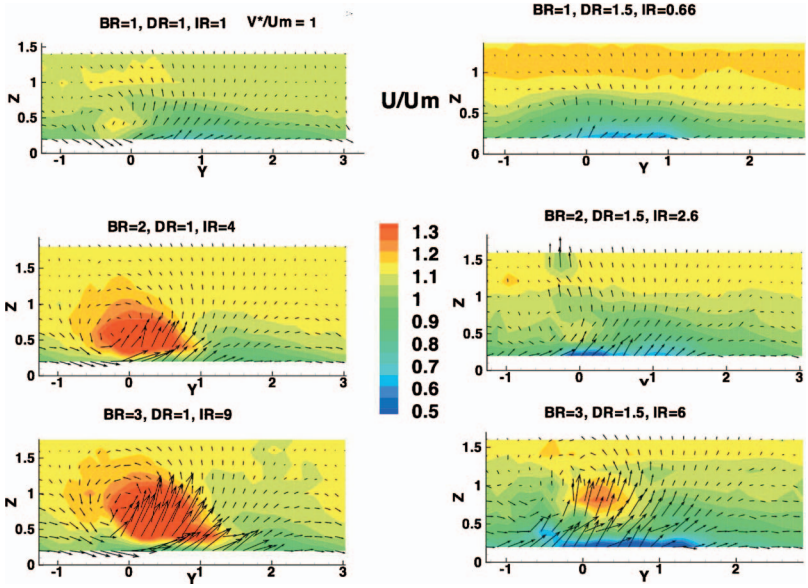

Fig. 5 Flow vectors and contours of normalized axial velocity at $X=2$ for different flow conditions

areas, one-step iterative refinement of the interrogation area with deforming windows, high accuracy subpixel refinement, and peak validation with a ratio between the minimum peak height and peak 2 of 1.1. A local moving average validation over 3×3 vectors with an acceptance factor of 0.1 is chosen as a local neighborhood validation. A Gaussian weighting function is applied to each interrogation area to deal with the particles at the border of the interrogation area. A detailed description of the options used can be found in the manufacturer's software manual [26].

The flow field is scanned in the Z direction in increments of 1 mm. All resulting planes are combined in a flow volume containing the three component flow vectors as well as a number of derivatives such as flow angle, vorticity, and shear stress. The flow volume consists of eight to nine planes with 79×63 vectors, giving a total number of roughly 50,000–60,000 data points.

Flow Conditions. The coolant was injected in a steady state manner. The Mach number of the freestream, M, was held constant at 0.3 while the BR and DR were varied. The flow conditions measured were

1. $M=0.3$, BR=1, DR=1.55, IR=0.64
2. $M=0.3$, BR=1, DR=1, IR=1
3. $M=0.3$, BR=2, DR=1.55, IR=2.6
4. $M=0.3$, BR=2, DR=1, IR=4
5. $M=0.3$, BR=3, DR=1.55, IR=6
6. $M=0.3$, BR=3, DR=1, IR=9

The parameters are defined globally. The momentum thickness was quantified before the PIV measurement campaign with a three hole pneumatic probe. The momentum thickness, nondimensionalized by the hole diameter, has a constant value of $\theta=0.051$, with a shape factor of $H=2.3$. However, this value is due to the fact that most of the boundary layer is sucked off by the suction apparatus upstream of the cooling holes. In spite of that, the velocity profiles show good correspondence to the 1/7-power approximation for turbulent boundary layers in the region of interest.

The density of the main flow is derived from the pressure and temperature taken just upstream of the cooling holes. The velocity of the main flow is derived from its directly measured mass flow rate, the cross section of main flow area, and the aforementioned density. The density of the coolant flow is derived from the pressure and temperature taken in the plenum upstream of the cooling holes. The velocity of the coolant flow is derived from its directly measured mass flow rate, the total cross section of all cooling holes, and the aforementioned density. With that, the above-stated parameters BR, DR, and IR are defined. The main flow Mach number is derived from the velocity and the speed of sound at the main flow temperature.

Results and Discussion

The PIV results are discussed in this section. In all the figures, the main flow direction is from $X=0$ to $X>0$. The actual hole center lies at the origin of the coordinate system and is not shown in any of the plots to obviate any noise from reflections near the holes. All the distances are nondimensionalized by the hole diameter $d=5$ mm. All the velocities are nondimensionalised by the freestream velocity U_m for that particular case. The vorticity is also given in a nondimensional form based on the nondimensional velocity and distances. Vectors in a 2D plot are tangent vectors in the plane shown.

First, a comparison of the secondary flow structure is made under varying BR, DR, and IR. Subsequently, some representative cases are analyzed to bring out details about the general structure of such a shallow angled, compound angle film-cooling flow.

Figure 5 shows a comparison of the flow structure for different BRs and DRs. The nondimensionalised horizontal velocity U/U_m is visualized as emerging out of the plane of the paper. The planes are visualized at $X=2$. If this flow structure is compared with the streamwise injection of Ref. [17], two features stand out even under a cursory glance, the foremost being the absence of a CVP, which is replaced by one large asymmetrical vortex as its partner vortex merges into the boundary layer (in Fig. 5, the boundary layer may be said to be limited by the green bands in the contours corresponding to $U/U_m=0.95$). This observation of the absence of the dominant single vortex is also visible in a computational work dealing with compound angled holes, e.g., Ref. [13].

The second feature is the large lateral extent or spread of the jet quite close to the point of injection compared to a streamwise injection case. It was this greater spread of the coolant over the surface that was the primary argument for using compound angled holes in the first place. With increasing IR, not only does the boundary layer become thinner but the size of the asymmetrical vortex is also seen to become greater. The figures in the right-hand column of Fig. 5, having a greater DR, show a more diffuse cen-

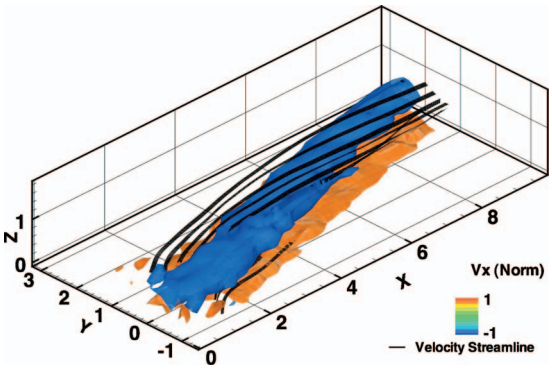

Fig. 6 Streamwise vorticity isosurfaces with velocity streamlines for BR=2, DR=1, and IR=4

tral jet core than a corresponding one at the same BR but lower DR. The figures suggest a greater transfer of horizontal momentum by the high DR jets to the boundary layer. The pileup of the boundary layer on one side of the vortex due to the higher DR is also a result of this. The lateral spread of the jet is responsible for the higher film-cooling effectiveness for compound angled holes with respect to streamwise holes, as conjectured in Ref. [7] and also observed in the experimental works [9,10]. On comparing the lateral spread with that of Ref. [17], the greater lateral spread of the coolant from a compound angled hole is apparent. Hence, this fact adds certainty to the conjectures expressed in those studies.

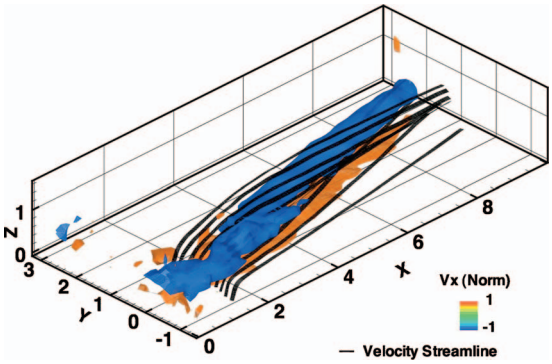

Fig. 7 Streamwise vorticity isosurfaces with velocity streamlines for BR=2, DR=1.55, and IR=2.6

Isosurface plots of vorticity in the *X* direction (streamwise) are shown for two representative cases in Figs. 6 and 7. It constitutes mainly the vorticity produced in the holes. The velocity streamlines are also plotted on the same graph to better visualize the effect of the primary vortex core. It is clear from Fig. 6 that the primary vortex core is highly asymmetrical in the sense that there are no two vorticity "tubes" of opposite signs extending side by side. The clockwise or positive vorticity (shown as the orange layer in the figure) merges into the shear layer from the wall-bounded flow. The vortex core is responsible for piling up the boundary layer on one side while thinning it on the other. The velocity streamlines in the same figure describe the path taken by the fluid just downstream of the holes. The primary vortex core is seen to deviate the coolant fluid as well as the fluid entrained from the boundary layer away from itself, aligning it in the direction of the freestream flow. Figure 7 shows the same plot for a higher DR case. Owing to the greater DR, the IR is lower, and hence there is lesser vorticity. The vortex core has a smaller size as reckoned by its lateral spread, compared to Fig. 6. The velocity streamlines highlight the fact that hotter fluid from the layers above the coolant jet also get transported toward the surface. This may tend to increase the surface heat transfer in some regions even though the spread of the coolant is greater than that of a hole without a lateral angle.

The normal vorticity formed due to the interaction between the freestream flow and the emanating jet is shown in Fig. 8 for BR =2. This figure shows the normal vorticity, i.e., vorticity in the *Z* direction for two different DRs at the same BR. This normal vorticity consists of the wall-normal component from the jet and the freestream. These may be thought of as analogous to wake vortices in straight jets in cross flows. Wake vortices have been shown to be responsible for vorticity transport and mixing between the boundary layer and the jet in Ref. [21]. As a sign convention, in Fig. 8, the blue zones are regions of anticlockwise rotation while the warmer colors are those of clockwise rotation. Label A shows

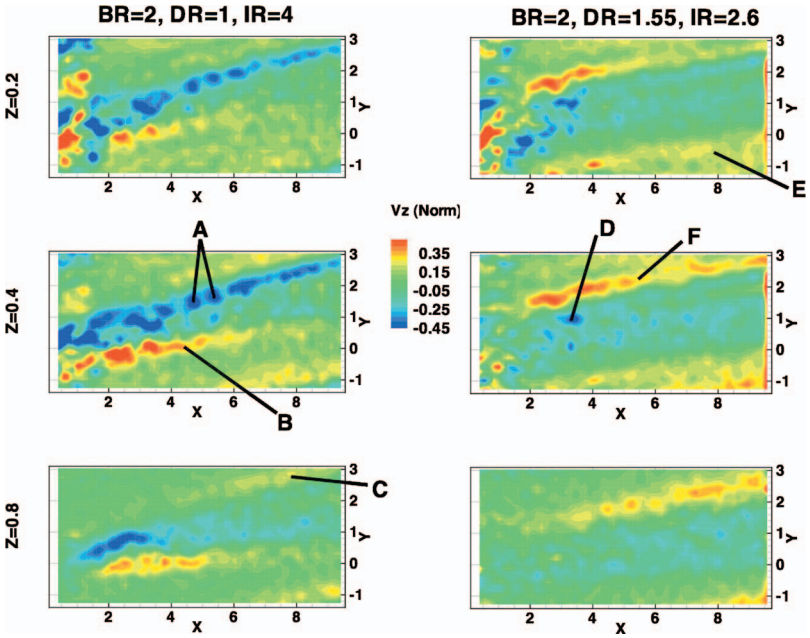

Fig. 8 Normal vorticity for BR=2, DR=1 and BR=2, DR=1.55 at different vertical *Z* planes

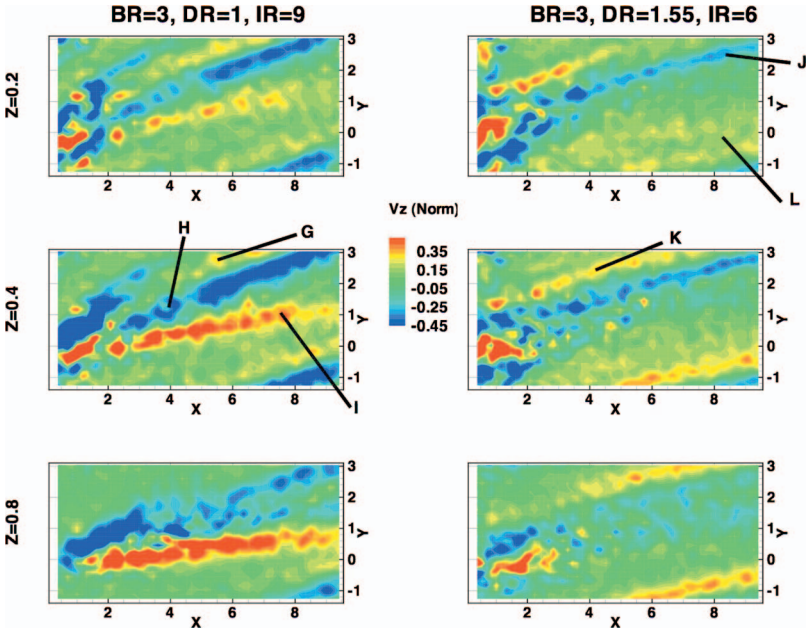

Fig. 9 Normal vorticity for BR=3, DR=1 and BR=3, DR=1.55 at different vertical *Z* planes

the vorticity directly involved in the mixing process between the boundary layer and the coolant jet. The region marked C is produced on the opposite side of the jet from the origin of A, and thus has an opposite sign. Region C, which appears symmetric to A in a streamwise injection, is seen to have reduced to some extent. This dwindling of C may be linked to the uneven shear layer due to the skewed surface proffered by the jet angled to the freestream. Region B, on the other hand, which was observed as a weak remnant of the horseshoe vortex for a streamwise injection in Ref. [17], is in this case seen to be enhanced in size and strength. For the higher DR case, D, which corresponds to A, is seen to be spread out over a spatially larger region as well as subjected to a greater deviation from its initial trajectory and is more aligned with the freestream flow. Zone E corresponding to B is much weaker. F, on the other hand, is clearly visible as the vortex street of opposite sign from that of D. Unlike C, F strongly participates in the mixing between the boundary layer and the jet. Figure 9 shows a similar plot as that of Fig. 8 for a BR=3 case. The zones G, H, and I correspond to J, K, and L, respectively, just like in the previous figure. It is observed that the vortex structure of the higher DR cases, for both BRs shown, is similar to each other but markedly different from the vortex structure for a flow with no temperature difference between the main and injected flows. The DR, through the temperature difference between the two streams, seems to affect the vorticity even more than the IR. The enhanced vorticity of K and the relatively greater separation between J and L, compared to the proximity between H and I, are similar to the observations in Fig. 8. For the DR=1.55 cases, the relatively spread out normal vorticity indicates a greater vorticity exchange between the boundary layer and the primary vortex core. The vorticity regions of G and K are found at the interface where the outermost extent of cool fluid interacts with the hotter freestream flow. The vortex structures suggest a greater transfer of momentum and vorticity between the emanating jet and the surrounding fluid, which are therefore the artifacts of the density differences between the two interacting flows. The heat transfer measurements of Ref. [7] bear this fact as the higher IR and lower DR jet in their study possesses greater lateral interaction leading to higher heat transfer coefficients along the direction of the hole angle β.

Echoes of the fact that boundary layer vorticity merges with the jet vorticity may be observed in Fig. 10, which shows two different isosurfaces of U/U_m (nondimensionalised streamwise velocity) for the IR=4 and IR=2.6 blowing conditions from two viewing angles for clarity. The freestream flow direction is from right to left in this case. One level (green) at $U/U_m=0.95$ indicates the boundary layer, and the second level (orange) at $U/U_m=1.25$ delineates the coolant jet.

The obvious difference in the trajectories of the wall boundary layer and the coolant jet can be explained by the combined mixing action of the "wake" vortices (normal vorticity) and primary vortex core (streamwise jet vorticity). By closely observing this figure in conjunction with Figs. 6 and 7, it can be seen that the streamwise vorticity, because of its asymmetrical nature, adds a horizontal velocity component to the coolant flow and causes it to swirl as well. This has the net effect of leaching the momentum of the coolant in its original injected direction until it gets aligned with the direction of the freestream. The temperature profiles of a

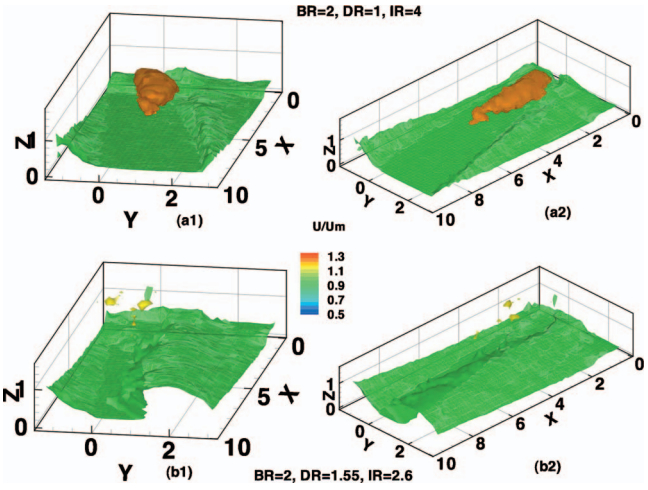

Fig. 10 Horizontal velocity isosurfaces for $U/U_m=0.95$ and $U/U_m=1.2$ at BR=2, DR=1 (*a*1) and (*a*2) and BR=2, DR=1.55 (*b*1) and (*b*2)

compound angle film-cooling jet in the computational works in Ref. [13] also predict the aligning of the jet with the freestream direction a few diameters downstream of the hole. This tendency of alignment is quite apparent in Fig. 10.

Additionally, the jet's high velocity core becomes very diffuse, as visible by the tapering shape of the isosurface of $U/U_m=1.25$ in Fig. 10. The streamwise vorticity causes the boundary layer to pile up on one side by entraining fluid from the other, as a consequence of its asymmetrical nature. The effect of this is visible as the spanwise spreading of the thinned boundary layers in ($a1$) and ($a2$) of Fig. 10. The growth and subsequent entrainment of the vortex increase the area over which this entrainment occurs. The heat transfer coefficient measurements in Ref. [7] show the enhancement along the direction of the hole angle β much in the same way that Fig. 10 shows the thinned boundary layers along the hole angle β. The higher heat transfer coefficients are, therefore, because of the trajectory of the thinned boundary layer, even though the jet trajectory aligns itself with the main flow direction a short distance from hole exit.

One of the important conclusions of the computational study in Refs. [13,7] is that compounding leads to higher heat transfer coefficients along the line of the lateral angle compared to streamwise injection. This can be explained by the thinning boundary layer following the trajectory of the primary vortex core aligned in the direction of the lateral hole. However, Ref. [13] also concluded that compounding causes greater film-cooling effectiveness because of greater flow uniformity and lateral spread. Figure 10 precisely emphasizes that conjecture.

For the lower IR case and DR=1.55 for the same BR=2, the coolant is almost enveloped by the wall-bounded flow. The lower vorticity combined with the faster diffusion of horizontal momentum from the coolant jet leads to a greater spread of the coolant. For this case, the boundary layer is piled up over a much greater spatial extent, while its trajectory is maintained. A higher adiabatic film effectiveness would be expected from this lateral spread, which is borne out by surface heat transfer measurements in Refs. [10,13] for a similar geometry.

These observations find resonance with the heat transfer measurements of Ref. [7]. For the same BR, it was observed that the lower DR (and, therefore, higher IR) flow had higher heat transfer coefficient. Figure 10 clearly shows the thinner boundary layer compared to that in the case of higher DR, thereby providing the explanation for the heat transfer observations.

Conclusions

3D PIV is used to investigate the flow structure of a shallow surface-angle compound angled film-cooling hole row over a flat plate at different BRs and DRs leading to different IRs. The results reveal the skewed vortex structure of the jet wherein one part of the classic CVP structure associated with jets in cross flows has diminished considerably, leading to the preponderance of a single vortex. The cross-plane velocity contours and vorticity plots provide data for a convenient comparison of computational efforts that would seek to capture the flow structure as a starting point in predicting heat transfer. The detailed analysis provides an intuitive understanding of the complex wall-bounded flow.

No injectant lift-off was observed even at BR=3 for this geometry. The trajectory of the jet vorticity is aligned with the initial injection angle, whereas the coolant jet with the highest momentum is considerably made to deviate from its initial injection angle by the vorticity and entrainment effects thereof and aligned with the freestream direction. Higher BR tends to increase the pileup of the boundary layer on one side of the emanating jet at the expense of the boundary layer from the other side, thereby thinning it, as was visible from the isovelocity contours. The isovelocity contours lead to an intuitive understanding by showing clearly the interaction of the jet with the boundary layer and the thinning of the boundary layer on one side, with a pileup on the other side due to the entrainment from the jet.

This thinning would lead to higher heat transfer to the surface which is borne out by existent wall heat transfer measurements. However, contradictorily, such an arrangement also causes greater film-cooling effectiveness because of the greater spread of the coolant. The vortical structure of a compound angled jet has some distinct characteristics that could explain this observation. The streamwise vortex is closely linked with the wall flow and maintains its trajectory after ejection from the hole. The bulk of the coolant mixes rapidly with the freestream by the combined action of the normal vortices and the primary streamwise vortex core, and it is made to deviate and align with the freestream direction after ejection. The high DR leads to some changes in the vortex structure, which causes a greater spread of normal vorticity in a spanwise direction. The loss of horizontal jet momentum and faster integration into the boundary layer of the coolant can also be noted for a high DR and a low IR injection. Compared to a simple streamwise injection, usage of a compound angled hole increases the coolant spread, and this is maintained even at high IR. Hence, a greater adiabatic film effectiveness is expected. This is borne out by many published surface measurements. The behavior of the jet and vortical flow for the compound angled film-cooling hole had previously been conjectured through surface heat transfer measurements. This study adds certainty to many of those conjectures and also explores the vortical structure of such flows in detail to better enable models to capture the precise flow physics.

The measurement of unsteady film-cooling flow structure for compound angled holes with some different lateral angles and surface heat transfer is proposed as future work to build on the experimental database.

Acknowledgment

The authors would like to acknowledge the support of GE Aviation through their University Strategic Alliance Program. Specifically, the technical interactions with Dr. Robert Bergholz and Dr. Fred Buck have been helpful in the formulation of this project. The facility would not have been built without Hans Suter, Thomas Kuenzle, Peter Lehner, and Christoph Raeber.

Nomenclature

- X = axial (streamwise) coordinate
- Y = lateral coordinate
- Z = vertical coordinate
- U,V,W = mean velocity components
- V^* = velocity magnitude YZ plane$=(V^2+W^2)^{1/2}$
- ρ = density
- M = Mach number
- P = static pressure
- T = total temperature
- D = hole diameter
- S = pitch distance between two holes
- L = length of the hole pipe
- β = injection angle with respect to the surface of the flat plate
- ϕ = surface lateral angle between the major axis of the hole and streamwise direction
- BR = blowing ratio, $\rho_c U_c/\rho_m U_m$
- DR = density ratio, ρ_c/ρ_m
- IR = momentum flux ratio, BR^2/DR
- V_x = normalized streamwise vorticity, $\partial W/\partial Y-\partial V/\partial Z$
- V_y = normalized cross-stream vorticity, $\partial U/\partial Z-\partial W/\partial X$
- V_z = normalized normal vorticity, $\partial V/\partial X-\partial U/\partial Y$
- Tu = turbulence intensity, U'/U_∞
- δ^* = displacement thickness, $\int(1-U/U_m)dx$
- θ = momentum thickness, $\int U/U_m(1-U/U_m)dx$
- H = shape factor, δ^*/θ

η = adiabatic effectiveness, $(T_{\text{recovery}} - T_{\text{adiabatic wall}})/(T_{\text{recovery}} - T_c^{\text{total}})$

h = heat transfer coefficient

Subscripts

c = coolant fluid

m = freestream fluid

Superscripts

$'$ = instantaneous value

∞ = time averaged value

References

[1] Abhari, R. S., and Epstein, A. H., 1994, "An Experimental Study of Film Cooling in a Rotating Transonic Turbine," ASME J. Turbomach., **116**, pp. 818–827.

[2] Abhari, R. S., 1996, "Impact of Rotor-Stator Interaction on Turbine Blade Film Cooling," ASME J. Turbomach., **118**, pp. 123–133.

[3] Ligrani, P. M., Ciriello, S., and Bishop, D. T., 1992, "Heat Transfer, Adiabatic Effectiveness and Injectant Distributions Downstream of a Single Row and Two Staggered Rows of Compound Angle Film Cooling Holes," ASME J. Turbomach., **114**, pp. 687–700.

[4] Ligrani, P. M., and Ramsey, A. E., 1997, "Film Cooling From Spanwise-Oriented Holes in Two Staggered Rows," ASME J. Turbomach., **119**, pp. 562–567.

[5] Reiss, H., and Boelcs, A., 2000, "Experimental Study of Showerhead Cooling on a Cylinder Comparing Several Configurations Using Cylindrical and Shaped Holes," ASME J. Turbomach., **122**, pp. 162–169.

[6] Honami, S., Shizawa, T., and Uchiyama, A., 1994, "Behaviour of the Laterally Injected Jet in Film-Cooling-Measurements of Surface-Temperature and Velocity-Temperature Field Within the Jet," ASME J. Turbomach., **116**(1), pp. 106–112.

[7] Ekkad, S. V., Zapata, D., and Han, J. C., 1997, "Heat Transfer Coefficients Over a Flat Surface With Air and CO_2 Injection Through Compound Angle Holes Using a Transient Liquid Crystgal Image Method," ASME J. Turbomach., **119**(3), pp. 580–586.

[8] Dittmar, J., Schulz, A., and Wittig, S., 2003, "Assessment of Various Film-Cooling Configurations Including Shaped and Compound Angle Holes Based on Large-Scale Experiments," ASME J. Turbomach., **125**, pp. 57–64.

[9] Sen, B., Schmidt, D., and Bogard, D., 1996, "Film Cooling Compound Angled Holes: Heat Transfer," ASME J. Turbomach., **118**, pp. 800–806.

[10] Schmidt, D., Sen, B., and Bogard, D., 1996, "Film Cooling With Compound Angle Holes: Adiabatic Effectiveness," ASME J. Turbomach., **118**, pp. 807–813.

[11] Jung, I. S., and Lee, J. S., 2000, "Effects of Orientation Angles on Film Cooling Over a Flat Plat: Boundary Layer Temperature Distributions and Adiabatic Film Cooling Effectiveness," ASME J. Turbomach., **122**(1), pp. 153–160.

[12] Walters, D. K., and Leylek, J. H., 2000, "A Detailed Analysis of Film-Cooling Physics: Part 1—Streamwise Injection With Cylindrical Holes," ASME J. Turbomach., **122**, pp. 102–112.

[13] McGovern, K. T., and Leylek, J. H., 2000, "A Detailed Analysis of Film-Cooling Physics: Part II—Compound Angle Injection With Cylindrical Holes," ASME J. Turbomach., **122**, pp. 113–121.

[14] Hyams, D. G., and Leylek, J. H., 2000, "A Detailed Analysis of Film-Cooling Physics: Part III—Streamwise Injection With Shaped Holes," ASME J. Turbomach., **122**, pp. 122–132.

[15] Brittingham, R. A., and Leylek, J. H., 2000, "A Detailed Analysis of Film-Cooling Physics: Part IV—Compound-Angle Injection With Shaped Holes," ASME J. Turbomach., **122**, pp. 133–145.

[16] Bons, J. P., MacArthur, C. D., and Rivir, R. B., 1996, "The Effect of High Freestream Turbulence on Film Cooling Effectiveness," ASME J. Turbomach., **118**(4), pp. 814–825.

[17] Bernsdorf, S., Rose, M., and Abhari, R. S., 2006, "Modeling of Film Cooling—Part 1: Experimental Study of Flow Structure," ASME J. Turbomach., **128**, pp. 141–149.

[18] Bernsdorf, S., 2005, "Experimental Investigation of Film Cooling Flow Structure," Ph.D. thesis, ETH Zurich, Zurich, Switzerland.

[19] Burdet, A., 2005, "A Computationally Efficient Feature-Based Jet Model for Prediction of Film-Cooling Flows," Ph.D. thesis, ETH Zurich, Zurich, Switzerland.

[20] Burdet, A., Abhari, R. S., and Rose, R. G., 2007, "Modeling of Film Cooling—Part II: Model for Use in Three-Dimensional Computational Fluid Dynamics," ASME J. Turbomach., **129**, pp 221–231.

[21] Fric, T. F., and Roshko, A., 1991, "Structure in the Near Field of a Transverse Jet," Turbulent Shear Flows, **7**, pp. 225–237.

[22] Kelso, R. M., Lim, T. T., and Perry, A. E., 1996, "An Experimental Study of Round Jets in Cross-Flow," J. Fluid Mech., **306**, pp. 111–144.

[23] Moussa, Z. M., Trischka, J. W., and Eskinazi, S., 1977, "The Near Field in the Mixing of a Round Jet With a Cross-Stream," J. Fluid Mech., **80**, pp. 49–80.

[24] Raffel, M., Willert, C. E., and Kompenhans, J., 2001, *Particle Image Velocimetry: A Practical Guide*, Springer-Verlag, Berlin/GmbH and Co., Heidelberg.

[25] Prasad, A. K., 2000, "Stereoscopic Particle Image Velocimetry," Exp. Fluids, **29**(2), pp. 103–116.

[26] Dantec Dynamics, 2002, Flow Manager Software and Introduction to PIV Instrumentation, Dantec Dynamics A/S.

A Criterion for Axial Compressor Hub-Corner Stall

V.-M. Lei

Z. S. Spakovszky

E. M. Greitzer

Gas Turbine Laboratory,
Department of Aeronautics and Astronautics,
Massachusetts Institute of Technology,
Cambridge, MA 02139

This paper presents a new criterion for estimating the onset of three-dimensional hub-corner stall in axial compressor rotors and shrouded stators. A simple first-of-a-kind description of hub-corner stall formation is developed which consists of (i) a stall indicator, which quantifies the extent of the separated region via the local blade loading and thus indicates whether hub-corner stall occurs, and (ii) a diffusion parameter, which defines the diffusion limit for unstalled operation. The stall indicator can be cast in terms of a Zweifel loading coefficient. The diffusion parameter is based on preliminary design flow variables and geometry. Computational simulations and single and multistage compressor data are used to show the applicability of the criterion over a range of blade design parameters. The criterion also enables determination of specific flow control actions to mitigate hub-corner stall. As an illustration, a flow control blade, designed using the ideas developed, is seen to produce a substantial reduction in the flow nonuniformity associated with hub-corner stall. [DOI: 10.1115/1.2775492]

Introduction

Modern compressor blades diffuse the flow efficiently over the middle 60–80% of the span, and the end wall and corner regions are thus key to aerodynamic blockage, loss production, and compressor stability. This paper is concerned with stalled flow in the hub region, more specifically the hub and suction surface corner region of rotors and shrouded stators. This hub-corner stall involves both the end wall and the blade suction surface. Its extent varies along both of these surfaces and it is thus inherently three dimensional.

Research on three-dimensional separation phenomena and stall covers a large range of flow situations. It is useful at the outset to define the regimes of interest in the present paper. Three-dimensional separation, as defined most generally, does not require a streamwise adverse pressure gradient to exist.[1] In the application addressed here, however, as shown by extensive computations (described below), the basic cause of the reversed flow in the corner of the blade suction surface and the end wall is the stagnation of low momentum fluid by adverse gradients.

Three-dimensional separation in axial compressors has been investigated in detail by Gbadebo et al. [3] who showed that reversed flow always occurs on the end wall as well as on the blade suction surface, irrespective of the pitchwise extent of the separated region. Put another way, separation always occurs, but does not imply stall,[2] which is defined in this paper as follows. In *qualitative* terms, stall can be viewed as a situation in which some aspect of the flow "has gone wrong"[3] and, as a result, a large extent of reversed flow exists, for example, the separation has become substantially larger than that at design conditions. In *quantitative* terms, we define below a stall indicator, denoted by S, which gives assessment of the extent of the separated region and indicates explicitly whether hub-corner stall occurs. In this context, the following nomenclature is used throughout the paper. If the stall indicator S is greater than 0.12, the terminology used is *hub-corner stall*, which is indicative of extreme excursions of the surface streamlines and large magnitude of flow reversals on *both* the blade suction surface and the end wall, as sketched in Fig. 1.

In capturing the physical mechanisms associated with hub-corner stall, the primary effects that must be described are the pressure rise and the state of the flow subject to this pressure rise. In this sense, the principal three-dimensional effect is the secondary flow, due to the cross-passage pressure gradient, which brings low stagnation pressure, low momentum fluid, into the hub-corner region. The criterion to be developed is based on this idea.

The mechanism of secondary flow is well described by Horlock et al. [4]. The end wall boundary layer has a lower velocity than, but experiences roughly the same cross-stream pressure gradient as, the freestream. The streamline radius of curvature near the end wall is thus smaller than in the freestream, leading to cross-passage motion and the accumulation of low stagnation pressure fluid near the suction surface hub corner. If the blade loading is high enough, this low stagnation pressure fluid is not able to negotiate the pressure rise in the blade passage and hub-corner stall occurs, increasing passage blockage, lowering the static pressure rise capability of the compressor blade row, and increasing the entropy rise from flow mixing downstream.

A large amount of work has been carried out on topology, numerical simulation, mitigation, and performance impact of hub-corner stall. What has not been provided, however, is a criterion for its occurrence. The development, evaluation, and application of such a criterion is the subject of this paper.

Scope and Organization of the Paper. The major goals of this paper are to develop a criterion for the formation of hub-corner stall in axial compressor blade rows and to assess it over a broad range of parameters using information from the literature and multistage compressor data from industry. The criterion consists of (i) a stall indicator, which defines *whether* three-dimensional hub stall exists, and (ii) a diffusion parameter, which defines *when* the flow diffusion limit associated with the onset of stall has been exceeded. A rough correspondence can be drawn between the diffusion parameter, and the well-known Lieblein diffusion factor (Lieblein [5], Kerrebrock [6], and Cumpsty [7]), which shows under what conditions two-dimensional blade stall occurs. Similarly, the three-dimensional stall indicator has an analogous role to

[1]For example, separation, with boundary layer fluid moving off the wall, occurs along the symmetry line on the end wall of a rectangular nozzle, where the streamwise pressure gradient is favorable (Greitzer et al. [1]). This type of three-dimensional separation, however, is associated with the confluence of boundary layer fluid due to cross-flow (Lighthill [2]) rather than by the inability of low stagnation pressure fluid to negotiate a pressure rise. In addition, there is no stagnation of the separating fluid, and the primary effect is rather a change of direction as the fluid leaves the wall.

[2]We are indebted to Professor N. A. Cumpsty for his clarifying comments on this point.

[3]We have found this phrase, due to Professor N. A. Cumpsty, useful in dispelling ambiguity surrounding discussions of the qualitative definition of compressor stall.

Contributed by the International Gas Turbine Institute of ASME for publication in the JOURNAL OF TURBOMACHINERY. Manuscript received July 28, 2006; final manuscript received February 12, 2007; published online May 2, 2008. Review conducted by David Wisler. Paper presented at the ASME Turbo Expo 2006: Land, Sea and Air (GT2006), Barcelona, Spain, May 8–11, 2006, Paper No. GT2006-91332.

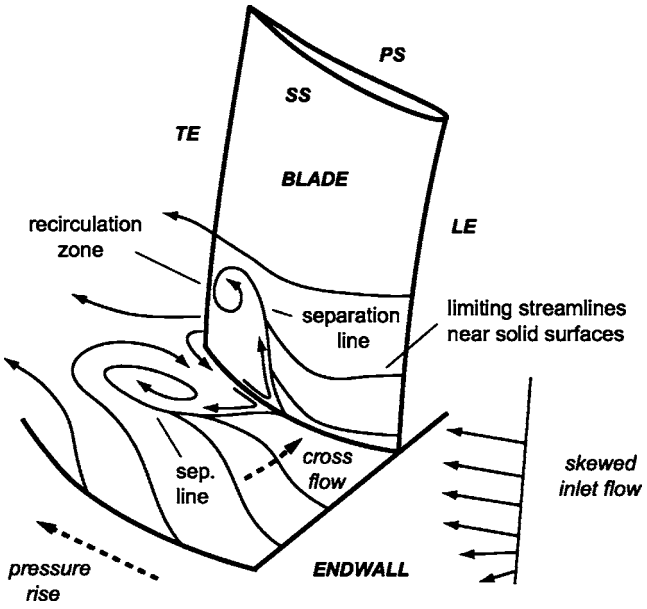

Fig. 1 Basic processes governing the formation of hub-corner stall together with limiting streamlines and separation lines

blade pressure distribution (loading), which shows whether (two-dimensional) stall has occurred.

The concept that underpins the formulation of the three-dimensional stall indicator is quantification of the extent of the hub-corner stall via local blade loading. The diffusion parameter is based on flow variables associated with hub-corner stall and geometric variables for an "equivalent" ideal blade passage. The approach involves the combination of numerical simulations, experiment, and modeling of flow mechanisms in the end wall region.

The paper is organized as follows. First, previous work on hub-corner stall is briefly reviewed. The hub-corner stall process and its characteristics are then described qualitatively and the features that underpin the criterion discussed. Following this, the stall indicator is formulated and cast in terms of a Zweifel loading coefficient. Next, the diffusion parameter is constructed, with justification for the steps in the formulation, from three-dimensional flow simulations. The diffusion parameter and its attributes are also compared with the Lieblein diffusion factor to place the two ideas in context. The criterion for the formation of hub-corner stall is then defined.

The applicability and the limitations of the criterion are evaluated using extensive CFD simulations as well as single and multistage axial compressor data. The criterion is also used to define the flow control processes necessary to alter the hub-corner stall. Results are reported from a linear compressor cascade flow control experiment based on these principles. Finally, the implications and conclusions of the research are summarized.

Previous Work on Three-Dimensional Separation. The impact of three-dimensional separation on end wall loss generation and compressor performance has been investigated by a number of researchers. Some features relevant to this discussion are the increase in the growth of the reversed flow region with blade loading (Joslyn and Dring [8] and Barankiewicz and Hathaway [9]), the use of three-dimensional blade designs (e.g., bowing) to increase compressor efficiency (Breugelmans et al. [10], Shang et al. [11], and Weingold et al. [12]), the transport of low momentum fluid by the secondary flow (Gallus et al. [13], Hah and Loellbach [14], and Schulz et al. [15]), and the overall characterization of the separation including reversed flow and recirculation near the end wall (Schulz and Gallus [16] and Weber et al. [17]).

The topology of three-dimensional compressor separation has been described in depth by Gbadebo et al. [3] using the concept of critical points. They established topological rules, which define the properties of the limiting streamlines and singularities. As the number of singularities increased, the thickness of the separated region and the losses also increased. Flow visualization (both experimental and numerical) showed flow reversal on both the blade suction surface and the end wall, although for the loading conditions examined, the separated region was confined mostly to the suction surface and thus did not resemble the hub-corner stall that we describe.

A further feature, to be addressed subsequently, is related to the interaction of the main gas path and the nongas path flows, for example, hub cavity leakages in shrouded stators. Demargne and Longley [18] and Wellborn and Okiishi [19] demonstrate that the strength of the secondary flow in the blade passage, which is affected by the leakage flow and the skew of the incoming end wall boundary layer, is related to the extent of the three-dimensional separation.

A final feature with which we will deal relates to attempts to mitigate the extent of compressor hub-corner separation through flow control, as first reported by Peacock [20] and Stratford [21]. More recently, Culley et al. [22] and Kirtley et al. [23] have explored the effects of suction surface blowing, both steady and unsteady, reporting a 25% reduction in loss from injection of 1% of compressor mass flow [22], although this did not account for work associated with the delivery of the injection fluid. Their results suggest that air injection from the suction surface is relatively ineffective in mitigating end wall loss, but it is shown below that this is not a general conclusion and that ideas developed herein enable reduction of three-dimensional separation using suction surface injection.

Development of a Criterion for Hub-Corner Stall

As introduced earlier, the basic processes governing the formation of hub-corner stall are (1) the adverse pressure gradient in the blade passage, (2) the cross-flow from pressure to suction side due to the overturning of the fluid near the end wall inside the blade passage, which brings low momentum fluid to the hub-corner region, and (3) the condition and skew of the incoming end wall boundary layer flow, which affects the strength of the cross-flow and the resistance to reversal. The situation is illustrated in Fig. 1 including the limiting streamlines near the solid surfaces and the separation lines that demarcate the region of separated flow. The three processes are fundamental pieces in establishing the three-dimensional flow diffusion parameter and the hub-corner stall indicator.

Hub-Corner Stall Indicator. Hub-corner stall, as defined in this paper, is characterized by extreme excursions of the surface streamlines and a large magnitude of flow reversal on both the blade suction side and the end wall. The consequences are an increase in blockage and a decrease in local blade loading relative to the midspan region. As depicted in Fig. 1, a distinct feature of hub-corner stall is the decrease of its chordwise extent away from the end wall. The idea behind the stall indicator is to quantify the extent of the hub-corner stall via the reduction in local blade loading relative to flow conditions outside the separated region. Assuming that such conditions occur at midspan, the size and strength of the hub-corner stall can be expressed as the difference between the loading at midspan and in the end wall region[4] as, where $AR = L/c$ is the blade aspect ratio,

[4]As shown later, the stall indicator S correlates best with the diffusion parameter if the loading near the end wall is evaluated at a spanwise location of 10% chord. This is within the end wall boundary layer thickness in multistage compressors but sufficiently away from the end wall surface to avoid interference with localized low pressure regions associated with spanwise turning of the cross-flow in the hub corner. To generalize different blade passage geometries, the calculations suggest nondimensionalizing the spanwise distance by chord.

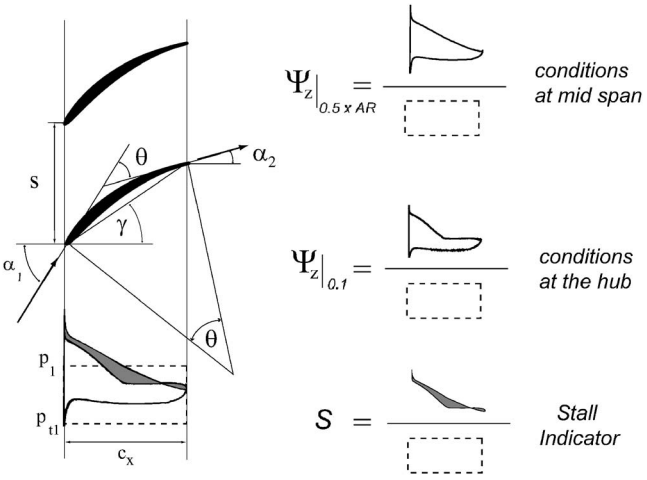

Fig. 2 Definition of the Zweifel loading coefficient and relation to the stall indicator *S*

$$S = \left[\int_0^1 \frac{p_{ps}(x) - p_{ss}(x)}{p_{t1} - p_1} \left(\frac{dx}{c_x} \right) \right]_{z/c=0.5\mathrm{AR}} - \left[\int_0^1 \frac{p_{ps}(x) - p_{ss}(x)}{p_{t1} - p_1} \left(\frac{dx}{c_x} \right) \right]_{z/c=0.1} \quad (1)$$

Introducing a Zweifel blade loading coefficient Ψ_z, the stall indicator S in Eq. (1) can be written compactly as

$$S = \Psi_z|_{0.5\mathrm{AR}} - \Psi_z|_{0.1} \quad (2)$$

The Zweifel loading coefficient is defined as the ratio of actual blade loading, to the blade loading, which would exist with isentropic diffusion to stagnation conditions. This ideal loading is represented by the inlet dynamic head times the chord length, as denoted by the rectangular area in Fig. 2. The Zweifel loading coefficient can be viewed as the ratio of the area defined by the chordwise integral of surface pressures (actual blade loading) to the rectangular area. As the separated flow region near the end wall occupies a larger and larger spatial extent, the Zweifel loading coefficient near the hubcorner decreases relative to the value at midspan. The stall indicator S thus increases.

Diffusion Parameter Development. Dimensional analysis shows that the stall indicator is a function of the following (many) nondimensional parameters:

$$S = S(M, \mathrm{Re}, \delta/c, \mathrm{AR}, \sigma, \gamma, \theta, \alpha_1, \alpha_2, \Delta\beta) \quad (3)$$

where M is the inlet relative Mach number, Re is the Reynolds number based on blade chord, δ is the incoming boundary layer thickness, AR is the blade aspect ratio, σ is the solidity, γ is the blade stagger angle, θ is the blade camber angle, α_1 and α_2 are the flow inlet and exit angles, respectively, and $\Delta\beta$ characterizes the additional flow turning associated with the skew of the incoming end wall boundary layer.

To establish a criterion for the formation of hub-corner stall, a parameter that reflects the three-dimensional diffusion limit needs to be formulated. The hypothesis is that those parameters, which measure the effects of streamwise pressure rise (and gradient), the cross-flow pressure difference (and gradient), and the state and skew of the incoming end wall boundary layer, will capture the mechanisms in the hub-corner stall process. If so, the groups related to these effects can be brought into a nondimensional diffusion parameter D such that

$$D = D(\sigma, \gamma, \theta, \alpha_1, \alpha_2, \Delta\beta) \quad (4)$$

The stall indicator can now be, at least notionally, reduced to

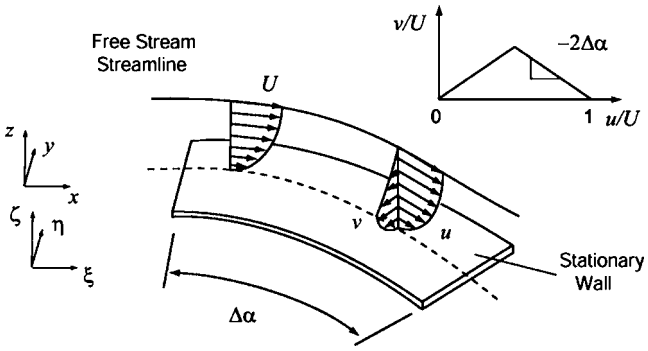

Fig. 3 Cross-flow in the end wall region

$$S = S(M, \mathrm{Re}, \delta/c, \mathrm{AR}, D) \quad (5)$$

Although Eq. (5) is, so far, little more than regrouping of terms, it gives a prelude to simplifications that are sought. To move further, numerical flow field simulations of candidate stator blade passage geometries were conducted to assess the sensitivity of the stall indicator S to inlet Mach number, Reynolds number, inlet boundary layer thickness, and blade aspect ratio. For fully turbulent, subsonic flow, the stall indicator was found to have little or no appreciable sensitivity to these parameters (this is discussed in depth later). The task of developing the stall criterion can therefore be reduced to determining the functional form of the diffusion parameter for hub-corner stall, Eq. (4).

In what follows, a rationale is presented in support of the development of this functional form. We emphasize that the different steps in the overall chain should be regarded as plausibility arguments, i.e., qualitative arguments which suggest what the form might be. These serve as a guide only and the final form is extracted from, and based on, the results of a large number of three-dimensional computations for blade rows of different geometries.

As a start, consider the overall pressure rise in a two-dimensional blade passage. Assuming constant axial velocity through the blade passage, the ideal static pressure rise coefficient can be expressed in terms of inlet and exit flow angles as

$$C_{p_i} = 1 - \left(\frac{\cos \alpha_1}{\cos \alpha_2} \right)^2 \quad (6)$$

For circular camber lines and negligible deviation, the inlet and exit flow angles can be expressed in terms of the incidence angle i and the geometric blade parameters $\alpha_1 = i + \gamma + \theta/2$ and $\alpha_2 = \gamma - \theta/2$. The ideal static pressure rise coefficient is thus

$$C_{p_i} = 1 - \left[\frac{\cos(i + \gamma + \theta/2)}{\cos(\gamma - \theta/2)} \right]^2 \quad (7)$$

A second process governing the hub-corner stall is the accumulation of low momentum fluid due to cross-flow toward the blade suction surface. The end wall region cross-flow is sketched in Fig. 3.

A basic inviscid description of the cross-flow is given by the well-known Squire and Winter expression for the relation between exit streamwise vorticity ξ and inlet normal vorticity η in terms of the flow turning angle $\Delta\alpha$ (Horlock et al. [4] and Cumpsty [7]),

$$\xi = -2\Delta\alpha\eta \quad (8)$$

Of direct interest is the cross-flow velocity, which is usefully depicted as a plot of cross-flow velocity component versus velocity component in the freestream direction, v/U versus u/U (Johnston [24]). The most basic representation of boundary layer cross-flow is a triangle as in Fig. 3. The outer leg corresponds to the inviscid outer portion of the boundary layer and the inner part corresponds

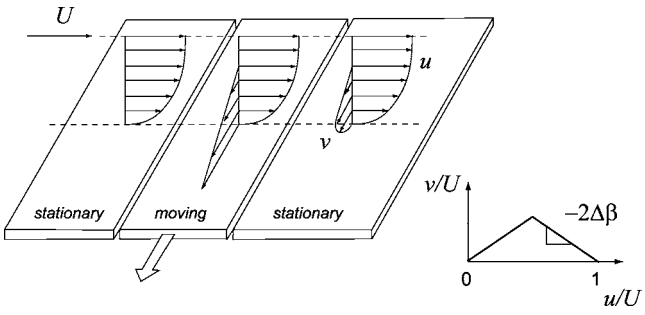

Fig. 4 Incoming end wall region skew due to moving end wall surfaces (i.e., rotor hubs or rotor drums underneath hub platforms in shrouded stators)

to the region dominated by viscous effects.[5] For the outer part,

$$\frac{v}{U} = -2\Delta\alpha\left(1 - \frac{u}{U}\right) \tag{9}$$

The slope of the outer leg is equal to the ratio of streamwise vorticity ξ to normal vorticity η, as can be seen by reference to Eq. (8). With the assumptions adopted, this ratio is $2\Delta\alpha = 2(i+\theta)$.

The cross-flow is affected by the exit conditions from the upstream blade row (which typically create a skewed inlet flow) and by moving surfaces such as rotor hubs or the rotating structures underneath shrouded stator platforms. One consequence is additional turning, which we characterize as $\Delta\beta$. A second is that the dynamic pressure in the end wall region may be higher than in the freestream (Koch [25] and Smith [26]), as in the middle picture in Fig. 4. While it is recognized that these two effects are different in nature, the approach taken amounts to assuming that they are linked in the applications of interest and can be captured through the single parameter, $\Delta\beta$. With reference to the polar plot representation in Fig. 4, the slope of the inviscid leg of the skewed end wall boundary layer then becomes $-2\Delta\beta$. The combined turning, $\Delta\epsilon$, which is the result of the cross-passage pressure gradient acting on the skewed incoming boundary layer, is associated with a cross-flow velocity in the inviscid region of the end wall region as

$$\frac{v}{U} = -2\Delta\epsilon\left(1 - \frac{u}{U}\right) = -2(i + \theta - \Delta\beta)\left(1 - \frac{u}{U}\right) \tag{10}$$

The principal point of Eq. (10) is that the cross-flow velocity is modified by inlet skew.

Cross-flow and overall pressure rise in the blade passage have so far been put forth as important parameters. A third parameter is blade solidity. For a given overall pressure rise (blade turning), the magnitude of the pressure rise the suction surface fluid must negotiate depends on the solidity, i.e., for a given overall turning, the pressure difference across the passage is proportional to blade pitch; lower solidity means a larger pressure rise on the suction surface.

The three nondimensional parameters thus proposed as being candidates for inclusion in the hub-corner stall diffusion parameter are (i) the overall pressure rise, expressed in terms of blade and incidence angles, (ii) the magnitude of the cross-flow, expressed in terms of the turning of the end wall region flow, and (iii) the solidity, which leads to a more local measure of the pressure rise (or pressure gradient) at the hub suction corner compared to the average value.

In the next section, we discuss the process of assessing this hypothesis in quantitative terms. To give a context for viewing the steps in the process, however, we anticipate the results to be described and state that the computations show that a relevant and useful diffusion parameter, which can be readily calculated from blade row geometry and inflow conditions, is found having the form

$$D = \frac{C_{p_i}\Delta\epsilon}{\sigma} \tag{11}$$

where C_{p_i} and $\Delta\epsilon$ are defined in Eqs. (7) and (10), respectively, and σ is the solidity c/s.

Table 1 Parameter range of nondimensional groups used in three-dimensional steady RANS simulations

Group	Parameter range
θ	20–65 deg (11 points)
γ	5–57 deg (21 points)
i	−6 to +5 deg (5 points)
σ	1.0, 1.5, 2.0
Re	2.5×10^4, 2.5×10^5, 2.5×10^6
AR	1.36, 5
δ/c	0.1, 0.2
$\Delta\beta$	0–42 deg (10 points)

Stall Indicator and Diffusion Parameter Evaluation. A large set of numerical simulations (about 100 geometries) was initially carried out to assess whether a simple criterion in terms of the parameters introduced above would unify the description of hub stall onset for different compressors. The simulations were done with a commercially available, steady three-dimensional RANS solver with the $k-\epsilon$ turbulence model. Prismatic blades with a modified NACA 65 thickness distribution on circular camber lines were used. For all these initial cases, the boundary layers were fully turbulent, the Reynolds number was fixed at 2.5×10^5, the blade aspect ratio was 1.36, and the incoming end wall boundary layer thickness was $\delta/c = 0.1$. A detailed description of the numerical tools and implementation can be found in Ref. [27].

Table 1 summarizes the parameter range of the nondimensional groups that characterize the blade geometries and flow conditions included in the simulations. In selected simulations, additional turning due to a skewed incoming end wall boundary layer $\Delta\beta$ was generated by injecting flow on the hub end wall upstream of

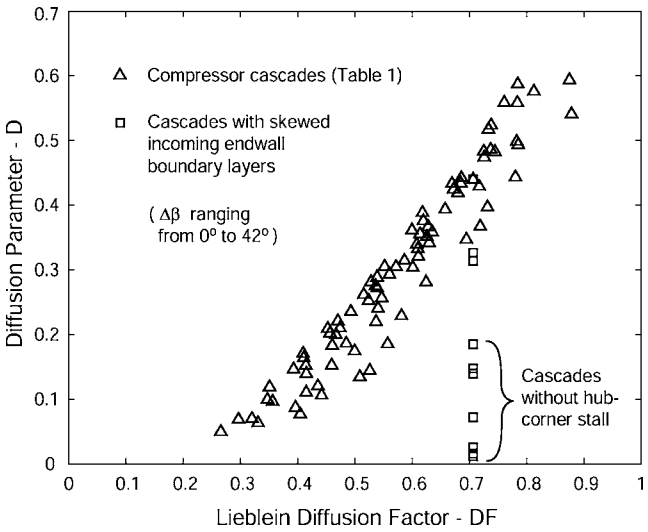

Fig. 5 Comparison between the Lieblein DF and the diffusion parameter *D*. Squares denote cascades with skewed incoming end wall boundary layer.

[5]Vorticity of the opposite sign to the inviscid part of the flow, which is associated with the cross-stream pressure gradient, is created at the wall and diffused into the end wall region. Since u/U is almost always monotonic with distance from the wall, the opposite sign of the vorticity can be inferred from the opposite slopes of the two sides of the triangle.

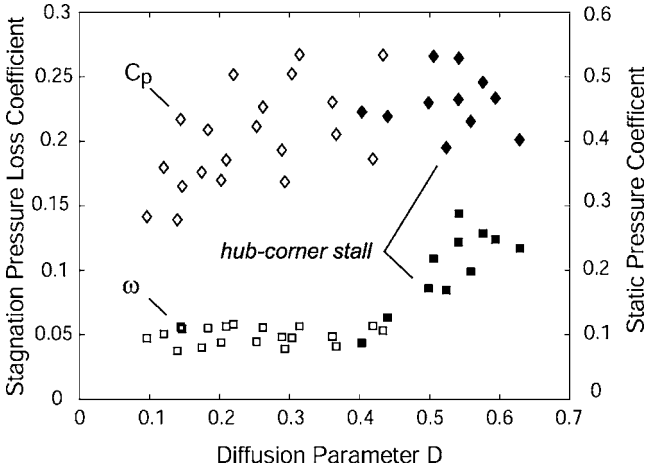

Fig. 6 Stagnation pressure loss coefficient ω (squares) and static pressure rise coefficient C_p (diamonds) as a function of diffusion parameter D for cascades with zero incidence. Solid symbols indicate hub-corner stall.

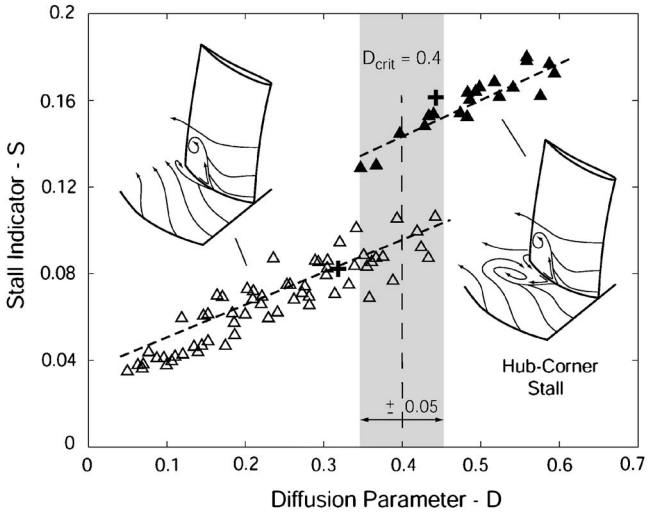

Fig. 7 Formation of hub-corner stall for diffusion parameters $D>0.4$ (upper branch, $S>0.12$)

the stator, as in shrouded stators due to leakage from underneath the hub platform. The leakage mass flows ranged from 0.35% to 0.84% of the passage mass flow, and the ratio of the leakage velocity to incoming velocity in the tangential direction $(v_{\text{leak}}/v)_\theta$ was set between 0.5 and 1.25, based on values reported by Demargne and Longley [18].

Some guide to the form of a nondimensional diffusion parameter comes from the qualitative reasoning given previously; it might be expected that the parameter would be proportional to the *overall pressure rise* and the *turning* (or some power of these). The *solidity* can affect hub-corner stall in several ways. One is that higher solidity enables higher blade turning and thus increases the pressure rise in the hub and suction surface corner; this might argue for the solidity to enter additively. Another effect is that for high solidity, the cross-flow will be suppressed by the blades. In fact, the relation between the Johnston polar plot and the velocity given by simple integration of the Squire-Winter result only holds in regions where there are negligible potential flow effects due to the passage boundaries. This might argue for the solidity to enter as an inverse power. A power law behavior (assuming $D \propto C_{p_i}^p \sigma^q \Delta\epsilon^r$) was therefore evaluated using the numerical simulations, with the observed best fit found to be $p=1$, $q=-1$, and $r=1$. As given in Eq. (11), the nondimensional diffusion parameter is

$$D = \frac{s}{c}\left\{1 - \left[\frac{\cos(\iota + \gamma + \theta/2)}{\cos(\gamma - \theta/2)}\right]^2\right\}(i + \theta - \Delta\beta) \tag{12}$$

Stated in a more direct manner, the numerical results showed that good correlation existed between the onset of three-dimensional hub-corner stall, as expressed by the criterion $D \approx 0.4$, and the stall indicator S. In the remainder of this paper, we will relate the diffusion parameter to the Lieblein criterion for two-dimensional stall, describe the features of the correlation, show its applicability to other data than used in the initial simulations, and use it in the design of an approach to hub-corner stall flow control.

Relation to the Lieblein Diffusion Factor. Both blade stall and hub-corner stall are diffusion driven and one would expect some correspondence between the diffusion parameter D and the well-known Lieblein diffusion factor (DF). The latter was originally defined (for two-dimensional cascades) in terms of a correlation between deceleration of the suction surface flow and the wake momentum thickness. It was expressed in terms of cascade area ratio and turning through the blade row. For incompressible flow with equal axial velocity into and out of the cascade,

$$\text{DF} = \left(1 - \frac{\cos\alpha_1}{\cos\alpha_2}\right) + \frac{\cos\alpha_1}{2\sigma}(\tan\alpha_1 - \tan\alpha_2) \tag{13}$$

The D parameter and the Lieblein DF both account for static pressure rise and flow turning in the blade passage. An explicit difference, however, is that D incorporates the effect of incoming boundary layer skew. To illustrate this difference, the diffusion parameter D, which is used here as the metric for occurrence of

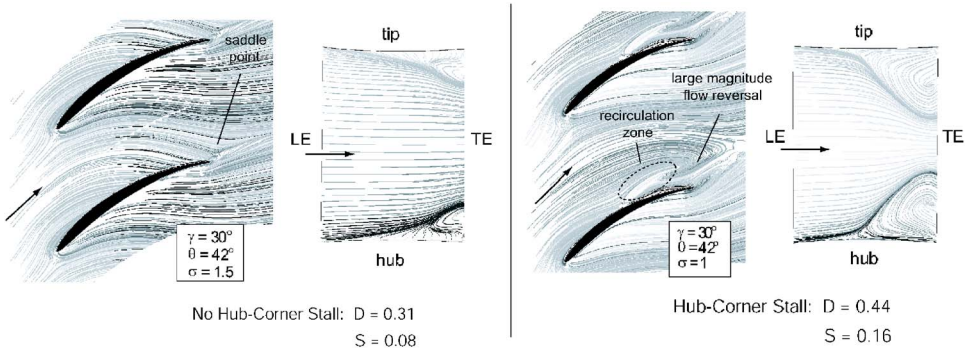

Fig. 8 Limiting streamlines for two different compressor cascades: without (left) and with (right) hub-corner stall

hub-corner stall, is plotted in Fig. 5 as a function of DF for all the compressor cascades in Table 1. For cases without incoming end wall boundary layer skew (triangles), there is a rough correlation between the two parameters. However, the diffusion parameter D does not correlate with DF when cases with incoming boundary layer skew are included. Also, for skewed incoming boundary layers, there are compressor geometries with a DF=0.7 greater than the "critical value" of 0.6 (Kerrebrock [6] and and Cumpsty [7]) in which the passages are free of hub-corner stall.

Hub-Corner Stall Criterion

To show features of the blade row performance, the static pressure rise coefficient C_p and the stagnation pressure loss coefficient ω are plotted as a function of the diffusion parameter D in Fig. 6 for cascades in Table 1 with zero incidence.

Solid symbols refer to cases with hub-corner stall present. It is seen that the static pressure rise coefficient does not correlate with diffusion parameter. There is, however, a critical value of diffusion parameter, $D_{\text{crit}} \approx 0.4$, above which hub-corner stall is found. Corresponding to this finding, the stagnation pressure loss coefficient is nearly constant for diffusion parameters $D < 0.4$ and abruptly increases at this critical value. Further, for all the cases in Fig. 6, passages with hub-corner stall have stagnation pressure loss coefficients a factor of 2 or 3 larger than those without large magnitude flow reversal on the end wall.

A more useful correlation is achieved if the data are plotted in terms of stall indicator, as in Fig. 7 which shows results for stall indicator versus diffusion parameter from all the initial simulations. Two distinct branches in S can be seen, with the condition for which hub-corner stall occurs defined by the diffusion parameter reaching critical value, $D_{\text{crit}} = 0.4 \pm 0.05$. There is a region of overlap of the upper and the lower branch in S near this critical value. For the same D parameter (and different combinations of blade passage geometry and flow conditions), the stall indicator S can either yield a low or a high value. The effects responsible for this double-valued behavior have not yet been identified.

For values of D less than 0.4 (the lower branch in S), the magnitude of flow reversal is small at the hub end wall, although suction surface separation can occur in the manner indicated by the limiting streamlines and the suction surface separation line sketched in Fig. 7. Increasing the turning and/or the overall diffusion, and/or reducing the solidity, all of which raise the diffusion parameter, increases the extent of the suction surface separation. Only if D exceeds 0.4, however, will hub-corner stall occur. The upper branch ($S > 0.12$) is therefore indicative of extreme excursions of the surface streamlines and large magnitude flow reversal on both the hub end wall and the suction surface, as sketched on the right of Fig. 7.

To illustrate the formation of hub-corner stall as the diffusion parameter increases, a series of simulations has been carried out by lowering the solidity from 1.5 to 1.0 to increase the diffusion parameter from 0.31 to 0.44. The computed limiting streamlines on the hub end wall and blade suction surface for a diffusion parameter of 0.31 (resulting in $S=0.08$ on the lower branch in Fig. 7 marked by the plus sign) are shown in the left-hand side of Fig. 8. A small magnitude flow reversal occurs on the end wall as evidenced by a saddle point downstream of the trailing edge, but extreme excursions of the surface streamlines exist on the suction surface. At a solidity of $\sigma=1$, with diffusion parameter of 0.44 (in excess of the critical value), as shown on the right of Fig. 8, a relatively large recirculation zone on the hub end wall is observed. For this situation, the suction surface reverse flow region is nearly twice the size of that in the left-hand figure and the stall indicator is doubled to $S=0.16$ on the upper branch, as marked by another plus sign in Fig. 7.

In summary, the results so far show a simple criterion for the formation of hub-corner stall consisting of a stall indicator S, which quantifies the extent of the reversed flow, and a diffusion parameter D, which defines the three-dimensional flow diffusion limit. Two distinct branches related to different flow patterns are identified, with a critical diffusion parameter of 0.4 separating the two. On the lower branch, large magnitude reversed flow is confined to the blade suction surface. On the upper branch, hub-corner stall exists, i.e., extreme excursions of the surface streamlines occur on both the hub end wall and the blade suction surface.

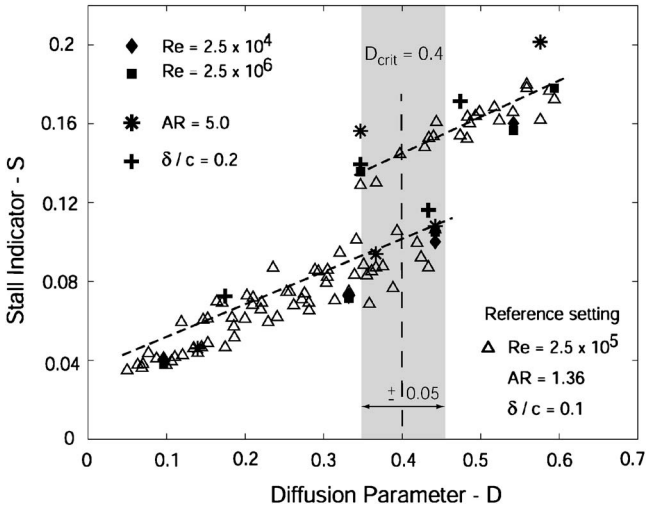

Fig. 9 Effects of blade aspect ratio, Reynolds number and incoming boundary layer thickness on hub-corner stall criterion

Applicability and Limitations of the Hub-Corner Stall Criterion

To assess the applicability and limitations of the hub-corner stall criterion, additional numerical simulations have been conducted. Further, the criterion has also been evaluated against compressor data from industry and literature.

Effects of Reynolds Number, Blade Aspect Ratio, and Incoming Boundary Layer Thickness. Computational results for a range of Reynolds number, aspect ratio, and end wall boundary layer thickness are shown in Fig. 9. For reference the results from Fig. 7 are plotted as triangles. For cases on both the lower and the upper branches, the Reynolds number was increased and decreased by a factor of 10 (to 2.5×10^6 and 2.5×10^4, respectively). In all the computations, the flow was fully turbulent. The results are marked by the solid diamonds and the solid squares in Fig. 9. For fixed value of diffusion parameter, the criterion is insensitive to changes in Reynolds number, as is the stall regime, i.e., small magnitude reversed flow on the hub end wall does not develop into hub-corner stall and vice versa.[6]

To investigate the effects of aspect ratio, simulations were conducted for three cascade geometries on the lower branch and two on the upper branch. The blade aspect ratio was increased from the reference value of 1.36–5.[7] The results are plotted in Fig. 9 as stars. As with Reynolds number, changing the aspect ratio does not change the flow regime, but there can be an appreciable change in the stall indicator. The simulations show that the spanwise extent of reversed flow is little affected by aspect ratio so the changes in S are indicative mainly of changes in reference loading. Reducing the aspect ratio increases the ratio of blocked area to geometric passage area, reducing the midspan loading. For the

[6]This and the insensitivity to inlet blockage are reminiscent of the situation with straight diffusers where the flow regimes are not much affected by Reynolds number (Johnston [28]).

[7]An aspect ratio of 0.5 was also considered but for such low values, the two end wall flows tend to merge developing full span stall and, under these circumstances, the separation indicator is no longer applicable.

Table 2 Evaluation of diffusion parameter and hub-corner stall criterion with compressor data from literature

Reference	Compressor description	Hub-corner stall	Inferred D
Kang and Hirsch [29]	Linear cascade, NACA 65-1810 airfoil	No	0.15
Shang et al. [11]	Linear cascade, NACA 65–24A_{10}-10 airfoil	No	0.18
Gbadebo et al. [3]	Linear cascades, NACA 65 and PVD airfoils	No	0.23, 0.24
Horlock et al. [4]	Linear cascade, C4 airfoil	Yes	0.33
Dong et al. [30]	Single stage, rotor, C4 airfoil, twist	No	0.34
Schulz and Gallus [16]	Annular cascade	Yes	0.35
Barankiewicz and Hathaway [9]	Four stage, stator, GE E^3 airfoil, twist	Yes	0.41
Wellborn and Okiishi [19]	Four stage, stator, GE E^3 airfoil, twist	Yes	0.41
Joslyn and Dring [8]	Two stage, stator, NACA 65 airfoil	Yes	0.41
Dong et al. [30]	Single stage, stator, C4 airfoil, twist	Yes	0.46

higher aspect ratio, the midspan loading is less affected yielding higher values of stall indicator. The change made in aspect ratio does not alter the trends in stall indicator.

To assess the sensitivity of the hub-corner stall criterion to incoming end wall boundary layer thickness, simulations were conducted for selected compressor cascade geometries with an end wall boundary layer thickness of 20% chord, twice the reference value. These results are also given in Fig. 9, with the thicker boundary layer behavior marked by plus signs. The stall indicator behavior as a function of diffusion parameter is unchanged, with the results for the thicker boundary layer within the scatter of the reference data.

Application of the Hub-Corner Stall Criterion to Compressor Data. The development of the hub-corner stall criterion was based on untwisted compressor cascades. To assess its applicability more generally, single and multistage compressor data from industry and literature, as well as other cascade data, have been used. Table 2 summarizes the compressor geometries and observed hub stall patterns found in the literature. The diffusion parameter has been inferred from the available information. For twisted blades, the diffusion parameter can change from hub to midspan and the span-averaged value has been used.

The proposed criterion is that all geometries with diffusion parameters below 0.4 ± 0.05 will not have hub-corner stall, i.e., in terms of Table 2, the third column will say "No." The data are in reasonable agreement with this. The linear cascade experiment by Horlock et al. [4] has a subcritical D parameter of 0.33 but hub-corner stall was observed. The amount of information is limited and it is not clear what the cause is. In the experiments conducted by Schulz and Gallus [16], the rather thick blade profiles had a highly curved suction surface and much flatter pressure surface. The reported camber angle is 29 deg, which yields a diffusion parameter of 0.16, but hub-corner stall was observed. The flow angle difference inferred from the suction surface curvature is almost 60 deg and, if this were the turning, the diffusion parameter would be 0.54. For purposes of listing the data, we have taken the average of the two values (0.35) as our best estimate, realizing that there is a large uncertainty. The reader should note that this approach has been taken for this one data point. Another possible explanation is the effect of the thick blade on the flow diffusion as described by the generalized diffusion ratio[8] (Koch and Smith [32]). This aspect is not explicitly captured by the D parameter.

Aeroengine compressor data, from five different production and research compressors, ranging from 5 to 14 stages, were also used to assess the criterion.[9] A total of 49 rotor end walls and 71 stator end walls were investigated. All were end walls with no tip leakage, i.e., rotor hubs, stator casings, and shrouded stator hubs. The results are shown in the histograms on the left- and right-hand sides of Fig. 10 for rotors and stators, respectively. The abscissa gives the value of diffusion parameter and the ordinate shows the percentage of the cases at that value.

For the rotors, all the cases shown are reported to be free of hub-corner stall.[10] All the rotor data are thus suggested to be in accord with a critical DF of 0.4 for the onset of hub stall. The inference is that designers recognize (at least implicitly), and avoid, flow conditions that the criterion states will lead to hub stall.

The majority of the stators had a diffusion parameter calculated to be between 0.21 and 0.24, with 18% of the stators yielding diffusion parameters above the critical value. Information on the stall pattern is not available for the stators and no direct comparison can be made. However, two points can be inferred from the stator data. First, the criterion is in accord with industrial design and development practices, in which performance-affecting stall is to be minimized. Second, most of the cases with diffusion parameters above 0.4 are reported to represent outlet guide vanes, which are naturally higher turning blade rows, and, even with the higher solidity commonly used, may be difficult to design without large magnitude flow reversal in the end-wall-suction corner.

Mitigation of Hub-Corner Stall via Flow Control

The criterion developed can also be employed to guide the design of flow control to mitigate hub-corner stall. The overall concept is to ensure that the diffusion parameter is below the critical value of 0.4. One way to accomplish this is to decrease the cross-flow due to the overturning of the fluid near the end wall by introducing cross-flow of the opposite sign. Such control cross-flow could be established via upstream flow leakage from underneath the hub platform in shrouded stators or by injecting air from the hub or blade suction surface inside the passage, as sketched in Fig. 11.

Effects of Hub Cavity Leakage Flow on Hub-Corner Stall. To illustrate the above scheme, simulations were conducted for leakage flow rates of 0.35%, 0.7%, and 0.84% of the blade passage mass flow and tangential velocity ratios $(v_{\text{leak}}/v)_\theta$ of 0.5, 1.0, and 1.25. The additional turning due to leakage, $\Delta\beta$ (see Eq. (10)), was extracted from the numerical results using the polar plot description. The resulting diffusion parameters and stall indicators are plotted in Fig. 12, marked by circles, plus signs, and stars. The upper and lower branches in S, identified earlier, are marked by dashed lines.

Tangential injection ratios of 0.5, indicated by the dotted line, yield increased values in stall indicator compared with the no-leakage case, indicative of a larger hub-corner stall region. This is in concert with the results reported by Demargne and Longley [18]; for the same leakage mass flow, the formation of hub-corner

[8]We thank Dr. L. H. Smith for pointing this out.

[9]This information, and the analysis, has been provided by Wellborn [31].

[10]The assessment was based on CFD analysis.

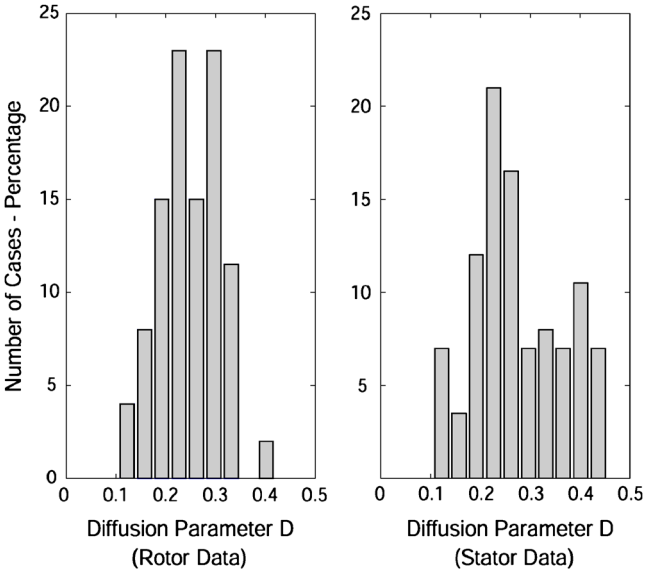

Fig. 10 Evaluation of the hub-corner stall criterion for rotor and stator blade rows of five different production and research compressors (data courtesy of Rolls-Royce, Wellborn [31]).

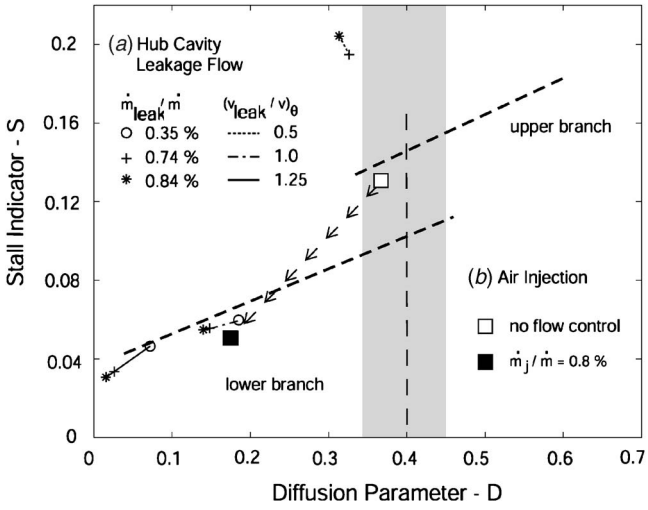

Fig. 12 Effect of flow control on stall indicator and diffusion parameter: (*a*) hub cavity leakage flows and (*b*) suction surface air injection (squares)

stall is promoted if the injected tangential momentum is less than the freestream value so fluid particles near the end wall overturn toward the blade suction side. For a tangential velocity ratio of 1.0, Fig. 12 shows that the separation indicator has a value on the lower branch for all the leakage mass fractions examined (dash-dotted line). At this condition, the tangential momentum imparted by the flow injection suppresses the overturning of the end wall fluid toward the suction surface and thus the tendency toward the stall. An increase in tangential velocity ratio to 1.25 further reduces the reversed flow region on the suction surface as evidenced by the decreasing stall indicator *S* marked by the solid line.

Hub-Corner Stall Control Scheme. A flow control scheme based on the concept in Fig. 11, with air injected from the blade suction surface, was constructed and tested in a linear compressor cascade. The cascade had five interchangeable blades, two of which were instrumented with an array of static pressure taps on suction and pressure surfaces. An exit stagnation pressure was surveyed by a Kiel probe mounted on a three-axis traverse table. The blades were based on GE's E^3 geometry. The flow control scheme consisted of an externally fed blade cavity and a spanwise injection slot on the suction side near the leading edge. Flow control air was supplied from the end wall through a feed channel near the blade trailing edge. The cavity was designed with an internal recirculation zone so that the flow exiting through the injection slot had a strong spanwise velocity component. The spanwise velocity on the blade suction surface created a cross-flow that opposed the existing passage secondary flow, as shown in Fig. 11. A single injection slot was located at 21% of chord on the blade suction side, extending radially from the hub to one-third span. The injection slot width was 0.04% of chord. Injection mass flow rates were from 0.4% to 0.8% of the passage flow. For more details on the experiment, see Ref. [27].

To illustrate the effect of air injection on the separated flow region, Fig. 13 depicts computed contours of stagnation pressure at the cascade exit for a datum case A (no control) and for two methods of air injection through a slot on the blade suction surface (Cases B and C). The injection mass flow rate was 0.8% of the compressor flow. In Case B, air is injected in the streamwise

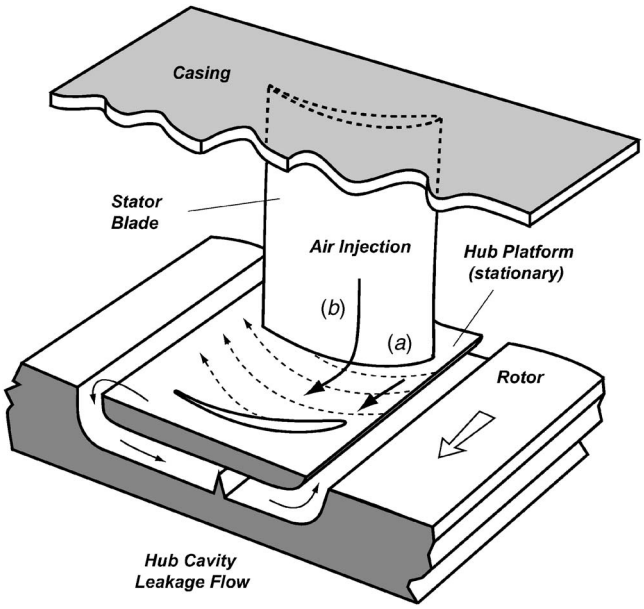

Fig. 11 Flow control of hub-corner stall via cross-flow of opposite sign to blade passage secondary flow: (*a*) upstream hub cavity leakage flow and (*b*) air injection in the blade passage

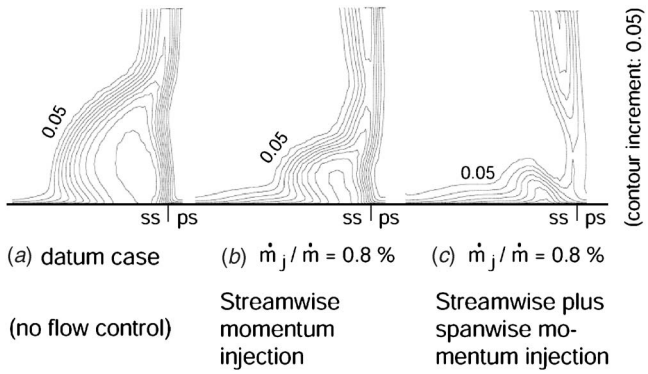

Fig. 13 Contours of computed stagnation pressure at cascade exit for (A) datum case, (B) streamwise air injection, and (C) streamwise plus spanwise air injection

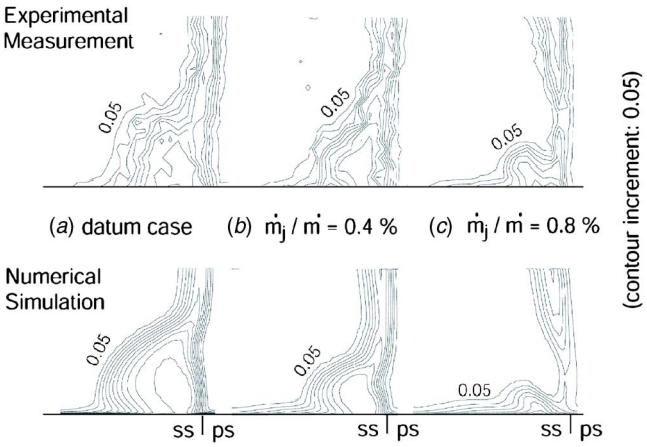

Fig. 14 Contours of stagnation pressure at compressor cascade exit: (A) datum case, (B) flow control with 0.4% of passage mass flow, and (C) flow control with 0.8% of passage mass flow. Top: Linear compressor cascade experiment; bottom: numerical simulation results.

direction (the injection angle was pitched 24 deg from the suction surface to impart streamwise momentum). In Case C, air is injected along the span toward the hub (the injection angle was pitched 24 deg from the suction surface and angled 53 deg from the streamwise direction toward the hub). Although injection in the streamwise direction (Case B) energizes the blade surface boundary layers and thins the wake, it has little effect on hub-corner stall. Introducing the spanwise velocity component (Case C), however, markedly reduces the extent of the hub-corner stall in accord with the stall criterion.

The experimental results are compared to the numerical simulations in Fig. 14. This figure compares two rates of spanwise flow injection. For 0.8% injection flow rate, the hub-corner stall is much reduced and the wake is thinned near the hub. The deduced diffusion parameter D drops from 0.37 to 0.18 so the stall indicator jumps from the upper to the lower branch as marked by the squares in Fig. 12, consistent with the observed change in stall pattern. Examination of the stagnation pressure taking into account the work associated with the delivery of the injection fluid shows that injection rates higher than 0.8% (not presented here) do not yield further reductions in stagnation pressure loss. The 0.8% injection flow rate thus gave the best results (roughly 10% reduction in overall loss coefficient) for the conditions examined. Although we regard the experiments (and simulations) primarily as an additional assessment of the ideas presented above, and although the reduction is small, the reduction of flow nonuniformity has potential for enhancing the performance of downstream blade rows.

Summary and Conclusions

A new criterion has been developed for estimating the geometries and flow conditions under which hub-corner stall will occur in axial compressors. The criterion consists of a diffusion parameter, which defines at what conditions the hub-corner stall will occur, and a stall indicator, which defines whether a large magnitude flow reversal exists on the blade suction surface and the hub end wall.

The diffusion parameter is expressed in terms of overall blade row parameters (flow angles, solidity, and incoming end wall boundary layer skew) so that the criteria can be applied in the preliminary design stage. The stall indicator can be related directly to the difference between Zweifel loading coefficients near the end wall and at midspan. Based on numerical simulations of over 100 different cascade geometries, the critical value of the diffusion parameter marking the onset of separation is $D = 0.4 \pm 0.05$.

The criterion has been found to be in general agreement with the available data in the literature. The criterion has also been found to be in agreement with multistage aeroengine compressor data. More specifically, it is in agreement with all rotor data provided (49 cases). For the stators, information was not provided for direct comparison, but it is suggested that the trends shown are consistent with the criterion.

The ideas leading to the criterion were used to design and test a stator flow control scheme in a linear compressor cascade. The experimental results, and the numerical simulations, are found to be in accord with the ideas presented in the paper.

Acknowledgment

The authors would like to thank Dr. S. Wellborn at Rolls-Royce for insightful discussions and for providing compressor data to assess the criterion. The research was sponsored by the NASA Glenn Research Center and monitored by Dr. A. Strazisar and Dr. G. Welch whose support is gratefully acknowledged. The comments of Professor N. Cumpsty, Dr. L. Smith, Dr. A. Strazisar, and Dr. P. Szücs of GE on drafts of this paper are also greatly appreciated.

Nomenclature

AR = blade aspect ratio
$\Delta\alpha$ = blade passage flow angle turning
$\Delta\beta$ = flow turning due to boundary layer skew
c, c_x = blade chord, axial chord
C_p = static pressure coefficient
D = diffusion parameter
DF = Lieblein diffusion factor
δ = boundary layer thickness
$\Delta\epsilon$ = total flow turning $\Delta\alpha - \Delta\beta$
γ = blade stagger angle
η = normal vorticity
i = incidence angle
L = blade span
M = Mach number
n = normal direction
p, p_t = static pressure, stagnation pressure
Ψ_z = Zweifel loading coefficient $\int_0^1 [p_{ps}(x) - p_{ss}(x)]/(p_{t1} - p_1)(dx/c_x)$
r = radius
Re = Reynolds number
ρ = density
s, S = blade pitch, stall indicator
σ = solidity (c/s)
θ = camber angle
u, U = streamwise velocity, freestream velocity
v = cross-flow velocity
ω = stagnation pressure loss coefficient
ξ = streamwise vorticity
1, 2 = upstream, downstream
ss, ps = suction side, pressure side

References

[1] Greitzer, E., Tan, C., and Graf, M., 2004, *Internal Flow: Concepts and Applications*, Cambridge University Press, Cambridge, UK.
[2] Lighthill, M., 1963, "Introduction: Boundary Layer Theory," *Laminar Boundary Layers*, L. Rosenhead, ed., Clarendon, Oxford.
[3] Gbadebo, S., Cumpsty, N., and Hynes, T., 2005, "Three-Dimensional Separations in Axial Compressors," ASME J. Turbomach., **127**, pp. 331–339.
[4] Horlock, J., Percival, P., Louis, J., and Lakshminarayana, B., 1964, "Wall Stall in Compressor Cascades," ASME Paper No. 64-WA/FE-29.
[5] Lieblein, S., 1959, "Loss and Stall Analysis of Compressor Cascades," ASME J. Basic Eng., **81**(3), pp. 387–400.

[6] Kerrebrock, J., 1992, *Aircraft Engines and Gas Turbines*, The MIT Press, Cambridge, MA.
[7] Cumpsty, N., 2004, *Compressor Aerodynamics*, reprint ed., Krieger, Malabar, FL.
[8] Joslyn, H., and Dring, R., 1985, "Axial Compressor Stator Aerodynamics," ASME J. Eng. Gas Turbines Power, **107**, pp. 485–493.
[9] Barankiewicz, W., and Hathaway, M., 1998, "Impact of Variable-Geometry Stator Hub Leakage in a Low Speed Axial Compressor," ASME Paper No.98-GT-194.
[10] Breugelmans, F., Carels, Y., and Demuth, M., 1984, "Influence of Dihedral on the Secondary Flow in a Two-Dimensional Compressor Cascade," ASME J. Eng. Gas Turbines Power, **106**, pp. 578–584.
[11] Shang, E., Wang, Z., and Su, J., 1993, "Experimental Investigations on the Compressor Cascades With Leaned and Curved Blade," ASME Paper No. 93-GT-50.
[12] Weingold, H., Neubert, R., Behike, R., and Potter, G., 1995, "Reduction of Compressor Endwall Losses Through the Use of Bowed Stators," ASME Paper No. 95-GT-380.
[13] Gallus, H., Hah, C., and Schulz, H., 1991, "Experimental and Numerical Investigation of Three-Dimensional Viscous Flows and Vortex Motion Inside an Annular Compressor Blade Row," ASME J. Turbomach., **113**, pp. 198–206.
[14] Hah, C., and Loellbach, J., 1999, "Development of Hub Corner Stall and Its Influence on the Performance of Axial Compressor Blade Rows," ASME J. Turbomach., **121**, pp. 67–77.
[15] Schulz, H., Gallus, H., and Lakshminarayana, B., 1990, "Three-Dimensional Separated Flow Field in the Endwall Region of an Annular Compressor Cascade in the Presence of Rotor-Stator Interaction—Part 1: Quasi-Steady Flow Field and Comparison With Steady-State Data," ASME J. Turbomach., **112**, pp. 669–678.
[16] Schulz, H., and Gallus, H., 1988, "Experimental Investigation of the Three-Dimensional Flow in an Annular Compressor Cascade," ASME J. Turbomach., **110**, pp. 467–478.
[17] Weber, A., Schreiber, H.-A., Fuchs, R., and Steinert, W., 2002, "3-D Transonic Flow in a Compressor Cascade With Shock-Induced Corner Stall," ASME J. Turbomach., **124**, pp. 358–365.
[18] Demargne, A., and Longley, J., 2000, "The Aerodynamic Interaction of Stator Shroud Leakage and Mainstream Flows in Compressors," ASME Paper No. 2000-GT-570.
[19] Wellborn, S., and Okiishi, T., 1996, "Effects of Shrouded Stator Flows on Multistage Axial Compressor Aerodynamic Performance," NASA Report No. CR–198536.
[20] Peacock, R., 1965, "Boundary-Layer Suction to Eliminate Corner Separation in Cascades of Airfoils," University of Cambridge Reports and Memoranda No. 3663, Cambridge, UK.
[21] Stratford, B., 1973, "The Prevention of Separation and Flow Reversal in the Corners of Compressor Blade Cascades," Aeronaut. J., **77**, pp. 249–256.
[22] Culley, D., Bright, M., Prahst, P., and Strazisar, A., 2003, "Active Flow Separation Control of a Stator Vane Using Embedded Injection in a Multistage Compressor Environment," ASME J. Turbomach., **126**, pp. 24–34.
[23] Kirtley, K., Graziosi, P., Wood, P., Beacher, B., and Shin, H.-W., 2005, "Design and Test of an Ultra-Low Solidity Flow-Controlled Compressor Stator," ASME J. Turbomach., **127**, pp. 689–698.
[24] Johnston, J., 1957, "Three-Dimensional Turbulent Boundary Layers," MIT Gas Turbine Laboratory Report No. 39.
[25] Koch, C., 1981, "Stalling Pressure Rise Capability of Axial Compressor Stages," ASME J. Turbomach., **103**, pp. 645–656.
[26] Smith, L., 2002, "Axial Compressor Aerodesign Evolution at General Electric," ASME J. Turbomach., **124**, pp. 321–330.
[27] Lei, V., 2005, "A Simple Criterion for Three-Dimensional Flow Separation in Axial Compressors," Ph.D. thesis, MIT, Cambridge, MA.
[28] Johnston, J., 1997, "Diffuser Design and Performance Analysis by Unified Integral Methods," Paper No. AIAA 97-2733.
[29] Kang, S., and Hirsch, C., 1991, "Three-Dimensional Flow in a Linear Compressor Cascade at Design Conditions," ASME Paper No. 91-GT-114.
[30] Dong, Y., Gallimore, S., and Hodson, H., 1987, "Three-Dimensional Flows and Loss Reduction in Axial Compressors," ASME J. Turbomach., **109**, pp. 354–360.
[31] Wellborn, S., 2005, private communication.
[32] Koch, C., and Smith, L., 1976, "Loss Sources and Magnitudes in Axial-Flow Compressors," ASME J. Eng. Power, **98**, pp. 411–424.

A Comparison of Cylindrical and Fan-Shaped Film-Cooling Holes on a Vane Endwall at Low and High Freestream Turbulence Levels

W. Colban
Combustion Research Facility,
Sandia National Laboratories,
Livermore, CA 94551-0969
e-mail: wcolban@sandia.gov

K. A. Thole
Department of Mechanical and Nuclear Engineering,
The Pennsylvania State University,
University Park, PA 16802-1412
e-mail: kthole@psu.edu

M. Haendler
Siemens Power Generation,
Muelheim a. d.,
Ruhr, Germany

Fan-shaped film-cooling holes have been shown to provide superior cooling performance to cylindrical holes along flat plates and turbine airfoils over a large range of different conditions. Benefits of fan-shaped holes include less required cooling air for the same performance, increased part lifetime, and fewer required holes. The major drawback, however, is increased manufacturing cost and manufacturing difficulty, particularly for the vane platform region. To this point, there have only been extremely limited comparisons between cylindrical and shaped holes on a turbine endwall at either low or high freestream turbulence conditions. This study presents film-cooling effectiveness measurements on an endwall surface in a large-scale, low-speed, two-passage, linear vane cascade. Results showed that film-cooling effectiveness decreased with increasing blowing rate for the cylindrical holes, indicating jet liftoff. However, the fan-shaped passage showed increased film-cooling effectiveness with increasing blowing ratio. Overall, fan-shaped holes increased film-cooling effectiveness by an average of 75% over cylindrical holes for constant cooling flow. [DOI: 10.1115/1.2720493]

Introduction

The primary goal of turbine cooling research during the past years was to develop cooling methods in which the amount of coolant could be decreased with at least the same, if not better, cooling performance. Fan-shaped holes have provided this opportunity to engine designers by providing significantly better cooling performance compared to cylindrical holes over a large range in blowing ratios and other conditions. However, the main drawback in implementing fan-shaped holes into current engine designs comes from the manufacturing side. Fan-shaped holes are on the order of four to eight times more expensive to manufacture than cylindrical holes on a per hole basis, depending on the technique. Fan-shaped holes are generally made using the electro-discharge machining technique, which is more expensive than the cheaper laser-drilling methods typically used to manufacture cylindrical holes.

The benefits of shaped hole cooling over cylindrical hole cooling for flat plates and airfoils were reviewed by Bunker [1]. Lateral expansion of the coolant promotes a better coverage of surface area downstream of the hole. Exit momentum of the jet is reduced as a result of the hole expansion, which keeps the jet attached to the surface. Both of these benefits were illustrated by the flow visualization study of Goldstein et al. [2].

Although shaped cooling holes have been widely used on the airfoil surface, there has been limited use on the vane platform. For this reason, the majority of endwall cooling studies have used cylindrical cooling holes. However, recent desires for more efficient cooling have promoted the use of shaped holes in the platform region. Unlike the majority of the airfoil surface, the endwall is a highly three-dimensional region, with intense secondary flows caused by the approaching boundary layer and cross-passage pressure gradient. This inevitably makes endwall film cooling more challenging to design and to predict.

This study was spawned from the lack of research of shaped hole endwall film cooling. It was necessary to directly compare the performance of shaped to cylindrical cooling holes, since cylindrical holes were used for most of the current research. This study contained two separate vane passages, one with cylindrical endwall film-cooling holes, and the other with shaped endwall film-cooling holes. A double row of staggered cylindrical film-cooling holes was located upstream of both passages. Comparisons were directly made based on matching coolant mass flow rates between the two passages. The coolant mass flow rates were determined by matching the percent coolant flow through the passage to typical engine operating conditions. The effect of freestream turbulence was also investigated because today's gas turbines can have a range of different freestream turbulence levels exiting the combustor.

Past Studies

Film-cooling has been studied at great length over the past 50 years [3,4]. Excellent reviews of film-cooling research can be found in Goldstein [5], Bogard and Thole [6], and for shaped film-cooling holes by Bunker [1]. A fair amount of endwall film-cooling research has been done using slots and discrete cylindrical holes, however only the studies by Vogel et al. [7], Vogel [8], and Barrigozzi [9] have employed shaped holes.

One of the main influences on endwall film cooling is the passage vortex and subsequent cross-passage flow. This tends to sweep the coolant away from the pressure side towards the suction side. This effect has been shown for upstream slot cooling by Blair [10], Granser and Schulenberg [11], Colban et al. [12], and Knost and Thole [13] and for cylindrical film-cooling holes by Harasgama and Burton [14] and Nicklas [15].

Not only does the endwall secondary flow affect the film cooling, but the film cooling also has an effect on the secondary flow

Contributed by the International Gas Turbine Institute of ASME for publication in the JOURNAL OF TURBOMACHINERY. Manuscript received July 14, 2006; final manuscript received July 26, 2006; published online May 2, 2008. Review conducted by David Wisler. Paper presented at the ASME Turbo Expo 2006: Land, Sea and Air (GT2006), Barcelona, Spain, May 8–11, 2006. Paper No. GT2006-90021.

field. Increased film cooling has been shown to reduce the strength of the passage vortex, as well as reduce the amount of cross passage flow. This effect has been shown by Sieverding and Wilputte [16] and Kost and Nicklas [17] for endwall cooling injection and Colban et al. [18] for upstream slot injection from a backward-facing step.

Friedrichs et al. [19] studied cylindrical endwall cooling in a rig specially designed to generate stronger secondary flows in order to isolate the effect of the secondary flow field on endwall cooling. They identified barriers to the endwall coolant flow in the form of three-dimensional separation lines on the endwall formed by the secondary flow structures. Coolant ejected near these separation lines was swept off the endwall surface, providing little cooling benefit. However, cooling ejection further from the secondary flow separation lines provided better cooling. They also reported that the addition of film cooling had an effect on the near wall secondary flow structures, redirecting the cross-passage flow in the direction of the inviscid streamlines. Friedrichs et al. [19] also found that the coolant trajectories were in large part dictated by the direction of the near wall flow, not the ejection angle of the hole. The insensitivity of the jet trajectory to the hole orientation angle has also been verified by Knost and Thole [20].

Studies of double rows of staggered cylindrical holes upstream of the leading edge have been performed by Oke et al. [21], Zhang and Jaiswal [22], and Zhang and Moon [23]. Oke et al. [21] measured thermal and velocity profiles in the vane passage downstream of 45 deg holes. Their results showed jet liftoff just downstream of the holes, which resulted in high mixing of the jets with the freestream. Both Zhang and Jaiswal [22] (using 45 deg holes) and Zhang and Moon [23] (using 30 deg holes) showed that at low flow rates the majority of the coolant was swept away from the pressure side towards the suction side because of the cross-passage flow. However, they found that at higher flow rates, the coolant ejection suppressed the endwall secondary flow, leading to both thermal and aerodynamic benefits.

To date, only the studies by Vogel et al. [7], Vogel [8], and Barigozzi et al. [9] have featured shaped hole film cooling on the endwall. The first two studies were primarily focused on the development of a unique experimental technique. However, a number of conclusions can be made about the behavior of shaped cooling holes on an endwall from the images presented in that work. The lateral spreading of coolant typically seen on flat-plate and airfoil surfaces with fan-shaped film cooling also occurred on the endwall. The coolant was still largely affected by the cross-passage flow, and was directed away from the pressure side toward the suction side. Also, jets that were located directly downstream of other coolant trajectories tended to provide the best film effectiveness.

Barigozzi et al. [9] measured film effectiveness, total pressure loss, flow field, and thermal field data for an endwall cooled with cylindrical holes and conical diffuser shaped holes. However, their comparison between cylindrical and conical shaped holes was not exact, since there were different hole patterns. Barigozzi et al. [9] showed that the size and vorticity of the passage vortex actually increased with decreasing film-cooling mass flow rates. As the flow rate increased above 1%, the passage vortex diminished in size and strength until it was no longer recognizable. The endwall cross flow was also eliminated at the highest mass flow rate (MFR), resulting in a nearly uniform two-dimensional exit flow. This result was confirmed with the film-effectiveness measurements, which showed that at low flow rates the jets were deflected toward the suction side, while at high flow rates the jets followed the potential flow streamlines. At low flow rates the cylindrical holes performed slightly better than the conical shaped holes, because the lower momentum jets exiting the shaped holes were more affected by the secondary flows. However, at higher flow rates, the conical shaped holes provided much better cooling than the cylindrical holes, in part because of the increased coverage and reduced exit momentum.

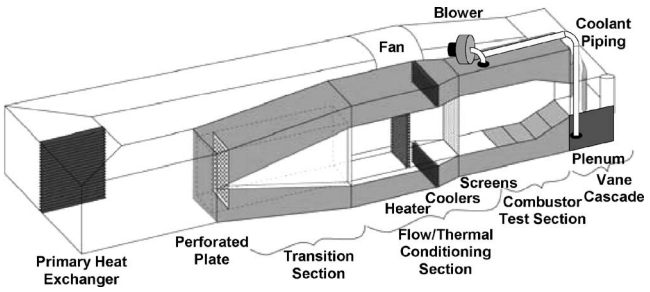

Fig. 1 Schematic of the low-speed recirculating wind tunnel facility

Experimental Facilities

The experiments were performed in the Virginia Tech Experimental and Computational Convection Laboratory low-speed, large-scale, recirculating wind tunnel facility shown in Fig. 1. The wind tunnel featured a flow split section, which divided the flow into three separate channels. The air in the center channel was heated by a 55 kW heater bank to simulate the combustor core flow, and then passed through a series of flow straighteners before entering the test section. The air in the two outer channels was cooled using heat exchangers supplied by a 44 kW chiller, and then used as supply coolant. The coolant was delivered to the endwall plenum by a 2 hp blower situated atop the wind tunnel. This process resulted in temperature differences between the coolant and mainstream of approximately 20°C.

The Reynolds number based on true vane chord and inlet velocity was 3.4×10^5 for all tests. Profiles of temperature and velocity were made upstream of each passage prior to testing to ensure periodicity among both passages. The tests were essentially incompressible, with a jet-to-freestream density ratio of approximately 1.06. The inlet turbulence intensity was measured at a location of $X/C=-0.3$ upstream of the test section with a hot wire anemometer. Turbulence intensity for the low freestream conditions was measured to be 1.2%. High freestream turbulence was generated using three 7.2-cm-diameter normal jets in crossflow, which were located 2.7 chord lengths upstream of the vane leading edge. This resulted in 8.9% turbulence intensity with a length scale of $\Lambda_x/P=0.15$. The approaching boundary layer thickness was also measured to be $\delta/Z_{\max}=0.12$ at a distance $X/C=-0.3$ upstream of the vane leading edge. A summary of important inlet conditions and geometrical parameters is given in Table 1.

Test Section Design. The two-passage linear vane cascade test section described in detail by Colban et al. [24] was used. A contoured upper endwall was designed to ensure the engine static pressure distribution around the vane surface was matched. It was critical to match the static pressure distribution around the vane surface, as the location of minimum static pressure has a significant effect on the development of the passage secondary flows. The pressure coefficient distributions around the vane at engine conditions and in the low speed facility both with and without the contour are shown in Fig. 2. The contoured vane was aft loaded,

Table 1 Operating conditions and vane parameters

Scale	3×
C (m)	0.53
$S_{\max,PS}$ (m)	0.52
$S_{\max,SS}$ (m)	0.68
U_{in} (m/s)	10
Re_{in} (–)	3.4×10^5
ΔT_{FC} (°C)	20
Vane pitch (m)	0.465

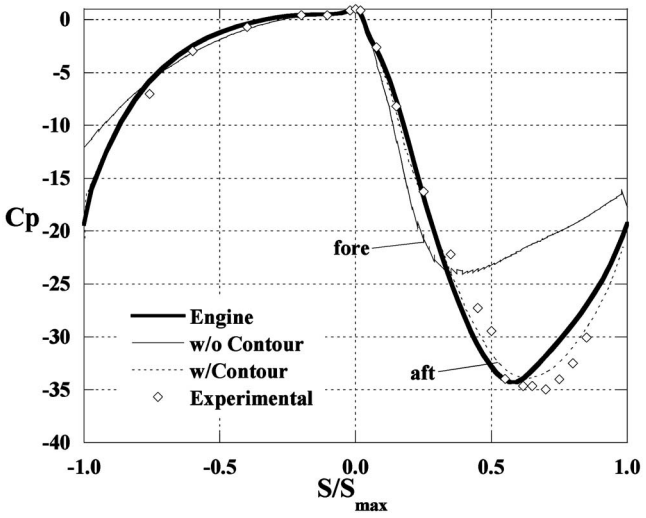

Fig. 2 Static pressure distribution around the center vane

which leads to weaker secondary flows since the minimum driving pressure is further from the leading edge. Without the contoured endwall, the vane is more fore loaded, which tends to strengthen the secondary flow structures because of a larger driving pressure difference in the passage. Clearly with the contoured endwall, the pressure distribution around the vane was very similar to the engine conditions, which led to closely simulated engine representative secondary flows in the vane cascade.

Some modifications to the previously described [24] test section were made. A film-cooled endwall surface was placed on the lower flat platform, and a feed plenum was constructed below. The inner passage of the cascade featured cylindrical holes, while the outer passage featured fan-shaped holes. Figure 3 shows the hole layout on the endwall, including the two rows of staggered cylindrical holes that were placed upstream of each passage. The layout of the film-cooling holes was identical for each passage, which allowed a direct comparison of the respective cooling performance of each hole geometry.

The endwall was constructed from medium density foam with a low thermal conductivity ($k=0.028$ W/m K) to allow adiabatic

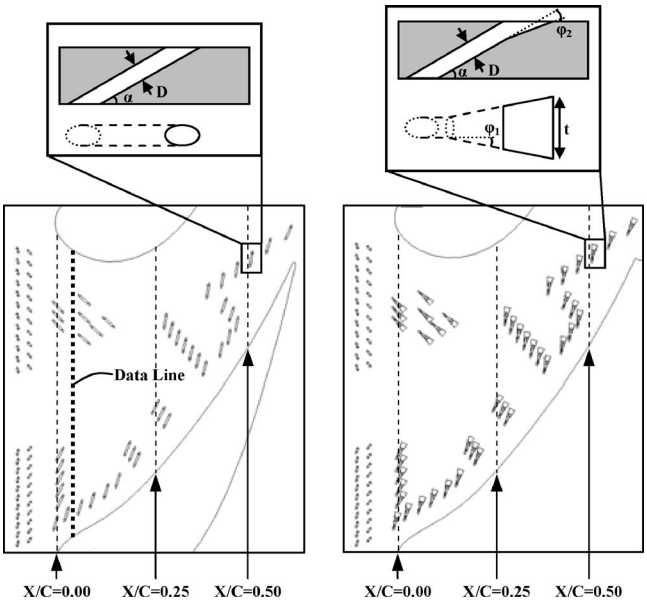

Fig. 3 Film-cooling hole layout and specifications

Table 2 Film-cooling hole parameters

	Upstream	Cylindrical	Shaped
D (cm)	0.26 ± 0.015	0.26 ± 0.015	0.26 ± 0.015
α (deg)	60	35	35
φ_1 (deg)	0	0	10
φ_2 (deg)	0	0	10

film-cooling effectiveness measurements and it was manufactured using a five-axis water jet cutting machine. The relevant geometrical parameters of the film-cooling holes are summarized in Table 2. All of the holes had a cylindrical diameter of 0.26 ± 0.015 cm. The two upstream rows of holes had a surface angle of 60 deg, while the holes in the passage had a surface angle of 35 deg. The fan-shaped holes had both a 10 deg lateral and forward expansion angle, which caused a breakout distance of $t=0.81$ cm on the endwall surface. The area ratio from the inlet area to the exit area for the shaped holes was 4.6. The vane–endwall junction was fitted with an elliptical manufacturing fillet, which extended out a distance of $10D$ normal to the vane surface and to a span height of $12D$ normal to the endwall surface.

Each passage could be sealed off from below, so that it was possible to provide film cooling to a single passage individually. This allowed for the total coolant flow rate to be measured directly with a laminar flow element (LFE) placed upstream of the plenum.

Surface temperature measurements were taken for each passage using an infrared (IR) camera positioned atop the test section. The IR camera was perpendicular to the surface for five of the seven images required to capture the complete endwall. The remaining two pictures were taken at an angle with respect to the surface, which required a linear surface transformation for those images. The IR camera provided an image resolution of 240×320 pixels, while the spatial resolution of the camera was approximately 0.72 mm/pixel ($0.28D$) at the measurement distance.

A one-dimensional conduction correction, described by Etheridge et al. [25], was applied to the film-effectiveness measurements to obtain the final adiabatic film-cooling effectiveness. This method involved measuring the endwall surface effectiveness with coolant inside the plenum but no blowing and using those values to correct the ultimate measured values of film-cooling effectiveness. The heat transfer coefficients inside the plenum were matched by letting the coolant exit the plenum through the adjacent passage. The uncooled effectiveness ranged from 0.06 to 0.15 with the highest values occurring near the entrance to the passage.

Experimental Uncertainty. The partial derivative and sequential perturbation method given by Moffat [26] was used to calculate uncertainties for the measured values. The uncertainties for the adiabatic effectiveness measurements were ± 0.012 for a high value of $\eta=0.9$ and ± 0.011 for a low value of $\eta=0.2$.

Test Design. This study was designed to independently investigate the effect of three separate variables: (1) coolant flow rate; (2) cooling hole shape; and (3) freestream turbulence intensity. The test matrix for this study is shown in Table 3, and contained a total of 12 cases. Coolant flow rates are reported in this study in terms of percent difference from the baseline case, with a 125%,

Table 3 Test matrix for endwall cases (shaded values are baseline operating conditions)

	Cylindrical passage			Fan-shaped passage		
TI=1.2%	75%	100%	125%	75%	100%	125%
TI=8.9%	75%	100%	125%	75%	100%	125%

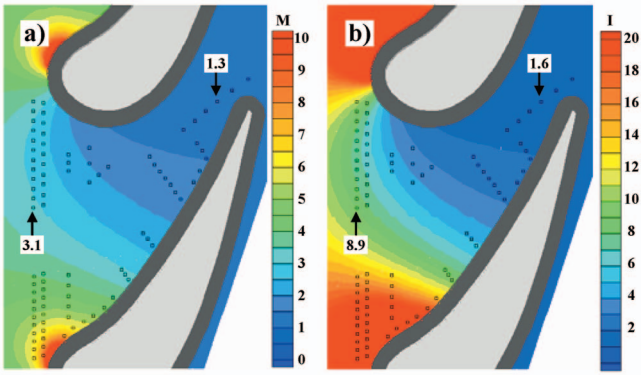

Fig. 4 Contours of calculated (*a*) blowing ratio and (*b*) momentum flux ratio for the baseline conditions

100%, and a 75% flow case. The complete test matrix is shown in Table 3. Note that flow rates have been normalized by the design conditions.

Local inviscid blowing ratios and local inviscid momentum flux ratios were computed for each hole. Local values mean that the local inviscid velocity was used in the scaling. The static pressure distribution on the endwall was approximated using a three-dimensional (3D) computational fluid dynamics (CFD) prediction without film-cooling in FLUENT 6.1.2. The measured total pressure in the plenum during the experiments was then used to make an inviscid prediction for the coolant velocity in the metering area of the cooling holes. Local freestream velocities on the endwall were also calculated using the CFD static pressure distribution, and the mainstream and coolant densities were measured during testing. The resulting blowing ratios and momentum flux ratios are presented in the form of contours shown in Figs. 4(*a*) and 4(*b*) for the baseline 100% flow conditions, with the hole locations outlined as well. Figures 4(*a*) and 4(*b*) are essentially design maps, showing the resulting blowing ratio at any location on the endwall. As expected, blowing ratios are highest at the inlet to the passage, especially near the stagnation point, where the freestream velocity is lowest. Fairly uniform blowing ratios of approximately $M=3.0$ are seen in the two upstream rows nearest the suction side, while the blowing ratios on the two upstream rows nearest the pressure side vary from $M=2.8$ to 5.9. The blowing ratios for the majority of the holes in the passage are less than 2.0, as the flow accelerates to nearly five times the inlet velocity in the throat region.

It is worth noting that because of the expansion through the fan-shaped holes, the velocity at the exit of the fan-shaped holes would be reduced by the area ratio (AR) of the holes (AR=4.6) from the velocity at the inlet to the holes. That means that the exit blowing ratios for the fan-shaped holes would be approximately 22% of the values shown in Fig. 4(*a*). Similarly, the momentum ratios at the fan-shaped hole exits would be 4.7% of the reported values in Fig. 4(*b*), again because of the reduction in jet velocity through the hole.

Experimental Results

Results are presented in terms of adiabatic film-cooling effectiveness. Contours are shown in Figs. 5(*a*)–5(*f*) for the low freestream turbulence cases and in Figs. 6(*a*)–6(*f*) for the high freestream turbulence cases. Analysis plots of laterally averaged and area-averaged effectiveness are also given, along with film-effectiveness augmentation plots of laterally averaged effectiveness, which show the effects of blowing ratio, hole shape, and freestream turbulence.

Cylindrical Holes at Low Freestream Turbulence. The adiabatic effectiveness contours for the cylindrical passage at low

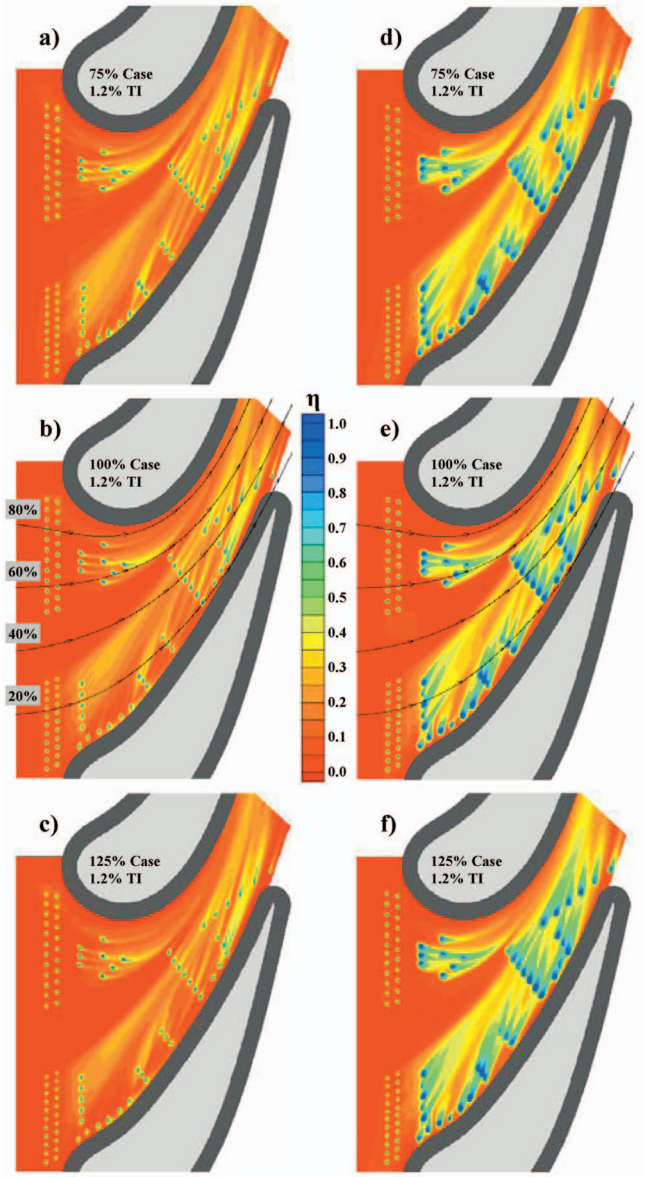

Fig. 5 Effectiveness contours at low freestream turbulence for the cylindrical passage (*a–c*) and fan-shaped passage (*d–f*)

freestream turbulence are shown in Figs. 5(*a*)–5(*c*). Overall, effectiveness levels were very low, especially in the region downstream of the double rows of holes at the entrance to the passage, which had a steeper surface angle than the passage holes (60 deg as opposed to 35 deg for the passage). Nearly all of the cooling flow from those two rows lifted off the surface, which is not surprising considering that blowing ratios for these holes ranged from 2.8 to 5.9. Only for the 75% case were slight cooling footprints visible downstream of the double cylindrical rows.

The row of pressure side holes running along the edge of the fillet just downstream of the leading edge separated completely. Blowing ratios for the holes in that region were extremely high between $M=3.9$ and 8.5 (see Fig. 4(*a*)), which is well above the range for cylindrical jet attachment.

The majority of the cooling footprints showed individual jets, indicating that there was not good lateral spreading downstream of most of the cylindrical holes. Most of the holes had a hole-to-hole spacing of greater than 5 hole diameters, which is generally too large to show significant jet merging. The exception was the first row of holes on the pressure side ($X/C=0$), which seemed to

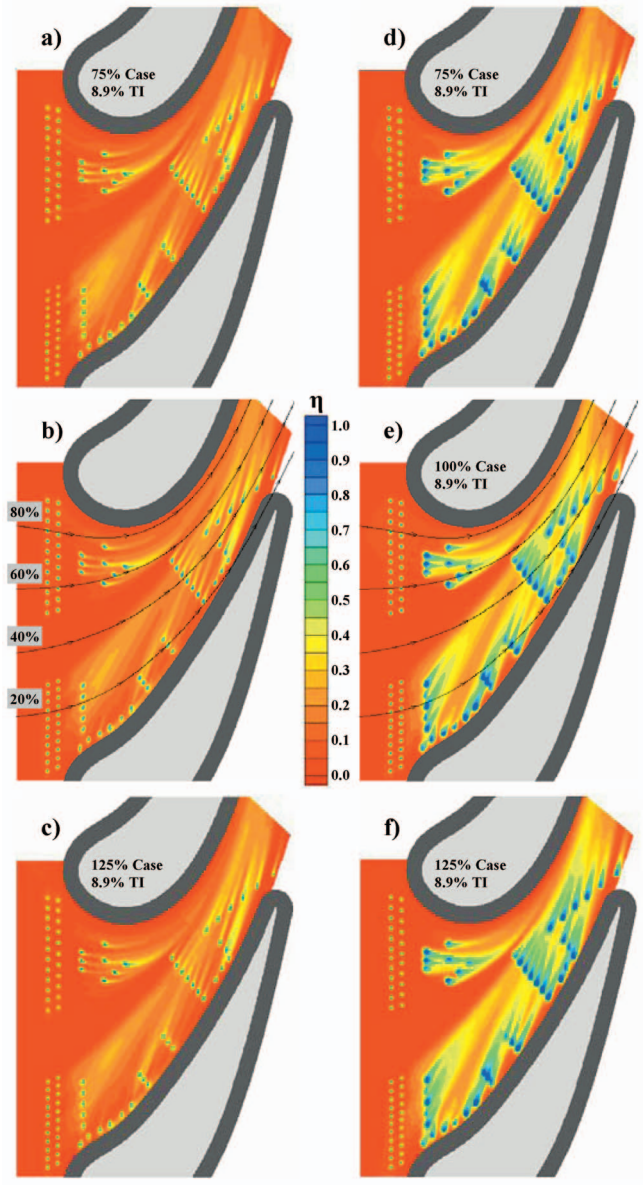

Fig. 6 Effectiveness contours at high freestream turbulence for the cylindrical passage (*a–c*) and fan-shaped passage (*d–f*)

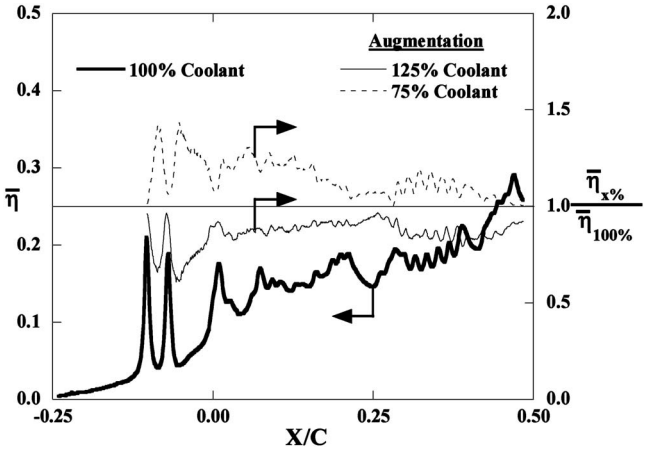

Fig. 7 Laterally averaged effectiveness for the 100% baseline case and augmentation of laterally averaged effectiveness for the 75% and 125% cases on the cylindrical passage at low freestream turbulence

have relatively good lateral spreading despite a hole-to-hole spacing of 6.2. This spreading was perhaps due to the effect of the upstream double row of holes.

Holes placed directly upstream of other holes seemed to increase the cooling benefit from that downstream hole. This phenomenon has been seen on the vane surface in the near pressure side region as well by Colban et al. [27], where the upstream cooling prevented the natural jet lift-off that would occur otherwise.

Streamlines are shown for the baseline contour in Fig. 5(*b*). The streamlines were calculated from the velocity vectors at 2% span from a 3D CFD computation in FLUENT 6.1.2. Near the suction side, the holes were clearly swept in the direction of the streamlines, despite their orientation angles toward the pressure side. This partially confirms the observances of Friedrichs et al. [19] and Knost and Thole [20] that the coolant trajectories of the film-cooling holes are primarily dictated by the near-wall streamlines and not by the hole orientations. However, near the pressure side region, the orientation angles of the holes were in the direction of the cross-passage pressure gradient, and not in line with the streamline. The coolant in this case followed the orientation angle direction and not the near-wall streamline direction. These results seem to modify the suggestions of the previous studies, such that the injected coolant will follow the near-wall streamline direction unless it is oriented in the direction of the cross-passage pressure gradient.

To quantify the development of the coolant through the passage and examine the effect of flow rate on effectiveness, pitch-wise lateral averages were done for each data set. Figure 7 shows $\bar{\eta}$ for the baseline 100% cylindrical case at low freestream turbulence. The two spikes in $\bar{\eta}$ were caused by the leading edge rows, but overall the leading edge rows had very little effect on increasing $\bar{\eta}$. Beginning at $X/C=0.0$, there was a continual increase in $\bar{\eta}$ throughout the passage by the addition of coolant from each successive row.

Also shown in Fig. 7 is the augmentation in $\bar{\eta}$ for the 125% and 75% cases relative to the baseline 100% case. It is immediately evident that better cooling performance was achieved at the lower mass flow rate, with a continual decrease in $\bar{\eta}$ with increased blowing. This was a result of jet liftoff from the cylindrical holes. The same trend of increased cylindrical jet liftoff with increased blowing ratio was also observed in the work done by Jabbari et al. [28].

Fan-Shaped Holes at Low Freestream Turbulence. The effectiveness contours for the fan-shaped passage at low turbulence are shown in Figs. 5(*d*)–5(*f*). It is immediately obvious that the fan-shaped cooling holes provided much better cooling to the end-wall than their cylindrical counterparts for the same coolant flow rate. Specifically, the fan-shaped holes had much better lateral spreading, which allowed the jets to stay attached to the surface because of the reduction in jet momentum. It should be pointed again that the blowing ratios given in the contour in Fig. 4(*a*) are valid for the cylindrical metering area of fan-shaped holes, and that the effective blowing ratio at the fan-shaped hole exit would be approximately 22% of those values, corresponding to an area ratio of 4.6 for the fan-shaped holes.

It is interesting to note that in the area of highest blowing ratio near the pressure side leading edge next to the fillet some of the jets appear to be lifting off, just as in the cylindrical passage. This seems to suggest that the liftoff in that region was not only due to high blowing ratios, but also because of strong secondary flows. Again, the holes near the suction side were swept toward the suction side following the near-wall streamlines, while the holes near the pressure side were directed along the path dictated by their orientation angles.

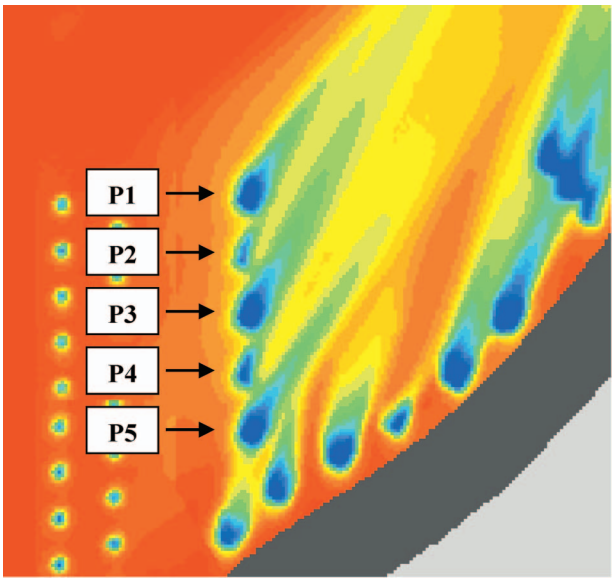

Fig. 8 Closeup view of region near the pressure side leading edge (baseline 100% case)

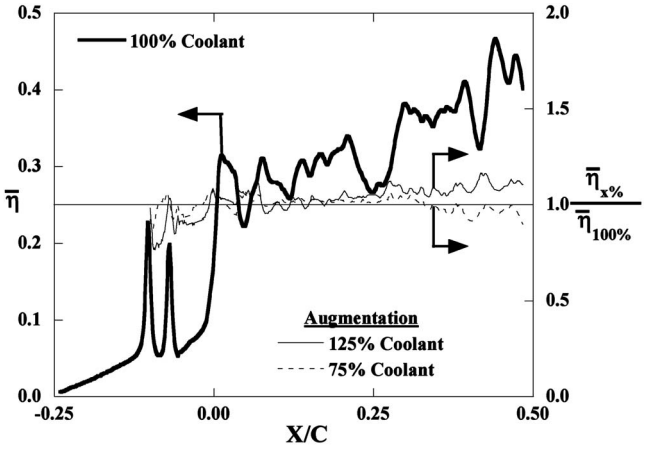

Fig. 9 Laterally averaged effectiveness for the 100% baseline case and augmentation of laterally averaged effectiveness for the 75% and 125% cases on the fan-shaped passage at low freestream turbulence

Upon closer examination of Fig. 5(*e*) for the baseline 100% case, the region shown in Fig. 8 near the pressure side leading edge displayed an interesting physical phenomenon. The jets in the first pressure side row exhibited an alternating pattern of separation and attachment. The first hole (labeled *P*1) produced a typical coolant footprint downstream of a fan-shaped hole. However, the next hole in the line, *P*2, lifted off of the surface entirely. The following hole, *P*3, again produced a coolant footprint typical of a fan-shaped hole, as did *P*5. However, as with *P*2, *P*4 again lifted off of the surface completely. Because of the orientation angle and close hole spacing, the jet from *P*2 was blocked by the coolant exiting *P*1. This caused jet *P*2 to flow up and over jet *P*1 and lift off of the surface. Because jet *P*2 did not remain attached to the surface, jet *P*3 had a clear path and behaved normally. However, the path of jet *P*4 was again blocked by the downstream jet from *P*3, causing jet *P*4 to lift off of the surface. This alternating pattern of flow blockages was caused by the combination of compound angle and hole spacing, and could probably be eliminated by increasing the hole spacing in this location.

To evaluate the cooling development through the passage, $\bar{\eta}$ values for the baseline case in the fan-shaped passage are shown in Fig. 9. As with the cylindrical passage, the upstream double row of holes had little cooling benefit for the endwall surface, and was mainly wasted in mixing with the freestream. $\bar{\eta}$ was seen to increase continually throughout the passage, reaching a consistent level as high as $\bar{\eta}=0.45$ near the end of the passage.

Also shown in Fig. 9 are the augmentations of $\bar{\eta}$ for the 75% and 125% cases in the fan-shaped passage relative to the baseline 100% case. In comparison with the cylindrical passage, changing the flow rate did not elicit nearly as large of an effect on $\bar{\eta}$ for the fan-shaped holes, causing only a minor increase in cooling performance with increased flow rate. The relative insensitivity to flow rate was perhaps because of the lateral jet spreading witnessed with the fan-shaped holes, which allowed the fan-shaped holes to provide excellent coverage for all blowing rates. Similar results of small increases in cooling performance with increased blowing were reported for the vane surface with full coverage fan-shaped film cooling by Colban et al. [27].

Hole Geometry Comparison at Low Turbulence. As stated previously, the primary goal of this study was to quantify the thermal benefit of using fan-shaped holes instead of cylindrical holes on the endwall. Figure 10 shows the augmentation in $\bar{\eta}$ at all three flow rates for fan-shaped holes over cylindrical holes. The benefits in film-cooling effectiveness were both substantial and remarkable. Depending on location in the passage and flow rate, increases in $\bar{\eta}$ were seen anywhere from 50% to 150% from the cylindrical cases to the fan-shaped cases. The highest increases in $\bar{\eta}$ were observed just downstream of the hole exits. The highest flow rate yielded the largest increases in $\bar{\eta}$ augmentation, in part because of the flow rate insensitivity in the fan-shaped passage coupled with the jet liftoff in the cylindrical passage. Also, the trend was that decreased flow rate decreased the difference in $\bar{\eta}$ between the cylindrical and fan-shaped passages, a result noted previously in flat plate and vane studies.

Effects of High Freestream Turbulence. The many different combustor arrangements used in industry lead to a wide range of turbulence intensity levels somewhere between 5% and 20% entering the turbine section [29]. For this reason, we also performed the same measurements of adiabatic film-cooling effectiveness for both passages at a comparably high freestream turbulence level of TI=8.9%. The contours of film-cooling effectiveness for the cylindrical passage at high freestream turbulence are shown in Figs. 6(*a*)–6(*c*). Overall, the general patterns look quite similar to the cases with low turbulence (Figs. 5(*a*)–5(*c*)). To quantify the ef-

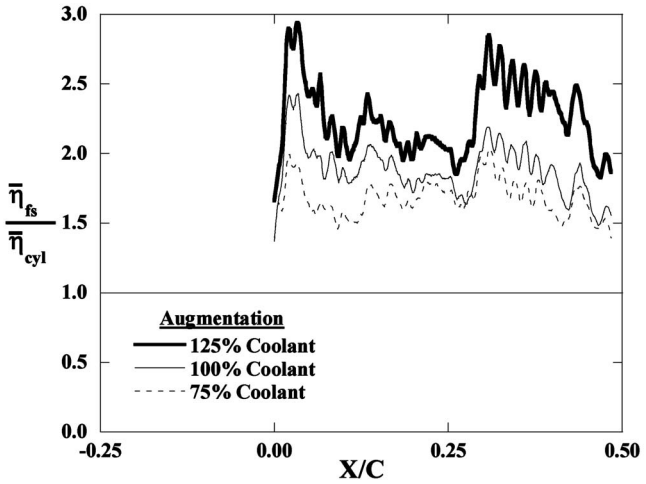

Fig. 10 Augmentation of laterally averaged film-cooling effectiveness for fan-shaped cooling holes over cylindrical cooling holes

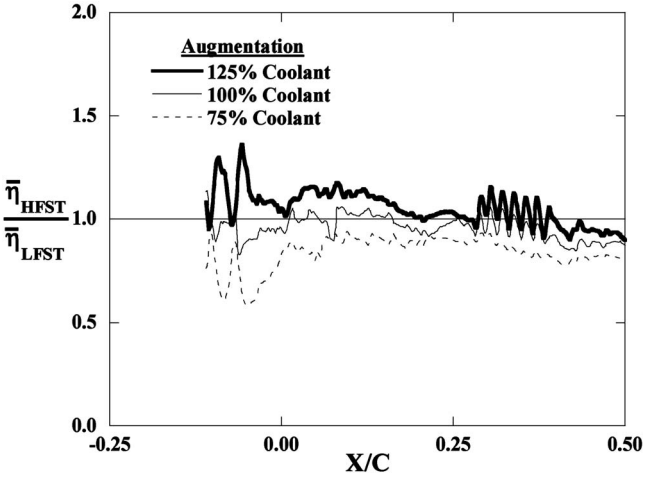

Fig. 11 Augmentation of laterally averaged film-cooling effectiveness for the cylindrical passage at high freestream turbulence

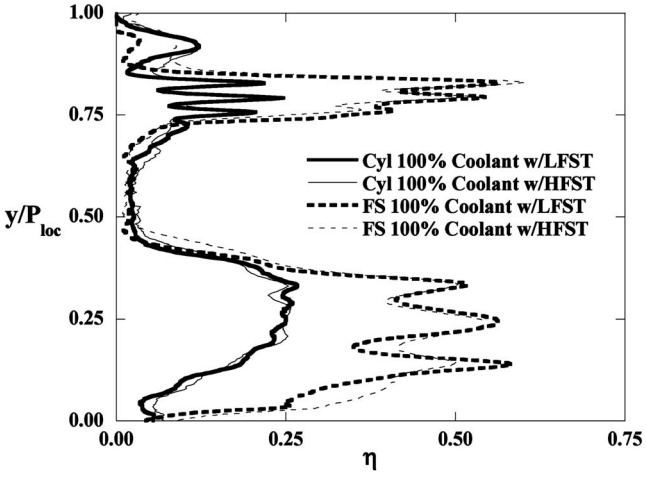

Fig. 13 Effectiveness along the data line shown in Fig. 3 for each baseline case

fects of elevated levels of turbulence intensity, augmentation levels of $\bar{\eta}$ for the high turbulence condition over the low turbulence condition are shown in Fig. 11 for the cylindrical passage. High freestream turbulence reduced film effectiveness for the 75% case near the entrance to the passage, likely as a result of increased mixing with the freestream. The baseline flow case showed little effect from elevated turbulence levels. The 125% case at high freestream turbulence showed a slight augmentation near the entrance to the passage, indicating that the extreme liftoff seen at low turbulence was somewhat counteracted by the high levels of turbulence, making the coolant more effective.

The effectiveness contours for the fan-shaped passage at high freestream turbulence are shown in Figs. 6(*d*)–6(*f*). Increased freestream turbulence had no noticeable effect on the overall flow pattern for the fan-shaped passage. Augmentations in $\bar{\eta}$ for the fan-shaped passage at high freestream turbulence are shown in Fig. 12 for all three flow rates. No significant change can be seen from the results, indicating that fan-shaped film cooling is relatively insensitive to the level of turbulence entering the turbine section.

As a way to further evaluate the effect of both hole shape and turbulence intensity, segments of effectiveness along the data line shown in Fig. 3 are shown in Fig. 13 for each of the baseline cases. Again, the superior performance of the fan-shaped holes to the cylindrical holes is immediately evident from the elevated effectiveness levels. The effect of high freestream turbulence on the fan-shaped holes nearest the pressure side ($0.10 < y/P_{loc} < 0.40$) was to decrease the peak-to-valley distance in effectiveness, or essentially smear out the coolant from elevated turbulent mixing.

Another way to visualize the results are in terms of the effectiveness along streamlines released from different vane pitch locations. The baseline contours shown in Figs. 5(*b*) and 5(*e*) and Figs. 6(*b*) and 6(*e*) each include four streamlines released from $Y/P=0.2$, 0.4, 0.6, and 0.8. The streamlines were taken from a CFD prediction without film cooling in FLUENT 6.1.2 at 2% span. The effectiveness along the 40% and 80% streamlines for each baseline case are shown in Figs. 14 and 15. For the streamlines released from $Y/P=0.4$, the benefit from the fan-shaped holes is clear and fairly consistent throughout the passage. However, the streamline at 80% pitch, which follows very close to the vane suction side, gives nearly the same levels for both hole geometries.

Area-Averaged Film-Cooling Effectiveness. To quantify the cooling benefit for the entire endwall surface, area-averaged values of adiabatic film-cooling effectiveness were calculated for

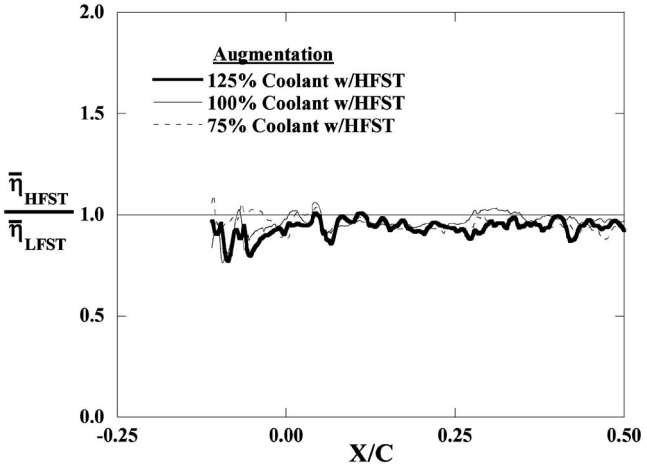

Fig. 12 Augmentation of laterally averaged film-cooling effectiveness for the fan-shaped passage at high freestream turbulence

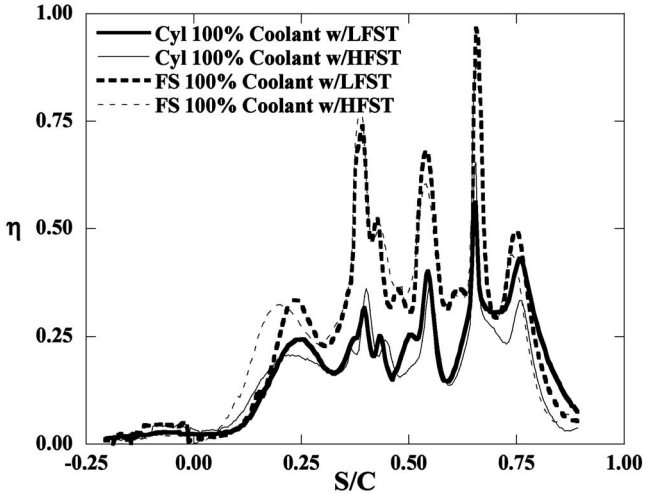

Fig. 14 Effectiveness along a streamline released from 40% pitch for each baseline case

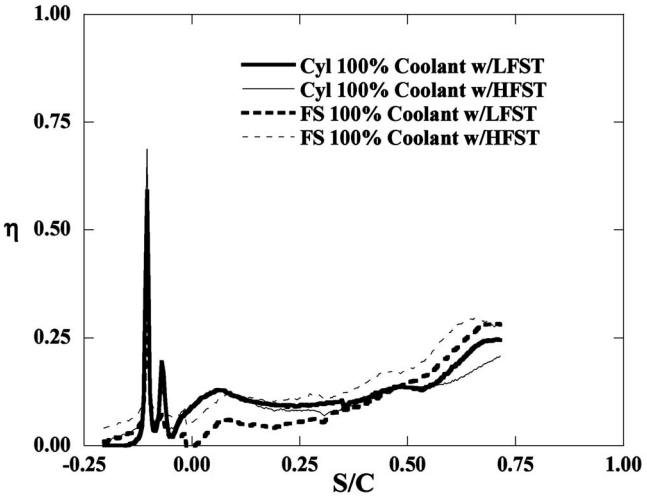

Fig. 15 Effectiveness along a streamline released from 80% pitch for each baseline case

each case. The area included in the calculation encompassed one vane pitch, beginning at a distance of $X/C=-0.25$ upstream of the vane leading edge and ending at the vane trailing edge ($X/C=0.5$). Area-averaged values are shown in Fig. 16 for each case listed in Table 3. The superior cooling performance of the fan-shaped holes is clear, with area-averaged film-effectiveness values 75% higher than for the cylindrical cases across the full range of flow rates. The effect of freestream turbulence was to decrease the film effectiveness by an average of 6% for the fan-shaped passage. Freestream turbulence had a stronger effect on the cylindrical passage because it changed the dependency of film effectiveness on flow rate. For low freestream turbulence, film effectiveness in the cylindrical passage decreased with flow rate as a result of coolant lift off. However, at high freestream turbulence, a slight increase in film effectiveness was observed with flow rate as a result of increased jet mixing that led to coolant spreading. Overall, the effect of turbulence on the cylindrical passage was to reduce the sensitivity of effectiveness to flow rate.

Area-averaged film-cooling effectiveness was also compared to the results reported in the study by Friedrichs et al. [19], and found to be in close agreement. The hole pattern used in the study of Friedrichs et al. [19] was very different from the pattern used in this study. They had four rows of holes located at axial positions

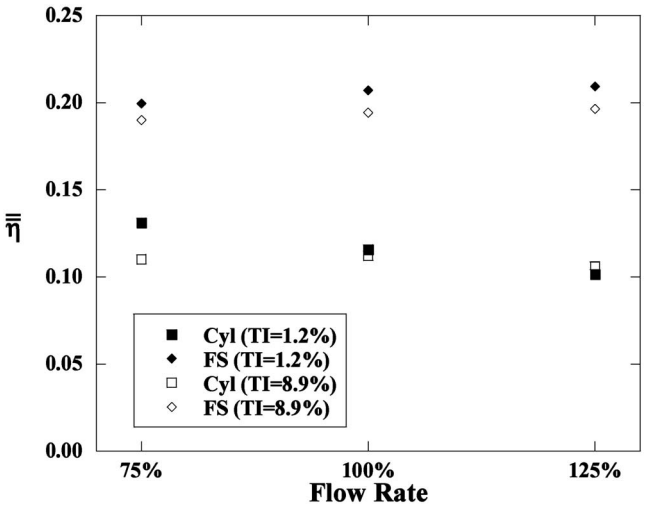

Fig. 16 Area-averaged film-cooling effectiveness for all cases

of $X/C\approx 0$, 0.3, 0.6, and 0.9. The difference in cooling hole layout between the two studies suggests that even though local effectiveness may vary significantly, perhaps there is an insensitivity of area-averaged effectiveness to hole layout. More investigation into this hypothesis will be needed.

Conclusions

This paper has presented high-resolution measurements of adiabatic film-cooling effectiveness for both cylindrical and fan-shaped holes on a turbine vane endwall surface. Results were presented at both high and low values of freestream turbulence. The measurements were performed in a large-scale, low-speed, two-passage, linear turbine vane cascade, with the identical cooling hole pattern in each passage but with different hole shapes.

The major conclusion from this work was a superior performance of fan-shaped holes in the platform region was found relative to cylindrical holes. An increase in film effectiveness of 75% based on area averages was seen by using fan-shaped holes instead of cylindrical holes. The effect of high freestream turbulence was to reduce cooling performance by 6% in the fan-shaped passage, and to change the dependency of film effectiveness on flow rate for the cylindrical passage.

Little benefit from a cooling standpoint was seen from the double row of staggered cylindrical holes placed upstream of each passage. Further work is planned to investigate the effect of the upstream blowing on the cooling performance of the downstream holes. Work is also planned to compare the aerodynamic performance of the two hole shapes.

Acknowledgment

The authors are grateful to Siemens Power Generation for their funding and support of this project.

Nomenclature

C = true vane chord
C_p = static pressure coefficient, $Cp=(p_{s,\mathrm{loc}}-p_{s,\mathrm{in}})/0.5\rho_{\mathrm{in}}U_{\mathrm{in}}^2$
D = film-cooling hole diameter
I = local momentum flux ratio, $I=\rho_c U_c^2/\rho_{\mathrm{loc}}U_{\mathrm{loc}}^2$
k = thermal conductivity
M = local blowing ratio, $M=\rho_c U_c/\rho_{\mathrm{loc}}U_{\mathrm{loc}}$
MFR = % total coolant mass flow per total passage mass flow
p = pressure
P = vane pitch
Re = Reynolds number, $\mathrm{Re}=U_{\mathrm{in}}C/\nu$
t = hole breakout width
s = distance measured along a streamline
S = streamwise distance around the vane
T = temperature
TI = turbulence intensity
U = velocity
X = axial coordinate measured from the vane stagnation
y = local pitchwise coordinate
Y = pitchwise coordinate

Greek

α = inclination angle
δ = boundary layer thickness
ν = kinematic viscosity
η = adiabatic film-cooling effectiveness
Λ_x = integral length scale
ρ = density
φ_1 = lateral diffusion angle
φ_2 = forward expansion angle

Subscripts

- c = coolant
- cyl = cylindrical holes
- fs = fan-shaped holes
- HFST = high freestream turbulence condition (TI=8.9%)
- in = inlet condition
- LFST = low freestream turbulence condition (TI=1.2%)
- loc = local value
- max = maximum value of given variable at that location
- s = static

Overbar

- - = lateral average
- = = area average

References

[1] Bunker, R. S., 2005, "A Review of Shaped Hole Turbine Film-Cooling Technology," ASME J. Heat Transfer, **127**, pp. 441–453.

[2] Goldstein, R. J., Eckert, E. R. G., and Burggraf, F., 1974, "Effects of Hole Geometry and Density on Three-Dimensional Film Cooling," Int. J. Heat Mass Transfer, **17**, pp. 595–607.

[3] Kercher, D. M., 2003, *Film-Cooling Bibliography: 1940–2002*, private publication.

[4] Kercher, D. M., 2005, *Film-Cooling Bibliography Addendum: 1999–2004*, private publication.

[5] Goldstein, R. J., 1971, "Film Cooling," Adv. Heat Transfer, **7**, pp. 321–379.

[6] Bogard, D. G., and Thole, K. A., 2007, "Gas Turbine Film Cooling," Turbine Science and Technology (AIAA Progress in Astronautics and Aeronautics: AIAA).

[7] Vogel, G., Wagner, G., and Bölcs, A., 2002, "Transient Liquid Crystal Technique Combined With PSP for Improved Film Cooling Measurements," *Proceedings 10th International Symposium on Flow Visualization*, Kyoto, Japan, Vol. F0109.

[8] Vogel, G., 2002, "Experimental Study on a Heavy Film Cooled Nozzle Guide Vane With Contoured Platforms," Ph.D. dissertation, École Polytechnique Fédérale de Lausanne, Lausanne, Switzerland.

[9] Barigozzi, G., Benzoni, G., Franchini, G., and Perdichizzi, A., 2005, "Fan-Shaped Hole Effects on the Aero-Thermal Performance of a Film Cooled Endwall," ASME Paper No. GT2005-68544.

[10] Blair, M. F., 1974, "An Experimental Study of Heat Transfer and Film Cooling on Large-Scale Turbine Endwalls," ASME J. Heat Transfer, **96**, pp. 524–529.

[11] Granser, D., and Schulenberg, T., 1990, "Prediction and Measurement of Film Cooling Effectiveness for a First Stage Turbine Vane Shroud," ASME Paper No. 90-GT-95.

[12] Colban, W., Thole, K. A., and Zess, G., 2003, "Combustor Turbine Interface Studies—Part 1: Endwall Effectiveness Measurements," ASME J. Turbomach., **125**, pp. 193–202.

[13] Knost, D. G., and Thole, K. A., 2003, "Computational Predictions of Endwall Film-Cooling for a First Stage Vane," ASME Paper No. GT2003-38252.

[14] Harasgama, S. P., and Burton, C. D., 1992, "Film Cooling Research on the Endwall of a Turbine Nozzle Guide Vane in a Short Duration Annular Cascade: Part 1—Experimental Technique and Results," ASME J. Turbomach., **114**, pp. 734–740.

[15] Nicklas, M., 2001, "Film-Cooled Turbine Endwall in a Transonic Flow Field: Part II—Heat Transfer and Film-Cooling Effectiveness," Paper No. 2001-GT-0146.

[16] Sieverding, C. H., and Wilputte, P., 1981, "Influence of Mach Number and Endwall Cooling on Secondary Flows in a Straight Nozzle Cascade," Trans. ASME: J. Eng. Gas Turbines Power, **103**, pp. 257–264.

[17] Kost, F., and Nicklas, M., 2001, "Film-Cooled Turbine Endwall in a Transonic Flow Field: Part I—Aerodynamic Measurements," ASME Paper No. 2001-GT-0145.

[18] Colban, W., Lethander, A. T., Thole, K. A., and Zess, G., 2003, "Combustor Turbine Interface Studies—Part 2: Flow and Thermal Field Measurements," ASME J. Turbomach., **125**, pp. 203–209.

[19] Friedrichs, S., Hodson, H. P., and Dawes, W. N., 1995, "Distribution of Film-Cooling Effectiveness on a Turbine Endwall Measured Using the Ammonia and Diazo Technique," ASME J. Turbomach., **118**, pp. 613–621.

[20] Knost, D. G., and Thole, K. A., 2005, "Adiabatic Effectiveness Measurements of Endwall Film-Cooling for a First Stage Vane," ASME J. Turbomach., **127**, pp. 297–305.

[21] Oke, R. A., Burd, S. W., Simon, T. W., and Vahlberg, R., 2000, "Measurements in a Turbine Cascade over a Contoured Endwall: Discrete Hole Injection of Bleed Flow," ASME Paper No. 2000-GT-214.

[22] Zhang, L. J., and Jaiswal, R. S., 2001, "Turbine Nozzle Endwall Film Cooling Study Using Pressure-Sensitive Paint," ASME J. Turbomach., **123**, pp. 730–738.

[23] Zhang, L., and Moon, H. K., 2003, "Turbine Nozzle Endwall Inlet Film Cooling—The Effect of a Back-Facing Step," ASME Paper No. GT2003–38319.

[24] Colban, W., Gratton, A., Thole, K. A., and Haendler, M., 2006, "Heat Transfer and Film-Cooling Measurements on a Stator Vane With Fan-Shaped Cooling Holes," ASME J. Turbomach., **128**, pp. 53–61.

[25] Ethridge, M. I., Cutbirth, J. M., and Bogard, D. G., 2000, "Scaling of Performance for Varying Density Ratio Coolants on an Airfoil With Strong Curvature and Pressure Gradient Effects," ASME Paper No. 2000-GT-239.

[26] Moffat, R. J., 1988, "Describing the Uncertainties in Experimental Results," Exp. Therm. Fluid Sci., **1**, pp. 3–17.

[27] Colban, W., Thole, K. A., and Haendler, M., 2005, "Experimental and Computational Comparisons of Fan-Shaped Film-Cooling on a Turbine Vane Surface," ASME J. Turbomach., **129**, pp. 23–31.

[28] Jabbari, M. Y., Marston, K. C., Eckert, E. R. G., and Goldstein, R. J., 1994, "Film Cooling of the Gas Turbine Endwall by Discrete-Hole Injection," ASME Paper No. 94-GT-67.

[29] Goebel, S. G., Abauf, N., Lovett, J. A., and Lee, C.-P., 1993, "Measurements of Combustor Velocity and Turbulence Profiles," ASME Paper No. 93-GT-228.

Computations of Turbulent Flow and Heat Transfer Through a Three-Dimensional Nonaxisymmetric Blade Passage

Arun K. Saha

Sumanta Acharya

Turbine Innovation and Energy Research (TIER) Center,
Louisiana State University,
Baton Rouge, LA 70803

The design of a three-dimensional nonaxisymmetric end wall is carried out using three-dimensional numerical simulations. The computations have been conducted both for the flat and contoured end walls. The performance of the end wall is evaluated by comparing the heat transfer and total pressure loss reduction. The contouring is done in such a way to have convex curvature in the pressure side and concave surface in the suction side. The convex surface increases the velocity by reducing the local static pressure, while the concave surface decreases the velocity by increasing the local pressure. The profiling of the end wall is done by combining two curves, one that varies in the streamwise direction, while the other varies in the pitchwise direction. Several contoured end walls are created by varying the streamwise variation while keeping the pitchwise curve constant. The flow near the contoured end wall is seen to be significantly different from that near the flat end wall. The contoured end wall is found to reduce the secondary flow by decreasing radial pressure gradient. The total pressure loss is also lower and the average heat transfer reduces by about 8% compared to the flat end wall. Local reductions in heat transfer are significant (factor of 3). This study demonstrates the potential of three-dimensional end-wall contouring for reducing the thermal loading on the end wall.
[DOI: 10.1115/1.2776952]

Introduction

The flow in blade passages is strongly three dimensional because of the secondary vortical flows established by the radial and pitchwise pressure variations in the passage. These secondary flows enhance mixing, increase aerodynamic loss in the passage, and entrain higher temperature gases from the midspan regions to the end wall, increasing the near-wall thermal loading. The curvature of the blade, the junction at the blade/end wall (or leading edge of the blade), and the inlet velocity profile all contribute to the strength of the secondary flows. In a low aspect ratio turbine blade, the effect of secondary flow is significant and accounts for a major portion of the total loss. In view of the increased aerodynamic loss, considerable research has been done by turbine designers in developing design strategies for reducing the secondary flow. There are various ways by which the pressure variation responsible for the secondary flow generation can be minimized. One promising concept is to modify the junction region with a sharp-edged fillet (Pierce et al. [1], Davenport et al. [2], Pierce and Shin [3], Zess and Thole [4], and Shih and Lin [5]). The use of fillet modifies the pressure distribution locally near the junction, thus reducing the strength and size of secondary vortices. A combined numerical and experimental study on leading-edge airfoil fillet by Zess and Thole [4] showed that the pointed/sharp type of fillet can eliminate or reduce horseshoe vortices. They also reported that the turbulent kinetic energy is greatly reduced in the end-wall region. This approach suffers from the drawback that the sharp edges must be aligned with the stagnation flow. However, Sauer et al. [6], using a bulb-type fillet, showed that the strength of the horseshoe vortices is enhanced on the suction side, leading to a reduction in the strength of the overall passage secondary flow. Other studies where modification of the end wall have shown a reduction in the secondary flows include Harvey et al. [7], Hartland et al. [8], Kopper and Milano [9], and Shih and Lin [5].

In the recent past, two-dimensional end-wall contouring has been performed to minimize the intensity and size of the secondary vortices. The contouring is achieved by contracting the flow area upstream of the blade in the streamwise direction, which accelerates the flow through the blade passage (Dossena et al. [10], Duden et al. [11], Burd and Simon [12], Shih et al. [13], and Lin et al. [14,15]). Kopper and Milano [9] have conducted an experimental investigation of (end-wall) contouring for a low aspect ratio nozzle vane configuration and observed 17% reduction in the full passage mass average loss compared to the flat end wall. In a separate experimental study by Burd and Simon [12], the advantages of 2D end-wall contouring are demonstrated. Their experiments are performed in cascade wind tunnel having low aspect ratio guide vanes. They also reported a significant variation in the near-wall flow structures between the flat and contoured end walls.

To reduce the secondary loss further by reducing the near-wall pitchwise pressure gradient, three-dimensional nonaxisymmetric contouring of the end wall has been proposed in a few recent studies (Hartland et al. [8], Yan et al. [16], and Harvey et al. [7]). Hartland et al. [8] designed a three-dimensional end wall using algebraic equations. However, no reduction in the pressure loss is observed. Yan et al. [16] adopted a different design strategy of using convex curvature near the pressure surface to reduce the static pressure and concave curvature near the suction surface to increase it. The study involves both experiments and computations. A reduction of about 20% in the pressure loss is found and a more uniform exit flow is also achieved with shaped end wall.

All the reported studies on 3D end-wall contouring have focused attention on the aerodynamics and pressure loss. There is absolutely no study that shows the influence of three-dimensional

Contributed by the International Gas Turbine Institute of ASME for publication in the JOURNAL OF TURBOMACHINERY. Manuscript received October 8, 2006; final manuscript received May 31, 2007; published online May 2, 2008. Review conducted by David Wisler. Paper presented at the ASME Turbo Expo 2006: Land, Sea and Air (GT2006), Barcelona, Spain, May 8–11, 2006. Paper No. GT2006-90390.

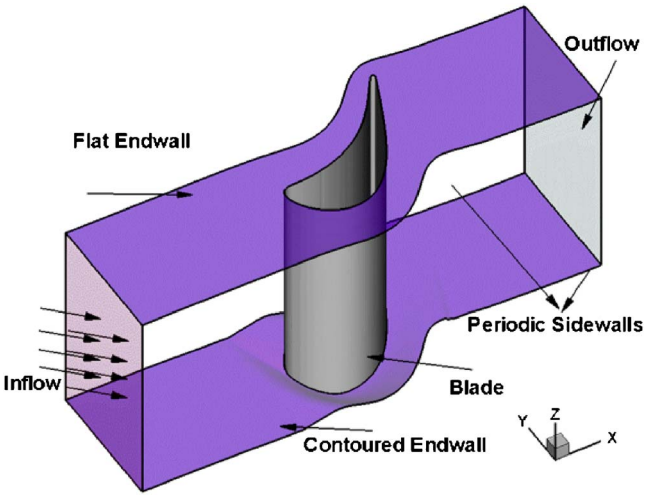

Fig. 1 Flow model and the confining boundaries

nonaxisymmetric contouring on end wall and blade surface heat transfer. This is the primary motivation for the present paper.

In the present study, three-dimensional contouring of the end wall is explored. Various end walls are studied and their performance is evaluated by comparing the reduction in heat transfer and total pressure loss. Based on the results of the various test cases, a specific end-wall contour is selected, and its results are compared in detail with those of a flat end wall.

End-Wall Design

The incompressible flow computations are performed for a scaled up GE-E^3 first stage blade passage. The rotor blades have a constant axial chord length of 31.2 cm and aspect ratio (span to actual chord, the actual chord being 35.86 cm) of 1.28. The blade leading-edge pitch is 29.08 cm. The inlet of the computational domain is placed at about 1.5 times the axial chord from the leading edge, while the outlet is located at 1.5 times the axial chord from the trailing edge. The schematic of the computational domain along with the different boundaries is presented in Fig. 1.

The three-dimensional end-wall profile is calculated algebraically by combining the streamwise and pitchwise algebraic variations shown in Figs. 2(*a*) and 2(*b*). Each variation is expressed as an analytical profile. The combination of the two profiles is achieved by multiplying the two analytical profiles and scaling them. Profiling of the end wall is done in such a way to have convex curvature in the pressure side and concave curvature on the suction side. The convex surface increases the velocity by reducing the local static pressure, while the concave surface decreases the velocity by increasing the local pressure. Four major categories of streamwise profiles but with the same pitchwise profile (Fig. 2(*b*)) are combined, leading to a total of nine different three-dimensional end-wall contours. The details of the four streamwise profiles are as follows: (i) an initial linear profile followed by a sinusoidal (sine) profile, (ii) an initial linear profile followed by a plateau, and then followed by another linear profile, (iii) an initial sinusoidal (sine) profile followed by a linear profile, and (iv) an initial sinusoidal (sine) profile followed by another sinusoidal (sine) profile. Different combinations of streamwise and pitchwise variations result in various contoured end walls. In the present paper, various streamwise variations studied are listed in Table 1. The details of the streamwise profile and the maximum and minimum heights of the end wall are also shown in the table.

The surface averaged Nusselt number and the peak Nusselt numbers in the throat area (TA) and in the leading-edge area (LEA) are shown in Table 2. Comparison of Nusselt numbers for the various cases reveals that Case 10 shows a better overall heat transfer reduction. Therefore, the results are discussed for this contoured end wall and the flat end wall. The contours of vertical height on the bottom end wall for Case 10 are shown in Fig. 3(*a*). Figure 3(*b*) depicts the three-dimensional view of the end wall that clearly shows the convex curvature near the pressure side and concave curvature along the suction side.

Computational Details

The computations were carried out using one blade with periodic boundary conditions imposed along the boundaries in the circumferential (pitch) direction. At the inlet, a temperature of 302.15 K and a velocity of 10.26 m/s are specified along with an inlet flow angle of −55 deg with the axial direction. This results in a Reynolds number of 2.1×10^5 based on the actual chord and a zero angle of attack for the blade. A turbulence intensity of 5% and a length scale of 0.055 times the actual chord are specified at the inlet. At the exit, outflow boundary conditions are employed. No-slip velocity boundary conditions are used for all solid walls. Uniform heat flux (840 W/m^2 K) conditions are applied along the

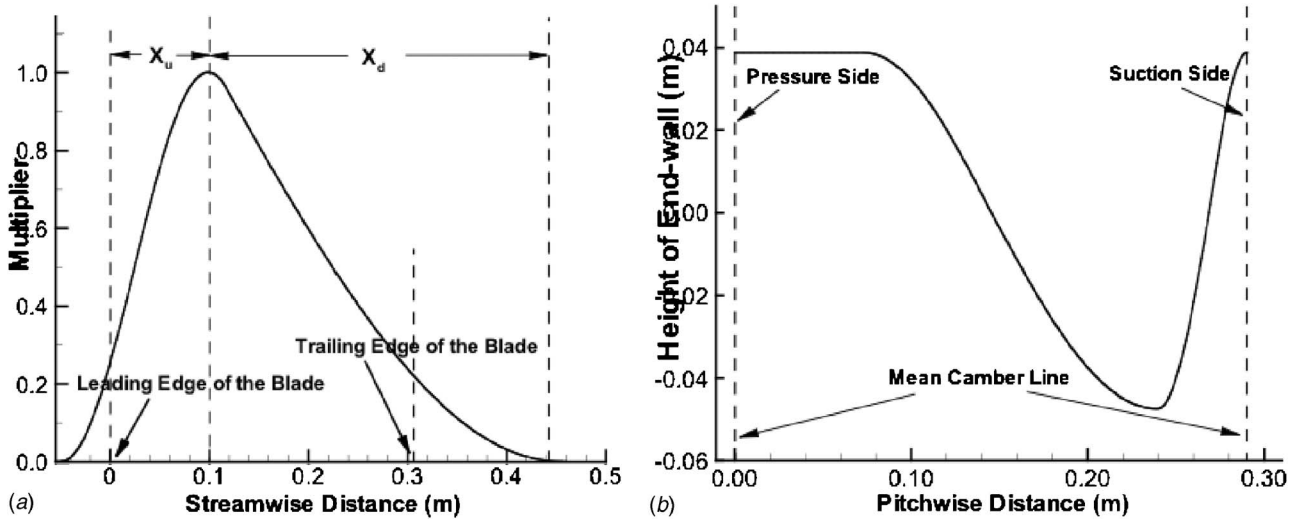

Fig. 2 The distribution used in (*a*) streamwise and (*b*) pitchwise directions to generate the end wall

Table 1 Description of the different streamwise variations

Cases	Streamwise distribution of the contoured end-wall	Salient parameters of the end-walls
1	Baseline or flat end-wall	
2	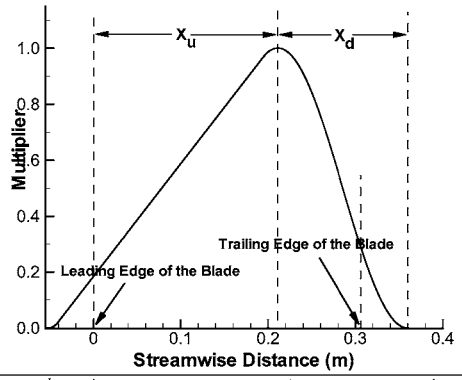	X_u=0.21, X_d=0.15 Height of End-wall, Max. Z=0.039 Min. Z=–0.047
3		X_u=0.18, X_d=0.18 Max. Z=0.039 Min. Z=–0.046
4		X_u=0.16, X_d=0.2 Max. Z=0.039 Min. Z=–0.045
5		X_u=0.13, X_d=0.23 Max. Z=0.039 Min. Z=–0.045
6	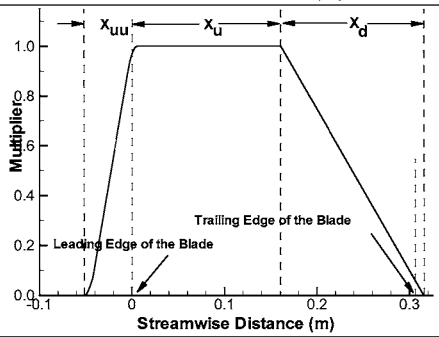	X_{uu}=–0.05, X_u=0.16 X_d=0.16 Starting location of uniform height=SL_u=0, Max. Z=0.029 Min.Z=–0.035
7		X_{uu}=–0.11, SL_u=0.07 Max. Z=0.019 Min. Z=–0.023
8		X_{uu}=–0.11, SL_u=0.07 Max. Z=0.029 Min. Z=–0.035
9	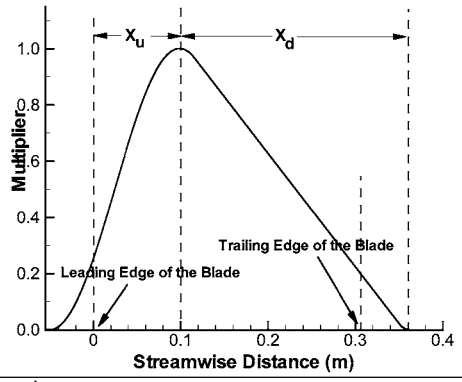	X_u=0.1, X_d=0.26 Max. Z=0.039 Min. Z=–0.046
10	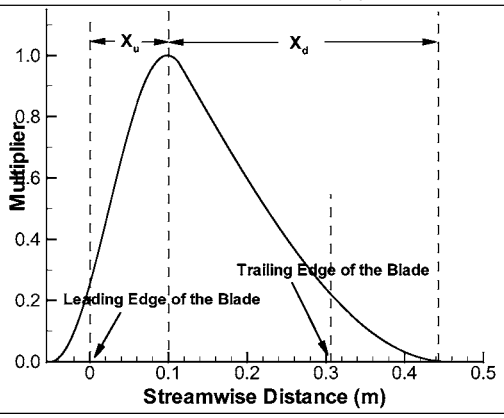	X_u=0.1, X_d=0.34 Max. Z=0.039 Min. Z=–0.046

bottom end wall, while the top wall and blade surface are insulated. The working fluid is air whose Prandtl number is 0.7.

All the calculations were performed with the commercial code FLUENT. The three-dimensional incompressible Reynolds-averaged Navier–Stokes equations are solved using a finite volume formulation to discretize these equations. Grid generation was done using GRIDPRO that produces a structured mesh. A typical grid along the confining surfaces and also on the contoured end wall is presented in Fig. 4. A zoomed-in grid (Fig. 4(*c*)) has also been presented to show the quality of the blade–end-wall

Table 2 Nusselt number of the end wall for the various cases

Cases	Heat transfer characteristics of the end wall, Nu
1	Avg=736 Peak: leading-edge area (LEA)=2200, throat area (TA)=1050
2	Avg=710, Peak: LEA=1620, TA=2100
3	Avg=709.4, Peak: LEA=2148, TA=1980
4	Avg=703.8, Peak: LEA=2158, TA=1797
5	Avg=696.9, Peak: LEA=2157, TA=1525
6	Avg=692.1, Peak: LEA=2288, TA=1300
7	Avg=690.8, Peak: LEA=2215, TA=1375
8	Avg=678.2, Peak: LEA=2250, TA=1404
9	Avg=688.9, Peak: LEA=2041, TA=1400
10	Avg=677.7, Peak: LEA=2158, TA=1075

junction grid. The number of grid points used is generally over 1×10^6 with near-wall stretching of the grid points toward the bottom end wall. A realizable k-ε model by Shih et al. [17] with a two-layer near-wall formulation is employed to simulate the turbulence. In all the simulations, the Y^+ values of the first grid point away from the wall are maintained below 2.0. The pressure equation, momentum equations, and the transport equations for k and ε are all discretized using second order schemes. All the flow variables presented here are converged to residual levels of order of 10^{-4}, while the residual level for the temperature field was 10^{-7}. The residual levels are normalized with respect to the inlet mass flow rate (for conservation of mass) and inlet momentum (for conservation of momentum equations).

Grid Independence Study

Grid independence is carried out by comparing solutions of flat end wall using two different grids having 972,320 and 2,204,688 cells. For all cases, the grid is clustered near the bottom end wall and blade surfaces. Though the number of grid points is increased in the whole domain, the bottom end-wall and blade wall regions are refined the most. The Y^+ values for the coarse and fine grids near the bottom end wall were 1.71 and 1.15, respectively, while keeping the corresponding values on the blade wall below the permissible limits ($Y^+\cong1.0$ for fine mesh). Figure 5 shows the pitchwise variation of the Nusselt number and static pressure coefficient, $C_{p,s}$ on the bottom end wall at an axial location 15% ($X=0.15C_x$) downstream the leading edge of the blade for the two grids. There is no significant difference in both Nusselt number and the pressure coefficient for the two grid sizes. The local Nusselt number and static pressure coefficient distribution on the end wall for the two grids is also presented in Fig. 6. There are no significant differences between the simulations with two different grids. The difference in the averaged values of the Nusselt number

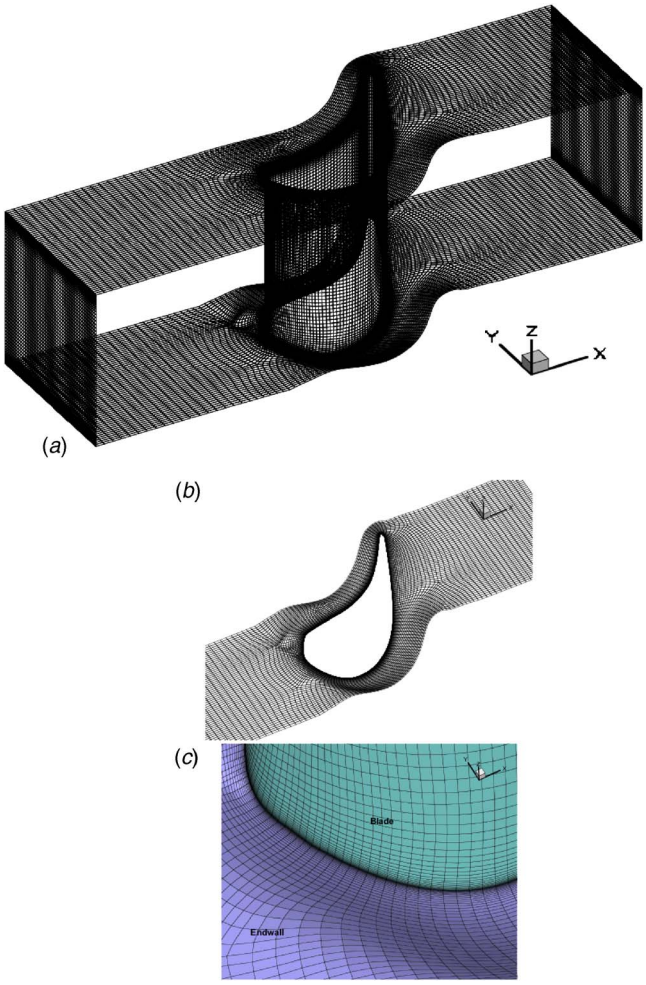

(a)
(b)
(c)

Fig. 4 (*a*) Three-dimensional view of the grid on the confining boundaries, (*b*) grid used on the end walls, and (*c*) a close-up view of the grid near the end-wall–blade junction

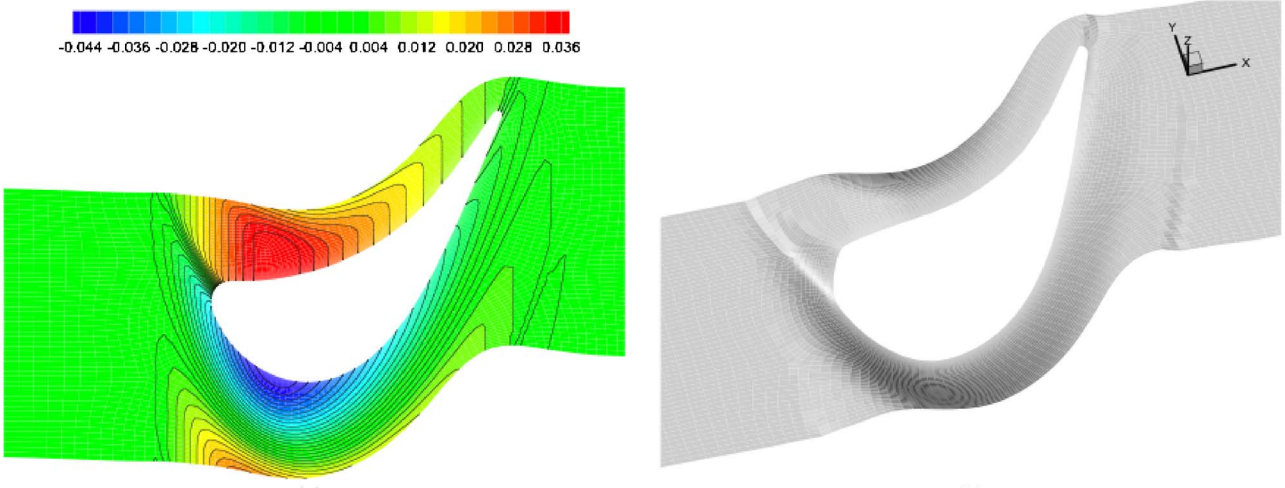

(a)
(b)

Fig. 3 (*a*) Contours of the end-wall height in meters and (*b*) three-dimensional view of the end wall

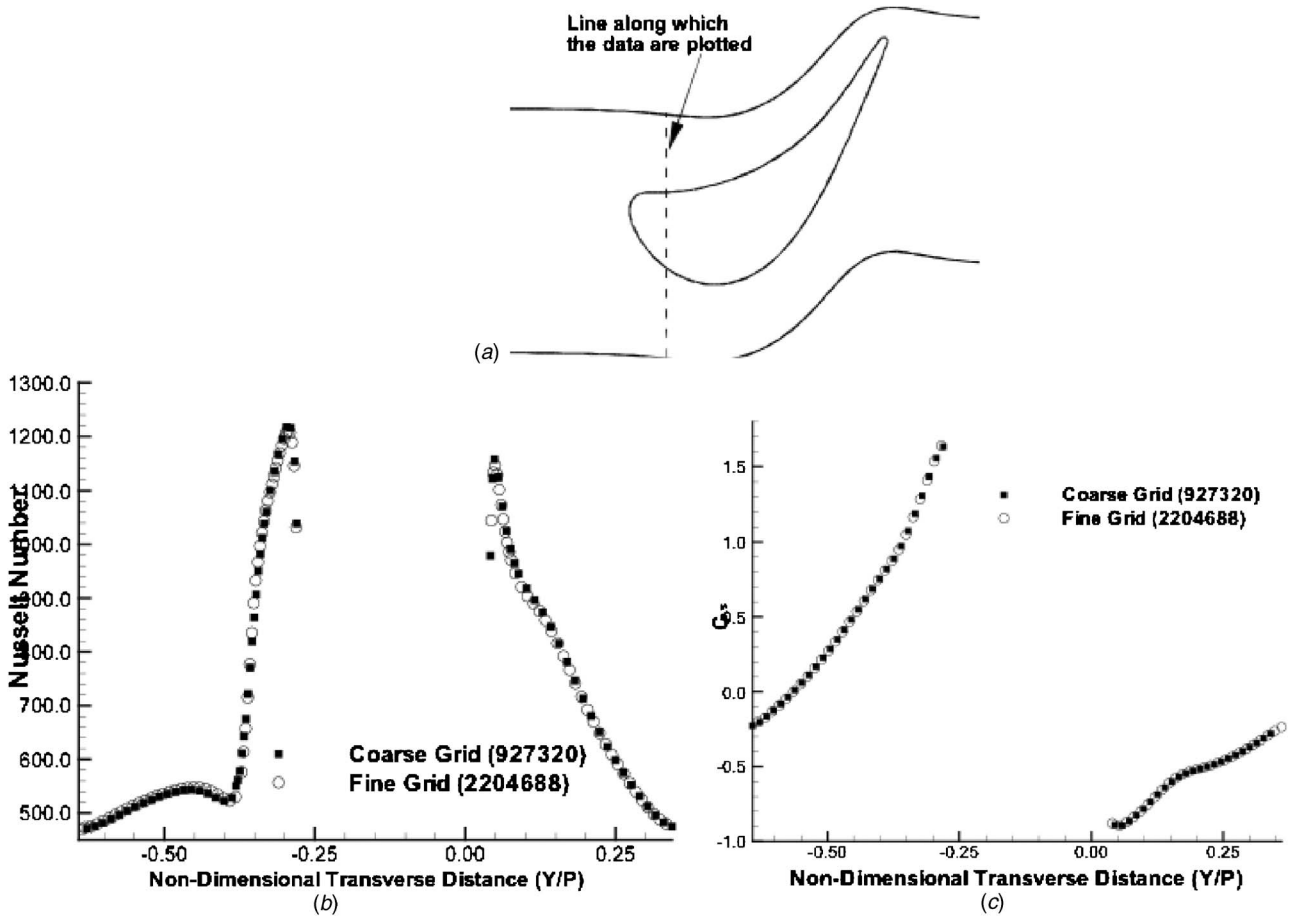

Fig. 5 (*a*) **Plane along which the line plots of Nusselt number and static pressure coefficient versus transverse distance in** (*b*) **and** (*c*) **are drawn. Note that** $Y/P=0$ **represents the intersection of the axial chord line shown with the pressure surface.** $Y/P>0$ **represents the pressure side.**

for the coarse and fine grids is only 1.3%. Therefore, calculations with 927,320 cells appear to be grid independent.

In an earlier study with the same blade [18,19], the present calculation procedure and turbulence model were validated against measurements and shown to provide blade tip heat transfer predictions that agree with experimental data to within 10–15%. All the correct qualitative trends were predicted including the location and size of low and high heat transfer coefficient regions. It is therefore expected that the results of the present numerical study can be used to evaluate trends and the effects of the end wall on the heat transfer.

The present code is also validated against the experimental results of Jin and Goldstein [20] and Srinivasan and Goldstein [21] for a similar blade geometry and cascade dimensions. The blade

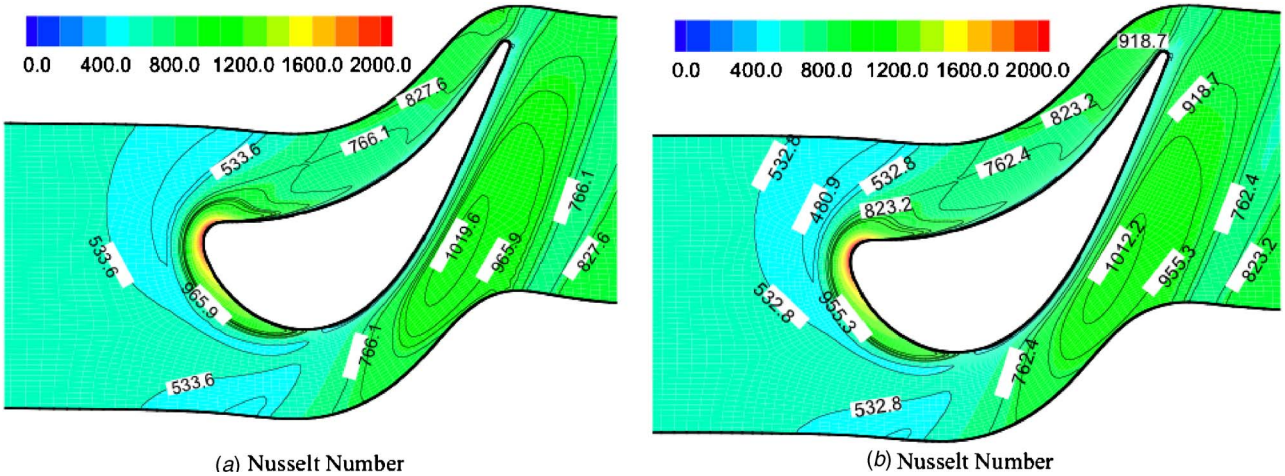

Fig. 6 Grid independence study showing contours of Nusselt number on the end wall using two grids: (*a*) **size=927,320 (coarse) and** (*b*) **size=2,204,688 (fine)**

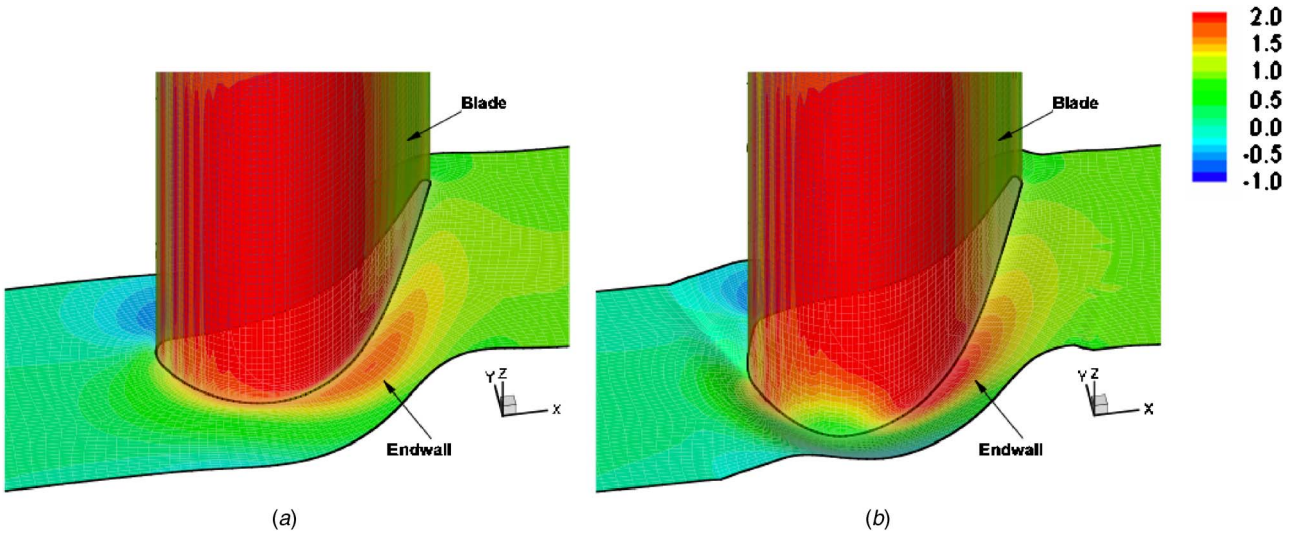

(*a*) (*b*)

Fig. 7 Static pressure coefficient on both the blade and end wall: (*a*) flat end wall and (*b*) contoured end wall

surface pressure coefficient and the blade tip heat transfer distribution were chosen for the basis of comparison. A good match between the two sets of data (experiments and computations) is found and reported elsewhere (Saha and Acharya [22]).

Results and Discussion

The static pressure coefficient ($C_{p,s}=(p_{s,\text{in}}-p_s)/0.5\rho U_\infty^2$) on the blade wall and the end wall is presented in Fig. 7 for the two cases. The reference static pressure at the inlet in the above definition of the static pressure coefficient is computed here as an area-averaged value. The flow near the end wall is three dimensional and is reflected in the pressure distribution with lower pressures (higher $C_{p,s}$) along the suction surface, a pitchwise pressure gradient from the pressure to the suction surface and a spanwise pressure gradient from the end wall to the midspan. Figure 7(*b*) shows that with end-wall contouring, the near-wall pitchwise pressure gradients along the suction surface and immediately downstream of the leading edge are reduced. This can also be seen in the distribution of static pressure coefficient on the end wall shown in Fig. 8. The pressure side does not show significant differences in the pressure distribution between the two end walls with the contoured case showing a smaller region of the peak pressures (e.g., an arbitrary value of $C_{p,s}$ of −0.5 can be compared). However, the suction side pressure distribution reveals greater differences. The primary intention of profiling the end wall is to decrease the local pressure gradient near the end wall between the pressure side and the suction side. This is clearly achieved and can be seen by comparing Figs. 8(*a*) and 8(*b*). To get a clearer picture, a line plot at a location $X=0.15C_x$ is shown in Fig. 8(*c*). From the line plot, it is obvious that with contouring the pressure on the suction side is increased ($C_{p,s}$ is decreased), leading to a reduction in the pitchwise pressure gradient.

To illustrate the near-wall flow structure, surface streamlines are generated using the two components of the shear stresses. Because of the formation of horseshoe vortex ahead of the blade leading edge, the flow near the surface shows a line of separation and a saddle point (Fig. 9). For the contoured end wall, the position of the saddle (marked by S) moves toward the leading edge and the separation-line pattern is different. Since the region between the saddle point and the leading edge where the flow separates to yield horseshoe vortices is shorter for the contoured end wall, this implies that the size and extent of the leading-edge horseshoe vortices are smaller for the contoured case. The horse shoe vortices represent the origin of the passage vortex, and therefore a reduction in its size, as achieved by the contoured end wall, is desired. The separation line along the suction side that is quite distinct for the flat end wall is not clearly seen for the contoured end wall. Further, in examining the orientation of the streamlines, it can be seen that for the contoured case the streamlines are oriented more in the flow direction (parallel to the suction surface) than for the flat-end-wall case where the near-wall streamlines are oriented from the pressure side to the suction side and feed the development of the passage vortex. Thus, the yaw angle of the near-wall flow is reduced for the contoured case which, in turn, will reduce the development of the passage vortex (seen later in Figs. 10 and 11). From the streamline distribution, it can be clearly said that the flow near the contoured end wall is significantly different from that in the flat end wall.

The three-dimensional pathlines near the end-wall region for the two cases are depicted in Fig. 10. The particles are released from the same location for both the cases. Close examination of the pathlines for the two cases reveals significant difference in the flow structures. The spreading of the pathlines is found to be more for the base line case than for the contoured end wall. This suggests that the contouring helps in reducing the size of the secondary flow vortex significantly. The stronger cross flow for the base line case results in higher losses (presented later).

Figure 11 presents the streamtraces superimposed on streamwise vorticity (ω_x) at $X=0.2C_x$. In both the plots, the presence of cross flow from the pressure to the suction side of the blade is clearly seen. Additionally, the formation of roll up near the pressure side is due to the development of the passage vortex. Comparison of the flow structures and the magnitude of the vorticity of the both cases reveals that the contoured end wall reduces the strength and size of the secondary flow structure significantly. Although the vortex is not necessarily aligned with the axial plane shown, the size of the passage vortex can be estimated from Fig. 11 and is reduced more than twice by end-wall contouring. At this axial chord location, the 3D separation line is roughly at the same position for the two cases. However, the contoured end wall shows the existence of a saddle point (S) near the end wall in the axial chord plane shown, and it is clear from the zoomed out view of the streamtraces that a similar flow pattern is not observed for the flat end wall. This behavior is linked to the orientation and the axial location of the line connecting the saddle point to the leading edge (LE). As can be seen in Fig. 9, the saddle point is moved slightly downstream with end-wall contouring, and the LE-S line is more aligned with the axial plane.

The streamtraces superimposed on the streamwise vorticity contours at $X=0.8C_x$ are shown in Fig. 12. Note that since the

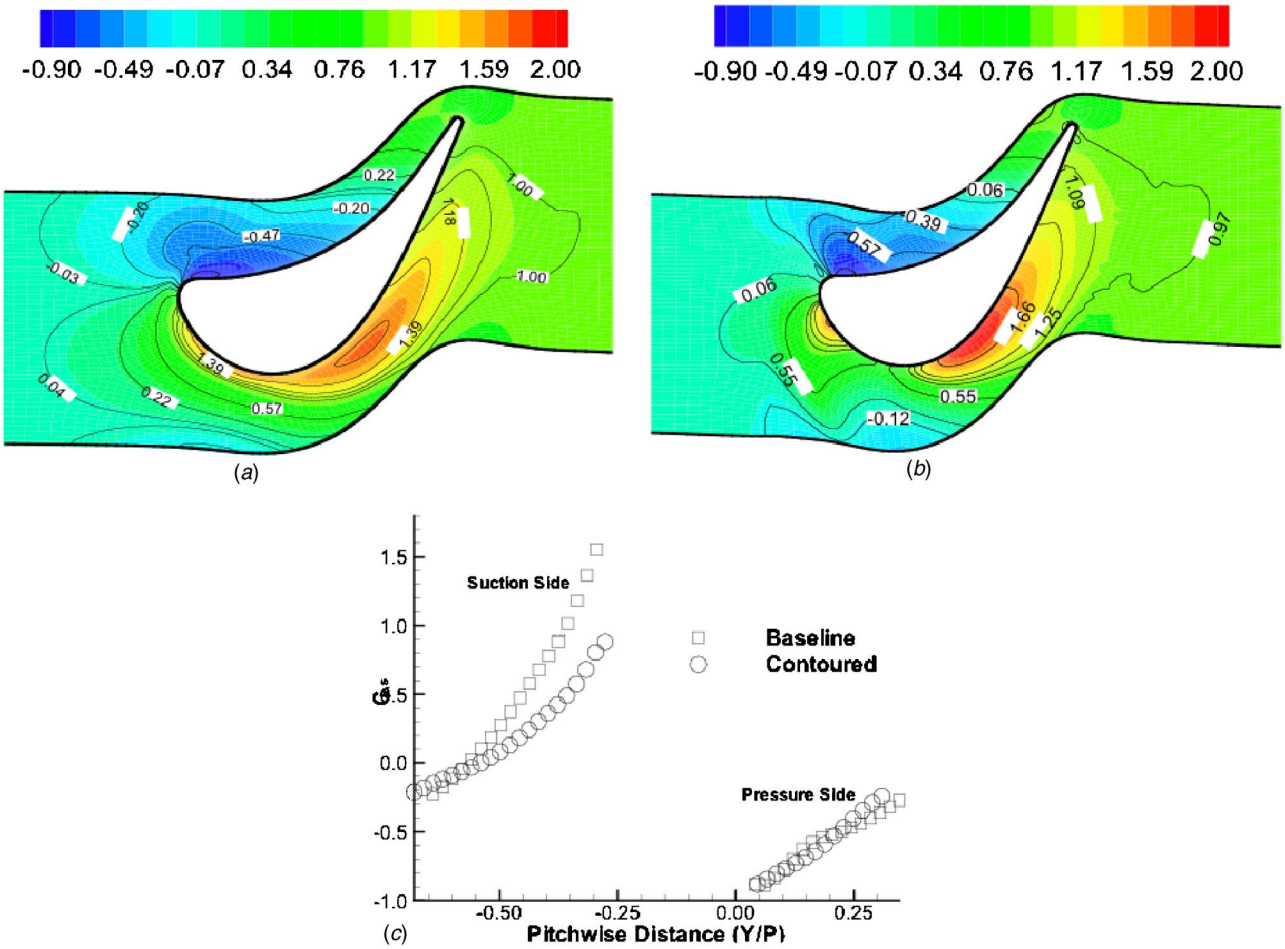

Fig. 8 Contours of the static pressure coefficient on the bottom wall: (*a*) flat and (*b*) contoured end walls. (*c*) Line plot at 15% of the C_x. Note that $Y/P=0$ represents the intersection of the 15% axial chord line with the pressure surface. $Y/P>0$ represents the pressure side.

passage vortex is not aligned with the axial chord plane at this location, the streamlines in this plane do not show the closed contours associated with a vortex. Rather, the vorticity magnitude is a measure of the passage vortex and strength at this location. The magnitude and the size of the vorticity associated with the passage vortex near the corner of the suction side decrease in the case of the contoured end wall compared with the base line case. An estimate of the passage vortex size can be made by examining the size of the high-vorticity patch. The contoured-end-wall case shows greater than a twofold reduction in the size of the vortex. The core of the passage vortex is also seen to be closer to the end wall for the contoured case.

The contours of the total pressure loss coefficient at $X=1.2C_x$ are shown in Fig. 13. This location is downstream of the trailing edge and the contoured regions of the end wall and can be used to evaluate the overall effects of the end-wall profiling. Even at this location, with contouring (Fig. 13(*b*)), the core of the passage vortex (region with the highest pressure loss coefficient) is smaller and closer to the end wall. The magnitude of the peak is also lower (nearly 10%) for the contoured case. The total mass-averaged pressure loss, calculated between the inlet and exit sections of the blade passage, is 0.281 and 0.272 for the flat and the contoured end wall, respectively. This represents a small reduction of about 3.2% with contouring in the mass-averaged loss values at the passage exit.

Figure 14 presents the heat transfer distribution on the end wall for the two cases. The flat end wall has larger patches of high heat

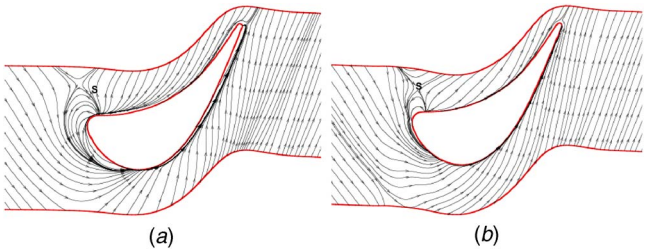

Fig. 9 Surface streamlines on the end wall: (*a*) flat and (*b*) contoured end walls

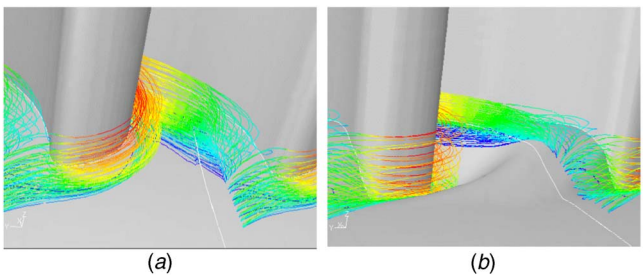

Fig. 10 Three-dimensional pathlines near the end wall: (*a*) flat and (*b*) contoured end walls

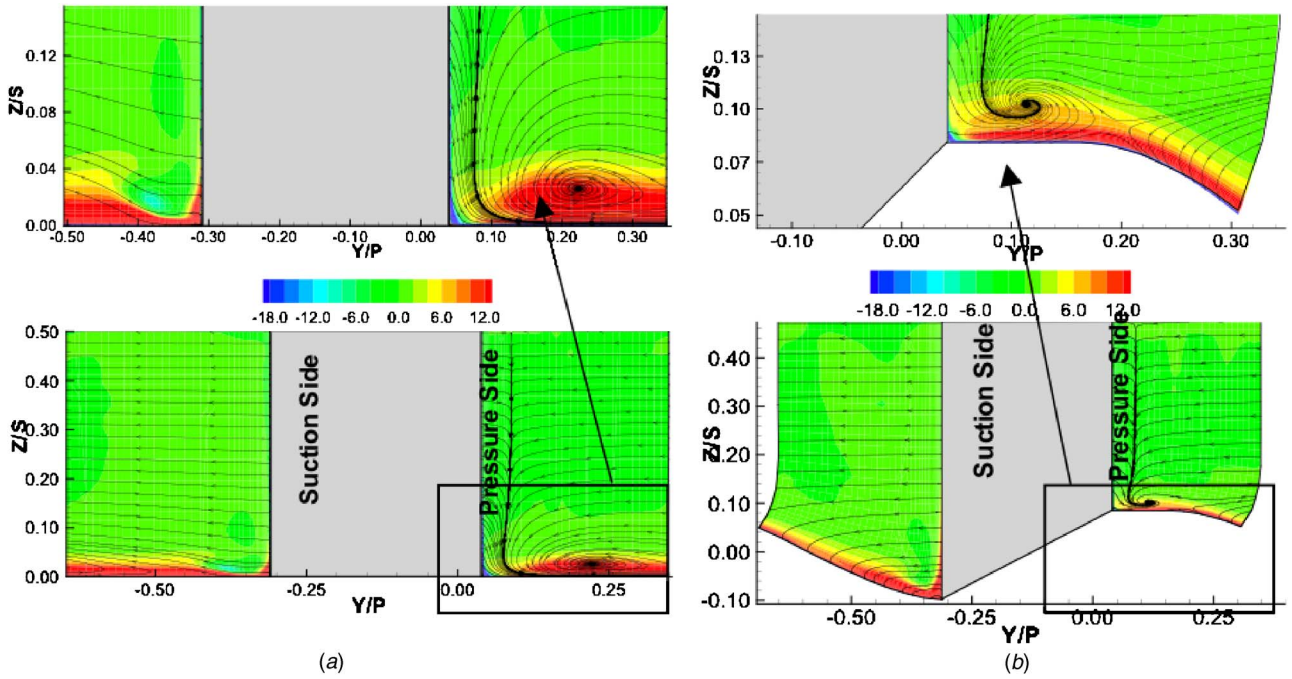

Fig. 11 Streamtraces superimposed on the contours of nondimensional streamwise vorticity at 20% of the axial chord: (*a*) base line (flat end wall) and (*b*) contoured end wall

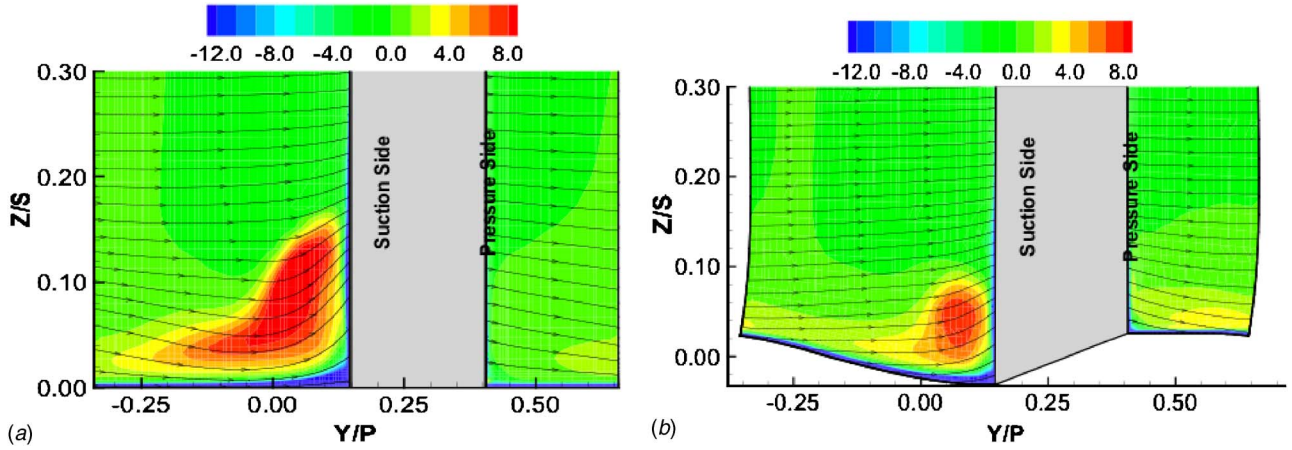

Fig. 12 Streamtraces superimposed on the contours of nondimensional streamwise vorticity at 80% of the axial chord: (*a*) base line (flat end wall) and (*b*) contoured end wall

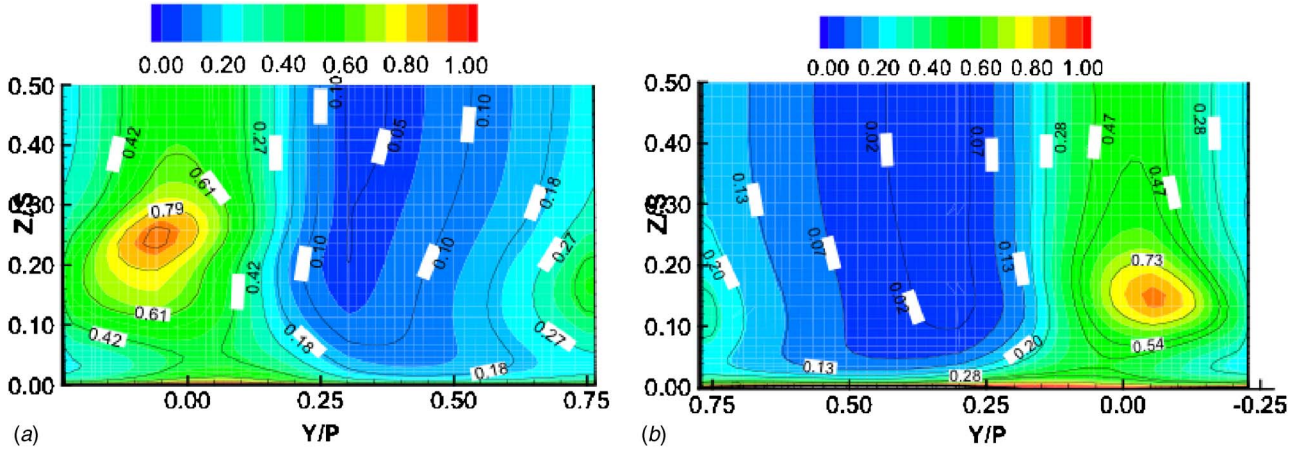

Fig. 13 Contours of total pressure loss coefficient at 120% of the axial chord: (*a*) base line (flat end wall) and (*b*) contoured end wall

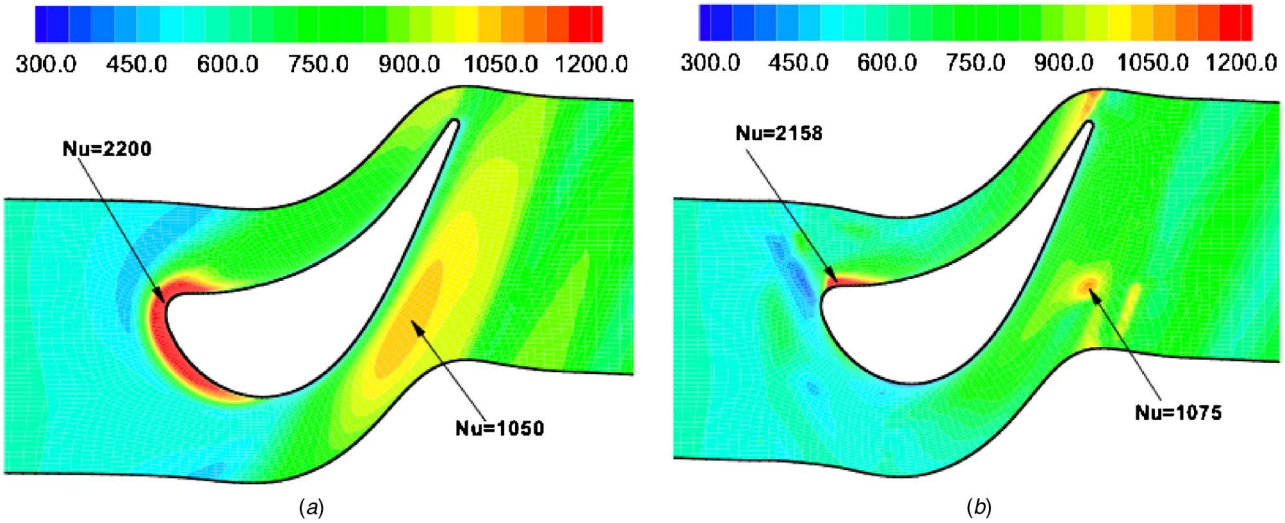

Fig. 14 Contours of the Nusselt number on the bottom wall: (*a*) flat and (*b*) contoured end walls

transfer zones, particularly near the blade LE where horseshoe vortices are formed. The horseshoe vortex system generates secondary flows and makes the flow strongly three dimensional near the junction. As a result, higher heat transfer coefficients are obtained near the LE. As shown earlier in Fig. 9, end-wall contouring reduces the size of the LE separation and the horseshoe vortex region. Consequently, with contouring, there is a significant reduction in the heat transfer coefficient near the LE. On the suction side immediately downstream of the LE (see Fig. 12 for corresponding secondary flow patterns), there is nearly a threefold reduction in the Nu values. As the flow accelerates through the TA, the heat transfer is enhanced. However, the region of high heat transfer coefficient (say, greater than 1000) is considerably reduced for the contoured-end-wall case despite the fact that there is a stronger initial acceleration in the passage due to the nature of the contouring. The peak Nusselt number values in the LEA and the TA are indicated in Fig. 14 and are comparable for the two

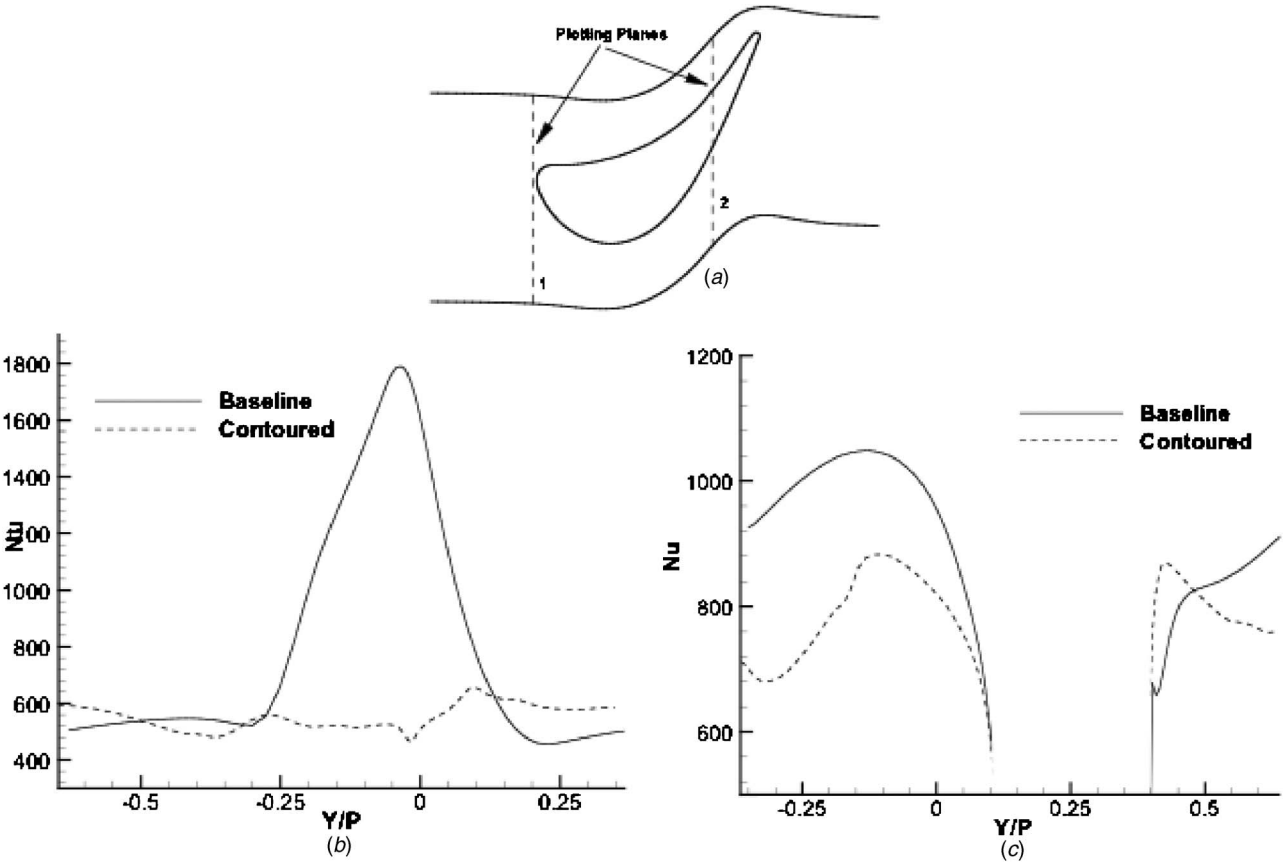

Fig. 15 Variation of Nusselt number along axial chord lines 1 and 2 shown in (*a*). In (*b*), Nu is shown along line 1. In (*c*), Nu is shown along line 2.

cases. It is the extent of the high heat transfer coefficient region that is considerably reduced by the end-wall contouring.

The line plots at two different axial locations (shown in Fig. 15(*a*)) are plotted in Figs. 15(*b*) and 15(*c*) to provide quantitative comparisons. Close to the LE (Fig. 15(*b*)), peak Nu reductions with contouring are greater than threefold. Closer to the throat (Fig. 15(*b*)), typical reductions in Nu with contouring are in the range of 15–25%. These reductions are linked to a decrease in the size and strength of the secondary flow structures with contouring.

The Nusselt number averaged over the entire end wall is shown in Table 2. The average value for the flat end wall is 736, while that for the contoured end wall is 677.7, giving a reduction of 8%. As noted earlier, local reductions are significantly higher.

Conclusions

The design of three-dimensional nonaxisymmetric end wall has been undertaken in the present study and the performance of the end wall is compared with that of a flat end wall with end-wall heat transfer, total pressure loss, and the size and strength of the passage secondary flows as the metrics for comparison. The following are the main conclusions drawn from the present work.

1. The pitchwise pressure gradients near the end wall are reduced with three-dimensional contouring of the end wall. Therefore, with contouring, the near-wall flow has lower yaw angle and the flow is more aligned with the midspan inviscid streamwise flow direction.
2. The strength and size of the secondary passage vortice reduces with a contoured end wall. An estimate of the size based on vorticity values indicates that contouring can lead to greater than twofold reductions in the size of the LE and passage vortices.
3. With contouring, there is a significant reduction in the heat transfer near the LE (threefold reduction in local values) and in the passage region (15–25% reduction in local values). The area-averaged Nu in the computational domain reduces by 8% with contouring. These reductions in Nusselt number are linked to a decrease in the size and strength of the secondary flows.
4. The three-dimensional end wall is found to be effective in bringing down the total pressure loss across the blade. Downstream of the blade trailing edge, the region of high pressure loss coefficient associated with the passage vortex is smaller in size, peak values are lower by about 10%, and the vortex is located closer to the end wall. The mass-averaged loss values are reduced by about 3.2% with contouring.

Acknowledgment

This work was supported by a grant from the DOE-UTSR program. Their support is gratefully acknowledged.

Nomenclature

C_{ac} = actual chord length
$C_{p,s}$ = static pressure coefficient (loss), $(p_{s,in}-p_s)/0.5\rho U_\infty^2$
$C_{p,t}$ = total pressure coefficient (loss), $(p_{t,in}-p_t)/0.5\rho U_\infty^2$
C_x = axial chord length
h = local convective heat transfer coefficient
K = thermal conductivity
Nu = Nusselt number, $q''C_{ac}[(T_w-T_\infty)K]$
p = local static pressure
p_t = total pressure
$p_{s,in}$ = static pressure at inlet
$p_{t,in}$ = total pressure at inlet
P = pitch of the blade cascade
Pr = ν/α
Re = Reynolds number, $U_\infty C_{ac}/\nu$
q'' = heat flux
S = span of the blade
T_w = wall temperature of the end wall
T_∞ = mainstream temperature of the flow
Tu = turbulence intensity at the inlet
U_∞ = mainstream velocity of the flow
u_τ = friction velocity
X = axial distance
y_p = distance from the wall
Y^+ = dimensionless distance from the wall, $u_\tau y_p/\nu$
α = thermal diffusivity
ν = kinematic viscosity
ω_x = nondimensional streamwise vorticity

References

[1] Pierce, E. J., Frangistas, G. A., and Nelson, D. J., 1988, "Geometry-Modification Effects on a Junction-Vortex Flow," *Proceedings of the Symposium on Hydrodynamics Performance Enhancement for Marine Applications*, Oct., pp. 37–44.
[2] Davenport, W. J., Agarwal, N. K., Dewitz, M. B., Simpson, R. L., and Poddar, K., 1990, "Effects of a Fillet on the Flow Past a Wing-Body Junction," AIAA J., **28**, pp. 2017–2024.
[3] Pierce, E. J., and Shin, J., 1992, "The Development of a Turbulent Junction Vortex System," ASME J. Fluids Eng., **114**, pp. 559–565.
[4] Zess, G. A., and Thole, K. A., 2002, "Computational Design and Experimental Evaluation of Using a Leading Edge Fillet on a Gas Turbine Vane," ASME J. Turbomach., **124**, pp. 167–175.
[5] Shih, T. I.-P., and Lin, Y.-L., 2003, "Controlling Secondary-Flow Structure by Leading-Edge Airfoil Fillet and Inlet Swirl to Reduce Aerodynamic Loss and Surface Heat Transfer," ASME J. Turbomach., **125**, pp. 48–56.
[6] Sauer, H., Mueller, R., and Vogeler, K., 2000, "Reduction of Secondary Flow Losses in Turbine Cascades by Leading Edge Modifications at the End-Wall," ASME Paper No. 2000-GT-0473.
[7] Harvey, W. N., Rose, M. G., Taylor, M. D., Shahpar, S., Hartland, J., and Gregory-Smith, D. G., 2000, "Nonaxisymmetric Turbine End-Wall Design: Part 1—Three-Dimensional Design System," ASME J. Turbomach., **122**, pp. 278–285.
[8] Hartland, J., Gregory-Smith, D. G., Harvey, W. N., and Rose, M. G., 2000, "Nonaxisymmetric Turbine End-Wall Design: Part 2—Experimental Validation," ASME J. Turbomach., **122**, pp. 286–293.
[9] Kopper, F. C., and Milano, R., 1981, "Experimental Investigation of End-Wall Profiling in a Turbine Vane Cascade," AIAA J., **19**, pp. 1033–1040.
[10] Dossena, V., Perdichizzi, A., and Savini, M., 1999, "The Influence of End-Wall Contouring on the Performance of a Turbine Nozzle Guide Vane," ASME J. Turbomach., **121**, pp. 200–208.
[11] Duden, A., Raab, I., and Fottner, L., 1999, "Controlling the Secondary Flow in Turbine Cascade by Three-Dimensional Airfoil Design and End-Wall Contouring," ASME J. Turbomach., **121**, pp. 191–199.
[12] Burd, S. W., and Simon, T. W., 2000, "Flow Measurements in a Nozzle Guide Vane Passage With a Low Aspect Ratio and End-Wall Contouring," ASME J. Heat Transfer, **122**, pp. 659–666.
[13] Shih, T. I.-P., Lin, Y.-L., and Simon, T. W., 2000, "Control of Secondary Flow in Turbine Nozzle Guide Vane by End-Wall Contouring," ASME Paper No. 2000-GT-0556.
[14] Lin, Y.-L., Shih, T. I.-P., Stephens, M. A., and Chyu, M. K., 2001, "A Numerical Study of Flow and Heat Transfer in a Smooth and a Ribbed U-Duct With and Without Rotation," ASME J. Heat Transfer, **123**, pp. 219–232.
[15] Lin, Y.-L., Shih, T. I.-P., Chyu, M. K., and Bunker, R. S., 2000, "Effects of Gap Leakage on Fluid Flow in a Contoured Turbine Nozzle Guide Vane," ASME Paper No. 2000-GT-0555.
[16] Yan, P. J., Gregory-Smith, D. G., and Walker, P. J., 1999, "Secondary Flow Reduction in a Nozzle Guide Vane Cascade by Non-Axisymmetric End-Wall Profiling," ASME Paper No. 99-GT-339.
[17] Shih, T.-H., Liou, W. W., Shabbir, A., Yang, Z., and Zhu, J., 1995, "A New-Eddy Viscosity Model for High Reynolds Number Turbulent Flows—Model Development and Validation," Comput. Fluids, **24**(3), pp. 227–238.
[18] Yang, H., Acharya, S., Ekkad, S., Prakash, C., and Bunker, R., 2002, "Flow and Heat Transfer Predictions for a Flat-Tip Turbine Blade," ASME Paper No. GT-2002-30190.
[19] Yang, H., Acharya, S., Ekkad, S., Prakash, C., and Bunker, R., 2002, "Flow and Heat Transfer Predictions for a Squealer-Tip Turbine Blade," ASME Paper No. 2002-GT-30191.
[20] Jin, P., and Goldstein, R. J., 2003, "Local Mass/Heat Transfer on a Turbine Blade Near-Tip Surfaces," ASME J. Turbomach., **125**, pp. 521–528.
[21] Srinivasan, V., and Goldstein, R. J., 2003, "Effect of End-Wall Motion on Blade Tip Heat Transfer," ASME J. Turbomach., **125**, pp. 267–273.
[22] Saha, A. K., Acharya, S., Prakash, C., and Bunker, R., 2006, "Blade Tip Desensitization With Pressure Side Winglet," Int. J. Rotating Mach., Article ID 17079.

Clearance Effects on the Evolution of the Flow in the Vaneless Diffuser of a Centrifugal Compressor at Part Load Condition

Matthias Schleer[1]

Reza S. Abhari

Turbomachinery Laboratory,
Swiss Federal Institute of Technology Zürich,
CH 8092 Zürich, Switzerland

This work reports on flow measurements taken within the vaneless diffuser of a scaled-up model of a small-scale, highly loaded unshrouded compressor with large relative tip clearance. The aims are to describe and to analyze the influence of the clearance flow on the flow structure at the impeller exit in part load operation. The kind of compressor described herein is widely used in distributed power applications and automotive turbocharging. It demands further enhancement of the operation range, as well as a high head rise and an improved efficiency. Therefore, the understanding of flow features and their interaction is crucial. The interaction and mixing of the flow pattern downstream of the impeller are shown using spatially and temporally resolved 3D-velocity data. The measurements have been obtained by using a 3D laser Doppler anemometry system throughout the vaneless parallel wall diffuser. This unique data set provides insight into the development of the flow within the diffuser and allows conclusions on the mixing and migration of the three-dimensional pattern. The flow structure in part load condition is strongly affected by the flow across the large relative tip gap. Due to the large relative tip clearance, a low momentum zone is formed as an additional pattern at the shroud. This clearance flow is highly vortical and interacts with the channel wake structure but remains stable throughout the vaneless diffuser. At the pressure side hub corner, a jet structure is formed, which interacts rapidly with the blade wake. This flow behavior does not comply with the classical jet-wake pattern. It is proposed that in a centrifugal compressor with large relative tip clearance, a modified flow model that includes tip leakage is more appropriate to describe the flow structure at part load condition.
[DOI: 10.1115/1.2776955]

Introduction

The requirements for compressors used in distributed power applications and automotive turbocharging are very ambitious as a wide operating range and high efficiency throughout the complete operational envelope are required. The challenge for further development of centrifugal compressors is to broaden the operation range by shifting the stall line without diminishing the maximum mass flow rate, the pressure ratio, or the efficiency. The problems faced here involve, e.g., complex 3D flows, loss generation mechanisms, impeller/diffuser interactions and also stability issues such as stall mechanism and the detection of stall precursors. Throughout all developments, the special need of mass production demands cost effective solutions as turbocharging becomes feasible only if economical solutions are available. For the small-scale compressors in distributed power and automotive turbocharging, an unshrouded impeller is typically used. The performance of this kind of impeller suffers from the pressure loss over the tip gap and the formation of secondary flows. The effect of the tip clearance flows on small turbomachines is very strong as the manufacturing accuracy determines a minimum clearance and thus the relative clearance becomes large.

The governing feature usually found at the exit of a centrifugal impeller is the so-called jet-wake flow pattern, which was introduced by Dean and Senoo in 1960 [1]. In the classical jet-wake model, it is assumed that most of the flow leaves the impeller in the jet region. The jet is found on the pressure side of the blade and shows the highest radial velocity. This region has an appropriate stagnation pressure for a nearly loss-free flow in the relative frame of reference. The wake region is found on the suction side of the blade and shows a much lower radial velocity but a very high tangential velocity. The wake is explained as a region where flow that has experienced high loss has accumulated. The high loss zone grows throughout the impeller passage and is finally recognized at the impeller exit as a wake. The influence of tip clearance flows, hub-to-shroud variation, or changed operating conditions is typically ignored. Since its introduction, the two-dimensional model was constantly improved and has been widely used in a two-zone approach for the preliminary design of centrifugal compressors (Jakipse [2]).

Experimental evidence for this model was given by Fowler [3], who showed the existence of a nonuniform flow in a huge slowly rotating impeller. Eckardt [4,5] and Krain [6] measured the meridional velocity at several measurement planes inside the impeller and confirmed the model. Rohne and Banzhaf [7] presented experimental results where the wake region was covering most of the exit area and was displaced toward the shroud. They concluded that the classical jet-wake theory is not universally valid and needs improvement for backswept impellers. Johnson and Moore [8,9] and Inoue and Cumpsty [10] concluded that the position of the wake is governed by secondary flows due to curva-

[1]Present address: ABB Turbosystems Ltd., 5401 Baden, Switzerland.

Contributed by the International Gas Turbine Institute of ASME for publication in the JOURNAL OF TURBOMACHINERY. Manuscript received November 23, 2006; final manuscript received December 10, 2006; published online May 2, 2008. Review conducted by David Wisler. Paper presented at the ASME Turbo Expo 2006: Land, Sea and Air (GT2006), Barcelona, Spain, May 8–11, 2006, Paper No. GT2006-90083.

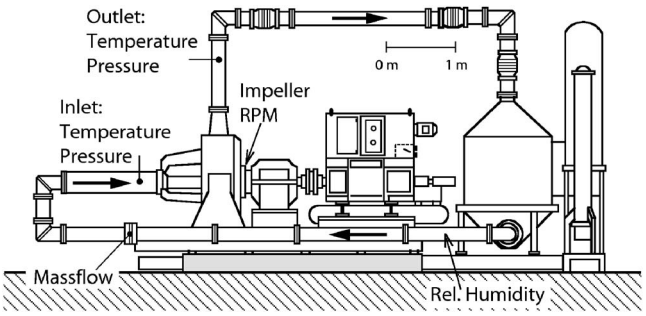

Fig. 1 Rigi research facility

ture, as well as due to rotational effects. They showed that for purely radial blading, the position of the wake is controlled by the Rossby number, which is the ratio of inertia of a particle in the relative frame to the centrifugal Coriolis force. Gyarmathy et al. [11] extended the description of the secondary flow development for nonradial blading by using the ratio of accelerations in the meridional and circumferential directions. Their model is understood as an extension to the Rossby number for the explanation of the flow pattern at different operating conditions in the impeller with nonradial blading. They explained the displacement of the wake as a result of the changed forces on the flow at different mass flow conditions.

Only little work has been done in centrifugal compressors on the interaction of the tip clearance flow with the passage flow and its influence on the stability. Based on measurements in several centrifugal impellers, Senoo and Ishida [12] described the deterioration of the compressor performance due to tip clearance. For all compressors, an increased tip clearance width results in increased leakage ratios and higher losses, and thus a deteriorated performance. Goto [13] measured the discharge flow from a mixed-flow water pump impeller at five different tip clearances and investigated the flow fields by applying an incompressible version of a computational fluid dynamics (CFD) code. Ishida et al. [14] measured the discharge flow from a low speed centrifugal impeller and discussed the secondary flow due to the tip clearance. Hong et al. [15] showed experimental results on the influence of the relative tip clearance on the flow structure and efficiency in radial compressors. However, none of these authors commented on the applicability of the classical models for the description of the secondary flow at the impeller exit at increased tip clearance. In the current paper, experimental evidence that the classical jet-wake model is not sufficient for the description of the flow in a highly loaded compressor with large relative tip clearance is shown. A modified flow model that includes tip clearance flows is presented, which is more appropriate for the description of the flow evolution in the vaneless diffuser.

Experimental Setup and Data Evaluation

The experimental investigations are performed on the "Rigi" research facility in the Turbomachinery Laboratory of the Swiss Federal Institute of Technology in Zurich, Switzerland. The compressor facility is a scaled-up model of a one-stage centrifugal compressor used in small-scale distributed power generation or automotive turbocharging. It was designed to match the main design criteria and nondimensional parameter typical for these small devices. As shown in a previous publication by the authors [16], the operating behavior of the true-scale and the enlarged compressor is similar. Thus, measurements within the large-scale research facility are representative of the flow structures found in small-scale compressors.

Research Facility. The Rigi facility consists of a single stage, vaneless centrifugal compressor system operating in a closed loop, as shown in Fig. 1. It is operated with air and delivers a design volume flow rate of $V=3.5\ \mathrm{m}^3/\mathrm{s}$ at a design pressure ratio of $\pi=2.8$. The compressor is equipped with a centrifugal impeller of an outer diameter $D_2=400$ mm. The rotor is followed by a parallel vaneless diffuser with an exit diameter of $D_5=580$ mm. The mass flow is measured in the backflow duct with a standard orifice, while the inlet and outlet conditions are measured in the suction and pressure pipe at the locations indicated in Fig. 1.

The closed-loop facility is driven by a 440 kW electrical dc engine. The compressed air has to be cooled down using a counterflow air-water heat exchanger before reentering the test section. The inlet pressure is reduced to inlet conditions by the throttle and is controlled by a pressure regulation system within the range of 16 to 125 kPa. The closed-loop arrangement facilitates measurements under repeatable and constant conditions without depending on the atmospheric conditions. A flow straightener mounted in the suction pipe ensures axial flow at the stage inlet. A large toroidal collecting chamber follows the radial diffuser. This arrangement ensures a virtually uniform circumferential pressure distribution at the impeller exit under all through-flow conditions and allows accurate measurement of the flow in the vaneless diffuser at one representative location.

Experiments have been conducted at two different relative clearances. The relative clearance ratio is defined as the ratio of the tip gap width t and the blade height b_2 at the impeller exit:

$$\mathrm{CR} = t/b_2 \tag{1}$$

In the experiment, the different clearance ratios could be adjusted by shimming the shroud casing in the axial direction. The base line tip clearance ratio at the impeller exit was set to a value of CR=12.7%. This very large tip clearance ratio is common for small-scale applications as the axial displacement in the bearing is large compared to the diffuser width. For comparison, a reduced gap configuration with a clearance ratio of CR=4.5% was tested. The different tip gap configurations are sketched in Fig. 2 and are summarized in Table 1.

In order to identify the evolution of flow features at part speed, laser Doppler anenometer (LDA) measurements have been performed for both tip clearance cases at an operating condition of Mu=0.6. In Fig. 3, the operating lines are plotted for both clearance configurations. An improved characteristic is seen for the reduced clearance case where the pressure head is improved by 6% and the stall inception is shifted to lower mass flow rates. In Schleer et al. [16], a similar relationship between compressor performance and clearance ratio was seen for all impeller speeds. Time resolved LDA measurements have been performed at a specific flow coefficient of $\phi=0.0513$. At this operating condition, the design incidence of 2 deg is present at the leading edge. The tested operating conditions are summarized in Table 2.

Measurement Setup. The flow velocities have been measured using a commercial 3D LDA system available from TSI Inc. by applying a similar setup as Stahlecker et al. [17]. For the base line clearance case (CR=12.7%), time resolved LDA data were acquired at a total of 31 radial and 29 axial locations within the vaneless diffuser at a spatial resolution of 0.5 mm in the axial and 1.5 mm in the radial direction, respectively. For the reduced clearance case (CR=4.5%), the acquisition of data was restricted to a radial location of $R/R_2=105\%$. Due to limitations of the optical setup, no data were obtained by the LDA system in neither case in a region very close to the diffuser hub wall and directly at the impeller exit.

The LDA measurement system is a noncontact measurement system for measuring optically the velocity of seeding particles in a flow. The flow was seeded with polydisperse liquid paraffin oil particles with a mean particle size of 0.4 μm. The proportion of the particles above 1 μm in diameter is negligible and thus the particles will experience only little slip relative to the flow and a good accuracy is achieved. The size of the measurement volume is $100\times100\times500\ \mu\mathrm{m}^3$. The velocities are acquired in a cross-

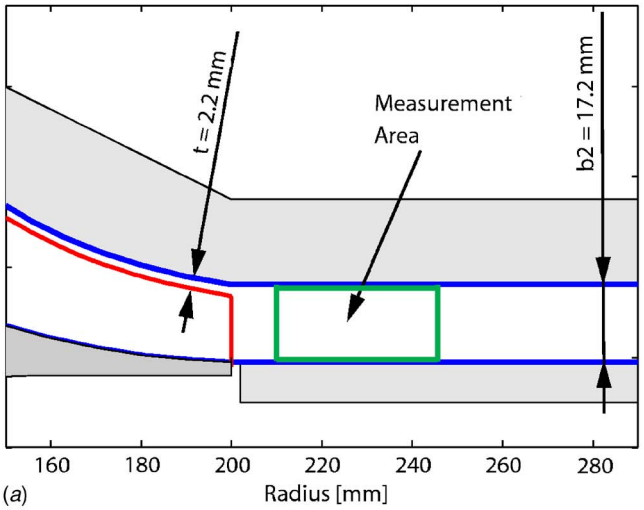

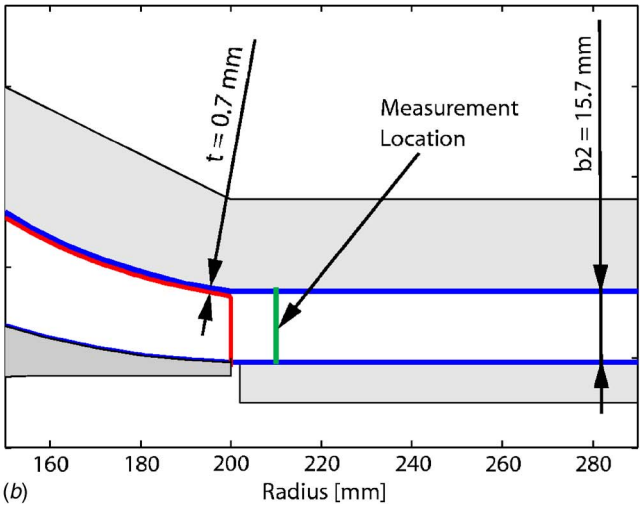

Fig. 2 Investigated clearance configurations

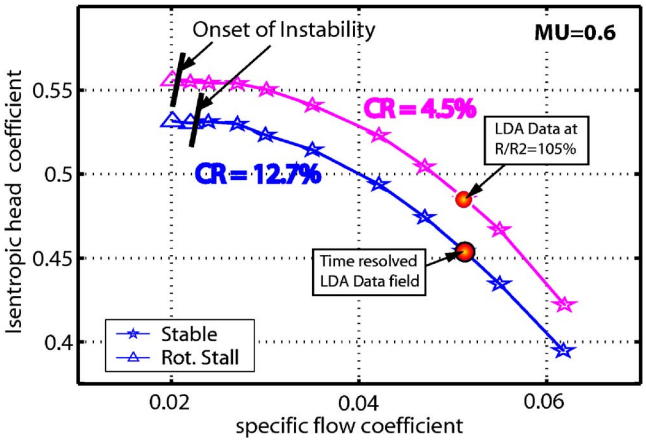

Fig. 3 Investigated operating conditions

backscatter mode in the parallel wall diffuser. The setup of the LDA system is shown in Fig. 4. The red box indicates the area where data were taken while the arrows depict the acquired velocity components. For each traversing point, 35,000 data points have been stored together with the impeller positions for the later postprocessing.

Data Evaluation. The LDA data are evaluated according to the angle definition given in Fig. 5. All angles are measured from the radial direction and the sign of the angle is positive in the direction of impeller rotation.

The circumferential velocity component is defined to be positive in the sense of rotation of the impeller. The axial velocity component is positive in the flow direction at the inlet, i.e., in the shroud-to-hub direction. This definition leads to a right-hand cylindrical coordinate system ($R\theta Z$ system), in which the signs of all the three velocity components, v_r, v_θ, v_z, are positive in the direction of the coordinate systems.

By using a time resolving technique such as the LDA measuring system, the pitchwise flow variation can be resolved. Based on the rotor position, the circumferential flow structure within the diffuser is determined by a phase locked ensemble averaging approach. As no downstream or upstream disturbances are present, the flow structure is assumed to be circumferentially periodic and the time axis and circumferential axis coincide. Using this assumption, the flow is resolved relative to the impeller position and the secondary flow structures can be studied. By using this phase lock averaging approach, data were resolved at a total of 31 $\times 180 \times 29$ locations within the vaneless diffuser.

Table 1 Investigated clearance configurations

	Base line clearance	Reduced clearance
Tip clearance t (mm)	2.2	0.7
Diffuser width b_2 (mm)	17.2	15.7
Diffuser width b_5 (mm)	17.2	15.7
Clearance ratio CR=t/b_2 (%)	12.7	4.5

Circumferentially Averaged Diffuser Flow

In Fig. 6, measurements of the circumferentially averaged radial and absolute tangential velocities are shown for the base line clearance case at seven radial positions within the vaneless diffuser. For this plot, the data have been time averaged for each axial and radial locations. The black dotted lines define the radial

Table 2 Operating conditions for flow measurements

	Base line clearance	Reduced clearance
Impeller tip Mach number Mu	0.6	0.6
Specific flow coefficient ϕ	0.0513	0.0513
Isentropic head coefficient ψ	0.454	0.488

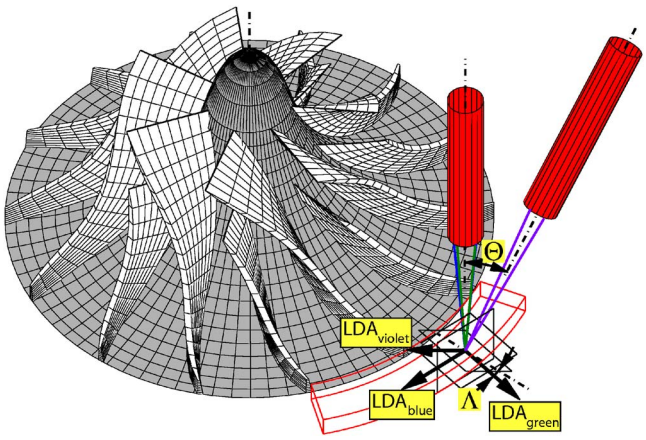

Fig. 4 Optical setup of the LDA system

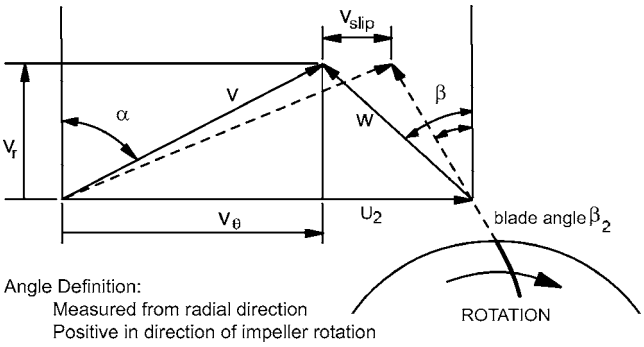

Fig. 5 Convention of the angles and velocities

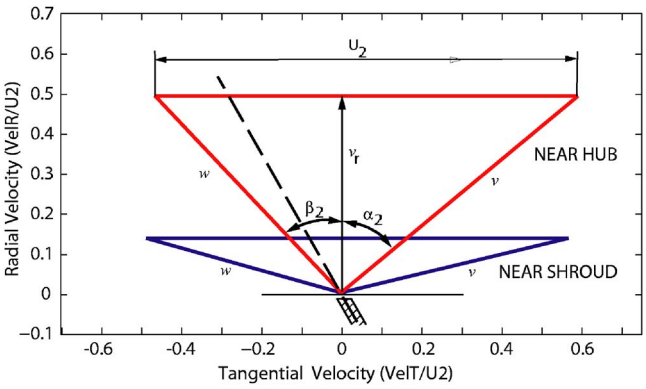

Fig. 7 Velocity triangles near the hub and shroud wall (z/b_2 =15% and 85%, respectively)

position of the measurement, while the colored lines show the magnitude of the radial and tangential velocities in the absolute frame. For negligible tangential velocities at the inlet, the absolute exit tangential velocity is proportional to the Euler work input. The component of the radial velocity is equivalent to the mass flow distribution throughout the diffuser channel.

Even at the stable operating condition shown, a blocked zone with zero radial velocity is present very close to the shroud wall. The zone of low radial velocity extends from the shroud wall up to one-third of the channel width. Very close to the shroud wall, reversed flow is encountered. The radial velocities at midheight and at the hub wall are positive and no flow reversal is observed at the diffuser hub wall. At the diffuser exit, no flow reversal is found at the shroud. The absolute tangential velocity is high throughout the diffuser. The highest values are measured at midspan, while toward the diffuser walls, the velocities are slightly lower. The diffusion process in the vaneless diffuser is seen in smaller absolute tangential and radial velocities at diffuser exit compared to the values at the inlet. Toward the diffuser exit, mixing takes place and the radial velocity gradient becomes smaller. The low radial velocities near the shroud indicate a separated zone where high loss fluid due to tip clearance flows has accumulated. According to the system analysis presented by Schleer et al. [16], the local flow reversal at the shroud does not seem to affect the stability of the compressor system. The system is stabilized by the mixing processes throughout the diffuser, which is seen in the positive radial velocity at the diffuser exit.

In Fig. 7, the velocity triangles are shown for the design incidence operating condition (phi=0.051) at two axial locations near the hub and the shroud wall. The triangles have been calculated from the circumferentially averaged data obtained at axial locations of z/b=15% and 85%, respectively. The velocity triangles visualize the strong hub-to-shroud variation of the flow approaching the diffuser. The slip of the flow relative to the impeller in both triangles is remarkable. The slip results in relative flow angles β_2, which are much larger than the exit angle χ_2=30 deg of the blading. The unequal velocity triangles indicate skewed flows near the shroud due to the influence of the large relative tip gap and the meridional curvature of the channel. The deficit in the radial velocity near the shroud indicates lack of mass flow in the shroud region. Therefore, simplifying assumptions that neglect axial gradients at the impeller exit may not be valid for the description and modeling of the flow entering the vaneless diffuser. A similar skew of the flow in the diffuser was also found to a lower extent in the tip region of an industrial impeller in a previous investigation performed in the Rigi facility (Schleer et al. [18]).

Three-Dimensional Flow Features in the Diffuser

For further understanding and interpretation of the flow structure in the vaneless compressor, time resolved measurements are performed. Based on these measurements, the three-dimensional flow structure, mixing, and evolution of the secondary flows are studied in detail. First, the flow structure is observed in a hub-to-shroud view for the base line clearance configuration CR =12.7% (Figs. 8–10). Later, the evolution of the flow pattern throughout the diffuser is studied based on isoradial plots for both

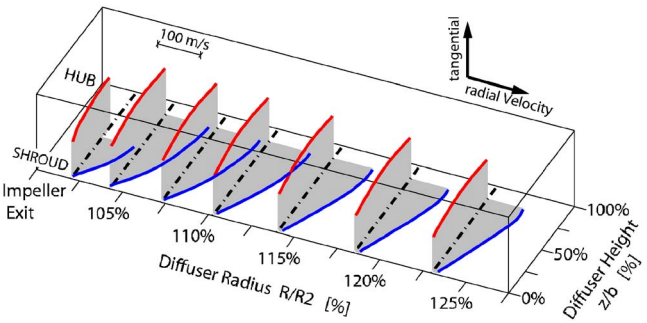

Fig. 6 Measured distribution of the radial and tangential velocities in the vaneless diffuser

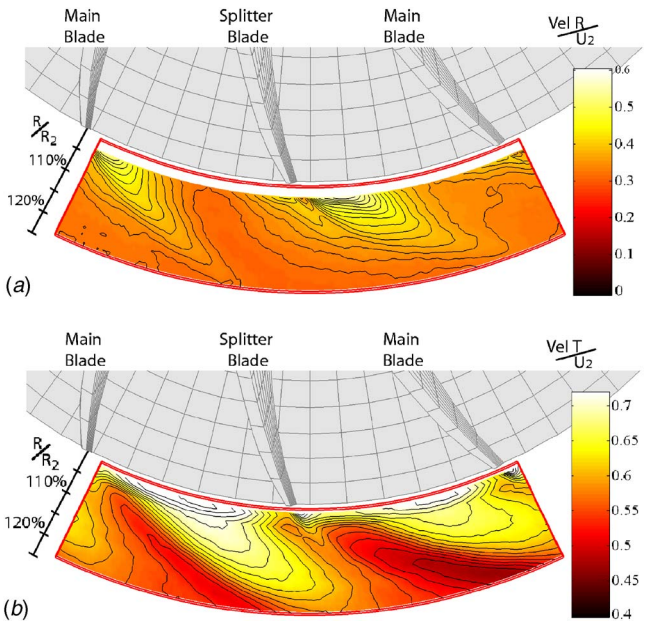

Fig. 8 Measured contours of the radial and tangential velocities at midspan (z/b_2=50%) for the base line clearance ratio CR=12.7%

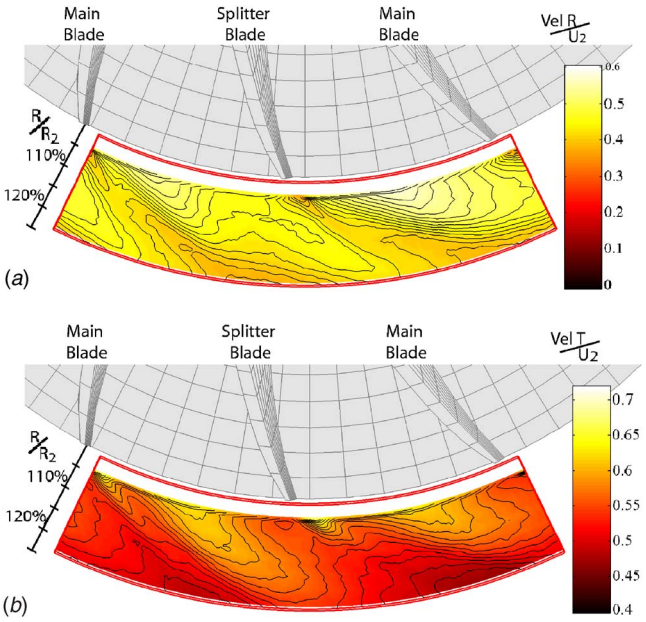

Fig. 9 Measured contours of the radial and tangential velocities near the hub (z/b_2=85%) for the base line clearance ratio CR=12.7%

clearances. For comparison, the effect of the clearance ratio on the flow pattern is shown in Fig. 15 for the reduced clearance case. The findings are summarized in Table 3.

In Fig. 8, contours of the radial and absolute tangential velocities are plotted for a midspan cut. Near the suction side, high radial and absolute tangential velocities are found. On the pressure side, the radial velocity is low while the tangential velocity is high. This does not agree with the classical jet-wake model described by Dean and Senoo in 1960 [1]. According to their jet-wake flow model, a jet appears on the pressure side as a region of high radial velocity and low tangential velocity at the pressure side. On the suction side, the wake region is expected, which shows lower radial and higher absolute tangential velocities than the jet region on the pressure side.

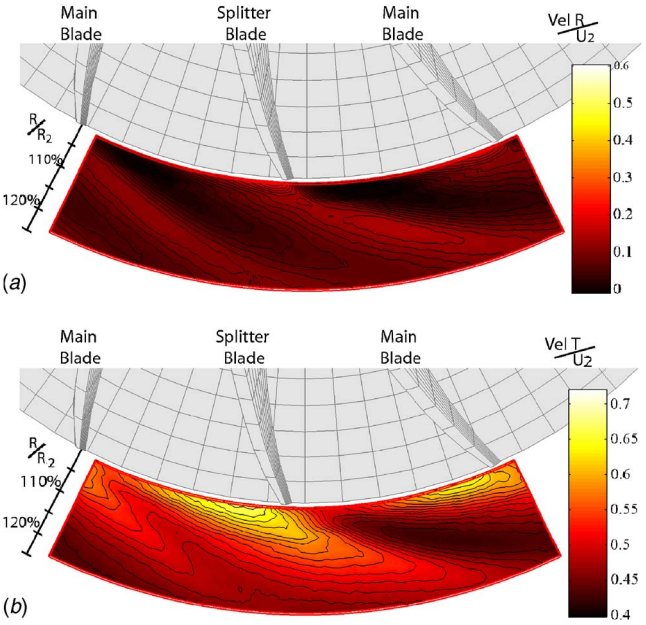

Fig. 10 Measured contours of the radial and tangential velocities near the shroud (z/b_2=9%) for the base line clearance ratio CR=12.7%

Table 3 Summary of the characteristics of the flow pattern in the hub-to-shroud view

		Radial velocity	Absolute tangential velocity	Pattern
Classical jet-wake model	SS	Very low	High	Wake-
	PS	Very high	Low	Jet
Midspan (z/b=50%)	SS	High	High	Unclear
	PS	Low	High	
Near the hub (z/b=85%)	SS	Very high	High	Unclear
	PS	High	Low	jet
	Blade	Very low	High	blade wake
Near the shroud (z/b=9%)	SS	Reversed	Low	Swirling tip
	PS	Very low	High	Gap flow

In Fig. 9, the circumferentially resolved pattern of the radial and tangential velocities is plotted for an axial location close to the hub wall. Close to the hub, the blade-wake pattern can be identified as a region of lower absolute tangential velocity in the contour plot (Fig. 9(*b*)). The jet region is found close to the pressure side, while the wake region has been established as a region of high absolute tangential velocity on the suction side, as expected in the classical 2D jet-wake model.

The reason for the high radial velocity near the suction side becomes clear if the flow pattern is investigated near the shroud wall (Fig. 10). As an additional pattern, tip leakage flow is seen in this figure. This tip leakage flow pattern is seen at the shroud wall as a zone of very low and in some locations even reversed radial velocity next to the suction side. The tangential velocities in those regions are low as well. Evidence for the presence and influence of the clearance flow was also seen in the velocity triangles near the hub and shroud wall (Fig. 7). The velocity triangles indicate severely skewed layers and showed nonuniformity in the hub-to-shroud direction with low radial velocities on the shroud side.

The observations on the inverted jet-wake pattern and the assignment of the flow pattern locations are summarized in Table 3. From this comparison, is concluded that for the machine and operating condition investigated, the classical jet-wake model is not sufficient for the description of the flow entering the diffuser. The reason for the observed disagreement is the strong hub-to-shroud variation of the flow. The classical jet-wake flow model was proposed as a 2D description of the flow and hub-to-shroud variation was not taken into consideration. This assumption is not fulfilled for the present case. In the following section, an improved description that takes the effect of tip leakage into consideration is proposed.

Evolution and Mixing of the Flow Pattern

Next, the interaction of flow structure, which leads to the disagreement with the classical jet-wake model, is studied. Figure 11 shows a 2D isoradial view of the absolute tangential and radial velocities at a radial location of R/R_2=104.25%. Figure 12 shows the same velocity components at a radial location of R/R_2 =116.25%. The constant radius plots reveal a strongly nonuniform flow in the axial and circumferential directions. The main flow features are marked in the figures. The positions of the blades are marked according to the signal of the shaft encoder. As the velocity contours are plotted 4.25% and 16.25% impeller radii downstream in the diffuser, the flow features appear shifted relative to the fixed position of the blade.

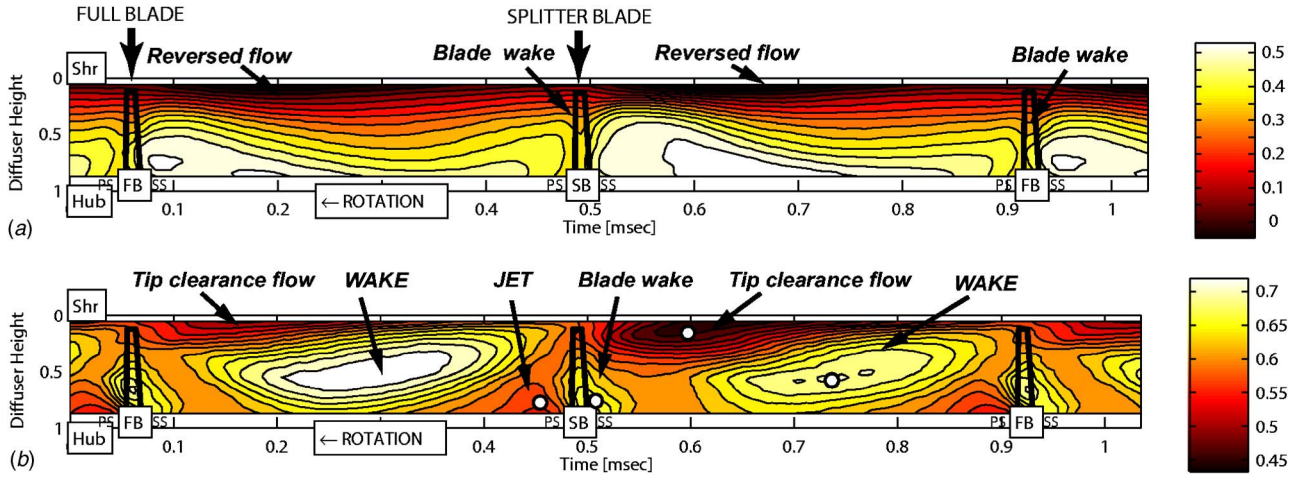

Fig. 11 Measured contours of radial and absolute tangential velocities at $R/R_2=104\%$ for CR=12.7%

In both figures, the complex flow features appear, which cannot be explained by a simple two-zone jet-wake model. The flow structure is highly three dimensional. In addition to the circumferential variation due to the blade loading, the flow is affected in the axial direction by a skewed shear layer. In these time resolved representations, additional three-dimensional flow patterns are newly seen. The flow does not follow one single log spiral as a quasisteady rigid body, as it is assumed in the 2D models. Instead, the flow follows different trajectories for each axial and circumferential locations. The flow patterns interact with each other and are able to change their location as they pass through the diffuser. In the following, the three-dimensional secondary flow patterns are discussed and their trajectories within the diffuser are analyzed.

In Fig. 11, the *channel wake* is seen as a region of high tangential velocities at midspan and near the suction side of the blades. It appears strongest in the middle of the channel and interacts with the clearance flow. Farther downstream, the wake area starts to mix out but is still visible as a region of high tangential velocity. The *jet* appears as a region of low tangential velocities in the pressure side hub corner. The dominating pattern seen in the radial velocity distribution is the mass flow deficit toward the shroud. Due to the hub-to-shroud skew, a clear distinction of the jet-wake pattern based on the radial velocities (Fig. 11(*a*)) cannot be made. This is not found in the 2D prediction by Dean and Senoo, where the jet is described as the region with the highest radial velocity. In Fig. 12, the jet has mixed out completely.

The third flow pattern in Fig. 11 is the *blade wake*. This small region next to the blades shows a low outward radial velocity and a high tangential velocity. It has the attributes of a wake but it appears directly at the trailing edge of the blade. As the jet region has already experienced a slip relative to the blade position while the trailing edge wake experiences only little slip, the blade wake and the jet interact strongly and interchange momentum. As seen in Fig. 9, the blade wake mixes out rapidly with the jet flow. At a radius of $R/R_2=110\%$, the blade wake has mixed completely with the jet flow. For comparison, the channel wake region diffuses but still visible throughout the diffuser until the last measurement location 125% downstream of the impeller exit.

The low radial velocity zone near the shroud is caused by the *flow through the tip clearance*. The tip clearance flow is seen at both radii as a layer of reversed flow near the shroud wall. In the clearance zone flow, the lowest tangential velocity and a very large slip velocity are found. In the contour plots, the strongest tip clearance flow pattern occurs behind the tip of the splitter blade. At the full blade, the reversed flow is also present but not as pronounced. Farther downstream, the clearance flow remains dominant (Fig. 12). It migrates from the shroud wall toward the midheight of the diffuser. During its migration, the flow mixes with the channel flow and flow reversal is no longer observed. This clearance flow region has been also identified in an accompanying paper by the authors [19] as a region of high flow distortion and turbulence. Based on large pressure deviations, a vortical structure that interacts with the channel flow was postulated. In the same study, the differences in the intensity of the clearance

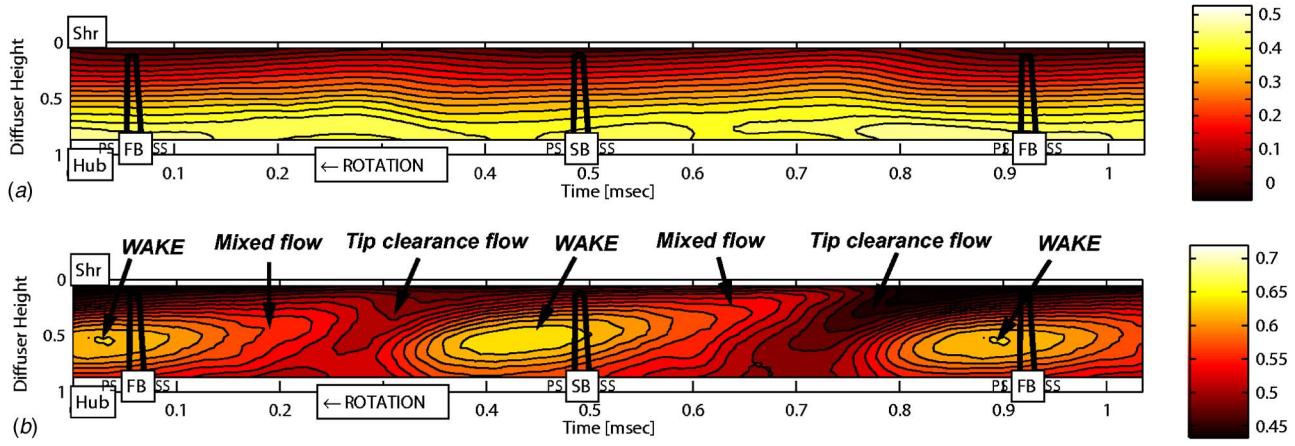

Fig. 12 Measured contours of radial and absolute tangential velocities at $R/R_2=116\%$ for CR=12.7%

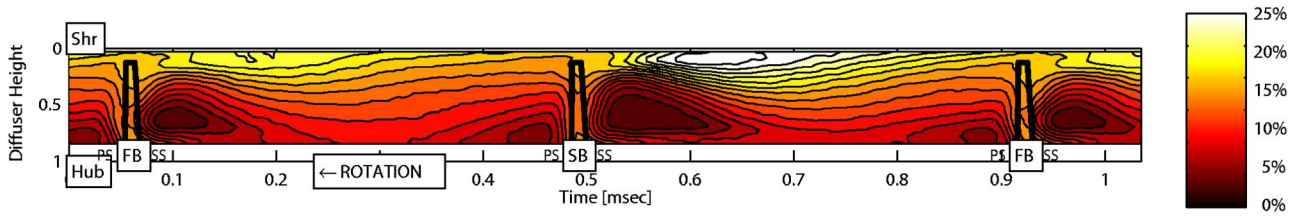

Fig. 13 Measured contours of the turbulence level at a radial location (R/R_2=104%) for CR=12.7%

flow at the main and splitter blade channels were also postulated.

The tip leakage flow results in a blockage of the diffuser channel. Due to this blockage effect, the streamlines of the wake are diverted toward the hub and the flow is accelerated radially. Therefore, the radial velocity in the wake region is higher than expected and the wake appears in the vicinity of the blocked zone as a region of high mass flow. No significant difference of this flow mechanism is seen between the main and splitter blades.

In Fig. 13, the turbulence level of the flow is shown. The local turbulence level $\mathrm{Tu}_{(r,z)}$ is defined as

$$\mathrm{Tu}_{(r,z)} = \frac{\sqrt{1/N\sum_{i=1}^{N}[\nu_{i(r,z)} - \bar{\nu}_{(r,z)}]^2}}{\bar{\nu}_{(r,z)}} \tag{2}$$

where the square root describes the deviation of the local velocity readings obtained by the LDA system, which are normalized by the mean absolute value of the local velocity vector. In the tip clearance flow zone, very high turbulence levels of above 25% are measured, while the lowest turbulence levels are recorded in a region at the suction side of the blades and in the pressure side hub corner. In the blade wake, elevated turbulence intensities are also measured. This supports the existence of a vortical structure in the tip gap region and a strong interaction with the channel flow. The interaction mechanism of the tip clearance flow and the channel flow is different for the main and splitter blade channels. In the case of the splitter blade, the interaction is strongest as the clearance jet interacts with rotational channel flow, while at the main blade, the leakage interacts with the nonrotational fluid entering the impeller. The interaction of the tip gap and the channel flow was also seen in the wall pressure fluctuation shown in the accompanying paper [18]. A similar conclusion on the existence of vortices can be drawn for the blade trailing edge region, where turbulent mixing of the blade wake and the jet is seen.

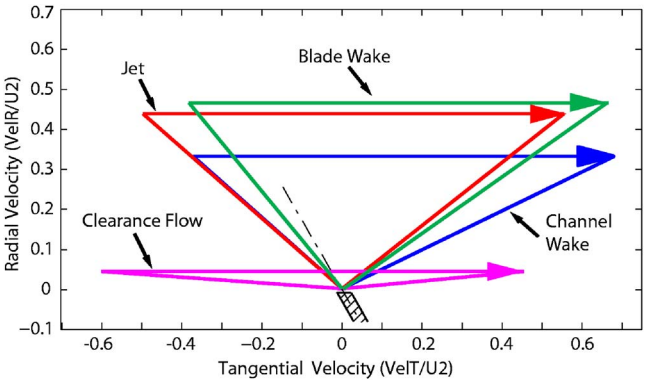

Fig. 14 Velocity triangles of the flow pattern

Velocity Triangles for the Secondary Flow Pattern. The velocity triangles for the main zones at the impeller exit are plotted and labeled in Fig. 14. The circumferential and axial positions of the specific velocity triangles are marked in Fig. 11(*b*) with small circles. In the velocity triangles, the classical distinction between the jet and the channel wake pattern is found. The wake shows the highest absolute tangential velocity, while the relative tangential velocity is higher in the jet region.

No significant difference is found in the relative flow angle of the channel wake and the jet flow pattern. The wake near the blade shows a similar tangential velocity as the channel wake pattern but the radial velocity is substantially elevated due to the blockage effect of the tip clearance vortex. In the blade wake, a lower slip velocity is found than in the channel wake or in the jet pattern. In this region, the highest radial velocities are found. The clearance flow can be identified very clearly as an additional zone in the velocity triangles. In the tip clearance region, the radial and absolute tangential velocities are very low, while the relative tangential velocity and the slip velocity become very large. The flow does

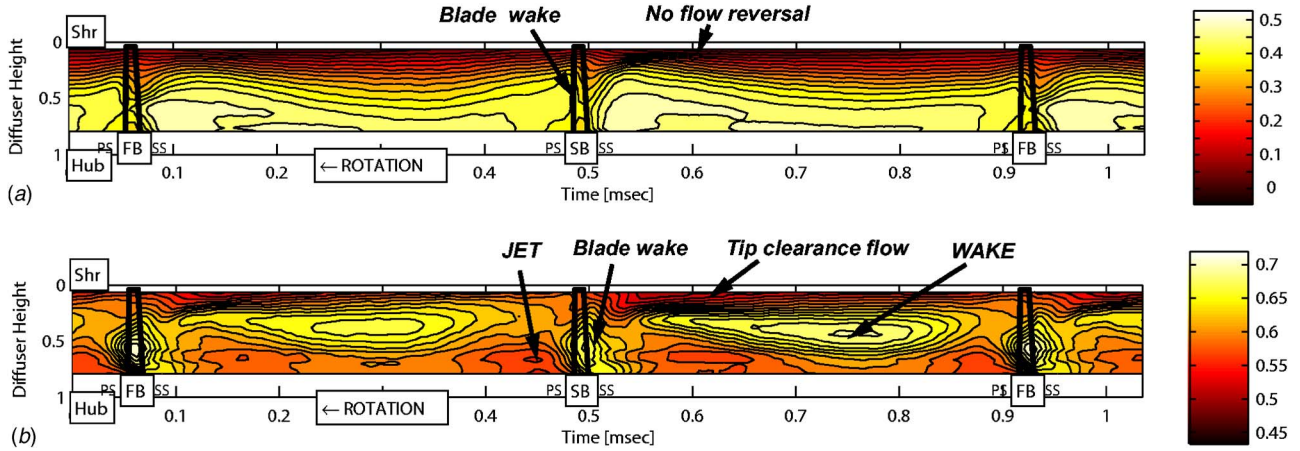

Fig. 15 Measured contours of radial and absolute tangential velocities at a radial location (R/R_2=105%) for a reduced clearance configuration (CR=4.5%)

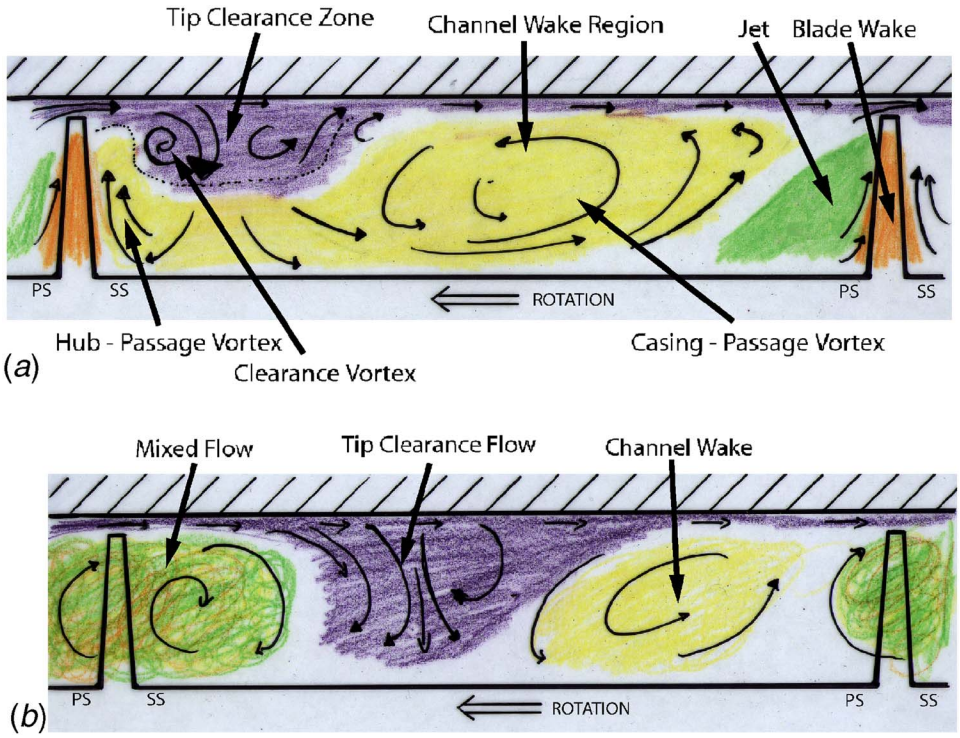

Fig. 16 Schematic model of the secondary flow pattern at the impeller exit and downstream in the vaneless diffuser

not follow the blade direction but crosses the blade through the tip gap and appears as a zone of flow mass flow and high blockage.

Reduced Tip Clearance Configuration

In Fig. 15, the radial and absolute tangential velocity components are displayed for the reduced clearance case CR=4.5%. The color scale is similar to the representations shown above. As in the base line clearance case discussed above, no clear jet-wake structure is observed. The pattern of the radial velocity is dominated by the skew of the flow. For the reduced relative clearance configuration, the influence of the tip clearance flow on the flow structure is attenuated. No local flow reversal is seen near the shroud and the axial gradients of the radial velocity are reduced.

Compared to the base line clearance case, the channel wake zone is enlarged and shifted. Contrary to the base line configuration, the channel wake is not replaced by the leakage flow and appears toward the suction side of the blades. This position of the channel wake agrees more with the location where, based on the classical jet-wake model, a wake region is expected. The position of the jet remains on the pressure side/hub corner.

Summary and Conclusion

The measurements of the flow structure in the vaneless diffuser reveal a significant nonuniformity of the flow at the discharge of the impeller. Near the hub, high radial velocities are present, while near the shroud, the flow is locally reversed. Due to the high blade loading, pitchwise flow variations are present. In this centrifugal compressor, the tip clearance flow has a dominant effect on the evolution of the flow structure. The flow pattern is dominated in the axial direction by the skew of the flow vectors. The skew is caused by reduced work and high losses in the clearance zone. Due to the skewed flow, the classical jet-wake model does not apply and the flow pattern appears, in contradiction to the classical jet-wake model by Dean and Senoo [1]. The channel wake zone is much larger than the jet area and covers most of the channel area. As an additional flow feature, a strong tip clearance flow pattern was identified near the suction side shroud corner.

In the clearance zone, only little work is done to the fluid and low absolute tangential velocities are found. The clearance flow is highly turbulent and appears to the channel flow as a zone of high blockage. Farther downstream in the diffuser, the jet structure mixed with the blade wake. The mixing process of the flow pattern takes place at two different time scales: The jet and the blade wake mix out rapidly at the impeller exit while the channel wake and the clearance flow remain stable throughout the diffuser. As the tip clearance was reduced, no flow reversal at the shroud could be identified. For the reduced clearance configuration, the tip clearance flow does not shift the channel wake toward the adjacent pressure side and the flow structure appears more, as predicted in the classical jet-Wake model.

A schematic description of the secondary flow pattern is provided for two radial locations (Fig. 16). This model applies to the description of a highly loaded centrifugal compressor with large relative tip clearance. It includes the strong effect of the low work leakage flow on the flow pattern and the different mixing scales for the blade wake and the clearance zones. The secondary flow patterns behave similarly to the predictions of the model proposed by Eckardt [3] for an impeller without backsweep. The area covered by the tip clearance flow is larger than that in the Eckardt model due to the higher backsweep of the blading in the current study. The circular movement of the channel wake and the skewed layers along the blades are in good agreement with this flow model. Near the impeller exit, the classical jet-wake structure and superimposed effects of the tip clearance flow are seen as dominant flow features. Measurements of the turbulence level reveal a highly turbulent and vortical structure of the tip clearance flows. The jet and the blade-wake pattern interact and mix out rapidly near the exit of the impeller. They cannot be identified farther downstream in the vaneless diffuser. The clearance flow region and the channel wake remain stable and can be seen up to the diffuser exit.

Acknowledgment

The authors would like to acknowledge the dedicated support by the Swiss Federal Institute of Technology, Zurich, and its permission to publish the paper. The authors would also like to thank Professor Seung Jin Song for his expertise in analyzing and interpreting the data. The assistance of the staff at the Turbomachinery Laboratory, both in the mechanical and the electronic laboratory, has been very much appreciated at all times.

Nomenclature

b = axial diffuser width (m)
D = diameter (m)
$\dot{m}$ = mass (kg/s)
p = pressure (kPa)
R = radius (m)
t = tip gap width (m)
U = circumferential speed (m/s)
$\dot{V}$ = volume flow rate (m^3/s)
ρ = density (kg/m^3)
v = absolute velocity (m/s)
w = relative velocity (m/s)
α = absolute flow angle (deg)
β = relative flow angle (deg)
Δh_{ts} = total-static enthalpy rise (kJ/kg)

Dimensionless Numbers

$\phi = V_0/(D_2^2 U_2)$ = specific flow coefficient
$\psi = \Delta h_{ts}/U_2^2$ = isentropic head coefficient
$\mathrm{Mu} = U_2/\sqrt{\kappa RT}$ = impeller tip Match number
$\pi = p_{2s}/p_{0t}$ = total-static pressure ratio
$\mathrm{CR} = t/b_2$ = tip clearance ratio

Subscripts

0 = stage inlet
2 = impeller outlet
5 = diffuser outlet

References

[1] Dean, R. C., and Senoo, Y., 1960, "Rotating Wakes in Vaneless Diffusers," ASME J. Basic Eng., **82**, pp. 563–574.
[2] Japikse, D., 1996, *Centrifugal Compressor Design and Performance*, Concepts ET1, Wilder, VT.
[3] Fowler, H. S., 1968, "Distribution and Stability of Flow in a Rotating Channel," ASME J. Eng. Power, **90**(3), pp. 229–236.
[4] Eckardt, D., 1975, "Instantaneous Measurements in Jet-Wake Discharge Flow of a Centrifugal Compressor Impeller," ASME J. Eng. Power, **97**(3), pp. 337–346.
[5] Eckardt, D., 1976, "Detailed Flow Investigations Within a High-Speed Centrifugal-Compressor Impeller," ASME J. Fluids Eng., **98**(3), pp. 390–402.
[6] Krain, H., 1988, "Swirling Impeller Flow," ASME J. Turbomach., **110**(1), pp. 122–128.
[7] Rohne, K. H., and Banzhaf, M., 1991, "Investigation of the Flow at the Exit of an Unshrouded Centrifugal Impeller and Comparison With the Classical Jet-Wake Theory," ASME J. Turbomach., **113**(4), pp. 654–659.
[8] Johnson, M. W., and Moore, J., 1983, "The Influence of Flow-Rate on the Wake in a Centrifugal Impeller," ASME J. Eng. Power, **105**(1), pp. 33–39.
[9] Johnson, M. W., and Moore, J., 1983, "Secondary Flow Mixing Losses in a Centrifugal Impeller," ASME J. Eng. Power, **105**(1), pp. 24–32.
[10] Inoue, M., and Cumpsty, N. A., 1984, "Experimental Study of Centrifugal Impeller Discharge Flow in Vaneless and Vaned Diffusers," ASME J. Eng. Gas Turbines Power, **106**(2), pp. 455–467.
[11] Gyarmathy, G., Hunziker, R., Ribi, B., and Spirig, M., 1991, "On the Change of Impeller Flow Non-Uniformities With Flow Rate in a Centrifugal Compressor," *Turbomachinery: Latest Developments in a Changing Scene, European Conference*, 1991, IMechE, Paper No. C423/054, pp. 143–154.
[12] Senoo, Y., and Ishida, M., 1987, "Deterioration of Compressor Performance Due to Tip Clearance of Centrifugal Impellers," ASME J. Turbomach., **109**(1), pp. 55–61.
[13] Goto, A., 1992, "The Effect of Tip Leakage Flow on Part-Load Performance of a Mixed-Flow Pump Impeller," ASME J. Turbomach., **114**(2), pp. 383–391.
[14] Ishida, M., Ueki, H., and Senoo, Y., 1990, "Effect of Blade Tip Configuration on Tip Clearance Loss of a Centrifugal Impeller," ASME J. Turbomach., **112**(1), pp. 14–18.
[15] Hong, S.-S., Schleer, M., and Abhari, R. S., 2003, "Effect of Tip Clearance on the Flow and Performance of a Centrifugal Compressor," FEDSM'03, Fourth ASME/JSME Joint Fluids Engineering Conference, Honolulu, HI.
[16] Schleer, M., and Abhari, R. S., 2005, "Influence of Geometric Scaling on the Stability and Range of a Turbocharger Centrifugal Compressor," ASME Paper No. GT 2005-68713.
[17] Stahlecker, D., and Gyarmathy, G., 1998, "Investigations of Turbulent Flow in a Centrifugal Compressor Vaned Diffuser by 3-Component Laser Velocimetry," ASME Paper No. 98-GT-300.
[18] Schleer, M., Hong, S. S., Zangeneh, M., Roduner, C., Ribi, B., Ploger, F., and Abhari, R. S., 2004, "Investigation of An Inversely Designed Centrifugal Compressor Stage—Part II: Experimental Investigations," ASME J. Turbomach., **126**(1), pp. 82–90.
[19] Schleer, M., Song, J. S., and Abhari, R. S., 2008, "Clearance Effects on the Onset of Instability in a Centrifugal Compressor," ASME J. Turbomach., **130**, p. 031002.

Inner Workings of Shrouded and Unshrouded Transonic Fan Blades

A. R. Wadia

P. N. Szucs

GE Aircraft Engines,
Cincinnati, OH 45215

This paper reports on the numerical assessment of the differences in aerodynamic performance between part span shrouded and unshrouded fan blades generally found in the first stage of multistage fans in low bypass ratio aircraft engines. Rotor flow fields for both blade designs were investigated at two operating conditions using a three-dimensional viscous flow analysis. Although designed to the same radius ratio, aspect ratio, and solidity, the unshrouded fan rotor had a slightly increased tip speed (+3%) and somewhat lower pressure ratio (−3.2%) due to engine cycle requirements. Even when allowing for these small differences, the analysis reveals interesting differences in the level and in the radial distribution of efficiency between these two rotors. The reason for the improved performance of the shrouded rotor in part can be attributed to the shroud blocking off the radial migration of boundary layer fluid centrifuged from the hub on the suction side. As a result, the shock boundary layer interaction seems to be improved on the shrouded blade. At the cruise condition, the efficiency is the same for both rotors. The slightly better efficiency of the shrouded blade in the outer panel is nullified by the large efficiency penalty in the vicinity of the shroud. As there is no significant radial migration of fluid in the suction side boundary layer, as indicated by the analysis at this condition relative to the design speed case, the benefit due to the shroud is greatly reduced. At this speed and at lower speeds, the shroud becomes a net additional loss for the blade. Also of interest from the numerical results is the indication that significant blade ruggedization penalties to performance can be reduced in the case of the unshrouded blade through custom tailoring of its mean camber line. [DOI: 10.1115/1.2776957]

Introduction

The trend in using wide chord fan blades to improve the aerodynamic performance of transonic blading has been one of the more significant technological evolutions in aircraft engine design technology. Wide chord fan technology has matured and is now well established for high bypass ratio turbofans used in commercial aircraft engines. Similarly, the trend in going from very high aspect ratio tip or part span shrouded fan blades with dovetails to low aspect ratio wide chord blade/disk (blisk) assemblies has also found a home in multistage fans for low bypass engines such as the one reported by Wadia and James [1].

As described in their paper, the cornerstone of advancing the state of the art in multistage fan design was derived from a higher airflow long chord, part span shrouded first stage fan blade developed for a low bypass ratio turbofan. The first stage of this advanced multistage fan incorporated wide chord fan aerodynamics technology using blisks, thus eliminating the need for the part span shroud and dovetail used in the previous design.

The losses through transonic rotors due to part span shrouds have been experimentally studied by many researchers including Esgar and Sandercock [2] Benser et al. [3], Reid and Tysl [4], Lewis and Urasek [5], Messenger and Keenan [6], and Ware et al. [7]. Koch and Smith [8] presented a part span shroud loss correlation represented in terms of a drag coefficient. Roberts [9] developed a design point loss correlation for part span shrouds using experimental data from 21 shrouded, transonic axial flow fan rotors with design pressure ratios between 1.5 and 2.0. The correlation has found wide usage in industry to estimate a priori the loss in blade element performance due to part span shrouds. In addition to identifying the parameters contributing to the shroud loss such as the Mach number, the part span shroud's thickness, chord, angle of attack, location along the blade span, and rotor airfoil geometry at the shroud location, he noted that the blockage and losses associated with a part span shroud cause significant flow shifts toward the end-wall regions that can have a detrimental effect on the performance of the entire blade. He correctly observed that the flow in the region of the shroud is highly complex and three dimensional in nature but was unable to analytically or numerically calculate this flow field due to the lack of three-dimensional computational fluid dynamics (CFD) capability at that time.

This paper reports on a numerical assessment of the differences in aerodynamic performance between a part span shrouded/dovetailed rotor and an unshrouded/blisk fan blade that is typically used in the first stage of a multistage fan. Figure 1 shows a three-dimensional pictorial view of the part span shrouded rotor and the unshrouded/blisk rotor. Rotor flow fields for both blade designs are investigated at two operating conditions using a three-dimensional viscous flow analysis.

The shrouded rotor, which has demonstrated excellent performance in service on the B2 aircraft, was designed in the early 1980s using two-dimensional through-flow analysis without mixing but with capability to model the local part span shroud blockage and inviscid cascade analysis for transonic blade rows. The design of the base line shrouded rotor is a true example of Cumpsty and Greitzer's [10] statement that in the past, although analyses were unable to capture many features of the flows, this did not preclude aeroengine turbomachinery from being successfully developed using methods that were far from a complete description. On the other hand, the unshrouded rotor/blisk version of the shrouded blade was designed in the late 1990s using through-flow analysis with mixing (Adkins and Smith [11]) and three-dimensional viscous analysis. The availability of the three-dimensional analysis was critical in helping reduce the penalty in performance due to the added ruggedization of the unshrouded rotor design.

Contributed by the International Gas Turbine Institute of ASME for publication in the JOURNAL OF TURBOMACHINERY. Manuscript received January 2, 2007; final manuscript received January 13, 2007; published online May 2, 2008. Review conducted by David Wisler. Paper presented at the ASME Turbo Expo 2006: Land, Sea and Air (GT2006), Barcelona, Spain, May 8–11, 2006, Paper No. GT2006-90992.

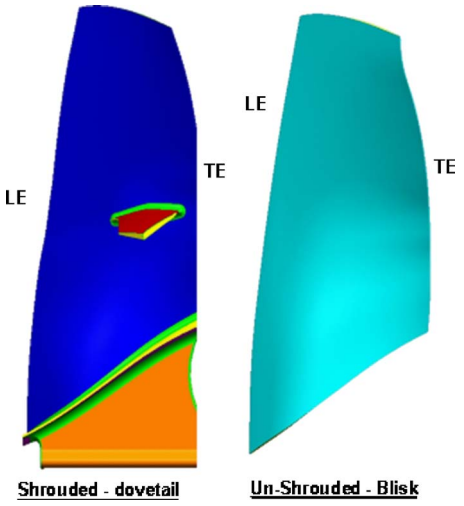

Fig. 1 Shrouded and unshrouded blades for low bypass ratio aircraft engine applications

Although designed for modestly different wheel speed and pressure ratio requirements, the analyses reveal interesting variation in the efficiency level and radial trends between the two rotors. The reason for the improved performance of the shrouded rotor in part can be attributed to the shroud blocking off the radial migration of boundary layer fluid centrifuged from the hub on the suction side. As a result, the shock boundary layer interaction seems to be improved on the shrouded blade.

At the cruise condition, the efficiency is the same for both rotors. The slightly better efficiency of the shrouded blade in the outer panel is nullified by the large efficiency penalty in the vicinity of the shroud. As there is no significant radial migration of fluid in the suction side boundary layer, as indicated by the analysis at this condition relative to the design speed case, the benefit due to the shroud is greatly reduced. At this speed and at lower speeds, the shroud becomes a net additional loss for the blade.

Fan Rotor Aerodynamic Design

The base line fan's part span shrouded first stage fan blade, as described in the paper by Wadia and James [1], was selected as the aerodynamic technology base to be improved on by employing unshrouded/blisk fan blade mechanical technology. An aerodynamic synthesis of the part span shrouded base line fan's test data served as the basis for the vector diagrams used to design the blading for the unshrouded/blisk fan. As the unshrouded fan was being designed for a different application than the existing shrouded fan, its design speed was increased by 3% at the same overall fan pressure ratio to better match the first stage fan blade with the inlet and to provide better overall distortion handling capability. This resulted in the unshrouded blade to operate on a slightly lower (−3.2%) operating line relative to the shrouded blade. In addition to keeping the inlet corrected flow and overall multistage fan pressure ratio requirements the same, the unshrouded first stage rotor was designed to retain the passage area distribution qualities of the shrouded rotor in terms of throat margin, start margin, and effective camber (Wadia and Copenhaver [12]) to ensure that the perceived performance change with the new blading is mostly a consequence of the blisk design without a part span shroud. Rotor chords were identical for both blades. Three-dimensional viscous analysis was extensively used in the design and analysis of the unshrouded rotor. Some of the aerodynamic attributes of the fan blades are summarized in Table 1. The rotor inlet and hub casing radii were retained such that on a one-dimensional basis, the specific flow into the rotor was constant between both configurations.

Table 1 Fan rotor aerodynamic parameters

Parameter	Shrouded/Unshrouded
Radius ratio	0.373
Rotor pressure ratio	1.96/1.9
Rotor inlet tip relative mach number	1.43/1.4
Rotor pitch line solidity	1.6
Rotor aspect ratio	1.7
Rotor pitch line T_{max}/C	0.04/0.06
Rotor mean camber line shape and thickness distributions	Custom tailored

Dictated by the engine application and its manufacturing, added mechanical constraints were placed on the unshrouded rotor design that represents a realistic aircraft engine product implementation, resulting in significant geometrical changes being made to the unshrouded rotor relative to its shrouded counterpart.

Mechanical design of a blisk from a base line bladed and shrouded design requires increased airfoil thickness to overcome the stiffness lost by removing the part span shroud. Shroud removal drops the fundamental resonant mode responses, and the increased thickness then overcomes this, driving the frequencies back up to acceptable levels. Blisk designs also have a fundamentally less (effectively zero) friction damping than their bladed counterparts. This too requires a judicious addition of material to reduce stresses by overcoming those loads with more material. The added material from the above two impacts could overcome some of the weight savings inherent to a blisk design. One positive benefit of the lack of friction damping in blisks is that unlike bladed designs wherein friction can depart over time due to wear, blisks cannot succumb to these phenomena. Counteracting this is the current relatively new science of mistuning, which typically increases the allowable limits on leading edge nicks and dents for safe operation.

Figure 2 shows the comparison of the radial distribution of maximum thickness-to-chord ratio between the shrouded and unshrouded rotor configurations. As shown in Fig. 2, to compensate for the loss of the part span shroud and dovetail in the blisk fan rotor, the hub airfoil section is 35% thicker than the shrouded blade. This additional thickness increases to 65% at 80% span before it starts to taper back toward the shrouded blade configuration. While the maximum thickness locally at the tip was not increased, the maximum thickness near the tip region was also increased slightly on the unshrouded blade to enhance its bird-strike and foreign-object-damage (FOD) capabilities. In general, the unshrouded rotor required slightly thicker leading edges and slightly more forward positioning of maximum thickness to re-

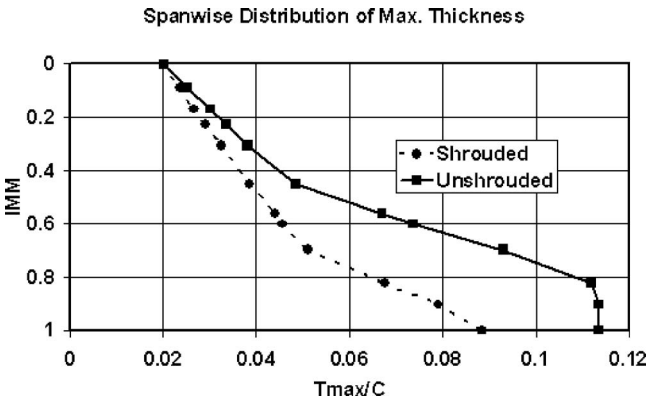

Fig. 2 Comparison of spanwise distribution of maximum thickness-to-chord ratio for part span shrouded and unshrouded rotor configurations

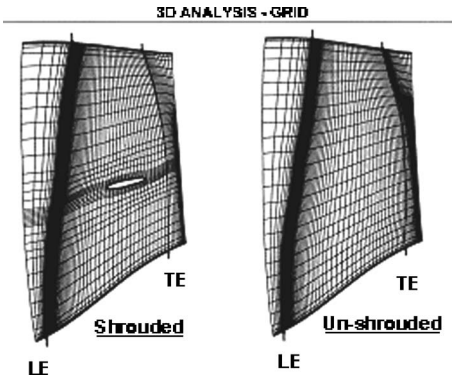

Fig. 3 Grid for three-dimensional viscous analysis

duce the leading edge stresses. The thicker sections represent increased blade blockage and thicker leading edges with larger wedge angles. In spite of the added thickness and wedge angles, proper mean camber line tailoring, shaping the hub flow path, and using three-dimensional viscous analysis in the design phase helped reduce the compromise in performance due to the added mechanical design constraints imposed on the unshrouded blade.

Three-Dimensional Viscous Analysis of Shrouded and Unshrouded Rotors

The details of the three-dimensional viscous code used herein, which has found wide usage within General Electric Company for compressor and turbine designs, has been reported by Jennions and Turner [13]. Although the capability to account for the presence of the downstream stator exists, for our comparative analysis, it was not utilized.

Grid Description

The three-dimensional calculations for both rotors were performed using the grids shown in Fig. 3. The calculations for the shrouded blade were performed with an attempt to resolve the details of the flow in the vicinity of the part span shroud. A stretching parameter between 1.0 and 1.2 was used in all three directions to model the gradients in the flow field near the end walls and the blade surfaces. Special care was taken to model the leading edge region accurately to obtain the correct shock structure in the analysis. Both rotor configurations were modeled with the same tip clearance of 0.03 in.

Boundary Conditions

The inlet boundary conditions for the analysis of both rotor configurations consisted of prescribing rotor inlet (inlet guide vane exit) total pressure, temperature, and tangential flow velocity that were obtained from a through-flow synthesis of engine test data for the base line fan. The total pressure loss across the front frame and inlet guide vane was measured using a radial traverse rake in the base line engine test. The exit boundary condition consisted of prescribing the exit tip static pressure level such that the flow-pressure ratio characteristic calculated by the three-dimensional analysis would be on the same operating line as calculated by the through-flow analysis. The data points selected for the three-dimensional analyses were on the fan operating line at 95% and 100% corrected speeds.

Code Validation

The three-dimensional viscous analysis was validated using data from an instrumented engine test with the shrouded rotor configuration. A typical comparison of the analysis with the data is shown herein for the fan peak efficiency condition only.

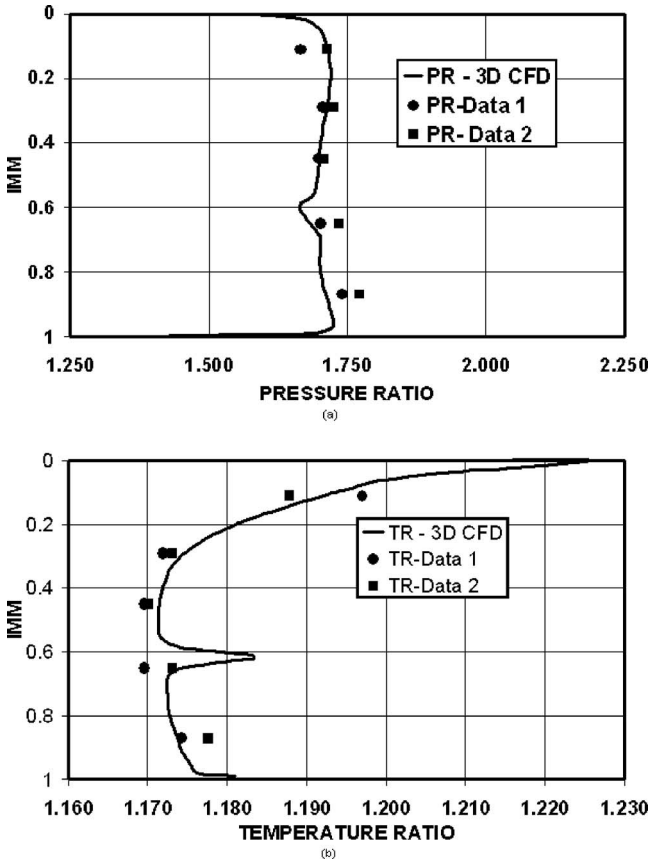

Fig. 4 Comparison of measured and calculated radial profiles of total pressure and temperature for the shrouded blade at 95% speed

Comparison of the radial profiles of rotor total pressure and total temperature ratios calculated by the three-dimensional viscous analysis at the rotor grid exit with the measured stator 1 leading edge (vane mounted) data with the shrouded rotor configuration at 95% speed is illustrated in Fig. 4. The calculated total pressure and temperature ratios are generally in good agreement with the measured data in the top 50% immersion of the shrouded blade. The three-dimensional analysis captures the loss (wake) of the part span shroud as a total pressure loss and an increase in temperature. The data miss the part span shroud effects due to the physical limitations in having more than five stator 1 leading edge mounted probes in the test. The calculated total pressure in the bottom 40% of the shrouded blade is lower than data with a corresponding decrease in work input, resulting in equal or lower efficiency relative to data. Similar comparison of calculated radial profiles with data was obtained at 100% speed.

Comparison of Three-Dimensional Analysis Calculations at Design Speed

Figures 5 and 6 show the isentropic Mach number contours on the suction and pressure surfaces of both rotors, in the meridional plane, at 100% speed. The suction surface shock extends across the entire span on both rotors. Unlike the inlet relative Mach number level, on the suction surface along most of the span, both blades exhibit a nearly constant Mach number level ahead of the shock. Per design intent, the shroud is tucked behind the passage shock due to its aft location and potential blockage field. In Fig. 6, a pressure side leg from the passage shock is indicated extending nearly 50% of the span for both rotors and this pressure side leg is located closer to the leading edge in the case of the shrouded blade.

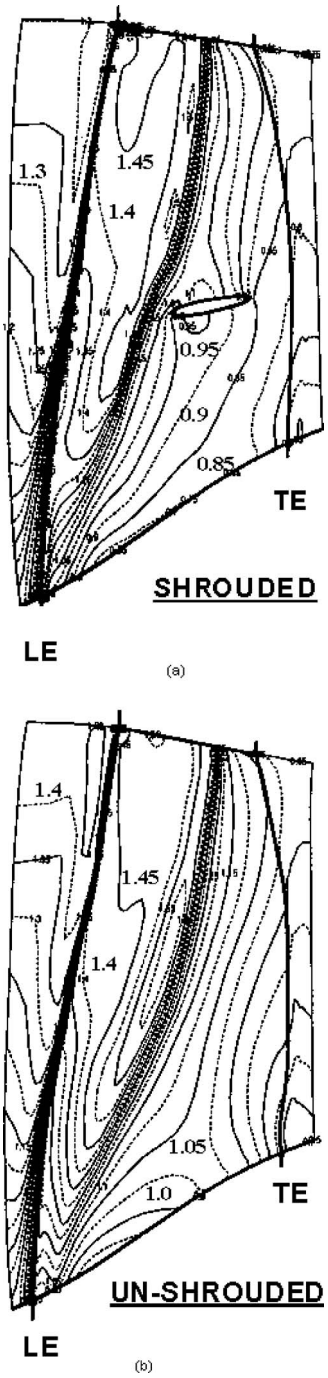

Fig. 5 Comparison of isentropic Mach number contours on suction surface at 100% speed

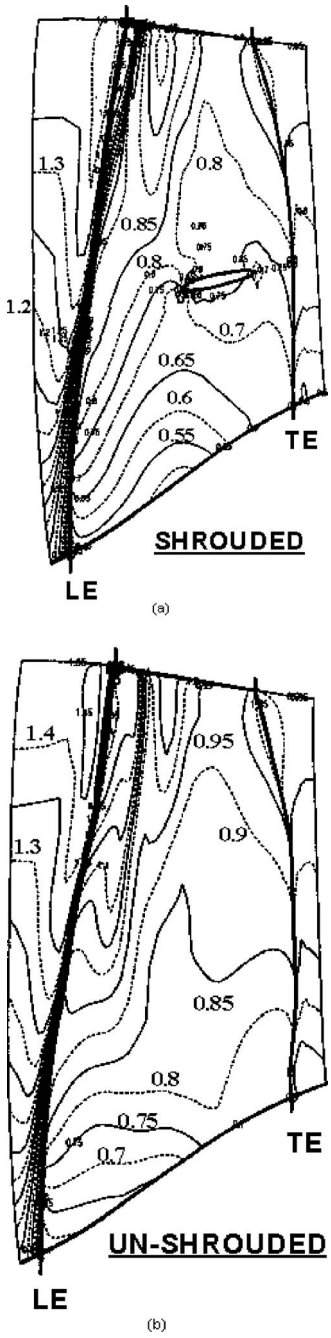

Fig. 6 Comparison of isentropic Mach number contours on pressure surface at 100% speed

Comparison of the blade-to-blade isentropic Mach number contours for both rotors at the blade tip at 100% speed is presented in Fig. 7(*a*) and the corresponding blade tip isentropic surface Mach number distributions are illustrated in Fig. 8. The shock structure at the blade tip, measured using over-the-rotor-tip kulites, for the shrouded rotor is presented for comparison in Fig. 7(*b*).

In Fig. 8, consistent with its slightly lower speed and higher pressure ratio, the exit Mach number for the shrouded blade is lower and its airfoil section loading is higher. The agreement between the calculated (Fig. 7(*a*)) and the measured (Fig. 7(*b*)) shock structure for the shrouded rotor at design speed lends credibility to the details of the 3D CFD solution. In spite of its ruggedization and 3% higher speed, Fig. 8 shows that the mean camber line tailoring for the unshrouded blade kept the suction side Mach number increase along the airfoil section's front half and the subsequent expansion of the shock to a minimum and reduced the strength of the pressure side shock bifurcation.

Similar blade-to-blade and blade surface Mach number results at the shroud immersion (59.2%) are presented in Figs. 9 and 10, respectively. In detail, for the shrouded blade, this immersion represents the shroud's lower surface.

Of interest here, as is evident in Fig. 9, is the pressure field from the shroud blockage and the section area ruling for the shrouded rotor. In this region, mean camber line tailoring for the much thicker unshrouded blade was used to make the passage shock more oblique and weaken its strength near the pressure surface.

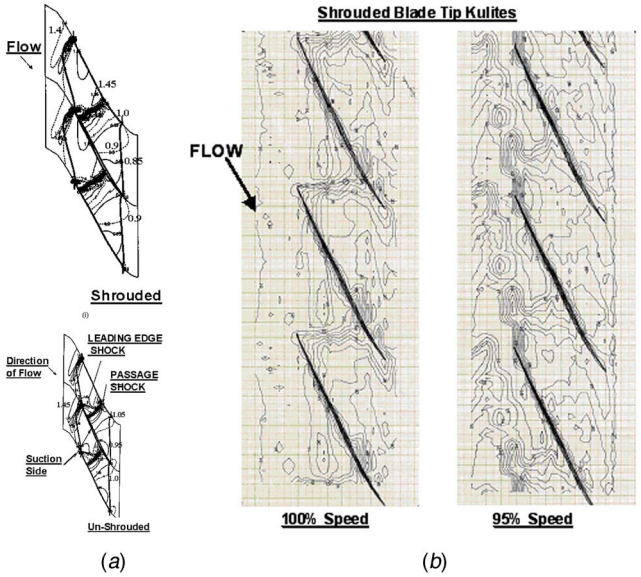

Fig. 7 (*a*) Comparison of the calculated blade-to-blade Mach number contours at the blade tip for both rotors at 100% speed and (*b*) shrouded blade's tip shock structure, measured using over-the-rotor-tip kulites, at 100% and 95% speeds

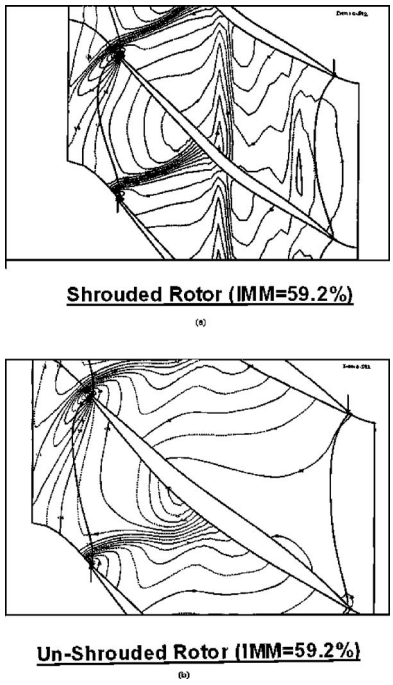

Fig. 9 Comparison of blade-to-blade Mach number contours at design speed at 59.2% immersion

The blade surface Mach number distributions for both rotors at design speed at this immersion are presented in Fig. 10. Comparison of the blade surface Mach number distribution confirms the shroud presence and its rather aft chordwise location. The consequence of the higher leading edge wedge angle is evident in the higher leading edge region Mach number distribution with the unshrouded blade.

The presence of the part span shroud is also clearly evident in the surface Mach number distribution in Fig. 10. The suction side shocks shown in Fig. 10 are located at 40% and 45% chord from the leading edge for the shrouded and unshrouded blades, respectively. While not shown in the main body of this paper but presented in detail in Appendix B, the part span shroud has lift (circulation) at this condition. The shroud alignment with the free-stream flow is also shown in Appendix B and in the velocity vectors presented later in the paper.

The hub blade surface Mach number distribution for both rotors at design speed is illustrated in Fig. 11. The consequence of the increased airfoil thickness (Fig. 2) in the case of the unshrouded blade is evident in the hub surface Mach number distribution comparisons presented in this figure.

Figure 12 shows the comparison of the radial distribution of the adiabatic efficiency at the stator 1 inlet plane between the shrouded and the unshrouded rotors as calculated by the three-dimensional analysis at 100% speed. The efficiency loss due to the part span shroud is evident in the figure. In spite of the unshrouded rotor's much larger thickness distribution (Fig. 2), the efficiency for both rotors below the part span shroud is very similar, the unshrouded rotor showing approximately 0.5 point lower efficiency than the shrouded blade.

The most glaring difference in efficiency between the unshrouded and the shrouded rotors occurs in the outer panel above the part span shroud. The shrouded rotor is between 2.5 and 5 points higher in efficiency from 10% to 60% immersion. The tip region of the shrouded rotor is significantly higher in performance than the unshrouded blade even though the airfoil thicknesses at the tip are identical between the two. The unshrouded blade shows

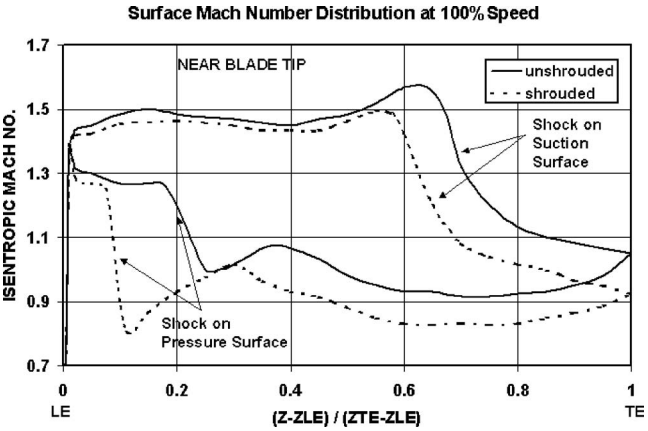

Fig. 8 Comparison of blade surface Mach number distribution near the blade tip at 100% speed

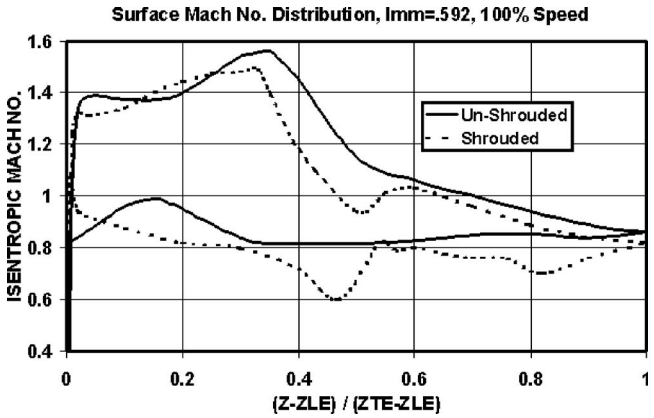

Fig. 10 Comparison of blade surface Mach number distribution at 59.2% immersion at 100% speed

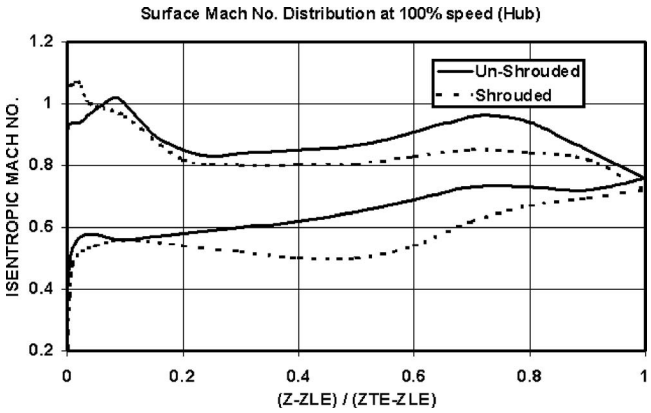

Fig. 11 Comparison of hub blade surface Mach number distribution at 100% speed

an overall efficiency penalty of 1.9 points relative to the blade with the midspan shroud. Taking the most pessimistic view and allowing for the full mixing out of the shroud wake, this 1.9 point overall efficiency advantage for the shrouded rotor would reduce to a still significant 1.1 points.

While some of the differences in performance in the outer panel of the two blades can be assigned to the thicker airfoils and higher through-flow Mach numbers of the unshrouded rotor, there is another occurrence that could make a significant contribution. As noted in Fig. 13, starting at a certain blade height level, the velocity vectors deep within the boundary layer fluid ($y^+ \sim 20$) indicate centrifugation outward on the suction side downstream of the shock. For the unshrouded blade, this initiates at a spanwise height of 39% (Fig. 13), and for the shrouded blade (Fig. 13), this is delayed to 60% spanwise height from the hub. This apparent gained resilience in the shock boundary layer interaction for the shrouded blade is attributed to the part span shroud blocking off the radial migration of low momentum fluid. This lessened migration of boundary layer fluid benefits the entire outer panel of the shrouded blade, contributing significantly to its higher performance there. Counting in the average 3.5 point performance advantage with the shrouded rotor in the outer panel as the base, and subtracting the inferred 2.0 point performance disadvantage due to the lower pressure ratio, higher speed, and thicker airfoils in the outer panel of the unshrouded rotor, quantifies this lessened migration of boundary layer fluid as providing a 1.5 point efficiency advantage for the outer panel of the shrouded rotor.

Note that the shroud is well aligned with the incoming through flow and no separated flow was observed in the calculations along

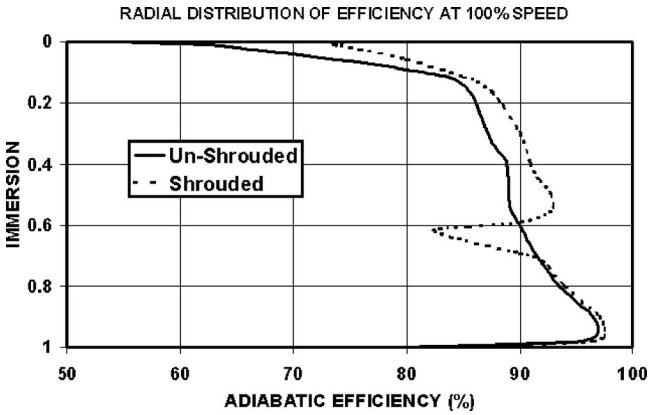

Fig. 12 Comparison of radial distribution of adiabatic efficiency calculated by the three-dimensional analysis at 100% speed

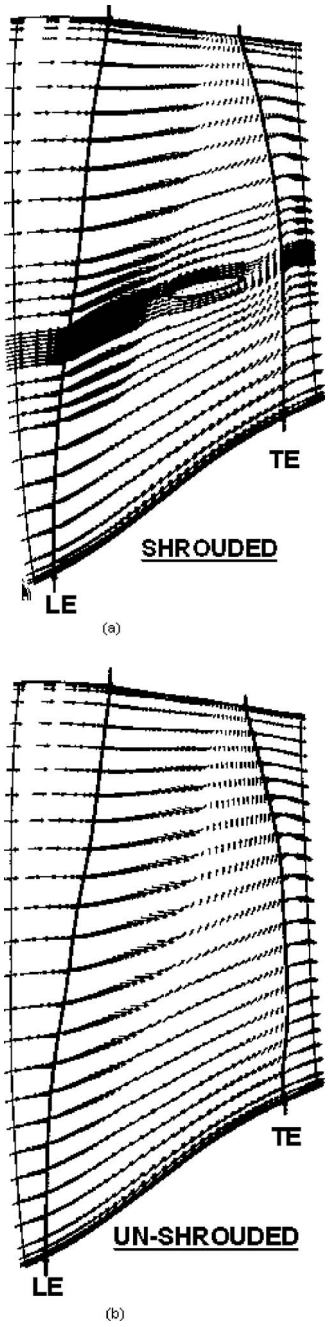

Fig. 13 Comparison of velocity vectors deep in the suction side boundary layer ($y^+ \sim 20$) at 100% speed

the shroud surface on the suction side. The good shroud leading edge alignment with the through flow was also evident in the blade surface Mach number distribution presented earlier in Fig. 10. The upward pointing arrows downstream of the shroud in Fig. 13 represent the rather orderly shroud wake migration.

Figure 14 shows a similar comparison of the velocity vectors deep within the boundary layer ($y^+ \sim 20$) on the pressure side of the two rotors. The calculations show no evidence of any separated flow regions on either rotor. In this case as well, the upper and lower part span shroud surfaces show no sign of any separated flow.

The reason for the higher efficiency of the shrouded blade at design speed was explored further by comparing the circumferential distribution of loss near the tip sections of both rotors, as presented in Fig. 15. The higher loss coefficient in the free-stream

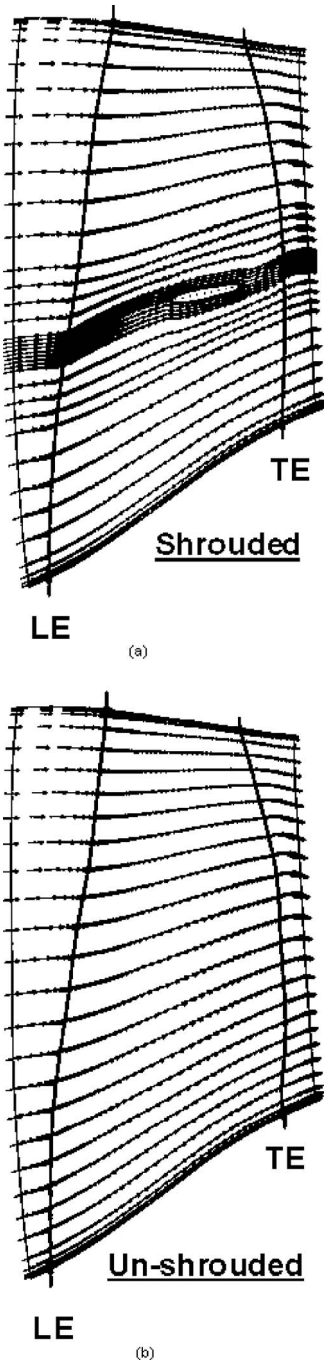

Fig. 14 Comparison of velocity vectors deep within the boundary layer on the pressure side ($y^+ \sim 20$) at 100% speed

region of the blade passage at the tip of the unshrouded blade is attributed to the stronger passage shock (Fig. 7(*a*)) and higher blade surface Mach numbers (Fig. 8). The wider wake and higher loss coefficient near the suction side of the unshrouded blade may be in good part a consequence of the more severe shock/centrifuged boundary layer interaction along the suction surface, as shown in Fig. 13, where the part span shroud behaves as a fence that prevents the lossy fluid centrifuged from the hub to reach the blade outer region. The higher surface Mach numbers on the pressure surface of the unshrouded blade appear to have a similar but less pronounced effect on the loss on the pressure side.

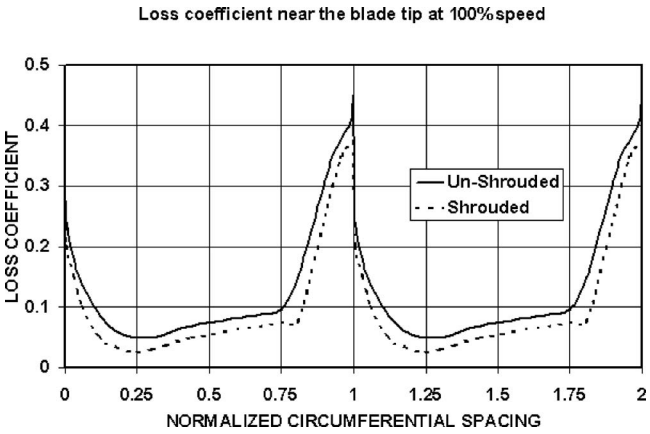

Fig. 15 Comparison of circumferential distribution of loss coefficient near the blade tip at design speed

Comparison of Three-Dimensional Analysis Calculations at 95% Speed

Similar three-dimensional calculations were conducted at 95% speed where the rotors achieve their peak efficiency along a prespecified operating line. Figures 16 and 17 show the comparison of the calculated Mach number contours on the suction and pressure side of the rotors, respectively. The Mach numbers are lower, and consistent with the airfoil sections moving closer to unstart, the shock is pulled further forward toward the leading edge relative to the design speed condition. The bifurcation of the shock has been eliminated. The shock is at the leading edge on the pressure surface at this condition.

The comparison of the calculated blade-to-blade Mach number contours near the tip of the rotors at 95% speed is illustrated in Fig. 18. Figure 7(*b*) (figure on the right) presents the measured shock structure obtained by tip kulites mounted in the casing over the rotor tip of the shrouded blade at 95% speed. At this condition, both blades have a normal shock structure with a single shock at the leading edge as opposed to a bifurcated shock at design speed. The passage shock is slightly more oblique for the unshrouded rotor. There is no shock on the pressure surface of the airfoil at this condition. The test data for the shrouded blade, in Fig. 7(*b*), show the normal shock that is further detached from the leading edge of the airfoil relative to that calculated by the three-dimensional analysis.

The comparison of the tip blade surface Mach number distributions at this condition is presented in Fig. 19. Being closer to unstart, the leading edge loadings are increased relative to those at design speed (Fig. 8). The benefit of mean camber line tailoring on the passage shock strength near the pressure side with the unshrouded rotor is evident at this condition as well.

Comparison of the radial distribution of efficiency between the rotors at 95% speed is presented in Fig. 20. The overall mass-averaged efficiency is approximately the same for both rotors. The shrouded rotor's slightly better efficiency in the outer panel is nullified in a large part by the significant increase in the loss in the vicinity of the shroud. Taking a pessimistic view at this condition, the shrouded rotor is about one point shy of the unshrouded rotor's performance level when debited for the full mixing out of its shroud's wake.

Figure 21 shows the comparison of the velocity vectors deep within the suction side boundary layer at 95% speed. Consistent with the reduced surface Mach numbers and shock strength at this condition, the migration of boundary layer fluid on the suction surface in the outer panel of both rotors is much reduced. As a consequence, the blocking benefit from the part span shroud is

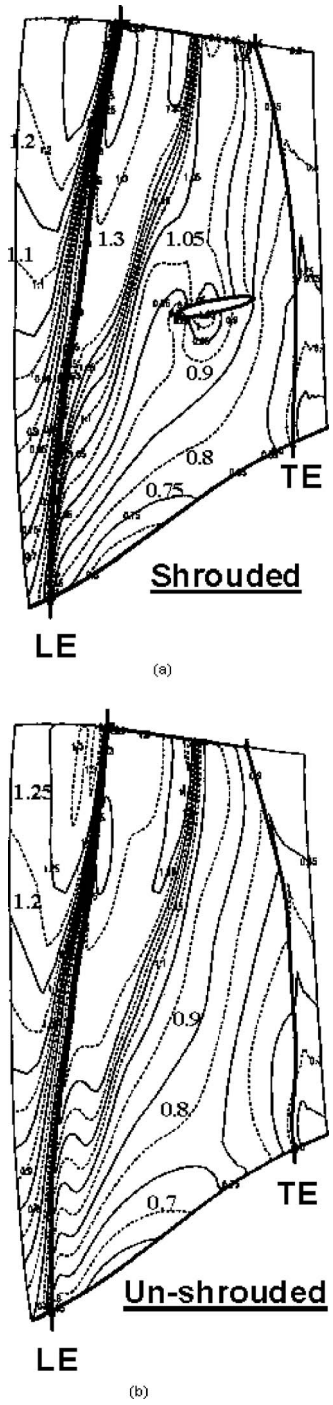

Fig. 16 Comparison of suction side Mach number contours at 95% speed

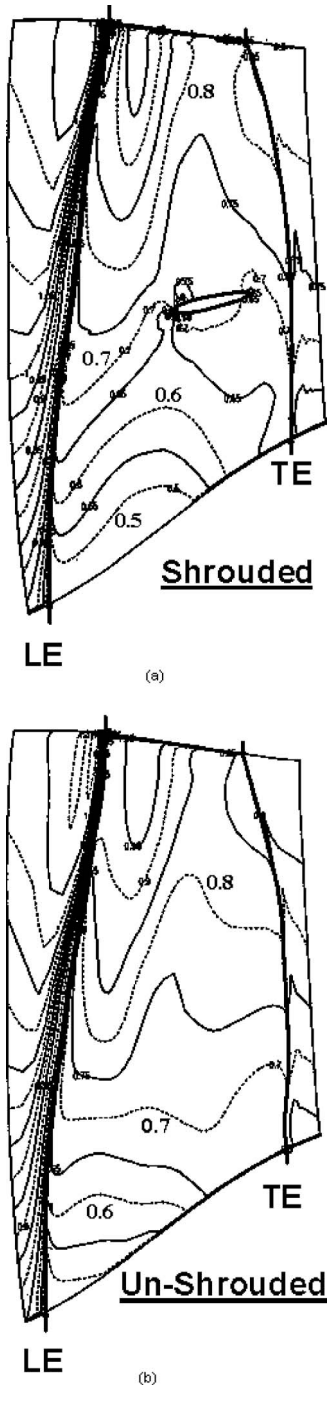

Fig. 17 Comparison of pressure side Mach number contours at 95% speed

eliminated. At 95% speed and at lower speeds, the part span shroud represents a net additional loss resulting in lower performance relative to the unshrouded rotor.

Concluding Remarks

Detailed analytical results of a study on the effect of part span shrouded transonic rotor with dovetail attachment and an unshrouded transonic rotor in a blisk configuration have been presented. The rotor configurations are representative of the first stage in a multistage low bypass ratio fan featuring consistent mechanical configuration attributes that are consistent with each configuration meeting its respective life mission requirements. The analysis reveals significant variation in the efficiency capability for the two rotors.

At design speed, aside from the slightly reduced relative Mach numbers and thinner airfoils, an improvement in the shock boundary layer interaction on the suction surface of the shrouded blade's outer panel contributes to its better performance relative to that with the unshrouded. The part span shroud's utility in preventing radial outward migration of boundary fluid is the key enabler for this improvement in the shock boundary layer interaction.

At the cruise condition, the as calculated efficiency is the same for both rotors. The slightly better efficiency of the shrouded blade in the outer panel is nullified by the large efficiency penalty in the

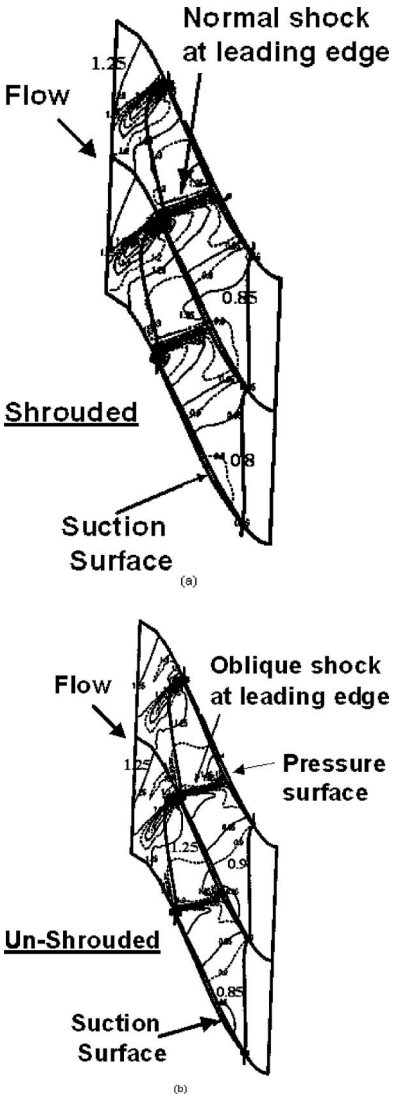

Fig. 18 Comparison of the calculated blade-to-blade Mach number contours near the blade tip at 95% speed

vicinity of the shroud. Due to the reduced shock strength at this condition, the shock boundary layer interaction is much reduced and hence there is no benefit to be gained from the presence of the

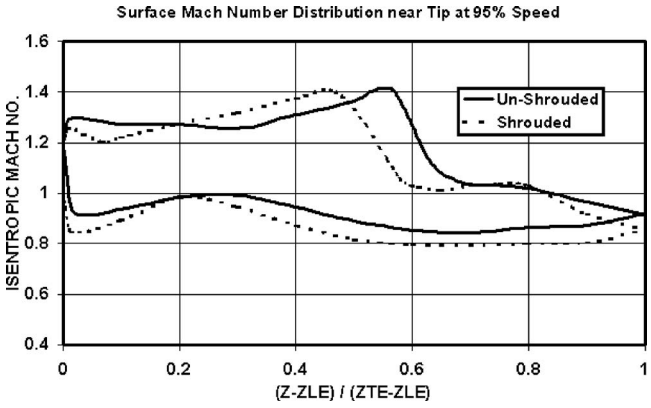

Fig. 19 Comparison of blade surface Mach number distribution near the tip at 95% speed

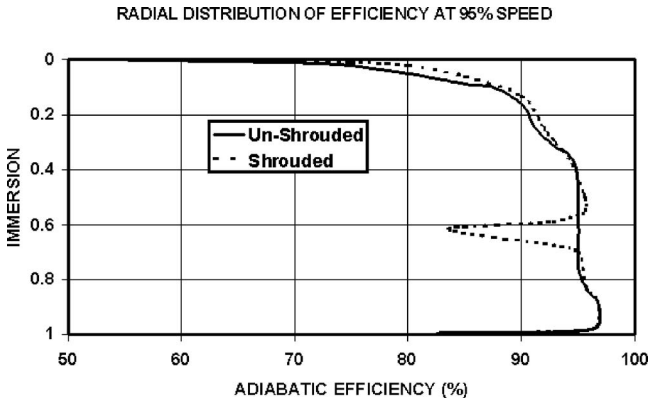

Fig. 20 Comparison of spanwise distribution of adiabatic efficiency calculated by the three-dimensional analysis at 95% speed

shroud. At this speed and at lower speeds, the shroud becomes a net additional loss for the blade that results in lower efficiency relative to the unshrouded blade.

In spite of the unshrouded blade's massive thickness ruggedization, higher tip speed, and lower pressure ratio, its attainment of equal performance with the shrouded blade at the cruise condition is a testament to the enhanced performance achievable with special tailoring of the mean camber lines.

The purpose of this paper is to show that the performance levels in turbomachines is significantly impacted by detailed geometrical features and internal flow field interactions. When making preliminary design estimates, just considering the obvious is often quite misleading. In this case, based on some 3D CFD enlightened reasons, the removal of an obvious loss source (in this instance, a part span shroud), when coupled with some mission alterations, forced geometrical and aerodynamic matching changes for the unshrouded rotor which turned out to be an aerodynamic design challenge on the performance side.

Acknowledgment

The authors would like to thank GE Aircraft Engines for permission to publish this paper.

Appendix A: Comparisons With Shroud Loss Correlations Developed by Roberts

There are still instances when quick estimates for the loss associated with part span shrouds have to be given. For such occasions, we include here our engine test experience derived from traversing behind the shrouded rotor. These are included in a way to reinforce and to augment Roberts [9] correlation for part span shroud loss.

Figure 22 shows the radial variation of the loss in efficiency due to the part span shroud as indicated by the radial traverse test data obtained in the engine test with the shrouded rotor at design speed. The three-dimensional CFD results have also been included in the figure together with the exponential type of shape postulated by Roberts [9]. The x axis in the figure represents the normalized local region of influence in the radial direction (approximately 20% of the total blade height) due to the part span shroud with the zero representing the spanwise location of the trailing edge of the part span shroud. The x axis range from 0 to -1 is in the direction from the shroud toward the tip and the range from 0 to +1 is in the direction from the shroud to the hub.

The agreement between the test and the three-dimensional CFD results is respectable. The spanwise distribution of the loss due to the shroud is more complex and is lopsided relative to the trends estimated from the paper by Roberts. The loss in the outer panel of the blade above the shroud is more concentrated toward the

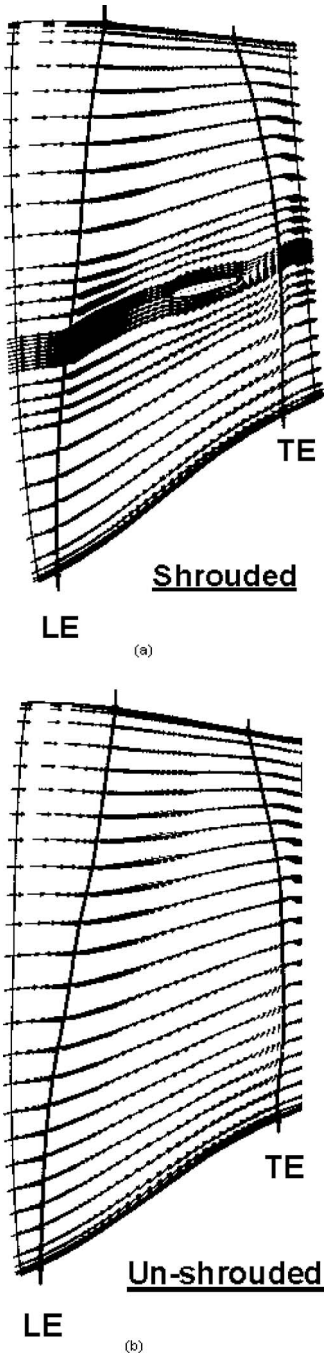

Fig. 21 Comparison of velocity vectors deep within the boundary layer on the suction side at 95% speed

shroud. The agreement in shape is better in the inner panel of the blade. The three-dimensional CFD underpredicts the maximum loss due to the shroud but the shape of the spanwise distribution in loss is in much better agreement with the data.

The integrated average total pressure loss coefficient increase in the region of the shroud at design and off-design conditions was also calculated using the correlations developed by Roberts [9] and Roberts et al. [14] and compared with the traverse data from the engine test. Figure 23 shows the comparison between the calculated and the measured average total pressure loss coefficient increase attributed to the shroud at 100%, 97.5%, and 95% corrected speeds. The agreement is quite good in spite of the differences in the distribution and the maximum loss coefficient levels.

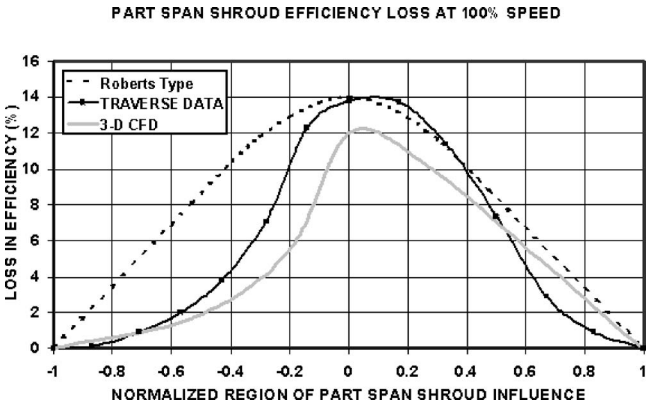

Fig. 22 Comparison of radial variation of loss in efficiency attributed to the part span shroud at design speed for the shrouded rotor

Appendix B: Part Span Shroud Surface Mach Number Distribution

As recognized by other researchers, the shape and alignment of the part span shroud do play a critical role in the overall performance of a shrouded blade. It was stated earlier in the paper that the shrouded rotor was designed before the advent of modern computational tools. The introduction of 3D CFD as part of the turbomachinery design system has provided a unique opportunity, in this case, to look into the fine details of the flow over the upper and lower surfaces of the part span shroud as the shock surface intersects the shroud airfoil.

Figure 24 shows the isentropic Mach number distribution along the upper and lower surfaces of the part span shroud near the pressure side of the shrouded rotor at 95% and 100% corrected speeds. Similar Mach number distributions at both speeds along the shroud surface at midpassage (blade to blade), i.e., between two adjacent blades, is presented in Fig. 25 and the Mach number distribution on the part span shroud near the suction side of the shrouded rotor is presented in Fig. 26.

The plots conclusively show the existence of circulation on the shroud. It is significant that only at the pressure side is there an indication of higher leading edge incidence level on the shroud. The tendency for this behavior has been known for some time now, resulting in designers drooping the part span shroud leading edge near the pressure side. This comes about as a result of the

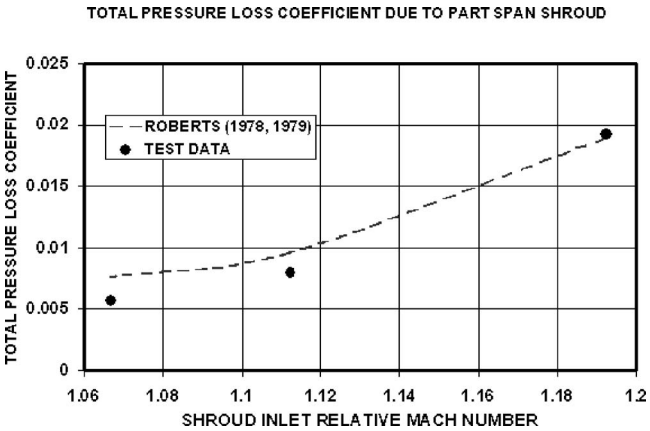

Fig. 23 Comparison of the design and off-design integrated average total pressure loss coefficient due to the part span shroud

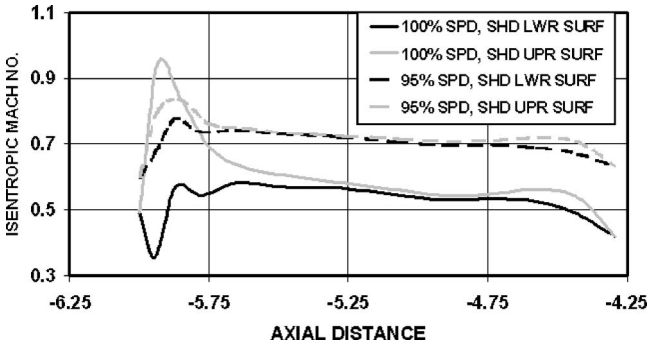

Fig. 24 Isentropic Mach number distribution along the upper and lower surfaces of the part span shroud near the pressure side of the shrouded rotor

flow path and shock inclination and that the passage shock is strongest near the pressure side. As a result, the radial deflection of the flow (incidence) is the largest there.

In terms of the noted lift on the part span shroud, there are two sources for it. One is stopping the radial migration of the boundary layer fluid on the suction side, as presented in Fig. 13. The other source, and this pertains to all along the shroud, is the part span shroud's mean line contour in the meridional sense. The shroud mean line contour was set on a circumferential average basis in the through-flow analysis with the shroud being a limp body (no lift). As a result, the chordwise energy distribution and the radial total pressure profile and flow distribution all had an impact on it. Relative to design intent, the downstream stators in the multistage fan were set closed to get the best performance on test. This made the radial total pressure profile behind the rotor less hub strong and the radial flow distribution to be less concentrated toward the hub (in effect moving the no lift on the shroud streamline radial location out toward the tip). Hence, to keep the shroud streamline at its designed position, lift will have to be generated on the shroud.

The indication that the shroud lift lessens at 95% speed is consistent with the lessened radial migration of the suction side boundary fluid, as shown in Fig. 21, and the added inlet guide vane closure providing a more hub concentrated radial flow distribution through the rotor (closer to design intent).

One reason for the lift on the part span shroud to be increasing toward the suction side in the passage at both speeds is the higher velocities (dynamic head) there. Consistent with this, the static pressure coefficients between the midpassage and the suction side shroud location are nearly the same.

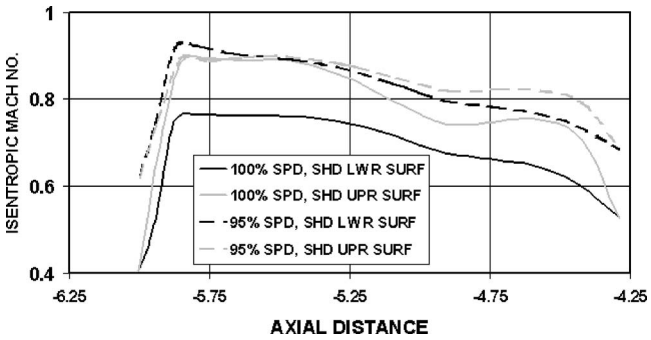

Fig. 25 Isentropic Mach number distribution along the upper and lower surfaces of the part span shroud at midpassage (blade to blade) between two adjacent rotor blades at 95% and 100% speeds

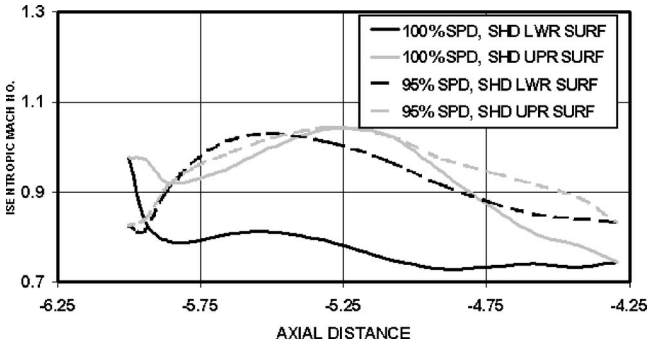

Fig. 26 Isentropic Mach number distribution along the upper and lower surfaces of the part span shroud near the suction surface of the shrouded rotor at 95% and 100% speeds

Nomenclature

C = chord
IMM = radial immersion (0=tip, 1=hub)
LE = leading edge
TE = trailing edge
T_{max} = maximum thickness

References

[1] Wadia, A. R., and James, F., 2001, "F110-GE-129 EFE—Enhanced Power Through Low Risk Derivative Technology," ASME J. Turbomach., **123**, pp. 544–551.

[2] Esgar, G. M., and Sandercock, D. M., 1973, "Some Observed Effects of Part Span Dampers on Rotating Blade Row Performance Near Design Point," NASA Paper No. TM X-2696.

[3] Benser, W. A., Bailey, E. E., and Gelder, T. F., 1975, "Holographic Studies of Shock Waves Within Transonic Fan Rotors," ASME J. Eng. Power, **97**, pp. 75–84.

[4] Reid, L., and Tysl, E. R., 1974, "Performance of a Transonic Rotor With an Aspect Ratio of 6.5," NASA Paper No. TN D-7662.

[5] Lewis, G. W., and Urasek, D. C., 1972, "Comparison of the Effect of Two Damper Sizes on the Performance of a Low Solidity Axial Flow Transonic Compressor Rotor," NASA Paper No. TMX-2536.

[6] Messenger, H. E., and Keenan, M. J., 1974, "Two Stage Fan 2: Data and Performance With Redesigned Second Stage Rotor Uniform and Distorted Inlet Flows," NASA Paper No. CR-134710.

[7] Ware, T. C., Kobayashi, R. J., and Jackson, R. J., 1974, "High Tip Speed Low Loading Transonic Fan Stage. Part 3: Final Report," NASA Paper No. CR-121263.

[8] Koch, C. C., and Smith, L. H., Jr., 1975, "Loss Sources and Magnitudes in Axial-Flow Compressors," ASME Paper No. 75-WA/GT-6.

[9] Roberts, W. B., 1978, "A Design Point Correlation for Losses Due to Part Span Dampers on Transonic Rotors," ASME Paper No. 78-GT-153.

[10] Cumpsty, N. A., and Greitzer, E. M., 2004, "Ideas and Methods of Turbomachinery Aerodynamics: A Historical View," J. Propul. Power, **20**(1), pp. 15–26.

[11] Adkins, G. G., and Smith, L. H., 1982, "Spanwise Mixing in Axial Flow Turbomachines," ASME J. Eng. Power, **104**, pp. 97–110.

[12] Wadia, A. R., and Copenhaver, W. W., 1996, "An Investigation of the Effect of Cascade Area Ratios on Transonic Compressor Performance," ASME J. Turbomach., **118**, pp. 760–770.

[13] Jennions, I. K., and Turner, M. G., 1993, "Three-Dimensional Navier–Stokes Computations of Transonic Flow Using an Explicit Flow Solver and an Implicit K-E Solver," ASME J. Turbomach., **115**, pp. 261–272.

[14] Roberts, W. B., Crouse, J. E., and Sandercock, D. M., 1979, "An Off-Design Correlation of Part Span Damper Losses Through Transonic Axial Fan Rotors," ASME Paper No. 79-GT-6.

Development and Demonstration of a Stability Management System for Gas Turbine Engines

D. Christensen
P. Cantin
D. Gutz
P. N. Szucs
A. R. Wadia

GE Aircraft Engines,
Cincinnati, OH 45215

J. Armor
M. Dhingra
Y. Neumeier
J. V. R. Prasad

Georgia Institute of Technology,
Atlanta, GA 30332

Rig and engine test processes and in-flight operation and safety for modern gas turbine engines can be greatly improved with the development of accurate on-line measurement to gauge the aerodynamic stability level for fans and compressors. This paper describes the development and application of a robust real-time algorithm for gauging fan/compressor aerodynamic stability level using over-the-rotor dynamic pressure sensors. This real-time scheme computes a correlation measure through signal multiplication and integration. The algorithm uses the existing speed signal from the engine control for cycle synchronization. The algorithm is simple and is implemented on a portable computer to facilitate rapid real-time implementation on different experimental platforms as demonstrated both on a full-scale high-speed compressor rig and on an advanced aircraft engine. In the multistage advanced compressor rig test, the compressor was moved toward stall at constant speed by closing a discharge valve. The stability management system was able to detect an impending stall and trigger opening of the valve so as to avoid compressor surge. In the full-scale engine test, the engine was configured with a one-per-revolution distortion screen and transients were run with a significant amount of fuel enrichment to facilitate stall. Test data from a series of continuous rapid transients run in the engine test showed that in all cases, the stability management system was able to detect an impending stall and manipulated the enrichment part of the fuel schedule to provide stall-free transients. [DOI: 10.1115/1.2777176]

Introduction

Rig and engine test processes and in-flight operation and safety for modern gas turbine engines can be greatly improved with the development of accurate on-line measurement to gauge the aerodynamic stability level for fans and compressors. Having a stability management capability during engine development testing would ensure stall-free operation resulting in enhanced engine acceleration/thrust capabilities and significant reductions in development cycle time by avoiding attendant hardware failures due to unexpected surge events in the compression components.

Since reliable early stall warning measurement systems and algorithms are in the experimental phase, modern high stage loading compressors are currently being designed with conservative steady state stall margin requirements that have to include effects due to deterioration, engine control tolerance, engine transient/thermal effects, and inlet distortion. Conservative stall margin requirements result in efficiency penalties that impact the overall engine fuel burn and temperature margins. A robust and reliable stability management system could alleviate the conservative stall margin requirements by active regulation of routine control devices available, such as variable stator and/or fuel schedules and bleed and/or exhaust nozzle actuation.

Active compressor stall control by suppressing the stall inception phenomenon was originally proposed by Epstein et al. [1] in 1986. The stall inception process was investigated further by Camp and Day [2], Hoying et al. [3], Breuer and Servaty [4], and Garnier et al. [5]. Camp and Day proposed two typical stall inceptions: a long-wavelength pattern referred to as "modal oscillation" and a short-wavelength pattern typically of the order of one or two blade passages referred to as "spike." Using numerical experiments, Hoying et al. [3] showed that the short length-scale inception process was linked to the behavior of the blade passage flow field structure, specifically the tip clearance vortex and claimed that a criterion for stall inception for the short length-scale phenomena required the tip vortex trajectory be perpendicular to the axial direction. Tryfonidis et al. [6] investigated prestall behavior of several high-speed compressors and proposed a new technique based on the spectral analysis of the spatial Fourier harmonics of measured case wall pressures. Day et al. [7] reported test results from four high-speed compressors and suggested that an alternative approach to active stall control would be to disregard the physical details of the flow generating the incoming signals and to simply pay attention to deriving a stall risk index from the sum of all the inputs. Hoenen and Arnold [8] proposed a monitoring algorithm for the prediction of unstable compressor operation that involved analyzing the signal patterns of dynamic pressure transducers mounted above the first rotor. As the compressor approached stall, the amplitude of the blade passing frequency was reduced but new frequency peaks occurred and grew until stall. By blanking out the blade passing frequency and its harmonics from the spectra and by means of numerical differentiation, taking absolute values and finally integration, the stability parameter was calculated from the remaining signal.

In addition to the study of prestall behavior, a variety of active control devices has been designed and tested in the last few years. One popular way of compressor operating range extension has been obtained by using air injection for stabilizing compressor flow in the vicinity of the tip gap. The stabilizing effect of air injection can be achieved with constant or modulated flow. Freeman et al. [9] demonstrated that starting a constant air injection at several circumferential positions when an on-line monitoring stability parameter derived from high frequency pressure data exceeded a threshold could eliminate spikes and delay the onset of stall to lower mass flows in a single spool turbojet engine. Spakovszky et al. [10], Weigl et al. [11], and Suder et al. [12] reported usage of modulated air injection to damp out modal dis-

Contributed by the International Gas Turbine Institute of ASME for publication in the JOURNAL OF TURBOMACHINERY. Manuscript received January 2, 2007; final manuscript received January 19, 2007; published online May 2, 2008. Review conducted by David Wisler. Paper presented at the ASME Turbo Expo 2006: Land, Sea and Air (GT2006), Barcelona, Spain, May 8–11, 2006, Paper No. GT2006-90324.

turbances that started growing at certain operating conditions near the stall line to further extend the operating range.

Leinhos et al. [13] used a combined approach of both constant and modulated air injection into the low-pressure compressor (booster) in a twin spool turbofan engine. The turbofan engine studied had a tip critical first booster rotor that exhibited different types of stall inception at different speeds. At low speeds, spikes initiated the instability, while there were some weak indications for a modal-type stall inception in the midspeed regime and strong evidence that a disturbance rotating at low-pressure compressor rotor frequency caused stall in the high-speed region [14]. In their test, the injected air was either taken from an external source or from bleed ports at the high-pressure compressor exit.

Dhingra et al. [15] proposed a new technique for detection of impending stall and surge in axial compressors based on the autocorrelation of pressure signal from a transducer located over the rotor. They analyzed data from both low speed and high-speed compressors and showed that their technique was sensitive to the actual location of the sensor over the rotor. Further, they found the rotor midchord location to be most suitable in the cases they studied.

Tahara et al. [16] proposed a stall-warning index based on pressure signals by high response transducers on the casing wall at the rotor leading edge. Tests conducted on a research compressor with both uniform inlet and with inlet distortion revealed that their stall correlation degradation first appeared at the midchord location and advanced toward the leading edge with a decrease in flow coefficient. The correlation degradation increased monotonically with a decrease in the flow coefficient and had the potential to generate a stall-warning signal sufficiently in advance of spike inception for the stall avoidance actuation to respond in a timely manner.

This paper describes the development of a robust real-time fan/compressor aerodynamic stability management system using over-the-rotor-tip dynamic pressure sensors. The real-time algorithm used for gauging the aerodynamic stability level is based on the method by Dhingra et al. [15]. This real-time scheme computes a correlation measure through signal multiplication and integration. The correlation measure has a value of unity for a purely periodic signal while the correlation of a completely chaotic or random signal would be zero. The algorithm uses the existing speed signal from the engine control for cycle synchronization. The correlation measure is computed for individual pressure transducers over rotor blade tips. The autocorrelation system samples a signal from a pressure sensor (Kulite) at 200 kHz (taken to be greater than ten times that of the blade passage frequency). A window of 72 samples is used to calculate the autocorrelation showing a value of near unity along the compressor operating line and dropping toward zero when the compressor approaches the surge line. When the correlation measure drops below a preset threshold level, the stability management system sends an electrical signal to the engine control system, which in turn takes corrective action using the available control devices to move the engine away from surge.

The algorithm is simple and is implemented on a portable computer to facilitate rapid integration with different experimental platforms such as compressor rigs or fielded gas turbine engines. It is very adaptable for rapid integration into the electronic control system of an engine.

This paper describes successful demonstration of this method on a full-scale high-speed advanced engine compressor rig and on an advanced aircraft engine. In the compressor rig test, the compressor was gradually "pushed" to stall at constant corrected speed by closing the rig discharge valve (throttling to stall). Test data presented show that the autocorrelation scheme is able to sense the impending stall. Further, the closed-loop test data presented show that the scheme is able to trigger corrective actions just prior to stall as the system is throttled toward the stall line. In the full-scale engine tests, rapid transients, often referred to as bodes (named after the pilot who developed this technique), were run. To facilitate stall, the engine was configured with a one-per-revolution distortion screen and the bodes were run with a significant amount of fuel enrichment to intentionally breach the stall line. Once the impeding stall was detected, stall prevention was achieved by deactivating the enrichment part of the fuel schedule resulting in stall-free bodes. Test data from a series of continuous rapid transient (bodes) run in the engine test show consistent performance of the correlation method in all the testing.

Correlation Measure

The approach to the correlation measure was conceived in the School of Aerospace Engineering at the Georgia Institute of Technology [15,17]. Further development and a detailed theoretical discussion of the method are given in a companion paper [18]. For the sake of completeness, we provide in the following section a brief description of the method.

The autocorrelation measures the repeatability of a pressure time trace, as observed by a sensor located over the rotor. The pressure time trace is mostly periodic when the compressor is operating away from the surge line. However, as the boundary of stable operation is approached, occasional loss of periodicity in the pressure signal is observed.

Figures 1 and 2 show pressure time traces obtained on the Georgia Tech axial compressor research rig. The trace corresponding to the compressor operation in a safe regime is presented in Fig. 1. The compressor operates far away from stall and a comparison of the current pressure trace to one shaft period ago shows strong similarity between the two traces. Some differences are to be expected due to phenomena such as natural turbulence and measurement noise. However, as shown in Fig. 2, when the compressor operates close to its stall boundary, the pressure traces vary significantly from one cycle to another.

The developed method quantifies the periodicity using a correlation measure expressed as

$$C(t) = \frac{\sum_{i=t\text{-wnd}}^{t} (P_i P_{i\text{-shaft}})}{\sqrt{\sum_{i=t\text{-wnd}}^{t} P_i^2 \sum_{i=t\text{-wnd}}^{t} P_{i\text{-shaft}}^2}} \tag{1}$$

Although wnd can be any value up to the number of samples in one shaft rotation, the experience to date is that a value, which spans two to four blades, is a good choice. By its very mathematical definition, the correlation measure is bound by 1 from above and −1 from below. When the behavior of the compressor is accounted for, the measure usually stays between 1 and 0, with a value of 1 implying perfect repetition of the pressure trace.

Figure 3 shows the time traces of the correlation measure obtained with the Georgia Tech research compressor operating at constant speed at several different points along the speed line as the compressor is throttled from a low pressure ratio toward stall. The input to the correlation measure was from a dynamic sensor located over the midchord of the rotor. When the compressor was operated with 12.2% stall margin, the timewise fluctuation of the correlation measure (dark blue line) was between 0.9 and 1. As the compressor was operated very close to the stall line, not only did the average value of the correlation measure (red line) decrease but also the fluctuations (randomness) increased suggesting an impending stall in the compressor.

The capability of the correlation measure to identify impending stall was further tested on a multistage low-speed research compressor and on a state-of-the-art multistage high-speed research compressor at GE Aircraft Engine's test facilities [15]. As an example, Fig. 4 shows the variation of the correlation measure obtained on the multistage high-speed compressor. For these tests, a Kulite pressure sensor was flush mounted in Stage 2 over the rotor midchord, which was believed to be ahead of the stalling stage. The compressor was run at constant speed and was loaded (throttled) by closing the discharge valve in the back of the com-

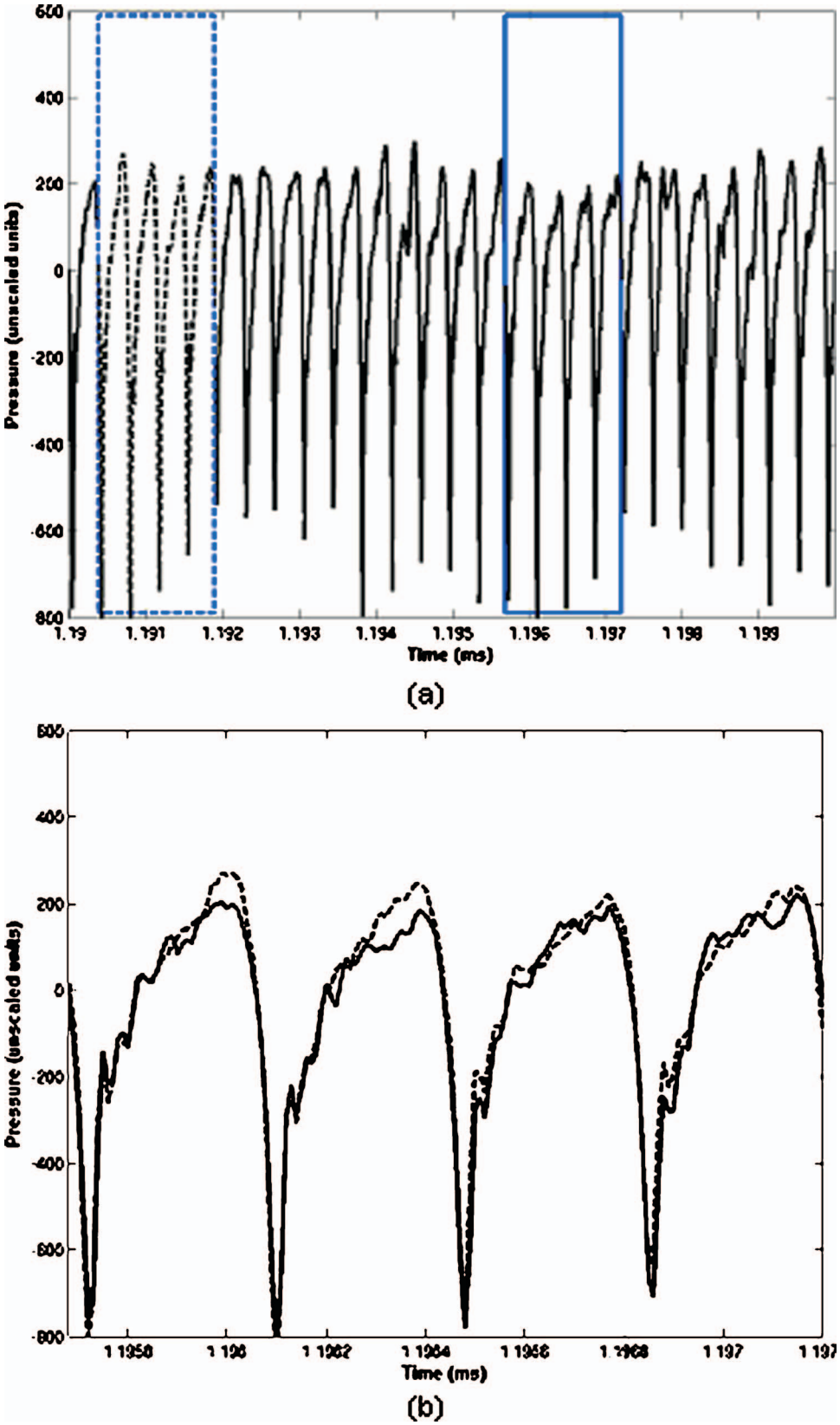

Fig. 1 Illustration of periodicity as observed by over-the-rotor dynamic pressure measurements when the compressor is operating far away from stall

pressor. Figure 4 shows time traces of the correlation measure at 97% rpm. The correlation measure was computed for a window size (wnd) that spanned two blade passages. The blue line is for the case of the compressor operated with a large stall margin of about 21% and the red line is for the case of an operation very close to the stall line. Figure 4 indicates that, with large stall margin, the correlation measure rarely drops below 0.8, whereas for the case when the compressor is on the verge of stall, the

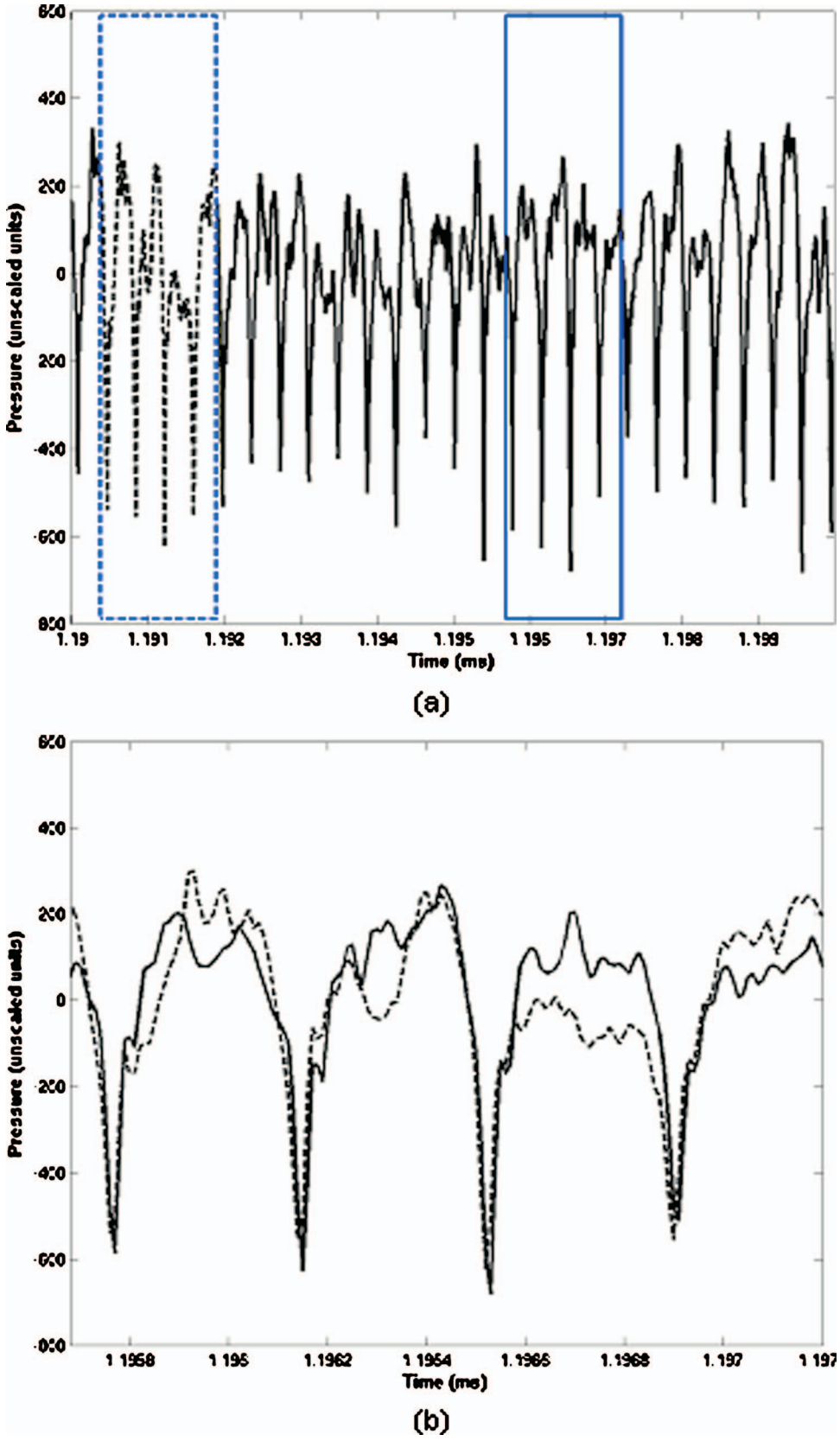

Fig. 2 Illustration of loss of periodicity when the compressor is operating close to stall

correlation measure dips well below 0.3.

After having established the capability of the correlation measure approach in detecting an impending stall event, the remainder of the paper deals with the applications of the correlation measure scheme for stall avoidance in a full-scale high-speed compressor rig test and in an advanced aircraft engine test.

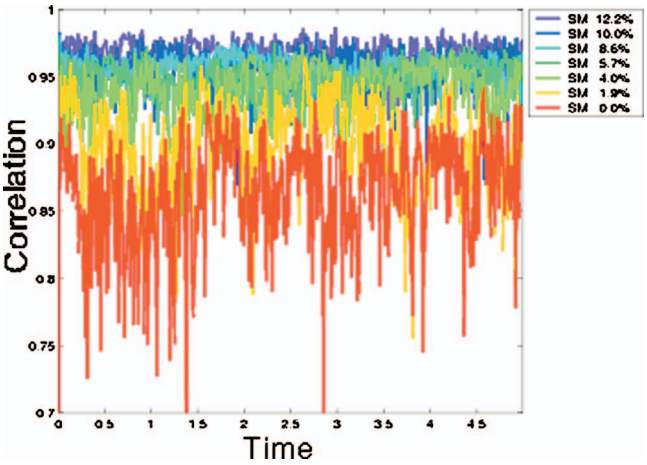

Fig. 3 Time variation of the correlation measure at various stall margins obtained with the Georgia Tech compressor along a constant speed line

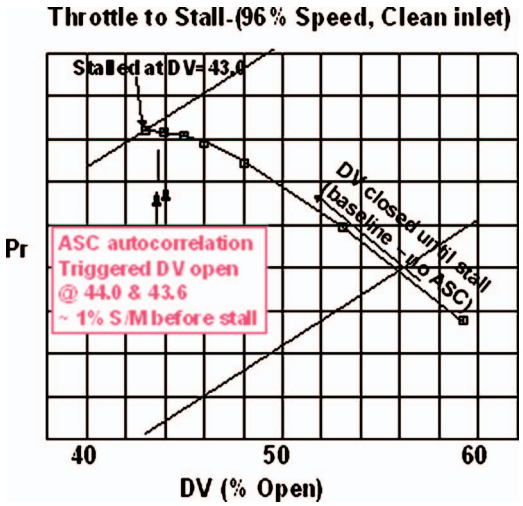

Fig. 5 Compressor speed line at 96% corrected speed

Full-Scale High-Speed Compressor Rig Application

The autocorrelation scheme was applied in closed loop for stall prevention in a full-scale six-stage high-speed compressor rig test. This compressor is different from the research compressor discussed in the previous section. The compressor has a row of inlet guide vanes and two variable stator rows. Because of hardware limitations, only the second stage was equipped with over the rotor flush-mounted sensor that was used as an input for the correlation measure.

As before, the autocorrelation system sampled a signal from the dynamic pressure sensor (Kulite) at 200 kHz. This relatively high value of sampling frequency ensures that the data are sampled at a rate at least ten times than that of the blade passage frequency. A window of 72 samples was used to calculate the autocorrelation.

In these tests, the compressor pressure ratio was increased at constant speed (throttling to stall) by closing the rig discharge valve (DV). At a preset threshold level of the autocorrelation, the stability management system sent an electrical signal to the rig control, which in turn took corrective action by opening the DV to move the compressor away from surge.

Figure 5 shows the increase in compressor pressure ratio (throttling) as the rig DV is closed at 96% corrected speed. Shown in this figure are the points at which the closed loop activated the DV at a stall margin of roughly 1% in two different runs. Figure 6 shows the correlation measure signal when the DV is opened to a condition away from stall. It shows that the correlation measure remains high with occasional drop no lower than 0.7. Figure 7 shows the pressure signal and the corresponding autocorrelation with time as the compressor is throttled transiently from an already close to stall condition into stall. In the test results presented in Fig. 7, an alarm was issued when the correlation measure dropped below 0.2, but no action (open loop) was taken to avoid the surge. Figure 7 shows progressive dips in the correlation measure as the compressor slowly approaches the stall line. Figure 8 shows the traces of the dynamic pressure and the corresponding correlation measure in the stall prevention test. In this test, the alarm was triggered when the correlation measure dropped below

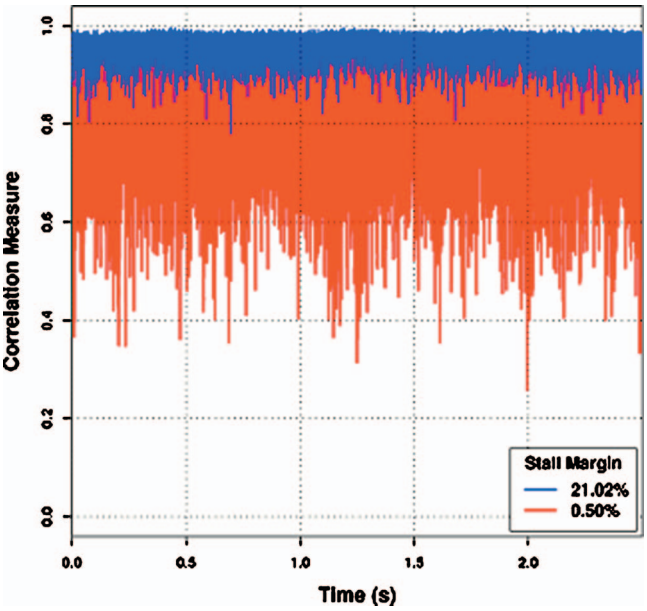

Fig. 4 Correlation measures obtained on a multistage high-speed compressor at 97% rpm corresponding to stall margins of 21% and 0.5%

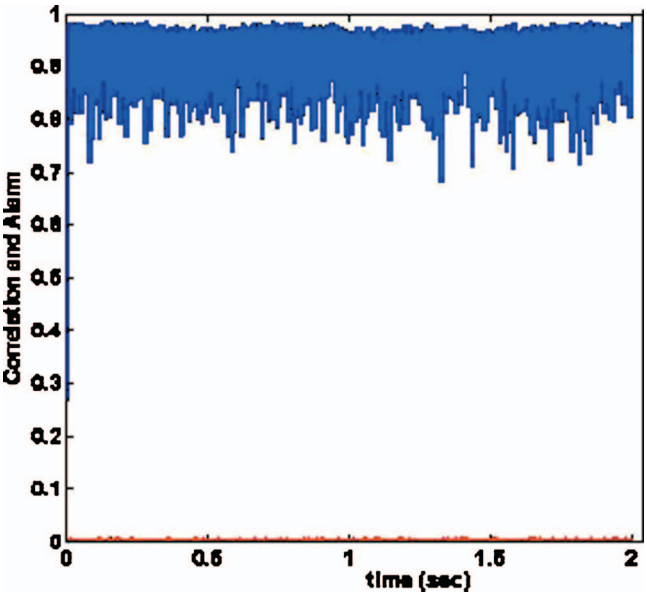

Fig. 6 Correlation measure shown in blue, and alarm shown in red (constantly at 0) at an operating condition away from stall

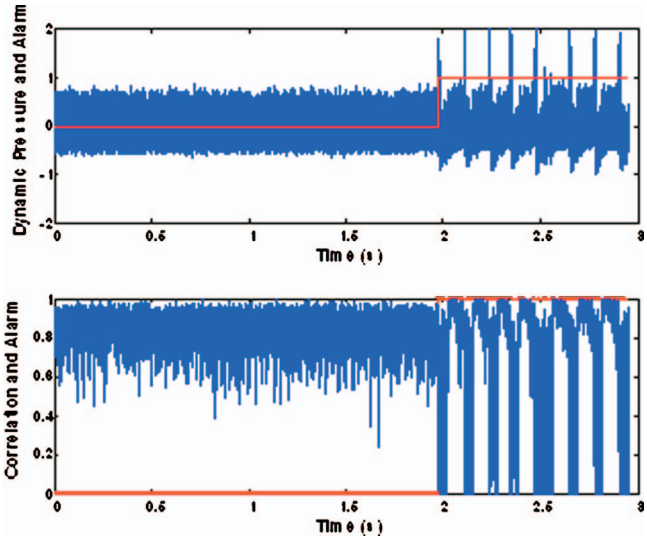

Fig. 7 Distribution of Rotor 2 midchord Kulite signal (dynamic pressure) and correlation measure with time as the compressor is throttled to stall

0.2 with the DV at 43.6%, see Fig. 5. Figure 8 clearly indicates that once the DV is activated by the alarm signal, the correlation measure goes up accordingly.

While not shown in detail herein, similar successful results were obtained on the compressor rig during deceleration from high speed to idle with the variable stators held fixed at their starting speed nominal position.

The successful demonstration of the capability of the correlation measure in detecting an impending stall event would suggest its usefulness in routine engine testing. One should appreciate the wear and tear that could be avoided in engine rig tests by establishing stability limits using the correlation measure in place of actual hard stalls. Also, controller manipulation of the DV in collaboration with the correlation measure could well be employed to simulate stall-free engine-type transient migration of the operating line in a component rig test.

Engine Application

Rapid transients, often referred to as bodes, are frequently run with enriched fuel flow in full-scale engine tests to demonstrate excess stability margins during engine certification or qualification tests. This type of testing is used herein to demonstrate the feasibility of the stability management system.

The compressor in the engine has seven stages and is different from the rig application discussed previously. It was instrumented with over-the-rotor tip Kulites at the leading edges of all the rotors and midchord Kulites over Rotors 2, 3, and 6. Unfortunately, during the initial engine tests with ram inlet conditions, all the rotor tip midchord Kulites as well as some of the rotor leading edge Kulites malfunctioned. Based on the past results, it was expected that the leading edge Kulites could not provide adequate signal [15]. Moreover, they were mounted on a waveguide cavity leading to significant attenuation of the signal in the blade passing frequency. In spite of this limitation, as the results presented here will demonstrate, advance warning could still be issued by the correlation measure. An example is shown in Fig. 9. It shows clear dips in the correlation measure 70 ms before stall and a final drop of the correlation measure below 0.2 threshold about 30 ms ahead of the stall. It is important to note that because of the "low quality" signal, excessive filtering of the correlation measure was required, around 50 Hz low pass, which further limited the advance warning. In view of the expected degradation in the performance of the correlation measure, a second measure for stall was constructed. It was based on the sharp increase of the pressure behind the inlet guide wave (IGV) at the onset of the stall, as presented in Fig. 10. A limited band derivative was performed on the signal from the IGV sensor and when the derivative level exceeded a preselected threshold, an alarm signal was generated. The alarms from the correlation measure and the IGV signal derivative were combined into an overall alarm. The correlation measure based alarm was given a value of 1 and the IGV signal derivative alarm was given a value of 2. Thus, an overall alarm level of 0 means no

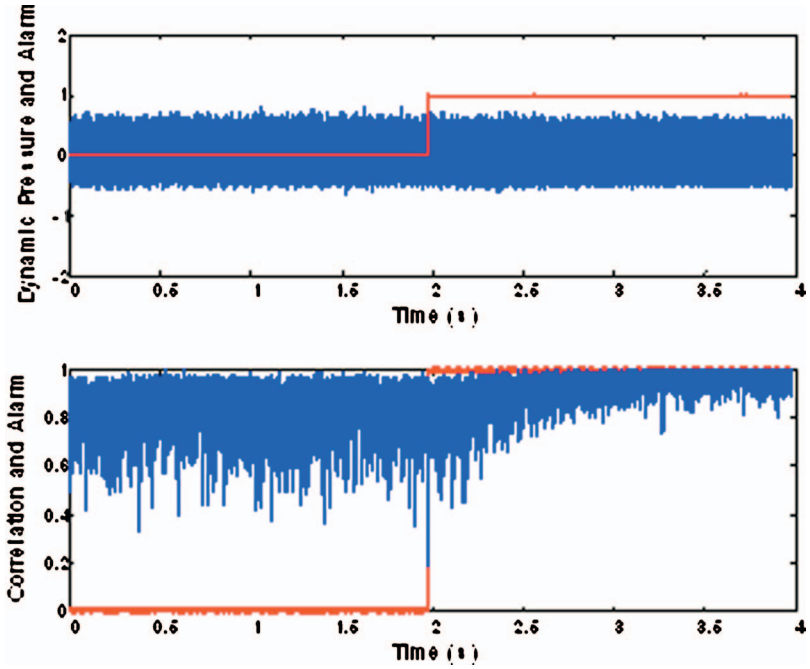

Fig. 8 Pressure and correlation measure behavior in the stall prevention rig test; the alarm was triggered at DV of 43.6

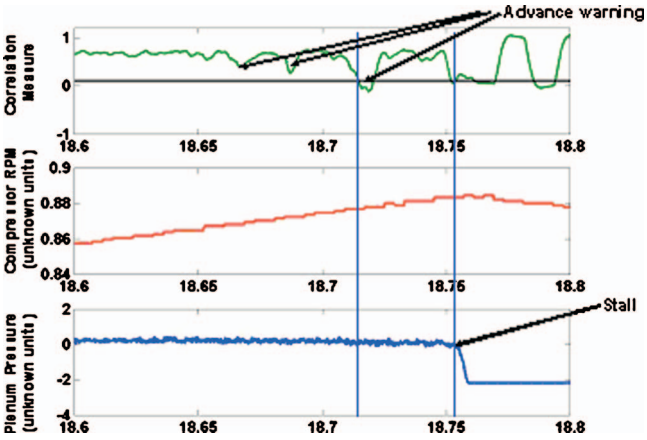

Fig. 9 Open loop event showing dips in the correlation measure 70 ms before the stall event

alarm, a level of 1 means only the correlation measure captured the alarm, a level of 2 means only the IGV signal derivative captured the alarm, and a level of 3 means both the correlation measure and the IGV signal derivative captured the alarms. Any level above zero was set to trigger the active stall control.

A block diagram illustrating the overall system operation is shown in Fig. 11. The alarm level delivered a binary on/off logic to the engine full authority digital electronic control (FADEC) with the "on" action logic triggered by the overall alarm at 1, 2, or 3.

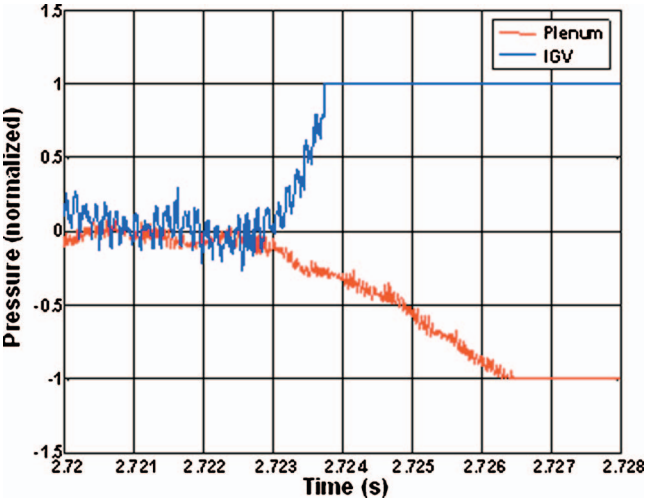

Fig. 10 Traces of plenum and behind IGV dynamic pressure just before and during a stall event; the straight horizontal lines are due to saturation of the pressure sensors

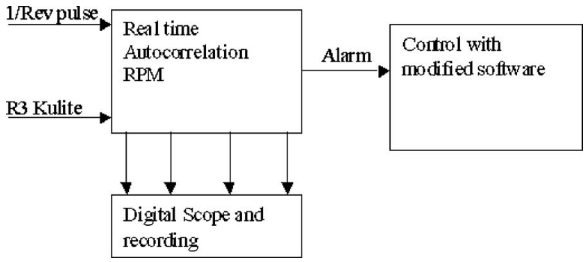

Fig. 11 Schematic of the stability management system on the engine

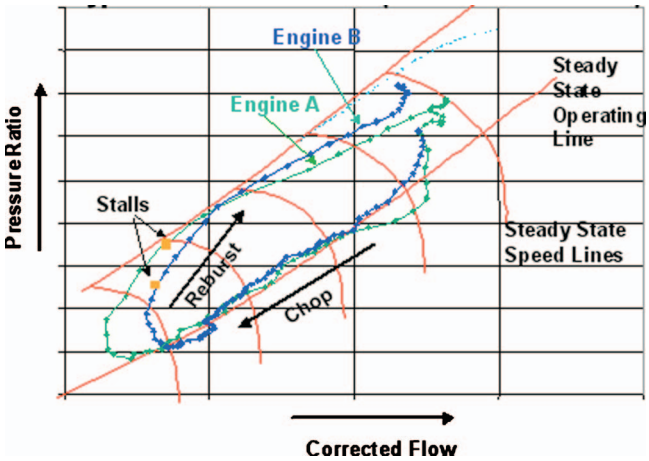

Fig. 12 Typical rapid engine transients with enriched fuel flow illustrating the migration of the compressor operating line toward stall

The engine was configured with a one-per-revolution inlet distortion screen and transients were run with a significant amount of fuel enrichment to intentionally force the engine to stall. A typical result from an engine transient is presented in Fig. 12. The transient begins with a quick reduction in speed from high power operation to idle with the engine operator pulling the throttle back, commonly referred to as a "chop," followed by an immediate increase in speed by pushing the throttle forward from idle to high power, commonly referred to as a "reburst." A continuous sequence of a chop and a reburst is sometimes referred to as a "bode."

The steady state speed lines, operating line, and stall line are shown in red in Fig. 12. Typical transient paths the compressor takes for two engines (A and B) are presented in blue and green in the same figure. The path is closely related to the thermal state of the engine during the chop and the reburst. The engine operating line is seen to follow the steady state operating line during the chop followed by a significant increase in pressure ratio at the turnaround point as the engine begins to accelerate. Recall that in addition to thermal effects, the engine runs with inlet distortion, which has lowered the stall line to some extent and the rapid increase in fuel (enrichment) backpressures the compressor further, resulting in engine stalls close to the turnaround speed, as illustrated in Fig. 12. The difference in the transient paths taken by the compressors in Engines A and B during bodes can be attributed to engine-to-engine variation and measurement accuracies.

Figure 13 shows an example of a stall that occurred during the reburst on a bode sequence. For comparison, the correlation measure computed from the remaining useful sensors from Stages 3 and 6 is shown in Fig. 13. The stall is manifested by a short duration of about 50 ms during which the rpm drops before picking up again. Note that both Stages 3 and 6 leading edge sensors provide similar trends in correlation measure, suggesting that with the remaining useful sensors, the correlation measure, albeit attenuated and greatly delayed, picks up the impending stall nearly simultaneously. However, as evident from Fig. 13, the correlation measure from stage 3 provided a slightly better lead time compared to that from Stage 6, and hence, the stage 3 sensor was used in the closed-loop experiments.

Figure 14 shows a record capturing eight bodes. There was approximately a 12 s span for each bode. The compressor went through stalls during the first two cycles, which were evident by loud booms, followed by stall-free operation during the remaining cycles. Noticeably, the alarm went off only in the first two cycles. The alarm level was 1 in the first cycle and it jumped all the way to 3 during the second cycle. Moreover, an expanded view of the second cycle shown in Fig. 15 revealed that the alarm jumped to

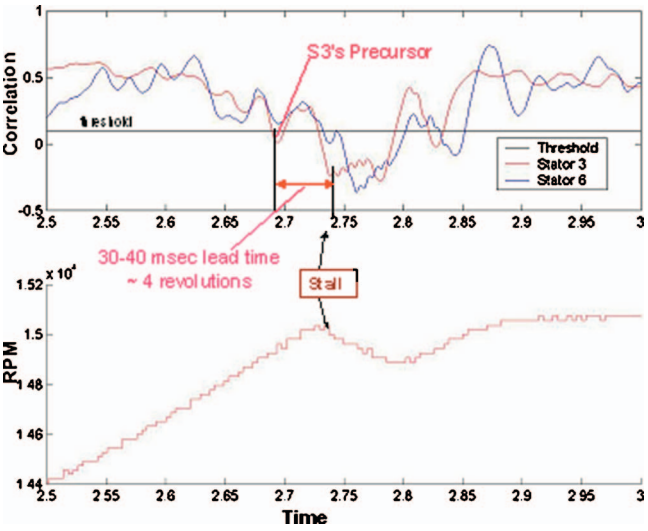

Fig. 13 Autocorrelation from sensors on Stages 3 and 6 and rpm during a blip encountered in open loop bode sequence

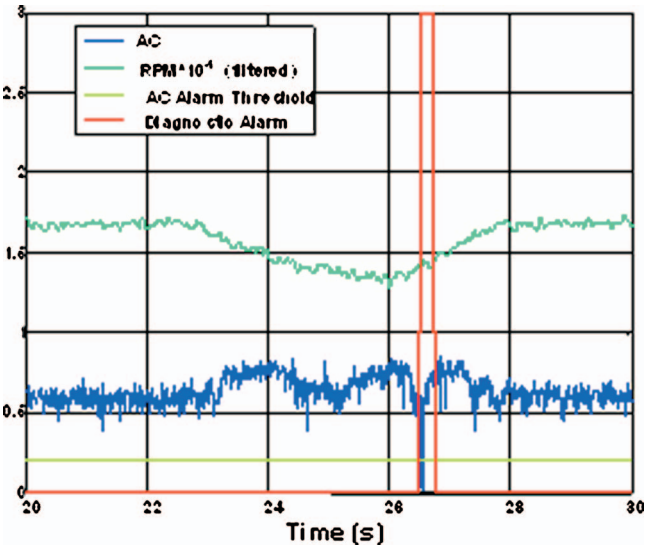

Fig. 15 Expanded view of second cycle of open loop bodes of Fig. 14.

1 (triggered by the correlation measure crossing the threshold) first before it jumped to 3 (triggered by the correlation measure as well as the derivative of the IGV signal crossing their individual thresholds) indicating that the correlation measure provided an indication of the impending stall event first. Note also that the correlation measure for Cycles 7 and 8 dipped very close to the threshold without crossing it. Hence, there was no alarm from the correlation measure. More significantly, there was no alarm from the derivative of the IGV signal either. Due to the low resolution of the data, the short drop in rpm cannot be clearly seen in Fig. 15.

The engine was run next with the stability management system in the "closed-loop" control mode, generating a 10 V signal when the alarm level went to 1, 2, or 3. The control software was programed to accept the 10 V stall alarm trigger and respond by deactivating (cutback) the enrichment part of the acceleration fuel schedule during the reburst.

The bode sequence (similar to the one shown in Fig. 14) was repeated with the closed loop and resulted in two cycles with alarms but no audible sounds of blips. Figure 16 shows the expanded timewise distribution of compressor corrected speed (rpm), compressor exit static pressure (PS3), and fuel flow (the electric current of the torque motor driving the metering valve of fuel flow) during the first bode on the engine where the compressor without the stability management system previously went through a stall (blip in rpm) event. The time scale shown in the figure is ten times than that of the actual value in seconds. In Fig. 16, the rpm is shown in blue, Stage 3 leading edge pressure sensor signal in pink, and the fuel flow in yellow.

In the test, the operator pulled the throttle back (chop ~3 s) reducing the fuel flow (initial spikedown to idle fuel flow shown in yellow) to the engine at 63 units of time that started the drop in PS3 followed by the drop in compressor speed (rpm) soon thereafter. The throttle was pushed forward again (reburst ~1.5 s) to reach high power at 100 units of time shown by the spikeup in fuel flow followed shortly by an increase in PS3 and slightly later by compressor rpm. This time lag between the spikeup in fuel

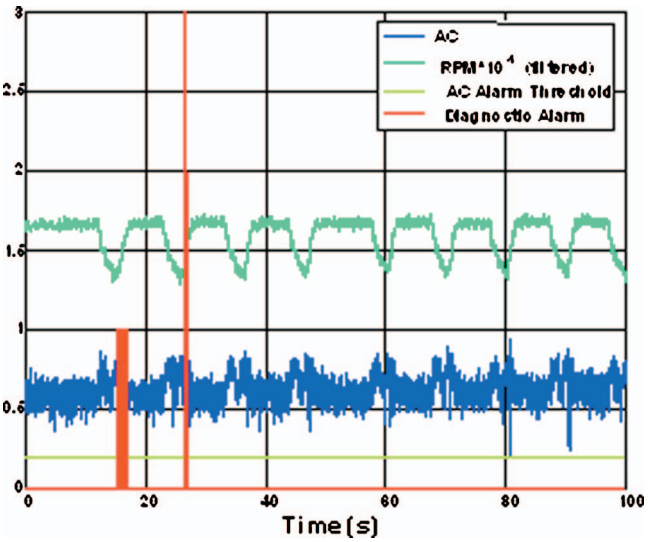

Fig. 14 Engine transients showing rpm in green, autocorrelation in blue, and alarm signals from the correlation measure and IGV in red; the alarm threshold in light green is set at 0.2

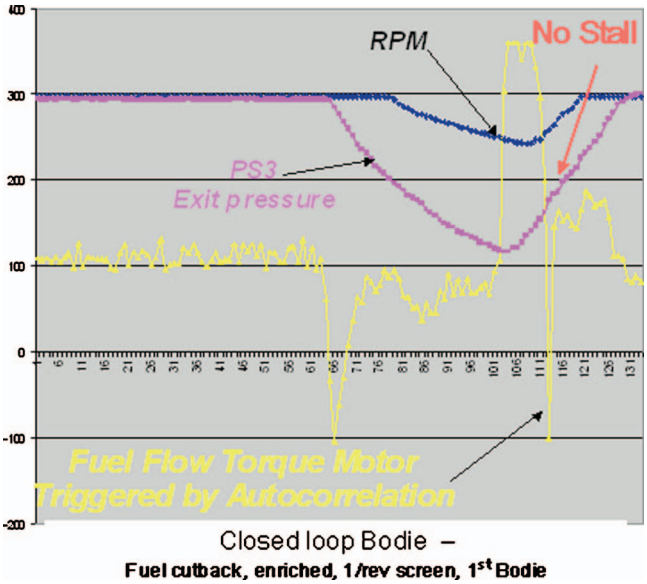

Fig. 16 Stability management used to cut back the enrichment part of the fuel schedule during acceleration and avoid stall during engine transients

flow and increase in compressor rpm can be attributed to the inertia of the compressor disk. At approximately 108 units in time, the autocorrelation crossed the threshold and sent an alarm to the control to cut back the acceleration fuel flow to the engine, as illustrated by the spikedown in fuel flow in Fig. 16. The engine accelerated (with the deactivated fuel flow enrichment as commanded by the control) through this critical region stall free when previously there was a stall event at this juncture. The fuel flow was restored back to its original enriched acceleration schedule by the control as soon as the correlation measure had recovered to a level above the threshold resulting in stall-free engine operation in this local region.

The transient bode demonstration was repeated again with and without the stability management system. The compressor did not go through any stall event with the system in place. The correlation method performed consistently in all the testing. In all cases, (a) the impending stall was detected by the correlation measure, and (b) when an impending stall was detected by the correlation method, the system triggered/deactivated the enrichment part of the fuel schedule resulting in stall-free transients.

Concluding Remarks

This paper presents the application of a robust real-time algorithm for gauging the fan/compressor aerodynamic stability level using over-the-rotor dynamic pressure sensors on a variety of systems suggesting that the method is "general" enough and could be used in practical systems. However, because of the nature of these tests, only one stage, if at all, was equipped with an over the rotor sensor. Thus, comparison of the behavior of the correlation measure for various stages and the dependence of warning time on individual stages could not be resolved. This aspect needs to be addressed in future.

The results obtained in this study suggest that the existing control software with only a slight modification, and more importantly, existing hardware such as the fuel control system, can be employed along with the correlation method to provide effective stall management. From the findings of this study, it is suggested that the stall management system can potentially be used in routine engine testing where it is desirable to establish the stability limits of an engine without driving it to hard stalls.

The operational benefits that a stall avoidance system can offer to military engines that are subjected to severe transient are easily grasped. However, it should be noted that such a system offers benefits to the design of commercial engines as well. A key goal in the compressor design of a commercial engine is that the line of maximum efficiency will have adequate stall margin. In order to achieve this goal, the designer often pays with excess solidity (e.g., number of blades) and consequently extra weight. An active stall management system, which facilitates safe and optimal operations, can bring upon the same results without the weight penalty.

Acknowledgment

The authors would like to thank GE for giving the permission to publish this paper.

Nomenclature

ASC = active stall control
$C(t)$ = correlation measure
DV = discharge valve (used to throttle the compressor)
i = index
P = pressure signal
P_r = pressure ratio
t = current sample time
rpm = Compressor shaft speed (revolutions per minute)
shaft = shaft time period
wnd = correlation window size

References

[1] Epstein, A. H., Efowcs Williams, J. E., and Greitzer, E. M., 1989, "Active Suppression of Aerodynamic Instabilities in Turbomachines," J. Propul. Power, **5**(2), pp. 204–211.
[2] Camp, T. R., and Day, I. J., 1998, "A Study of Spike and Modal Stall Phenomena in a Low-Speed Axial Compressor," ASME J. Turbomach., **120**, pp. 393–401.
[3] Hoying, D. A., Tan, C. S., and Grietzer, E. M., 1998, "Role of Blade Passage Flow Structures in Axial Compressor Rotating Stall Inception," ASME Paper No. 98-GT-588.
[4] Breuer, Th., and Servaty, S., 1996, "Stall Inception and Surge in High Speed Compressors," Paper No. AGARD CP-571 26/1-17.
[5] Garnier, V. H., Epstein, A. H., and Grietzer, E. M., 1991, "Rotating Waves as a Stall Inception Indication in Axial Compressors," ASME J. Turbomach., **113**, pp. 290–301.
[6] Tryfonidis, M., Etchevers, D., Paduano, J. D., Epstein, A. H., and Hendicks, G. J., 1995, "Prestall Behavior of Several High Speed Compressors," ASME J. Turbomach., **117**, pp. 62–80.
[7] Day, I., Breuer, T., Escuret, J., Cherrett, M., and Wilson, A., 1999, "Stall Inception and the Prospects for Active Control in Four High Speed Compressors," ASME J. Turbomach., **121**, pp. 18–27.
[8] Hoenen, H., and Arnold, T., 2003, "Development of a Surge Prediction System for Multi Stage Axial Compressors," 2003, IGTC2003 Tokyo Paper No. TS-040.
[9] Freeman, C., Wilson, A., Day, I., and Swinbanks, M., 1998, "Experiments in Active Control of Stall on an Aero engine Gas Turbine," ASME J. Turbomach., **120**, pp. 637–647.
[10] Spakovszky, Z., Weigl, H., Paduano, J., van Schalkwyk, C., Suder, K., and Bright, M., 1999, "Rotating Stall Control in a High-Speed Stage With Inlet Distortion," ASME J. Turbomach., **121**, pp. 510–524.
[11] Weigl, H., Paduano, J., Frechette, A., Epstein, A., Greitzer, E., Bright, M., and Strazisar, A., 1998, "Active Stabilization of Rotating Stall in a Transonic Single Stage Axial Compressor," ASME J. Turbomach., **120**, pp. 625–636.
[12] Suder, K., Hathaway, M., Thorp, S., Strazisar, A., and Bright, M., 2001, "Compressor Stability Enhancement Using Discrete Tip Injection," ASME J. Turbomach., **123**, pp. 14–23.
[13] Leinhos, D., Scheidler, S., Fottner, L., Grauer, F., Hermann, J., Mettenleiter, M., and Orthmann, A., 2002, "Experiments in Active Stall Control of a Twin-Spool Turbofan Engine," ASME Paper No. 2002-GT-30002.
[14] Hoss, B., Leinhos, D., and Fottner, L., 2000, "Stall Inception in the Compressor System of a Turbofan Engine," ASME J. Turbomach., **122**, pp. 32–44.
[15] Dhingra, M., Neumeier, Y., Prasad, J. V. R., and Shin, H. W., 2003, "Stall and Surge Precursors in Axial Compressors," presented at 39th AIAA/ASME/SAE/ASEE Joint Propulsion Conference and Exhibit, Huntsville, AL.
[16] Tahara, N., Kurosaki, M., Ohta, Y., Outa, E., Nakakita, T., and Tsurumi, Y., 2004, "Early Stall Warning Technique for Axial Flow Compressors," ASME Paper No. 2004-GT-53292.
[17] Dhingra, M., Armor, J., Neumeier, Y., and Prasad, J. V. R., 2005, "Compressor Surge: A Limit Detection and Avoidance Problem," presented at AIAA Guidance, Navigation, and Control Conference and Exhibit, San Francisco, CA.
[18] Dhingra, M., Neumeier, Y., Prasad, J. V. R., Breeze-Stringfellow, A., Shin, H.-W., and Szucs, P. N., 2006, "A Stochastic Model for a Compressor Stability Measure," ASME Paper No. GT2006-91182.

Rapid Prototyping Design Optimization Using Flow Sculpting

W. N. Dawes
CFD Laboratory,
Department of Engineering,
University of Cambridge,
Cambridge CB2 1PZ, UK

Computational fluid dynamics has become a mature art form and its use in turbomachinery design has become commonplace. Simple blade-blade simulations run at near interactive rates but anything involving complex geometry—such as turbine cooling—turns around too slowly to participate in realistic design cycles; this is mostly due to the difficulty of modifying and meshing the geometry. Simulations for complex geometries are run afterwards as a check—rather than at the critical conceptual design phase. There is a clear opportunity for some sort of rapid prototyping but fully 3D simulation to remedy this. This paper reports work exploring the relationship between solid modeling, mesh generating, and flow solving in the general context of design optimization but with the emphasis on rapid prototyping. In particular, the work is interested in the opportunities derived by tightly integrating these traditionally separate activities together within one piece of software. The near term aim is to ask the question: how might a truly virtual, rapid prototyping design system, with a tactile response such as sculpting in clay, be constructed? This paper reports the building blocks supporting that ambition.
[DOI: 10.1115/1.2777178]

1 Introduction

Computational fluid dynamics (CFD) has become a mature art form and its use in turbomachinery design has become commonplace. However, there is a real spectrum of usage in practice: For simple blade to blade flows, steady Reynolds-averaged Navier–Stokes (RANS) simulations are essentially interactive and fast enough for use within automatic design optimization loops. Whereas for complex geometries, the relative slowness of the CAD-to-mesh-to-solver process means that simulations cannot be performed fast enough to fit within realistic design cycle times. For something like turbine cooling design, full-authority, full-geometric fidelity CFD simulations are used to check a design rather than guide and scope out a whole series of designs at a more conceptual level. This conceptual design continues to be performed with lower order modeling, correlations, etc., and clearly limits the performance the designer can achieve. Some sort of rapid prototyping system capable of utilizing fully 3D simulations would greatly help design optimization.

An orthodox "CFD Process" imports geometry from CAD (IGES, STEP, STL, etc.), creates and heals a watertight surface, creates a surface mesh, creates a volume mesh, runs a flow solver (possibly with mesh adaption), and then permits postprocessing. This "process" is usually assembled from a combination of "best-in-class" pieces of software—some commercial, off the shelf, and some custom written. However, it is a big challenge to make this a robust, guaranteed, and fully automated procedure. A number of bottlenecks exist, which must be overcome in various ways (see, for example, Dawes et al. [1]) otherwise the process can break down without human interaction (which can be very slow and costly and divert human time away from the higher level design task). Critically also, only the flow solver will run in parallel—all the other elements of the process represent a serial bottleneck.

Design optimization is then often viewed as a kind of software wrapper enclosing the selected CFD process and—provided the process does not break—automatically driving it to produce better design for selected figures of merit. At the core of this activity is changing the geometry since if you cannot change the geometry, you cannot change the flow. More importantly—and less well recognized—the flexibility and generality with which the geometry can be changed is the critical enabling factor in our ability to properly explore design space and change the flow for the better (see, for example, Samareh [2,3] and Dawes et al. [4]).

Roughly speaking, design optimization operates on three classes of geometry description. The first, and most pragmatic, simply intercepts and edits whatever basic ASCII datasets are in routine use to describe a turbomachinery blade profile or wing section—or the parametrized model which writes that dataset (see for example Harvey, et al. [5,6]). The second class assumes a "boundary representation" (BREP) geometry model and edits the boundary patches either by directly modifying control points or solving surrogate equations Bloor et al. (1990) or using techniques such as "free-form deformation" (see Lamousin and Waggenspack [7] and Kellar [8,9]). The third class acts directly on a solid model description—obviously a parametrized one—as described by Haimes and Follen [10] or Sederberg and Barry [11], for example.

It seems clear that from the point of view of the integrity of the process, it is better to have control as close as possible to the solid model—and this is the philosophy adopted in this paper. However, the generality and usefulness of the design process will be fatally compromised firstly if the CFD process cannot operate automatically (for example, if manual intervention is needed to import the edited CAD model into the mesh generator) and/or secondly if the CAD modeling does not permit a sufficiently automated or general or flexible way to edit the model, for example, to permit topology (genus) change in the model.

So, is there an alternative? This paper describes the building blocks for a quite different approach with its heart the integration of the solid modeling directly with the mesh generation and the flow solution. The following sections will first summarize the key features of solid modeling and then a relatively new field of 3D computer graphics—interactive volume sculpting—will be reviewed. Then the current research into an integrated flow solver/geometry engine will be presented and then some example applications will be described.

Contributed by the International Gas Turbine Institute of ASME for publication in the JOURNAL OF TURBOMACHINERY. Manuscript received January 15, 2007; final manuscript received January 16, 2007. published online May 5, 2008. Review conducted by David Wisler. Paper presented at the ASME Turbo Expo 2005: Land, Sea and Air (GT2005), 2005, Reno, NV, June 6–9, 2005, Paper No. GT2005-68239.

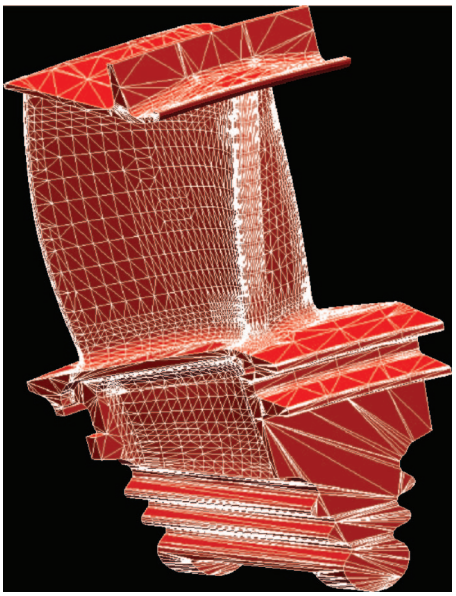

Fig. 1 Typical tessellated surface extracted by CAPRI (Haimes and Follen [10]) from a Parasolid solid model of a turbine

2 Solid Modeling Basics

It will be helpful here to review the principles of solid modeling. There are three basic types of solid model.

Constructive solid geometry (CSG) is based on the definition and manipulation of simple analytical bodies (cube, sphere, ellipse, etc.), which can be scaled, translated, and rotated. The body primitives are then combined via Boolean logic together with inside/outside conventions to enable quite complex solid models to be produced. The advantages are simplicity and compactness of storage; the disadvantages are difficulty in representing the more free-form sorts of shapes encountered in aerodynamics.

BREP solid modeling is based on combining patches, edges, and topology bindings into a "watertight" solid. Typically nonuniform rational B-splines (NURBS) patches are used and complex, multiply curved surfaces can be stored very economically (the geometry needs only to be reconstructed for viewing or manipulation). The big disadvantages are in producing—and maintaining under manipulation—the watertight bindings and supporting topology (genus) change.

Spatial occupancy solid models consist of Cartesian hexahedral cells (perhaps stored in an octree data structure for efficiency) with cells occupied, or vacant, or cut (with perhaps some local surface shape data stored). The big advantages are simplicity and generality—topology change is trivially supported—but the disadvantage is the elevated storage overhead compared to BREP and CSG.

Commercial CAD uses mostly BREP with CSG constructs where possible coupled with octreelike data structures if needed, to make searching operations efficient.

The kernel vendors license access (for example, UG sits on Parasolid) and direct read of the kernel can interrogate the solid model to return data such as curvature, inside/outside, etc. Of particular interest is access to the tessellation of the surface of the solid model, which is used to render it. We use CAPRI (Haimes et al. [10]), which combines kernel queries with visualization and is implemented for UG (Parasolid), PRO/E (Pro/Toolkit), and CATIA. However, the tessellations themselves are not directly suitable as a flow mesh and thus must be used as a driver for a more flow oriented mesher (see Fig. 1). In a more general sense, tessellated surfaces—especially those held in STL or VRML formats—have become the de facto standard geometry representation.

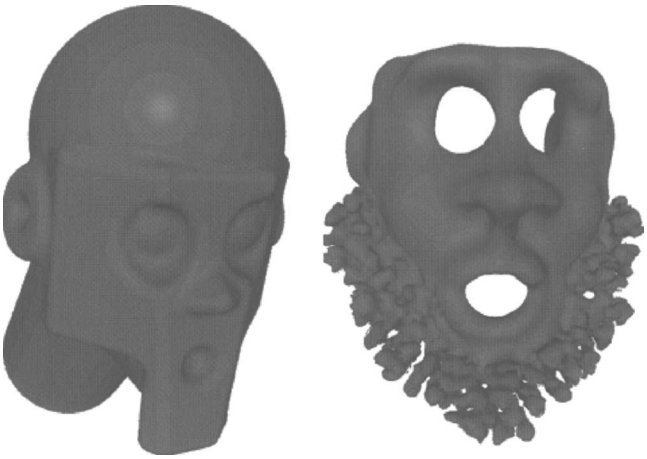

Fig. 2 Basic head (left) sculpted simply via CSG Boolean operations enacted via a spatial occupancy solid model of tool and workpiece; the head right results from much more complex tool/workpiece interactions (from Baerentzen [16])

3 Topology Editing: Interactive Design Via Sculpting

Imagine having a turbine blade with both external and internal cooling geometries fully meshed and mounted within a virtual reality wind tunnel with the current flow solution displayed and then adding extra film cooling holes or modifying the internal passages—perhaps with a VR glove—and seeing the predicted flow field respond in real time.

It is difficult to imagine achieving these levels of generality with a conventional CFD process linked to conventional CAD modeling. A modern trend is to combine the basic elements of the CFD process together in more coupled ways to address the needs of the designer. Flow solvers are already available as plug-ins into CAD packages (and vice versa); software is available based on free-form deformation to morph meshes, but subject to mesh distortion limits and without topological change. However, this trend is limited by its absolute lack of inherent parallelism—the key to exploiting CFD in design on personal computer (PC) clusters is to avoid serial bottlenecks at any stage in the process.

However, a very interesting recent development in the field of computer graphics has been real-time sculpting in virtual reality—first proposed by Galyean and Hughes [12]. This draws heavily on the rapidly expanding field of 3D volume graphics, which is driven particularly by medical imaging (see, for example, Jones and Satherley [13]). The basic principles are very simple: space is divided up into a 3D mesh of cells, "voxels;" a work-piece and a tool are defined and manipulated as basic spatial occupancy solid models; interactions between the tool and the workpiece result in modified geometry; these interactions can be via adding or removing of material (basic CSG type operations) or spraying of new material onto an existing solid or anything else that can be devised. The whole procedure is similar in concept to sculpting with clay, and quite complex and sophisticated results can be produced (see, for example, Bremer et al. [14]). Of course, the surface of the emerging solid body must be managed carefully. There are two main approaches: One is based on the classic graphics rendering algorithm called "marching cubes," which simply aims to remove aliasing; (see Perng et al. [15]; a more sophisticated approach is based on level set techniques (for example, Baerentzen [16] and Fig. 2) this is capable of faithfully representing multiply curved surfaces.

4 Distance Fields and Level Sets

When a solid model is presented using spatial occupancy each cell—or voxel—can have associated with it the signed distance to the nearest point on the body (or bodies). This is known as a

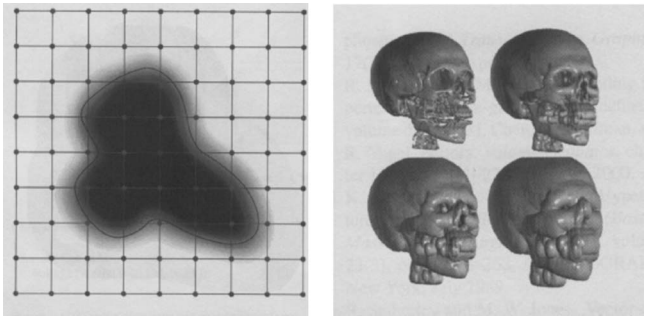

Fig. 3 Scanned spatial density variation (black is high density, white is low) stored on a Cartesian grid; a "voxel raster" (left), which can be rendered (right) by extracting various isosurfaces (Jones and Satherley [13])

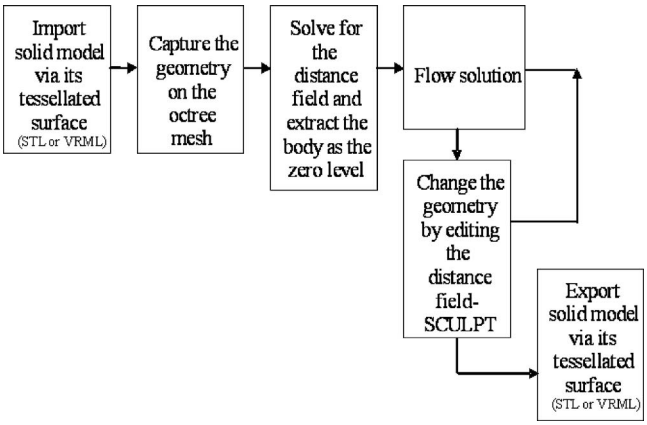

Fig. 4 The basic flow of activities within BOXER

"distance field" or "level set." This concept arises quite naturally, for example, in medical imaging applications as illustrated in Fig. 3, which shows various isosurfaces extracted from a scanned density variation stored on a Cartesian grid (a "voxel raster"). A distance field is created, stored, and managed in just the same way. Boundaries are represented as the zero isosurface of the level set. *Sculpting*, as outlined above, simply means editing the distance field. Topological changes are trivially supported since the underlying solid model is based on spatial occupancy rather than conventional BREP. Typical solid modeling operations from CSG are Boolean sums of the form

$$C = A \cup B \tag{1}$$

(which forms the union of solid A with B) are replicated in distance fields via simple and inexpensive voxelwise logic

$$d_C = \min(d_A, d_B) \tag{2}$$

with material added or removed simply by selecting the inside/outside sign on the distance itself.

The level set method (see, for example, Sethian (1987), Osher and Sethian [17], and Adalsteinsson and Sethian [18]) has its key idea the representation of a propagating interface as the zero value of a signed distance function

$$\phi(x, t > 0) = \pm \delta \tag{3}$$

It is easy to show that ϕ has an associated evolution equation

$$\phi_t + F|\nabla \phi| = 0 \tag{4}$$

where F is the speed function in the normal direction (a function of curvature, deposition/etch rate, etc.). At any time, the distance function can be reinitialized by solving $|\nabla \phi| = 1$ using simple iterative techniques that mimic time marching evolution.

5 BOXER: An Integrated Flow Solver and Geometry Engine

5.1 Overview. The heart of the new work presented here is the exploration of the possibilities offered by the integration of editable solid modeling directly with the mesh generation, flow solving, and postprocessing coupled together with very efficient and inherently parallelizable data structures within a single piece of software. This research combines the ideas from solid modeling and virtual sculpting described in previous sections with a simple, cut-Cartesian mesh flow solver implemented on an efficient octree data structure/mesh.

The inspiration for the present work was the amazing paper published by Viecelli [19] who, over 30 years ago, presented a method for the simulation of flows with free surfaces on Cartesian meshes bounded by arbitrarily moving walls. Since then, other very interesting flow solvers have been presented for adapted Cartesian meshes by Young et al. [20] (the well-known full-potential solver TRANAIR) and Aftosmis et al. [21] (the CART3D code using the Euler equations). However, the present work is the first to explore a completely integrated viewpoint.

5.2 Data Structures. The core of the new code ("BOXER") is a very efficient octree data structure acting *simultaneously* as a search engine, as a spatial occupancy solid model, and as an adaptive, unstructured mesh for the flow solver. This provides unlimited geometric flexibility and very robust mesh generation. The generation of such a mesh is rather straightforward (see, for example, Yerry and Shephard [22]) and can be implemented in a relatively short code. Maximum advantage is taken of the basic hexahedral element being axis aligned and neighbors are not allowed to differ by more than one level (partly to simplify the data structures but also since that makes sense for flow solver accuracy). All searching operations have a cost directly proportional to no more than the number of levels.

5.3 Flow Chart. Figure 4 shows the basic flow of activities within BOXER; the whole process is controlled by a simple top level graphical user interface (GUI). The iteration between the flow solver and the continually reedited geometry is closely coupled so that the previous flow solution is used as the next initial guess.

5.4 Geometry Capture and Extraction of the Distance Field. The solid model is initialized by the import of a tessellated surface from a variety of potential sources (most CAD engines have an STL export) or by direct interrogation of the CAD solid model kernel itself. The solid model is "captured" on the adaptive, unstructured Cartesian hexahedral mesh very efficiently by cutting the tessellated boundaries using basic computer graphics constructs developed for interactive 3D gaming (aimed at real-time collision detection)—see Glassner [23]. This geometry capture is very fast; for example, a body represented by about 1M surface triangles can be imported into a mesh of around 11M cells (with six to seven levels of refinement) in approximately 5 min on a single, top-end PC. As an example, Fig. 5 shows a captured generic turbocharger housing; this was imported in VRML format.

Adaptive mesh refine/derefine for the flow and for the geometry

Fig. 5 The capture of a generic turbocharger housing

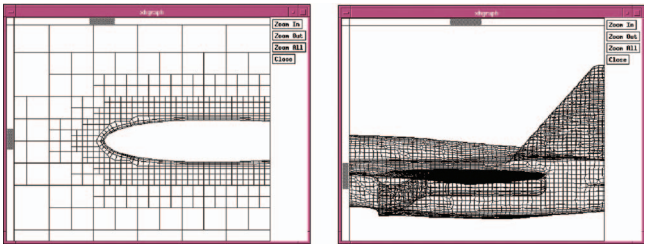

Fig. 6 Viscous layers can be inserted between cut cells and the body—above is such a layer near the LE of an airfoil: this creates a new, quadrilateral surface definition illustrated by showing the midsection of an F18 geometry originally imported as a tessellated surface

enables both moving bodies and topology editing—*flow sculpting*—once the level set has been extracted from the distance field. A key novelty is to regard the body (represented within the distance field) as just another field variable—like the flow properties themselves—and thus subject to—and controlled by—the same mesh adaptivity and to its own evolution.

5.5 Flow Solver. The present 3D RANS solver is perfectly standard and was adapted from an existing unstructured mesh RANS solver (see Dawes et al. [1]). The solver uses explicit Runge–Kutta time marching on a second order accurate finite volume discretization of spatial fluxes. Standard, blended second and fourth differences are used for smoothing. A modest novelty is the opportunity to use the distance function also as the length scale in the turbulence modeling; this copes tidily and economically with arbitrary geometries. Simple modifications to the solver were made to manage the additional complications of handling hanging nodes and the cut cells. The aim of the present paper is not to report development to the solver itself but to explore the opportunity of integration and no further detail is felt appropriate. However, it is worth noting that it would be straightforward to use the mesh which quite naturally is generated within the geometry solid as the basis for solving other equation sets, especially for heat transfer or mechanical stress, coupled directly with the flow mesh simulation. Indeed, this work is in progress now.

The *cut cells* are the big disadvantage of the Cartesian approach. For the present, rather exploratory research, the simple ghost cell approach of Viecelli [19] was adopted as it is very robust; this relies on storing for each cut cell the local body normal (which is efficiently grabbed on the fly during the geometry capture/editing stages and is simply the gradient of the distance field). More accurate approaches are certainly possible and, although not used in this paper, BOXER has also the ability to delete out the cut cells and build layered viscous meshes along body normals—illustrated in Fig. 6.

5.6 Sculpting. Modifying the geometry in response to the flow solution—*sculpting*—is the next part of the process. A tool is selected from the menu presented by the GUI and then maneuvered via 6DOF input to interact with and change the geometry of the current body. This is coupled within the flow solver like a moving body as the ultimate aim is interactive response. The flow solver can then be relaunched with the previous solution as the initial guess, and then the geometry can be edited again. Tools are currently simple geometries—spheres and cylinders (see Baerentzen [16] and Perng et al. [15])—but could in principle themselves be tessellated surface solids. The distance field associated with the tools is combined with that of the current body and the new body extracted by reinitializing the new distance field; the main complication is ensuring adequate mesh support in previously less refined areas of the mesh. The only human input to the process is via this sculpting; all other aspects of the CFD process are completely automated. In principle, the sculpting also could be automated for example, drilling holes in specified locations or morphing geometries in accordance with a specified schedule.

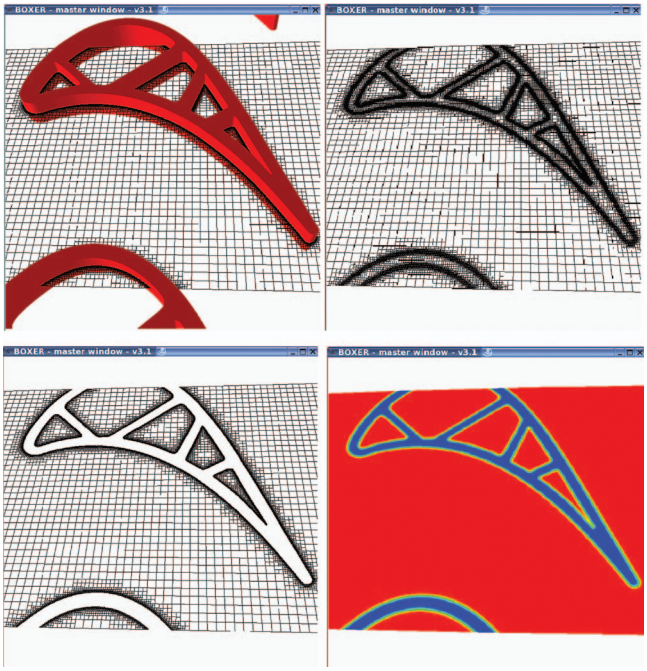

Fig. 7 Stages in the capture of a generic film cooled turbine blade: top left, the tessellated geometry; top right, the octree mesh, bottom left, the flow mesh; bottom right, the clipped distance field

5.7 Geometry Export. The sculpted geometry naturally emerges in STL/VRML tessellated format as the geometry surface is held and rendered as a triangulated isosurface. This may be exported direct to rapid prototyping systems for actual manufacture and test or converted back into conventional BREP form (using a number of commercially available software products) and hence reenter the CAD world [24].

6 Example Application: Rapid Prototyping Topological Editing of a Turbine Cooling Configuration

This example is based on the important practical problem of turbine cooling. Blades in the high pressure sections of high-performance aeroengines and land-based gas turbines are very commonly cooled using air from compressor exit delivered via an internal air system to within the blade—in complex serpentine cooling passages—and to the blade surface via film cooling holes. Much research, development and testing go into the design of this critical technology. Inadequate cooling is responsible for a significant fraction of in-service problems and rectifying poorly performing design can be very expensive.

The essential difficulty of applying modern analysis tools such as CFD to the design process in the complexity of the geometry combined with the vulnerability of the CFD process to rapid changes in geometry. Even with obvious shortcuts such as parametrizing the CAD model and templating the CFD process, it takes an unacceptable time to turn around simulations of new geometries—sometimes over a week per new geometry. This is exacerbated by the need to make frequent *topological* changes to the cooling concept—a blade always looks like a blade but the internal cooling system could have two or three or five passages with or without interconnection with an a priori unknown number of film cooling passages in a priori unknown locations. This means that in practice there is little scope within realistic design timescales to try innovative design.

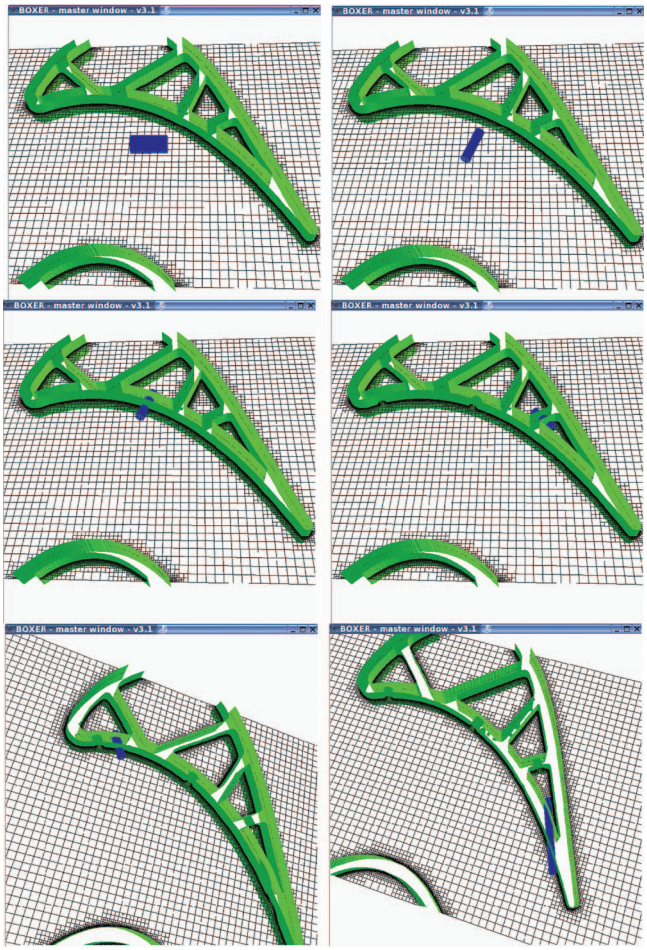

Fig. 8 Sculpting a new film cooling passage through the distance field (the zero isosurface, the blade, is rendered green) with a cutting tool (blue)

The development of BOXER was started with exactly this sort of problem area in mind with the ultimate ambition of providing a rapid prototyping tool with sufficient speed, generality and accuracy to allow design to be optimized. This section shows the stages in a simple design study on a generic cooled section.

Figure 7 shows the stages in the "capture" of the blade geometry. The geometry is imported as a tessellated surface and then the octree mesh is generated with four refinement levels. The mesh contains 1.4*M* cells and took about 2 min to generate and 400 Mbytes of RAM on a 2 GHz laptop PC. The two mesh shots show the total mesh and the mesh within the flow domain. The next stage is to extract the distance field which is shown as the last shot in Fig. 7; the distance is clipped for economy to $\pm 5\Delta$, the mesh spacing on the finest level, and red is positive, blue is negative.

This is followed by the sculpting stage. In this example, Fig. 8, a cylindrical tool, shown in blue, is selected and, via a 6DOF motion applied via the front-end GUI, scaled and maneuvered toward the blade pressure side; a new film cooling passage "drilled" into the internal air supply. This operation takes about 30 s/hole and can be repeated as often as desired before restarting the flow simulation. This is the only stage which requires human intervention but needs no specialist CAD or meshing or CFD training—rather it feels like, via the GUI, a simple computer game.

Then the distance field associated with the tool and that of the current blade geometry (the zero value of the distance is rendered green in the figure) are combined and a new spatial rendered

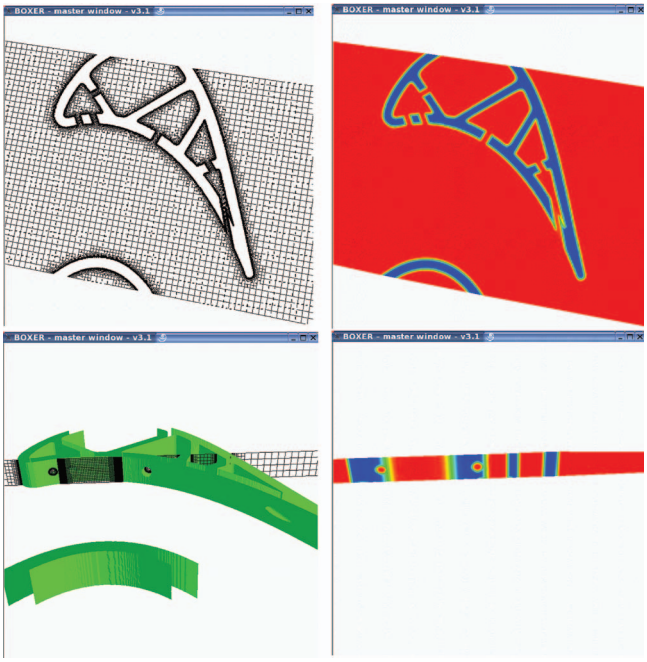

Fig. 9 The newly sculpted mesh and examples of the current distance field

green in the figure) are combined and a new spatial occupancy solid model created ready for the next flow solve (using the previous solution, which presumably inspired the need for the extra cooling, as its guess). This stage takes about 1.5 min and Fig. 9 shows some shots of this.

The final figure in this example, Fig. 10, shows a couple of sample shots of the predicted flow field—the total temperature field near the pressure side film cooling holes and the midspan Mach number field. No more flow analysis will be attempted here since the aim of this paper is to describe the building blocks and demonstrate their integrated assembly.

It is important to stress that all the stages represented in Figs. 7–10 were carried out within a single piece of software, all under the control of a GUI—from the moment the initial geometry is captured there is no need to pass data to any other code—nor return to the CAD engine. It is believed that the dramatic speed up afforded to the designer will allow much more creative and extensive conceptual design within realistic timescales.

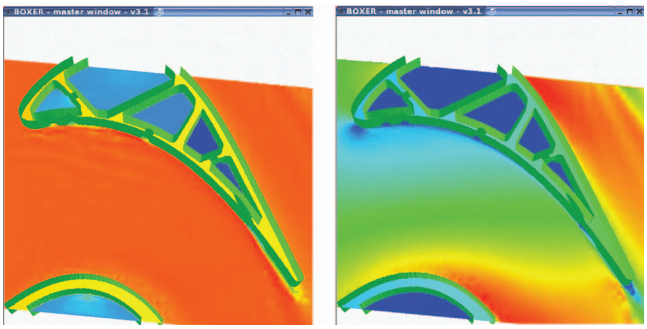

Fig. 10 Two snapshots of the new flow solution; total temperature (left) and Mach number (right)

7 Concluding Remarks and Future Plans

This paper has attempted to show the potential benefits of integration of the solid model, mesh generator, and flow solver within a single software system, bound together with efficient data structures.

Adopting concepts from volume sculpting together with editable distance fields then allows the designer essentially arbitrary geometric flexibility within a VR-like environment.

In terms of the flow solver, more work is needed on cut cell boundaries—and layers—plus parallel load balancing to allow the ultimate goal of real-time, interactive response to be achieved.

The key to real-world exploitation is likely to be effective presentation of captured geometry and virtual sculpting tools via a VR environment to users and this is being pursued now. Links to the world of rapid prototyping as well as more interdisciplinary hierarchical design are very attractive and also are being planned.

Acknowledgment

It is my great pleasure to acknowledge the help and support of Dr. Caleb Dhanasekaran.

Appendix

Some of the les familiar acronyms and terms are gathered here with brief explanation.

6DOF	six degrees of freedom
BREP	boundary representation solid model consisting of patches, edges and topology bindings
CAD	computer aided design software, for example, PRO/E or Unigraphics (UG) or CATIA each of which sits on a geometry kernel
CSG	constructive solid geometry
GUI	graphical user interface
IGES/STEP/STL	are various standard formats for importing and exporting geometry out of and in to CAD software
NURBS	nonuniform rational B-splines
VR	virtual reality
VRML	is the VR version of the STL format and consists of a geometry represented by its tessellated (triangulated) surface and stored as a set of (x,y,z) vertex coordinates bound together in triplets to make up a set of triangles

References

[1] Dawes, W. N., Dhanasekaran, P. C., Demargne, A. A. J., Kellar, W. P., and Savill, A. M., 2001, "Reducing Bottlenecks in the CAD-to-Mesh-to-Solution Cycle Time to Allow CFD to Participate in Design," ASME J. Turbomach., **123**(3), 552–557.

[2] Samareh, J. A., 1999, "Status and Future of Geometry Modelling and Grid Generation of Design and Optimisation," J. Aircr., **36**(1), pp. 97–104.

[3] Samareh, J. A., 2001 "Survey of Shape Parameterisation Techniques for High-Fidelity Multi-Disciplinary Shape Optimisation," AIAA J., **39**(5), pp. 877–883.

[4] Dawes, W. N., Kellar, W. P., Harvey, S. A., Dhanasekaran, P. C., Savill, A. M., and Cant, R. S., 2003, "Managing the Geometry is Limiting the Ability of CFD to Manage the Flow," AIAA Paper No. 2003-3732.

[5] Harvey, S. A., Dawes, W. N., and Gallimore, S. J., 2003, "An Automatic Design Optimisation System for Axial Compressors Part I: Software Development," ASME Paper No. GT2003–38115.

[6] Harvey, S. A., Dawes, W. N., and Bolger, J. J., 2003, "An Automatic Design Optimisation System for Axial Compressors Part II: Experimental Validation," ASME Paper No. GT2003–38650.

[7] Lamousin, H. J., and Waggenspack, W. N., 1994, "NURBS-Based Free-Form Deformation," IEEE Comput. Graphics Appl., **14**(6), pp. 59–65.

[8] Kellar, W. P., Savill, A. M., and Dawes, W. N., 1999, "Integrated CAD/CFD Visualisation of a Generic F1 Car Front Wheel Flowfield," Lect. Notes Comput. Sci. **1593**, pp. 90–98.

[9] Kellar, W. P., 2003, "Geometry Modelling in CFD and Design Optimisation," Ph.D thesis, Cambridge.

[10] Haimes, R., and Follen, G. L., 1998, "Computational Analysis Programming Interface," *Proceedings of the Sixth International On Numerical Grid Generation in Computational Field Simulations*, M. Cross, P. R. Eiseman, J. Hauser, B. K. Soni, and J. F. Thompson, eds.

[11] Sederberg, T. W., and Parry, S. R., 1986, "Free-Form Deformation of Solid Geometric Models," Comput. Graphics, **20**(4), pp. 151–160.

[12] Galyean, T. A., and Hughes, J. F., 1991, "Sculpting: An Interactive Volumetric Modelling Technique," ACM Trans., Computer Graphics, **25**(4), pp. 267–274.

[13] Jones, M. W., and Satherley, R., 2000, "Voxelisation: Modelling for Volume Graphics," Annual SIGGRAPH Conference, Los Angeles.

[14] Bremer, P.-T., Porumbescu, S. D., Kuester, F., Hamann, B., Joy, K. I., and Ma, K.-L., 2001, "Virtual Clay Modelling Using Adaptive Distance Fields."

[15] Perng, K.-L., Wang, W.-T., Flanagan, M., and Ouhyoung, M., 2001, "A Real-Time 3D Virtual Sculpting Tool Based on Modified Marching Cubes," *SIGGRAPH*.

[16] Baerentzen, A., 1990, "Volume Sculpting: Intuitive, Interactive 3D Shape Modelling," CAD, **22**(4), pp. 202–212.

[17] Osher, S., and Sethian, J. A., 1988, "Fronts Propagating With Curvature-Dependent Speed: Algorithms Based on Hamilton-Jacobi Formulations," J. Comput. Phys., **79**, pp. 12–49.

[18] Adalsteinsson, D., and Sethian, J. A., 1995, "A Level Set Approach to a Unified Model for Etching, Deposition and Lithography II: Three Dimensional Simulations," J. Comput. Phys., **122**, pp. 348–366.

[19] Viecelli, J. A., 1971, "A Computing Method for Incompressible Flows Bounded by Moving Walls," J. Comput. Phys., **8**, pp. 119–143.

[20] Young, D. P., Melvin, R. G., Bieterman, M. B., Johnson, F. T., Samant, S. S., and Bussoletti, J. E., 1991, "A Locally Refined Rectangular Grid Finite Element Method: Application to Computational Fluid Dynamics and Computational Physics," J. Comput. Phys., **92**(1), pp. 1–66.

[21] Aftosmis, M. J., Berger, M. J., and Melton, J. E., 1998, "Robust and Efficient Cartesian Mesh Generation for Component-Based Geometry," AIAA J., **36**(6), p. 952.

[22] Yerry, M. A., and Sheppard, M. S., 1983, "Automatic Three-Dimensional Mesh Generation by the Modified Octree Technique," Int. J. Numer. Methods Eng., **20**, pp. 1965–1990.

[23] Glassner, A. S., 1990, *Graphics Gems* Academic, New York.

[24] Sussman, M., Smereka, P., and Osher, S., 1994, "A Level Set Approach for Computing Solutions to Incompressible Two-Phase Flow," J. Comput. Phys., **114**, pp. 146–159.

Paolo Boncinelli
e-mail: Paolo.Boncinelli@icad.de.unifi.it

Roberto Biagi

Antonio Focacci

Umberto Corradini

Andrea Arnone

"Sergio Stecco" Department of Energy Engineering,
University of Florence,
Via di Santa Marta, 3,
Florence 50139, Italy

Marco Bernacca
e-mail: m.bernacca@termomeccanica.com

Massimiliano Borghetti

TM.P. S.p.A.-Termomeccanica Pompe,
Via del Molo 3,
La Spezia 19126, Italy

Bowl-Type Diffusers for Low Specific-Speed Pumps: An Industrial Application

In this paper, the aerodynamic design of a bowl-type diffuser for a low specific-speed pump is presented and described in detail. The main goal was to achieve an optimal configuration in terms of diffuser recovery capacity and stage aerodynamic efficiency, while satisfying severe constraints concerning stage size and multistage feasibility. Both geometrical parametrization tools and a fully viscous three-dimensional numerical solver were exploited in the design process. The geometrical parametrization allowed one to control and modify the geometry of the component by changing a limited number of parameters. Computational fluid dynamics analysis was exploited to assess the effectiveness of the geometrical modifications on the performance and to identify critical problems. A number of aerodynamic 1D coefficients with simple physical meanings were also introduced and used as a support to the design to synthesize the main feature of the strongly three-dimensional flow evolving in the component. As a result, a new stage configuration was developed according to the imposed constraints, whose performance is at the same level as standard pumps of the same class. [DOI: 10.1115/1.2777182]

Introduction

In recent years, the industrial process related to the aerodynamic design of pumps has undergone a significant evolution, due to both changes in industrial requirements and constraints and the development of new and more powerful design tools. Two interesting discussions concerning modern trends in industrial pump design are reported in two papers by Gopalakrishnan [1] and Hergt [2].

Gopalakrishnan [1] emphasizes that today the primary pump characteristics, required by end users to manufacturers supplying a worldwide customer base, mainly relate to cost and reliability. Technical performance is not ignored, but it represents a minimum requirement for a pump to be an acceptable offering.

Similarly, Hergt [2] highlights how, from the early 1970s to present, the main focus of pump design has moved from the so-called "primary task of turbomachinery design" to the "second task:" that is, from finding the best geometry, which provides maximum efficiency and reliability for given operating data, to designing the hydraulic contours, which make it possible to meet the requirements of modern, low-cost manufacturing methods, while satisfying the desired operating characteristics (head, efficiency, operating range, and behavior). Nevertheless, the cost-benefit principle, which has by now become the judging factor for the final choice on the end-user side, has pushed industries to concentrate efforts on improving pump efficiency within stricter and stricter manufacturing constraints. This often implies the understanding of complex flow physics, so, to achieve this target, a closer cooperation between industries and basic research carried out in universities has proved to be fruitful.

A significant contribution in this sense has come from the development of more and more accurate and powerful numerical codes for turbomachinery flow analysis, which allow the designer to predict the machine performance and understand the flow phenomena of interest, helping him in achieving the optimum design. Many examples of different applications of numerical techniques to industrial pump analysis and design can be found in recent literature, exploiting both research and commercial solvers (Zangeneh et al. [3], Goto et al. [4], Miner [5], Shi and Tsukamoto [6], and van Esch and Kruyt [7]). As a matter of fact, computational fluid dynamics (CFD) has by now asserted itself as one of the most effective instruments in turbomachinery research and design.

In this context, Termomeccanica Pompe S.p.A. and the "Sergio Stecco" Department of the University of Florence started a joint research project for the design and the optimization of pump stages, mainly based on the use of CFD techniques. A number of centrifugal and mixed-flow pumps were selected, characterized by different values of the specific speed n_s. For each one, specific design targets were identified, based on industrial needs. An example of application carried out during this activity has already been reported in a previous paper by Bonaiuti et al. [8], concerning the optimization of a mixed-flow pump stage corresponding to a specific speed $n_s=155$. In the present paper, attention is focused on a different kind of application: the design of a bowl-type diffuser for a low specific-speed stage ($n_s=40$).

In industrial pumps, a critical problem is represented by radial dimension and weight, especially for low specific-speed pumps ($n_s<50$), whose typical stages are usually composed of a centrifugal impeller coupled with a radial vaned/vaneless diffuser. The presence of the radial diffuser contributes to increase the pump radial size noticeably. For this reason, particular efforts are devoted to the investigation of alternative configurations, capable to reduce this problem while maintaining an acceptable level of performance.

An interesting design solution, already presented and discussed, for example, by Goto and Zangeneh [9], is to couple the radial impeller with a bowl-type diffuser, similar to those ones used in mixed-flow stages. However, the matching of the diffuser with the upstream centrifugal impeller is not an easy task to accomplish.

Contributed by the Turbomachinery Division of ASME for publication in the JOURNAL OF TURBOMACHINERY. Manuscript received January 15, 2007; final manuscript received February 22, 2007; published online May 5, 2008. Review conducted by David Wisler. Paper presented at the Eighth Biennial ASME Conference on Engineering Systems Design and Analysis (ESDA2006), Torino, Italy, July 4–7, 2006.

The reduction of the outer diffuser diameter determines an increase of the blade load, which must be carefully controlled to avoid flow separations, responsible for unwanted performance deterioration. The handling of the resultant highly 3D flow cannot be simply achieved by means of traditional semiempirical 1D correlations and requires a complete 3D analysis, including viscous effects.

As far as the diffuser geometry design is concerned, two possible approaches can be followed. In the first one, the so-called "conventional design," the diffuser blade is designed by providing the blade angle distribution, together with the meridional channel geometry, according to both physical considerations and previous experience. The second one exploits the inverse design method, which is capable of producing a blade geometry starting from an assigned loading distribution. Both approaches make use of CFD computations to assess overall performance and analyze the flow field structure.

Advantages related to the use of the inverse design method are extensively discussed by Goto and Zangeneh [9] and Goto et al. [10]. In particular, attention is focused on the capability of this method to produce a geometry, which directly provides the desired blade load. However, not all geometrical features can be determined in an inverse manner. Both the meridional geometry and the blade stacking condition must be supplied separately, usually from an existing database and previous experience, and optimized by means of a trial-and-error process, coupled with the blade load distribution (Goto et al. [10]). As a consequence, in the authors' opinion, the effort needed to produce the optimum geometry is not much different from that one required by the more direct conventional approach, which relies mainly on the physical analysis of the flow development and the designer's expertise. This approach was used in the present work.

Here, the main steps of the diffuser design process are illustrated. The centrifugal impeller was first analyzed in order to investigate the thermofluid dynamics properties of the flow at the impeller outlet, and a preliminary diffuser geometry was set. Then, the flow across the stage was computed to assess the stage performance and identify critical problems. Successive modifications to the diffuser geometry were applied in order to achieve an optimized configuration in terms of diffuser recovery capacity and stage aerodynamic efficiency.

Pump geometry was handled in parametric way, in order to describe the complex 3D geometry of the diffuser using a limited set of parameters. This allowed one to account for the structural and manufacturing requirements and to assess the relative importance of each parameter in impacting on the pump performance. A number of aerodynamic 1D coefficients with simple physical meaning were introduced and used as a support to the design, too, to synthesize the main feature of the strongly three-dimensional flow evolving in the component.

Pump Stage Description

The pump under investigation is a multistage vertical one, characterized by a value of specific-speed number $n_s=40$ at design operating point (DP). This value is set as a constraint over the whole design process of the diffuser.

The original pump stage consisted of a seven-blade shrouded centrifugal impeller and a diffuser composed of 11 hydraulic channels, with an increasing passage section in the streamwise direction. This design solution, even if allowing an optimum control of the diffusion process with minor losses, had the severe drawback of increasing considerably the pump weight and radial size (up to 1.60 times the outer impeller radius).

In the new stage design, the impeller was left unchanged, while the channel diffuser was substituted by a bowl-type one. The main constraint for the new diffuser design was to reduce the maximum radial size of the stage to less than 1.30 times the outer impeller radius. Moreover, as an essential industrial requirement, the new pump stage should be suitable for use in a multistage pump.

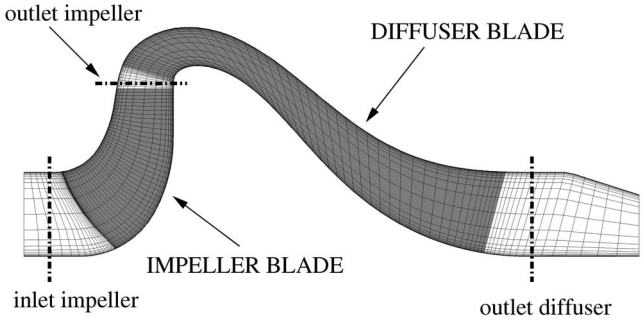

Fig. 1 Meridional view of computational domain and performance evaluation sections

Numerical Procedure

All computations were performed using the HYDRO code, which is the incompressible version of the TRAF code (Arnone [11]), a fully viscous, multigrid, multirow solver developed at the University of Florence, capable of solving 3D cascade flows in coupled fixed and rotating blade passages using nonperiodic *H*-type or *C*-type grids. The concepts of artificial compressibility of Chorin [12] are used to handle incompressible fluids with a time-marching approach. The eddy-viscosity hypothesis is used to account for the effect of turbulence. The eddy viscosity is computed using the two-layer mixing length algebraic model of Baldwin and Lomax [13].

The 3D unsteady incompressible Reynolds-averaged Navier–Stokes (RANS) equations are discretized in space using a cell-centered finite volume scheme. The solution is advanced in time using an explicit four-stage Runge–Kutta scheme, until the steady-state solution is reached. In order to reduce the computational cost and speed up convergence to the steady solution, four computational techniques are employed (local time stepping, residual smoothing, multigrid full approximation storage (FAS) scheme, and grid refinement).

Boundary conditions are imposed on solid walls (no slip), on periodic boundaries, at inlet (total pressure and flow angles) and outlet (static pressure at hub) of the computational domain. In the clearance region, the conservation of physical quantities across the blade is imposed without modeling the flow inside. Coupling between rows is achieved by using mixing planes. Further details on the numerical procedure can be found in Refs. [14–17].

Nonperiodic *H*-type grids were employed in all computations presented here. The removal of periodicity allows grids to be only slightly distorted, even for cascades having a large camber or a high stagger angle and twist. The computational domain was divided into two blocks, one for the impeller and one for the diffuser, respectively. A pinch was used downstream of the diffuser in order to suppress regions of separated flow at the outlet section, which may affect the convergence and make it complex to evaluate the component performance. About 400,000 grid cells were used for each computational block.

The flow was pressurized to some extent with respect to physical pressure at the stage inlet, in order to prevent cavitation from arising at the impeller mouth, which would make it impossible to perform computations.

Stage performance was evaluated considering fluid-dynamic area-averaged quantities at two axial sections, the first one just upstream of the impeller leading edge and the second one downstream of the diffuser trailing edge. In Fig. 1, the position of the two sections is illustrated, together with a meridional view of the computational grid, while in Fig. 2, a 3D view of the grid is reported. For the sake of clarity, only half of grid cells are shown.

The whole pump operating range was covered by starting from a high flow rate condition and increasing the backpressure progressively until a stall point was reached. As stall is characterized

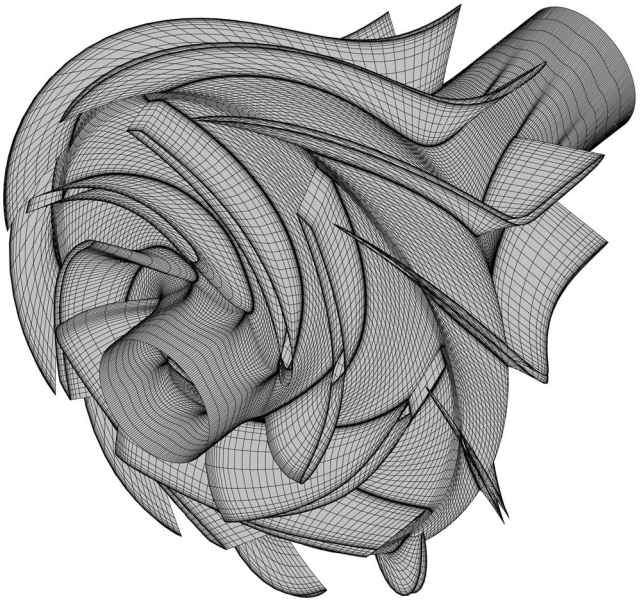

Fig. 2 3D view of the computational grid

by unsteady flow phenomena, it is not possible to investigate it using a steady-state approach. However, the designer's main interest is prevalently focused on identifying stall inception, in order to foresee the pump operative range in terms of deliverable mass flow. Here, the stall inception is established by following this procedure. When approaching stall, finer and finer adjustments of backpressure are performed, which cause smaller and smaller reductions in the computed mass flow rate, until a point is reached where computations do not converge anymore. Then, it is assumed that the stall inception occurs at the last computed point for which the code converges. Convergence was assumed when the rms of the residual reduced its initial value of four-order magnitude.

Geometrical Parametrization

In an iterative direct design procedure, it is essential to parametrize the component geometry using as few geometrical parameters as possible. To achieve this goal, the geometrical properties of integral Bézier curves are exploited, for which the shape of the curve can be controlled using a few control points (Hoschek and Lasser [18]). Bézier curves are defined parametrically as

$$\mathbf{X}(t) \equiv \sum_{i=0}^{n} \mathbf{b}_i B_i^n(t), \quad t \in [0,1] \tag{1}$$

where $\mathbf{X}(t) \equiv [x(t), y(t)]$ is the point on the curve for the parametric value t, n is the degree of the Bézier curve, $\mathbf{b}_i \equiv (x_i, y_i)$ with $i=0,1,\ldots,n$ are the control points, and

$$B_i^n(t) \equiv \binom{n}{i} t^i (1-t)^{n-i} \quad i = 0,1,\ldots,n$$

are the so called Bernstein polynomials. Figure 3 shows an example of a Bézier curve $\mathbf{X}(t)$ and its control points $\mathbf{b}_i$. Many efficient algorithms, developed especially for computer graphics applications, are already available (see, for example, Refs. [19,20]).

In the present work, a geometrical parametrization tool was set up to produce the component geometry using as an input the following geometrical data.

Meridional layout. In general, both hub and shroud meridional contours are described by a single Bézier curve, defined using a variable number of control points, while leading edge (LE) and trailing edge (TE) meridional contours are described by a three-control-point Bézier curve. In the present case, two nine-control-point curves are used for the hub and shroud parametrization and a linear contour for LE and TE, as shown in Fig. 4.

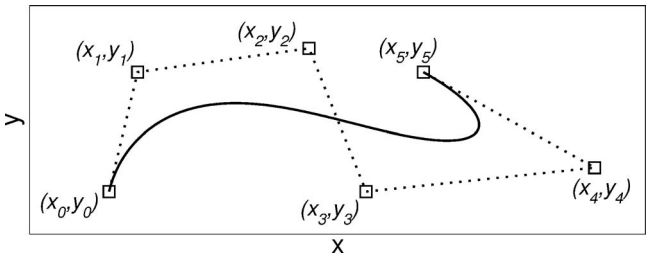

Fig. 3 Example of a Bézier curve of degree *n*=5

Blade turning angle (β_{bl}). The blade geometry is built by stacking in the (m,r) plane a number of blade-to-blade sections described in the $(m,R\theta)$ plane, where R is the LE radius at the hub. The camber line of each section is parametrized in terms of the turning angle β_{bl} along the meridional abscissa m. The β_{bl} angle is related to the azimuthal blade angle θ by

$$\tan \beta_{bl} \equiv r \frac{d\theta}{dm} \tag{2}$$

The use of β_{bl} angle instead of θ allows the designer to easily control the blade load distribution. Here, two β_{bl} distributions at the hub and the shroud are described by five-control-point Bézier curves, as shown in Fig. 5, together with the corresponding θ distributions.

Blade thickness. In order to define the blade profile, a thickness distribution is assigned for each section by means of GC^1 patches of Bézier curves [18]. In the present case, blade sections have a constant thickness over the whole camber line except that near the LE and TE.

Stacking law. The stacking of the blade is determined by assigning the value of $\Delta\theta$ at a fixed m for each section with respect to a reference one (usually the hub one) (Fig. 5).

Impeller Analysis

To define a preliminary diffuser configuration, the centrifugal impeller was first analyzed over the whole operating range in order to investigate the flow structure at the impeller outlet (Fig. 1). Attention was focused on spanwise distributions of the flow angle and the thermofluid dynamics properties at DP. The flow rate was set equal to the flow rate of the original stage configuration at $n_s=40$.

Blade loads are reported in Fig. 6 at three different spanwise sections. The load distribution is quite uniform along the impeller blade, and the flow incidence is correct, assessing the good behavior of the impeller at DP.

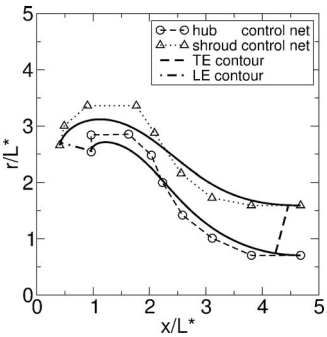

Fig. 4 Meridional contour parametrization

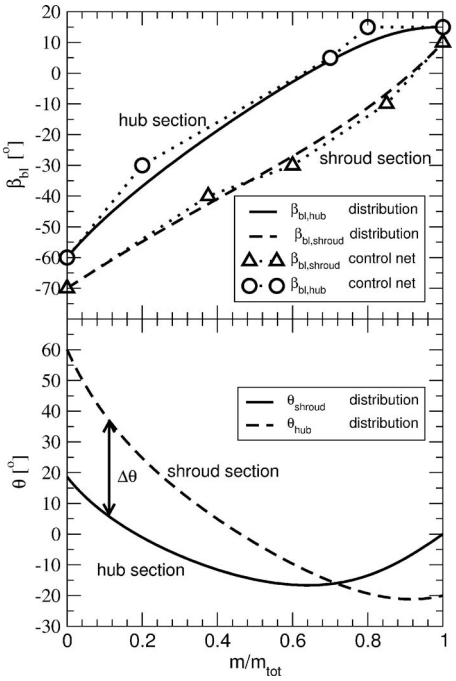

Fig. 5 β_{bl} angle parametrization and corresponding θ angles

The flow angle distribution at DP was used to choose the blade turning angle at the diffuser LE. A high value of the absolute flow angle is observed (Fig. 7). This is determined by the geometry of the impeller blades, which are not highly backwarded.

Diffuser Design Process

The new diffuser was designed to accomplish the following main targets and constraints.

1. Reduce the maximum radial size to less than 1.30 times the outer impeller radius.

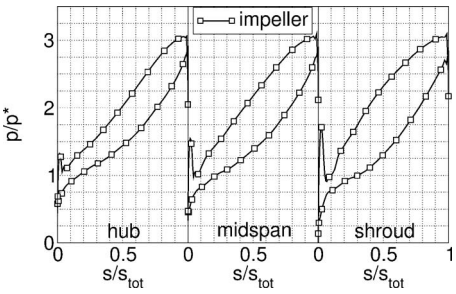

Fig. 6 Impeller blade load distributions at DP

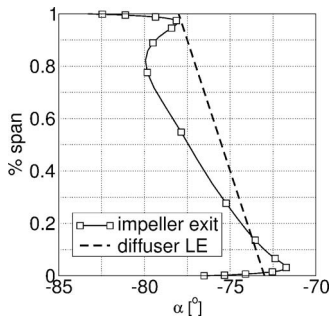

Fig. 7 Impeller outlet absolute flow angle at DP

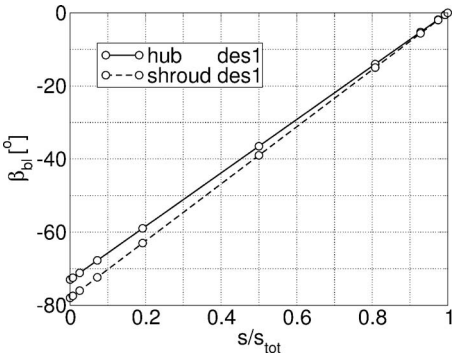

Fig. 8 β_{bl} angle distribution ("des1")

2. Change the diffuser type from a channel to a bowl-type one. Consequently, a weight reduction is expected.
3. Design a diffuser suitable for multistage feasibility, maintaining the original impeller in all stages. This required setting the outlet hub and shroud diameters of the diffuser equal to the impeller inlet ones. Moreover, similar flow conditions (axial flow) should be provided at the impeller inlet in all stages.
4. Produce a blade geometry with ruled surfaces, in order to simplify the manufacturing process.
5. Maintain the specific-speed number n_s of the stage equal to the original one at the peak efficiency.

A preliminary diffuser geometry (identified by "des1") was generated using both the results of the impeller analysis and past experience on bowl-type diffusers of pump stages with similar n_s. This is the classical approach followed in the traditional design process, where 1D relationships, standard criteria, and the preexisting industrial database are exploited.

The preliminary des1 diffuser geometry was analyzed and critical problems affecting stage performance were highlighted. Subsequently, a number of configurations, based on the geometrical parameters, were produced to assess the relative impact of each parameter on the diffusion process. Two different configurations were generated, optimizing the blade turning angle distribution and the meridional channel shape successively. The intermediate one, referred to here by "des2," is characterized by an optimum blade load distribution. Then, the final configuration ("des3") was optimized for the meridional channel shape, too.

The three diffuser configurations were analyzed using CFD and compared in terms of efficiency and diffusion performance.

Preliminary Geometry. The preliminary diffuser geometry des1 was defined by assigning the meridional channel shape, including LE and TE linear contours, and the blade angle and thickness distributions for hub and shroud sections, in the following way.

Meridional layout. The channel shape was chosen using past industrial experience on bowl-type diffusers. The outlet hub and shroud diameters were set equal to the impeller inlet ones. The maximum diameter was selected within design constraints. LE and TE positions were chosen relying on past experience.

Blade turning angle. Blade angles at LE were chosen so that the resulting spanwise linear distribution approximates the flow angle at the impeller outlet (Fig. 7). At TE, a constant distribution equal to zero was set, in order to produce an axial flow for multistage feasibility. A constant β_{bl} gradient was selected along the blade (Fig. 8).

Blade thickness. Thickness distribution was set constant throughout the blade and smoothed using Bézier curve to profile LE and TE.

Stacking law. Sections were stacked so that $\Delta\theta$ between the hub and the shroud was kept within 20 deg, for manufacturing

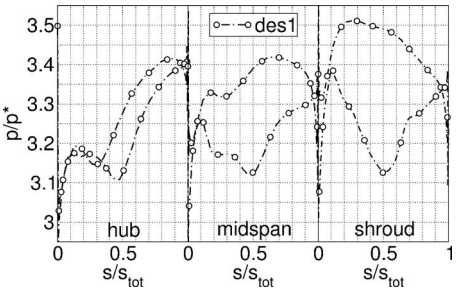

Fig. 9 Blade load distribution at DP ("des1")

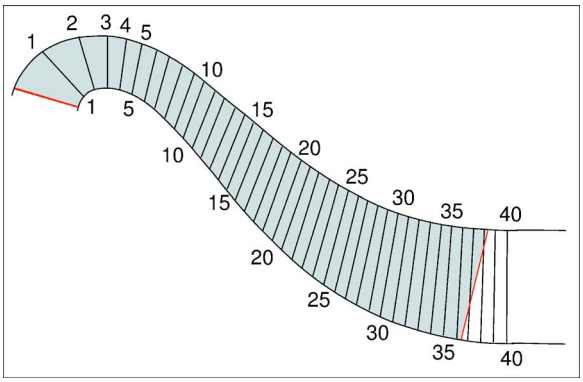

Fig. 12 Sections along the diffusion channel

reasons.

The number of diffuser blades was set equal to 11, as for the original channel diffuser.

The stage configuration composed of the original impeller and the des1 diffuser was analyzed, focusing attention on the DP flow rate condition. In Fig. 9, static pressure distributions at three different sections (10%, 50%, and 90% of the span) are reported. The flow incidence is substantially correct. However, a strongly nonuniform pressure distribution is observed. In the forepart, the blade is almost unloaded at all sections. At the hub, it remains unloaded for most of its length, while, near the shroud, load is concentrated at midchord, with a strong adverse pressure gradient on the suction side at about 60% of the blade length.

Looking at the spanwise flow angle distribution at the diffuser outlet (Fig. 10), an average swirl of about −10 deg is observed, with a maximum peak over −40 deg at about 90% of the span. Typically, this is a sign of the presence of flow recirculation.

This result is confirmed by the analysis of flow stream lines in the meridional plane, obtained by means of particle traces (Fig. 11). Two strong recirculations are seen in the meridional channel near the hub and at the diffuser exit, near the shroud. For these flow structures, views in the blade-to-blade planes are reported, too. At the hub, the region of recirculating flow extends across the whole vane, explaining the absence of blade load previously discussed. At the shroud, the high adverse pressure gradient determines the observed separation, which is responsible for the peak in the swirl angle at the outlet.

As seen before, the flow evolving in the diffuser is strongly three dimensional. In the optimization process, this makes it difficult to relate geometrical changes to their effects on the flow behavior. For this reason, a number of aerodynamic 1D coefficients were introduced to synthesize the main features of the flow. Distributions of these coefficients along the diffuser meridional channel were computed by area-averaging fluid-dynamic quantities at a number of sections, which are reported in Fig. 12. Here, attention is focused on the recovery coefficient C_p, the loss factor ξ, and the flow passage area A_f. The last one, computed as the ratio of the volume flow Q and the absolute velocity modulus c, represents the effective geometrical area seen by the evolving flow. It allows one to manage the three-dimensional diffuser as a one-dimensional one, accounting for any nonalignment of the flow with the channel.

Distributions of C_p, ξ, and A_f, reported in Fig. 13, confirm that both the irregular blade load observed in Fig. 9 and the flow separations are associated with an irregular diffusion process. In the first part of the vane, C_p increases only due to the increase of the channel radius, as it can be deduced from the C_p distribution. As the maximum radius is reached, the effective geometrical area A_f keeps on increasing, but a steep reduction in the recovery factor is observed, up to Section 15, in correspondence of the separation at the hub. Despite the increasing A_f, the area blockage induced by the presence of the recirculation bubble at the hub determines a flow acceleration. A significant increase of the loss coefficient is associated with this phenomenon. When the maximum blockage is reached, C_p starts increasing again until Section 25, corresponding approximately to the reattachment of the flow. From this point on, the flow passage area A_f remains almost constant, and the diffusion process stops, as confirmed by the behav-

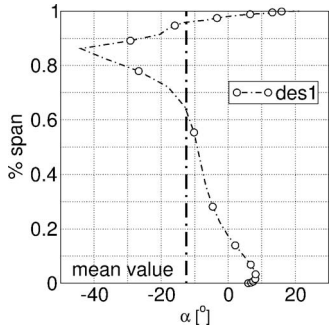

Fig. 10 Swirl angle distribution at diffuser outlet ("des1")

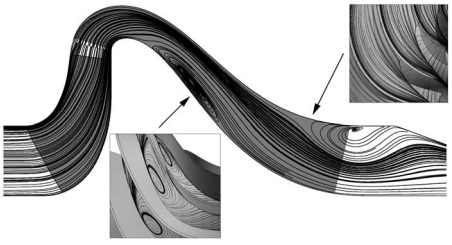

Fig. 11 Stream lines and velocity flow field at DP ("des1")

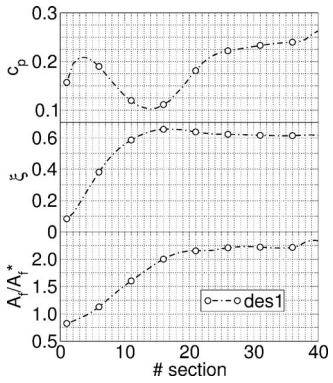

Fig. 13 Flow properties along the diffusion channel at DP ("des1")

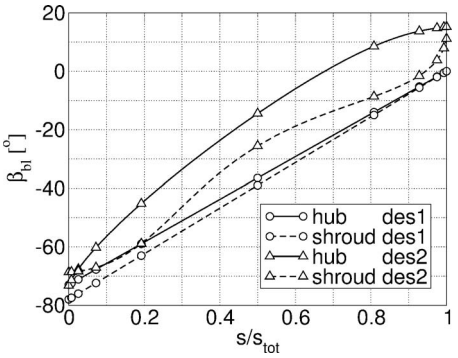

Fig. 14 Comparison of β_{bl} angle distributions

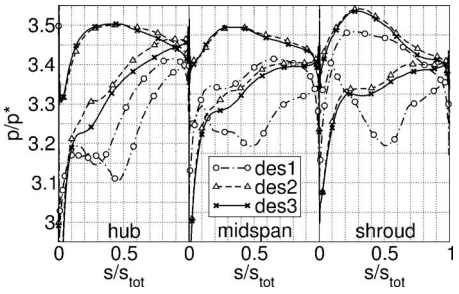

Fig. 16 Comparison of blade load distributions at DP

ior of C_p in the aft part of the channel. The impact of the recirculation at the shroud on the diffusion process seems to be negligible. Several effects can be put forward to explain this behavior. First of all, as seen in the flow structure (Fig. 11), the separation extends over the whole passage only at the vane exit, where the blockage due to blades ends. Moreover, the increase in the geometrical area, determined by the opening of the vane at almost constant radius, balances the area blockage due to the recirculation bubble.

Design of Intermediate and Optimized Geometries. The intermediate geometry des2 was generated by acting on the β_{bl} distribution, while the meridional layout was left unchanged with respect to the preliminary configuration. The main target was to increase the load in the forepart of the blade. This result was achieved by imposing a higher β_{bl} gradient at the hub, while at the shroud, the inlet β_{bl} was increased so that positive flow incidence is expected (Fig. 14). Moreover, a counter-rotating angle was imposed at the blade exit, both at the hub and at the shroud, in order to have zero-swirl flow at midspan, with a symmetrical spanwise distribution. Reasons for which a uniform zero-swirl distribution was not pursued are discussed in detail later on.

In the optimized configuration des3, the meridional shape was modified while keeping the same β_{bl} distribution as the intermediate one, so that the increase of the flow passage area A_f was more uniformly distributed along the channel. Major changes were performed in the central part of the channel, as illustrated in Fig. 15.

Results. Both intermediate and optimized configurations were investigated over the whole operating range. Detailed comparisons were carried out at DP condition and on performance characteristic curves.

At DP, as expected, in both configurations, blade load was increased in the forepart and more regularly distributed along the blade and the span (Fig. 16). In the des3 configuration, this improvement, coupled with modifications carried out on the meridional channel, produced a better flow guidance of the diffuser blade and a more uniform flow throughout the channel, with the removal of the previously observed recirculations, as shown in Fig. 17.

The improvement of the diffusion process is assessed by the distributions of aerodynamic 1D coefficients C_p, ξ, and A_f reported in Fig. 18. Both des2 and des3 achieve a larger recovery coefficient with significant lower losses with respect to des1. Most of the pressure recovery is again obtained in the increasing radius region (Sections 1–4). However, the C_p value is kept almost unchanged all along the component, avoiding the previous acceleration and subsequent deceleration of the flow. As far as the flow passage area A_f is concerned, the impact of geometrical changes in the meridional shape can be clearly observed by comparing des2 and des3 results. At the beginning, both configurations have higher A_f values than the des1 one, due to changes in the blade angle distributions. However, while des2 presents a behavior similar to des1 up to midchord (Section 20), des3 distribution has a lower gradient. As a result, the diffusion process is more uniform, with a further slight reduction in the loss coefficient.

In Fig. 19, computed characteristic C_p and ξ curves of the diffuser are compared for the three configurations. Flow rates are scaled with the corresponding DP flow rate of each stage. Improvements in the pressure recovery coefficient (Fig. 19(*a*)) and reduction of losses (Fig. 19(*b*)) are extended over the whole operating range.

The stage efficiency curve reported in Fig. 20(*a*) confirms the good matching between the des3 diffuser and the original impel-

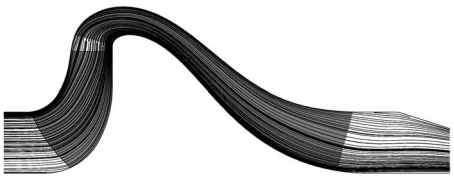

Fig. 17 Stream lines and velocity flow field at DP ("des3")

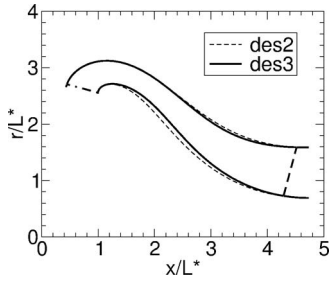

Fig. 15 Comparison of diffuser meridional channel geometries

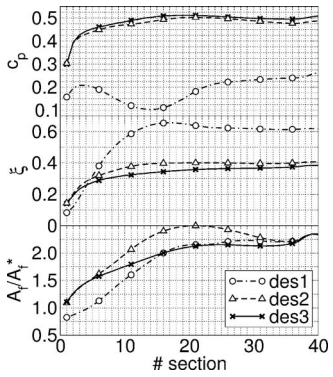

Fig. 18 Comparison of flow properties along the diffusion channel at DP

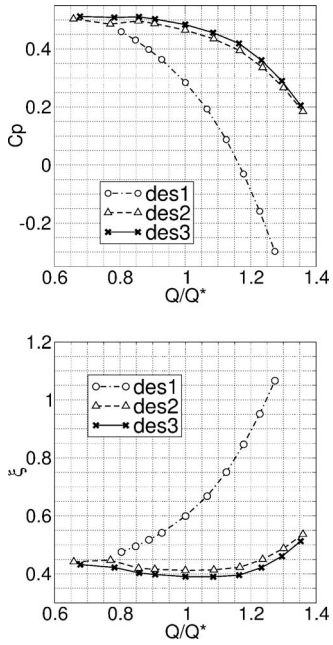

Fig. 19 Comparison of diffuser performance

ler. Peak efficiency is achieved at the DP flow rate corresponding to $n_s=40$, as required by design constraints. Moreover, the efficiency curve is almost flat for a range of flow rates around DP. The effectiveness of the new stage design is assessed by comparing the stage peak efficiency value to the optimum hydraulic efficiency data provided in literature for standard pumps of the same class (Stepanoff [21] and Japikse et al. [22]), as shown in Fig. 20(*b*). Reported data used for reference purposes refer to single-stage pumps. The obtained efficiency value is about 1% lower than the reference one. This result was judged good considering the severe constraints imposed on the design.

Exit Swirl and Recovery Coefficient. In Fig. 21, the spanwise swirl angle distributions at the outlet are reported for the three

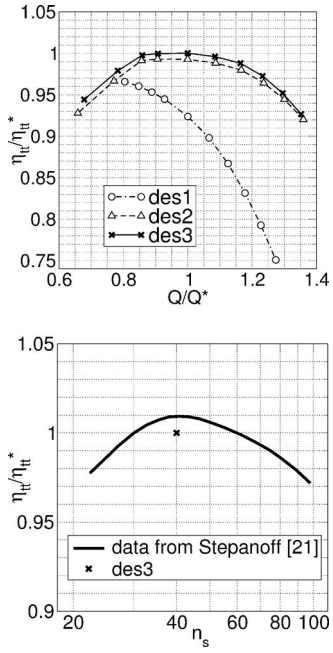

Fig. 20 Comparison of stage efficiency

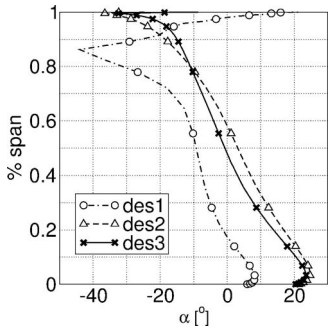

Fig. 21 Comparison of diffuser outlet flow angle distributions at DP

diffuser configurations. As far as des3 configuration is concerned, even if the section-averaged swirl is about zero, its distribution varies linearly within ±20 deg when moving from the hub to the shroud. As discussed before, an axial flow exiting the diffuser would be preferable for multistage feasibility. However, due to the assigned geometrical and flow rate constraints, this goal could not be achieved.

The exit swirl angle is strictly related to the pressure recovery coefficient C_p and, as a consequence, to the outlet/inlet area ratio and the length of the diffuser vane. Higher C_p values correspond to lower values of the velocity modulus at the outlet section. The meridional component of the velocity is fixed by the given mass flow rate and the geometrical area. A value of the velocity modulus higher than the meridional component causes swirl to occur at the exit. For this reason, higher values of C_p would allow one to decrease swirl.

In order to estimate the maximum allowable limit for C_p, a simplified configuration corresponding to a 2D straight diffuser was taken as a reference. For such configuration, a wide range of experimental data concerning diffusion capabilities is available in literature (Japikse [23] and ESDU [24]). In Fig. 22, a map of the pressure recovery coefficient C_p is reported as a function of the outlet/inlet area ratio w_3/w_2 and the relative diffuser length L/w_2. Data are taken from ESDU [24]. Values of L/w_2 and w_3/w_2 equivalent to the des3 diffuser configuration are also highlighted,

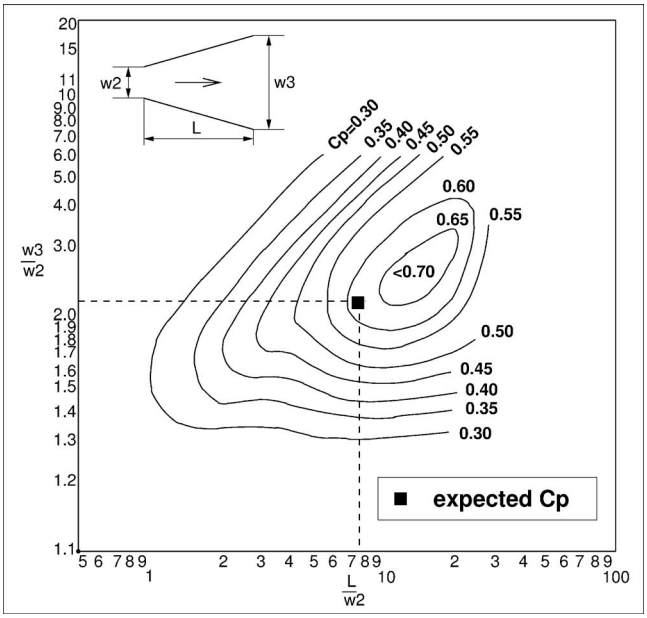

Fig. 22 Map of pressure recovery coefficient for a given blockage range (0.05< *B* ≤0.08) [24]

together with the corresponding expected C_p. Since the effects of strong curvature in both the meridional and the blade-to-blade planes in this simplified configuration are not accounted for, this value of C_p can be reasonably assumed as an upper limit for the pressure recovery coefficient achievable by the diffuser. For the des3 configuration, $C_p=0.51$ as compared to an expected value $C_p \approx 0.61$. This result was judged to be satisfactory for the aims of the present work. No significant improvements in the pressure recovery coefficient and, consequently, no reductions of the spanwise exit swirl angle are expected for further geometrical modifications within the imposed constraints.

Conclusions

In this paper, the aerodynamic design of a bowl-type diffuser for a low specific-speed pump was presented and described in detail. The original pump was equipped with a radial impeller and a channel diffuser, and the original impeller was not changed. The main goal was to reduce the pump stage radial size, while maintaining an optimal configuration in terms of diffuser recovery capacity and stage aerodynamic efficiency. Moreover, multistage feasibility and simple diffuser blade geometry with ruled surfaces were imposed as constraints. The stage specific-speed was kept unchanged.

The aerodynamic design of the diffuser was carried out by means of both geometrical parametrization tools and by exploiting results of fully viscous three-dimensional analysis. A preliminary diffuser geometry, designed using both the results of the impeller analysis and the existing industrial database, was investigated, and critical problems affecting stage performance were highlighted. A key point was the use of a number of aerodynamic 1D coefficients to synthesize the main features of the diffusion process, as a support to the design. The final configuration was generated by successively optimizing the blade turning angle distribution and the meridional channel shape.

As a result, the new bowl-type diffuser allows a reduction of about 21% of the radial size of the pump, from 1.60 to 1.27 times the impeller outer diameter. Moreover, the new stage is suitable for use in a multistage configuration. Comparisons with data provided in literature show that the performance of the stage is at the same level as standard pumps of the same class.

Acknowledgment

The authors would like to express their appreciation for the financial support from the Ministero dell'Istruzione, Università e Ricerca (MIUR) under the Research Project F.R.E.C.A. No. S636-P/DSPAR/01.

They would also like to express their gratitude to Professor Ennio Carnevale of the University of Florence and Dr. Edoardo Garibotti of Termomeccanica Pompe, for encouraging and promoting this joint research activity.

Nomenclature

A_f = flow passage area $A_f=Q/c(\mathrm{m}^2)$
B = blockage
c = absolute velocity (m/s)
C_p = diffuser recovery coefficient $C_p=(p_3-p_2)/(p_{02}-p_2)$
H = head (m)
m = meridional abscissa
n_s = specific speed $n_s=\omega(Q^{0.5}/H^{0.75})(\mathrm{rpm\ m}^{0.75}/\mathrm{s}^{0.5})$
p = pressure (Pa)
Q = volume flow rate (m^3/s)
s = curvilinear abscissa
x,r,θ = cylindrical coordinates
BEP = best efficiency point
DP = design point
L = length (m)
LE = leading edge
TE = trailing edge
w = width (m)

Greek

α = absolute flow angle $\alpha=\arctan(c_\theta/c_m)$ (deg)
β_{bl} = Blade turning angle $\beta_{bl}=\arctan(r(d\theta/dm))$ (deg)
η = efficiency
ω = impeller rotational speed (rpm)
ξ = diffuser loss factor $\xi=(p_{02}-p_{03})/(p_{02}-p_2)$

Subscripts

0 = stagnation quantities
1 = impeller inlet
2 = impeller outlet
3 = diffuser outlet
max = maximum value
tt = total to total

Superscripts

$*$ = reference value
tot = total value

References

[1] Gopalakrishnan, S., 1999, "Pump Research and Development: Past, Present and Future—An American Perspective," ASME J. Fluids Eng., **121**, pp. 237–247.
[2] Hergt, P. H., 1999, "Pump Research and Development: Past, Present and Future," ASME J. Fluids Eng., **121**, pp. 248–253.
[3] Zangeneh, M., Goto, A., and Takemura, T., 1996, "Suppression of Secondary Flows in a Mixed-Flow Pump Impeller by Application of Three-Dimensional Inverse Design Method: Part 1—Design and Numerical Validation," ASME J. Turbomach., **118**, pp. 536–543.
[4] Goto, A., Takemura, T., and Zangeneh, M., 1996, "Suppression of Secondary Flows in a Mixed-Flow Pump Impeller by Application of Three-Dimensional Inverse Design Method: Part 2—Experimental Validation," ASME J. Turbomach., **118**, pp. 544–551.
[5] Miner, S. M., 2000, "CFD Analysis of the First Stage Rotor and Stator in a Two Stage Mixed Flow Pump," *Proceedings of the Eigth ISROMAC Conference*.
[6] Shi, F., and Tsukamoto, H., 2001, "Numerical Study of Pressure Fluctuations Caused by Impeller-Diffuser Interaction in a Diffuser Pump Stage," ASME J. Fluids Eng., **123**, pp. 466–474.
[7] van Esch, B. P. M., and Kruyt, N. P., 2001, "Hydraulic Performance of a Mixed-Flow Pump: Unsteady Inviscid Computations and Loss Models," ASME J. Fluids Eng., **123**, pp. 256–264.
[8] Bonaiuti, D., Arnone, A., Corradini, U., and Bernacca, M., 2003, "Aerodynamic Redesign of a Mixed-Stage Pump Stage," 21st Applied Aerodynamics Conference, Orlando, FL.
[9] Goto, A., and Zangeneh, M., 2002, "Hydrodynamic Design of Pump Diffuser Using Inverse Design Method and CFD," ASME J. Fluids Eng., **124**(2), pp. 319–328.
[10] Goto, A., Nohmi, M., Sakurai, T., and Sogawa, Y., 2002, "Hydrodynamic Design System for Pumps Based on 3-D CAD, CFD, and Inverse Design Method," ASME J. Fluids Eng., **124**(2), pp. 329–335.
[11] Arnone, A., 1994, "Viscous Analysis of Three-Dimensional Rotor Flow Using a Multigrid Method," ASME J. Turbomach., **116**, pp. 435–445.
[12] Chorin, A., 1967, "A Numerical Method for Solving Incompressible Viscous Flow Problems," J. Comput. Phys., **2**, pp. 12–26.
[13] Baldwin, B. S., and Lomax, H., 1978, "Thin Layer Approximation and Algebraic Model for Separated Turbulent Flows," AIAA Paper No. 78–257.
[14] Arnone, A., Liou, M. S., and Povinelli, L. A., 1993, "Multigrid Calculation of Three-Dimensional Viscous Cascade Flows," J. Propul. Power, **9**(4), pp. 605–614.
[15] Arnone, A., and Pacciani, R., 1995, "Three-Dimensional Viscous Analysis of Centrifugal Impellers Using the Incompressible Navier-Stokes Equations," *First European Conference on Turbomachinery—Fluid Dynamic and Thermodynamic Aspects*, Erlangen, pp. 181–195.
[16] Arnone, A., and Benvenuti, E., 1994, "Three-Dimensional Navier-Stokes Analysis of a Two-Stage Gas Turbine," ASME Paper No. 94-GT-88.
[17] Arnone, A., Boncinelli, P., Munari, A., and Spano, E., 1999, "Application of CFD techniques to the Design of the *Ariane 5* Turbopump," *14th AIAA Computational Fluid Dynamics Conference*, AIAA Paper No. 99–3380, pp. 1087–1097.
[18] Hoschek, J., and Lasser, D., 1993, *Fundamentals of Computer Aided Geometric Design*, A. K. Peters, Wellesley, MA.

[19] Boehm, W., and Müller, A., 1999, "On de Casteljau's Algorithm," Comput. Aided Geom. Des., **16**, pp. 587–605.
[20] Mann, S., DeRose, T., and Winkenbach, G., 1993, "Computing Values and Derivatives of Bézier and B-Spline Tensor Products," Computer Science Department, University of Waterloo, Ontario, Research Report No. CS-93–31.
[21] Stepanoff, A. J., 1957, *Flow Pumps*, Wiley, New York.
[22] Japikse, D., Marscher, W. D., and Furst, R. B., 1997, *Centrifugal Pump Design and Performance*, Concepts ETI, Wilder, VT.
[23] Japikse, D., 1986, "A New Diffuser Mapping Techniques Part 1: Studies in Component Performance," ASME J. Fluids Eng., **108**(2), pp. 148–156.
[24] ESDU, 1974, "Performance in Incompressible Flow of Plane-Walled Diffusers With Single Plane Expansion," ESDU International, Engineering Sciences Data Item No. 74015.

Control of Rotor Tip Leakage Through Cooling Injection From the Casing in a High-Work Turbine

Thomas Behr
Turbomachinery Laboratory,
ETH Zurich,
CH-8092 Zurich, Switzerland
e-mail: behr@lsm.iet.mavt.ethz.ch

Anestis I. Kalfas
Department of Mechanical Engineering,
Aristotle University of Thessaloniki,
GR-54124 Thessaloniki, Greece

Reza S. Abhari
Turbomachinery Laboratory,
ETH Zurich,
CH-8092 Zurich, Switzerland

This paper presents an experimental investigation of a novel approach for controlling the rotor tip leakage and secondary flow by injecting cooling air from the stationary casing onto the rotor tip. It contains a detailed analysis of the unsteady flow interaction between the injected air and the flow in the rotor tip region and its impact on the rotor secondary flow structures. The experimental investigation has been conducted on a one-and-1/2-stage, unshrouded turbine, which has been especially designed and built for the current investigation. The turbine test case models a highly loaded, high pressure gas turbine stage. Measurements conducted with a two-sensor fast-response aerodynamic probe have provided data describing the time-resolved behavior of flow angles and pressures, as well as turbulence intensity in the exit plane of the rotor. Cooling air has been injected in the circumferential direction at a 30 deg angle from the casing tangent, opposing the rotor turning direction through a circumferential array of ten equidistant holes per rotor pitch. Different cooling air injection configurations have been tested. Injection parameters such as mass flow, axial position, and size of the holes have been varied to see the effect on the rotor tip secondary flows. The results of the current investigation show that with the injection, the size and the turbulence intensity of the rotor tip leakage vortex and the rotor tip passage vortex reduce. Both vortices move toward the tip suction side corner of the rotor passage. With an appropriate combination of injection mass flow rate and axial injection position, the isentropic efficiency of the stage was improved by 0.55 percentage points. [DOI: 10.1115/1.2777185]

Introduction

Modern gas turbine designs aim to reach the highest possible turbine entry temperatures in order to increase cycle efficiency and turbine specific work. Different cooling strategies have been developed in order to achieve adequate life for all components that are exposed to these high temperature gas flows. One critical region for cooling in a high-pressure turbine is the blade tip area, which experiences high thermal loads and which is difficult to cool. A second aspect in optimizing turbine efficiency is the reduction of aerodynamic losses. The unshrouded design of high-pressure rotor blade rows introduces high losses due to tip leakage flows. Booth [1] found tip leakage losses to be in the order of up to one-third of the overall stage losses.

Several strategies for reducing losses due to blade tip gap flows have been the subject of a number of investigations over the past decade. According to Denton [2], the loss related to tip leakage flows is proportional to a discharge coefficient. Further, the loss scales with the velocity distribution around the blade tip, and thus with the loading of the blade tip.

One way of changing the discharge coefficient without affecting significantly the pressure distribution around the tip profile is to modify the blade tip geometry. Contouring can be done by including squealer rims or radii along the edges of the tip. Booth [3] presented test on a series of different tip geometries and evaluated the related discharge coefficients. Bindon and Morphis [4] tested three different tip geometries in a linear cascade. They found that the discharge coefficient is not necessarily representative of the overall loss associated with the tip leakage flow. It does not account for losses due to mixing of the tip leakage flow downstream of the rotor. In the investigation of Kaiser and Bindon [5] in a 1.5-stage rotating rig, the plain tip was shown to have the best performance compared to other geometries tested. With a tip that is radiused along the edges of the pressure side, the vena contracta that usually forms inside the tip gap could be almost completely eliminated. Other studies in rotating rigs concerning this area of research have been presented by Yoshino [6] and Camci et al. [7]. A numerical analysis examining the influence of improved tip concepts has been described by Mischo et al. [8] and Chander et al. [9].

The possibility of reducing tip leakage flows through a reduced loading of the tip region has been discussed by De Cecco et al. [10] and Yamamoto et al. [11]. Staubach et al. [12] achieved the off-loading of the tip by applying 3D design strategies to the profiles. Tip lean was found to be beneficial for this purpose; however, its application is limited due to stresses within the rotor blade.

Offenburg et al. [13] investigated the effect of different trenches within the casing around the rotor on efficiency of the stage. The function of trenches within the casing was found to be dependent on the tip gap height. Up to a relative tip gap of 2.3% blade span, a straight casing contour has been shown to yield the best results.

On the effect of tip leakage in a multistage environment, Harvey [14] concluded that no benefit results from the tip leakage flow once it has formed into a vortex. In order to limit the losses that this vortex generates in subsequent blade rows, the tip leakage flow and thus the strength of the vortex have to be reduced.

Another approach in order to reduce the losses due to tip leakage has been examined by Dey and Camci [15] and Rao and Camci [16,17]. Coolant was injected from the blade tip into the tip gap in order to reduce the mixing losses due to the tip leakage.

Contributed by the International Gas Turbine Institute of ASME for publication in the JOURNAL OF TURBOMACHINERY. Manuscript received January 26, 2007; final manuscript received March 16, 2007; published online May 5, 2008. Review conducted by David Wisler. Paper presented at the ASME Turbo Expo 2007: Land, Sea and Air (GT2007), Montreal, Quebec, Canada, May 14–17, 2007, Paper No. GT2007-27269.

Jets at different discrete positions and blowing ratios were evaluated. An influence of the injection rate on the radial position of the tip leakage vortex and of the injection position on its strength could be detected.

The concept of injecting air from the rotor casing through circumferential slots onto the rotor blade tip was proposed by Auyer [18]. Minoda et al. [19] injected air in a similar way through arrays of inclined holes at three axial positions. The inclined jets at an angle of 30 deg opposed the rotor turning direction. It was found that the flow could be influenced down to a radial position of 50% span; across this range, the relative rotor exit angles were increased from 100% to 70% span and reduced from 70% to 50% span. The promising observations of these investigations are based on steady state measurements in the stator relative frame.

In gas turbine engines, the external side of the high-pressure turbine rotor casing is generally cooled with compressor discharge air. The cooling is necessary for the casing part to withstand the temperatures of the rotor inlet gas that may be 1400°C and higher. After cooling the casing, the cooling air is purged into the gas path of the turbine, where it mixes out with the main flow. The current approach investigates the injection of cooling air from the rotor casing onto the rotor tip. This injection is used to control and reduce the development of the rotor tip secondary flows and hence improve the aerodynamic performance. In contrast to previous work and to understand the aerodynamics of this complex problem, unsteady measurement techniques are applied, which allow a study of the time-resolved flow in the rotor-relative frame. This experimental approach is supported by a numerical study by Mischo et al. [20].

Experimental Method

Turbine Test Rig Facility. The experiments for the current investigation have been conducted on the 1.5-stage unshrouded axial turbine test rig at the Turbomachinery Laboratory of ETH Zurich. A cross section view of the turbine module is presented in Fig. 1. Global parameters of the turbine at the design operating point are shown in Table 1. The characteristics of each blade row are presented in Table 2.

The air loop of the facility is of a quasiclosed type and includes a radial compressor, a two-stage water to air heat exchanger, and a calibrated venturi nozzle for mass flow measurements. Before the flow enters the turbine section, it passes through a 3 m long straight duct, which contains flow straighteners to ensure an evenly distributed inlet flow field. Downstream of the turbine, the air loop is open to atmosphere. A dc generator converts the turbine power and controls the rotational speed of the turbine. A torque meter measures the torque that is transmitted by the rotor shaft to the generator. The turbine entry temperature is controlled to an accuracy of 0.3% and the rpm is kept constant within ± 0.5 min^{-1} by the dc generator. The pressure drop across the turbine is stable within 0.3% for a typical measurement day. More detailed information on the test rig can be found in Ref. [21].

Measurement Techniques. The flow field data presented in the paper are derived from time-resolved probe measurements in a plane 15% rotor axial chord downstream of the rotor trailing edge. The unsteady pressure measurement technology of the fast-response aerodynamic probes (FRAPs) has been developed at the LSM (Kupferschmied et al. [22] and Pfau et al. [23]). The mainstream flow field was measured using a novel 1.8 mm tip diameter, two-sensor FRAP in virtual-four-sensor mode to provide two-dimensional, time-resolved flow field information. Each measurement plane is resolved by a grid of 27 points in the radial direction clustered close to the end walls, and 20 equally spaced points in the circumferential direction, covering one stator pitch. The time-resolved pressure signals are acquired at each measurement point at a sampling rate of 200 kHz over a period of 2 s. The data sets are processed to derive basic flow quantities, i.e., total and static pressures, flow yaw and pitch angles, velocity components, and Mach number, by applying a phase lock average over 85 rotor revolutions. For the data evaluation, three consecutive rotor passages were selected. Each rotor pitch is resolved in time by 82 samples. The frequency response of the probe allows flow features to be captured at frequencies up to 35 kHz. With this two-sensor probe technology, it is also possible to determine flow turbulence information (Porreca et al. [24]). The FRAP technology also provides temperature data at a frequency of up to 10 Hz.

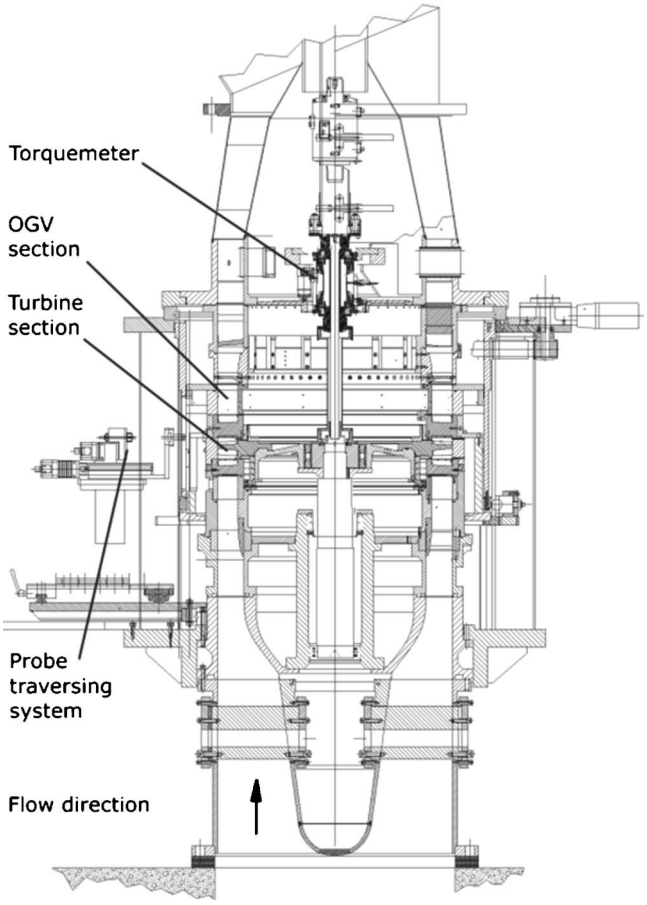

Fig. 1 "LISA" 1- and –1/2-stage axial turbine facility

The time-resolved static pressure distribution of the base line configuration at the rotor casing has been measured using miniature piezoresistive differential pressure transducers (Endevco 8507C-5) having a head diameter of 2.67 mm and a resonance frequency of 85 kHz. A sector of the rotor casing of the size of

Table 1 Main parameter of "LISA" 1.5-stage axial turbine research facility at design operating point (measured)

Turbine	
Rotor speed (rpm)	2700
Pressure ratio (1.5 stage, total to static)	1.60
Turbine entry temperature (°C)	55
Total inlet pressure (bar abs norm)	1.4
Mass flow (kg/s)	12.13
Shaft power (kW)	292
Hub/tip diameter (mm)	660/800
First stage	
Pressure ratio (first stage, total to total)	1.35
Degree of reaction (—)	0.39
Loading coefficient $\psi=\Delta h/u^2$ (—)	2.26
Flow coefficient $\phi=c_x/u$ (—)	0.65

Table 2 Characteristic geometry and performance parameters of the 1.5-stage turbine configuration (performance values are derived from five-hole-probe measurements at the design operating point)

	Stator 1	Rotor	Stator 2
Number of blades	36	54	36
Inlet flow angle (deg) (midspan)	0	54	−42
Exit flow angle (deg) (midspan)	73	−67	64
Aspect ratio (span/chord)	0.87	1.17	0.82
Blade row relative exit Mach numbers (—) (average)	0.54	0.50	0.48
Reynolds number based on true chord and blade row relative exit velocity (—)	7.1×10^5	3.8×10^5	5.1×10^5

one stator pitch has been resolved with a mesh of 7 axial and 40 equidistant circumferential positions. Data from all sensors have been acquired simultaneously at a sampling rate of 100 kHz.

Cooling Air Injection. The cooling air injection is applied through an injection window that covers a sufficiently representative sector of five rotor pitches. A picture of the injection window arrangement is shown in Fig. 2. The inner contour of the rotor casing ring and the injection window have been machined together in order to ensure a continuous inner contour. The part of the window that faces the rotor tip area is interchangeable. In this way, different injection plate configurations can be tested with a short changeover time.

The cooling air is provided by both an air supply system that dehumidifies the air and controls the temperature and the mass flow. A detailed description of the system can be found in Ref. [25]. In order to achieve a uniform distribution of the injected air, the injection window module has a symmetric shape. The air enters the plenum of the module from two sides. To further homogenize the air, the plenum is divided into two chambers. The air enters Plenum 1, before it passes through a screen of 3×40 large holes to reach Plenum 2. The total pressure and total temperature are measured in Plenum 2.

For the current investigation, three axial injection positions were tested (Table 3). The axial positions were chosen to counteract the formation of the tip leakage vortex. With all configurations, air is injected circumferentially against the rotor turning direction at an angle of 30 deg relative to the casing's tangent in order to oppose the rotor tip leakage flow. For each configuration, cooling air is injected at two mass flow rates representing an injection of 0.7% and 1.0% of the turbine mass flow on the full annulus at the conditions shown in Table 4. Differences between the discharge characteristics of the injection configurations have been found to be negligible. Reference measurements for all three configurations with no injection are made with the holes sealed from the inside of the plenum with tape.

Table 3 Geometric parameters of injection configurations

Configuration	A	B	C
Rotor axial chord	30	50	30, 50
Number of holes/rotor	10	10	10+10
Hole diameter (mm)	1.0	1.0	0.7
Hole angle relative to	30	30	30
Length/diameter ratio	8.0	8.0	11.4

Rotor Tip Flow and Casing Injection

In axial flow turbines, the required clearance between the tips of the rotor blades and the surrounding casing results in secondary flows. Fluid that passes through the tip gap of the rotor forms a tip leakage vortex, which has a major contribution to the loss production inside the rotor. A detailed literature review on the studies of tip clearance flow in unshrouded axial turbines has been presented by Sjolander [26]. The following section gives an overview of the secondary flow phenomena in the rotor blade row of the turbine configuration under investigation. In the following, the problem of the casing air injection will be addressed. Based on the experimental findings, the interaction between rotor secondary flows and injection fluid will be discussed.

In Fig. 3, a schematic view of the secondary flow development inside a rotor is shown. The incoming boundary layers at the hub and tip end wall experience a strong adverse pressure gradient as

Table 4 Injection air conditions

Injection rate (% of passage mass flow)	0.7	1.0
Plenum total pressure $p_{t,I}$ (kPa)	128	140
Plenum total temperature $T_{t,I}$ (°C)	32.5	32.5
Average density ratio DR (—)	1.0	1.0
Average blowing ratio BR (—)	2.2	3.2
Average momentum flux ratio IR (—)	4.8	10.3

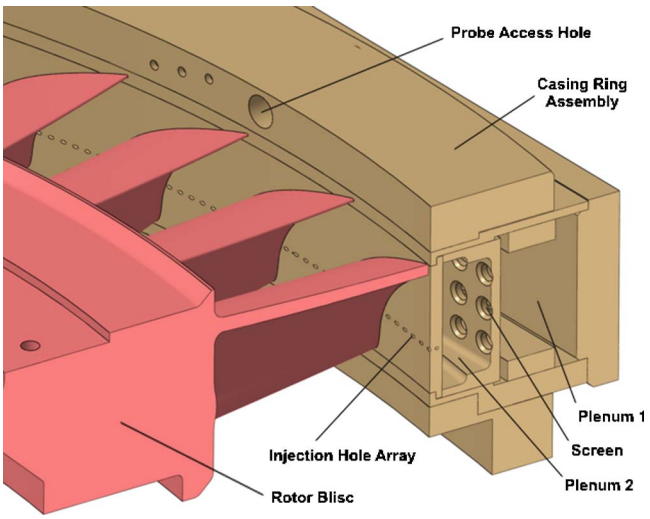

Fig. 2 Air injection system and probe access within traversable rotor casing ring assembly

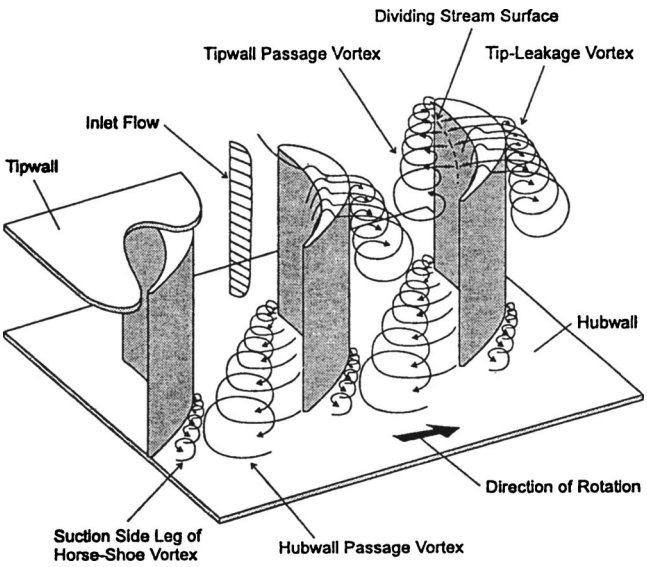

Fig. 3 Secondary flow model after Sjolander [26]

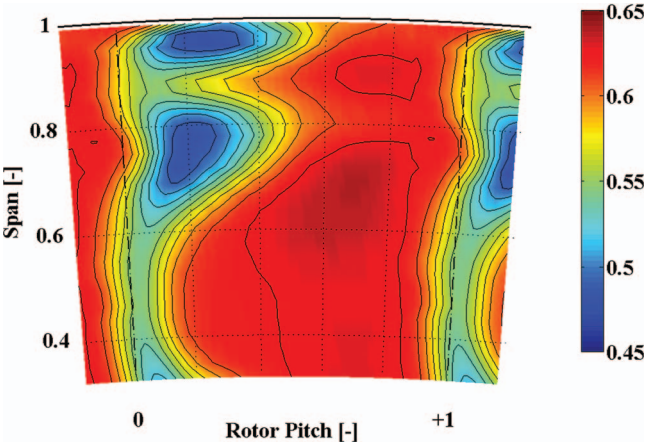

Fig. 4 Relative total pressure coefficient $C_p t_{rel}$ (-) measured at the rotor exit (rotor-relative frame, time averaged)

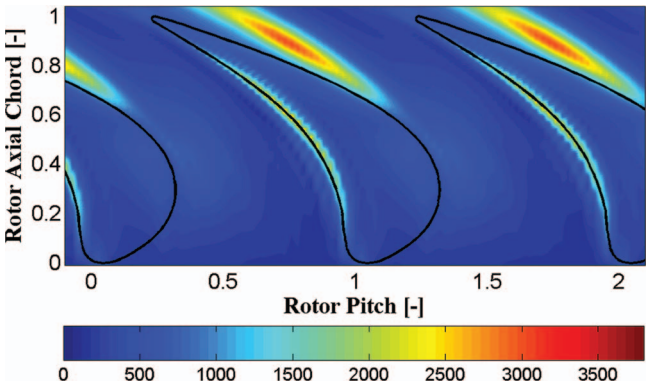

Fig. 5 rms of nondeterministic pressure variation (Pa) measured at the rotor casing (rotor-relative frame, time averaged)

they approach the leading edge of the rotor, which leads to the formation of a "horseshoe" vortex that wraps around the profile. The incoming end wall flow that enters the passage is influenced by the pressure gradient between the pressure and suction sides. Due to the difference in momentum across the boundary layer, the pressure gradient drives the fluid that is adjacent to the end wall closer to the suction side. This crossflow on the end wall subsequently rolls up into the passage vortex, which often merges with the pressure side leg of the horseshoe vortex.

In the tip region of an unshrouded rotor blade, the characteristics of secondary flows differ from the previously described model. Due to the reduced strength of the adverse pressure gradient at the tip gap, the horseshoe vortices appear only at small clearances. In addition, a tip leakage vortex develops. At the blade tip, the pressure gradient between pressure and suction side sucks off mass flow from the tip region of the pressure side into the tip gap. The inlet flow to the gap separates along the pressure side corner of the tip gap and forms a separation bubble. The unseparated flow passes through a vena contracta that is between the separation bubble and the casing. This vena contracta region is characterized by a maximum in the flow velocity and a minimum in the static pressure.

The tip leakage flow leaves the gap at a high velocity and interacts with the flow on the blade suction side. The passage flow and the passage vortex cause the leakage jet to roll up into the tip leakage vortex. In the rotor exit plane, this counter-rotating pair of tip leakage vortex and tip passage vortex are observed to be attached to the suction side. The tip leakage vortex is additionally confined by the casing end wall.

In Fig. 4, the position of the secondary flows in the rotor tip region can be confirmed from the distribution of the relative total pressure coefficient. In this plane at 15% rotor axial chord downstream of the rotor trailing edge, the vortices can be identified as regions of low relative total pressure. Hence, the tip leakage vortex extends from 90% to 100% span, adjacent to the tip passage vortex from 60% to 90% span. Further, radially inward on the left side of the vortices, the low-pressure field of the rotor wake can be identified. A more detailed discussion of the flow field has been presented in Ref. [21].

Figure 5 shows the nondeterministic pressure distribution at the casing wall measured with fast-response pressure sensors. The value plotted represents the variation (or rms) of the phase-locked pressure signal $\sigma(p'_w)$ calculated out of 180 values. The distribution of this parameter has been calculated for each stator-rotor relative position. Afterward, all these distributions have been averaged in the rotor-relative frame. At the position of the vena contracta and the separation bubble at the pressure side corner of the tip, a region with high levels of pressure unsteadiness can be found from 20% to 80% axial chord. This region marks the position where the tip leakage fluid enters the tip gap. At the opposite side of the tip, the region of the tip leakage vortex can clearly be distinguished. The position of the start of the vortex development at 60% rotor axial chord coincides with the approximate position of the peak suction pressure. Inside the vortex region, the maximum level of unsteadiness is at a position of 90% rotor axial chord. Xiao and Lakshminarayana [27] investigated the development of tip leakage vortices using laser Doppler velocimetry (LDV). They found that a reduction of the vortex circulation downstream 90% rotor axial chord coincided with a slower growth of the vortex. If one assumes that the circulation and the unsteadiness of a vortex are correlated, this effect is also seen in the present measurement.

Due to the fact that the rotor is embedded in between two stators, the rotor exit flow as well as the development of rotor secondary flows are influenced by blade row interactions. Figure 6 shows the nondeterministic pressure distribution on the rotor casing at 104% rotor axial chord versus the time of two stator blade passing periods. The tip leakage vortex is again indicated by high levels of pressure unsteadiness. The relative circumferential position of the tip leakage vortex to the rotor trailing edge varies with its position relative to the subsequent stator leading edge. The unsteady casing pressure measured further upstream shows that the blade row interaction affects the development of the entire tip leakage vortex up to the position where the vortex first leaves the tip gap. This effect is seen in a modulation of unsteadiness and a variation of the relative position of the vortex. This phenomenon is also discussed in Ref. [21].

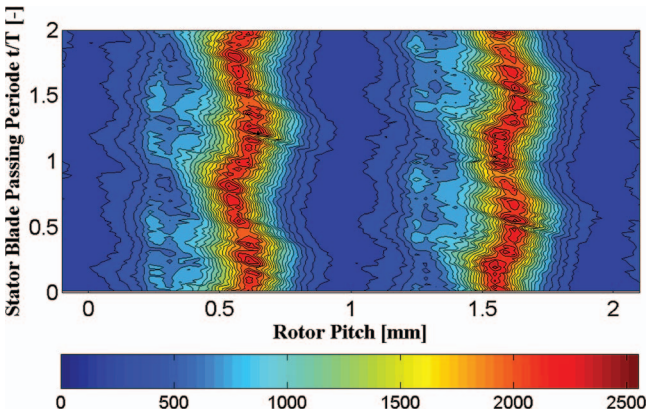

Fig. 6 rms of nondeterministic pressure variation (Pa) measured at the rotor casing at 104% rotor axial chord versus stator blade passing period (rotor-relative frame)

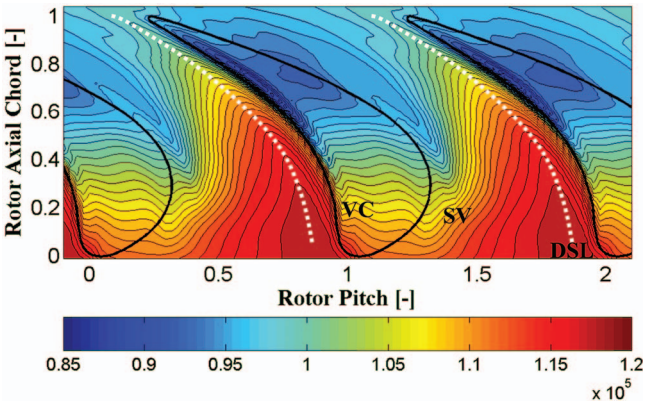

Fig. 7 Static pressure (Pa) measured at the rotor casing (rotor-relative frame, time averaged)

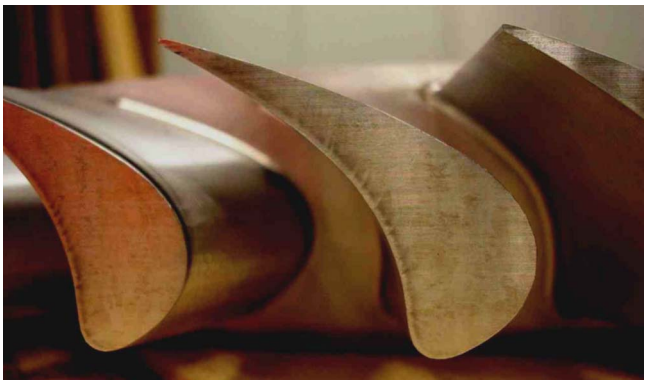

Fig. 9 Model of the flow directions at the casing in the rotor-relative frame of reference

The acceleration of the flow into the tip gap reduces the static pressure close to the pressure side. The maximum static pressure at the tip occurs along the dividing stream surface (see Fig. 3) that is close to the blade pressure side. Fluid on one side of this surface goes into the tip gap. The fluid on the other side forms the cross-passage flow that is then accelerated toward the suction side and forms the passage vortex. Another secondary flow feature develops at the tip of rotating blade rows (not shown in Fig. 3) and is caused by the relative movement of the blade to the tip casing wall. The casing boundary layer is scraped by the suction side of the blade tip and moves down the suction surface. This shear layer eventually rolls up into the scraping vortex, which rotates counter to the tip leakage vortex. The scraping vortex results in a low static pressure region at the end wall.

The previously described secondary flow features at the casing are evident in the distribution of static pressure at the casing (see Fig. 7). The trace of the dividing stream surface at the casing is indicated by the static pressure maxima of the dividing stream line (DSL) that is offset from the pressure side toward the passage. On the pressure side, a line of static pressure minima is also seen and is a result of the vena contracta (VC) region. A second line of static pressure minima, which is offset from the suction side toward the passage, is caused by fluid that has been accelerated due to the proximity of the blade. This fluid goes along the suction surface, and is referred to as the scraping vortex (SV).

The oil flow visualization near the pressure side on the blade tip surface (Fig. 8) shows the position of the line of the separation bubble as well as the flow direction across the separation bubble. The region along the pressure side corner of the tip is blank, whereas further inward oil deposits from the recirculation are seen.

In summary, the interaction between the injected fluid and the main flow can be subdivided into two regions. These regions are distinguishable depending on the manner in which the injected fluid enters the main flow path. Region A (shown as the gray shaded region in Fig. 9) is comprised of the cross flow from the pressure side to the suction side and the SV that is close to the suction side. Fluid in this region tends to move from the pressure to the suction side across the passage in the rotor-relative frame of reference. Region B is dominated by the fluid that passes through the tip clearance and eventually forms the tip leakage vortex. This region extends circumferentially from the dividing stream surface close to the suction side across the rotor tip until the rotor tip suction side. It further includes the region downstream of the rotor suction side, which is dominated by the tip leakage vortex. The flow in this region moves faster in the circumferential direction than the rotor. Therefore, it moves in the opposite circumferential direction in the rotor-relative frame then the flow of region A.

The mass flow rate of the cooling air injection is determined by the pressure difference between the plenum total pressure and the static pressure at the exit of the injection hole and the discharge coefficient. Each injection hole is exposed to a static pressure field that varies with the relative position of the rotor blades. Thus, the injection mass flow rate changes accordingly. The maximum mass flow occurs with the lowest static pressure and vice versa. Figure 10 shows the circumferential distribution of static casing pressure at the two axial injection positions considered in the current investigation. The vertical blue lines in the plots mark the approxi-

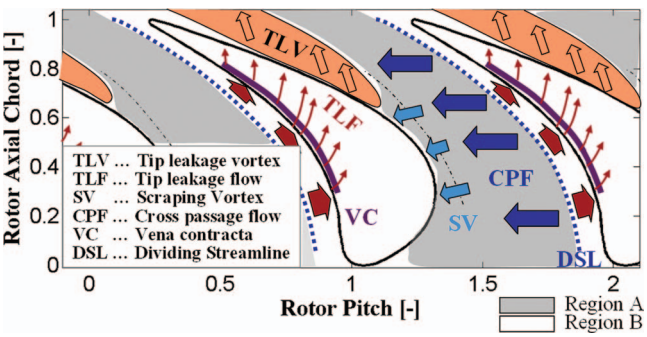

Fig. 8 Flow visualization on rotor tip surface

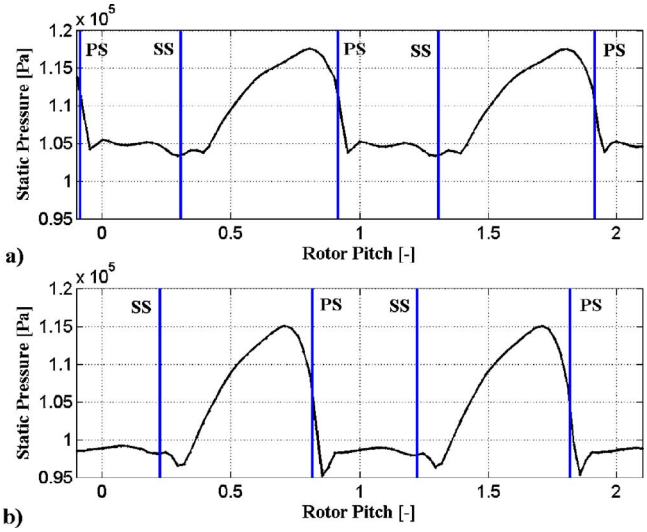

Fig. 10 Static pressure distribution measured at the rotor casing (rotor-relative frame, time averaged) at two rotor axial chord positions; (*a*) 30% and (*b*) 50%

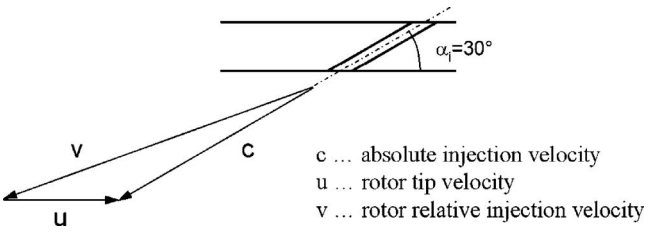

Fig. 11 Velocity triangle of casing injection

mate positions of the pressure and suction sides. It is evident that on the surface of the blade tip, the highest injection rate occurs at relatively constant level. Within the passage, the injection rate reduces from this level until the dividing stream surface that is close to the pressure side at which the static pressure reaches its maximum.

The inclined injection at an angle of 30 deg introduces a circumferential velocity component that is opposite to the rotor turning direction. In the rotor-relative frame, the injection angle is reduced to approximately 20 deg relative to the casing tangent. The velocity triangle of the injection is shown in Fig. 11.

In order to show the evolution of the injected fluid within the rotor passage, the axial velocity in the rotor exit plane can be considered. Figure 12(*a*) shows the distribution of axial velocity of the base line case. The midpassage flow of the rotor has an average axial velocity of around 70 m/s. The regions occupied by the tip leakage vortex and tip passage vortex show a reduction of axial velocity of up to 30%. Figure 12(*b*) visualizes the change in axial velocity due to an injection of 1% cooling mass flow at 30% rotor axial chord (injection configuration A). The velocity change is the difference between the axial velocities of the injection and the base line case. The mass flow difference derived from the measured data of both flow fields is equivalent to the injected mass flow. A substantial increase in axial velocity is seen in the core of the tip passage vortex (see also Fig. 4). Also, in the region of the tip leakage vortex, there is a slight increase. The rest of the flow field is nearly unaffected. This indicates that at the exit of the rotor, most of the injected fluid has accumulated within the tip passage vortex.

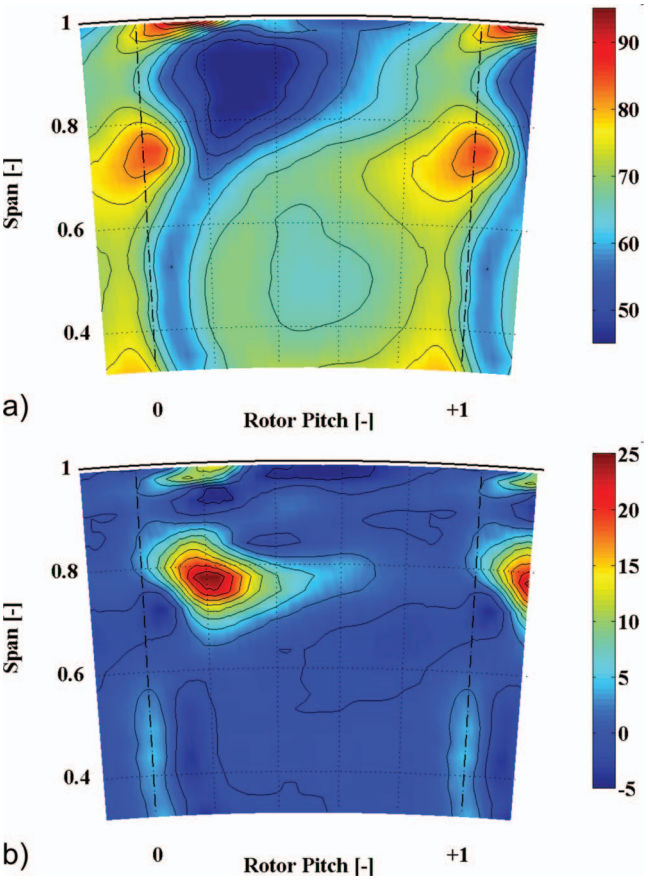

Fig. 12 Rotor-relative frame, time-averaged contours: (*a*) axial velocity c_x (m/s) measured at the rotor exit, baseline, (*b*) axial velocity difference Δc_x (m/s) measured at the rotor exit between injection A-1% and base line case

Based on the flow models and experimental data described above, the main effects of cooling air injection can be described as follows:

(1) Within the tip gap region until the dividing stream surface, the cooling jets oppose the direction of the tip leakage fluid. Due to the momentum exchange between the jets and the leakage fluid and the increased static pressure upstream of the holes, the leakage fluid is reduced and deflected to a more downstream position. Therefore, the leakage vortex leaves the suction side at a more downstream position. Within the rotor exit plane, the vortex has a reduced strength and is closer to the suction side.

(2) The upstream border of the passage vortex marks the position of an end wall separation line, where the boundary layer of the incoming flow and the new boundary layer of the cross-passage flow meet each other. This separation line moves upstream due to the casing air injection, such that the secondary flow of the passage vortex then impinges on the suction side of the opposing blade at a more upstream position. The reason for this effect is the increase in static pressure upstream of the injection holes, which displaces the incoming low momentum fluid. Secondly, the injection is directed in the same direction as the cross-passage flow. Therefore, it will add to it a circumferential velocity component, which will accelerate the development of the passage vortex.

In the next section, this description of the flow is verified with experimental data.

Effect of the Injection Mass Flow

For all injection configurations considered in this investigation, the following effects are seen and are more pronounced with *increasing* injection.

Tip Leakage Vortex and Tip Passage Vortex

Reduction of Vortex Turbulence Intensity. The position and the size of secondary flow features in the flow field can be identified from the turbulence intensities derived from the FRAP data. The distributions of turbulence intensity have been calculated for each measured stator-rotor relative position and then averaged in the rotor-relative frame. The measurements at the rotor exit of the base line case are presented in Fig. 13(*a*). The turbulence levels correlate well with the relative total pressure shown in Fig. 4. At the position of the tip leakage vortex, the highest turbulence levels are measured, and high levels are also seen in the region of the tip passage vortex.

With injection, the levels of turbulence intensity in the region of the rotor tip vortices are reduced by up to 35%. This effect is shown from the turbulence intensity differences of two cases with different injection mass flows in Figs. 13(*b*) and 13(*c*). The largest reduction of turbulence is in the tip passage vortex, as can be seen in blue contours at around 70% span. Hence, the injected fluid stabilizes the passage vortex.

In the region of the tip leakage vortex, a similar effect is seen; however, the largest reduction in turbulence occurs at midpitch and not at the center of the leakage vortex in the base line case

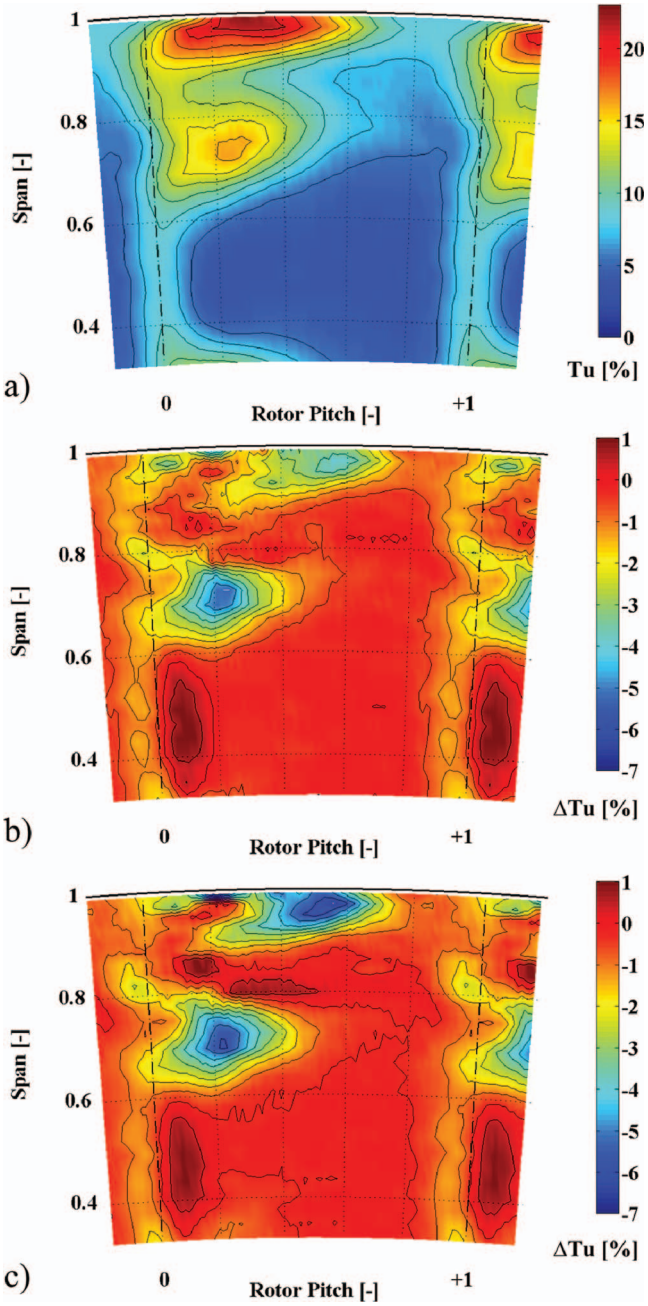

Fig. 13 Rotor-relative frame, time-averaged contours, injection configuration A; (*a*) turbulence Tu [%] measured at the rotor exit, baseline case, (*b*) turbulence difference ΔTu (%) measured at the rotor exit between injection A-0.7% and base line case, and (*c*) turbulence difference ΔTu (%) measured at the rotor exit between injection A-1% and base line case

(see Figs. 13(*b*) and 13(*c*)). It is thought that the injection reduces the vortex diameter. Hence, the vortex moves closer to the suction side of the blade and occupies less space in the midpitch region. Since the turbulence levels are reduced in the entire region from 90% to 100% span, it is concluded that the tip leakage vortex is changed not only in size and position but also reduces its turbulence intensity.

To quantify the overall effect on the flow field, the pitchwise mass-averaged values are presented in Fig. 14. The largest reductions of turbulence intensity are also seen in the vortex span regions, with reductions at around 2% for the tip leakage vortex and 1.5% for the tip passage vortex at an injection rate of 1% of the turbine mass flow.

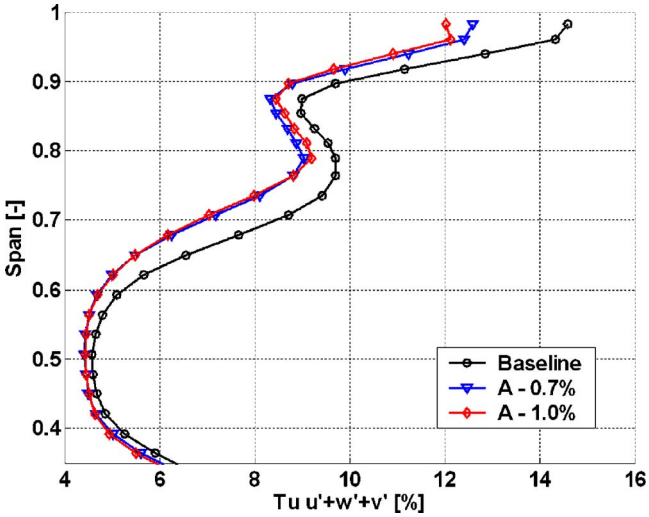

Fig. 14 Turbulence intensity (%) measured at the rotor exit (pitchwise mass averaged) of baseline case and injection configuration A at injection rates of 0.7% and 1.0%

Reduction of Vortex Size. The effect of the casing air injection on the vortex size has been described above. Another indication of this is seen in the pitchwise mass-averaged distribution of the flow yaw angle (see Fig. 15). In the flow region from 60% to 100% span, the characteristic overturning-underturning of the flow due to rotation of the vortices can be seen. The position of the minimum underturning due to the tip passage vortex is at around 75% span. This position moves radially outward with an increasing injection rate. Cooling injection of 1% of the turbine mass flow displaces the minimum by 4% span compared to the base line. This observation indicates that the passage vortex affects less fluid in the midspan region.

Increase of Vortex Overturning-Underturning. A second effect is seen in the distribution of flow yaw angles in Fig. 15. With an increasing injection rate, the underturning of the tip passage vortex and the overturning of tip leakage and tip passage vortex are

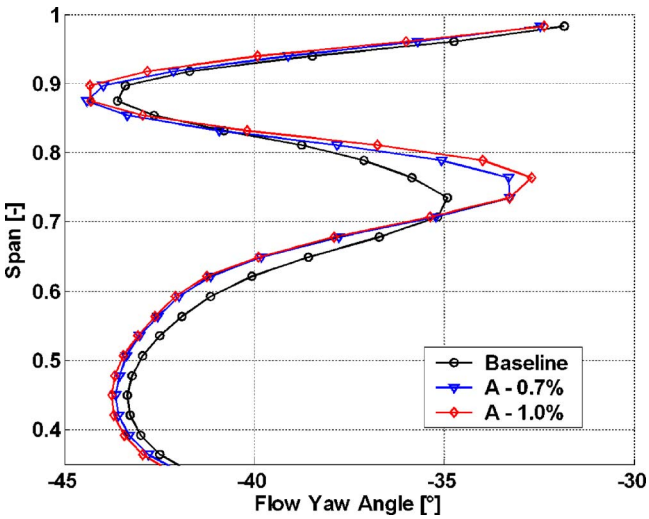

Fig. 15 Absolute yaw angle (%) measured at the rotor exit (pitchwise mass averaged) of baseline case and injection configuration A at injection rates of 0.7% and 1.0%

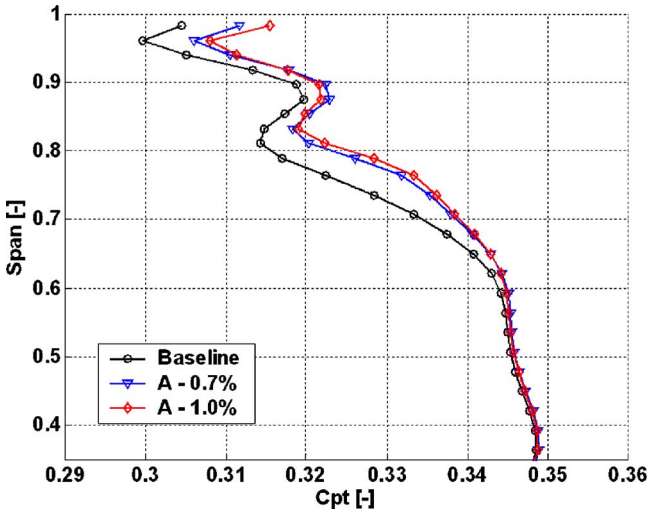

Fig. 16 Total pressure coefficient $C_p t$ (-) measured at the rotor exit (pitchwise mass averaged) of baseline case and injection configuration A at injection rates of 0.7% and 1.0%

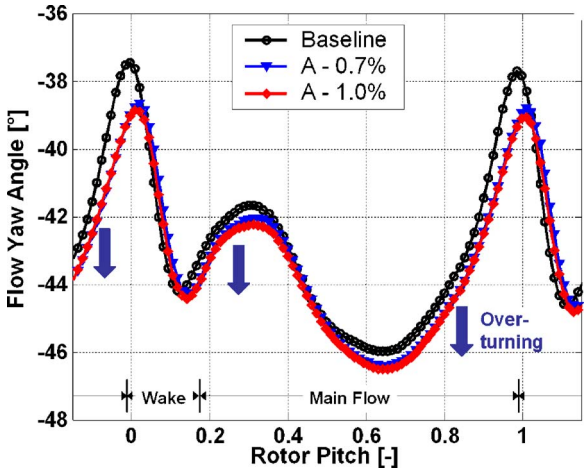

Fig. 18 Flow yaw angle at 50% span (deg) measured at the rotor exit for base line case and two injection mass flows (rotor-relative frame)

increased. This indicates that the casing injection increases the rotation of the tip passage vortex, which results in larger deviation of the flow from the design.

Increase of Total Pressure. The injection of cooling air from the casing adds energy to the flow, which increases the total pressure in the affected region. Figure 16 shows the pitchwise mass-averaged distribution of total pressure. An effect of the injection on the main flow is seen in the region between the casing and 60% span. The largest increase in total pressure occurs at the positions of the vortex centers, that is, at 75% and close to the casing end wall.

Rotor Wake

Shift Away From Suction Side. The injection of casing cooling air is seen to have secondary effects on other secondary flow features such as the rotor wake. In Fig. 17, the pitchwise distribution of axial velocity at the midspan of the rotor exit is presented. The wake of the rotor is identified from the deficit of the axial velocity that is a minimum at a rotor pitch position of 0.08. The wake is clearly displaced away from the suction side as the injection rate is increased (see also Fig. 12(*b*)). This suggests that the development of the suction side boundary layer on the rotor blade is altered in the presence of injection. It is thought that the modified passage vortex has an effect on the pressure distribution on the blade surface. The changed 3D loading on the blade then modifies the boundary layer and the wake development.

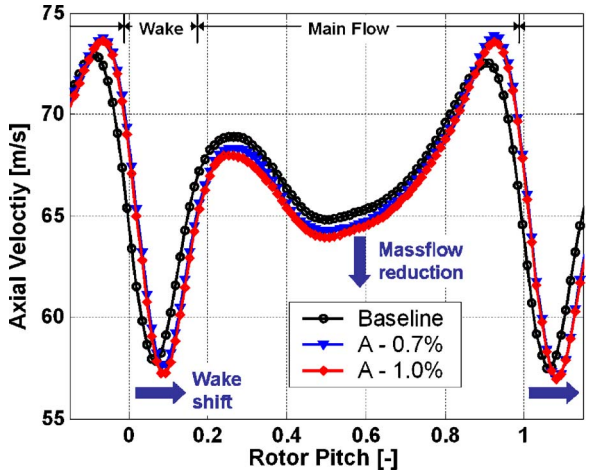

Fig. 17 Axial velocity c_x at 50% span (m/s) measured at the rotor exit for base line case and two injection mass flows (rotor-relative frame)

Increased Turning. In addition to the displacement of the wake, a change in the yaw exit angle of the fluid on both sides of the wake toward higher turning is observed. This effect is seen in the pitchwise distribution of absolute flow yaw angle at midspan, Fig. 18. At both rotor pitch positions of 0 and 0.3, the maxima of the exit angle are changed by up to 1 deg.

Main Flow

Reduction of Axial Velocity. The flow that is not directly affected by the rotor secondary flows is termed the main flow. It is observed that with injection, the axial velocity of the main flow at the midpitch is reduced. In Fig. 17, the distribution at the midspan shows a reduced axial velocity between rotor pitch positions of 0.3 and 1.0. This effect is also seen in the other injection configurations (see Fig. 19). The reason for this redistribution of mass flow is still under investigation.

Increased Turning. With injection, the exit angle of the rotor flow between 30% and 70% span changes toward higher turning. This effect is seen in the pitchwise mass-averaged yaw angle distribution in Fig. 15. The previously described reduction of axial velocity in this region results in the opposite effect, and is thus not the source of this increase.

Effect of the Injection Position

The injection of casing air into the rotor tip region has been investigated with three injection configurations at different axial positions:

(A) at 30% rotor axial chord
(B) at 50% rotor axial chord
(C) at 30% and 50% rotor axial chord

In the previous section, the detailed effects on the flow field have been described for the injection configuration A. In this section, the other injection configurations with 1.0% injection rate are also presented. The results are presented in terms of pitchwise mass-averaged radial distributions. In order to clarify the effect of the injection position, the differences relative to the base line case are also presented.

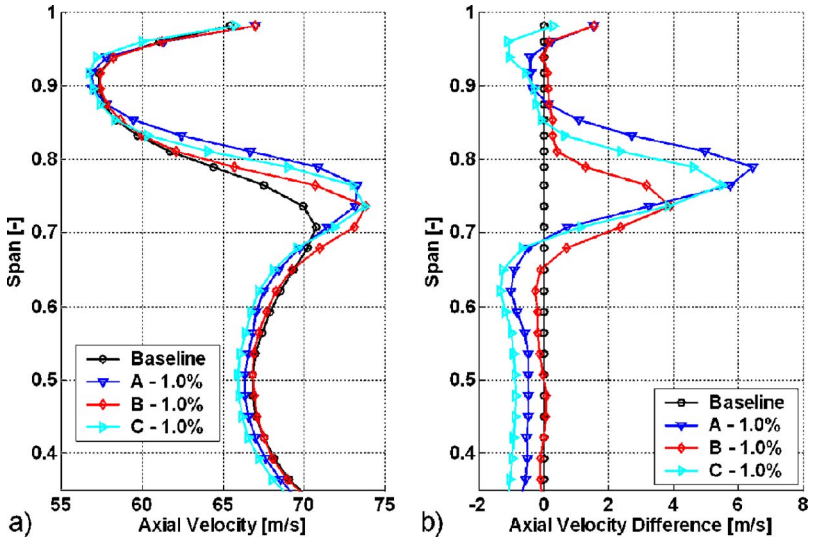

Fig. 19 Pitchwise averages of base line and three injection configurations at an injection rate of 1.0% turbine mass flow: (*a*) axial velocity (m/s) and (*b*) axial velocity difference from baseline case (m/s)

From the distribution of axial velocity presented in Fig. 19(*a*), it can be seen that the axial position of the injection has different effects. Interestingly, a more upstream injection (Case A) does not cause a deeper penetration of the cooling flow into the main flow compared to a more downstream injection (Case B). This is more clearly seen in the difference plot in Fig. 19(*b*). It is thought that the reason for this behavior is the effect the injection fluid has on the development of the rotor tip passage vortex. It has been shown above that the injection fluid accumulates mostly inside the passage vortex. Hence, depending on its radial position, an increase of axial velocity occurs.

The axial velocity distributions also show the extent of the redistribution of mass flow within the rotor passage. A more upstream injection (Case A) has the highest level of mass flow redistribution. In this case, the axial velocity is reduced in the midspan region of the wake between 30% and 70% span, whereas the axial velocity increases in the passage vortex region. A more downstream injection (Case B) shows a similar effect in the wake region, however, a smaller effect in the vortex region. The simultaneous injection at both axial positions (Case C) shows in the region of the passage vortex values in between the other two cases, which indicates a quasilinear behavior.

The change of radial position of the rotor passage vortex, which is inferred from the distribution of axial velocity, is confirmed in the distribution of flow yaw angles (see Fig. 20). The position of the passage vortex is changed the most for the most upstream injection case. The smallest radial shift occurs at the 50% rotor axial chord injection position. From the difference plot (Fig. 20(*b*)), it can be seen that the yaw angle distributions are almost linearly related to the axial injection position. The simultaneous injection at both axial positions (Case C) results in an angle distribution that is in between the two single-row injections (Cases A and B).

The effect of the casing injection to reduce the turbulence intensity of the rotor tip vortices is evaluated for the three injection cases in Fig. 21. Also, the turbulence distributions show a quasi-

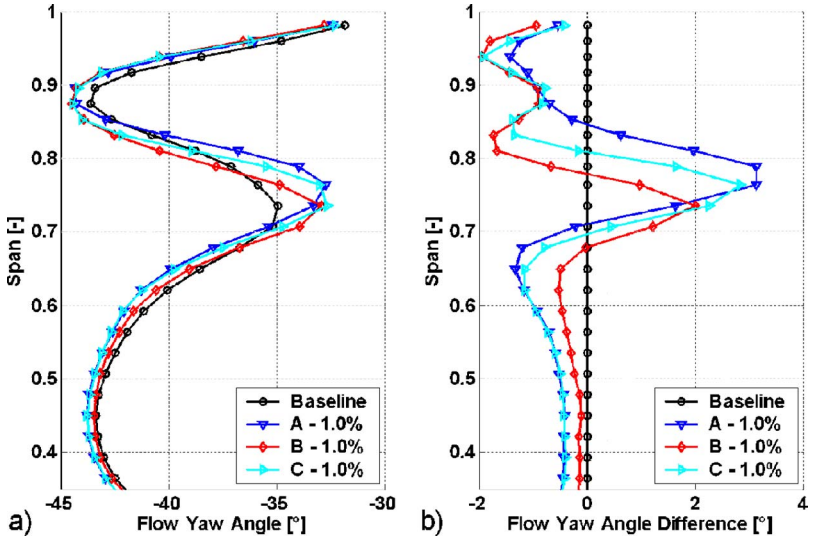

Fig. 20 Pitchwise averages of base line and three injection configurations at an injection rate of 1.0% turbine mass flow: (*a*) flow yaw angle (deg) and (*b*) flow yaw angle difference from base line case (deg)

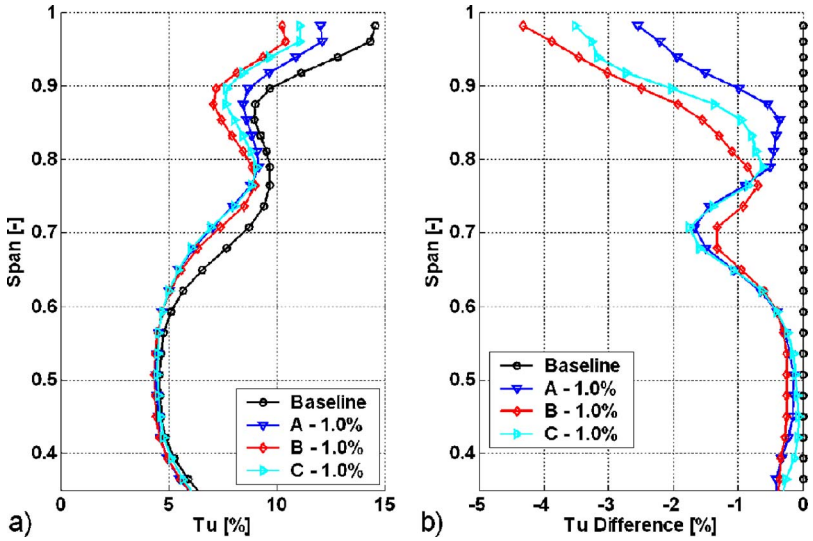

Fig. 21 Pitchwise averages of base line and three injection configurations at an injection rate of 1.0% turbine mass flow: (*a*) turbulence intensity (%) and (*b*) turbulence intensity difference from base line case (%)

linear relation to the axial injection position. The most upstream injection case yields the largest reduction of turbulence in the passage vortex. However, the same case shows a smaller reduction of turbulence in the tip region between 80% span and the casing end wall. It is thought that this behavior depends on which flow features are most affected by the casing injection. In Case A, the cross-passage flow and hence the passage vortex seem to be most changed. In Case B, the tip leakage is most affected by the casing air injection.

Discussion

The concept of injecting casing cooling air through an array of inclined holes into the tip region of a rotor increases the complexity of the flow in this region. The experimental data show that there are significant effects on the entire flow field of the rotor. Depending on where the injected air enters the rotor passage, it may attenuate or intensify the existing flow features, which are illustrated in Fig. 9.

Due to the fact that the injection is modulated by the pressure field of the rotor, a portion of the injected fluid interacts with the rotor tip leakage flow. The other portion of the flow is entrained into the cross-passage flow of the rotor, which generates the rotor tip passage vortex. Calculation of the pitchwise distribution of the injection yields a 1:1 ratio of the two mass flows. This ratio will depend on the specific turbine configuration, especially on the pitch area covered by the metal surface of the blade tip. The experiments have shown that both parts of the injected fluid can improve the aerodynamic performance of the rotor due to the mechanisms described below. Their final effect on the overall performance will be evaluated in the next section.

From the measurements of turbulence intensity, it is shown that the tip leakage vortex moves with injection closer to the rotor suction side and occupies a smaller pitch area in the rotor exit plane (see Fig. 13). In the opinion of the authors, this effect is a result of the injected air that counteracts the tip leakage flow and moves the onset of the tip leakage vortex to a more downstream position. As a result, the vortex occupies a smaller volume of the rotor passage and therefore reduces its interaction with the main flow on the blade suction side. The reduced turbulence intensity of the vortex implies a reduced level of turbulent kinetic energy, which should decrease the related loss. It is suggested that the injection stabilizes the rotating flow of the vortex, and hence causes a reduction of the turbulence intensity.

The portion of the injected air that is entrained in the cross-passage flow shows that there is potential to control the rotor tip passage vortex. The yaw angle measurements show that there is a modification of the vortex characteristic angle distribution. The increased level of overturning-underturning and the radial outward shift of this region indicate that the passage vortex is altered. Its rotational strength is increased but the diameter is reduced. As a consequence, the passage vortex moves further radial outward.

From measurements of axial flow velocity, it was concluded that the injected cooling mass flow accumulates mostly inside the tip passage vortex and the tip leakage vortex. Furthermore, probe measurements have shown an increased level of turbulent kinetic energy and temperature in the flow regions of the vortices with respect to the main flow. Downstream of the blade row, the hotter fluid of the vortex mixes with the colder fluid of the main flow. Hereby, the creation of losses is also a function of the temperature difference. The accumulation of colder air of the injection inside the vortex will reduce its temperature. Hence, the temperature gradient to the blade surface and thus the heat load on the blade as well as the mixing losses reduce.

A secondary effect of the air injection on the rotor wake and the rotor main flow is observed. It is thought that the modified shape and position of the tip leakage vortex and the tip passage vortex cause a change of the 3D pressure distribution on the rotor blade surface. Consequently, the development of the rotor wake is changed with injection, and results in a more detached position of the wake from the rotor suction side surface (see Fig. 17). In addition, the exit angle in the span region of the wake increases toward higher turning with the injection.

Performance

This section presents performance data of the injection cases investigated. On the basis of these values, the overall effect of the injection on the flow field and the performance of the turbine can be evaluated. From the turbulent velocity fluctuations of the flow, the turbulent kinetic energy (TKE) can be derived as

$$\mathrm{TKE} = 0.5(c'^2_{\mathrm{sw}} + c'^2_r + c'^2_\theta)$$

Figure 22 shows the relation between the TKE and the injection rate. The plot shows mass-averaged values in order to account for the mass flow redistribution in the flow field due to the injection. Even though the injected mass flow mainly accumulates in the vortex regions, the mass-averaged value of TKE reduces with in-

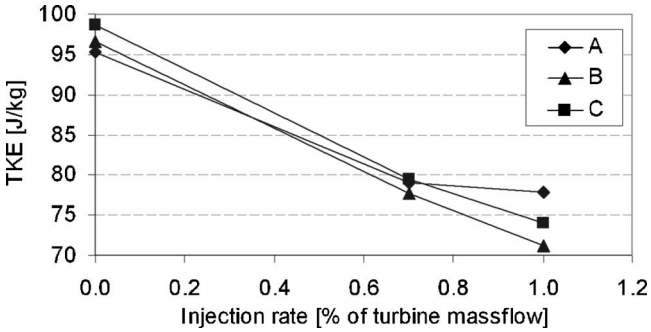

Fig. 22 TKE (J/kg) (mass averaged) versus injection rate (% of turbine mass flow)

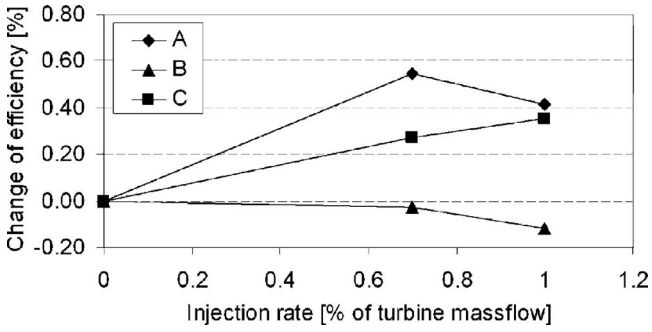

Fig. 23 Change of isentropic efficiency (%) compared to the base line case versus injection rate (% of turbine mass flow)

jection. All three injection cases show a reduction of 20–25% at an injection rate of 1% compared to the base line.

In Ref. [28], the high turbulent flow of the rotor tip vortices could be related to a periodically appearing region of reduced total pressure at the exit of the subsequent stator. Consequently, a reduced level of turbulence of the rotor vortices is thought to have a positive effect on the generation of total pressure loss within the next stator row.

In order to evaluate the overall effect of the injection on the performance of the turbine, the efficiency of the different injection cases is analyzed. The aerodynamic efficiency can be defined as the ratio of the real and isentropic enthalpy flux difference,

$$\eta = \frac{\Delta \dot{H}_{\text{real}}}{\Delta \dot{H}_{\text{is}}} \quad \text{where } \Delta \dot{H} = \dot{m}(h_{t,\text{in}} - h_{t,\text{out}}) \text{ and } h_t = c_p T_t$$

If various mass flows of different total temperatures and pressures are involved in the expansion process, as in the case of cooling injection, a general definition can be formulated,

$$\eta = \frac{\sum_{i=1}^{I} \dot{m}_i c_p T_{t,i} - \sum_{j=1}^{J} \dot{m}_j c_p T_{t,j}}{\sum_{i=1}^{I} \dot{m}_i c_p T_{t,i} - \sum_{j=1}^{J} \dot{m}_j c_p T_{t,\text{is},j}} \quad \text{with } T_{t,\text{out,is}} = T_{t,\text{in}} \left(\frac{p_{t,\text{out}}}{p_{t,\text{in}}} \right)^{(\kappa-1)/\kappa}$$

Based on the total pressure ratio and the inlet total temperature of each mass flow, its isentropic exit temperature can be derived.

In the current cases, the turbine inlet mass flow $\dot{m}_M$ and the injection mass flow $\dot{m}_I$ introduced energy into the system. The sum of both mass flows $\dot{m}_T = \dot{m}_M + \dot{m}_I$ leaves the rotor. The total temperatures and total pressures of the passage mass flows were measured with FRAP. The 2D temperature and pressure data of each plane are mass-averaged values. The values of the injection mass flow were measured inside the plenum with three PT100 sensors and three total pressure sensors.

According to the above equations, a thermodynamic isentropic efficiency value can be defined for the current case as follows:

$$\eta = \frac{\dot{m}_M c_p \overline{T_{t,M}} + \dot{m}_I c_p \overline{T_{t,I}} - \dot{m}_T c_p \overline{T_{t,T}}}{\dot{m}_M c_p \overline{T_{t,M}} \left(1 - \overline{\frac{p_{t,T}}{p_{t,M}}} \right)^{(\kappa-1)/\kappa} + \dot{m}_I c_p \overline{T_{t,I}} \left(1 - \overline{\frac{p_{t,T}}{p_{t,I}}} \right)^{(\kappa-1)/\kappa}}$$

The change of efficiency of the three injection cases compared to the base line is presented in Fig. 23. The most upstream injection at 30% axial chord (Case A) achieves the maximum efficiency gain of 0.55% at the injection rate of 0.7%. At 1% injection rate, the efficiency is increased only by 0.41%. The injection at 50% axial chord (Case B) reduces the efficiency by –0.12% at 1% injection. If air is injected from both axial positions (Case C), the efficiency is in between the two single-row injections.

These results reflect two competing mechanisms, which influence the effect of injection on the stage efficiency. From the momentum balance on the rotor, it can be seen that the injection against the rotor turning direction reduces the torque on the rotor. The differential torque of the injection is calculated as $\Delta M_I = r_{\text{tip}} \dot{m}_I c_{I,\theta}$. If the injection mass flow is increased, the injection velocity increases proportional to that. Therefore, the differential torque of the injection on the rotor is proportional to the square of the injection mass flow, $\Delta M_I \propto \dot{m}_I^2$. At the same time, the injection causes an increase in efficiency compared to the base line case. This positive effect comes from an improved aerodynamic performance of the stage due to the reduction of secondary flow losses in the tip region of the rotor. The results of this investigation suggest that an improvement of efficiency can be achieved with an injection in the upstream part of the tip leakage and cross-passage flow development region and a moderate injection rate.

Conclusions

A novel approach of using rotor casing cooling air for the control of rotor tip secondary flows is presented. The cooling air is injected in the circumferential direction at a 30 deg angle from the casing tangent, opposing the rotor turning direction through a circumferential array of ten holes per rotor pitch. Three different cooling air injection configurations are investigated at injection rates of up to 1% of the turbine mass flow. FRAPs and fast-response wall pressure sensors were used to measure the rotor flow field.

The effects of the casing air injection on the unsteady rotor flow field are analyzed in the current paper. A flow model that describes the interaction of the injected fluid with the main flow is presented. It subdivides the interaction between injected fluid and main flow in two regions. In one region, the injected fluid counteracts with the tip leakage fluid. In the other region, the fluid is injected into the cross-passage flow and influences the development of the passage vortex.

With the casing injection, it was possible to reduce the size of the rotor tip leakage and the tip passage vortex. Both vortices move toward the tip suction side corner of the rotor passage. In accordance to the flow model, the more upstream axial injection position at 30% axial chord affected more the passage vortex, whereas the injection at 50% axial chord had more effect on the tip leakage vortex.

The turbulence intensity of the rotor tip vortices reduces with the injection. The overall TKE of the rotor exit flow field reduces linearly with the injection rate. With an injection of 1% of the turbine passage mass flow, the TKE reduces by 25% with respect to the noninjection case.

From the isentropic efficiencies of the injection cases, it can be concluded that the aerodynamic performance of the rotor improves with injection. However, the negative momentum of the injected fluid reduces the work output of the rotor. In the current study, the optimum between both effects was found at an injection

of 0.7% of the turbine mass flow at 30% axial chord, which improved the isentropic efficiency by 0.55% percentage points.

Nomenclature

c = absolute flow velocity (m/s)
v = rotor-relative velocity (m/s)
u = rotor velocity (m/s)
c_p = specific heat capacity at constant pressure (J/kg K)
h = enthalpy (J/kg)
$\dot{m}$ = mass flow (kg/s)
p = pressure (Pa)
r = radius (m)
$\dot{H}$ = enthalpy flux (W)
M = torque (N m)
T = temperature (K)
tu = turbulence intensity (%)
TKE = turbulent kinetic energy (J/kg)
C_p = pressure coefficient $C_p=(p-p_{s,3})/(p_{t,0}-p_{s,3})$
DR = density ratio (ρ_c/ρ_m)
BR = blowing ratio $(\rho_c c_c/\rho_m c_m)$
IR = momentum flux ratio $(\mathrm{BR}^2/\mathrm{DR})$

Greek

ρ = density $(\mathrm{kg/m}^3)$
η = efficiency
ψ = loading coefficient $(\psi=\Delta h/u^2)$
ϕ = flow coefficient $\phi=c_x/u$
κ = isentropic coefficient $(\kappa c_p/c_v)$
σ = standard deviation

Abbreviations

FRAP = fast-response aerodynamic probe
PS = pressure side
SS = suction side
RMS = root mean square

Subscripts

0 = turbine inlet is isentropic
3 = turbine exit
x = axial coordinate
sw = streamwise coordinate
r = radial coordinate
θ = circumferential coordinate
c = coolant jet
m = local main flow
is = isentropic
rel = rotor relative
s = static
t = total
w = wall
I = rotor injection flow
M = first stage main inlet flow
T = first stage total exit flow

Superscripts

$\bar{}$ = mass average
$\cdot$ = turbulent fluctuation

References

[1] Booth, T. C., Dodge, P. R., and Hepworth, H. K., 1982, "Rotor-Tip Leakage Part I-Basic Methodology," ASME J. Eng. Power, **104**, pp. 154–161.
[2] Denton, J. D., 1993, "Loss Mechanisms in Turbomachines," ASME J. Turbomach., **115**, pp. 621–656.
[3] Booth, T. C., 1985, "Importance of Tip Leakage Flows in Turbine Design," *Tip Clearance Effects in Axial Turbomachines* (VKI Lecture Series 1985-05), von Karman Institute, Rhode-St-Genèse, Belgium.
[4] Bindon, J. P., and Morphis, G., 1990, "The Development of Axial Turbine Leakage Loss for Two Profiled Tip Geometries Using Linear Cascade Data," ASME Paper No. 90-GT-152.
[5] Kaiser, I., and Bindon, J. P., 1997, "The Effect of Tip Clearance on the Development of Loss Behind a Rotor and a Subsequent Nozzle," ASME Paper No. 97-GT-53.
[6] Yoshino, S., 2002, "Heat Transfer in Rotating Turbine Experiments," Ph.D. thesis, Oxford University, Oxford.
[7] Camci, C., Dey, D., and Kavurmacioglu, L., 2003, "Tip Leakage Flows in Near Partial Squealer Rims in an Axial Flow Turbine Stage," ASME Paper No. GT2003-38979.
[8] Mischo, B., Behr, T., and Abhari, R. S., 2007, "Flow Physics and Profiling of Recessed Blade Tips: Impact on Performance and Heat Load," ASME Paper No. GT2006-91074.
[9] Chander, P., Lee, C.-P., Cherry, D., Wadia, A., and Doughty, R., "Analysis of Some Improved Blade Tip Concepts," ASME Paper No. GT2005-68333.
[10] De Cecco, S., Yaras, M. I., and Sjolander, S. A., 1995, "Measurement of Tip Leakage Flows in Turbine Cascade With Large Clearances," ASME Paper No. 95-GT-77.
[11] Yamamoto, A., Tominaga, J., Matsunuma, T., and Outa, E., 1994, "Detailed Measurements of Three-Dimensional Flows and Losses Inside an Axial Flow Turbine Rotor," ASME Paper No. 94-GT-348.
[12] Staubach, J. B., Sharma, O. P., and Stetson, G. M., 1996, "Reduction of Tip Clearance Losses Through 3-D Airfoil Designs," ASME Paper No. 96-TA-13.
[13] Offenburg, L. S., Fischer, J. D., and Hoek, T. J. V., 1987, "An Experimental Investigation of Turbine Case Treatments," Paper No. AIAA-87-1919.
[14] Harvey, N. W., 2004, "Aerothermal Implications of Shroudless and Shrouded Blades," *Turbine Blade Tip Design and Tip Clearance Treatment* (VKI Lectures Series 2004-02), von Karman Institute, Rhode-St-Genèse, Belgium.
[15] Dey, D., and Camci, C., 2000, "Development of Tip Clearance Flow downstream of a Rotor Blade With Coolant Injection From a Tip Trench," *Proceedings of the Eighth ISROMAC Conference*, Honolulu, HI, pp. 572–579.
[16] Rao, N. M., and Camci, C., 2004, "Axial Turbine Tip Desensitization by Injection From a Tip Trench, Part 1: Effect of Injection Mass Flow Rate," ASME Paper No. GT2004-53256.
[17] Rao, N. M., and Camci, C., 2004, "Axial Turbine Tip Desensitization by Injection From a Tip Trench, Part 2: Leakage Flow Sensitivity to Injection Location," ASME Paper No. GT2004-53258.
[18] Auyer, E. L., 1954, "Dynamic Sealing Arrangement for Turbomachines," U.S. Patent No. 2,685,429.
[19] Minoda, M., Inoue, S., Usui, H., and Hiroyuki, N., 1988, "Air Sealed Turbine Blades," U.S. Patent No. 4,732,531.
[20] Mischo, B., Burdet, A., Behr, T., and Abhari, R. S., 2007, "Control of Rotor Tip Leakage Through Cooling Injection From the Casing in a High-Work Turbine: Computational Investigation Using a Feature-Based Jet Model," ASME Paper No. GT2007-27669.
[21] Behr, T., Kalfas, A. I., and Abhari, R. S., 2007, "Unsteady Flow Physics and Performance of a One-and-1/2-Stage Unshrouded High Work Turbine," ASME J. Turbomach., **129**, pp. 348–359.
[22] Kupferschmied, P., Köppel, O., Gizzi, W. P., and Gyarmathy, G., 2000, "Time Resolved Flow Measurements With Fast Aerodynamic Probes in Turbomachinery," Meas. Sci. Technol., **11**, pp. 1036–1054.
[23] Pfau, A., Schlienger, J., Kalfas, A. I., and Abhari, R. S., 2002, "Virtual Four Sensor Fast Response Aerodynamic Probe (FRAP)," *Proceedings of the XVIth Bi-Annual Symposium on Measuring Techniques in Transonic and Supersonic Flows in Cascades and Turbomachines*, Cambridge, UK, Sept. 23–24.
[24] Porreca, L., Hollenstein, M., Kalfas, A. I., and Abhari, R. S., 2005, "Turbulence Measurements and Analysis in a Multistage Axial Turbine," ISABE Conference, Munich, Germany, Paper No. 2005-1032.
[25] Bernsdorf, S., Rose, M. G., and Abhari, R. S., 2006, "Modeling of Film Cooling—Part I: Experimental Study of Flow Structure," ASME J. Turbomach., **128**, pp. 141–149.
[26] Sjolander, S. A., 1997, "Overview of Tip-Clearance Effects in Axial Turbines," *Secondary and Tip Clearance Flows in Axial Turbines* (VKI Lecture Series 1997-01), Von Karman Institute for Fluid Dynamics, Rhode-St-Genèse, Belgium.
[27] Xiao, X., and Lakshminarayana, B., 2002, "Experimental Investigation of End-Wall Flow in Turbine Rotor," J. Propul. Power, **18**, pp. 1122–1123.
[28] Behr, T., Kalfas, A. I., and Abhari, R. S., 2007, "Stator Clocking Effects on the Unsteady Interaction of Secondary Flows in a 1.5-Stages Unshrouded Turbine," Seventh European Turbomachinery Conference, Athens, Greece, Paper No. B217.

Film Cooling Effectiveness Distributions on a Turbine Blade Cascade Platform With Stator-Rotor Purge and Discrete Film Hole Flows

Lesley M. Wright
Department of Aerospace and Mechanical Engineering,
The University of Arizona,
Tucson, AZ 85721-0119

Sarah A. Blake

Je-Chin Han
Distinguished Professor and
Marcus Easterling Endowed Chair

Turbine Heat Transfer Laboratory,
Department of Mechanical Engineering,
Texas A&M University,
College Station, TX 77843-3123
e-mail: jc-han@tamu.edu

An experimental investigation to obtain detailed film cooling effectiveness distributions on a cooled turbine blade platform within a linear cascade has been completed. The Reynolds number of the freestream flow is 3.1×10^5, and the platform has a labyrinthlike seal upstream of the blades to model a realistic stator-rotor seal configuration. An additional coolant is supplied to the downstream half of the platform via discrete film cooling holes. The coolant flow rate through the upstream seal varies from 0.5% to 2.0% of the mainstream flow, while the blowing ratio of the coolant through the discrete holes varies from 0.5 to 2.0 (based on the mainstream velocity at the exit of the cascade). Detailed film cooling effectiveness distributions are obtained using the pressure sensitive paint (PSP) technique under a wide range of coolant flow conditions and various freestream turbulence levels (0.75% or 13.4%). The PSP technique clearly shows how adversely the coolant is affected by the passage induced flow. With only purge flow from the upstream seal, the coolant flow rate must exceed 1.5% of the mainstream flow in order to adequately cover the entire passage. However, if discrete film holes are used on the downstream half of the passage, the platform can be protected while using less coolant (i.e., the seal flow rate can be reduced). [DOI: 10.1115/1.2777186]

1 Introduction

As the temperature of the mainstream gases in the turbine continues to rise, in an effort to increase the efficiency and power output of the engine, it is necessary to ensure that the turbine components can withstand these extreme temperatures. A wide variety of cooling techniques can be employed to protect the airfoils while lowering their temperature. Film cooling is commonly used to provide a protective film between the hot gases and the airfoil. Film cooling is utilized on the airfoil surface, as well as on the vane end wall and blade platforms. With the end walls and platforms comprising a large percentage of the area exposed to the mainstream gases, it is vital to ensure that these areas are well protected. As with the airfoil, the platform must be adequately protected while minimizing the amount of coolant used for protection. Several comprehensive reviews of platform (end wall) flow, heat transfer, and film cooling are available. The reviews completed by Han et al. [1], Langston [2], Chyu [3], and Simon and Piggush [4] offer valuable insight into the fundamentals of end wall and platform cooling.

The platform is a difficult area to properly cool due to the complex flow that varies depending on the profile of the airfoil. Langston et al. [5,6] performed flow measurements to gain insight into this complex secondary flow. They showed that at the inlet of the passage, the boundary splits at the leading edge of the blade. A horseshoe vortex forms with one leg on the pressure side of the blade and the other leg on the suction side of the blade (in the adjacent passage). The pressure side leg of the horseshoe vortex travels from the pressure side of the passage to the suction side; this pressure side leg of the horseshoe vortex becomes indistinguishable from the passage vortex. This passage vortex will eventually meet the suction side leg of the horseshoe vortex that has remained near the junction of the suction surface and end wall. Goldstein and Spores [7] also studied the flow through a blade passage. They identified multiple "corner" vortices that developed throughout the passage. A pressure side corner vortex develops just downstream of the leading edge, and the vortex carries about one-third of the chord length. Two suction side corner vortices develop along the suction surface in the latter half of the passage. After the passage vortex carries to the suction side of the passage, it lifts from the end wall surface. Below the passage vortex, along the junction where the suction surface meets the end wall, suction side, counter-rotating, corner vortices form. Wang et al. [8] also observed similar small, but strong, vortices developing downstream of the passage vortex (after the passage vortex crosses to the suction side of the passage).

Film cooling can be used in several forms to protect the platform. Traditionally, film cooling is thought of as coolant from discrete holes. Takeishi et al. [9] obtained heat transfer and film effectiveness distributions on a vane end wall with discrete film cooling holes placed at three locations in the passage. They found that the effectiveness is very low near the leading edge on the suction side; with the roll-up of the horseshoe vortex, the film coolant lifted from the surface and offered little or no protection. The path of the coolant was also influenced by the passage vortex transporting the coolant from the pressure to the suction side of the passage. Harasgama and Burton [10] used film cooling near the leading edge, just inside the passage, with the film cooling holes located along an iso-Mach line. Although the row of film cooling holes was evenly distributed to span the passage, no coolant reached the pressure side of the passage. The film cooling configuration used by Jabbari et al. [11] consisted of discrete holes placed on the downstream half of the passage. Similar to the up-

Contributed by the Turbomachinery Division of ASME for publication in the JOURNAL OF TURBOMACHINERY. Manuscript received February 10, 2007; final manuscript received February 28, 2007; published online May 5, 2008. Review conducted by David Wisler. Paper presented at the 2006 ASME International Mechanical Engineering Congress (IMECE2006), Chicago, IL, November 5–10, 2006.

stream design [10], the film cooling effectiveness varied significantly through the passage, with the coolant moving to the suction side of the passage.

Friedrichs et al. [12–14] studied the film cooling effectiveness using the ammonia and diazo technique. They found that a simple layout of the film cooling holes throughout the passage can result in areas being overcooled (or undercooled) due to the secondary flow. With their proposed "improved design," the film holes were placed so the strong secondary flow could be used advantageously. Using the same amount of coolant, they were able to provide improved coolant coverage. Recently, Barigozzi et al. [15] compared the film cooling effectiveness on a passage end wall with cylindrical or fan-shaped film cooling holes. With their cooling designs, they showed that by increasing the blowing ratio, the passage vortex is weakened, and the passage cross flow is reduced; therefore, coolant coverage is more uniform across the passage. Similar to flat plate film cooling, shaped film cooling holes offer better protection than cylindrical holes.

A similarity between the vane end wall and the blade platform is the existence of a slot (or gap) upstream of the airfoil leading edge. A gap is commonly in place in the transition from the combustion chamber to the turbine vane (stator). Similarly, a gap exists between the stator and rotor, so the turbine disk can rotate freely. To prevent ingestion of the hot mainstream gases, it is a common practice to inject coolant air through these slots. If this preventive measure is utilized properly, unnecessary discrete film holes can be eliminated, so the coolant is not wasted by overcooling areas on the rotating platform. Blair [16] measured the film cooling effectiveness with upstream injection in his pioneering study; he showed large variations in the film cooling effectiveness over the entire passage due to the strong secondary flow. Granser and Schulenberg [17] injected coolant from a slot upstream of their airfoils; they concluded that the boundary layer is reenergized with the coolant injection, and thus the secondary flows through the passage are reduced. Roy et al. [18] placed coolant slots upstream of their vane. They showed that the heat transfer near the leading edge was reduced due to the secondary air injection. Because the slots were placed directly upstream of the blades, a large area in the center of the passage did not receive adequate film cooling coverage. Slot injection has been the focus of many studies performed at the University of Minnesota [19–21]. It was found that using slots, which span the majority of the passage upstream of their vanes, can provide film coverage over most of the passage to the trailing edge of the vane [19,20]. It was also found that increasing the amount of coolant through the slot can reduce the effect of the secondary flow. In addition, strategically blocking the slot so the coolant does not exit the slot uniformly provides thermal advantages (and disadvantages) [21].

The heat transfer coefficients and the film cooling effectiveness were measured on the end wall of a vane passage with film cooling combined with upstream slot injection by Nicklas [22]. He found that in the upstream region, the film cooling effectiveness was elevated due to the large amount of cooling flow from the slot. However, the effectiveness near the discrete holes located near the center of the passages suffered due to the passage vortex. Liu et al. [23] used a dense array of discrete holes upstream of their vanes to emulate the effect of upstream slot injection. He determined that the film cooling effectiveness was primarily affected by the blowing ratio of the injection; in addition, as the blowing ratio increases, the uniformity of the coverage increases.

The film cooling effectiveness has been measured using pressure sensitive paint by Zhang and Jaiswal [24] and Zhang and Moon [25]. They first measured the effectiveness with two upstream injection geometries: two rows of discrete holes and a single row slot. The effect of a backward facing step was also considered with the discrete hole configuration. They confirmed that increasing the coolant flow can significantly increase the effectiveness, and they reported that the use of a backward step significantly decreases the effectiveness within the passage. Knost and Thole [26] showed that with increased slot flow, the critical areas of the leading edge and pressure side junction can be adequately cooled. Cardwell et al. [27] extended this work to include midpassage misalignment. With the misalignment that may occur between two adjacent vanes, the film cooling effectiveness is dramatically reduced.

Although significant effort has been directed toward vane end wall and blade platform cooling, most of the studies do not model realistic cooling designs and flow conditions. It is imperative to couple the available upstream purge flow with limited discrete film holes to maximize the coverage of the coolant while minimizing the amount of coolant. The current study is an attempt to fill many of the gaps that still exist in the area of turbine platform cooling. The pressure sensitive paint (PSP) technique will be used to obtain detailed film cooling effectiveness distributions on the platform of a high pressure turbine blade placed in a linear cascade. An advanced, labyrinthlike seal geometry will be used to simulate an advanced gap design between the stator and rotor. Although the advanced seal is used to prevent ingestion of the hot mainstream gases, purge flow is also used to ensure that ingestion does not occur. The flow rate of purge flow through the labyrinthlike seal will be varied from 0.5% to 2.0% of the mainstream flow, while the freestream turbulence intensity will be varied from 0.75% to 13.4%. The film cooling effectiveness will also be obtained from 12 discrete film cooling holes on the downstream half of the passage over a range of blowing ratios (0.5–2.0). The upstream seal flow will be combined with the downstream film cooling to provide a more realistic model of a cooled high pressure turbine blade platform. With these various flow conditions coupled with the advanced stator-rotor seal geometry, the detailed film cooling effectiveness distributions will provide additional understanding of the secondary flow behavior around the high pressure turbine blade. In addition, areas that may require additional cooling can be identified, while areas that have the potential to be overcooled can be eliminated.

Experimental Facility

Low Speed Wind Tunnel. An existing low speed wind tunnel facility was used to study the platform film cooling effectiveness, and a schematic view of the facility is shown in Fig. 1. Modifications were made to the end wall of the wind tunnel that was previously used by Wright et al. [28]. The open-loop wind tunnel operates in suction with two mesh screens located at the inlet of the wind tunnel. To produce uniform flow entering the cascade, a 4.5:1 contraction nozzle guides the flow to the linear cascade. The test area is 25.4 cm high by 75.0 cm wide, and has a 107.49 deg turning angle to match the turning of the five-blade cascade. Head- and tailboards further guide the flow into the cascade. The cascade inlet velocity was maintained at 20 m/s and was set using a variable frequency controller attached to the 15 hp (11.2 kW) blower. The inlet velocity was measured (and continuously monitored) using a Pitot tube placed inside the wind tunnel. The mainstream accelerates through the cascade, so the mainstream velocity at the cascade exit is 50 m/s.

The freestream turbulence through the cascade was varied by placing a turbulence grid 30 cm upstream of the cascade. The grid is made of square bars that are 1.3 cm wide, and they are spaced 4.8 cm in both the horizontal and vertical directions. Zhang and Han [29] used hot wire anemometry and showed that the inlet turbulence intensity increases from 0.75% (without the grid) to 13.4% with a length scale of 1.4 cm. The turbulence intensity decreases with the flow acceleration through the passage to a level of 5% at the cascade exit.

Linear Cascade Design. Figure 2 shows the typical, advanced, high pressure turbine blade used for this study. The blade, which was scaled up five times, has a 107.49 deg turning angle with an inlet flow angle of 35 deg and an outlet flow angle of −72.49 deg. The chord length of the blade is 22.68 cm and the height of the

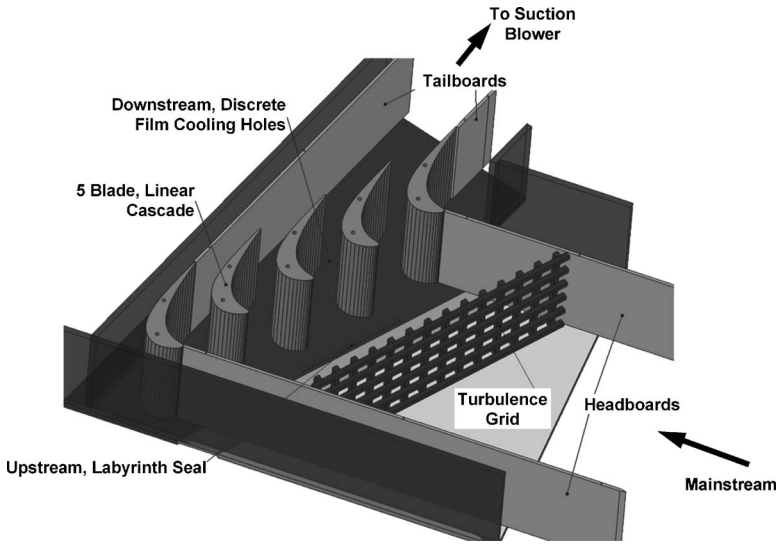

Fig. 1 Overview of the low speed wind tunnel used to study platform cooling

blade is 25.4 cm. The blade-to-blade spacing at the inlet is 17.01 cm with a throat-to-span ratio of 0.2. The mainstream flow accelerates from 20 m/s at the inlet to 50 m/s at the outlet of the cascade. The inlet flow periodicity and uniformity for the blade design have been measured and reported by Zhang and Han [29]. In addition, the velocity (pressure) distributions along the pressure and suction surfaces of the blades have also been measured. With the turbulence grid placed in the wind tunnel, the streamwise freestream turbulence ranges from 13.4% at the cascade inlet to 5% at the outlet of the cascade, as measured using a hot wire anemometer [29]. The mainstream Reynolds number (based on the inlet velocity, inlet fluid properties, and blade chord) is 3.1×10^5.

Platform Cooling Design. The platform within the linear cascade has been altered to incorporate an advanced, labyrinthlike seal upstream of the blades. This design models the more advanced seals used to prevent ingestion of the mainstream gases into the engine cavity. Unlike previous studies using inclined slots, this seal design is a more accurate representation of the stator-rotor seals in advanced engines. As shown in Fig. 3, the seal covers 1.5 passages within the linear cascade. The width of the slot is 0.44 cm, and the coolant travels through the labyrinthlike geometry ($l_s/w=6.84$), turning 180 deg before being expelled onto the passage end wall. The seal is located upstream of the leading edge of the blades. It is placed 4.34 cm upstream of the blades, so it is approximately halfway between the leading edge of the blades and trailing edge of the stator vanes (as the vanes would be located in the actual engine). An ASME orifice meter is used to measure the coolant flow rate before the coolant fills a plenum and is then expelled onto the platform. The flow rate of the coolant is varied, so the film cooling effectiveness can be measured over a range of flow rates varying from 0.5% to 2.0% of the mainstream flow.

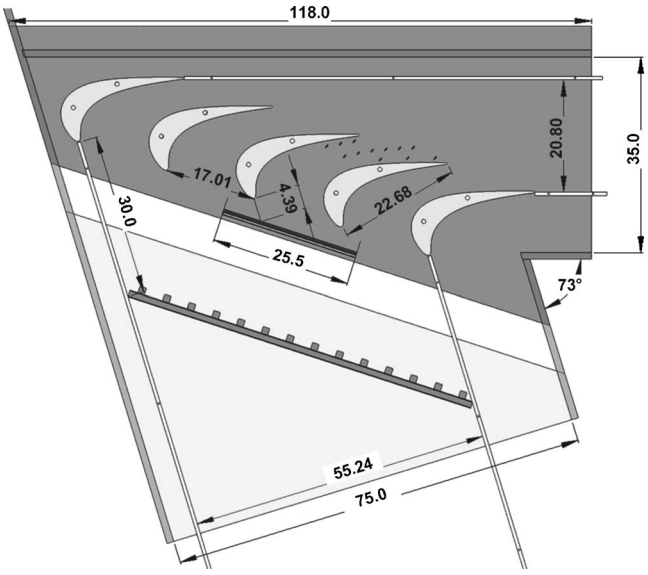

Fig. 2 Low speed wind tunnel and turbine blade details

Figure 3 also shows the location of the discrete film holes. With the upstream seal providing protection to the upstream half of the passage, additional holes are limited to the downstream half of the passage. Twelve holes are positioned to follow the potential streamlines through the passage. However, they are placed at a compound angle to the approximate streamlines. The holes are turned 45 deg toward the pressure side of the passage from the streamline injection angle. With this compound angle, the coverage area of the coolant should increase. Table 1 gives the detailed location and flow angle for the 12 film cooling holes. Although the flow angle of the holes varies, the injection angle through the platform remains constant for each hole at 30 deg. A second plenum supplies coolant to the holes after the coolant is metered through a volumetric flow meter. The flow rate is varied to achieve average blowing ratios varying from 0.5 to 2.0 (based on the velocity of the mainstream at the exit of the cascade).

Pressure Sensitive Paint Measurement Technique

The film cooling effectiveness has been measured using an array of measurement techniques over several decades. Thermocouples, thermochromatic liquid crystals, infrared thermography, and, recently, temperature sensitive paint have been used for surface temperature measurements, which can be converted to the film cooling effectiveness with knowledge of the mainstream and coolant flows. Although these techniques can be used to obtain the film cooling effectiveness, the accuracy near the film cooling holes is questioned. Near the holes, the test material can be very thin, and therefore, heat conduction through the test surface can give false representations of the film cooling effectiveness. This is a problem that is inherent to heat transfer experiments.

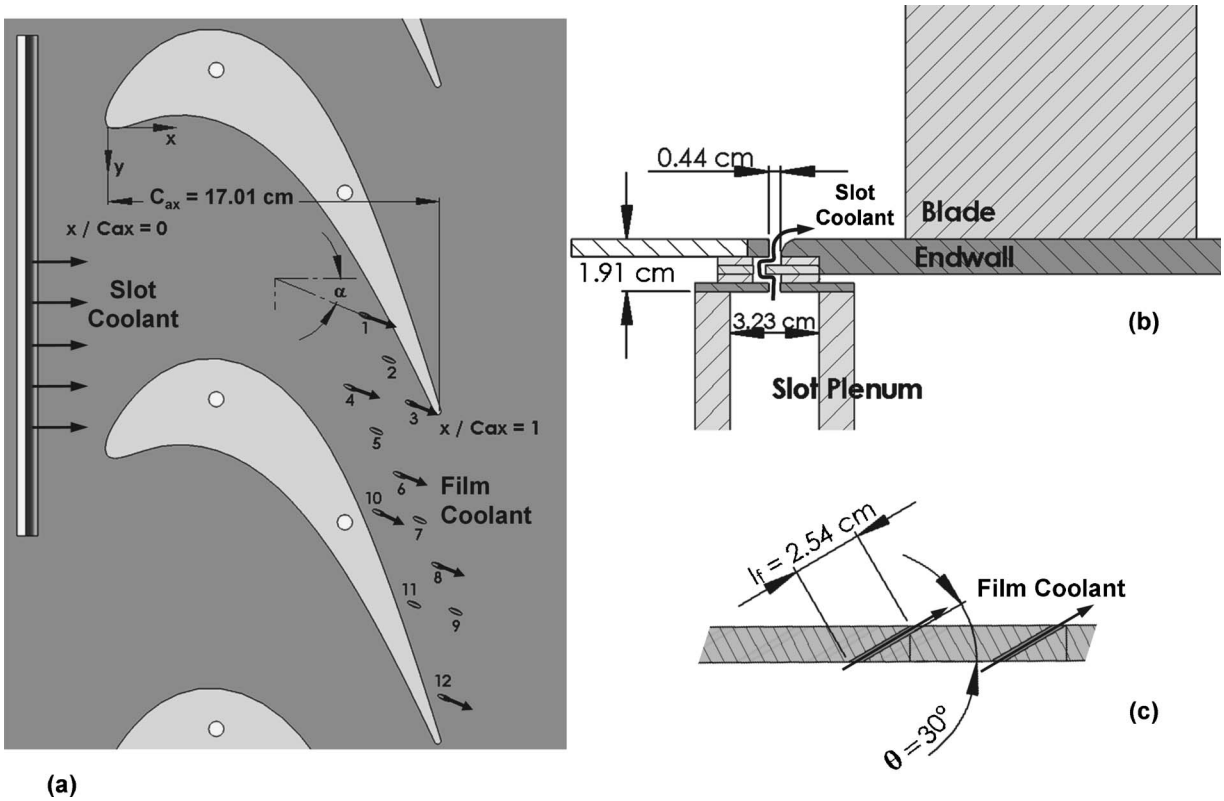

Fig. 3 Platform film cooling details: (*a*) detailed view of the cooled passage, (*b*) labyrinthlike stator-rotor seal, (*c*) cross-sectional view of two discrete film holes

Numerical correction of the film cooling data is one alternative for producing more accurate film cooling data. Another alternative is to avoid heat transfer experiments. This approach was used by Zhang et al. [24,25] as they used PSP to measure the film cooling effectiveness on a cascade end wall. Wright et al. [30] used PSP to measure the film cooling effectiveness on a flat plate with compound angle film cooling holes, and they provided a detailed review of the PSP theory and application. In addition, PSP has also been used to the measure the effectiveness on a cylinder placed in a low speed wind tunnel [31]. Both of these studies demonstrate the advantages of PSP measurements compared with other traditional measurement techniques, including steady state liquid crystal thermography, steady state infrared thermography, and transient infrared thermography. The PSP technique has also been applied by Ahn et al. [32,33] to measure the film cooling effectiveness on the leading edge of a rotating blade placed in a three stage research turbine. Additional film cooling effectiveness distributions have been obtained on the blade tip in a blowdown facility [34,35].

Table 1 Discrete film hole location and orientation

Film hole No.	x (cm)	y (cm)	d (cm)	α (deg)	θ (deg)
1	13.3	9.8	0.25	16	30
2	14.5	12.1	0.25	16	30
3	15.7	14.4	0.25	16	30
4	12.6	13.5	0.25	10.5	30
5	13.9	15.8	0.25	16	30
6	15.1	18.0	0.25	19	30
7	16.1	20.4	0.25	12	30
8	17.1	22.7	0.25	27	30
9	18.0	25.1	0.25	27	30
10	14.0	20.0	0.25	27	30
11	15.9	24.7	0.25	27	30
12	17.4	29.6	0.25	27	30

The premise behind PSP is an oxygen quenching effect. As the oxygen partial pressure of the gas in direct contact with the surface increases, the intensity of light emitted by the PSP decreases (hence, oxygen is quenched). The PSP can be calibrated to determine the relationship between the emission intensity of the paint and the surrounding pressure. A test plate is sprayed with the Uni-FIB PSP (UF470-750) supplied by Innovative Scientific Solutions, Inc. (ISSI) and placed inside a vacuum chamber. At each measurement point, the PSP sample was excited using a strobe light equipped with a 500 nm broadband pass filter. A charge-coupled device (CCD) camera with a 630 nm filter records the intensity emitted by the PSP. Figure 4 shows a typical calibration curve relating a known pressure ratio to a measured intensity ratio (where the reference conditions are taken at atmospheric pressure).

After the PSP has been properly calibrated, the film cooling effectiveness can be measured on the desired test surface. Due to the size of the end wall passage, two sets of images are required to capture the entire passage. The procedure to measure the effectiveness on both the upstream and downstream halves of the passage is identical, and the results are combined to give a complete picture of the film cooling effectiveness on the platform. The film cooling effectiveness is measured based on a mass transfer technique. Two similar tests are required to calculate the film cooling effectiveness: one with air as the coolant and one with nitrogen as the coolant. The film cooling effectiveness can be calculated based on the concentration of oxygen, which is related to the partial pressure of oxygen. Therefore, the film cooling effectiveness can be calculated using the following equation:

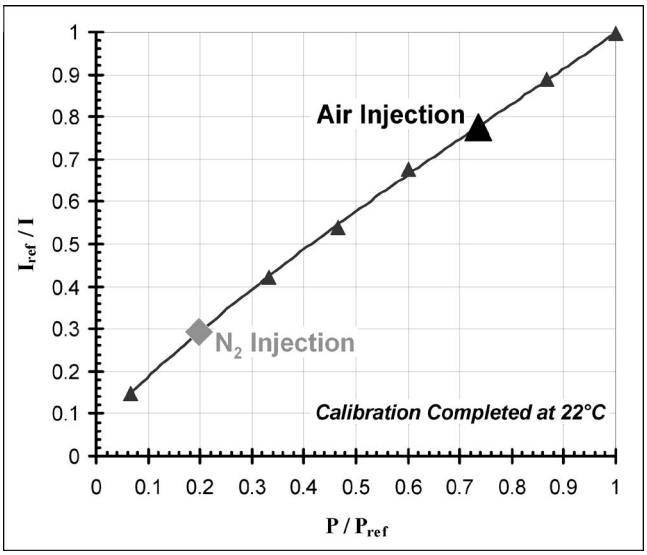

Fig. 4 PSP calibration curve

$$\eta = \frac{C_\infty - C_{\text{mix}}}{C_\infty} = \frac{(P_{O_2})_{\text{air}} - (P_{O_2})_{N_2}}{(P_{O_2})_{\text{air}}} \approx 1 - \frac{I_{\text{air}}}{I_{N_2}} \quad (1)$$

To accurately determine the film cooling effectiveness, a total of four images are required: (1) a black image to remove any background noise from the optical components (no mainstream flow, no coolant flow, no excitation light), (2) a reference image to establish the intensity at the reference atmospheric pressure (no mainstream flow, no coolant flow, PSP is excited with the strobe light), (3) an air image to measure the partial pressure of oxygen with air as the coolant (mainstream flow, air as coolant flow, excitation by strobe light), and (4) a nitrogen image to measure the partial pressure of oxygen with nitrogen as the coolant (mainstream flow, nitrogen as coolant flow, excitation by strobe light). As shown in Fig. 4, in the presence of oxygen, the emission intensity falls, so the intensity ratio (I_{ref}/I) increases, as shown by representative point for film cooling with air injection. When nitrogen is injected as the coolant, the emission intensity increases (due to the lack of oxygen), and the intensity ratio decreases, as shown by the point for nitrogen injection. The partial pressure of oxygen with air or nitrogen injection is determined based on the calibration of the emission intensity and pressure. The film cooling effectiveness can be determined at every pixel, giving a detailed film cooling effectiveness distribution on the passage end wall.

Experimental uncertainty was considered using a 95% confidence level, as presented by Coleman and Steele [36]. The uncertainty of the film effectiveness measurements varies depending on the intensity level measured by the CCD camera. The experimental uncertainty is less than 2% for film effectiveness measurements greater than 0.5. However, as the effectiveness begins to approach zero (where the measured light intensities are relatively low), the uncertainty rises. For a film cooling effectiveness of 0.07, the uncertainty is approximately 10% and continues to rise as the effectiveness approaches zero. All experimental results were repeated multiple times to confirm the repeatability of the data. The data proved to be repeatable for the entire range of film effectiveness that was measured.

Results and Discussion

The presentation and discussion of the results can be divided into three groups: film cooling effectiveness with coolant injection from the upstream seal, film cooling effectiveness due to the downstream, discrete film cooling holes, and film cooling effectiveness due to the combined seal and discrete film cooling hole flows. Table 2 summarizes the 24 experimental cases considered in the present study. Although the seal injection rate is commonly considered as a percentage of the mainstream flow, the corresponding blowing ratio is also given for reference. This seal blowing ratio is based on the mainstream velocity at the inlet of the cascade (20 m/s). However, the blowing ratios for the downstream film holes are based on the exit velocity of the mainstream flow (50 m/s). The effect of increased freestream turbulence is considered for the independent upstream seal and downstream film hole flows. In addition to the discussion of the detailed film cooling effectiveness distributions, the results are averaged, so direct comparisons can be made among the cases considered.

Table 2 Experimental conditions considered in the present study

Upstream slot injection				
Slot injection rate (m_s) (%)	M_s	I_s	DR	Tu (%)
0.5	0.29	0.084	1.0	0.75, 13.4
1.0	0.57	0.325	1.0	0.75, 13.4
1.5	0.86	0.740	1.0	0.75, 13.4
2.0	1.14	1.30	1.0	0.75, 13.4

Downstream discrete film holes			
M_f	I_f	DR	Tu (%)
0.5	0.25	1.0	0.75, 13.4
1.0	1.00	1.0	0.75, 13.4
1.5	2.25	1.0	0.75, 13.4
2.0	4.00	1.0	0.75, 13.4

Combined upstream slot and downstream film				
Slot injection rate (m_s) (%)	M_s	M_f	$\text{MFR}_{\text{total}}$ (%)	Tu (%)
1.0	0.57	0.5	1.11	0.75
1.0	0.57	1.0	1.22	0.75
1.0	0.57	1.5	1.34	0.75
1.0	0.57	2.0	1.46	0.75
2.0	1.14	0.5	2.11	0.75
2.0	1.14	1.0	2.22	0.75
2.0	1.14	1.5	2.34	0.75
2.0	1.14	2.0	2.46	0.75

Upstream Slot Injection. The base line case of the measured film cooling effectiveness on the platform with upstream injection from the labyrinth seal is shown in Fig. 5 (Tu=0.75%). The effect of the passage secondary flow is clearly seen in this figure. At the lowest coolant flow rate of 0.5%, the coolant exits the seal, and as the coolant travels into the blade passage, it is quickly carried from the pressure to the suction side of the passage. As other studies have shown, the pressure side leg of the horseshoe vortex, which forms near the leading edge of the blades, becomes indistinguishable from the passage vortex as it crosses the passage from the pressure side to the suction side. Beginning at the leading edge of the blades, the film cooling effectiveness quickly diminishes, and the coverage area is skewed to the suction side of the passage. With the stator-rotor seal located upstream of the leading edge of the blades, the coolant exits the seal uniformly over the entire length of the seal. This trend was not observed with an inclined slot located at the leading edge of the blades [28]. The combination of the advanced seal configuration and the location of the seal, with respect to the blades, offers added protection against the ingestion of the hot mainstream gases into the engine cavity.

Increasing the coolant flow rate offers added protection to the downstream half of the passage. However, coolant protection does

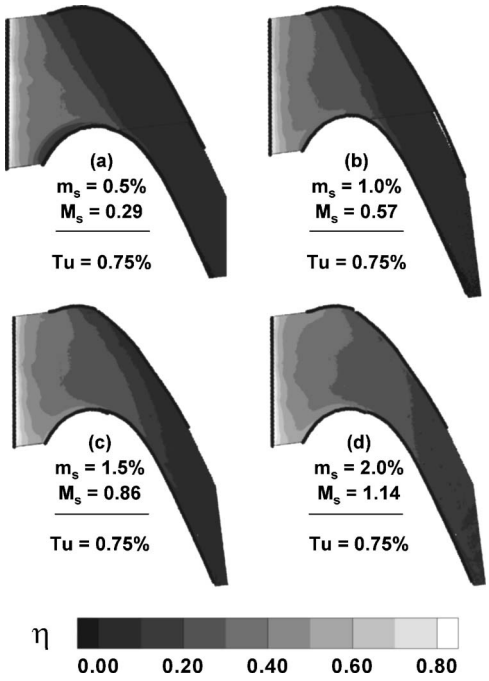

Fig. 5 Film cooling effectiveness with various seal injection rates (Tu=0.75%)

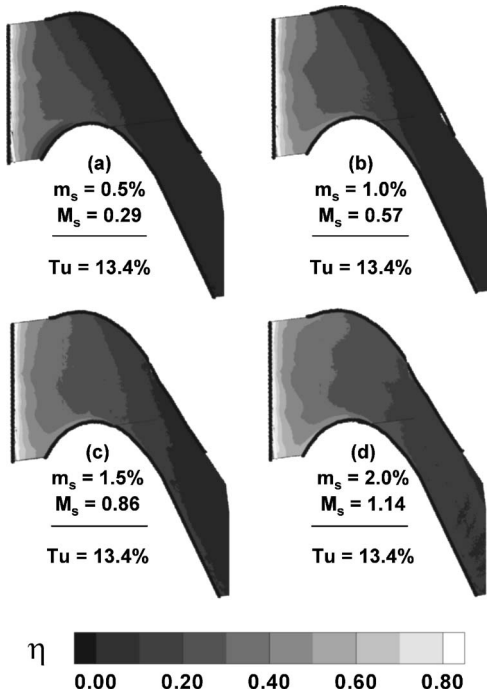

Fig. 6 Film cooling effectiveness with various seal injection rates (Tu=13.4%)

not reach the exit of the passage until the seal flow rate is increased to 2.0%. With the intermediate flows of 1.0% and 1.5%, a large area of the platform is left unprotected, and the coolant is adversely affected by the passage induced secondary flow. At the greatest flow rate of 2.0%, the film cooling effectiveness distributions are the most uniform from the pressure side to the suction side of the passage. As other studies [8,28] have indicated, the effect of the passage vortex is weakened by the upstream purge flow. Therefore, the coolant from the seal is more uniformly distributed across the passage.

Although it is convenient to measure the film cooling effectiveness with a low freestream turbulence level of 0.75%, this flow condition poorly represents the actual engine environment. To combat this problem, a turbulence grid is added to the wind tunnel upstream of the blades, so the freestream turbulence intensity is raised to 13.4% at the cascade inlet. Figure 6 shows the measured film cooling effectiveness on the passage platform with this increased freestream turbulence. A quick comparison of Figs. 5 and 6 does not reveal an appreciable difference between the two mainstream flow conditions. However, upon a more careful assessment, several differences can be observed. At the lowest two flow rates of 0.5% and 1.0%, the coverage area extends further into the passage with the increased turbulence intensity of 13.4%. From previous studies [28], this could be anticipated as increasing the freestream turbulence has been shown to weaken the effect of the passage vortex. The reduced effect of the passage vortex is further shown at the increased flow rate of 1.5%. At this coolant flow rate, a large area of the passage remains protected by the coolant, but the film cooling effectiveness distributions are more uniform from the pressure side to the suction side of the passage. With a final comparison of the greatest seal flow rate of 2.0%, the film cooling effectiveness distributions obtained under the two freestream turbulence levels show only marginal differences.

The film cooling effectiveness on the platforms is averaged to yield a direct comparison between the various cases. Figure 7 shows the laterally averaged effectiveness through the passage with both freestream turbulence levels. With the seal placed upstream of the turbine blades, the effectiveness is averaged beginning at the exit of the seal, through the passage, to the trailing edge of the blades. Immediately downstream of the seal, all flow rates give the same level of film cooling effectiveness. With the specific geometry of the seal, the film cooling effectiveness directly downstream of the seal is less than unity due to the current seal design with the coolant being injected perpendicular to the platform. However, downstream of the seal, the level of effectiveness begins to deviate depending on the coolant flow rate: the greatest film cooling effectiveness results from the greatest coolant flow rate. When considering the cases with the turbulence intensity of 0.75%, the effectiveness decreases to approximately zero at the same location in the passage with the lowest coolant

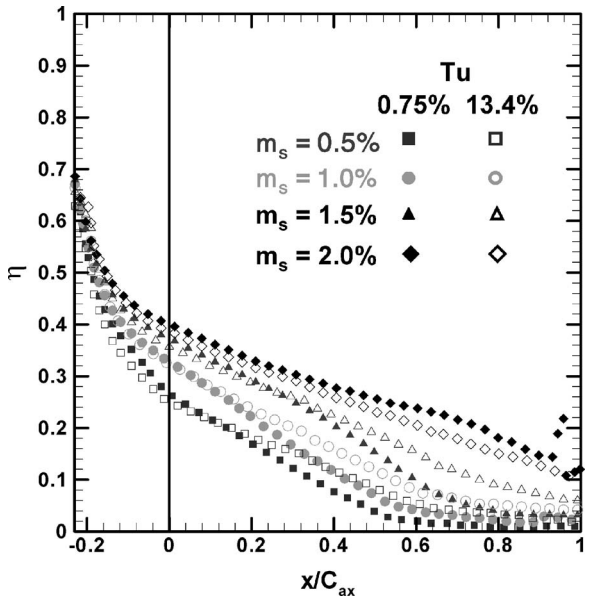

Fig. 7 Laterally averaged film cooling effectiveness on the passage end wall with upstream seal injection

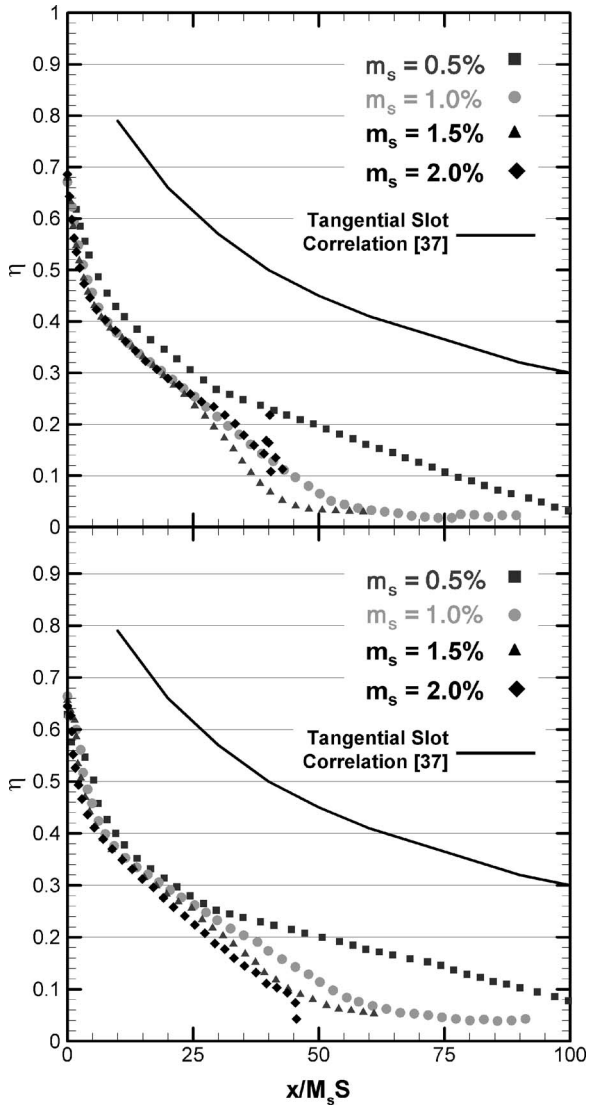

Fig. 8 Comparison of the laterally averaged film cooling effectiveness on the passage end wall with upstream seal injection and tangential slot injection over a flat plate

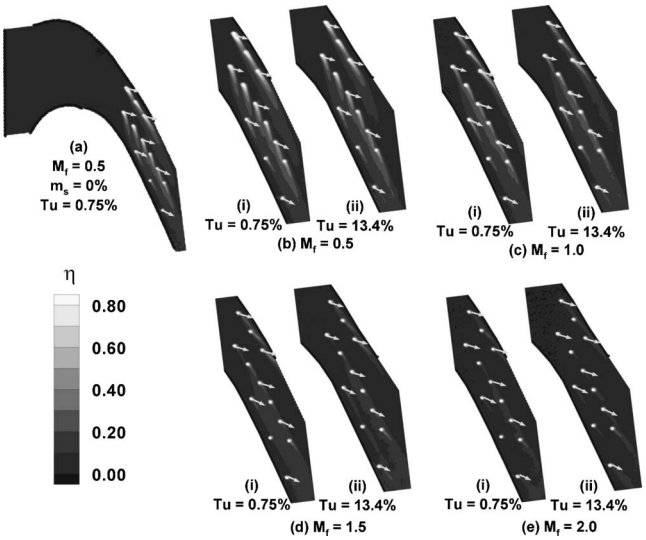

Fig. 9 Film cooling effectiveness with downstream discrete film cooling

rates of 0.5% and 1.0%. However, this point occurs further downstream with the increased flow rate of 1.5%, and with the greatest flow rate of 2.0%, this point is never reached.

In addition to the effect of the coolant flow rate, Fig. 7 also presents the effect of the freestream turbulence intensity. In general, increasing the turbulence intensity increases the film cooling effectiveness, as the adverse effect of the passage vortex is reduced. At the highest coolant rate of 2.0%, there is only a slight difference between the two turbulence intensities. The effect of the passage vortex has already been weakened by the large amount of coolant injected onto the platform upstream of the blades. Therefore, no additional weakening of the passage induced secondary flow is observed.

The laterally averaged film cooling effectiveness has been replotted in Fig. 8, so comparisons can be made with the fundamental, tangential slot injection over a flat plate. The film effectiveness has been plotted versus the nondimensional x/M_sS parameter, and it should be noted that for this plot, the starting point of $x=0$ is taken at the exit of the seal (and not at the leading edge of the blades). Near the exit of the slot, all the coolant flow rates collapse together; however, the trends begin to change beyond $x/M_sS=25$. For both freestream turbulence levels of 0.75% and 13.4%, the coolant flow rates of 1.0% and 1.5% approach an average effectiveness of zero. However, with the flow rate of 0.5%, the effectiveness does not approach zero until x/M_sS extends beyond 100.

Figure 8 also offers an interesting comparison with the fundamental tangential slot injection over a flat plate from Goldstein [37]. With the coolant exiting the seal at $x=0$, a dramatic difference in the film cooling effectiveness can be quickly observed. Wright et al. [28] previously observed that near the exit of their inclined slot, the effectiveness is comparable to that predicted by the tangential correlation, and deviation from the correlation was not observed until the effect of the passage induced secondary flow dominated the film cooling effectiveness on the platform. The present labyrinth geometry gives a much lower effectiveness than the tangential slot, so beginning at the exit of the seal, the large deviation from the correlation is observed. The difference continues through the passage, as the coolant is adversely affected by the passage vortex.

Downstream Discrete Film Cooling. Before considering the more realistic cooling design of seal flow combined with discrete film cooling, the isolated effects should be first understood. Therefore, it is necessary to consider the discrete film holes separately from the seal coolant. Figure 9 shows the measured film cooling effectiveness due to the downstream, discrete film cooling holes with both freestream turbulence levels of 0.75% and 13.4%. The entire passage is shown in Fig. 9(*a*), and Figs. 9(*b*)–9(*e*) more clearly show the detailed film cooling effectiveness in the area surrounding the film cooling holes. Before discussion of the discrete film cooling begins, several items should be noted and remembered as the discussion progresses. Although the elevated turbulence intensity is stated as 13.4%, this level occurs at the inlet of the cascade. At the exit of the cascade, near the discrete holes, the turbulence intensity reduces to approximately 5% [29]. In addition, as described earlier, the location of the holes follow the streamlines through the passage and have a compound angle 45 deg toward the pressure side of the passage. The blowing ratios stated for the holes are average blowing ratios based on the mainstream velocity at the exit of the cascade.

As Fig. 9(*b*) shows at the lowest blowing ratio of $M_f=0.5$, distinct traces are seen from each of the 12 film cooling holes. However, the path of each of the coolant traces is rather interesting. Arrows have been added to the plot to indicate the injection angles of selected holes. The deviation of the coolant traces from the injection angles is very apparent. The 12 holes can be divided

into three groups: pressure side, center of the passage, and suction side. The coolant from the three holes along the pressure side of the passage follows the curvature of the blade (mainstream flow). Although the injection of the coolant is directed toward the pressure side of the passage, the flow of the coolant is dominated by the mainstream flow.

Moving to the center of the passage, the path of the coolant changes dramatically. The traces are nearly from the pressure side to the suction side of the passage, especially with the upstream holes. For this center row of holes, the path of the coolant is dominated by the passage induced secondary flow. The passage vortex moving from the pressure side to the suction side of the passage severely influences the path of the coolant. This behavior was previously observed with holes angled with the streamlines [28]. With these compound angle holes, the coolant traces are wider, and the coolant spreads more as it is directed toward the suction side of the passage. These wider traces come at the expense of shorter traces, which can be expected when the same amount of coolant is used for both cooling designs. Near the trailing edge of the passage (still considering the middle row of holes), the deflection of the coolant toward the suction side of the passage is reduced. At this point, the passage vortex has already crossed the passage, so the effect is reduced, although the effect of the passage vortex is not mitigated.

Finally, with the three holes located along the suction side of the passage, the coolant traces are very weak. This is again a result of the passage vortex. Others have shown that after the passage vortex crosses to the suction side of the passage, it wraps around the suction leg of the horseshoe vortex and lifts off the platform near the trailing edge of the blade. With the passage vortex lifting off the surface, the coolant is also lifted off the surface, minimizing the protection offered by the coolant.

Increasing the blowing ratio beyond 0.5 decreases the film cooling effectiveness on the platform. Similar to flat plate studies, increasing the momentum of the jets causes the film coolant to blow off the surface. When the coolant lifts off the surface, the platform is left unprotected. Although increasing the blowing ratio decreases the film cooling effectiveness, the coolant traces are also altered. With the increased momentum, the coolant more closely follows the injection angle of the holes, although the true injection angle is never fully realized.

Figure 9 also shows the effect of freestream turbulence intensity on the discrete film cooling. However, there is no defining trend to characterize the effect of increased freestream turbulence. In other words, the film cooling effectiveness distributions obtained for both freestream turbulence levels are very comparable. On this latter half of the passage, the turbulence intensity is reduced (Tu $=5\%$). The effect of freestream turbulence is further reduced by the film cooling holes placed at a compound angle to the mainstream flow coupled with the strong effect of the passage induced secondary flow. Figure 10 shows the laterally averaged effectiveness with the downstream discrete film cooling holes. This figure reiterates that no clear differences can be seen between the two freestream turbulence levels.

Combined Upstream Slot Injection and Downstream Discrete Film Cooling. Finally, the film cooling effectiveness is measured with combined seal injection and discrete film holes. With the freestream turbulence having only a marginal effect on the film cooling effectiveness, the effectiveness is presented without the turbulence grid, so the freestream turbulence intensity is 0.75%. Figure 11 shows the measured effectiveness with a seal injection rate of 1.0% and various blowing ratios from the discrete film holes. Figure 5(*b*) clearly shows that a large area of the passage is left unprotected with only upstream injection, so the addition of the discrete holes should help alleviate this problem. All the trends observed for the upstream injection and the downstream film holes can be seen in these figures. The seal and hole flows are essentially independent of one another.

Although the holes adequately protect the downstream half of the passage, an area near the pressure side of the passage remains unprotected. One way to ensure that this area is adequately protected is to increase the coolant flow rate from the seal. Figure 12 shows an increased seal flow of 2.0% combined with the discrete film holes. Now the entire passage is protected, but much of the downstream half of the passage is overprotected. With this high flow rate of 2.0%, the downstream film cooling is not required, and therefore, this is wasted coolant. Figure 12(*a*) clearly shows the film accumulation due to the seal and hole coolant flows. Although this illustrates the power of the PSP measurement tech-

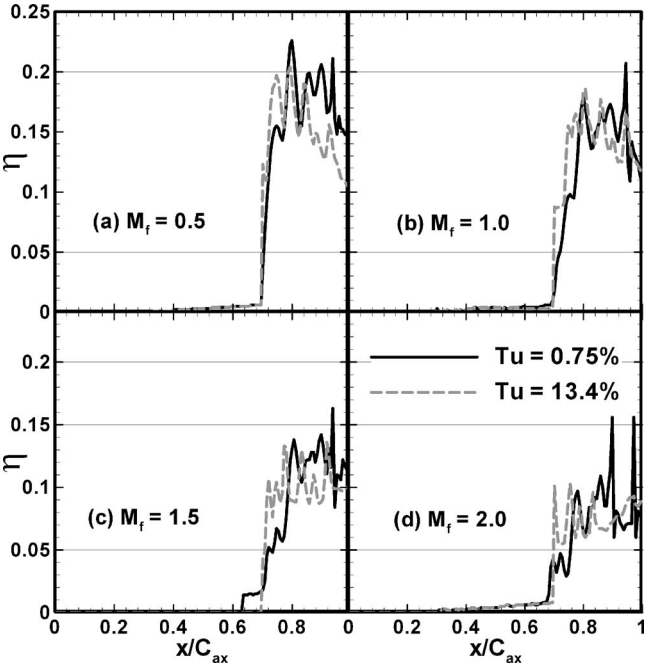

Fig. 10 Laterally averaged film cooling effectiveness on the passage end wall with downstream discrete film cooling

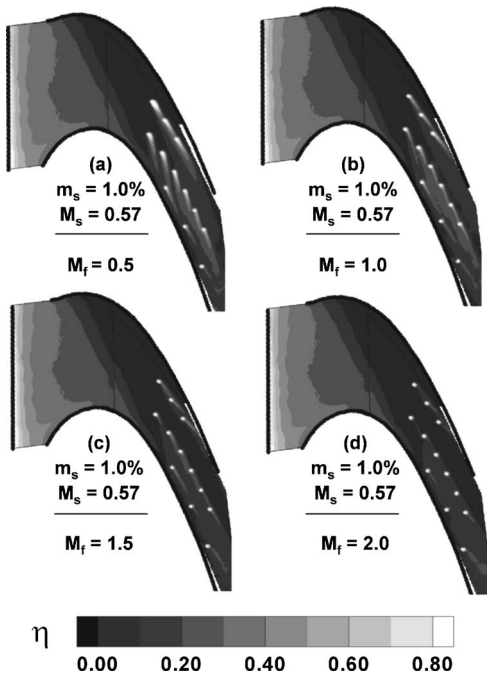

Fig. 11 Film cooling effectiveness with combined seal cooling (1%) and downstream film cooling (Tu=0.75%)

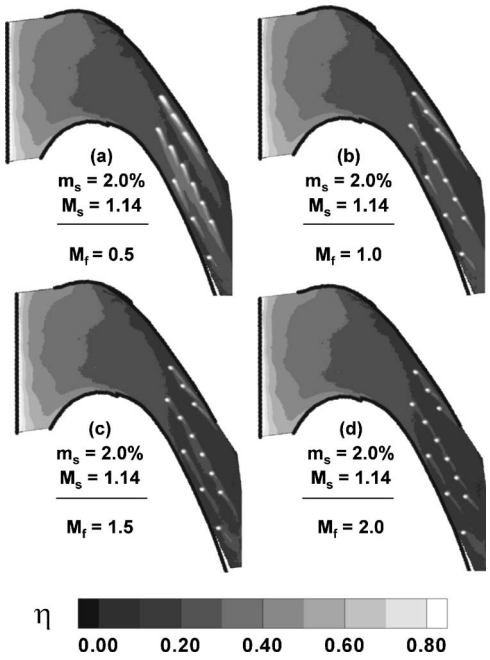

Fig. 12 Film cooling effectiveness with combined seal cooling (2%) and downstream film cooling (Tu=0.75%)

nique, it also clearly shows how the coolant is inefficiently used. The path of the coolant from the middle row of film holes nearly follows the streamlines through the passage. As stated earlier, increasing the flow rate of the coolant through the seal can weaken the effect of the passage induced secondary flow. This is seen by the path of the coolant from the holes; the coolant is no longer directed from the pressure side to the suction side of the passage (as dominant passage vortex would dictate).

The combined effect of the upstream injection and the discrete holes is shown by the laterally averaged effectiveness in Fig. 13. Beginning with the seal injection rate of 1.0%, from the reference case (only seal flow with m_s=1.0%), the effectiveness quickly drops into the passage. However, with the addition of the downstream discrete film cooling holes, the effectiveness increases dramatically with the additional cooling. With the seal injection of 2.0%, the effectiveness is obviously greater than that with the injection of 1.0%. The film cooling effectiveness is elevated with the film cooling holes; however, the increase is not as significant as with the injection rate of 1.0%.

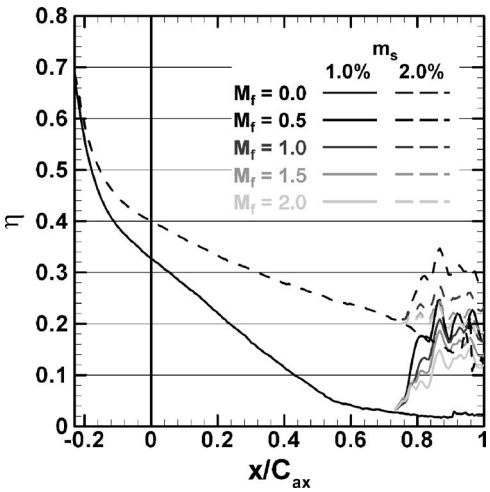

Fig. 13 Laterally averaged film cooling effectiveness on the passage end wall with combined upstream seal injection and downstream discrete film cooling (Tu=0.75%)

Conclusions

Detailed film cooling effectiveness distributions have been obtained on the platform of a high pressure turbine blade within a linear cascade. An advanced, labyrinthlike seal has been used to model the stator-rotor seal common to modern gas turbine engines. The purge flow through this seal is significantly affected by the complex secondary flow along the passage end wall. The PSP technique clearly demonstrates the impact of passage secondary flow on the film cooling effectiveness. The protection offered through the advanced seal of the current seal is less than that from an inclined slot and moreover from a tangential slot (as this should be anticipated due to the perpendicular injection of the present geometry). However, with this seal geometry, the coolant exits the seal more uniformly (across the entire length of the seal) than with the inclined slot. Although the effectiveness is reduced, the possibility of hot gas ingestion is also reduced, which is an obvious advantage of the advanced seal design.

The behavior of the discrete film cooling holes is best described from traditional flat plate film cooling studies with cylindrical holes. The maximum effectiveness occurs when the blowing ratio (M_f) is 0.5. As the blowing ratio increases beyond 1.0, the coolant tends to lift off the surface, and protection is inadequate. In addition, the path of the coolant from the holes is also affected by the passage induced secondary flow. Although the coolant is injected toward the pressure side of the passage, the coolant traces follow the passage vortex toward the suction side of the passage.

Finally, combining upstream slot injection with downstream discrete film hole cooling has the potential to further increase the end wall film cooling effectiveness. With the current cooling scheme, with an injection rate of 1.0%, an area near the pressure side of the passage is left unprotected. However, increasing the injection rate to 2.0% results in much of the passage being overcooled, and thus the coolant is wasted. Therefore, additional film cooling holes located near the pressure side of the passage can potentially offer additional protection while using less coolant through the stator-rotor seal.

Acknowledgment

This paper was prepared with the support of the U.S. Department of Energy, Office of Fossil Energy, National Energy Technology Laboratory.

Nomenclature

C = true chord length of the blade
C_{ax} = axial chord length of the blade
C_{mix} = oxygen concentration of mainstream-coolant mixture
C_∞ = oxygen concentration of mainstream
d = film hole diameter
I_f = discrete film hole momentum flux ratio ($=\rho_f V_f^2/\rho_m V_{m2}^2 \cong V_f^2/V_{m2}^2$)
I_s = slot injection momentum flux ratio ($=\rho_s V_s^2/\rho_m V_{m1}^2 \cong V_s^2/V_{m1}^2$)
l_f = discrete film hole length
l_s = slot length
M_f = discrete film hole blowing ratio ($=\rho_f V_f/\rho_m V_{m2} \cong V_f/V_{m2}$)
m_s = slot injection mass flow ratio (percentage of mainstream flow)
M_s = slot injection blowing ratio ($=\rho_s V_s/\rho_m V_{m1} \cong V_s/V_{m1}$)
MFR_{total} = total mass flux ratio (coolant to mainstream)
P_{O_2} = partial pressure of oxygen

Re = mainstream flow Reynolds number base on the inlet velocity and chord length
S = slot width (m)
Tu = turbulence intensity
V_f = discrete film hole velocity (m/s)
V_{m1} = mainstream velocity at the cascade inlet (m/s)
V_{m2} = mainstream velocity at the cascade exit (m/s)
V_s = slot injection velocity (m/s)
w = slot width (m)
x = axial distance from the cascade leading edge (m)
α = lateral injection angle
θ = streamwise injection angle
ρ_f = density of film coolant (kg/m^3)
ρ_m = density of mainstream (kg/m^3)
ρ_s = density of slot coolant (kg/m^3)
η = film cooling effectiveness $(=[(P_{O_2})_{air}-(P_{O_2})_{N_2}]/(P_{O_2})_{air})$

References

[1] Han, J. C., Dutta, S., and Ekkad, S. V., 2000, *Gas Turbine Heat Transfer and Cooling Technology*, Taylor & Francis, New York.
[2] Langston, L. S., 2001, "Secondary Flows in Axial Turbines—A Review," Ann. N.Y. Acad. Sci., **934**, pp. 11–26.
[3] Chyu, M. K., 2001, "Heat Transfer Near Turbine Nozzle Endwall," Ann. N.Y. Acad. Sci., **934**, pp. 27–36.
[4] Simon, T. W., and Piggush, J. D., 2006, "Turbine Endwall Aerodynamics and Heat Transfer," J. Propul. Power, **22**, pp. 310–312.
[5] Langston, L. S., Nice, L. M., and Hooper, R. M., 1976, "Three-Dimensional Flow Within a Turbine Cascade Passage," ASME Paper No. 76-GT-50.
[6] Langston, L. S., 1980, "Crossflows in a Turbine Cascade Passage," ASME J. Eng. Power, **102**, pp. 866–874.
[7] Goldstein, R. J., and Spores, R. A., 1988, "Turbulent Transport on the Endwall in the Region Between Adjacent Turbine Blades," ASME J. Heat Transfer, **110**, pp. 862–869.
[8] Wang, H. P., Olson, S. J., and Goldstein, R. J., 1997, "Flow Visualization in a Linear Turbine Cascade of High Performance Turbine Blades," ASME J. Turbomach., **119**, pp. 1–8.
[9] Takeishi, K., Matsuura, M., Aoki, S., and Sato, T., 1990, "An Experimental Study of Heat Transfer and Film Cooling on Low Aspect Ratio Turbine Nozzles," ASME J. Turbomach., **112**, pp. 488–496.
[10] Harasgama, S. P., and Burton, C. S., 1992, "Film Cooling Research on the Endwall of a Turbine Nozzle Guide Vane in a Short Duration Annular Cascade: Part 1—Experimental Technique and Results," ASME J. Turbomach., **114**, pp. 734–740.
[11] Jabbari, M. Y., Marston, K. C., Eckert, E. R. G., and Goldstein, R. J., 1996, "Film Cooling of the Gas Turbine Endwall by Discrete-Hole Injection," ASME J. Turbomach., **118**, pp. 278–284.
[12] Friedrichs, S., Hodson, H. P., and Dawes, W. N., 1996, "Distribution of Film-Cooling Effectiveness on a Turbine Endwall Measured Using the Ammonia and Diazo Technique," ASME J. Turbomach., **118**, pp. 613–621.
[13] Friedrichs, S., Hodson, H. P., and Dawes, W. N., 1997, "Aerodynamic Aspects of Endwall Film Cooling," ASME J. Turbomach. **119**, pp. 786–793.
[14] Friedrichs, S., Hodson, H. P., and Dawes, W. N., 1998, "The Design of an Improved Endwall Film Cooling Configuration," ASME Paper No. 98-GT-483.
[15] Barigozzi, G., Benzoni, G., Franchini, G., and Derdichizzi, A., 2005, "Fan-Shaped Hole Effects on the Aero-Thermal Performance of a Film Cooled Endwall," ASME Paper No. GT2005–68544.
[16] Blair, M. F., 1974, "An Experimental Study of Heat Transfer and Film Cooling on Large-Scale Turbine Endwall," ASME J. Heat Transfer **96**, pp. 524–529.
[17] Granser, D., and Schulenberg, T., 1990, "Prediction and Measurement of Film Cooling Effectiveness for a First-Stage Turbine Vane Shroud," ASME Paper No. 90-GT-95.
[18] Roy, R. P., Squires, K. D., Gerendas, M., Song, S., Howe, W. J., and Ansari, A., 2000, "Flow and Heat Transfer at the Hub Endwall of Inlet Vane Passages—Experiments and Simulations," ASME Paper No. 2000-GT-198.
[19] Burd, S. W., Satterness, C. J., and Simon, T. J., 2000, "Effects of Slot Bleed Injection Over a Contoured End Wall on Nozzle Guide Vane Cooling Performance: Part II—Thermal Measurements," ASME Paper No. 2000-GT-200.
[20] Oke, R., Simon, T., Shih, T., Zhu, B., Lin, Y. L., and Chyu, M., 2001, "Measurements Over a Film-Cooled Contoured Endwall With Various Coolant Injection Rates," ASME Paper No. 2001-GT-0140.
[21] Oke, R. A., and Simon, T. W., 2002, "Film Cooling Experiments With Flow Introduced Upstream of a First Stage Nozzle Guide Vane Through Slots of Various Geometries," ASME Paper No. GT-2002–30169.
[22] Nicklas, M., 2001, "Film-Cooled Turbine Endwall in a Transonic Flow Filed: Part II—Heat Transfer and Film Cooling Effectiveness," ASME J. Turbomach., **123**, pp. 720–729.
[23] Liu, G., Liu, S., Zhu, H., Lapworth, B. C., and Forest, A. E., 2004, "Endwall Heat Transfer and Film Cooling Measurements in a Turbine Cascade With Injection Upstream of Leading Edge," Heat Transfer Asian Res. **33**, pp. 141–152.
[24] Zhang, L. J., and Jaiswal, R. S., 2001, "Turbine Nozzle Endwall Film Cooling Study Using Pressure-Sensitive Paint," ASME J. Turbomach. **123**, pp. 730–735.
[25] Zhang, L. J., and Moon, H. K., 2003, "Turbine Nozzle Endwall Inlet Film Cooling—The Effect of a Backward Facing Step," ASME Paper No. GT2003–38319.
[26] Knost, D. G., and Thole, K. A., 2004, "Adiabatic Effectiveness Measurements of Endwall Film Cooling for a First Stage Vane," ASME Paper No. GT2004–53326.
[27] Cardwell, N. D., Sundaram, N., and Thole, K. A., 2005, "Effects of Mid-Passage Gap, Endwall Misalignment and Roughness on Endwall Film-Cooling," ASME Paper No. GT2005–68900.
[28] Wright, L. M., Gao, Z., Yang, H., and Han, J. C., 2006, "Film Cooling Effectiveness Distribution on a Gas Turbine Blade Platform With Inclined Slot Leakage and Discrete Film Hole Flows," ASME Paper No. GT2006–90375.
[29] Zhang, L., and Han, J. C., 1994, "Influence of Mainstream Turbulence on Heat Transfer Coefficients From a Gas Turbine Blade," ASME J. Heat Transfer **116**, pp. 896–903.
[30] Wright, L. M., Gao, Z., Varvel, T. A., and Han, J. C., 2005, "Assessment of Steady State PSP, TSP, and IR Measurement Techniques for Flat Plate Film Cooling," ASME Paper No. HT2005–72363.
[31] Gao, Z., Wright, L. M., and Han, J. C., 2005, "Assessment of Steady State PSP and Transient IR Measurement Techniques for Leading Edge Film Cooling," ASME Paper No. IMECE2005–80146.
[32] Ahn, J., Schobeiri, M. T., Han, J. C., and Moon, H. K., 2004, "Film Cooling Effectiveness on the Leading Edge of a Rotating Turbine Blade," ASME Paper No. IMECE2004–59852.
[33] Ahn, J., Schobeiri, M. T., Han, J. C., and Moon, H. K., 2005, "Film Cooling Effectiveness on the Leading Edge of a Rotating Film-Cooled Blade Using Pressure Sensitive Paint," ASME Paper No. GT2005–68344.
[34] Ahn, J., Mhetras, S., and Han, J. C., 2004, "Film-Cooling Effectiveness on a Gas Turbine Blade Tip Using Pressure Sensitive Paint," ASME Paper No. GT2004–53249.
[35] Mhetras, S., Yang, H., Gao, Z., and Han, J. C., 2005, "Film-Cooling Effectiveness on Squealer Rim Walls and Squealer Cavity Floor of a Gas Turbine Blade Tip Using Pressure Sensitive Paint," ASME Paper No. GT2005–68387.
[36] Coleman, H. W., and Steele, W. G., 1989, *Experimentation and Uncertainty Analysis for Engineers*, Wiley, New York.
[37] Goldstein, R. G., 1971, "Film Cooling," Adv. Heat Transfer **7**, pp. 321—379.

Optimized Shroud Design for Axial Turbine Aerodynamic Performance

L. Porreca[1]
e-mail: luca.porreca@ch.manturbo.com

A. I. Kalfas[2]

R. S. Abhari

Turbomachinery Laboratory,
Swiss Federal Institute of Technology,
CH-8092 Zurich, Switzerland

This paper presents a comprehensive study of the effect of shroud design in axial turbine aerodynamics. Experimental measurements and numerical simulations have been conducted on three different test cases with identical blade geometry and tip clearances but different shroud designs. The first and second test cases are representative of a full shroud and a nonaxisymmetric partial shroud geometry while the third test case uses an optimized partial shroud. Partial shrouds are sometimes used in industrial application in order to benefit from the advantage of shrouded configuration, as well as reduce mechanical stress on the blades. However, the optimal compromise between mechanical considerations and aerodynamic performances is still an open issue due to the resulting highly three-dimensional unsteady flow field. Aerodynamic performance is measured in a low-speed axial turbine facility and shows that there are clear differences between the test cases. In addition, steady and time resolved measurements are performed together with computational analysis in order to improve the understanding of the effect of the shroud geometry on the flow field and to quantify the sources of the resultant additional losses. The flow field analysis shows that the effect of the shroud geometry is significant from 60% blade height span to the tip. Tip leakage vortex in the first rotor is originated in the partial shroud test cases while the full shroud case presents only a weak indigenous tip passage vortex. This results in a significant difference in the secondary flow development in the following second stator with associated losses that varies by about 1% in this row. The analysis shows that the modified partial shroud design has improved considerably the aerodynamic efficiency by about 0.6% by keeping almost unchanged the overall weight of this component, and thus blade root stresses. The work, therefore, presents a comprehensive flow field analysis and shows the impact of the shroud geometry in the aerodynamic performance. [DOI: 10.1115/1.2777187]

Introduction

In any turbomachine, sealing between moving blade rows and stationary component at the casing is achieved using a number of different design strategies that focus on the reduction of leakage flow over the blades. The leakage flow that occurs in between this gap is still considered as a main source of aerodynamic loss and several researches have focused on this aspect (Denton [1], Gier et al. [2], and Peters et al. [3]). Typically, tip leakage loss accounts for almost 1/3 of the overall turbine stage loss. Obviously, the smaller the gap, the lower are the losses, however, mechanical and thermal considerations do not allow the reduction of this gap to less than, typically, 1% of the blade height. Minimizing aerodynamic losses and maintaining tight tip clearances over the life of the engine in such a hot environment are still very critical issues in modern turbomachinery design.

In the unshrouded blade design, the blade tip is extended toward the rotor casing while keeping a reasonable gap between rotating and stationary parts. Positioning a shroud around the blades ensures a better seal of this gap with a corresponding increase of aerodynamic efficiency. However, this design requires a more complicated cooling arrangement to ensure reasonable temperatures in the shroud part. This requires more coolant flow to be extracted from the compressor section, and therefore a higher efficiency penalty on the overall performance. This cooling arrangement also significantly increases the manufacturing cost per blade. Additionally, the increased weight at the highest radius of the blade increases considerably the blade/disk centrifugal stresses. For these reasons and in view of higher engine core temperature, higher blade speeds, and reduced airfoil number, several alternative solutions are under consideration. In some cases, partial shrouds are already in use in order to reduce the weight and maintain the aerodynamic benefit of the shrouded turbines. However, with a partial shroud, the resultant flow field is highly three dimensional and unsteady and care should be taken in the optimal match between the blade tip profile and shroud/cavity geometry.

The first published use of partial shroud design is from Patel [4]. The author claimed an efficiency improvement of 1.2% with respect to a plain tip. The measured angle shows that the winglet does not change the maximum underturning associated with the tip leakage vortex but it is suggested that the passage secondary vortex is reduced.

Yaras and Sjolander [5] conducted a study of the influence of winglets on the pressure side, suction side, and both sides of the blades in a low turning airfoil linear cascade. The authors claimed a modest reduction of tip leakage losses; particularly, the pressure side winglet seemed to reduce the discharge coefficient while the suction side winglet reduces the pressure difference across the tip. Harvey et al. [6,7] proposed a new concept design of blade "winglet" where a partial shroud is extended on the tip blade. Their intent was to find a way to reduce the exit velocities of the tip leakage flow and the free stream on the suction side tip in order to reduce mixing. Additionally, they sought to aerodynamically off-load the rotor tip by applying a tangential lean without compromising the mechanical design and to reduce the leakage mass flow. Experimental results on this geometry show an in-

[1]Present address: MAN Turbo AG Schweiz, Zurich, Switzerland.
[2]Present address: Aristotle University of Thessaloniki, Thessaloniki, Greece.

Contributed by the International Gas Turbine Institute of ASME for publication in the JOURNAL OF TURBOMACHINERY. Manuscript received February 12, 2007; final manuscript received March 6, 2007; published online May 5, 2008. Review conducted by David Wisler. Paper presented at the ASME Turbo Expo 2007: Land, Sea and Air (GT2007), Montreal, Quebec, Canada, May 14–17, 2007, Paper No. GT2007-27915.

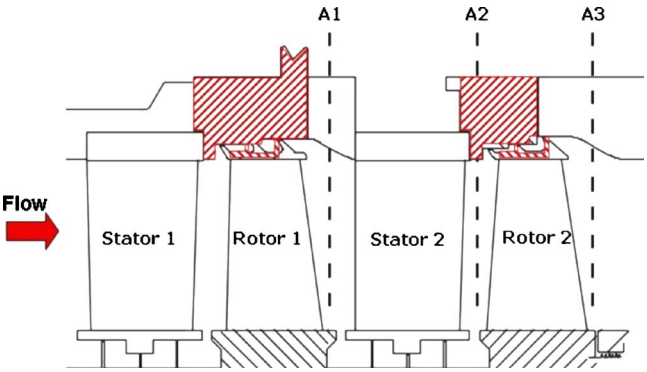

Fig. 1 Meridional view of the two-stage geometry and the shroud different configurations

creased performance of this new shroud design applied on a modern high pressure (HP) turbine section. The performance of the winglet is comparable to a fully shrouded blade with two fins. Despite the positive results obtained for winglets, none is known to have entered commercial service yet.

Nirmalan and Bailey [8] performed an extensive experimental and numerical study on a linear cascade with three different shrouds: full shroud, medium shroud, and deep scalloped shroud. The authors showed that the shroud geometry has a large impact on the performance loss. The unscalloped shroud (equivalent to a full shroud) shows the highest performance as expected, but as the tip gap increases (higher than 1% of the blade height), the shroud geometry does not play a major role. However, it should be noted that their study did not take into account rotation or flow unsteadiness.

This study presents a comparison of three test cases with the same blade geometry but different shrouds. The test cases are representative of a full shroud (FS) configuration, partial shroud (PS) configuration, and enhanced partial shroud (EPS) geometry. The overall effect of the partial shroud geometry on the turbine is an increase of flow unsteadiness due to the formation of a vortex pattern on the shroud cutback close to the trailing edge, which significantly affects the flow field in both rotating and stationary blade rows. A change in the turbine flow capacity is observed in the partial shroud cases due to the increased flow area of the rotor passage at the tip caused by the shroud geometry. Additionally, significant change in the aerodynamic efficiency has been measured in the second stage.

Test Cases

The test cases under investigation are representative of a modern gas turbine blading used for power generation purposes. The aerodynamic design of the two stages includes noncylindrical stacking of both stator and rotor and smooth geometry downstream the rotor shroud. Three test cases are taken in consideration in this work. The airfoil geometry is the same in all test cases except for the design of the shroud on both rotors 1 and 2 (shown in Fig. 1). The first test case (named FS in the following sections) uses an axis-symmetric full shroud typical of modern engine design that is adapted to the geometrical constraints of the parallel annulus of the facility. This shroud has three inclined forward fins and a one-step labyrinth path in the first rotor and two-step path in the second rotor. The other two test cases use partial shroud arrangements. The PS case has two vertical fins with a one-step labyrinth path and nonaxisymmetric shroud platform and cutback at the leading and trailing edges. Moreover, the shroud platform leaves the region from about 65% C_{ax} to the blade trailing edge (TE) uncovered.

The EPS has a similar geometry to the PS case but the shroud platform partially covers the blade passage at the TE, as shown in Fig. 2. In all cases, the tip clearance is identical and equal to 1% of the blade height. All test cases are examined at a constant turbine pressure drop and constant rotational speed. The mass flow is then a result of the slightly different flow capacity due to the different shroud geometry.

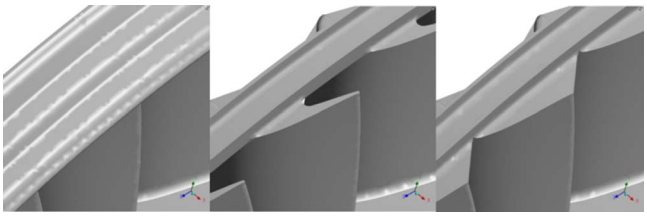

Fig. 2 Schematic of the shroud geometry: FS (left), PS (middle), and EPS (right)

Experimental Method

Research Facility. The experimental investigation has been performed in the research turbine "LISA" at the Turbomachinery Laboratory of the ETH Zurich. The facility can accommodate a maximum of two stages of an axial turbine. The air loop is of a closed type, and thus includes a radial compressor, a two-stage water to air heat exchanger, and a calibrated venturi nozzle for accurate mass flow measurements. A DC generator absorbs the turbine power and controls the rotational speed of the turbine shaft. The first and second rotors are mechanically decoupled by use of a twin spool shaft design. A pair of independent torquemeters allows the torque of each rotors to be separately measured.

To achieve the same rotational speeds, the shafts are coupled again before the DC generator. More details can be found in Porreca et al. [9]. The turbine is normally operated at constant pressure difference across the stages. The turbine entry temperature is controlled to an accuracy of 0.3% and the rpm is kept constant by the generator within the range of $\pm 0.02\%$ (± 0.5 rpm). The main operational parameters of the facility are listed in Table 1.

Measurement Technology. Flow parameters including total and static pressures, flow angles, velocity components, and Mach numbers are measured at frequencies of up to 40 kHz using a two-sensor fast response aerodynamic probe (FRAP). This probe is a modified version of the conventional single sensor probe; a second sensor that is sensitive to pitch angle variations of the flow is incorporated. This two-sensor FRAP has been used in previous investigations (Porreca et al. [9,10]). The FRAP also provides unsteady temperature measurements at a low frequency of up to 10 Hz. The absolute uncertainties in the measurements are listed in Table 2. Temperature measurements obtained with FRAP have an absolute uncertainty of the order of ± 0.3 K.

The measurement grid comprises 1502 points that are distributed uniformly in the circumferential direction at every 3.5% pitch (32 points in a pitch range of 1.1) and 47 points clustered toward the end walls in the radial direction. Data from the sensors are sampled at 200 kHz, which corresponds to 109 samples for each blade passing period. Phase-locked averaging of the data is done

Table 1 Main parameters of the "LISA" two-stage axial turbine research facility

Rotor speed (rpm)	2625
Overall pressure ratio	1.38
Mass flow (kg/s)	10.65
Blade count (stator/rotor)	42/42
Aspect ratio	1.8
Outer tip diameter (m)	0.8
Mach number (stator/rotor)	0.35/0.1
Reynolds number (rotor)	2×10^5

Table 2 Uncertainty in measurements of 5HP and FRAP

Probe type	φ (deg)	β (deg)	P_t (Pa)	P_s (Pa)	Ma
5HP	0.3	0.3	60	130	0.4
FRAP	0.3	0.3	100	150	0.5

Table 3 Quantity imbalance between turbine inlet/outlet of the computational domain for all test cases

Imbalance (%)	FS	PS	EPS
Mass flow	0.0028	0.0043	0.0048
Energy in R1	0.0156	0.0007	0.0036

over 80 rotor revolutions.

Steady state measurements are performed using miniaturized pneumatic five hole probes with a 0.9 mm diameter cobra head shape (Treiber et al. [11]). The probe is calibrated for ranges of ± 14 deg in yaw and ± 30 deg in pitch angle. The uncertainty of pneumatic probe measurements is reported in Table 2 for angles of ± 10 deg in yaw and ± 10 deg in pitch. For higher pitch angles, higher uncertainty is detected.

Numerical Method

The full stator and rotor passages for both stages are modeled in the computational mesh, except for the labyrinth path in the hub region. The tip clearance and shroud geometry are fully modeled in the meshing process (Fig. 3). To facilitate efficient meshing of the nonaxisymmetric partial shroud geometry and to reduce the turnaroundtime for grid generation, unstructured meshes covering both the main flow path and the tip leakage paths were chosen for all the test cases. Due to the same blade count number in both stator and rotor passages, the computational domain takes into account only one blade passage. Periodic boundary conditions are applied.

Following the hybrid meshing strategy of the commercial grid generator CENTAUR, prismatic elements were applied in regions of high flow gradients, and tetrahedra were used elsewhere with pyramids used in some locations to allow for a transition between the prisms and the tetrahedra. The total number of elements for both stages is about 2.7×10^6, corresponding to 1.2×10^6 nodes. The stator mesh is limited to 1.7×10^5 nodes, while the rotor blades, due to the resolved labyrinth seal passage, accounts for about 4×10^5 nodes. The resulting averaged nondimensional wall distance for all test cases is between 6.5 and 9.9 in the shroud region and to 25 on the rotor blades.

The simulations were performed using the commercial flow solver ANSYS CFX 10.0, which is an element-based conservative finite-volume method. All the calculations started with a frozen rotor, i.e., no averaging at the interface stator/rotor. Then the solution was switched using a mixing plane method which means that all the flow quantities are averaged in the circumferential direction at the interface stator/rotor. The solution residuals were monitored continuously for the momentum, energy, and turbulence equations. The residuals in all cases drop from 10^{-2} to 10^{-6} for the momentum equations, while the energy equation residual drops to 10^{-5}. The fidelity of the computational results is summarized in Table 3. Total computational time was about 4 hours using 16 parallel processors.

The measured total pressure profile and total temperature were prescribed at the inlet to the computational domain. The flow was assumed to be fully turbulent and turbulence closure was achieved using a standard k-ε turbulence model. The inlet turbulence intensity of 2% and a turbulent length scale of 0.1 m were chosen to reflect the flow conditions of the test facility. A reference static pressure at the exit and the radial equilibrium condition were prescribed at the outlet. All walls were assumed to be adiabatic to reproduce the thermal equilibrium conditions achieved during the experiments.

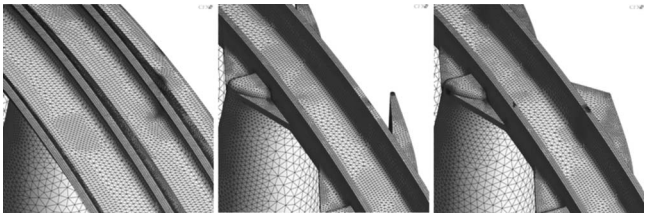

Fig. 3 Details of the numerical mesh on the shroud location: FS (left), PS (middle), and EPS (right)

Flow Field Analysis

First Rotor Exit. The leakage flow downstream of the first rotor still retains a large amount of the momentum of the upstream stator, as shown in numerous investigations. Therefore, in modern turbine design, an alignment between leakage flow and main stream is preferred in order to reduce the entropy production due to mixing process. For this reason, some designs adopt "bladelets" to turn the leakage flow in order to reduce the difference in tangential momentum. These devices have been found to be more effective when placed in the stationary frame (Rosic and Denton [12]) compared to the shroud (Wallis et al. [13]).

Figure 4 shows the mass-averaged absolute yaw angle downstream of the first rotor of the two test cases. In all cases, the flow has the same features from hub to midspan. Closer to the tip in the PS and EPS test cases, the measured data show that the fluid is underturned from approximately 60% span to the tip. The degree of underturning is much higher in the PS case. In the PS case, a vortex of considerable strength develops due to the TE cutback of the shroud. This feature is observed in the overturning-underturning behavior (of the order 10 deg) from the tip to 80% span. In the absence of the shroud platform, the main flow expands in the cavity region and rolls up in a vortex. This feature results in a marked underloading of the rotor blade from approximately 60% to 100% span (Fig. 4). In the EPS case, the presence of the shroud platform reduces the formation of this vortex even though there is a considerable degree of underturning/overturning from 60% to 100% blade span. Unsteady measurements show that this vortex is still shed by the rotor blade and is enhanced by the PS geometry. Close analysis of the tip region shows that the design intent of aligning the cavity flow with the main stream in the FS and EPS cases is quite well achieved. The flow is appropriately turned and the blading is fully loaded until 95% span. Closer to the tip region (from 95% to 100% span), the flow is underturned and better aligned with the cavity flow. In the PS case, the blade is underloaded from 60% span to the tip and the main flow mixes with the leakage layer and reaches an almost axial flow direction (yaw equal to zero). In all cases, a secondary flow structure is detected in the hub region. Previous investigations (Behr et al. [14] and Schlienger et al. [15]) have shown that the development of the hub passage vortex is greatly affected by the reentry of the labyrinth leakage flow of the upstream stator hub shroud.

Figure 4 right shows the comparison between the measured and calculated absolute yaw angles in the EPS case. CFD calculations show good agreement with the measured data at midspan. The difference between the computed and measured yaw angles in this region is limited in the range of ± 0.5 deg. At the tip, calculations can correctly predict the yaw angle trend up to the cavity. The underturning-overturning behavior at the hub region is not predicted. This is expected due to the fact that the stator hub leakage flow is not modeled in the CFD calculations. The vortical structures in this location result from the interaction between leakage

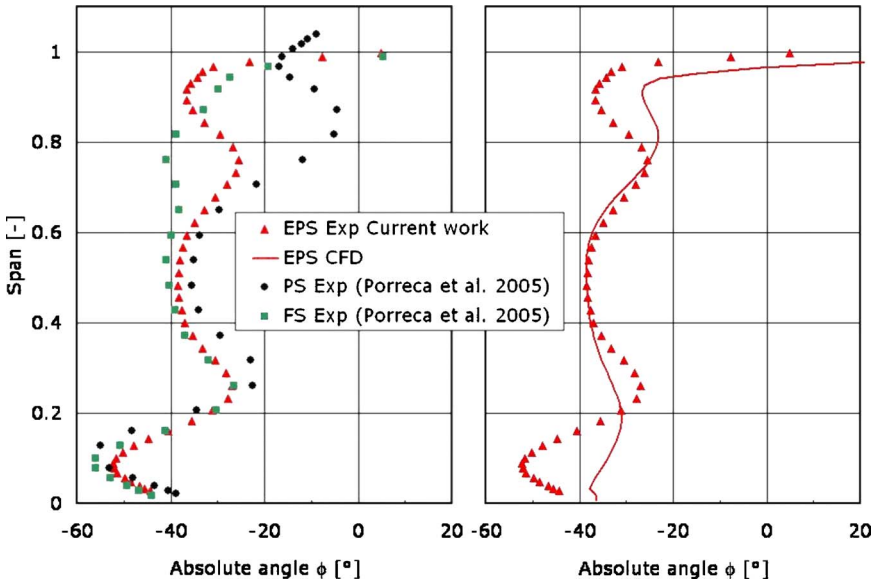

Fig. 4 Mass-averaged absolute yaw angle at the exit of the first rotor (Plane A1): expt. data (left), and expt. and CFD data of the EPS case (right)

from the stator cavity and hub rotor passage vortex.

The larger cavity of the PS test case at the exit of the first rotor produces a strong leakage flow interaction with the main stream. In the EPS case, even though the geometry of the cavity is the same as that of the PS case, the presence of the shroud platform prevents the main flow from expanding in the cavity and reaccelerating during the reentry in the main passage. Profile static pressure distributions at 75% span across the second stator blades show a typical negative incidence behavior in the PS test case. This is a result of the underloading of the PS tip rotor blade region and the incoming flow of the jet leakage. In the EPS case, a slight negative incidence is detected but with a smaller value compared to the PS case.

Total relative pressure measurements at the exit of the first rotor are presented in Fig. 5. Marked differences between the test cases are detected from 60% span to the tip. In the relative frame of reference, the total pressure reduction can be considered as a measure of loss. In the PS case, from 60% span where the yaw angle plot shows the start of the underturning, a considerable reduction of the relative total pressure is measured.

This is associated with the strong vortex at the tip at the TE cutback. A similar total pressure reduction is seen for the EPS case in this region but with a significantly lower absolute value. Additionally, the same trends in the FS and EPS are observed from 90% span up to the cavity region. One can conclude that the presence of the shroud platform in the EPS case guarantees a similar flow field at the blade tip compared to the FS case. In the FS case, the reduction of C_{pt} in both absolute and relative frames at 90–100% span is due to the wake generated by the rim at the TE of the shroud platform and the low momentum fluid coming from the labyrinth path.

Figure 6 shows the relative pressure coefficient plotted at the exit of the first rotor (Plane A1 in Fig. 1). For all test cases, the

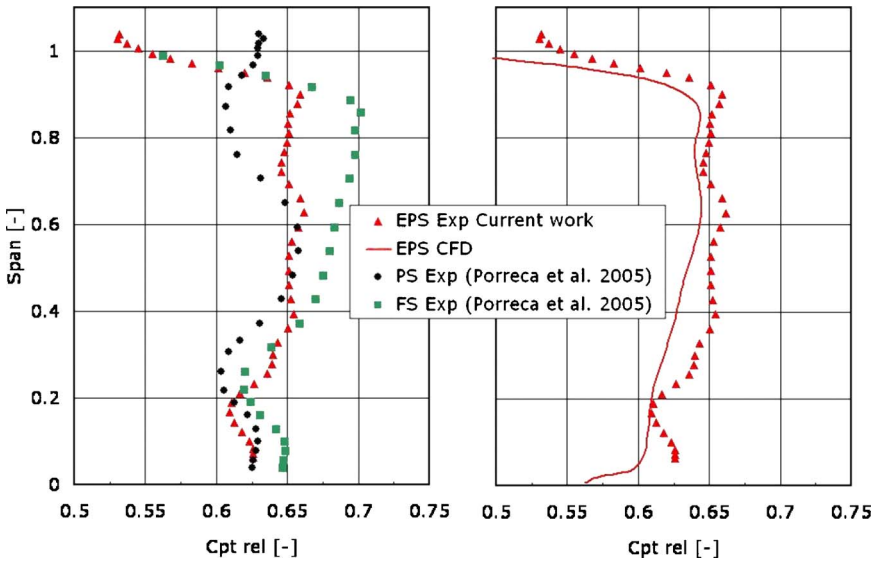

Fig. 5 Mass-averaged relative total pressure coefficient at the exit of the first rotor (Plane A1): expt. data (left), and expt. and CFD data of the EPS case (right)

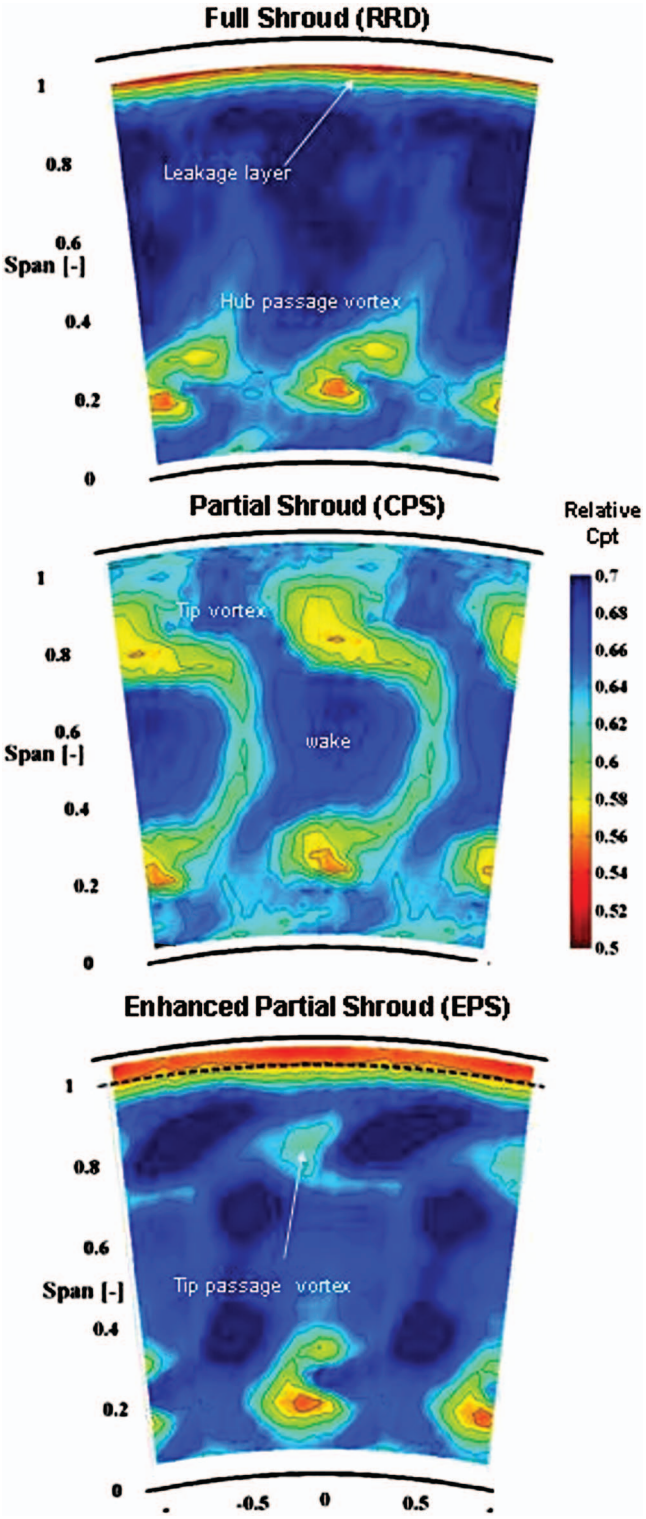

Fig. 6 Measured relative total pressure coefficient at the exit of the first rotor at one blade passing position (Plane A1)

same rotor blade fixed position is shown. In all cases, the hub passage vortex is identified by reduction of the total pressure coefficient between 20% and 30% blade span.

These flow structures appear to be quite similar in all test cases and their evolution and interaction with the wake and the downstream second stator row have been reported in detail and discussed by Behr et al. [14]. The wake is also identifiable in all cases. Significant differences appear close to the blade tip.

In the FS case, almost no pressure reduction corresponding to the tip passage vortex is observed. In this full shroud configuration, the boundary layer is sucked into the leakage path, and therefore, the passage vortex is rather weak. In the PS and EPS cases, however, a significant total pressure reduction is measured at about 80% blade span. In the PS case, this reduction is attributed to the tip vortex that originates from the uncovered region of the blade of the TE and expands on the cavity region. In the EPS case, the total pressure reduction is attributed to the growth of the passage vortex downstream of the shroud platform and mixing with the leakage layer. The formation and the evolution of this vortex are documented in the 3D-PIV measurements in Yun et al. [16]. In the FS and EPS cases, the low total pressure region very close to the blade tip that extends around the pitch is clearly visible. This pressure reduction is attributed to the presence of a low momentum fluid that comes from the leakage layer and is entrained in the main flow. In the PS case, the leakage layer is mixed with the vortex that is present due to the expansion of the main flow in the cavity region; thus the leakage layer is not visible in the upper blade span (span greater than 100%).

In Fig. 7, the time evolution of the relative total pressure coefficient is plotted as a function of the measurement position with respect to the stator blade pitch. The vertical dashed lines denote the position of the leading edge of the second stator. The regions of reduced relative total pressure associated with the vortical structure described previously in relation to Fig. 6 are seen to lie along the inclined lines in Fig. 7. This inclination indicates that the regions of lower total pressure move together with the rotor blade. At 80% span, the degree of interaction with secondary flow is relatively high and a broad region of decreased total pressure is observed. As the leading edge of the second stator is approached by the flow structures, the size of the region of low relative total pressure decreases.

Differences are clear between the three test cases. In the FS case, the tip passage vortex is relatively weak because the boundary layer at the inlet of the rotor tip casing is sucked into the leakage path. The new boundary layer develops in the lower part of the FS but, due to the full coverage of the shroud, the tip passage vortex does not expand in the labyrinth cavity. For this reason, the relative total pressure drop visible as inclined features (Fig. 7 top) is quite small at all circumferential positions. Corresponding with the LE of the second stator, a local total pressure reduction of the same magnitude as that corresponding to the vortex is measured showing that the flow field is mainly influenced by the potential field of the downstream second stator at this span.

In the PS case, a substantial relative total pressure reduction is observed (Fig. 6 middle). This reduction is associated with the tip vortex that is generated by the uncovered portion of the shroud platform. Moreover, this total pressure reduction is weakly influenced by the potential field of the second stator, i.e., the magnitude of the total pressure drop is nearly independent of the time.

The EPS Case (Fig. 7 bottom) shows similar features as the PS case but with a reduced magnitude. As shown in Fig. 6, the tip vortex originates at the blade tip but with a reduced pressure drop compared to the PS case. Additionally, the variation of the pressure drop along the time axis is more pronounced compared to the PS case. This variation suggests that there is a higher degree of unsteady interaction such as vortex stretching and growth in this geometry, compared to the other two, between the shed vortex from the first rotor and the second stator leading edge (LE). A detailed analysis of the unsteady loss mechanisms in this region is presented in Yun et al. [16].

Second Stator Exit. The flow detected at the exit of the first rotor significantly affects the aerodynamic behavior of the second stator row. The flow is similar for all test cases from hub up to midspan. At the hub, a passage vortex is established with typical overturning-underturning (Fig. 8). More radially outward, a marked underturning-overturning behavior is observed at 70% of

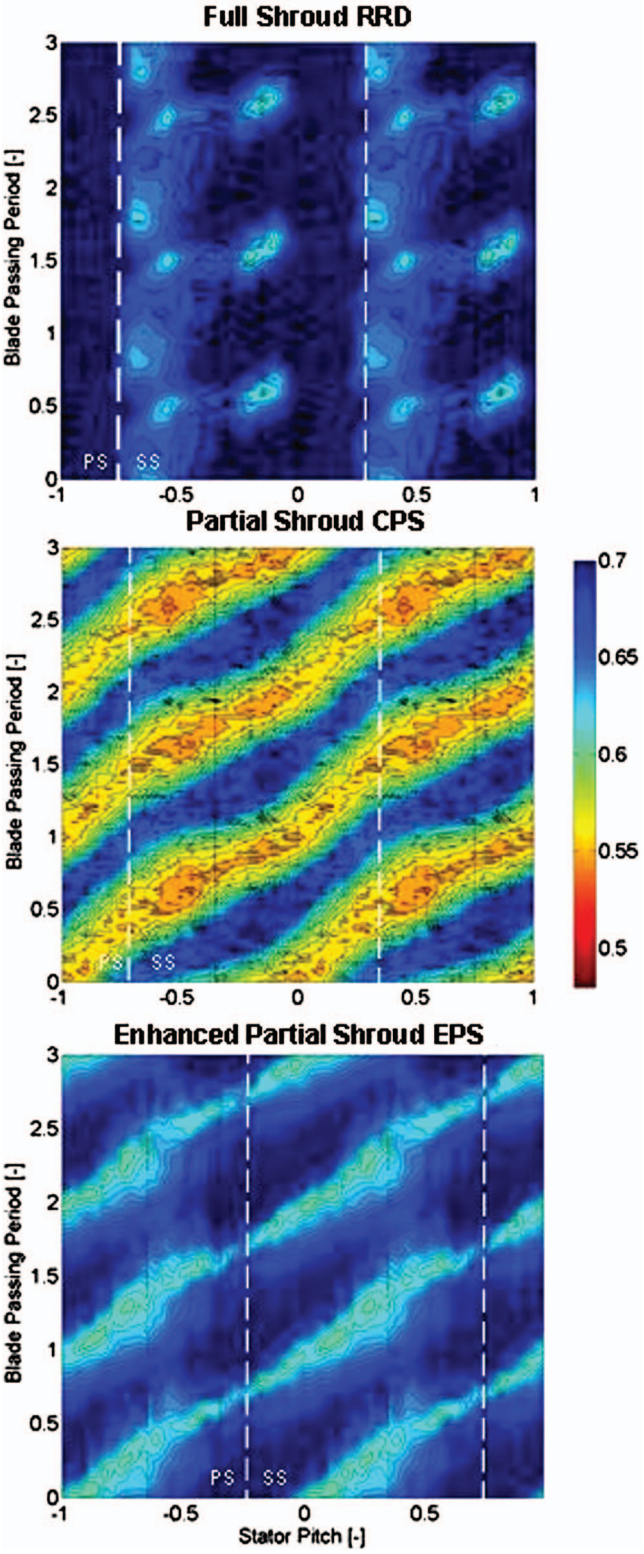

Fig. 7 Measured time-distance diagram of relative total pressure coefficient at 80% blade span at the exit of the first rotor (Plane A1)

the span in the FS test case. This feature is caused by the cavity flow in the first rotor that is accelerated by the reentry channel in the main stream and rolled up with the tip passage vortex. In the PS case, the turning from the stator row at the tip is reduced by as much as 25% with respect to the FS case, with the result that the inlet stator angle has a negative incidence. Consequently, the overturning-underturning of the tip passage vortex is decreased and occurs at 90% span due to the presence of the indigenous stator passage vortex. The local total pressure losses are decreased in the FS case. At midspan, a local decrease in the total pressure is identified and attributed to the compression of the wake structure due to the transported leakage vortex that comes from the first rotor. In the EPS case, the yaw angle profile follows the same trend as in the FS case. The flow behavior is almost unchanged until 60% span, then, closer to the tip, while the change in flow angle is the same, for the EPS case, the underturning-overturning occurs at larger angles. The comparison between the measured and computed data of the EPS case (Fig. 8 right) shows that the CFD is in reasonably good agreement with the experiment. Differences in the flow angles are limited to 2–3 deg. This comparison, together with the total pressure coefficient plot in Fig. 9, is representative of the other cases. The good agreement validates the use of the CFD results (presented below) to quantify the loss generation mechanisms.

Figure 10 shows the contour of the steady total pressure coefficient downstream of the second stator together with the secondary flow vectors. The vortex structures are very similar for all test cases from the hub to 40% span. The TE wake is identified in all three cases at approximately −20% blade pitch. The hub passage vortex that contributes to the total pressure reduction at about 10% span is very similar in all cases, as expected.

In the PS test case, a strong vortex is seen at midspan. This structure is thought to be the leakage vortex that originates from the first rotor. In the FS test case, the moderate leakage vortex is rolled up into the passage vortex and can be identified from the total pressure reduction that is between 60% and 80% blade span. The EPS case has secondary flow structures that are very similar to those measured in the FS case. Additionally, similar vortical structures that are associated with the secondary flow total pressure reduction cores can be seen. However, a close analysis of the EPS case shows that the low pressure region associated with the tip passage vortex between 60% and 80% span is more extended toward the middle of the stator passage (around a pitch of 0.4). This behavior in the EPS case is clearly shown in the mass-averaged total pressure coefficient profile shown in Fig. 9. The flow profile is almost identical when compared to the FS case until 70% span, beyond which there is a significant total pressure drop measured in the EPS case. It can be concluded from the analysis of Figs. 9 and 10 that the partial shroud of the PS case completely alters the secondary flow pattern at the exit of the second stator.

This is achieved by a lower blade loading at the tip (lower flow turning), and therefore reduced secondary losses at the blade tip. Moreover, due to the negative incidence at the LE, the radial pressure gradient is enhanced, which displaces vortical structures close to midspan. On the other hand, the EPS case has a similar blade loading and also similar secondary flow features; however, the associated losses at the tip are higher. The reason for this behavior is that greater losses are generated at the first rotor tip during the vortex mixing and dissipation in the interstage region. This high loss fluid is then reaccelerated in the second stator passage and entrained in the tip passage vortex. The results of this dynamic process is a lower total pressure value at the stator exit. Figure 11 shows the calculated streamlines and the entropy function coefficient $\exp(-\Delta s/R)$ (Denton [1]) on the suction surface of the second stator blade row.

These results are derived from the CFD simulation. The streamlines show that there is a well established two-dimensional flow between 20% and midspan, while at the hub, an identical lift-off of the passage vortex is observed for all three test cases. At the tip, major differences are seen in the secondary flow structures. The tip passage vortex appears quite weak in the PS case and has lower associated losses compared to the other cases. On the other hand, the EPS case has the highest secondary losses. By compar-

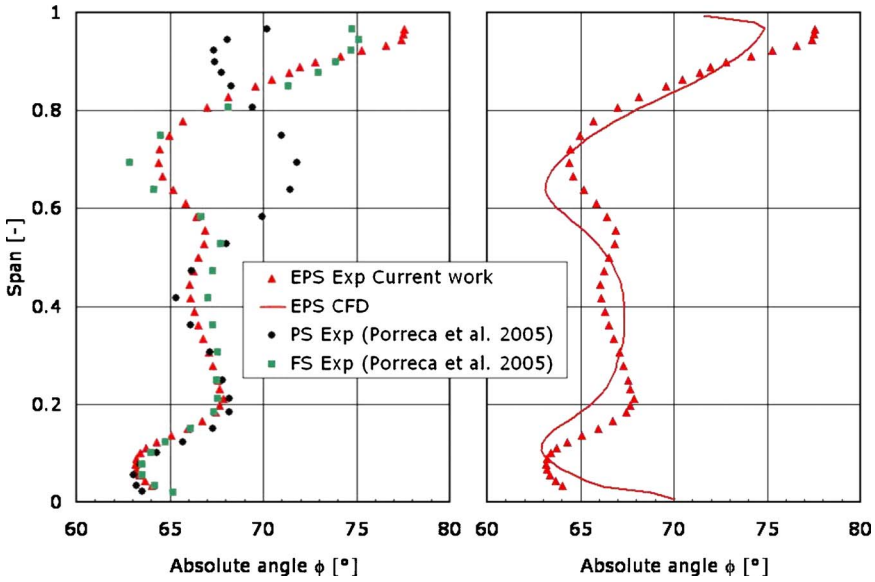

Fig. 8 Mass-averaged yaw angle at the exit of the second stator (Plane A2) expt. data (left), and expt. and CFD data of the EPS case (right)

ing the measurements of Fig. 10 streamlines and losses in Fig. 11, one can see excellent agreement in the details of the computed secondary flow structures induced by the shroud geometry on the second stator blade row. The aerodynamic efficiency of the blade row is quantified in a following section. To help our understanding of the vortex and loss transport mechanisms, the area-averaged meridional entropy function derived from the CFD computations is plotted in Fig. 12. The entropy function is set equal to 1 at the inlet of the first rotor, and thus, the losses are measured relative to this location. The upper plot represents the FS case, the middle the PS, and the lower the EPS. The main differences occur, as expected, in the upper part of the span height, from midspan to the blade tip. In the FS case, the highest entropy production is *inside* the labyrinth leakage path both in the first and second rotors as a result of strong flow recirculation and mixing between the shroud fins.

In the reentry process, e.g., downstream the first rotor, the leakage and the main flow mix together and results in the higher entropy level that is seen between 90% span and the casing of the interstage region. This high loss fluid enters the second stator passage and is then both convected downstream and radially moved downward by the tip passage vortex. Region A in Fig. 12 top denotes this loss core. In the same region, a total pressure drop was measured, as shown in Fig. 10. In the PS case, it is shown that the loss generation is less pronounced in the labyrinth path but more diffused over a large region that extends from 80% span up to the casing. Measurements of the relative total pressure shown in Fig. 6 confirm this behavior. Also, this high loss fluid is convected downstream into the second stator and the second rotor, thereby adversely affecting their performances.

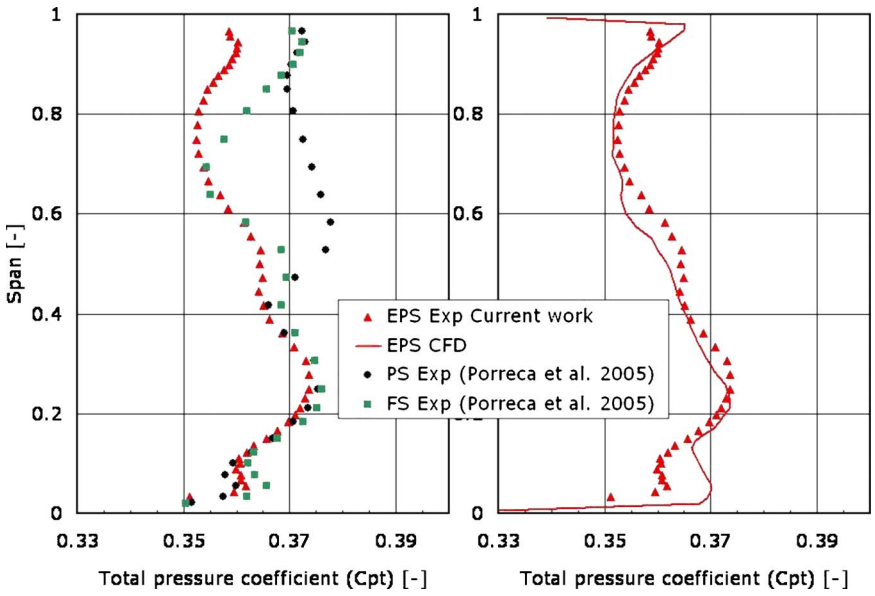

Fig. 9 Mass-averaged total pressure coefficient at the exit of the second stator (Plane A2): expt. data (left), and expt. and CFD data of the EPS case (right)

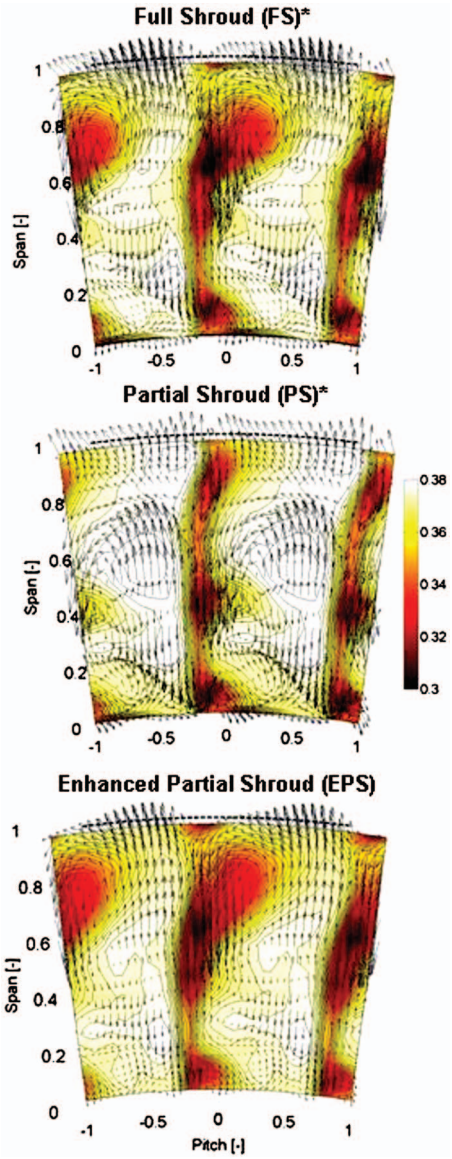

Fig. 10 Measured total pressure coefficient and secondary flow vector plot at the exit of the second stator FS* (top), PS* (middle), and EPS (bottom) (Plane A2) (data marked with asterisk are from Porreca et al. [9])

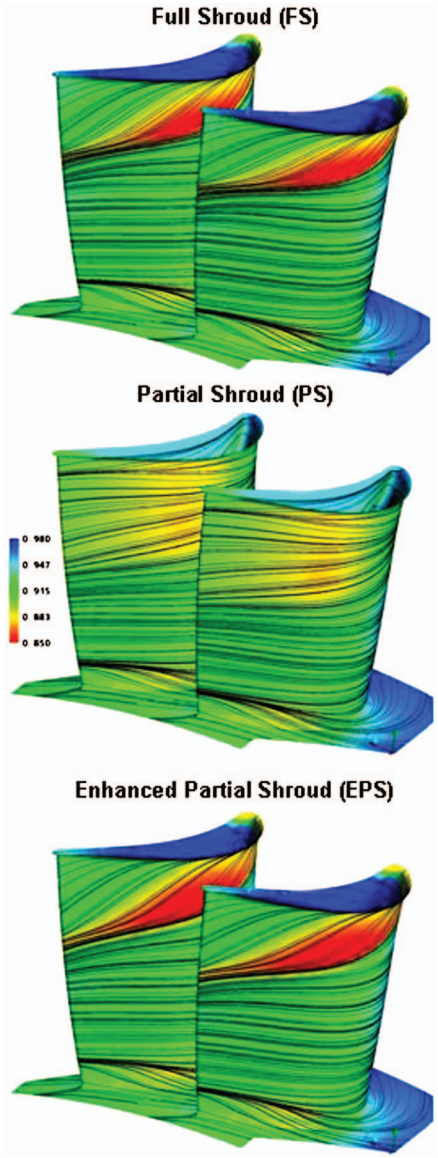

Fig. 11 Calculated streamlines and entropy function on the second stator suction surface: FS (top), PS (middle), and EPS (bottom)

The EPS case has similar features to the FS case, as in the labyrinth path there is considerable entropy loss and the reentry of the leakage flow into the main flow is also similar to the FS case. However, the losses are higher at the exit of the second stator, close to the tip (Region A), as also indicated by the total pressure measurements. From the analysis of Fig. 12, it can be concluded that the leakage flow and the flow structures generated over the upper height of the blade in the first rotor derive the loss production mechanisms and significantly affect the flow field of the second turbine stage. The analysis also shows that the EPS case has improved aerodynamic features, which are more similar to the PS case than to the reference FS case.

Turbine Exit. The turbine exit flow field is also influenced by the shroud geometry. The design intent at this location is to align the flow with the axial direction at midspan in order to minimize exit swirl, while at the hub and tip, moderate negative and positive swirls are still detected. Figure 13 shows the absolute yaw angle measured downstream of the second rotor. The same flow features are similar up to midspan. Closer toward the tip region, the flow angles are similar to those observed for the first rotor. A significant underturning occurs in the PS case, and the measured angles are about 20 deg different with respect to the reference FS test case. Moreover, the presence of underturning-overturning between 90% and 100% span shows the presence of the tip vortex that occurs in the PS case. Within the leakage layer (blade span greater than 100%), the PS case has only a moderate swirl, which indicates that mixing between the leakage flow and main stream has occurred upstream during the expansion of the main flow in the cavity region.

The FS case on the other hand has an almost constant yaw angle up to 90% span and then, similar to the first rotor, the main flow tends to be aligned with the leakage layer. The yaw angle of the EPS case presents a profile that lies in between the FS and PS cases. A moderate underturning is detected from 60% span, while close to the tip, an overturning-underturning is measured between 80% and 90% span as a result of the growth of the passage vortex as in the first rotor. The CFD results (Fig. 13 right) are in good agreement with the measured absolute yaw angle. The main flow,

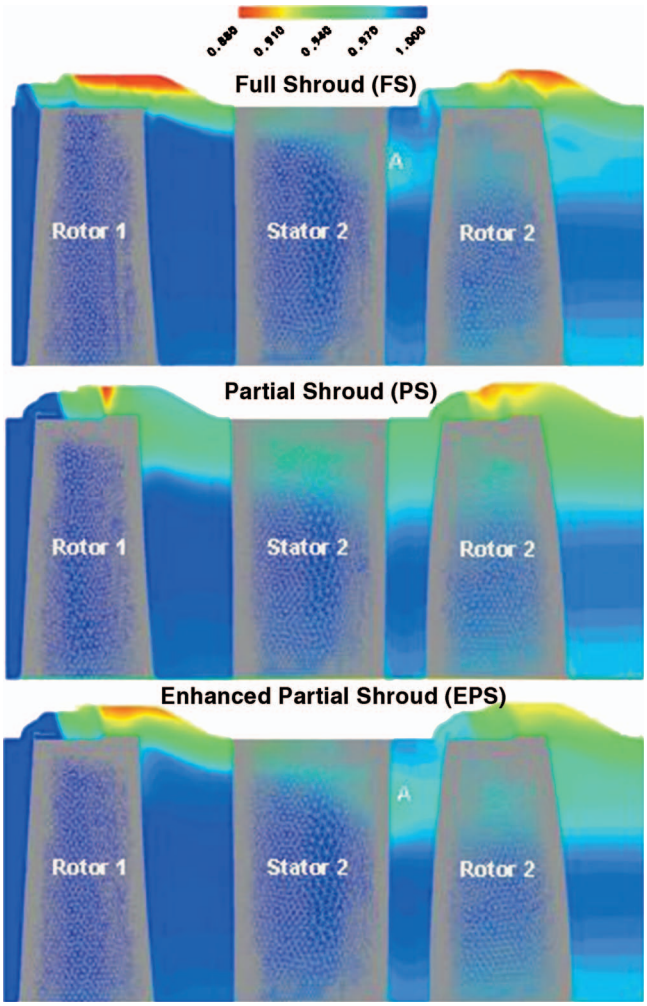

Fig. 12 Calculated area-averaged meridional entropy function: FS (top), PS (middle), and EPS (bottom) test cases

as well as the overturning/underturning, is well captured with differences limited to ± 1 deg at midspan and ± 2 deg in the tip secondary flow region.

To clarify the details of the flow structures that occur at the tip, the streamlines at several radial planes are presented in Fig. 14. The colored contours show the entropy function level with a reference at the inlet of the rotor row. In the FS case, as shown also in the circumferentially averaged plot in Fig. 12, a high loss level is detected in the labyrinth passage downstream of the last shroud fin. A circumferentially oriented vortex, which dissipates energy from the leakage flow, is seen. Downstream of the blade row, the effect of the leakage layer is visible only in a small portion of the boundary layer on the tip casing. Also, vortical streamlines due to the tip passage vortex do not appear. In the PS case, the expansion of the main flow in the leakage cavity and the roll up into a streamwise vortex are observed. Lower loss generation occurs in this case in the cavity; however, a higher level of entropy increase is diffused into the main flow. Higher entropy levels are also seen at the casing boundary layer and at the blade suction side surface.

The streamwise vortex drives the loss generation and diffusion processes. In the EPS case, the growth of the tip passage vortex in the streamwise direction can be seen along the radial planes in terms of associated losses. The entropy level is lower than the PS case and less diffused in the main flow region.

The analysis of Fig. 14, however, is not sufficient to draw a conclusion regarding the entropy production mechanism and to quantify the effect of the shroud geometry on the losses generated in different locations. Thus, a budget of the entropy production is performed in order to quantify the contribution on the losses of different flow structures in the second rotor, and then relate this to the measured aerodynamic efficiency.

Loss Generation Budget. A control volume analysis was used to evaluate the loss budget in the second rotor row. From the energy equation, it can be written that

$$\int_{\nu} \sigma d\nu + \int_{A} \frac{k \nabla T}{T} n dA = \frac{\partial}{\partial t} \int_{\nu} \rho s d\nu + \int_{A} \rho s V_n dA$$

where σ is the entropy production rate per unit volume, k is the thermal conductivity, and V_n is the normal velocity directed out of the volume. In the present analysis, the flow can be considered incompressible (as the maximum measured Mach number is equal

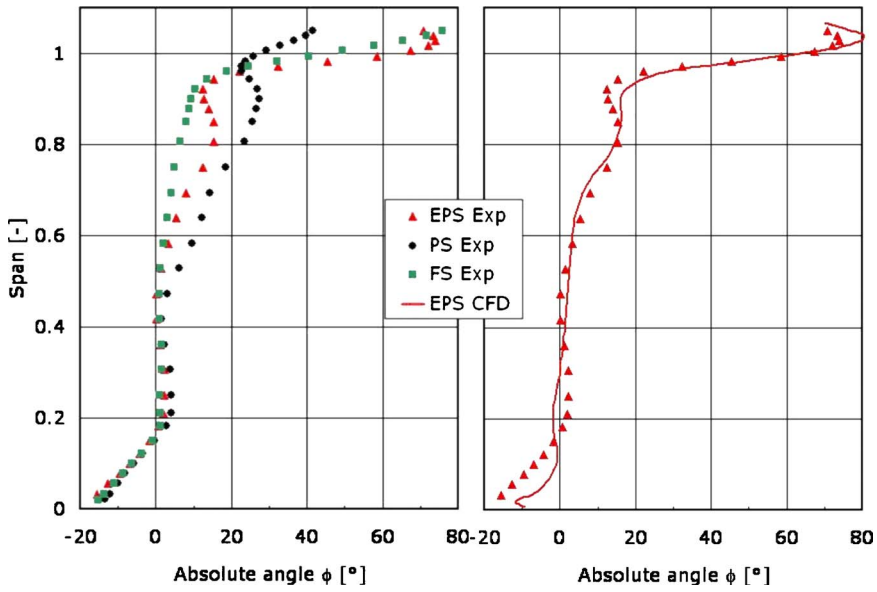

Fig. 13 Mass-averaged yaw angle at the turbine exit (Plane A3): expt. data (left), and expt. and CFD data of the EPS case (right)

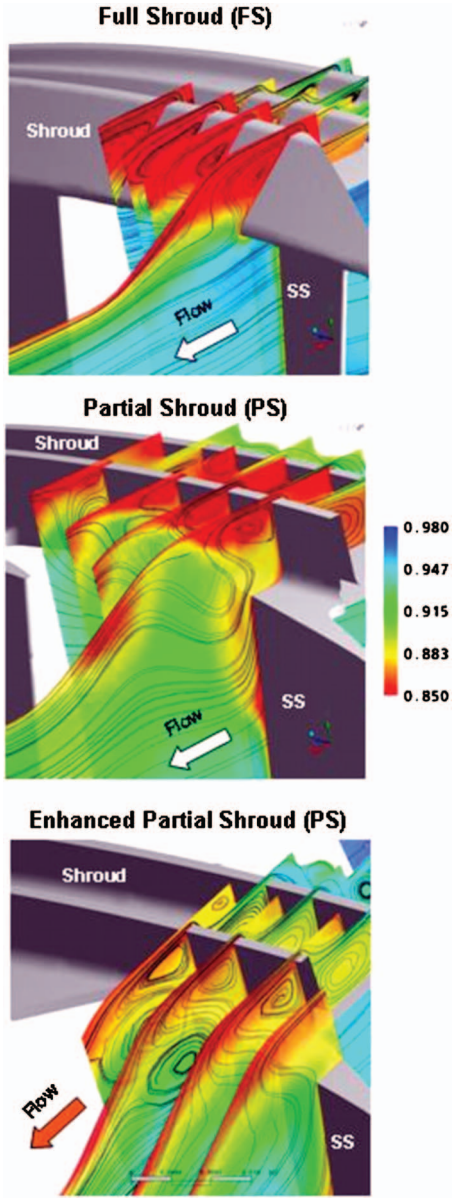

Fig. 14 Calculated streamline evolution at the turbine exit region (second rotor). Colors indicate entropy level.

to 0.31) and adiabatic. Therefore, the previous equation can be written, for steady state simulations, as:

$$\int_{\nu} \sigma d\nu = \int_{A} \rho s V_n dA$$

Since the CFD results are in good agreement with the measured flow field in the two stages, the entropy production rate is evaluated over four control volumes that quantify the contribution to the losses arising from different flow features. The control volumes are divided in the radial direction as follows. The "hub" control volume is defined as the volume from the hub to the 33% span where, based on the measurements, the hub passage vortex occurs. The "midspan" control volume is between 33% and 66% span in which the only identified feature is the wake structures, and the "tip" control volume lies between 66% and 98% span where the tip passage vortex is dominant. The remaining volume is the "leakage" control volume that includes the labyrinth path up to the rotor casing wall and the exit cavity where the leakage flow is prevailing. Table 4 summarizes the location of the control volumes used in this analysis. The inlet of the control volume is the axial plane at 13% C_{ax} upstream the LE and the outlet is placed at 36% C_{ax} downstream the TE.

Table 4 Control volume location in the loss generation budget analysis of the second rotor

Region	Location (% of blade span)
Hub	0–33
Midspan	33–66
Tip	66–98
Leakage	98–113

To show the contribution from the different control volumes, the overall entropy generation rate in the second stage was taken as 100% for each test case. Figure 15 shows the respective entropy production as a percentage of the stage value.

Figure 15 shows clearly that the contribution of the hub passage vortex is significant and accounts for about 20% of the overall entropy production for all test cases. The contribution of the wake structure is limited between 6% and 7.3%, while the contribution of the tip region is even smaller. These results can be explained by taking into account the fact that the second blade row has a relatively low loading at the tip, and therefore, the contribution of the tip passage vortex is rather small in all cases. Additionally, the PS and EPS cases, due to the shroud geometry, have a lower loading in the region between midspan and the tip; thus, the tip passage vortex is weakened.

Therefore, the entropy production in this case is lower (PS =4.3% and EPS=5.3%) compared to the FS case (5.45%). In the leakage region, significant differences are observed between the test cases. In the FS case, the entropy produced in the labyrinth path and in the mixing of the leakage with the main stream at the blade row exit contributes with 15.8% of the overall entropy generated in the second stage.

In the PS case, this is increased up to 25.8%, while the EPS case has an intermediate value. The reason for this improvement is related to the flow kinematics and interaction between the leakage flow, the tip passage vortex, and the main stream, which have been described in the above sections.

The entropy generation budget analysis quantifies clearly the relative contributions of the different flow regions to the total aerodynamic stage losses. Therefore, in order to improve the aerodynamic performance, the most beneficial design strategy is to pay more attention to the labyrinth path region and the mixing of the reentry of the leakage flow. The use of the partial shroud as in

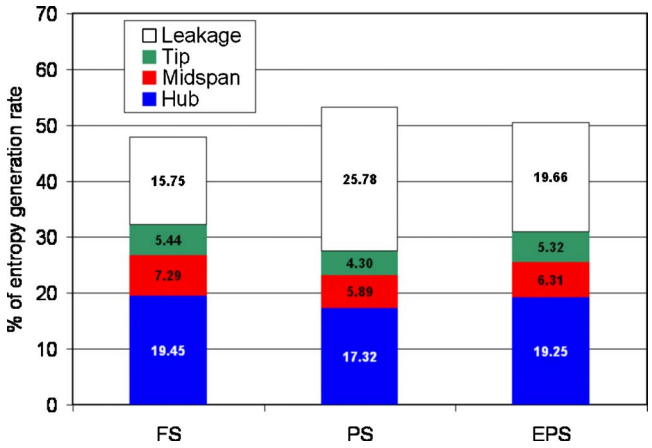

Fig. 15 Entropy generation rate in different regions of the second rotor blade row as a percentage of the total entropy production in the second stage

the PS case results in an aerodynamic penalty in this region of about 10% of the total stage losses (15.7% in the FS case compared to 25.8% in the PS case). On the other hand, the optimized configuration EPS shows that this penalty is reduced to only 3.9% when the matching between the main stream and the leakage flow is improved, as has been shown in the previous section.

Measured Aerodynamic Performance

A mechanical method is used to evaluate stage efficiency. The second stage torque is measured with a sampling frequency of 5 Hz during the entire time of the data acquisition. In the EPS test case, a second torquemeter has been installed, and thus, the turbine torque and second rotor torque are measured simultaneously. The second stage pressure ratio P_{03}/P_{01} is calculated by mass averaging the inlet total pressure over the area at the exit of the first and second rotors. By referring the measured shaft power to the isentropic power provided by the fluid, the efficiency can then be evaluated.

In the current arrangement and in all three test cases, mechanical dissipation is negligible and comparable to each other as the mechanical arrangement is the same in all test cases. The first torquemeter is in fact directly connected to the second stage shaft (power dissipation in the bearing is negligible because the relative motion between the first and second rotors is essentially zero), while the second torquemeter measures the torque immediately above the mechanical coupling between the inner and outer shafts.

The turbine reaches a constant thermal state after about 2 hours and afterward the measurement test starts; thus, heat transfer contribution to the efficiency calculation is negligible. The following equation is used to calculate the aerodynamic efficiency:

$$\eta = \frac{M_2 \omega / \dot{m}}{\overline{\overline{T_{01}}} C_p [1 - (\overline{\overline{P_{03}}}/\overline{\overline{P_{01}}})^{(\gamma-1)/\gamma}]}$$

The facility is open to the atmospheric pressure at the turbine exit. The turbine pressure drop may vary up to $\pm 0.3\%$ during a typical 10 hours operation. The measured pressures are corrected with a standard day condition. The error analysis (Pfau [17]) shows that the absolute overall uncertainty range of the efficiency (for a given geometry) is equal to 0.6%, while the relative uncertainty range between two test cases is equal to 0.3%. All test cases are operated at the same overall pressure drop and at the same rotational speed. The measured mass flow varies from case to case depending on the capacity of the turbine. In particular, the PS case experienced a higher mass flow of 3.3% while the EPS case has a mass flow almost identical to the FS case (difference of 0.1%). The reason of the increased mass flow is the increased flow area of the rotor passage due to the uncovering of the blade throat. The second stage performance is significantly affected by the flow field that is established in the first stage. In all three test cases, main differences in the aerodynamic efficiency are measured. The FS test case with a full shroud arrangement has the highest efficiency at all the operating points. This conclusion was expected since the turbine aerodynamic design process was based on this axis-symmetric shroud. However, the aim of evaluating the performance was to quantify the aerodynamic penalty of the PS and EPS cases in spite of their advantage of a reduced mechanical stress on the blades due to the reduced weight. The PS test case has an aerodynamic efficiency penalty of about 1.1% at design condition and between 0.8% and 1% at off-design conditions.

This penalty arises from the flow angle distribution along the radius in both rotors and the different flow field at the blade tip. High deviations between the measured and design flow angles are detected and a significant unloading from 60% to 100% span is observed. Moreover, a strong tip leakage develops due to the uncovering of the throat passage. Consequently, mixing process is enhanced and losses are generated.

In the EPS test case, the shroud is extended toward the TE of the rotor blade and covers partially the blade passage. The formation of the tip vortex is reduced and flow angles are in between the FS and the PS case. The blade loading control is also improved when compared to the PS case. The second stage efficiency is thus improved by 0.6%. Unfortunately measured data are missing at off-design pressure drop in the EPS test case. Figure 16 summarizes the measured efficiency on the second stage. The loss coefficient within the second stator passage is estimated for all test cases using the following equation, where $\overline{\overline{P_{01}}}$ and $\overline{\overline{P_{02}}}$ represent the mass-averaged second stator inlet and outlet total pressures and $\bar{p}_2$ is the stator static outlet pressure:

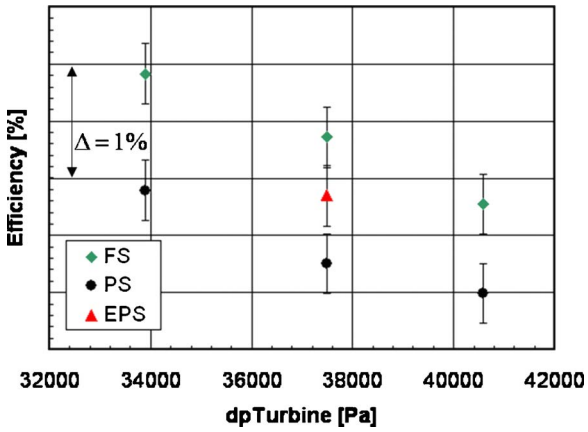

Fig. 16 Measured total to total second stage efficiency in the FS, PS, and EPS test cases

$$Y = \frac{(\overline{\overline{P_{01}}} - \overline{\overline{P_{02}}})}{(\overline{\overline{P_{02}}} - \overline{p_2})}$$

It was observed that the losses in the second stator are increased by almost 1% in the FS test case when compared to the PS geometry (Table 5). In the latter case, two opposing effects occur. On one hand, a strong negative incidence is detected from 60% to 100% span in the stator blade. This incidence mismatch obviously increases the profile losses at those locations. On the other hand, the flow turning in this region is decreased by around 25% when compared to the FS case. Therefore, the losses associated with the tip passage vortex are reduced. The extent of these two effects shows that the reduction of secondary flow losses is larger than the increase of the profile losses. This result again illustrates that for a low aspect ratio high turning blade row, the effect of the vortical structure is dominant compared to other loss generation mechanisms. In the EPS case, the stator total pressure losses are almost 1% higher with respect to the FS case. This behavior is once more attributed to the nonmatching conditions between the

Table 5 Measured total to total second stage relative efficiency and second stator loss coefficient for the PS and EPS test cases

Turbine pressure difference [Pa]	FS[a]	PS	EPS
Total to total efficiency (second stage) (%)			
33,900	100	−1.0	
37,485	100	−1.1	−0.5
40,575	100	−0.8	
Loss coefficient (second stator) (%)			
37,485	—	−1.06	+0.95

[a]Reference case.

exit flow field of the first rotor and the design of the inlet of the second stator.

Conclusions

Partial shrouds arrangements are used more and more in current industrial turbine design because of reduced weight, reduced blade stresses, and thus improved blade life. However, the actual impact of this geometry on the aerodynamic performance has often been not quantified. This study presents a unique and unprecedented experimental and numerical study of industrially relevant turbine shroud configurations.

The flow field downstream the first rotor is dominated by the effect of the different shroud geometries. The uncoverage of the blade throat in the PS case causes the flow to expand in the cavity region and reenter in the main path. The enhanced mixing process and the formation of a strong tip vortex decrease the aerodynamic efficiency by 1% in comparison with a classic fulll shroud case.

An optimized partial shroud geometry is used in the EPS case adopting a platform onto the trailing edge region of the rotor blade in order to prevent the flow expansion in the cavity region. Measurements and computations clearly show that this modification is effective and the flow field is significantly modified toward the design intent of an axis-symmetric full shroud.

Surprisingly, in the optimized shroud case, the second stator row total pressure losses increase by about 2% with respect to the PS case, showing that the mismatch of the flow field at the outlet of the first rotor and the inlet of the second stator still has a significant effect. However, the second stage aerodynamic efficiency has been improved by about 0.6% compared to the previous PS case.

A budget of the entropy production is also made in order to quantify various loss sources in the hub, midspan, tip, and leakage regions. Results show that the leakage and reentry flows in the PS case have the highest contribution (about 25%) to the overall stage loss.

A comprehensive flow field investigation is carried out and the effects of the shroud configuration in terms of the aerodynamic performance are quantified. The measurements show that an optimized partial shroud platform geometry has only 0.5% aerodynamic penalty compared to a 1.1% penalty for a non-optimal partial shroud. This finding quantifies the benefit of an improved matching between the blade and shroud design.

Acknowledgment

The support of the Alstom-ETH research and development forum "Centre of Energy Conversion" and the financial support of ALSTOM Power are acknowledged. The authors gratefully acknowledge ALSTOM Power Switzerland for the kind permission to publish the results presented in this paper. In particular, thanks are due to Dr. Michael Loetzerich for his support and suggestions during the course of this research activity.

Nomenclature

C_{ax} = blade axial chord
C_p = specific heat at constant pressure
C_{pt} = total pressure coefficient $(P_{0meas}-P_{Sexit})/(P_{0inlet}-P_{Sexit})$
$\dot{m}$ = mass flow
M = second stage torque
P = pressure
$\Delta s, s$ = entropy
T = temperature
CFD = computational fluid dynamics
PS = partial shroud test case
FS = full shroud test case
EPS = enhanced partial shroud test case
5HP = five hole probe
FRAP = fast response aerodynamic probe
PIV = particle image velocimetry

Greek

β = pitch angle
γ = isentropic exponent
η = aerodynamic efficiency
ρ = density
ϕ = yaw angle
ω = rotational speed

Subscripts/Superscripts

0 = total conditions
S = static conditions
1,2,3 = measurement plane A1, A2, and A3
$\bar{\bar{P}}, \bar{\bar{T}}$ = mass and area-averaged data
$\bar{P}, \bar{T}$ = area averaged data

References

[1] Denton, J. D., 1993, "Loss Mechanisms in Turbomachines," ASME J. Turbomach., **115**, pp. 621–656.
[2] Gier, J., Stubert, B., Brouillet, B., and De Vito, L., 2005, "Interaction of Shroud Leakage Flow and Main Flow in a Three-Stage LP Turbine," ASME J. Turbomach., **127**, pp. 649–658.
[3] Peters, P., Menter, J. R., Pfost, H., Giboni, A., and Wolter, K., 2005 "Unsteady Interaction of Labyrinth Seal Flow and Downstream Stator Flow in a Shrouded 1.5 Stage Axial Turbine," ASME Paper No. 2005-GT-68065.
[4] Patel, K. V., 1908, "Research on a High Work Axial Gas Generator Turbine," SAE Report No. 800618.
[5] Yaras, M. I., and Sjolander, S. A., 1991, "Measurements of the Effect of Winglets on Tip-Leakage Losses in a Linear Turbine Cascade," ISABE Report No. 91-7011, pp. 127–135.
[6] Harvery, N. W., and Ramsden, K., 2000, "A Computational Study of a Novel Turbine Rotor Partial Shroud," ASME Paper No. GT2000-668.
[7] Harvey, N. W., Newmann, D. A., Haselbach, F., and Willer, L., 2006, "An Investigation Into a Novel Turbine Rotor Winglet—Part 1: Design and Model Rig Test results," ASME Paper No. GT2006-90456.
[8] Nirmalan, N. V., and Bailey, J. C., 2005, "Experimental Investigation of Aerodynamic Losses of Different Shapes of a Shrouded Blade Tip Section," ASME Paper No. GT2005-68903.
[9] Porreca, L., Behr, T., Schlienger, J., Kalfas, A. I., Abhari, R. S., Ehrhard, J., and Janke, E., 2005, "Fluid Dynamics and Performance of Partially and Fully Shrouded Axial Turbines," ASME J. Turbomach., **127**, pp. 668–678.
[10] Porreca, L., Hollenstein, M., Kalfas, A. I., and Abhari, R. S., 2007, "Turbulence Measurements and Analysis in a Multistage Axial Turbine," J. Propul. Power, **23**(1), pp. 227–234.
[11] Treiber, M., Kupferschmied, P., and Gyarmathy, G., 1998, "Analysis of the Error Propagation Arising From the Measurements With a Miniature Pneumatic 5-Hole Probe," 14th Symposium on Measuring Techniques for Transonic and Supersonic Flows in Cascade and Turbomachines.
[12] Rosic, B., and Denton, J., 2006, "The Control of Shroud Leakage Loss by Reducing Circumferential Mixing," ASME Paper No. GT2006-90949.
[13] Wallis, A. M., Denton, J. D., and Demargne, A. A. J., 2001, "The Control of Shrouded Leakage Flows to Reduce Aerodynamic Losses in a Low Aspect Ratio, Shrouded Axial Flow Turbine," ASME J. Turbomach., **123**, pp. 334–341.
[14] Behr, T., Porreca, L., Kalfas, A. I., and Abhari, R. S., 2004, "Multistage Aspects and Unsteady Effects of Stator and Rotor Clocking in an Axial Turbine with Low Aspect Ratio Blading," ASME J. Turbomach., **128**, pp. 11–22.
[15] Schlienger, J., Kalfas, A. I., and Abhari, R. S., 2005, "Vortex-Wake-Blade Interaction in a Shrouded Axial Turbine," ASME J. Turbomach., **127**, pp. 699–707.
[16] Yun, Y. I., Porreca, L., Kalfas, A. I., Song, S. J., and Abhari, R. S., 2006, "Investigation of 3D Unsteady Flows in a Two Stages Shrouded Axial Turbine Using Stereoscopic PIV and FRAP—Part II: Kinematics of Shroud Cavity Flow," ASME Paper No. GT2006-91020.
[17] Pfau, A, "Loss Mechanisms in Labyrinth Seals of Shrouded Axial Turbines," ETH Ph.D. thesis, ETH, Zurich.

Unsteady Flow and Aeroelasticity Behavior of Aeroengine Core Compressors During Rotating Stall and Surge

M. Vahdati

G. Simpson

M. Imregun

Mechanical Engineering Department,
Imperial College of Science, Technology and Medicine,
London SW7 2BX, UK

This paper will focus on two core-compressor instabilities, namely, rotating stall and surge. Using a 3D viscous time-accurate flow representation, the front bladerows of a core compressor were modeled in a whole-annulus fashion whereas the rest of bladerows were represented in single-passage fashion. The rotating stall behavior at two different compressor operating points was studied by considering two different variable-vane scheduling conditions for which experimental data were available. Using a model with nine whole bladerows, the unsteady flow calculations were conducted on 32 CPUs of a parallel cluster, typical run times being around 3–4 weeks for a grid with about 60 $\times 10^6$ *points. The simulations were conducted over several engine rotations. As observed on the actual development engine, there was no rotating stall for the first scheduling condition while malscheduling of the stator vanes created a 12-band rotating stall which excited the rotor blade first flap mode. In a separate set of calculations, the surge behavior was modeled using a time-accurate single-passage representation of the core compressor. It was possible to predict not only flow reversal into the low pressure compression domain but also the expected hysteresis pattern of the surge loop in terms of its mass flow versus pressure characteristic.* [DOI: 10.1115/1.2777188]

1 Introduction

Unsteady turbulent high-speed compressible flows often give rise to complex aeroelasticity phenomena by influencing the dynamic behavior of structures on which they act. Under certain conditions, the energy transfer from the fluid to the structure can cause excessive vibration levels and structural integrity may be compromised. The problem is particularly severe for gas turbines where virtually all bladerows are susceptible to aeroelasticity effects either by inherent self-induced motion (flutter) or by response to aerodynamic flow distortions and blade wakes (forced response). The most complex and the least understood aeroelasticity phenomena occur in multistage core compressors, the subject of this paper, because of their wide operating envelope. The performance of an axial-flow compressor is often summarized in the form of a pressure rise versus mass flow characteristic map (Fig. 1), representing nominally steady and axisymmetric flow operation. At a given shaft speed, the operating zone is bounded by choke at high mass flow/low pressure (Point D) and by surge at low mass flow/high pressure (Point A). During engine development programmes, costly structural failures are known to occur because of a mixture of aeroelastic instabilities such as acoustic resonance, flutter, forced response, rotating stall, surge, etc. Apart from surge, which is a global event, most such phenomena are believed to be caused by at least one bladerow undergoing severe stall, but the overall compressor still managing to function because of the overall pressure ratio. Rotating stall is a disturbance that is *local* to the compressor bladerows, which is characterized by a circumferential nonuniform flow deficit, with one or more stall cells propagating around the compressor circumference at a fraction of the shaft speed, typically between 20% and 60%. In fully developed rotating stall, the overall flow through the compressor is constant in time, with the stall cells redistributing the flow around the annulus. The numerical modeling of such a situation is a formidable challenge as the analysis must be able to represent accurately not only the aerodynamic and structural properties of a large number of bladerows but also the interactions through these.

In contrast to part span rotating stall, surge is a *global* instability, which involves an axial oscillation of the flow inside the whole compression system, consisting of the bladerows as well as any ducting or plenum volume after the last bladerow. Surge occurs in cycles where the flow oscillates throughout the compression domain as the downstream volume (combustor) is filled and emptied periodically

Since the avoidance of stall and surge is a major design consideration, a considerable amount of research effort has been devoted to the understanding of the physical mechanisms that give rise to such instabilities. After the initial inception stage, it is not clear which conditions will cause surge or rotating stall, though a simplified nondimensional parameter, based on basic geometry, the mean flow speed and the speed of sound, has been proposed by Greitzer [1], who provided a means of assessing how design changes were likely to affect the stall/surge behavior of a particular compressor. However, in the general case, there are no rules to determine the speed of rotating stall, its circumferential, and radial extent as well as the number of rotating cells. So far, due to modeling difficulties, much of the stall and surge research has been experimental [2,3], or based on simplified models [4,5], though numerical simulations with simplified or partial geometries are beginning to emerge [6–8].

Unlike other instabilities of aeroelastic origin, core-compressor rotating stall and surge behavior needs to be simulated not only at the onset but also during the event itself. This requirement arises from the fact that on the other hand, design parameters such as axial gap and the size of variable-vane controllers are dictated by surge loads, hence the requirement for a full simulation.

From an industrial perspective, it is important to understand the factors that influence changes in stall characteristics as it may

Contributed by the International Gas Turbine Institute of ASME for publication in the JOURNAL OF TURBOMACHINERY. Manuscript received February 20, 2007; final manuscript received February 22, 2007; published online May 6, 2008. Review conducted by David Wisler. Paper presented at the ASME Turbo Expo 2006: Land, Sea and Air (GT2006), Barcelona, Spain, May 8–11, 2006. Paper No. GT2006-90308.

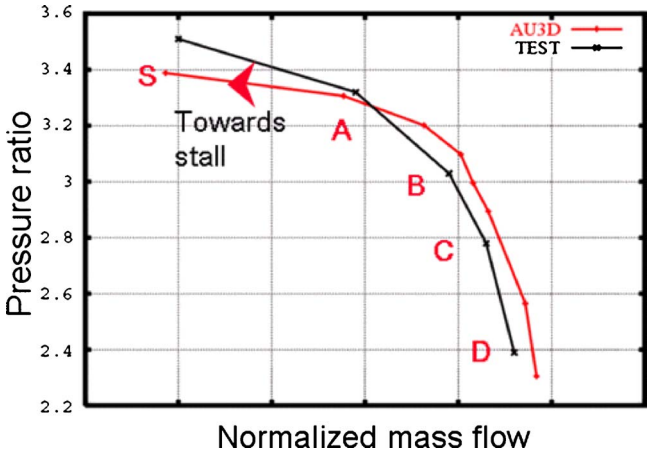

Fig. 1 Compressor characteristic

result in moving from a safe operating regime to one that causes rotor blade failure. These effects are normally assessed by engine strain gauge tests, which are used to map out stall boundaries. However, due to the high cost of these tests and the limited scope for varying engine configuration and operation, the objective of this work is to develop a predictive capability that will minimize rig and engine testing by means of advanced simulations that will cover the flight envelope in an efficient manner.

2 Theoretical Background

2.1 Flow Model. The unsteady, compressible Reynolds-averaged Navier–Stokes equations for a 3D bladerow can be cast in terms of absolute velocity **u** but solved in a relative reference frame rotating with angular velocity $\boldsymbol{\omega}$. This system of equations, written in an arbitrary Eulerian–Lagrangian conservative form for a control volume Ω with boundary Γ, takes the form

$$\frac{d}{dt}\int_{\Omega}\mathbf{U}d\Omega+\oint_{\partial\Omega}\left(\mathbf{F}-\frac{1}{\mathrm{Re}}\mathbf{G}\right)\cdot\mathbf{n}d\Gamma=\int_{\Omega}\mathbf{S}d\Omega \tag{1}$$

where **n** represents the outward unit vector of the control volume boundary Γ. The viscous term **G** on the left hand side of Eq. (1) has been scaled by the reference Reynolds number for nondimensionalization purposes. The solution vector **U** of conservative variables is given by

$$\mathbf{U}=\begin{bmatrix}\rho\\ \rho u_i\\ \rho\varepsilon\end{bmatrix} \tag{2}$$

The inviscid flux vector **F** can be written as

$$\mathbf{F}=\begin{bmatrix}\rho(u_i-w_i)\\ \rho u_i(u_i-w_i)+p\,\delta_{ij}\\ \rho E(u_i-w_i)+pu_i\end{bmatrix} \tag{3}$$

where δ_{ij} is the Kronecker delta, u_i and w_i are the absolute and the grid velocities, and i is the ith Cartesian coordinate direction. The pressure p and the total enthalpy h are related to density ρ by two perfect gas equations:

$$p=(\gamma-1)\rho\left(\varepsilon-\frac{|\mathbf{u}^2|}{2}\right)\quad h=\varepsilon+\frac{p}{\rho} \tag{4}$$

where γ is the constant specific heat ratio. The viscous flux vector **G** can be written as

$$G=\begin{bmatrix}0\\ \sigma_{ij}\\ u_k\sigma_{ik}+\dfrac{\gamma}{\gamma+1}\left(\dfrac{\mu_l}{\mathrm{Pr}_l}+\dfrac{\mu_t}{\mathrm{Pr}_t}\right)\partial T/\partial x_i\end{bmatrix} \tag{5}$$

where μ_l represents the molecular viscosity given by Sutherland's formula, and μ_t denotes the turbulent eddy viscosity, which must be determined using a suitable turbulence model. The model proposed by Spalart and Allmaras [9] was adopted here. The laminar Prandtl number Pr_l is taken as 0.7 for air, while the turbulent Prandtl number Pr_t is taken as 0.9. The viscous stress tensor σ_{ij} is expressed using the eddy viscosity concept which assumes that, in analogy with viscous stresses in laminar flows, the turbulent stresses are proportional to mean velocity gradients:

$$\sigma_{ij}=(\mu_l+\mu_t)\left(\frac{\partial u_i}{\partial x_j}+\frac{\partial u_j}{\partial x_i}\right)+\lambda\,\delta_{ij}(\nabla\cdot\mathbf{u}) \tag{6}$$

The value of λ is given by the Stokes relationship $\lambda=-2/3(\mu_l+\mu_t)$. Vector **S**, which contains the terms due to the rotation of the coordinate system, can explicitly be written as

$$\mathbf{S}=\begin{bmatrix}0\\ \rho\omega u_2\\ \rho\omega u_3\end{bmatrix} \tag{7}$$

Equation (1) is discretized on unstructured mixed-element grids via a finite volume method, the details of which are given by Sayma et al. [10]. As described by Sbardella et al. [11], the blades are discretized using a semistructured mesh, which consists of brick elements in the boundary layer and triangular prisms further away in the blade passage, i.e., the grid is only unstructured in a blade to blade plane. To achieve further computational efficiency, the mesh is characterized via an edge-based data structure, i.e., the grid is presented to the solver as a set of node pairs connected by edges, a feature that allows the solver to have a unified data structure. Furthermore, the edge-based formulation has the advantage of computing and storing the edge weights prior to the main unsteady flow calculation, hence reducing the CPU effort. The central differencing scheme is stabilized using a mixture of second- and fourth-order matrix artificial dissipations. In addition, a pressure switch, which guarantees that the scheme is total variation diminishing (TVD) and reverts to a first-order Roe scheme in the vicinity of discontinuities, is used for numerical robustness. The resulting semidiscrete system of equations is advanced in time using a point-implicit scheme with Jacobi iterations and dual time stepping. Such an approach allows relatively large time steps for the external Newton iteration. For steady-state calculations, solution acceleration techniques, such as residual smoothing and local time stepping, are employed. For unsteady computations, an outer Newton iteration procedure is used where the time steps are dictated by the physical restraints and fixed through the solution domain. Within the Newton iteration, the solution is advanced to convergence using the traditional acceleration techniques described previously.

The relative motion between the stator and the rotor blades can be modeled using one of the following two types of interface boundaries.

(1) *Mixing planes*. These boundaries are used to provide an interface between bladerows, which are represented as single passages. Since, there is no one-to-one correspondence between the rotor and stator bladerows, the information can only be exchanged in an average sense. In the approach taken here, a circumferential mass averaging of the flow variables is performed at each radial height on both sides of the mixing plane. The flow variables at the rotor side are imposed as boundary condition for stator domain, and the variables at the stator side are prescribed as boundary condition for the rotor domain. Mixing planes are

typically used in steady-state flow calculations, especially for multistage core compressors. Due to the averaging process, they do not allow a correct propagation of circumferential wave and hence they are not suitable for simulating unsteady flow phenomena such as forced response and rotating stall. However, they can still be used to capture global unsteadiness characteristics such as whole compressor surge where local unsteadiness, say, due to blade interactions, is of secondary interest.

(2) *Sliding planes*. Such boundaries can be used at both whole-annulus and single-passage bladerow interfaces. They model the bladerow interaction correctly and all waves, axial, radial, and circumferential, are propagated without any simplifying assumptions. For sliding planes placed at bladerow boundaries, the solution is updated at the interface by interpolating the variables in the stator computational domain to obtain rotor fluxes and in the rotor computational domain to obtain the stator fluxes [12,13]. The fluxes are computed using a characteristic technique, which allows the correct propagation of the information. In other words, flow data are exchanged between the two grids via specially formulated boundary conditions at the interface. Sliding planes are typically used in unsteady flow computations.

2.2 Aeroelastic Response During Surge and Rotating Stall. The determination of the blade response during rotating stall and surge is a difficult problem for which there are no reliable procedures. An accurate numerical simulation of core-compressor rotating stall phenomena requires the whole-annulus modeling of a large number of bladerows using grids containing several tens of millions of points. The time-accurate unsteady flow computations may need to be run for several engine revolutions for rotating stall to get initiated and many more before it is fully developed. Such an analysis is computationally very expensive because of the large number of engine rotations that must be simulated, as well as number of points required in the model. In the interest of computational feasibility, an approximate method will be used here. It is based on the time-accurate version of the single-passage steady-state flow model where mixing planes are used at the bladerow boundaries. A multibladerow single-passage analysis is a "reasonable" simplification from the full model and, in spite of its potential shortcomings, it provides some insight to flow behavior during surge. Strictly speaking, the model here assumes that flow has passed its rotating stall stage and a full surge has developed.

During rotating stall, the blades encounter the stall cells and the excitation depends on the number, size, exact shape, and rotational speed of these cells. The long-term aim is to minimize the forced response due to rotating stall excitation, should this occur under extreme conditions, by avoiding potential matches between the vibration modes and the rotating stall pattern characteristics. Furthermore, the knowledge of the loadings on the blade during surge is very important for determining the axial gap between rotors and stators, especially in the back stages of a core compressor. In contrast to part span rotating stall, surge is a *global* instability, which involves an axial oscillation of the flow inside the whole compression system, consisting of the bladerows as well as any ducting or plenum volume after the last bladerow. Surge occurs in cycles where the flow oscillates throughout the compression domain as the downstream volume is filled and emptied periodically.

The difficulty in rotating stall initiation arises from a lack of representation of the triggering disturbances, which are inherently present in aeroengines. Since the numerical model represents a symmetric assembly, the only random mechanism for rotating stall initiation is provided by numerical roundoff errors. In this work, rotating stall is initiated by introducing a small amount of geometric mistuning to the rotor blades. It has been verified, by trying several mistuning patterns, that the results are independent of the pattern used.

A major obstacle in modeling flows near stall is the specification of appropriate upstream and downstream boundary conditions. Obtaining reliable boundary conditions for such flows can be very difficult. Moreover, the imposition of steady-state flow conditions is invalid as the flow is totally unsteady within the compressor. Furthermore, the flow will be going out of the compressor's inlet and will be coming through its inlet during the surge cycle. In the present study, the low pressure compression (LPC) domain is placed upstream of the core compressor. With such an approach, only far field atmospheric boundary conditions are specified, which are obtained from aircraft speed and altitude. Moreover, the LP domain is used as a discharge volume during the surge. A choked variable-area nozzle, placed after the last compressor bladerow in the model, is used to impose boundary conditions downstream. Such an approach is representative of modeling an engine. A convenient indicator of the blade response is the modal force, which is a measure of the correlation between the structural mode shape and the unsteady pressure fluctuation, the other two key parameters being the amplitude and frequency of the fluctuation. The modal force represents the strength of the unsteady forcing in a particular mode of vibration and is given by

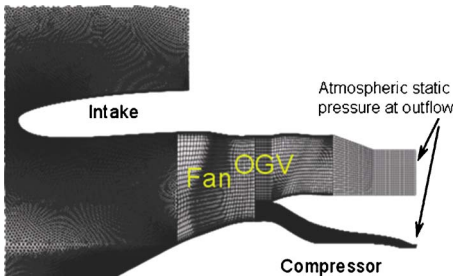

Fig. 2 Steady-state flow domain

$$f(x,r) = \tilde{p}(x,r)\,\eta\phi(x,r) \tag{8}$$

where ϕ is the mode shape vector and η is the area normal vector. The total modal force is obtained by summing the above over all the points on the blade. In simple terms, the modal force may be considered to be the product of the unsteady pressure and the structural mode shape. It can best be visualized by considering a rigid body motion where the blade is plunging only. In this case, the modal force is equivalent to the unsteady lift on the blade.

3 Boundary Conditions

A major difficulty in modeling flows near stall is the specification of appropriate upstream and downstream boundary conditions. The usual method for imposing boundary conditions in a core compressor is to specify total pressure, total temperature, and the flow angles at the inlet to the first bladerow and to specify the static pressure at the exit of the last bladerow. However, for flows near stall, obtaining reliable and accurate boundary conditions can be very difficult since the engine is operating very far from its design intent. Therefore, the imposition of time-invariant boundary conditions may not be valid as the flow is unsteady within the compressor. Moreover, under certain conditions, such as surge, the flow will be going out the compressor inlet. Therefore, alternative ways of prescribing the inlet and exit conditions for the core compressor are required. In the approach taken here, the upstream conditions are modelled by placing the low pressure compressor domain upstream of the core compressor (Fig. 2). The domain contains the intake, fan, the fan outlet guide vanes (OGV), and the engine section stator (ESS). With such an approach, only far field atmospheric boundary conditions are specified and the only information required for upstream boundary conditions is the aircraft speed and the ambient conditions at a given altitude. Moreover, with such approach the low pressure (LP) and intermediate pressure (IP) domain interactions, which can be very important at off design settings, are modeled automatically.

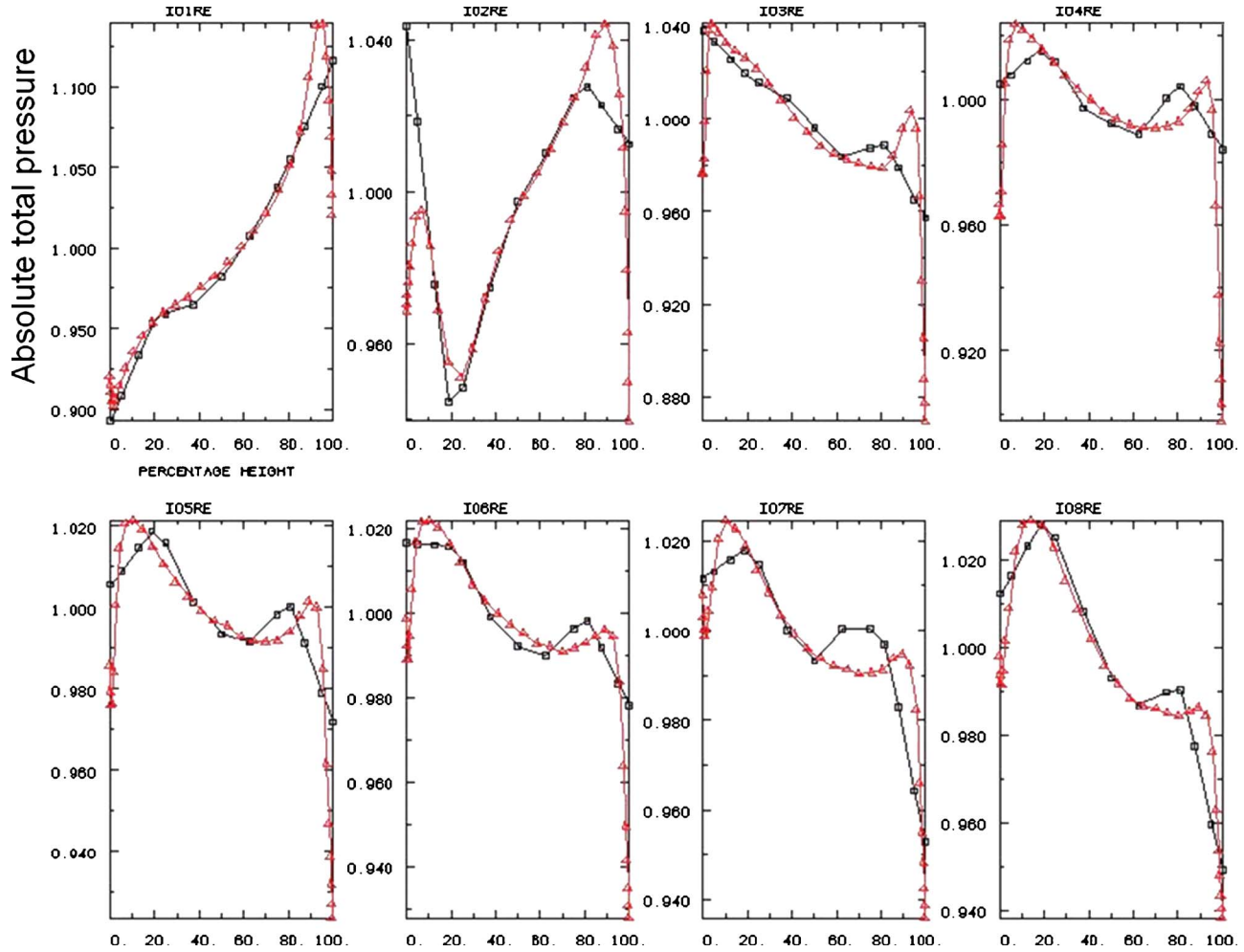

Fig. 3 Comparison of computed total pressure (△) at rotor exit against test data (□)

At the exit, it is a common engineering practice to specify a fixed static pressure as a downstream boundary condition. It is shown in Ref. [14] that rigid boundary conditions, based on imposing given fixed exit pressure distributions, are not suitable for numerical studies near stall because of the inherent unsteadiness of the boundary conditions. For instance, in the case of surge, the downstream exit pressure profiles are neither known nor constant in time. Similarly, at high working lines, the flow becomes genuinely unsteady near the stall boundary, and the imposition of a radially constant exit static pressure is likely to result in numerical instabilities, the so-called "numerical stall." As discussed in Ref. [14], the situation can be remedied for a single bladerow fan assembly by introducing a downstream variable nozzle, thus allowing the pressure behind the fan to adjust automatically, while the pressure behind the nozzle is fixed. Such an approach makes the computational domain "less stiff" and provides a powerful natural boundary condition for stall studies. Moreover, since the aim is to simulate, as much as possible, engine and rig tests, nozzle area changes can be used to move to any point on the compressor characteristic. In the present study, a similar approach is taken by placing a variable nozzle downstream of the last bladerow of the compressor. The flow in the nozzle is choked, hence the nozzle area change determines the mass flow and the operating point on the core-compressor characteristic and the solution is independent of prescribed boundary condition at the nozzle exit. With such an approach, nothing is fixed at the exit and hence it is very well suited for a genuinely unsteady flow.

The flow through the engine is controlled by using two downstream variable-area nozzles (Fig. 2). The variable-area bypass duct nozzle is placed downstream of the OGVs. This nozzle is adjusted to obtain the correct fan operating point and the bypass ratio. Once this is obtained, it is kept fixed for the rest of the computations and hence assuming that the fan operating point remains the same for all the compressor conditions. Atmospheric static pressure is assumed at the exit of the bypass nozzle. A second variable-area nozzle is used downstream of the compressor. The compressor nozzle is gradually closed until the flow approaches stall.

Figure 3 shows the comparison of computed and measured total pressure profiles downstream of rotor blades for an eight-stage compressor near stall (Point A in Fig. 1). It should be noted that stall can numerically be defined as the first point on the characteristic at which a converged steady-state position is no longer possible (Point S in Fig. 1). It is seen that the proposed methodology can produce reasonably good agreement with measured data for such flows. Such an imposition of the boundary conditions is a very powerful tool for simulating flows near stall. It will be shown that such a methodology will also allow emptying and filling of the compressor during surge.

4 Computational Domain

There are very few methods that allow a 3D time-accurate modeling of rotating stall and surge in a core compressor. A whole-assembly analysis of whole compressor is computationally very expensive because of the large number of engine rotations that need to be simulated as well as the number of points required in the model. However, given the computational cost, taking advan-

Fig. 4 Hybrid single-passage, whole-annulus model

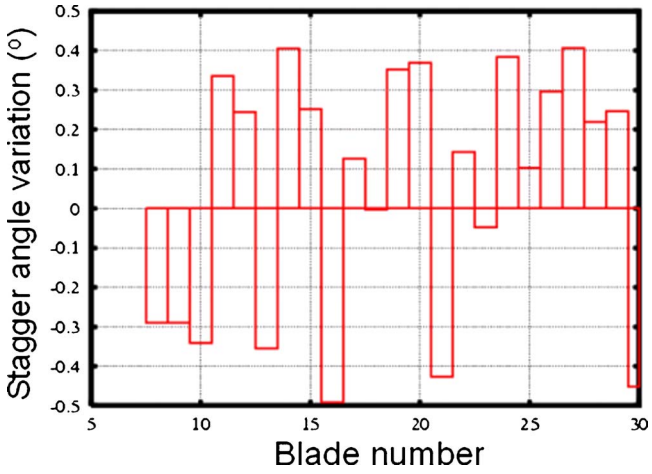

Fig. 5 Mistuning pattern to initiate rotating stall

tage of the circular symmetry, i.e., ignoring potential differences around the annulus, becomes quite critical. However, not all unsteady phenomena can be confined to the symmetry of a single passage. For instance, rotating stall can only be studied with a whole-annulus model. A possible compromise to reduce the computational cost is the use of a hybrid single-passage whole-annulus model. In this approach, the bladerows of interest are modeled in whole-annulus fashion, while the remaining bladerows are represented as single blade passages (Fig. 4). The interface boundaries between the whole-annulus bladerows are represented by sliding planes, while the remaining interface boundaries are treated as mixing planes. Depending on how the solution develops, any single-passage bladerow can be replaced by a whole-annulus bladerow and vice versa during the course of the computations. The approach is best suited for simulating the so-called "part-span stall," which is confined to a relatively small area of the compressor.

Another major difficulty is the initiation of rotating stall numerically. The analysis usually starts using an initial solution obtained using one passage steady-state flow analysis. For an instability to be triggered, the flow must be perturbed. If the whole-annulus unsteady flow analysis is performed for a perfectly symmetric geometry, there are no aerodynamic differences between the passages, the so-called aerodynamic mistuning; rotating stall can only develop, after perhaps 100 engine revolutions, when rounding off errors becomes significant enough to cause a perturbation. For computational efficiency, it is essential to drive the numerical model into rotating stall as quickly as possible. In the approach taken here, rotating stall is initiated by introducing a small amount of aerodynamic mistuning to the blade passages by changing the stagger angle of blades in a random fashion (Fig. 5). The amount of mistuning introduced is within the manufacturing and assembly tolerances. Prior to running the full configuration, a number of tests were conducted with a smaller geometry to ensure that the rotating stall behavior was independent of the pattern used.

The aerodynamically mistuned domain is obtained forming a tuned whole-annulus domain from a single-passage grid first. The blades are then moved according to the desired mistuning pattern. The grid movement algorithm described in [10] is used to ensure the quality of grid that does not degenerate.

5 Case Study: Surge

This section will demonstrate the strength of the proposed methodology for imposing boundary conditions by modeling a surge event in an eight-stage core compressor. The authors know of no such numerical simulations in the published literature. The domain used in the surge study is that used in the earlier steady-state flow analysis (Fig. 2). The method here is based on the time-accurate version of the single-passage steady-state flow model where mixing planes are used at the bladerow boundaries. The characteristic variables are imposed at the mixing plane and the number of conditions imposed is determined from the actual flow direction. Therefore, the interface boundaries can automatically change from inlet to exit or vice versa. A multibladerow single-passage analysis is a "reasonable" simplification from the full model and, in spite of its potential shortcomings, which will be discussed later, it provides considerable insight to the flow behavior during surge. It is assumed that full surge has developed and that the unsteadiness is mainly in the axial direction. The approach is useful to provide a first approximation to vane loading during surge.

Starting from a steady and stable solution, the nozzle at the back of the core compressor is gradually closed, until a situation is reached where the compressor is not able to produce the required pressure ratio and the flow becomes unstable and surges. The variation of negative axial velocity, indicative of stall regions, at midpassage plane at six different time levels is shown in Fig. 6. It is seen from this figure that there is no stall initially. As the time evolves, stall regions are formed and expand into the domain. The process continues until the whole compressor is filled with reversed flow and the flow starts to come out of the compressor. Due to the flow reversal, the volume upstream of the nozzle empties and the pressure at the end of compressor decreases. Hence, the required pressure rise across the compressor drops and consequently the compressor recovers from stall. With the filling of the volume, the pressure at the back of the compressor increases again, and the process above repeats itself. Surge occurs in cycles where the flow oscillates throughout the compression domain as the downstream volume (combustor) is filled and emptied periodically. Hence, the frequency of the surge is dictated by the size of

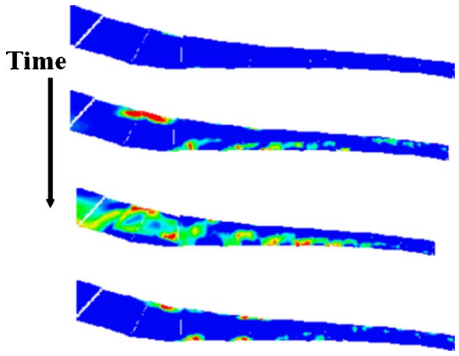

Fig. 6 Time history of negative axial flow at midpassage

the volume upstream of the nozzle. The time history of the mass flow/pressure ratio is shown in Fig. 7, which shows the hysteresis loop for the compressor. It is obvious that the above procedure creates a significant amount of unsteadiness, and hence as a result of interaction with blade modes a large amount of unsteady forcing is produced. The time history of mass flow and forcing on the blade, as well as the Fourier components of the forcing, are shown in Fig. 8. The forcing is for the first flap (1F) mode of the rotor assembly. It can be seen that, for such a chaotic event, the forcing on the blade almost repeats itself during each surge cycle. A Fourier transform of the forcing shows that all frequencies are present in the forcing and that the aeroelastic behavior during surge can be viewed as an impulse response where all modes are excited. The highest forcing corresponds to the surge frequency, and it is determined by the size of the control volume. Furthermore, it can be seen from these figures that the steady (averaged) forcing on the blade changes and hence the blade twist is due to changes in the aerodynamic loading.

The method offers good computational efficiency over an equivalent whole-annulus analysis but it cannot model the rotating stall to surge transition. It is inherently assumed that the unsteadiness is axial during surge. However, the method can produce a first-order approximation to the blade loadings during surge and could be used to determine the axial gap between blade rows. This approach would be of more interest if the blade loadings were higher during the surge than the rotating stall that precedes it. These assumptions can be examined by performing a full analysis of the flow during surge and is currently being undertaken. Moreover, such an approach can be used for determining the weakest stage in a multistage core compressor.

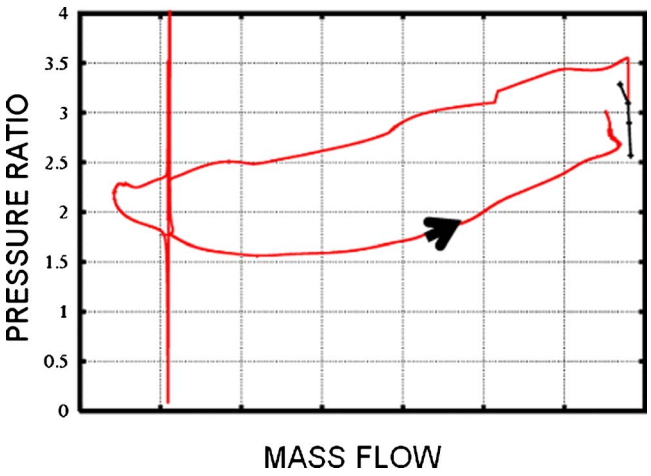

Fig. 7 Hysteresis loop for mass flow versus pressure ratio

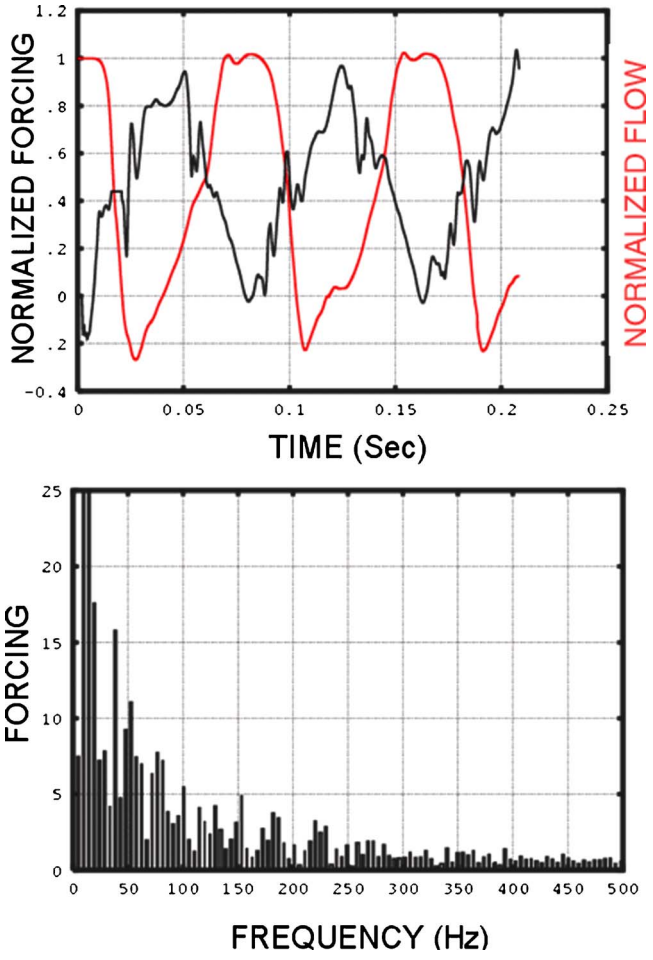

Fig. 8 Time history of mass flow and blade forcing (upper plot); Fourier components of forcing (lower plot)

6 Case Study: Rotating Stall

One of the objectives of this work is to develop a methodology that can predict the effects of multilobe rotating stall on blade vibration levels. Of particular importance is to link the variable-vane scheduling to the number, size, distribution, and speed of rotating stall cells so that the critical modes of vibration can be identified and avoided. The test case chosen is an eight-stage compressor where the first three stator bladerows have variable-angle vanes. Two vane settings, namely, datum and malscheduled, were used in the computations because of the availability of experimental data for these two conditions.

6.1 Steady-State Flow Results. In the steady-flow computations, the entire domain is modeled using single passages (Fig. 2). Steady-state flow results, obtained for two given variable stator vane (VSV) conditions, are shown in Figs. 9–11. The following differences between datum schedule (DS) and malschedule (MS) can be observed in the steady-state flow solution.

- The separated flow region on Rotor 1 extends much further radially for the MS case.
- The separated flow region extends into the upstream and downstream bladerows for the MS case.
- Compressor characteristics, such as the overall mass flow, pressure ratio, and efficiency, drop for the MS case.

As can be seen from Fig. 10, the inlet profiles to the compressor are significantly different between the two scheduling cases, the compressor having much weaker inlet profiles for the MS case.

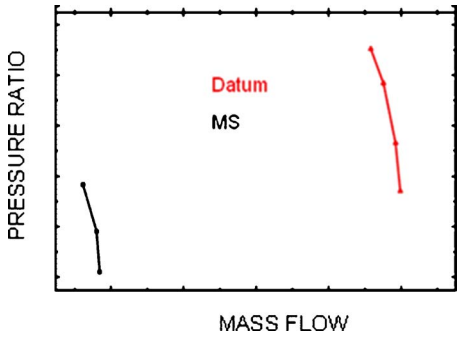

Fig. 9 Overall performance: DS versus MS

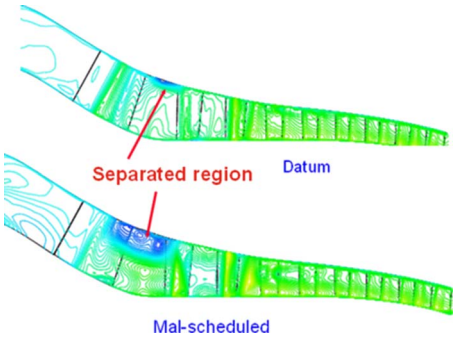

Fig. 11 Total pressure along compressor

This indicates that there is a strong interaction between the core and the LPC domains: The massive separation around the Rotor 1 tip affects the flow at the fan root, which in turn affects the flow into the core compressor. Therefore, the inclusion of the LP domain is critical for the correct prediction of the onset of rotating stall.

6.2 Unsteady-Flow Results. The first nine bladerows of the compressor are modeled in a whole-annulus fashion, whereas the rest of the compressor as well as the LP domain are modeled using single passages. It was known that Rotor 1 was affected by rotating stall and hence it was modeled in finer mesh resolution. The computational domain contained about 60×10^6 grid points. The variation of the static pressure upstream of Rotor 1 after 13 engine rotations is shown in Fig. 12. It is seen that the flow looks symmetric for the DS case, i.e., sign of no rotating stall, but a nonsymmetric pattern, i.e., rotating stall, develops for the MS case. It should be noted that the same amount of aerodynamic mistuning is used for both vane schedules and hence the formation of stall cells depends on how the flow solution develops, rather than which aerodynamic mistuning pattern is imposed. The variations of the instantaneous static pressure upstream of Rotor 1 along the circumference at 70% and 90% heights are shown in Fig. 13 together with the corresponding Fourier components. A close study of these figures reveals the existence of a 12-band rotating stall for the MS case. Moreover, the figure shows that the rotating stall is much stronger at 70% height. The variations of static pressure upstream of Rotor 1 at four different time levels are shown in Fig. 14. It is seen that about 13 engine rotations are required before an identifiable stall pattern, with about 12 cells, starts emerging. During the rig test, the number of rotating stall cells was observed to be between 10 and 13, which matches well the predicted value of 12.

The instantaneous variations of negative axial velocity, and stall region at 70% height for the MS case, are shown in Fig. 15. It is seen that a totally nonsymmetric profile has developed and the instantaneous variations of flow variables are different for each blade passage. Moreover, the fact that a gross amount of flow nonsymmetry can be obtained with a very little amount of aerodynamic mistuning lends support to the assumption that the final stall pattern is independent of the mistuning pattern. It is also seen that the rotating stall creates a significant amount of unsteadiness. A matching between this unsteadiness and any of the assembly vibration modes is likely to result in very high response levels. It is also noticeable from Fig. 15 that the rotating stall disturbances diffuse very rapidly downstream of Rotor 1, which is the only rotor that may suffer from excessive vibrations. Such an observation is typical of high-band rotating stall behavior where the unsteadiness remains confined to a single bladerow. This is further evident from Fig. 16, which shows the Fourier components of rotating stall at successive planes, just upstream of the rotor bladerows. The disturbances diffuse very rapidly and there is little evidence of rotating stall past Rotor 4. This finding suggests that similar results could have been obtained with a smaller model with fewer whole-annulus bladerows.

The unsteadiness due to rotating stall interacts with the assembly vibration modes, a feature that creates unsteady forcing on the blade. The Fourier components of the unsteady forcing for different nodal diameter (ND) modes arising from the blade 1F mode are shown in Fig. 17. In this case, the 1F natural frequency is 308 Hz and the 4ND forcing frequency is about 340 Hz. In the event of the two frequencies matching, the response in that mode is estimated to be about 20% of the chord length using a Q-factor damping value of 200, which corresponds to a structural damping loss factor of 0.5%. The above results are in a very good agreement with engine data.

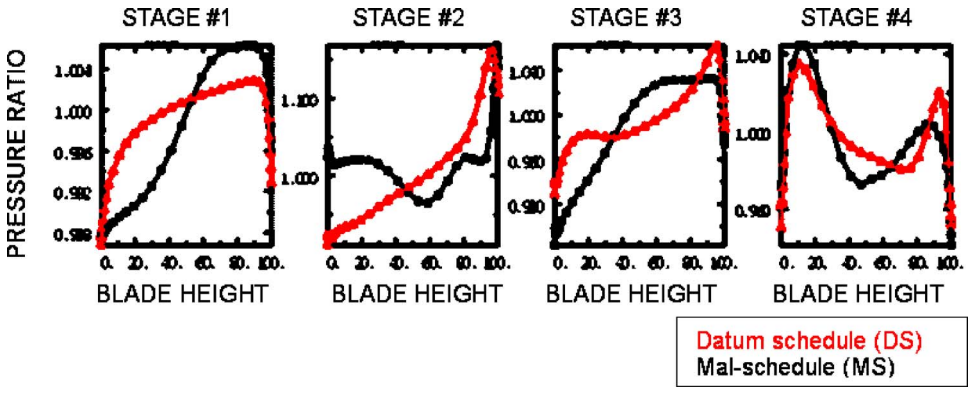

Fig. 10 Front stage performance

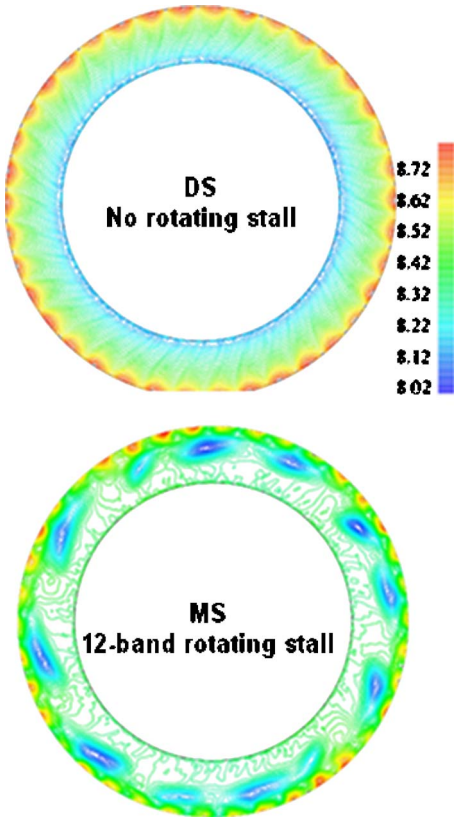

Fig. 12 Instantaneous static pressure upstream of Rotor 1: DS versus MS

7 Concluding Remarks

With a LP domain plus variable nozzle approach, it is not necessary to impose fixed stiff boundary conditions at the core-compressor inlet or exit and hence the unsteadiness is modeled naturally. Moreover, such an approach allows the modelling of LP/core domain interactions, which can be crucial in predicting the initiation of rotating stall.

Using the proposed methodology, not only can one model steady flow near stall but one can model a simplified axial surge event and produce the hysteresis loop for compressor. The method allows a total flow reversal (negative mass flow) and recovery from it. Although only simplified single-passage computations with mixing planes have been performed so far, the methodology can easily be applied to a full computations.

From an engineering viewpoint, the simple method can be used to obtain a first-order approximation to surge loading. The approach can be of more practical use, e.g., axial gap approxima-

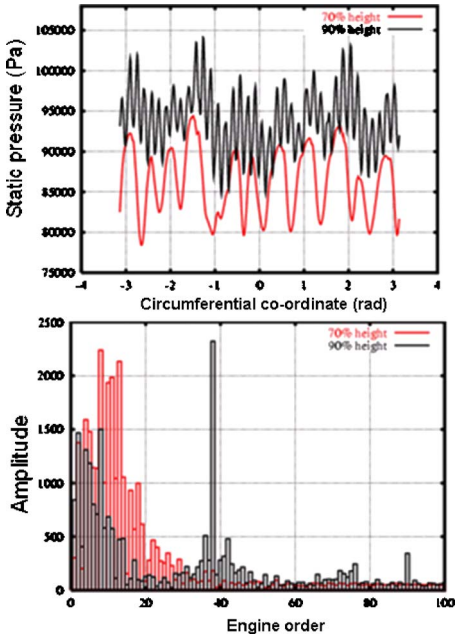

Fig. 13 Static pressure upstream of Rotor 1 and its Fourier components at 70% and 90% height

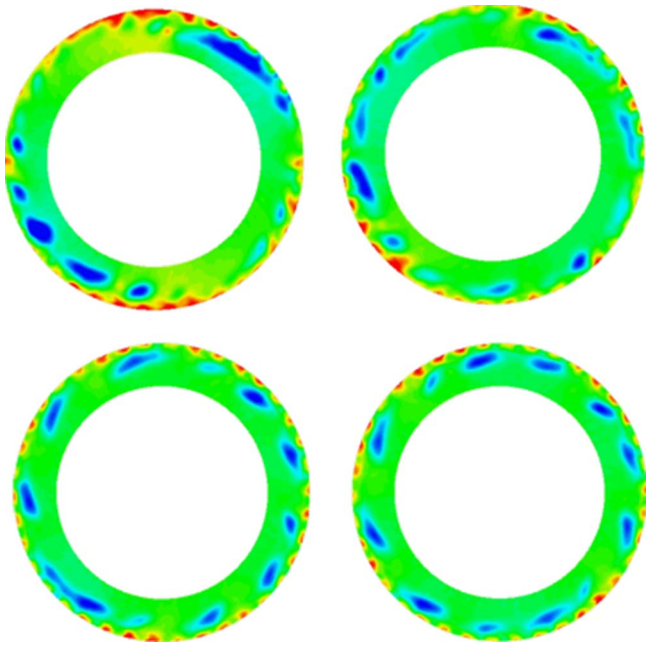

Fig. 14 Development of stall cell

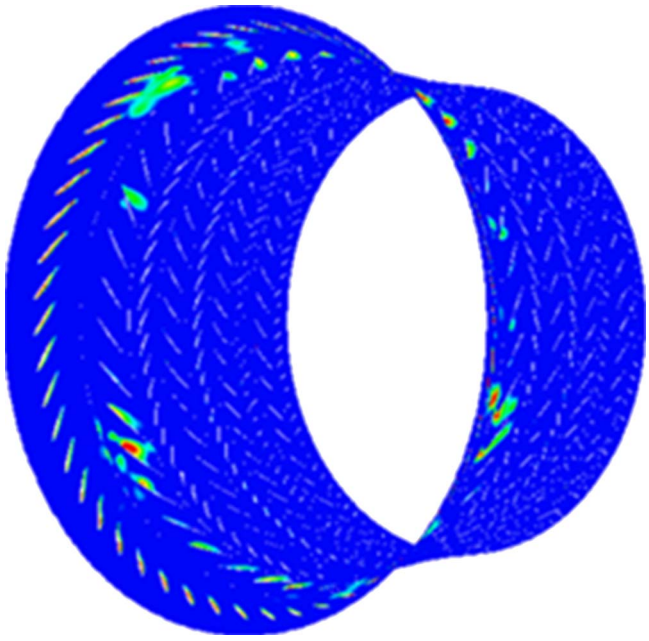

Fig. 15 Instantaneous negative axial velocity at 70% height

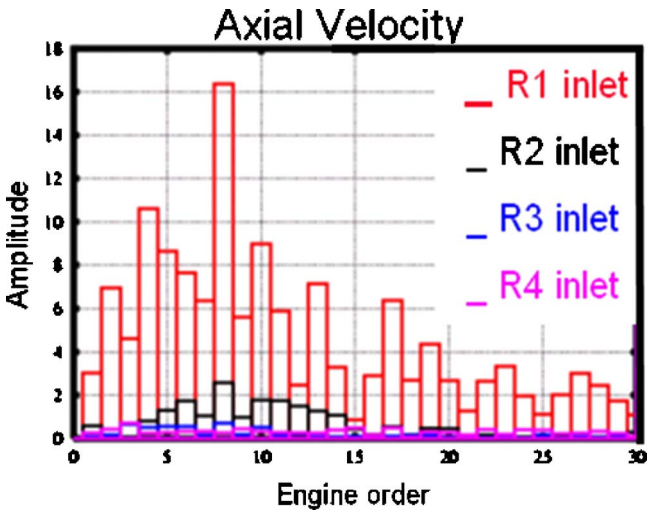

Fig. 16 Fourier components of axial velocity upstream of rotor blades

tions, provided that the unsteadiness during surge is mainly axial and the loadings during surge are higher than the rotating stall that precedes it.

From a rotating stall point of view, the most important conclusion of this work is the feasibility of simulating rotating stall with a large scale numerical model. Although the computational effort is significant, parallel processing on inexpensive personal computer (PC) clusters allows the runs to be undertaken in "advanced design" time scales. For instance, the nine-bladerow model has about 60×10^6 grid points and a typical run takes about 3 weeks on a 32-CPU cluster, each node consisting of a 2 GHz Intel Xeon CPU. Shorter time scales can be achieved by using more CPUs as the code is known to have an excellent parallel performance. It may also be possible to use relatively coarser meshes for stator bladerows, though the real computational savings are likely to come from hybrid models where remote bladerows are represented as single passages.

From a numerical viewpoint, stall initiation can be achieved by aerodynamically mistuning the rotor blade so that an initial perturbation is created. However, stall initiation is slow, requiring the simulation of about 13 full engine revolutions in this particular case.

The variable-vane scheduling plays an important role in determination of the nature of rotating stall. From a steady-state flow point of view, the MS results in a significant drop in flow, pressure ratio, and efficiency. In the case of the high-band rotating stall predicted here, the disturbances diffuse very rapidly downstream. Hence, only Rotor 1 is likely to experience high response levels.

From a design point of view, it is important to demonstrate that the compressor is free from rotating stall using a simple and cost effective design tool. From a diagnostic point of view, it is important to understand rotating stall in terms of both the exact pattern and speed of the stall cells so that any critical vibration modes can be identified and avoided. However, such a requirement may not only be beyond the available modeling accuracy, but it also relies on both the pattern and speed to remain constant between successive rotations. The latter issue needs to be studied by undertaking long rotating stall simulations, say, over 100 engine rotations, with representative inlet perturbations to see the stability or otherwise of the rotating stall structure.

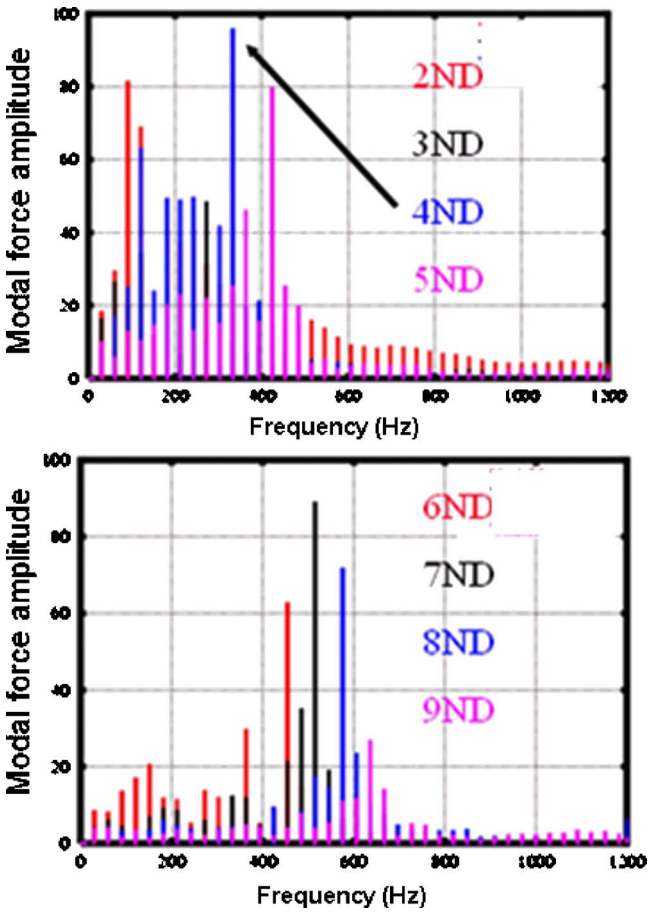

Fig. 17 Fourier components of forcing on the blade

Acknowledgment

The authors would like to thank Rolls-Royce plc for both sponsoring the work and allowing its publication.

References

[1] Greitzer, E. M., 1978, "Surge and Rotating Stall in Axial Flow Compressors. Parts 1 & 2," ASME J. Eng. Power, **98**, pp. 190–217.
[2] Longley, J., and Hynes, T. P., 1990, "Stability of Flow Through Multi-Stage Compressors," ASME J. Turbomach., **112**, pp. 126–132.
[3] Weigl, H. J., Paduano, J. D., Fréchette, L. G., Epstein, A. H., Greitzer, E. M., Bright, M. M., and Strazisar, A. J., 1998, "Active Stabilization of Rotating Stall and Surge in a Transonic Single-Stage Compressor," ASME J. Turbomach., **120**, pp. 625–636.
[4] Moore, F., and Greitzer, E. M., 1986, "A Theory of Post-Stall Transients in Axial Compressors," ASME J. Eng. Gas Turbines Power, **108**, pp. 371–379
[5] Paduano, J., Epstein, A. H., Greitzer, E. M., and Guenette, G., 1994, "Modelling for Control of Rotating Stall," Automatica, **30**, pp. 1357–1373.
[6] Niazi, S., 2000, "Numerical Simulation of Rotating Stall and Surge Alleviation in Axial Compressors," Ph.D. thesis, Georgia Institute of Tech, Atlanta, GA..
[7] He, L., 1997, "Computational Study of Rotating Stall Inception in Axial Compressors," J. Propul. Power, **13**(1), pp. 31–38.
[8] Davis, R. L., and Yao, J., 2005, "Prediction of Compressor Stage Performance From Choke Through Stall," AIAA Paper No. 2005-1005.
[9] Spalart, P. R., and Allmaras, S. R., 1992, "A One-Equation Turbulence Model for Aerodynamic Flows," AIAA Paper No. 92-0439.
[10] Sayma, A. I., Vahdati, M., Sbardella, L., and Imregun, M., 2000, "Modelling of 3D Viscous Compressible Turbomachinery Flows Using Hybrid Grids," AIAA J., **38**(6), pp. 945–954.
[11] Sbardella, L., Sayma, A., and Imregun, M., 2000, "Semi-Structured Meshes for Axial Turbomachinery Blades," Int. J. Numer. Methods Fluids, **32**(5), pp. 569–584.
[12] Rai, M., 1986, "Implicit Conservative Zonal Boundary Scheme for Euler Eqn Calculations," Comput. Fluids, **14**, pp. 295–319.
[13] Sayma, A. I., Vahdati, M., and Imregun, M., 2000, "Multi-Bladerow Fan Forced Response Predictions Using an Integrated 3D Time-Domain Aeroelasticity Model," Proc. Inst. Mech. Eng., Part C: J. Mech. Eng. Sci., **214**(12), pp. 1467–1483.
[14] Vahdati, M., Sayma, A., Freeman, C., and Imregun, M., 2005, "On the Use of Atmospheric Boundary Conditions for Axial-Flow Compressor Stall Simulations," ASME J. Turbomach., **127**(3), pp. 349–351.

Aerodynamic Design, Model Test, and CFD Analysis for a Multistage Axial Helium Compressor

X. Yan
e-mail: yan.xing@jaea.go.jp

T. Takizuka

K. Kunitomi

Japan Atomic Energy Agency,
Oarai-Machi, Ibaraki-ken 311-1394, Japan

H. Itaka
Mitsubishi Heavy Industries, Ltd.,
Akunoura-Machi, Nagasaki 850-8610, Japan

K. Takahashi
Mitsubishi Heavy Industries, Ltd.,
Takasago, Hyogo 676-8686, Japan

Results of an aerodynamic design study for the multistage axial helium compressor of a 300 MWe class nuclear gas turbine are presented. Helium compressor aerodynamics is challenged by the characteristically narrow and numerous-stage flow path, which enhances loss effects of blade surface and end wall boundary layer growth, secondary and clearance flows, and any occurrence of flow separation and stage mismatch. To meet the high efficiency and reliability requirements of the nuclear application, base line and advanced aerodynamic design techniques are incorporated with the intent to mitigate the flow path adverse working condition and losses. Design validation is carried out by test and test-calibrated 3D viscous CFD analyses of a subscale model compressor. In addition to verifying the success of the design intent, the data and computational insights of overall performance and internal flow behavior are used to establish a performance model based on Reynolds number and used for the full compressor performance prediction. The model applicable to all geometrically similar designs shows sensitive responses of helium compressor aerodynamic efficiency to Reynolds number and surface roughness. Presented in the paper is the first modern design with experimental validation for multistage axial helium compressor that concerned itself with a difficult past but which has strong current interest in countries now developing thermal and fast nuclear gas reactors. [DOI: 10.1115/1.2777190]

1 Introduction

Nuclear reactors employing steam turbine would have attainable levels of power generation efficiency around 40%. The advanced thermal and fast gas reactors under development in several countries utilize high temperature helium gas coolant. The HTTR reactor is presently testing in 950 °C helium [1]. Powering gas turbine directly with these high temperature reactors will increase efficiency to a level of 50%. Helium gas turbine is being developed to enable this type of efficient nuclear power generation services.

JAEA's 300 MWe class nuclear helium gas turbine design is shown in Fig. 1. The unit consists of a turbine and a compressor on single shaft. The turbine bell mouth intakes hot helium ducted from the reactor whereas the compressor radial diffuser discharges high pressure helium back to the reactor. The turbine exhaust and compressor inlet scroll casings in the unit midsection connect to the closed Brayton cycle heat exchangers. Bearings are located to the rotor ends. The shaft cold end drives a 3600 rpm synchronous generator directly. The unit's structural design follows largely the practice of industrial air gas turbines in that it employs similar rotor disks designed to comparable stresses, similar rotor orientations and bearing spans, and similar casings.

Use of helium as working fluid, however, creates several unique conditions of both pro and con in the unit's aerodynamic design. The sonic speed of the light molecule weight gas is sufficiently high, about three times of air's, making flow low subsonic and free of shocks in the turbine and compressor. Other working conditions are less than favorable especially in the compressor whose aerodynamic design targets contemporary performance goals of 90% polytropic efficiency and 20% surge margin in quest of baseload economy and reliable nuclear operation. The specific heat of helium is five times that of air, making helium about as many times less compressible than air such that it takes many more stages to compress helium given a pressure ratio. Furthermore, the volume flow remains small despite the unit's high power rating because the compressor is designed to an inlet of 35 times the atmospheric pressure as opposed to the usual 1 atm at air gas turbine compressor inlet. These unfavorable conditions lead to what appears to be a large number of blade rows, though pressure ratio is rated low, populating a narrow and essentially parallel compressor flow path, as seen in Fig. 1. The multistage slender flow path gives rise to the relative importance of aerodynamic losses associated with surface and end wall boundary layer growth, secondary and clearance flows, and any occurrence of flow separation and stage mismatch, making overall efficient compressor performance difficult to achieve.

2 Prior Experience and Present Approach

2.1 Prior Experience. The difficulty with helium compressor aerodynamics was evident on a 50 MWe rated unit, the world's largest helium gas turbine installed in the Energieversorgung Oberhausen (EVO) utility cogeneration plant in Germany [2]. The two shafts used are linked by a gear box. The 5500 rpm shaft includes a high pressure turbine and an intercooled compressor that includes a high pressure and a low pressure compressor section having 10 and 15 stages, respectively, whereas the 3000 rpm shaft includes a low pressure turbine and an electric generator. The higher speed was intended for compressor aerodynamic optimization. The mass flow is 84 kg/s in the compressor with 1 MPa inlet pressure.

The unit operated for about 24,000 accumulated hours until 1988 and achieved a maximum power of 30.5 MWe, well below the rated level. Problematic compressor aerodynamics was a major contributor to the power deficit [3]. An unexpected power loss of 4.0 MW or an efficiency falling short by several points was measured in the high pressure compressor section and the performance situation was similar in the low pressure compressor section. Major sources of the losses were identified to be blade profiles, which are conventional types designed to 100% reaction and

Contributed by the Turbomachinery Division of ASME for publication in the JOURNAL OF TURBOMACHINERY. Manuscript received May 10, 2007; final manuscript received June 7, 2007; published online May 6, 2008. Review conducted by David Wisler.

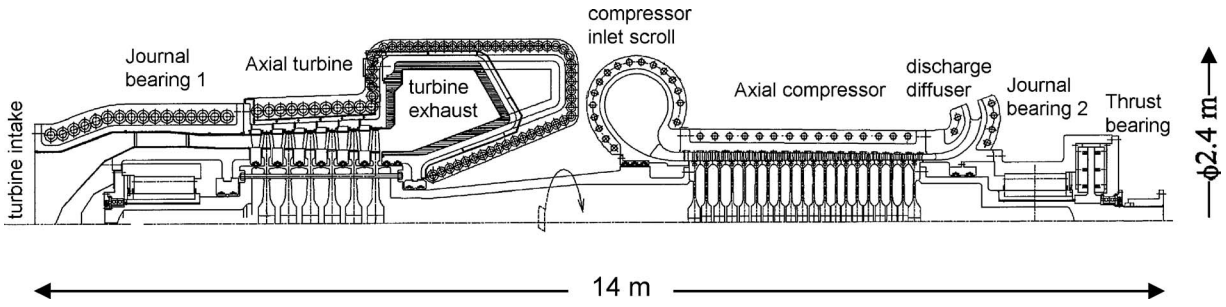

Fig. 1 300 MWe class helium gas turbine design

free vortex radial equilibrium, blade tips, inlet flow distortion, and inlet and outlet casings. No data have been published to describe the problems in detail.

2.2 Present Approach. The present base line design approach to high performing helium aerodynamics rules out compressor intercooling because intercooling optimizes cycle performance only at demanding high compression ratio that results in significant machinery complexity and inefficiency in delivering helium. To deliver a pressure ratio of 2.75, the EVO intercooled compressor used 25 stages in its original design and 41 stages in a later improved aerodynamic design from the operating experience [3]. The optimum pressure ratio is greatly reduced in the present non-intercooled compressor that, as shown in Fig. 2(*a*), employs 20 stages to deliver a design pressure ratio of 2.0. In addition to shortening bladed flow path, reducing pressure ratio in a given cycle heat rate boosts volume flow, which can effectively improve the flow area of a generally narrow helium flow path. The blades are allowed to be of sufficient span to keep blade essential core

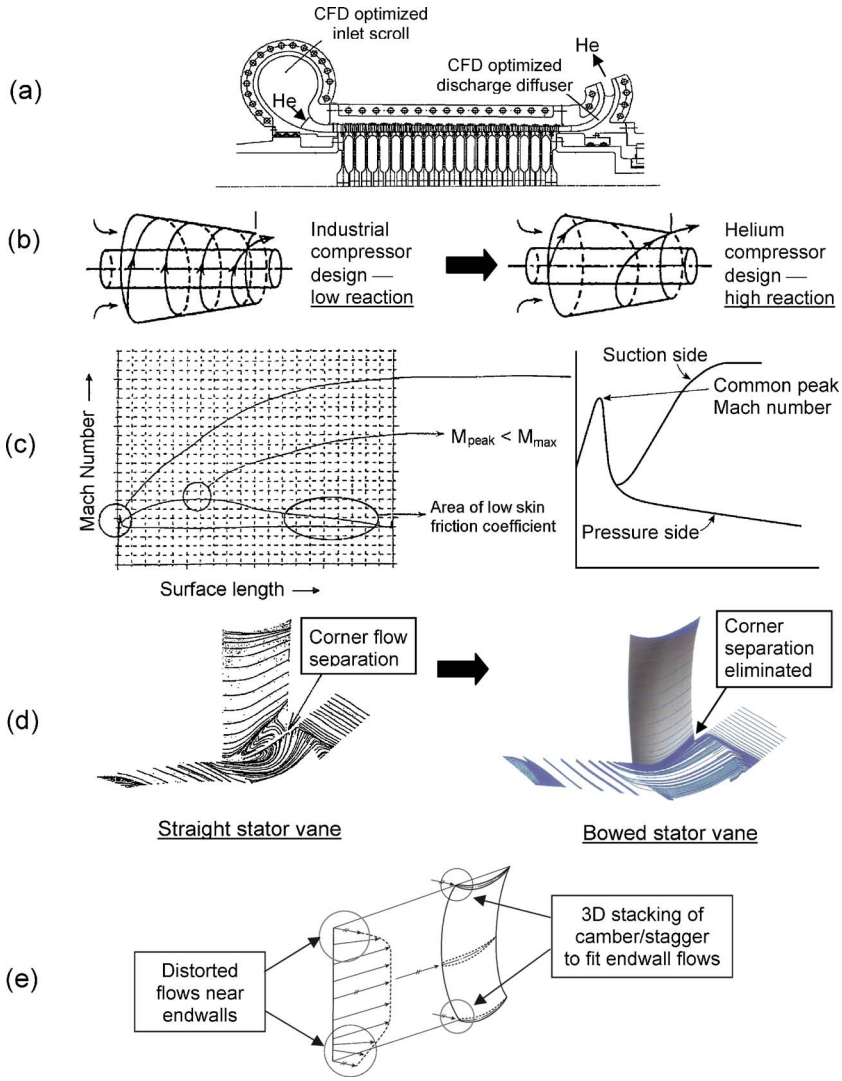

Fig. 2 Elements of base line and advanced design approach to high performing helium compressor

passage from end wall and tip clearance effects. This is done in the present design without resorting to high rotor speed. Instead, the speed is set to permit efficient gas turbine drive of both the compressor and the grid-synchronous generator on single shaft.

A further important design benefit gained by forgoing intercooling is the reduction of inlet and outlet casings to minimum. Constrained in sizing by economical installation of closed cycle, the casings engage in changing high velocity gas streams that can induce major losses, as was the case in the EVO unit and is confirmed also by the present data. Besides minimizing the number of casings, a CFD tool is thus used to configure the casings within the installation constraint to minimize pressure losses in inlet and diffuser and flow distortion before the inlet guide vane (IGV). One of the results of the configuration exercise is the outlet radial diffuser seen in Fig. 2(*a*) that incurs about a third of the pressure loss from an earlier scrolled design.

A second base line design choice made is the use of high reaction blading to balance the dual design goals of efficiency and surge margin achievable in a reasonable number of compressor stages. The classic air compressor practice has preferred use of lower reaction blading, as illustrated in Fig. 2(*b*). On the other hand, the EVO operating helium unit used a much higher reaction of 100%.

The present design experiments advanced blading techniques for the first time in helium compressor. Hubbs and Weingold [4] described the controlled diffusion airfoil (CDA) approach to air transonic blades. MHI had used double circular arc rotor blades and NACA65 stator vanes until CDA was developed and used on MF221 and M501G combustion gas turbine compressors in the 1990s, which gained efficiency and operating range over the conventional airfoils when given the same vector diagrams. The present helium design uses a type of CDA for subsonic flow with specific design goals depicted in Fig. 2(*c*), which include adjusting incidence to achieve single stagnation point near the leading edge, limiting peak Mach number on the suction surface, and achieving suction surface diffusion from the peak Mach number until the trailing edge without separation and with the well-known "Stratford" velocity profile of minimum skin friction. Wisler [5] showed through low speed model testing how custom-tailored airfoils were used to improve a range of performance goals such as reducing separation and end wall losses, which are particularly relevant to helium application. In a similar approach, the present design uses a proper degree of stator bow to take out suction surface corner separation (see Fig. 2(*d*)) and the 3D stacking of camber and stagger to restore flow incidence near end walls (see Fig. 2(*e*)).

3 Aerodynamic Design

Given the nominal aerodynamic design conditions in Table 1, the first in a series of reiterative design steps defines the backbone of the compressor flow path using a 1D pitch line code. The input to the code is largely experience based: the tip speed uses values typically found in existing products, velocity triangles draw on the flow and load coefficients that yield an efficient high reaction stage of interest, and a hub-constant contraction flow path is selected over alternatives mainly for distributing pressure rise coefficients evenly from front to rear stages. Because the resulting flow path averaging about 10 cm height can respond to blade clearance sensitively, the size of the design tip clearance is determined in detailed thermal and rotordynamic analysis of the integrated rotor bearing system that incorporates a proprietary magnetic bearing technique to control clearance. Empirical models are used to preliminarily estimate aerodynamic losses. The stagewise Mach numbers and diffusion factors at selected radii are checked to detect potential flaws. A preliminary performance map is then calculated to gauge the ability of the flow path to meet the eventual performance goals.

The flow path design from the pitch line code is scrutinized in depth and with added details using a 2D axisymmetric through-flow code. Stream surfaces of various span locations are computed at design and off-design points. More elaborated empirical models are used to account for flow losses, deviation, and blockade. An example is the loss model used to guide blade solidity selection by trading between viscous loss and stall margin while giving considerations to other design objectives such as cost and weight. Parametric survey is performed over the earlier pitch line design choices of stage count, flow path shape, and basic airfoil parameters such as solidity and aspect ratio to identify potential areas and margins for refinement. Figure 3 shows how the incidence has been improved in the core span section as a result of stage matching carried out by increasing airfoil design groups from two in the left graph to three in the right graph. Increase in airfoil design groups continues until satisfactory matching on the part of the blade core span has been obtained in all compressor stages. The incidence near either end wall will be adjusted in the next airfoil design step. Iteration with the pitch line code is necessary to finalize the flow path design.

Once the flow path design has been concluded, a potential flow CFD code is used to customize airfoil details utilizing the advanced blading techniques introduced in Sec. 2. The CDA goal design is performed on a number of span locations, followed by radial stacking of airfoil camber, stagger, and thickness location toward the end walls to complete the 3D blade profile. The radial

Table 1 Outline design parameters for full and test compressors

	Full compressor	Test compressor
Nominal design conditions		
Inlet pressure (MPa)	3.52	0.883
Inlet temperature (°C)	28.4	30
Pressure ratio, flange to flange	2.0	1.15
Mass flow (kg/s)	442	12.2
Rated speed (rmp)	3,600	10,800
Aerodynamic design pitch line values		
Number of stages	20	4
Tip diameter (first rotor) (m)	1.70	0.57
Hub diameter (first stator) (m)	1.50	0.50
Tip speed (first stage) (m/s)	321	321
Rotar/stator blade count (first stage)	72/94	72/94
Rotar/stator chord (first stage) (mm)	78/60	26/20
Rotar/stator solidity (first stage)	1.19/1.20	1.19/1.20
Rotar/stator aspect ratio (first stage)	1.3/1.7	1.3/1.7
Rotar tip/stator hub clearance	~1% blade span	~1% blade span
Flow coefficient	0.51	0.51
Load coefficient	0.63	0.63
Reaction	High reaction	High reaction

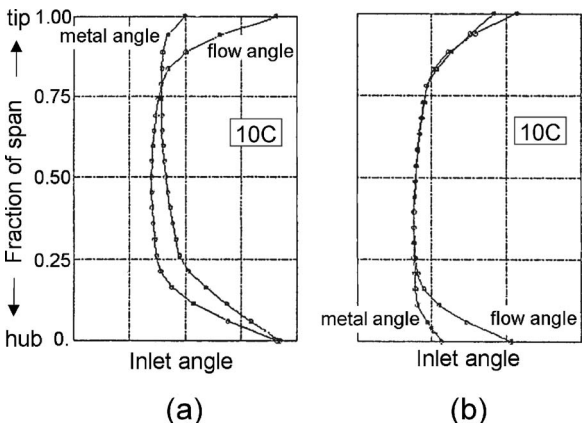

Fig. 3 Improved spanwise incidence by stage matching, shown for the tenth stator only

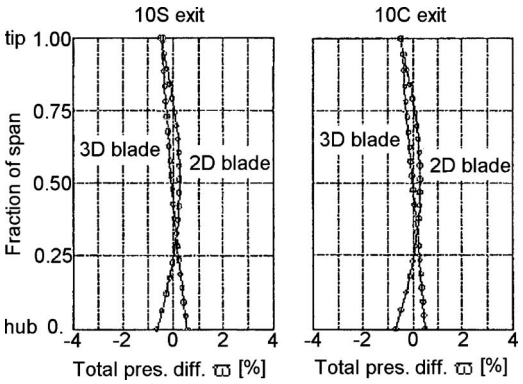

Fig. 4 Spanwise normalized total pressure difference (ϖ) at the tenth rotor and stator blade row exits

design has led to reduction of end wall boundary layers and spanwise loss profiles while enhancing hub total pressure. The improvement of the 3D blading over earlier 2D blading, which makes no particular end wall treatment, is shown in Fig. 4 for the spanwise distributed total pressure difference, ϖ at the tenth stage rotor (10S) and stator (10C) blade row exits.

Final check on the airfoil design is done row by row by a 3D viscous CFD code. Pitchwise Mach number contours, illustrated for a specific rotor span height in Fig. 5, are used to identify and correct any problem of inconsistence with or flow separation overlooked in the earlier design steps. The results of using the 3D viscous CFD to uncover stator hub corner separation and then to correct it by using the appropriate degree of stator bow were earlier shown in Fig. 2(*d*). The airfoil design is concluded when agreement between the 3D viscous and the radial potential flow design iterations has been satisfied.

4 Validation Test

4.1 Test Facility

4.1.1 Model Compressor. A minimum scale of one-tenth with tip diameter not less than 300 mm is required for a fan and flow model test [6]. A one-fifth scale regardless of diameter is specified elsewhere [7]. For aerodynamic validation test of the present helium compressor, a third of the full dimensional scale is chosen to provide the appropriate tolerance for the small-profile blade fabrication and for traverse measurement of the flow path while generating Reynolds numbers that are reliably large for performance data and evaluation.

The resulting test compressor shown in Fig. 6 includes four stages of rotor (S) and stator (C) blade rows in the main bladed flow path, a row each of inlet and outlet guide vanes, and inlet and discharge scroll casings. Four stages are selected for two reasons, (a) to observe end wall boundary layer growth through multiple

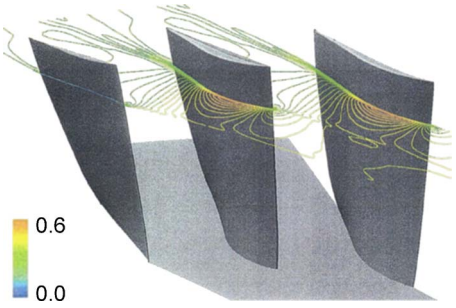

Fig. 5 Pitchwise Mach number contour for the second rotor blade row at 80% span

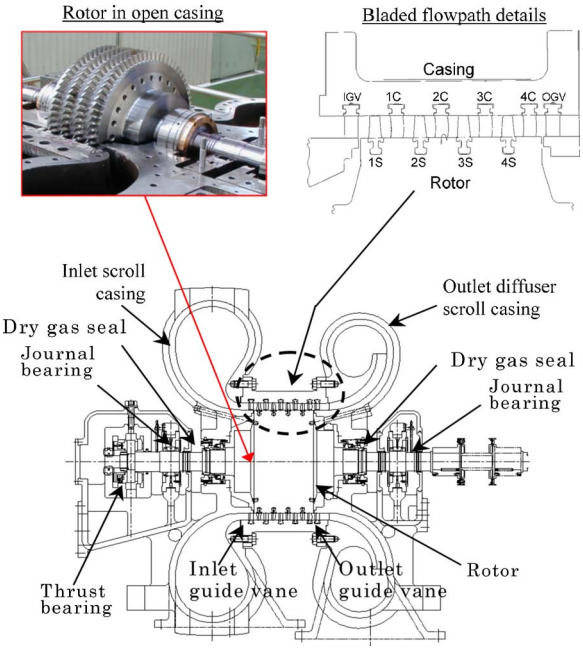

Fig. 6 Helium test compressor in one-third dimensional scale

rotating blade rows and (b) to test blading performance in a stage sufficiently removed from machine entry and exit effects. The main bladed flow path models the forward stages of the full compressor and comes equipped in two sets of airfoils, referred to as Case 1 and Case 2, with different cambers near end walls. Table 1 compares principal design values of the test and full scale compressors.

4.1.2 Test Rig. The photo of Fig. 7 shows operation in progress of the 15 kg/s helium flow, 3.65 MW motor driven test rig for the model compressor. Compressor inlet pressure is adjustable up to 1.0 MPa by varying helium inventory in the closed circuit. Compressor inlet temperature is controllable by a helium-to-water cooler. The helium circuit includes parallel valves for crude and fine flow throttling to accurately regulate compressor pressure ratio.

4.1.3 Data Measurement and Reduction. A computerized data acquisition system provides real-time measurement and data reduction from a total of 65 instrumented stations on the compressor and is put in place of the uppermost industrial quality assurance for the subject test operation, instrumentation calibration, and measurement.

To ensure nominal conditions of performance test, running blade clearances of all stages are monitored by sensors and confirmed as designed. Distortion of compressor inlet gas velocity is

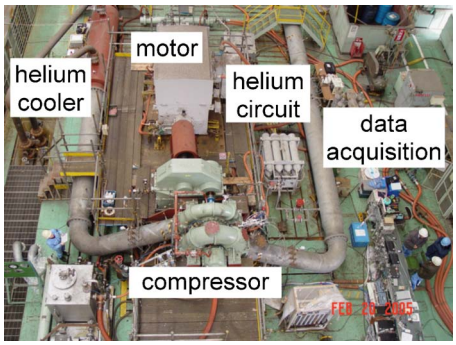

Fig. 7 Helium compressor test rig

Table 2 Measured design point performance

Test run No.	Blade airfoil design	Pressure ratio π	Corrected flow G^* (kg/s)	Poly. efficiency η_p (%)
Run 12	Case 1	1.171	12.289	88.7
Run 14	Case 1	1.170	12.174	88.6
Run 1	Case 2	1.170	12.005	88.1

determined from measurements of circumferentially spaced total pressure and temperature rakes in the annulus ahead of the IGV. Inlet distortion is controllable with the use of alternate inlet casing configurations and, when necessary, down to levels confirmed by test of negligible effects on downstream blade section performance. Pressure and temperature wall taps are present at all interstage locations for monitoring performance health of individual stages.

Steady data are logged only after the compressor discharged conditions have been confirmed to be steady, which takes typically 20 min to reach after a change of operating point in hot condition. Minor unsteadiness remains around a steady point, being a characteristic of closed circuit operation. The problem is corrected by averaging multiple sets of data taken in intervals of several minutes at a targeted point. Repeatability of data is confirmed by rerunning selected tests.

The combination of an effective flow straightener and a metering orifice located a short distance upstream of the compressor provides reading of mass flow with uncertainty of $\pm 0.1\%$. Four temperature taps and four pressure transducers peripherally distributed on the interior wall of each of the inlet and outlet ducts provide the mean static temperature and pressure of the compressor inlet and outlet. The mean static data are accurate to $\pm 0.025\%$ for pressure and $\pm 0.1\,^{\circ}\mathrm{C}$ for temperature in the scheduled measurement range. Other overall performance parameters such as total pressure, temperature, and efficiency are derived from the mass flow and static measurements.

Performance of the main bladed flow path is measured by the total pressure and temperature five-hole rakes positioned at four circumferential locations in an inlet plane approximately one and a half axial chord upstream of the IGV and in an outlet plane the same distance downstream of the outlet guide vane (OGV). The probes cross 10–90% blade span. The pressure probes are particularly calibrated by digital manometer in test. The measured temperature and pressure data are corrected by compressibility factors of individual probes obtained in the wind tunnel and mass averaged for inlet and outlet planes. Overall uncertainty of the final reduced data is $\pm 0.1\%$ for pressure ratio and $\pm 0.2\%$ for temperature ratio for the bladed flow path in the scheduled measurement range.

Traverse measurement is made in the wake of every running blade row and at fore of the IGV and aft of the OGV. The traversing plane is approximately 25% pitch line axial chord downstream of a rotor trailing edge and one and a half axial chord upstream of the IGV and downstream from the OGV. The mapped profiles of spanwise and stagewise velocities and flow angle indicate the growth of end wall boundary layers through the multistage narrow helium flow path. Piloted remotely, the traversing struts move cobra three-hole ($<\phi 1$ mm) Pitot probes between 5% and 95% span reaching wall surface proximity of 1.75 mm. The data are collected in steps of 5% span near the hub and casing walls and of 10% span away from the walls. Traverse uncertainty is less than 0.1 mm and ± 0.1 deg for linear and angular movements, respectively.

4.2 Test Results

4.2.1 Design Point. Table 2 includes the design point performance data of three test runs around the nominal inlet conditions of 0.883 MPa and 30 °C. The actual mean inlet conditions differ within 0.01 MPa and 2 °C among the three runs.

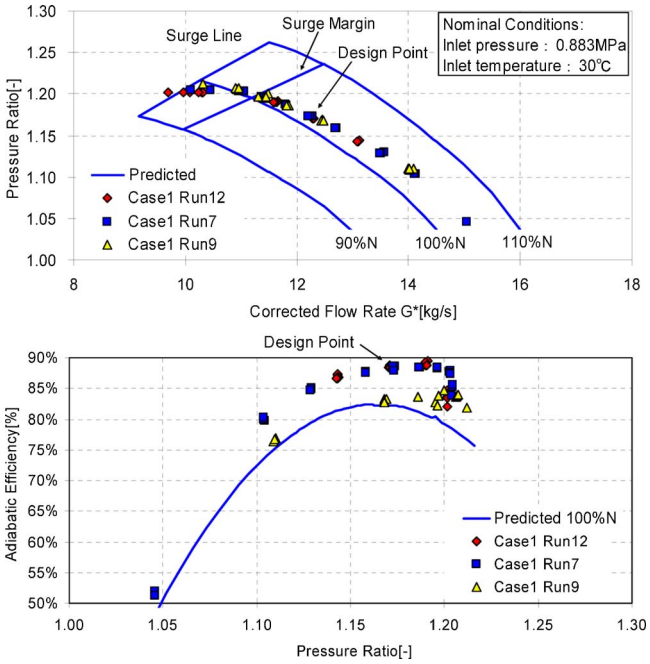

Fig. 8 Measured and predicted high speed compressor performance maps

The measured efficiencies of all three runs exceed design expectation by about 5% point. Little difference in efficiencies for the bladed section including IGV and OGV can be said between Run 12 and Run 14, which test an identical set (Case 1) of airfoil blades but use different inlet casings. While inlet distortion is limited in both runs, the casing of Run 14 results in a marginally higher level of distortion in circumferential gas velocity distribution before the IGV. However, efficiency seems unaffected by it.

On the other hand, the measured throughflows respond more to the inlet conditions. Though the measurements in both Run 12 and Run 14 tests come close to the design value of 12.2 kg/s, the design point corrected flow is reduced by 0.9% from Run 12 to Run 14, due mainly to the greater inlet distortion experienced in Run 14. The important effect of inlet distortion on throughflow capacity is clarified by further tests conducted in a broader range of inlet distortion.

Run 1 tests a different set of airfoils (Case 2). Because the same inlet casing is used in Run 1 and Run 14, the data give direct performance comparison between the airfoils. The measured design point is 0.5% point less efficient and 1.3% smaller in throughflow capacity in Run 1 than in Run 14. The Case 2 airfoil design adds more cambers near the blade tip and hub with the intent to extend stall incidence range in the end wall regions. The incidence angles are thus removed from optimum at the design point, which is consistent with the test results.

4.2.2 Performance Map. The full speed performance map is drawn in Fig. 8 of the measurements made around the nominal inlet pressure of 0.896 MPa in Run 12, and at two other inlet pressures of 0.543 MPa in Run 7 and 0.200 MPa in Run 9. The inlet temperatures that are not regulated in these tests are measured to be 28.7 °C for Run 12, 26.9 °C for Run 7, and 12.3 °C for Run 9 at their respective design points. The compressor ran about 1% over the nominal rotational speed during these tests. By factoring in the actual inlet temperatures, the corrected speed N^* is about 1.2%, 1.5%, and 4.0% overspeed at the design point of Run 12, Run 7, and Run 9, respectively. The predicted performance map is drawn by solid lines for the range of speeds and the nominal inlet conditions, as indicated.

The measured flow capacity in Run 12 matches the design prediction over a broad operating range extended from the design point when the slight overspeed of the test is factored in. The measured stall point extends beyond the predicted surge line but with a less rise in pressure ratio. This suggests an extended stall incidence range accompanied by rapid increase in loss near stall. The latter can be seen by the abrupt drop of the near-stall efficiency on the efficiency versus pressure ratio map.

The measured efficiency of Run 12 exceeds the design prediction substantially and broadly on the full speed line except near stall. Because of lack of direct helium compressor data, the loss models entered into the prediction were constructed based on pertinent air compressor data available, some of which are only remotely relatable such as the losses assumed for the stator hubs of the present cantilever type, whereas those of latest industrial compressors are typically shrouded with clearance seals. The internal flow measurements acquired in the present helium compressor tests will improve the loss models to be used in performance prediction.

The tests at the multiple pressure levels are intended to assess design and off-design performance responses to Reynolds number. The Reynolds number based on the first rotor chord and relative inlet velocity falls in the range of $(1.5–6.5)\times 10^5$ for the three inlet pressures tested. To single out Reynolds number effect on performance, the three tests are run with the same set of airfoils, as well as common inlet and outlet casing configurations. Inlet flow distortion is confirmed to be minimal.

The full speed lines of flow capacity at the three test inlet pressures coincide in a broad operating range extending both ways from the design point. Taking into account the higher corrected speed of Run 9 than those in the other two runs, the flow capacity is effectively less at the lowest inlet pressure in Run 9. The efficiency behaves similarly in that it remains nearly constant at the intermediate to high pressure levels but decreased markedly at the lowest inlet pressure tested.

The measured characteristics of flow and efficiency versus pressure ratio are consistent with the classic response of turbulent boundary layer to Reynolds number and surface roughness. Boundary layer loss is unaffected in the upper pressures or higher Reynolds number range where the surfaces are likely to be hydraulically rough in that surface roughness elements protrude the laminar sublayer of the turbulent boundary layer. Below the intermediate inlet pressure range, the appreciable changes in flow capacity and efficiency as measured indicate the behavior of a turbulent flow regime over hydraulically smooth surfaces, in which boundary layer thickness (flow blockade) and viscous loss increased with decreasing inlet pressure or Reynolds number.

4.2.3 Boundary Layer Growth. Figure 9 shows the spanwise traverse measurements of axial and tangential flow velocities in the wake of each of the four running blade rows. The measurements are made near the nominal inlet conditions of 0.883 MPa and 30 °C and in full speed. The design predicted velocity distributions are superimposed.

The measured velocity distributions in the midspan confirm the success of the design intent that the broad core span sections are kept from end wall effects. In the third rotor, which is least affected by machine entry and exit is the focus of blade passage performance test, the 20–85% span section is essentially free from the end wall effects. Outside this core span section, however, boundary layer effects are more expansive than expected near the walls. Note also that the end wall boundary layers grow rapidly from the first to the second stage and that the measured axial and tangential velocity distributions appear similar from the second to the third row, suggesting the presence of a repeating stage in the third stage, in which the growth of end wall boundary layers has slowed from the preceding stage. The velocity distributions in the fourth row depart from what are expected strictly of another repeating stage. The departure which occurs in the exit stage is believed to have been influenced by the skewed potential flow field generated in the outlet scroll casing.

Other interesting observations can be made of the traversed data. The axial velocity inclines distinctly to peak near the hub, which is a design intent to unload the hub while energizing the hub boundary layer momentum in order to prevent separation there and slow its development to stall. A spike in the tangential velocity profile appears near the casing wall of each rotor row, albeit less clear in the front row. It comes from interaction of tip clearance leak flow and vortex with the casing wall boundary layer. The spike is less visible in the first rotor row because the wall boundary layer there remains undeveloped with axial velocity near the wall still being high and because the first rotor blade tip is less loaded in design than the tips of the rear stage blades.

5 Test-Calibrated CFD Analysis

5.1 CFD Method. CFD has become sophisticated and widely used in product development [8]. In addition to being used to establish initial design, as described in Sec. 3, the CFD is used here to gain additional and greater insights on helium aerodynamics that could not be observed in the compressor model test.

The CFD code employed is a fully three-dimensional multistage viscous solver extensively used in-house for production gas turbine development. It is based on such application experience that the code calibration is focused on mesh refinement, selection of turbulence model parameters, and establishment of appropriate computational boundary conditions in benchmark against available test data.

The final CFD model for the helium test compressor is shown in Fig. 10, including the IGV, the four stages of rotor and stator blades, and the OGV. The computational model is constructed of structured H-mesh intersected by streamwise, quasiorthogonal, and meridional surfaces. The mesh refinements are adapted in surface and wall boundary layers, around leading and trailing edge planes and in wake of each blade row. Mesh count is 110 streamwise, 46 pitchwise, and 49 spanwise per blade row. Three out of the spanwise mesh count are in the clearances of the rotor tip and stator hub. The adjacent blade rows assume computational interface of a mixing plane. The extra mesh lengths extended outward from fore of the IGV and aft of the OGV are used to establish appropriate inlet and exit flow conditions.

The CFD solves the 3D Reynolds averaged Navier–Stokes equation in finite volume. Shear stress of turbulence is modeled by a thin-layer hypothesis with the "mixing length" eddy viscosity formulated based on the product of suitable velocity and length scales. The measured surface roughness data of blades and hub and casing walls of the test compressor are input to wall functions to compute skin friction.

The computational model boundary conditions include rotational speed and inlet pressure and temperature profiles as measured by the total pressure and temperature rakes before the IGV. Zero swirl angles are assumed though a swirl of about 10 deg is recorded in tests. The effect of this computation simplification is negligible on flow calculations in the relatively distant downstream main blade section. Solutions are generally achieved on the order of 10,000 iterations to a residual error of 0.01% of mean meridional velocity.

Successful use of CFD relies on proven procedures it employs. Internal flow path streamwise and spanwise measurements made of velocity, flow angle, temperature, and pressure from ten helium compressor test cases have been used to calibrate the CFD model. The graph on the left side of Fig. 11 shows a benchmark result of spanwise distribution of axial velocity in the third rotor wake, in which the measured data are seen to be accurately captured by the CFD. As a result of the calibration against the internal flow measurements, the CFD yields agreement with the measured overall performance data, as summarized in Table 3. Note that the 1% efficiency discrepancy from the measured value is sufficiently accurate in CFD analysis of this kind.

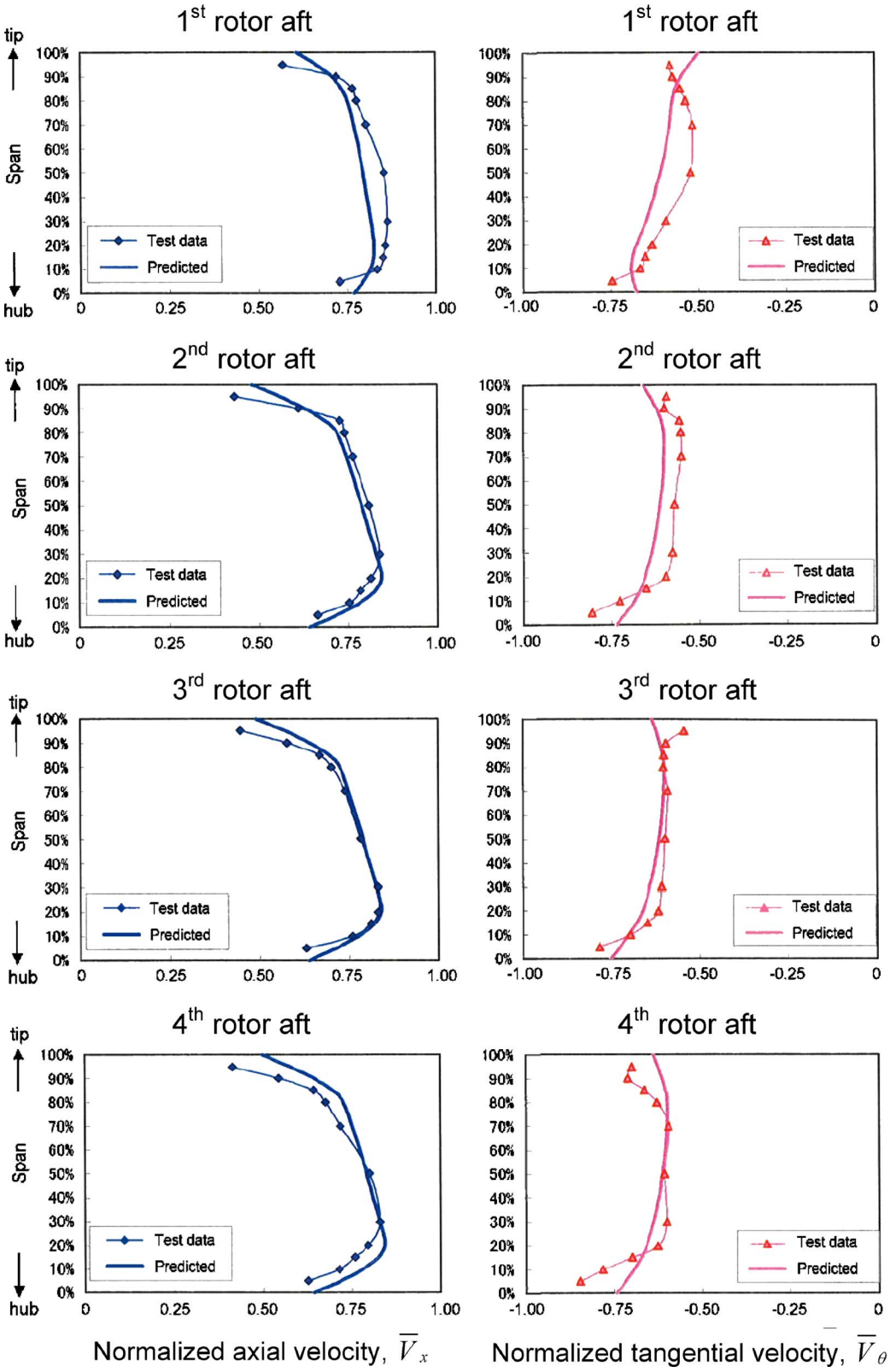

Fig. 9 Traversed measurements at nominal design point

5.2 CFD Results. Important aerodynamic insights are gained by the CFD to supplement the essential data for design validation. The graph on the right side of Fig. 11 shows the calculated spanwise distribution of axial velocity for the third stator wake, which is shown to be well behaved and for which measurement was not made in test. Indeed, the suction surface streaklines shown in Fig. 12 for the same stator blade shows no evidence of any significant separation, thanks to the successful advanced blading methods employed. Due to the passage pressure gradient, the secondary flow and boundary layer develop over a good portion of the pas-

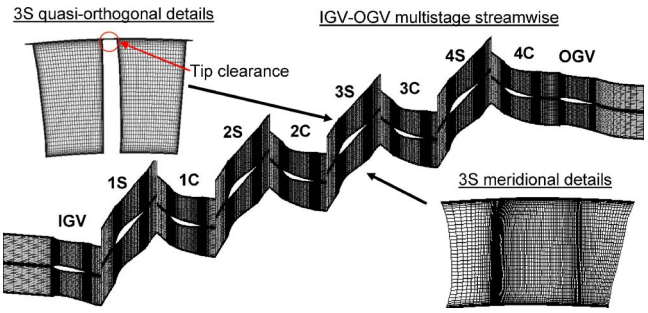

Fig. 10 Multistage 3D CFD mesh for helium test compressor

Table 3 Benchmarked CFD results

Item	Measured	CFD
Airfoil design	Case 1	Case 1
Rotation speed N (rpm)	10,911	10,911
IGV fore total pressure $P_{t,1}$ (MPa)	0.899	0.899
IGV fore total temperature $T_{t,2}$ (°C)	30.455	30.455
Reynolds number R_e	6.40×10^5	6.40×10^5
Raw mass flow G (kg/s)	12.47	12.42
OGV aft total pressure $P_{t,2}$ (MPa)	1.049	1.049
OGV aft total temperature $T_{t,2}$ (°C)	52.41	52.22
Pressure ratio π	1.168	1.166
Corrected flow G^* (kg/s)	12.31	12.20
Adiabatic efficiency η_{ad} (%)	88.4	87.4

sage hub wall and interacts strongly with the hub clearance leak flow to form a relatively thick, low momentum, and high loss hub wall flow layer, as shown in the wake Mach number contours for the stator row. Nonetheless, there is no sign of hub corner or end wall separation. The secondary flow boundary layer also forms across the casing passage wall toward the suction surface and rolls downward on the suction surface, which is seen by the oblique streaklines in the rear-tip corner region. The casing layer is less significant than the hub wall layer because of absence of leak flow and wall scraping there. Overall, the stator passage wake is thin in the broad core region away from the hub wall and the casing corner region. Evidently, stator performance could be improved by further thinning hub boundary layers, conceivably by incorporating hub seals to eliminate the clearance effect in future design.

The streaklines shown in Fig. 12 for the third rotor confirm the rotor suction surface to be essentially free of separation except for what appears to be a minor stall confined closely to the hub corner in the rearward passage. The corner stall that is visible also in the wake Mach number contours is caused by the transport and roll-up onto the hub suction surface of the end wall boundary layers of secondary flow, which is directed from pressure to suction surface. In contrast, the secondary flow and boundary layer on the passage casing wall are rather insignificant. The majority of casing end wall loss appears in the suction and casing corner region as a consequence of the mixing of tip clearance leak flow and vortex with the passage mainstream. With the clearance size of close to 1% span height, the clearance loss seems to be limited to a small tip-wall corner region. Apart from the immediate tip and hub corner regions, the rotor wake stays thin, which indicates essential success of the blade design.

6 Performance Prediction Model

The test data and CFD insights have provided the basis to develop a performance prediction model based on Reynolds number. Analogous to boundary layer thickness in tube and over plate, aerodynamic loss in compressor flow path is dependent on Reynolds number and has been correlated to it by a power law of Re^{-n} where the power index n equals zero for a hydraulically rough surface and a finite value less than unity in the case of laminar or turbulent flow over a smooth surface.

Wassell [9] surveyed data on some 20 multistage axial compressors and suggested that the power law index, which gauges how sensitive compressor loss responds to changing Reynolds number, be the product of two factors that depend on Mach number and mean flow path aspect ratio, respectively. The sensitivity decreases with increasing Mach number and decreasing aspect ratio. Schaffler [10] confirmed the predictability of Wassell's model through testing of four aeroengine transonic compressors that included from three to six intermediate to high pressure stages. The values of power law index for the four units fell to a narrow band of 0.10–0.15 in a turbulent flow regime over a smooth surface.

Wassell's model is the only known method linking the effect of Reynolds number on efficiency to easily available design parameters of a multistage axial compressor. By the Wassell model, the power law index estimated for the present helium test compressor is about 0.1, which cannot be agreed with by the measurements for at least two reasons. First, the Mach number factor in the Wassell model was evaluated tentatively, as the author cautioned,

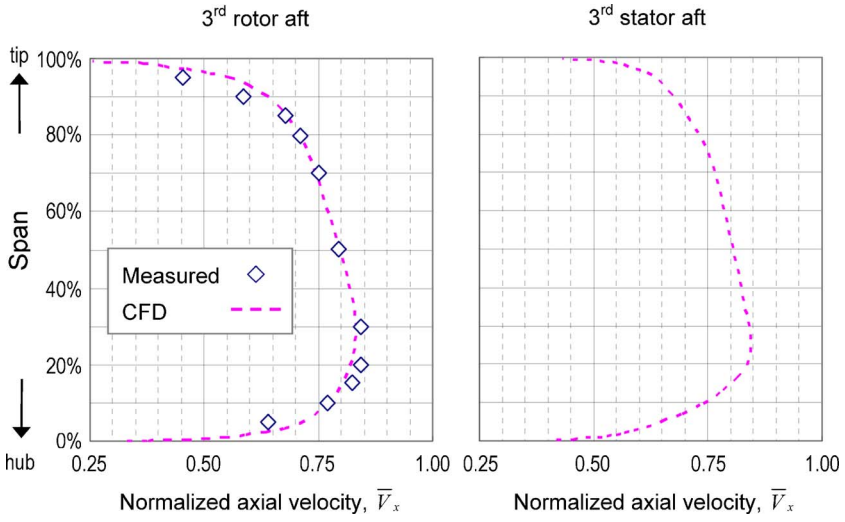

Fig. 11 Measured and CFD computed spanwise distributions of axial velocity

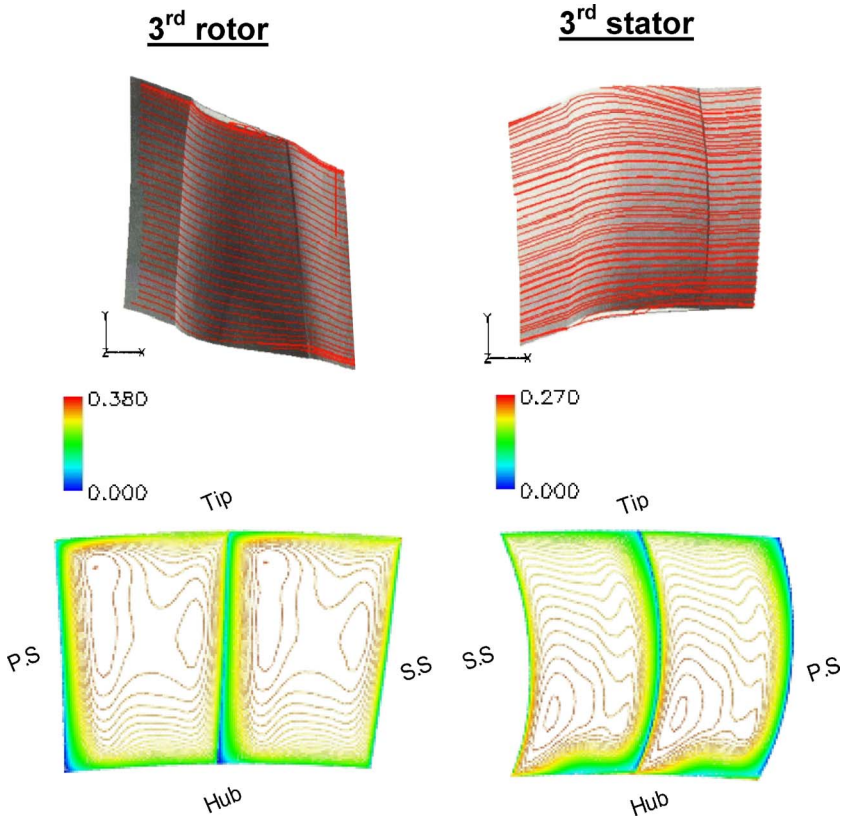

Fig. 12 CFD results of blade suction surface streaklines (upper) and wake Mach number contours of Case 1 airfoils at nominal design point

based on limited transonic data. Nevertheless, shock waves were shown to alter airfoil surface boundary layer from incompressible flow behavior and claim as much as 35–55% of overall blade passage loss in the majority of test cases reported by Schwenk [11]. The shock mechanisms and affected losses are absent in the low subsonic helium compressor.

Second, the flows in the compressor are complex, both three dimensional and interactive, say, between secondary and clearance flows, and can hardly be prescribed satisfactorily by the factor dependent on the single two-dimensional based flow path aspect ratio proposed by Wassell. Instead, the flows and their associated losses, not all coming from viscous effect, are influenced by other design features such as airfoil type, blade solidity, tip clearance, and so forth. The source and magnitude of losses will additionally be affected by recent CFD-enabled features such as CDA, 3D blading that are more effective than traditional means in tackling problems of stage matching and separation in the end wall regions.

In the absence of shock flow and in view of greater cares of modern practice that has been exercised in the present design to reduce premature losses, the effect of Reynolds number on helium compressor efficiency is expected to be more pronounced than it is foreseen in Wassell's model and likely by any other method based on either transonic or legacy data. The helium test data seem to have confirmed such expectation.

The design point data of the test cases that are run to reliably paint efficiency response to the Reynolds number are plotted in Fig. 13. The test cases cover the range of $(1.5–7.0)\times 10^5$ Reynolds numbers defined on machine inlet condition, pitch line inlet relative gas velocity, and chord length of the first rotor. Use of the rotor parameters and the first stage to prescribe overall compressor performance is rather justified because of the high reaction stage employed, which concentrates more loss in rotor than in stator, and because chord length varies little from stage to stage in the helium compressor.

The test cases involve several inlet configurations marked as Inlets A, B, and C. Inlets A and B result in negligible inlet distortion so far as impact on downstream blading performance is concerned. Inlet C is designed to distort inlet velocity substantially, measured to be about 8% circumferentially. Consequently, the blading efficiency in the run with Inlet C falls markedly from that

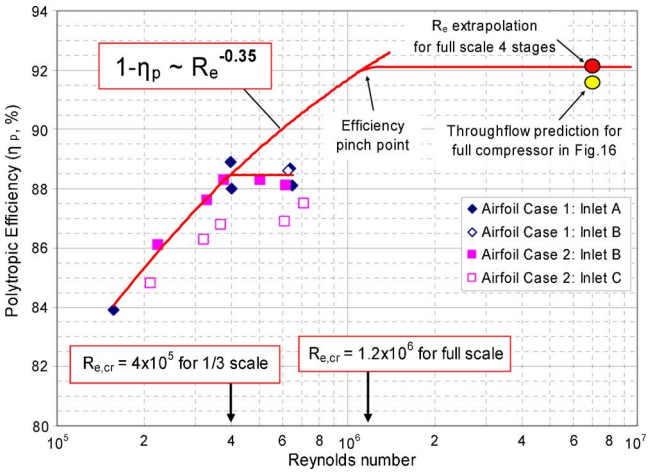

Fig. 13 Correlation of helium compressor efficiency data with Reynolds number

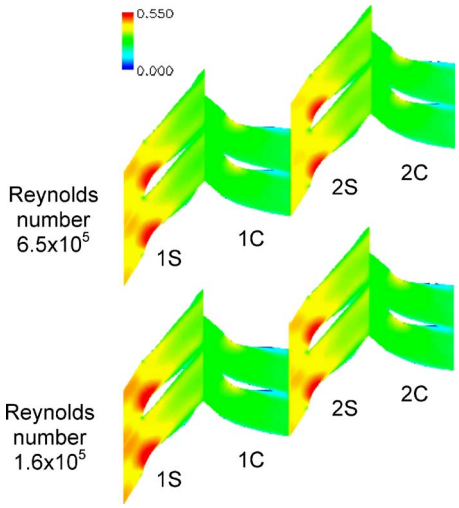

Fig. 14 Blade passage Mach number distribution at 50% span at two Reynolds numbers (IGV-to-OGV multistage CFD result)

demonstrated in the run of "Airfoil Case 2: Inlet B," which tests an identical set of airfoils but uses the inlet with minimal flow distortion. The data with Inlet C, which are considered not representative enough for the purpose of generalizing the Reynolds number effect, are nevertheless included here for reference.

Test data from two sets of airfoil designs, marked as Case 1 and Case 2, are included. The data suggest that the effect of Reynolds number on efficiency is basically independent of the specific airfoil design details, which differ by their radial stacking of camber and stagger near end walls.

With the valid data taken into account, the efficiency increases rapidly from the lowest Reynolds number tested until $R_e = 4 \times 10^5$ but levels off thereafter. Test measurements reported earlier in Sec. 4 suggested the presence of a turbulent flow regime during the steep ascend and leveling off of efficiency.

Figure 14 compares the multistage 3D viscous CFD results of pitchwise Mach number distribution at 50% span at two Reynolds numbers, in which only the first and second stages are shown and other stages are omitted for clarity. Note that the nature of the boundary layers on airfoil surfaces remain unchanged as the Reynolds number decreases and that the blade wakes increase with decreasing Reynolds number. Flow separation is seen to be limited to the very rear of the stator suction surfaces down to the lower Reynolds number. Figure 15 shows the wake Mach number contours of the third rotor and stator at the lower Reynolds number, in which flow separation is limited mainly to a local stall at the rotor suction hub. The CFD results corroborate the test data that a turbulent flow regime exists in the entire range of Reynolds numbers tested.

The steep change of efficiency data with Reynolds number as seen in Fig. 13 is thus attributed to the viscous effect of prevailing

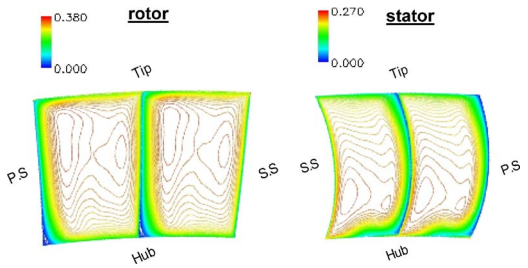

Fig. 15 Blade wake Mach contours of the third stage at Reynolds number of 1.6×10^5

turbulent attached flow on smooth surfaces until a critical Reynolds number $R_{e,cr} = 4 \times 10^5$ is reached. Above this critical Reynolds number, the surfaces become hydraulically rough and efficiency becomes independent of Reynolds number. More specifically, the data in Fig. 13 correlate polytropic efficiency (η_p) with Reynolds number (R_e) for the present helium compressor as follows:

$$1 - \eta_p \sim R_e^{-n} \quad \text{where } n = \begin{cases} 0.35 & R_e < R_{e,cr} \\ 0 & R_e \geq R_{e,cr} \end{cases} \tag{1}$$

The precise value of the critical Reynolds number $R_{e,cr}$ depends on surface roughness, more correctly on a design-permissible roughness Reynolds number. The Nikuradse experiments [12] correlated the roughness Reynolds number to the following expression:

$$R_{e,k} = k_s \frac{V}{\nu} \tag{2}$$

For a fully turbulent flow over a flat plate, the permissible roughness Reynolds number up to which a hydraulically smooth surface is expected is found to be $R^*_{e,k} = 100$ on the basis of free stream velocity [13]. The value is expected to be different inside a compressor passage wherein the boundary layer flow conditions are potential (pressure gradient and centrifugal) forced in addition to sheer stress driven. In practice of compressor, the roughness Reynolds number is equivalently expressed as follows:

$$R_{e,k} = k_{cla} \frac{R_e}{c} \tag{3}$$

where the sand roughness in Eq. (2) is replaced by the centerline average roughness for appropriate characterization of fabricated surface with distributed roughness, as is the case in compressor.

The surface roughness is measured as built on two rotor blades (1R and 3R) and two stator blades (1C and 3C) of the test compressor using on Olympus LEXT OLS3000 laser microscope scanner. The measurement is centered on a forward area of the suction surface, about 20% chord from the leading edge at 50% span height, where the boundary layer is about the thinnest on the suction surface and surface roughness there commands an influence on the rearward suction surface boundary layer. For each blade, a total of 100 measurements are taken in chordwise direction over a distance of about 4 mm. The surface roughness measurements of the four blades result in a mean value of $k_{cla} = 0.63$ μm.

With additional input to Eq. (3) of the critical Reynolds number $R_e = R_{e,cr}$ ($= 4 \times 10^5$ observed in test) and the test compressor first rotor chord length c (=26 mm), the permissible roughness Reynolds number for the present helium compressor is computed to be

$$R^*_{e,k} = 9.7 \tag{4}$$

Since aerodynamic similarity is retained between the test and full scale compressors, the correlations of Eqs. (1) and (4) found on the test unit are equally applicable to the full compressor.

The critical Reynolds number for the full scale is $R_{e,cr} = 1.2 \times 10^6$, obtained based on the experimentally derived permissible roughness Reynolds number (Eq. (4)) and by assuming the same quality of surface finish as the test compressor's. Extrapolation of the test data using Eq. (1) yields polytropic efficiency slightly above 92% for a full scale, four stage (i.e., the same number of stages used in the test compressor) unit. The method of extrapolation is depicted in Fig. 13. The extrapolated value is consistent with the 91.5% polytropic or 90.3% adiabatic design efficiency read from the performance map in Fig. 16, which is computed for the full scale, 20 stage compressor using a throughflow code that has been separately calibrated based on the data of the same test compressor.

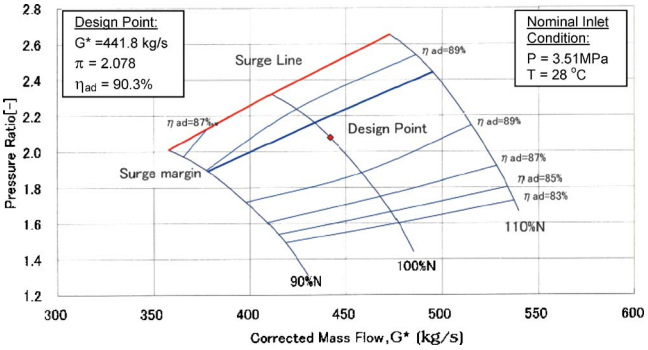

Fig. 16 Full helium compressor high speed performance map

Major design implications by the foregoing development of correlating efficiency with Reynolds number and surface roughness are given in the following.

(1) The power law index of $n=0.35$ for $R_e < R_{e,cr}$ in Eq. (1) is substantially larger than what have been reported or recommended for axial air compressors [9,10,14–16], which, along with the fact that it goes even larger than the one-fifth power law index known for one-dimensional turbulent boundary layer thickness, suggests unusually strong viscous loss contribution to the total aerodynamic inefficiency of the three-dimensional, low subsonic flow field in the present helium compressor.
(2) The permissible roughness Reynolds number of $R^*_{e,k}=9.7$ found in Eq. (4) for the helium compressor is rather small, below the range of values of 9.8–15.4 [10], 14.5 [14], and 16.0 [15] reported for axial air compressors, indicating exceptional sensitivity of the helium compressor to surface roughness.
(3) In light of the experimental evidences above, a high fabricating quality of surface finish is required for this and other helium compressor alike to avoid premature performance penalty, considering that Reynolds number as high as 7×10^6 is present in the full scale compressor.

7 Summary and Conclusion

An aerodynamically efficient and reliable multistage axial helium compressor is being developed to enable gas turbine to enter the services of advanced nuclear power generation. Aerodynamic performance of helium compressor with its characteristically narrow and numerous-stage flow path is limited by enhanced loss effects of surface and end wall boundary layer growth, secondary and clearance flows, and any occurrence of separation and stage mismatch. The difficulty with helium compressor aerodynamics was clearly evident in a prior utility plant installation.

New base line and advanced approaches are taken in the present aerodynamic design for the multistage axial helium compressor of a 300 MWe class nuclear gas turbine. The nonintercooled base line approach is selected to provide the flow path working conditions such as pressure ratio and volume flow that result in the flowpath configuration of a single bladed rotor with reasonable stage count and sufficient flow area to limit boundary layer growth effects and at the rotor speed that allows direct drive of a grid-synchronous generator, thereby avoiding a gear box or a frequency converter. The selection of the high reaction blading is intended to balance the dual design goals of efficiency and operating stability. The advanced design approaches include the use of CDA method to optimize blade profile and the 3D blading techniques to mitigate end wall boundary layers and corner separation. These advanced methods are experimented in a helium unit for the first time.

The intent of aerodynamic design is validated in the subscale model compressor test and test-calibrated CFD analyses. The results show that the surface and wall boundary layers are limited and free of significant separation and that the broad core span regions of the stator and rotor blade passages are kept from the end wall effects. The repeating stage is shown developed by the third stage from the entrance. Although confined generally close to the walls, the end wall boundary layers appear expansive and loss intensive. The thickness of the stator hub wall boundary layer seems most substantial under the influence of hub clearance flow. A meaningful gain in stator performance could be expected by incorporating hub clearance seals in future design. The overall performance has been confirmed to be of design flow capacity and operational range and strong efficiency potential.

Correlating efficiency with Reynolds number from the newly acquired data and CFD insights reveals the strong sensitivities of helium compressor aerodynamic efficiency to Reynolds number and surface roughness, suggesting that a quality fabricated surface is likely needed for high efficiency. The correlation model is used to predict the full scale compressor performance with the result that satisfies the design efficiency target and which agrees with another separately calibrated prediction.

The present study concludes that successful helium compressor aerodynamics is achievable with the design approaches taken here to meet the unique challenging working conditions of helium flow path and to address some specific performance difficulties previously experienced. A detailed multistage axial helium compressor design has been developed for prototypical demonstration next.

Acknowledgment

The present study includes the result of Nuclear Applied Heat System Technology Development entrusted to JAEA by the Ministry of Education, Culture, Sports, Science and Technology of Japan (MEXT). The authors wish to acknowledge the project contributions of S. Takada and N. Kurokochi of JAEA and E. Mori, Y. Mizokami, M. Tanihira, I. Minatsuki, and others of MHI.

Nomenclature

c = blade chord
G = mass flow rate
G^* = corrected mass flow rate $[=G\sqrt{\theta}/\delta]$
k_{cla} = centerline or arithmetic average roughness
k_s = sand grain type of roughness
n = power law index or exponent
N = rotational speed
N^* = corrected speed $[=N/\sqrt{\theta}]$
p_t = total pressure
P_t = spanwise mean total pressure
R_e = Reynolds number
$R_{e,cr}$ = critical Reynolds number
$R_{e,k}$ = roughness Reynolds number
$R^*_{e,k}$ = permissible roughness Reynolds number
V = gas velocity
V_f = reference velocity constant
V_x = axial gas velocity
$\bar{V}_x$ = normalized axial gas velocity $[=V_x/V_f]$
V_θ = tangential gas velocity
$\bar{V}_\theta$ = normalized tangential gas velocity $[=V_\theta/V_f]$
δ = ratio of measured to nominal compressor inlet total pressure
η_{ad} = adiabatic efficiency
η_p = polytropic efficiency
ν = kinematic viscosity
π = IGV fore to OGV aft total pressure ratio
θ = ratio of measured to nominal compressor inlet total temperature
$\bar{\omega}$ = normalized total pressure difference $[=(P_t - \overline{P_t})/P_t]$

References

[1] Fujikawa, S., Hayashi, H., Nakazawa, T., Kawasaki, K., Iyoku, T., Nakagawa, S., and Sakaba, N., 2004, "Achievement of Reactor Outlet Coolant Temperature of 950 °C in HTTR," J. Nucl. Sci. Technol., **41**, pp. 1245–1254.

[2] Zenker, P., 1988, "10 Jahre Betriebserfahrung mit der Heliumturbinenanlage Oberhausen," VGB Kraftwerkstechnik, **68**(7), pp. 616–621.

[3] Weisbrodt, I. A., 1994, *Summary Report on Technical Experiences from High Temperature Helium Turbomachinery Testing in Germany*, IAEA, Vienna, Austria.

[4] Hubbs, D. E., and Weingold, H. D., 1984, "Development of Controlled Diffusion Airfoils for Multistage Compressor Applications," ASME J. Eng. Power, **106**, pp. 271–278.

[5] Wisler, D. C., 1985, "Loss Reduction in Axial-Flow Compressors Through Low-Speed Model Testing," ASME J. Eng. Gas Turbines Power, **107**, pp. 354–363.

[6] JSME, 1984, "Testing Methods for Fan and Blower Performance Using Models," Japan Society of Mechanical Engineering Standard No. JSME S005-1984.

[7] AMCA, 1993, "Industrial Process/Power Generation Fans: Establishing Performance Using Laboratory Models," Air Movement and Control Association Publication No. 802-92.

[8] Horlock, J. H., and Denton, J. D., 2005, "A Review of Some Early Design Practice Using Computational Fluid Dynamics and a Current Perspective," ASME J. Turbomach., **127**, pp. 5–13.

[9] Wassell, A. B., 1968, "Reynolds Number Effects in Axial Compressors," ASME J. Eng. Power, **90**, pp. 149–156.

[10] Schaffler, A., 1980, "Experimental and Analytical Investigation of the Effects of Reynolds Number and Blade Surface Roughness on Multistage Axial Flow Compressors," ASME J. Eng. Power, **102**, pp. 5–13.

[11] Schwenk, F. C., Lewis, G. W., and Hartmann, M. J., 1957, "A Preliminary Analysis of the Magnitude of Shock Losses in Transonic Compressors," National Advisory Committee on Aeronautics Report No. NACA-RM-ES7A30.

[12] Nikuradse, J., 1932, "Laws of Flow in Rough Pipes," National Advisory Committee on Aeronautics Report No. NACA-TM-1292, 1950 translation.

[13] Schlichting, H., 1979, "*Boundary Layer Theory*," 7th ed., McGraw-Hill, New York.

[14] Koch, C. C., and Smith, L. H., Jr., 1976, "Loss Sources and Magnitudes in Axial-Flow Compressor," ASME J. Eng. Power, **98**, pp. 411–424.

[15] Miller, D. C., 1977, "The Performance Prediction of Scaled Axial Compressors from Model Tests," IMechE Paper No. C181/77.

[16] ASME, 1997, "Performance Test Code on Compressors and Exhausters," ASME Test Code No. PTC 10-1997, R2003.

Transonic Turbine Stage Heat Transfer Investigation in Presence of Strong Shocks

A. de la Loma
G. Paniagua
D. Verrastro

Turbomachinery and Propulsion Department,
von Karman Institute,
Rhode Saint Genèse B1640, Belgium

P. Adami
Energy Department "Sergio Stecco,"
University of Florence,
Florence 50139, Italy

This paper reports the external convective heat transfer distribution of a modern single-stage transonic turbine together with the physical interpretation of the different shock interaction mechanisms. The measurements have been performed in the compression tube test rig of the von Karman Institute using single- and double-layered thin film gauges. The three pressure ratios tested are representative of those encountered in actual aeroengines, with $M_{2,is}$ ranging from 1.07 to 1.25 and a Reynolds number of about 10^6. Three different rotor blade heights (15%, 50%, and 85%) and the stator blade at midspan have been investigated. The measurements highlight the destabilizing effect of the vane left-running shock on the rotor boundary layer. The stator unsteady heat transfer is dominated by the fluctuating right-running vane trailing edge shock at the blade passing frequency. [DOI: 10.1115/1.2777193]

Introduction

Compact aeroengines with higher thrust force the aerothermal engineer to load more and more the high-pressure stages. This design trend has a strong impact on the flow characteristics, performance, and engine life cycle. Concurrently, the growing tendency to increase the turbine inlet temperature lowers the life of engine components if the cooling scheme is not adequately adapted. The correct estimation of the external heat transfer around the blade rows is thus the first step to predict the hot-section-component life. In such scenario, the increase of stage loading motivates further advances in the heat transfer analysis and investigation for turbine design process, where experimental data still remain the reference for the designers.

The current paper analyzes the strong blade row interactions present in highly loaded high pressure (HP) stages, where the flow pattern and heat transfer are dominated by the trailing edge shocks in both the vane and the rotor (M_{2is}=1.25). The complex shock mechanisms encountered in turbomachinery flows and their influence on the heat transfer rates have been extensively studied by a community with an increasing interest in transonic flows. Experimental investigations have been carried out in different types of facilities. Measurements in linear cascades provide valuable information on the heat transfer mechanisms and physics, allowing to separate the effects of Mach number, Reynolds number, and turbulence intensity, e.g., Arts and Lambert de Rouvroit [1], Arts et al. [2], Popp [3], and Giel et al. [4]. However, the flow in blade rows is intrinsically three dimensional, and viscous effects in the end-wall region augment considerably the three dimensionality of the flow, becoming a dominant factor in low aspect ratio HP blade rows (Sieverding and Arts [5]).

Rotating devices in front of linear cascades allowed separating the effect of the stator wakes and shocks on the rotor heat transfer, e.g., the experiments of Doorly et al. [6], Doorly and Oldfied [7] or Ashworth et al. [8]. Interestingly, there is little agreement between rotating blade heat transfer data (Hilditch and Ainsworth [9]) with the corresponding values obtained in a linear cascade with bars and grid generated turbulence (Doorly and Oldfield [7]). The rotor unsteady heat transfer in a fully scaled transonic turbine measured at MIT by Guenete et al. [10] was compared with Oxford data taken in a linear cascade with passing bars (Ashworth et al. [8]). The amplitude of the fluctuations induced by the shock was larger in the turbine than in the cascade. Effectively, there are many coupled phenomena on the full-stage flow field that cannot be reproduced by superposition in linear cascades (Dunn [11]). However, the knowledge acquired in these simpler experimental setups has been effectively used in full rotating rigs, where a bigger effort is needed to meet the experimental objectives (Haldeman et al. [12]).

Since the 1980s, remarkable work on heat transfer with fully rotating turbines has been conducted by research groups at Calspan (Dunn et al. [13,14]), Oxford (Hildich and Ainsworth [9] and Moss et al. [15]), MIT (Guenette et al. [10] and Abhari et al. [16]), OSU (Haldeman et al. [12,17]), VKI (Denos et al. [18] and Didier et al. [19]), and WPAFB (Haldeman et al. [20] and Polanka et al. [21]). Dunn et al. [13,14] reported mean values of Stanton number around the nozzle guide vane (NGV) and rotor blade rows of the full-stage rotating turbine of the Garrett TFE 731-2 engine. The investigation, designed to determine the interaction between the vane and the blade rows, shows a comparison between the full-stage heat flux and the measurements obtained with a stator only, in the absence of a rotor. The presence of the rotor tends to move the transition forward on the airfoil, increasing the heat transfer levels around 20%, suggesting that caution should be exercised when applying stator-only results to full-stage predictions. Abhari et al. [16] reported time resolved rotor heat flux calculations and measurements in a transonic turbine with a 4:1 total pressure ratio and a NGV exit Mach of 1.18. A complex shock structure interaction is proposed, where as many as six shock waves moving through a single rotor passage are identified. Didier et al. [19] investigated the effect of Reynolds and pressure ratio for different blade heights in a transonic turbine stage at VKI. The variation of the stage pressure ratio causes changes in the relative inlet conditions to the rotor, explaining the changes in the heat transfer coefficient around the blade. When the strength of the NGV trailing edge shock is reinforced, the amplitude of the heat transfer fluctuations increases significantly.

The objective of this investigation is to provide a better understanding of hot-gas-side heat transfer in high-pressure turbine stages, focusing on shock interactions across the stage based on measurements and computational fluid dynamics (CFD). The dominant effects on the heat transfer fluctuations in the vane and rotor are addressed. The vane trailing edge shocks being reflected in the rotor and in the neighboring vane are clearly identified

Contributed by the International Gas Turbine Institute of ASME for publication in the JOURNAL OF TURBOMACHINERY. Manuscript received May 21, 2007; final manuscript received May 27, 2007; published online May 6, 2008. Review conducted by David Wisler. Paper presented at the ASME Turbo Expo 2007: Land, Sea and Air (GT2007), Montreal, Quebec, Canada, May 14–17, 2007. Paper No. GT2007-27101.

Table 1 Geometrical characteristics at midspan

	C_{ax}/h	Pitch/C_{ax}	Stagger (deg)	pitch	le/C
Vane	0.81	1.31	54	0.28	0.035
Rotor	0.74	0.91	32	0.40	0.037

using both experiments and numerical simulations. The analysis of the CFD data provides further insight on the origins of the large heat transfer variations.

Experimental and Computational Tools

Test Rig and Instrumentation. The measurements have been performed in the compression tube turbine test rig CT3 at the von Karman Institute. This facility built in the 1990s by Sieverding and Arts [5] allows a correct simulation of the operating conditions encountered in modern aeroengines. The operation cycle of the rig is fully described by Dénos and Paniagua [22]. The turbine stage is composed of 43 uncooled cylindrical vanes and 64 uncooled twisted blades. The main geometrical characteristics are listed in Table 1. In contrast with previous investigations, the vane trailing edge has no cooling slot and has been restaggered 2 deg. to allow a higher vane exit Mach number. Sieverding et al. [23] present the coordinates of the cooled cylindrical vane.

Table 2 summarizes the three operating conditions of the measurement campaign at midspan. The NGV exit Mach number is supersonic for all the conditions. Tests were performed around the nominal speed of 6500 rpm (108.3 rev/s) with a stage inlet turbulence level of ~5% (Yasa et al. [24]). The inlet total pressure and total temperature were 1.65 bar and 434 K. The axial distance between the rotor leading edge and the stator trailing edge at midspan is 40% of the stator axial chord.

The heat transfer process of a real engine is reproduced in a short-duration turbine test rig by a sudden release of hot gas over a cold turbine. The surface temperature increase experienced by the blades is monitored with thin film gauge resistors mounted on an insulating substrate (Macor or Upilex) around the airfoil. The use of such gauges for measuring heat transfer rates to turbine blades in short-duration transient facilities is well documented (Schultz and Jones [25]). In addition to the heat transfer rate measurement, the interpretation of these signals yields useful information about the gas flow and boundary layer.

Three different vanes have been instrumented at midspan with a total of 39 platinum thin film gauges. The gauges are deposited on an Upilex sheet, which is wrapped around the airfoils, made of Plexiglas (double-layered system). On the rotor, 18 blades were instrumented with 72 Macor-based gauges (single-layered system), spread at three different heights (15%, 50%, and 85%). In Fig. 1, an instrumented stator vane and a rotor blade are shown. The thermal properties of the different substrates, Upilex, Plexiglas, and Macor, have been obtained in a free jet facility, with known heat flux, using an optimization routine (Billiard et al. [26]).

Pressure measurements have been carried out with pneumatic and fast response pressure transducers, located at the same positions as the thin film gauges. Temperature and pressure rakes measure the flow field at the inlet of the NGV and the outlet of the rotor.

Table 2 Main operating conditions

	Re(10^6)	$M_{2,is}$	$M_{3r,is}$	P_{01}/P_{03}
Low	1.063	1.071	0.65	2.19
Normal	1.072	1.242	0.97	3.19
High	1.074	1.249	1.18	3.85

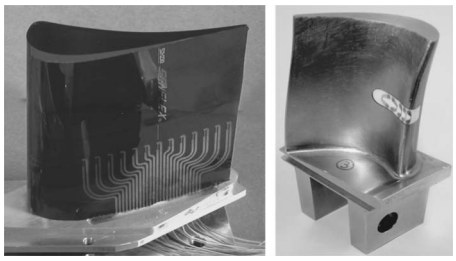

Fig. 1 Vane and rotor blades instrumented

Data Processing. At VKI, the heat flux is retrieved from the measured wall temperature using a numerical solution (Crank–Nicholson scheme) of the unsteady heat conduction equation in a multilayered substrate (Iliopoulou et al. [27]). Due to the short testing time (~300 ms), the heat penetration can be considered as a 1D process. Secondly, the blade appears as a semi-infinite body since its inner part does not experience any temperature change during the experiment. The Nusselt number is defined in terms of the airfoil axial chord, total inlet temperature minus the local profile temperature measured by the gauge, and thermal conductivity based on the local temperature. The Nusselt number computed in this way is rather like a scaled down heat flux. The overall uncertainty on the Nusselt number was evaluated to be 5%.

The thin film heat flux gauges measure both the steady and unsteady components of heat flux. Both components are recorded and processed separately since they carry information at different time scales. The steady component, at the blow-down time scale, is low pass filtered at 750 Hz and sampled at 1.5 kHz. The unsteady component, containing the high frequency phenomena, is high pass filtered at 100 Hz and sampled at 300 kHz. The measured surface temperature fluctuations occurring at the blade passing frequency (~6.9 kHz) or at the vane passing frequency (~4.7 kHz) are amplified before being digitized on a 12 bit acquisition system. An averaging technique is applied on the unsteady heat flux time series in order to extract a representative period of the whole time series (phase-locked averaging). The averaging is done over three rotor revolutions. The relative position of the rotor with respect to the stator is well known, thanks to an infrared diode system.

Numerical Simulations. Quasi-3D CFD computations have been performed to have a better understanding of the flow field in the stage. HYBFLOW, developed at the University of Florence (Adami and Martelli [28]), has been used as flow solver with k-ω turbulence model proposed by Wilcox, based on the Businesque hypothesis (details are given by Martelli et al. [29]).

In order to minimize the computational cost, the domain considered comprised two stator and three blade passages ($43/64 \approx 2/3$). Figure 2 (left) displays the blade to blade view of the final grid with 201,144 nodes and 110 structured and unstructured blocks. Figure 2 (right) depicts a detail of the unstructured grid matching with the structured grid around the blade leading edge.

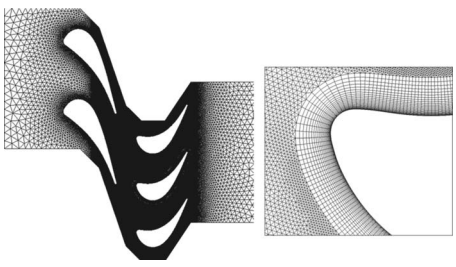

Fig. 2 (Left) Blade to blade view of the stage and (right) detail of the structured grid close to the airfoil

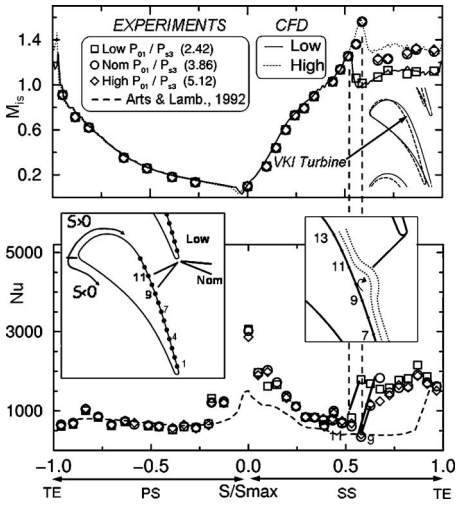

Fig. 3 Vane Mach and Nusselt number distributions

The grid is one layer deep. The first cell nondimensional y^+ distance is between 1 and 2. The time resolved sampling frequency used in the simulation is ~500 kHz.

Stator Heat Transfer

Stator Time-Averaged Nusselt Number. The convective heat transfer rate into an airfoil is strongly linked to the velocity distribution around the profile. Figure 3 presents the vane Nusselt number distribution, together with the isentropic Mach number, based on the measured local static pressure and total pressure at the inlet of the stage. The three different pressure ratios are shown. The repeatability was verified and proven to remain within 1%. Each data point is the result from averaging up to three different tests at each pressure ratio. Excluding the rear suction side, the velocity distribution around the profile is identical for the three pressure ratios. Consequently, the Nusselt distribution is similar in the pressure side and front suction side, which proves a high level of repeatability. Regarding the rear suction side, since the vane exit Mach number for *nominal* and *high* pressure ratios is identical ($M_{2,is} \sim 1.25$), the vane flow field for these two conditions is the same.

The highest heat flux levels are encountered in the stagnation region due to the lack of insulation from the boundary layer (Nu=2800–3000). An attempt has been done to correlate the stagnation region heat transfer data. The Frössling number ($Fr = Nu\sqrt{Re} = 1.65$) based on the vane LE diameter, for a 5% turbulence intensity, is ~30% higher than the value predicted in the correlation developed by Lowery and Vachon [30]. A possible explanation for this enhanced value is the degree of isotropy present in the turbulent flow, leading to increased stagnation heat transfer, as demonstrated by Van Fossen and Ching [31]. At the leading edge, 2D conduction effects are also present due to the high curvature in that region, leading also to an artificially increased heat transfer [32].

As the laminar boundary layer develops and thickens, the heat flux falls rapidly, both on the pressure and suction sides. Along the front pressure side, the flow is rapidly accelerated in the convex surface resulting in a substantial decrease of the Nusselt number, which remains practically constant further downstream (Nu =750). This plateau indicates a laminar/transitional state of the boundary layer. At this level of Reynolds number (10^6), the detrimental effect of the concave curvature does not disturb an accelerating boundary layer (Arts and Lambert de Rouvroit [1]).

At the suction side, the favorable pressure gradient and the convex curvature accelerate continuously the laminar boundary layer until locations 10/11 ($S/S_{max} \sim 0.48$) for the *low-pressure* ratio and location 9 ($S/S_{max} \sim 0.58$) for the nominal and high-*pressure* ratios. At those locations, a discontinuity exists in the Mach and Nusselt numbers. The sudden rise of heat transfer and static pressure is due to the impingement of the right-running trailing edge shock from the neighboring vane.

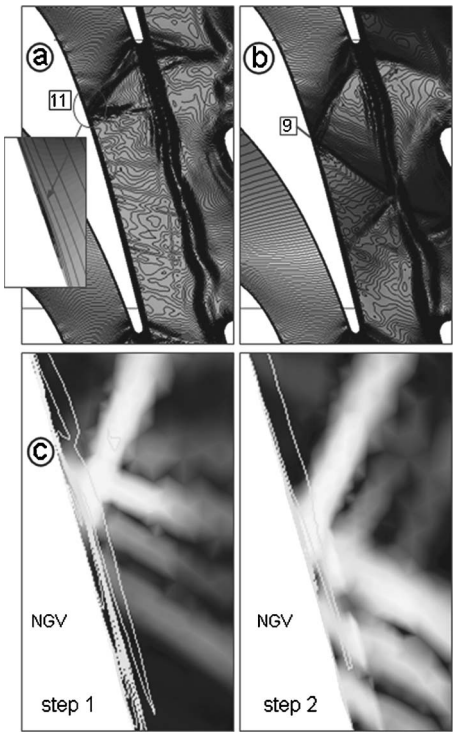

Fig. 4 (*a*) Time-averaged isopressure lines at *low-pressure* ratio, (*b*) Time-averaged isopressure lines at *high-pressure* ratio, and (*c*) instantaneous shock interaction at two time steps

A comparison between the actual heat transfer data and the VKI airfoil tested by Arts and Lambert de Rouvroit [1] in a linear cascade under similar operating conditions ($Re_2 = 1.09 \times 10^6$, $M_{2is} = 1.06$, Tu=6%) is also shown. The pressure side heat transfer levels match very well; however, the linear cascade data appear to indicate lower Nusselt numbers in the suction side than the corresponding full-stage data, where the presence of the rotor enhances the heat transfer. A normal shock standing on the rear suction side is present in the cascade data, leading to a sudden increase in heat transfer.

Figure 4 (top) displays the time-averaged isopressure lines in the vane for low- and high-pressure ratios. The large gradients of static pressure jointly with the complex system of compression waves indicate the vane shocks. The inclination and strength of the vane trailing edge shocks increase with the pressure ratio. Figure 3 showed that in Gauge 9 for the high-pressure ratio (11 for the low-pressure ratio), a lower level of heat transfer appears just preceding the sudden rise. This can be explained by the presence of a small separation bubble originated by the shock impinging on a laminar boundary layer, evidenced also in the CFD results for the low-pressure ratio (stream lines in Fig. 4(*a*)). Downstream of the separation bubble, the boundary layer becomes turbulent, enhancing the heat transfer levels; as the turbulent boundary layer develops, the heat flux tends to decrease.

Note that in the case of the high-pressure ratio, the time-averaged CFD results do not indicate any separation bubble (Fig. 4(*b*)). This is due to the highly unsteady nature of the vane shock for the case of the high-pressure ratio. By contrast, Fig. 4(*c*) shows the instantaneous presence of a separation bubble for the high-pressure ratio at two different instants.

Stator Time-Resolved Nusselt Number. The unsteady content

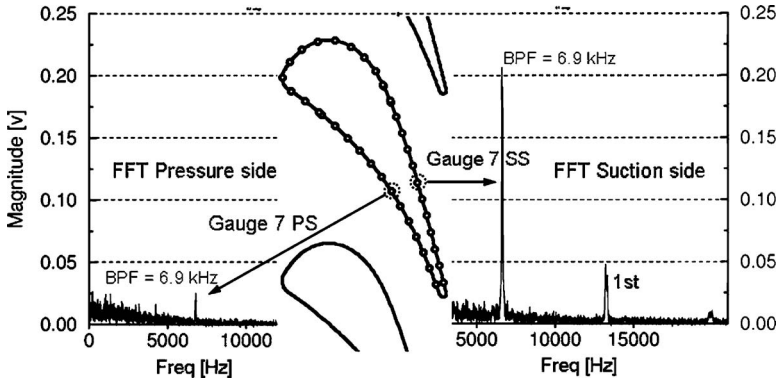

Fig. 5 FFT analysis of gauges mounted in the vane

of the data is analyzed by means of a phase-locked averaging (PLA) technique. This technique allows computing the mean period of an unsteady signal at a given frequency. Hence, it provides the periodic part of the signal, also called deterministic or time resolved. Furthermore, it provides an estimate of the time-unresolved (random) component, based on the root-mean-squared (rms) and correlation coefficients. At VKI, this averaging is done based on three rotor revolutions, i.e., 192 periods (Dénos and Paniagua [33]). In the following, the results are presented under the form of a Nusselt number over two blade passing events.

Figure 5 shows the fast Fourier transform (FFT) of two gauges located at the suction and pressure sides. Both FFTs show clearly a dominant frequency, at the blade passing frequency (64 blades/rev $\times$ 108.3 rev/s $\approx$ 6.9 kHz), and its harmonics. The amplitude of the fluctuations at the dominant frequency on the suction side is one order of magnitude higher than that on the pressure side. The rotor downstream has effectively a large influence on the vane rear suction side, which is directly exposed to the rotor. On the other hand, the stator pressure side is geometrically hidden from the rotor; besides, the right-running trailing edge shock prevents any major fluctuation to travel upstream of the throat.

Figure 6 shows the steady plus the periodic component of the unsteady signal for several gauges along the pressure side and suction side at low and nominal pressure ratios. Similarly to the time-averaged data, no significant difference has been encountered between the nominal and high-pressure ratios. In the pressure side, there is little difference between the low and nominal pressure ratios, with a single fluctuation per blade passage progressing upstream from Gauge 1 to 7.

On the rear suction side, the flow field is dominated by shock waves reflected by the rotor and to a lower extent the rotor blade potential field, resulting in several fluctuations traveling upstream. For the low-pressure ratio, the strength of the trailing edge (TE) shocks and their reflections is reduced, resulting in a decrease of the heat transfer fluctuations. However, close to the vane trailing edge, the amplitude of the fluctuations for both pressure ratios is very similar. In Gauges 1 and 2, along the suction side, the reflected shock intensity is lessened and the fluctuations might be dominated by the rotor potential effect. At nominal pressure ratio, the biggest fluctuation is encountered at Gauge 8, due to the fluctuating nature of the right-running TE shock (from the neighboring vane). The rotor blade passing in front of the vane channel produces a blockage effect, increasing the static pressure, so that the local pressure ratio across the vane channel decreases. The shock wave moves accordingly in order to match the new instantaneous pressure ratio, becoming less inclined. This effect produces a small up-and-down motion of the shock that sweeps Gauge 8 at the blade passing frequency. Coherently, the reflected shock also fluctuates, reaching for selected phase angles a higher intensity than the direct shock itself. The strong fluctuation at Position 8 is no longer present at low-pressure ratio, indicating a change in the position and the strength of the shock. As predicted in the steady analysis, the shock impinges the vane around Location 10.

The numerical simulations provided further insight into the stator-rotor interaction mechanisms. Figure 6 (right) shows several snapshots of the complex shock patterns present in the stator-rotor gap for the nominal/high-pressure ratio. The rotor is directly exposed to both the right and left shocks produced by the NGV trailing edge and each one is differently reflected back toward the upstream row. The resulting interaction of the shocks is a rather complex pattern. Figure 6 (Step a) shows that the left-running vane shock impinges directly onto the rotor crown forming a normal shock, which is subsequently reflected back to the NGV (shown in Step b). The reflected shock is followed by an expansion that travels upstream following the shock wave. Both the shock and the expansion are impinging on the NGV suction side and then reflected back again as shown in Step c. In Step d, it is possible to see how the reflected shock reaches again the rotor merging with the compression waves on the rotor crown. This complex wave interaction results in two different fluctuations traveling from Gauge 1 to Gauge 8, in agreement with the experimental data. Figure 6 (bottom) sketches the shock interaction mechanism.

For the low-pressure ratio, it has already been shown (Fig. 4(*a*)) that the right-running TE vane shock is weaker, so that the reflected shock from the vane suction side does not hit the rotor crown.

The magnitude of the fluctuations together with the time-averaged level of the Nusselt number is presented at the bottom of Fig. 6 for low- and nominal/high-pressure ratios. At Location 8, the magnitude of the fluctuation is higher than the time-averaged value for nominal/high pressure ratios. On the last three gauges of the suction side, the amplitude of the fluctuations is 40–70% of the corresponding time-averaged value. A correlation coefficient can be obtained by performing a linear regression between the magnitude of the phase-locked average and the magnitude of the raw signal. A coefficient of 1 means that the raw signal is equal to the phase-locked average, i.e., purely periodic fluctuations without random unsteadiness. High correlation coefficients ($\sim$0.7) and high levels of rms ($\sim$300) are encountered in the rear suction side, where the vane is directly exposed to strongly periodic phenomena caused by the reflected shocks. Low correlation coefficients ($\sim$0.2) are registered for gauges on the rest of the blade, indicating high level of randomness in the data.

Rotor Heat Transfer

Rotor Time-Averaged Nusselt Number. The ingested vane wakes and the stator left-running shock sweeping the rotor crown affect the boundary layer state at high frequency. Moreover, shock

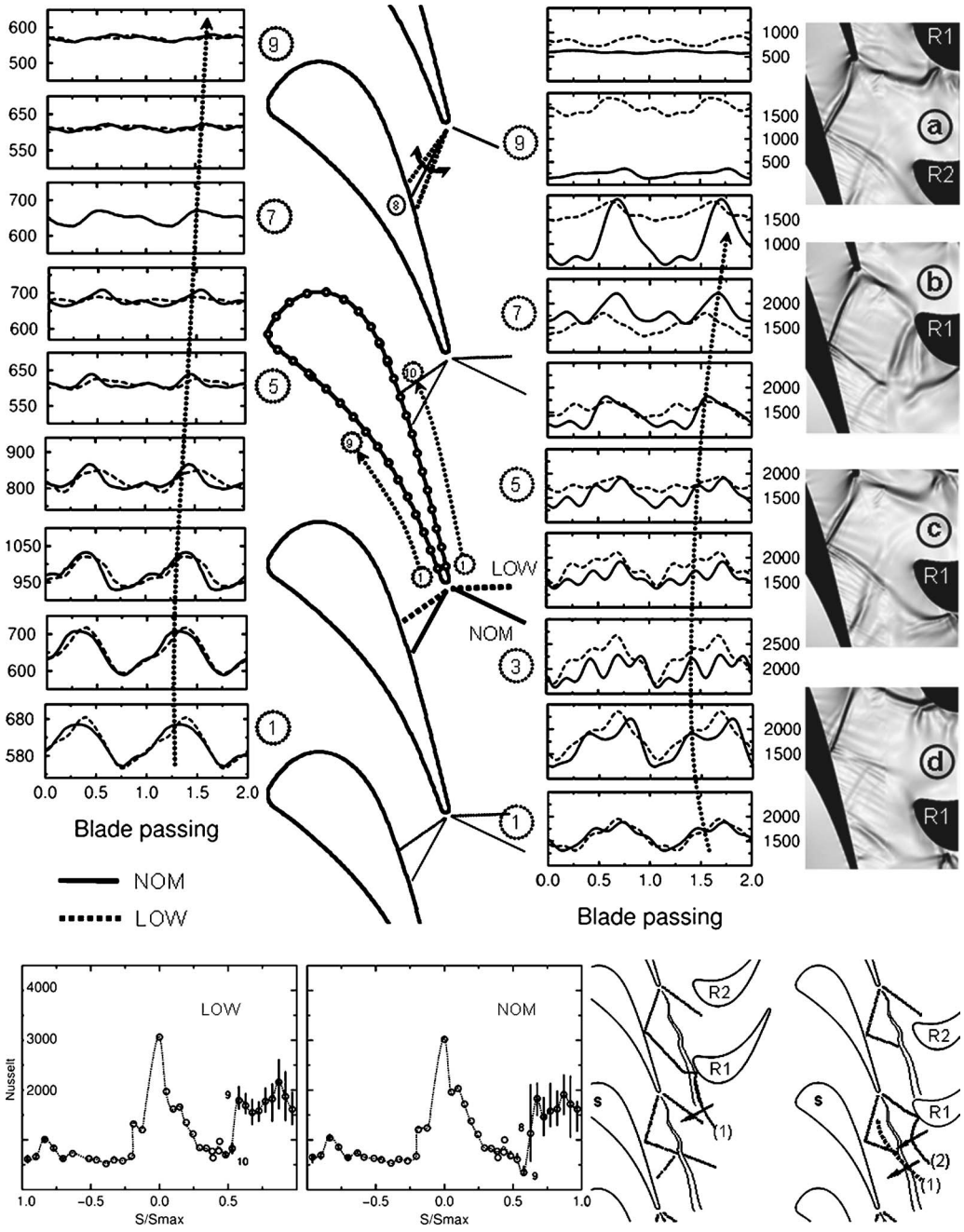

Fig. 6 Vane unsteady heat transfer and shock patterns present in the vane-rotor gap

wave reflections propagate along the blade channel. In such an environment, the turbulence level is difficult to evaluate. Besides, significant 3D phenomena take place on the twisted rotor blade. Consequently, the Nusselt number cannot be easily predicted as for linear cascades by means of simple correlations.

The effect of pressure ratio has been investigated at midheight of the blade. Figure 7 presents the time-averaged Nusselt number together with the velocity distribution around the blade for the three pressure ratios tested. The change in pressure ratio has a direct effect on the velocity distribution around the blades and consequently on the heat transfer rates. In the front region of the blade, the boundary layer is very thin and the heat transfer depends on the local Reynolds number and the free stream turbulence. In the stagnation region, the Nusselt number ranges from 3000 to 3300, and the Frössling number from 1.3 to.1.48. Periodic wake and shock ingestion may enhance considerably the heat transfer rate at the stagnation point with respect to a steady flow case with isotropic turbulence. No change in the stagnation point with the pressure ratio can be identified from the heat transfer data. The fact that the gauges might not be located exactly in the stagnation point, the poor spatial resolution on pressure side, and the high rate of decrease of heat flux in that region make it difficult to draw conclusions.

The differences in the measurements are confined principally to the suction side. On the pressure side, the Mach number distribution does not change significantly with the pressure ratio. As a result, no significant differences appear in the corresponding heat transfer distribution. At nominal/high-pressure ratios, the positive incidence (~14 deg) of the flow produces a stronger acceleration on the front suction side compared to low condition (~8 deg), see the velocity triangles in Fig. 7. This acceleration rate is associated

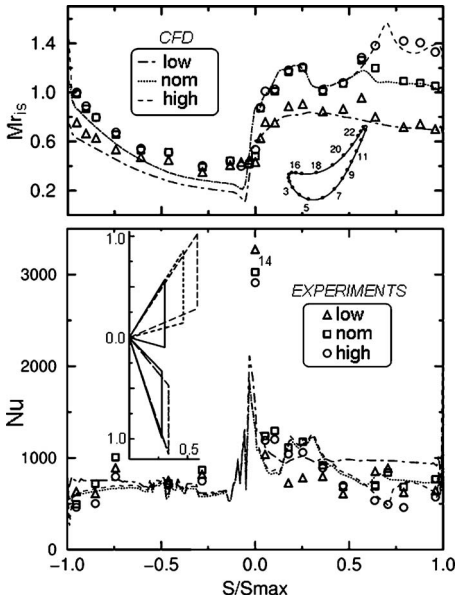

Fig. 7 Nusselt number and $M_{2r,is}$ at midspan for three pressure ratios

with a higher heat transfer level for nominal/high-pressure ratios in that part of the blade, being also present in the quasi-3D prediction. A thinner boundary layer with locally higher Reynolds number for nominal/high-pressure pressure ratios allows higher heat transfer rates on the front suction side.

At $S/S_{\max} \sim 0.25$, a deceleration can be seen in the Mach number distribution, which is not followed by an increase of the heat transfer rate. At $S/S_{\max} \sim 0.6$, a new deceleration is present at nominal and low pressure ratios whereas the flow continues accelerating at high-pressure ratio. The heat transfer data seem to follow this time the expected trend, showing a decrease at high-pressure ratio and higher values for the other two conditions.

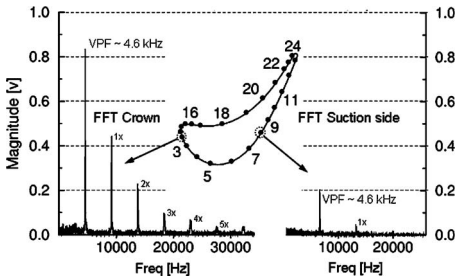

Fig. 8 FFT analysis of gauges mounted in the rotor blade

Rotor Time-Resolved Nusselt Number. The rotor flow field is dominated by the strong interaction between blade rows. Of particular interest is the actual effect of shock waves on the convective heat transfer rates. The rotor crown is submitted periodically to the trailing edge shocks that cause major fluctuations of pressure, temperature, and heat transfer on the rotor blades. Figure 8 shows the FFT analysis made on two different gauges located at the front suction side and rear suction side. At the front, the strong periodicity of the signal allows a clear identification of the vane passing frequency (43 vanes/rev $\times$ 108.3 rev/s $\approx$ 4.6 kHz) and six harmonics. The FFT of Gauge 9 indicates smaller fluctuations at this location and only two harmonics. This gauge, being hidden from the vane trailing edge shock, does not suffer from the strong fluctuations present in the crown. The instantaneous heat flux in the crown can be as much as twice the time-averaged values due to the strong shock interactions between blade rows.

Figure 9 reports the unsteady Nusselt number distribution around the blade at midspan for three different pressure ratios. In this plot, the time-averaged value of each signal is removed, which allows to track the propagation of fluctuations in time and space. The results are presented under the form of two periods, i.e., two vane passing events. Note that both Figs. 9 and 10 use sliding scales for the Nusselt number. The highest amplitude (A) of the oscillations is observed in the crown of the blade. This perturbation travels from the crown (Gauge 5) to the leading edge (Gauge 14) and is caused by the vane left-running trailing edge shock sweeping the blade as the rotor traverses in front of the stator. This statement is valid for all the test conditions and heights that have been investigated. The amplitude and the phase delay of the fluctuations depend on the pressure ratio. Again, nominal and high-pressure ratios are very similar since the heat flux fluctuations are mostly dictated by the vane trailing edge shocks. The perturbation (B) is originated by the right-running trailing edge shock being reflected on the neighboring stator blade and subsequently impinging on the rotor.

One can observe that the smaller peak (B) in Gauge 14 is in phase with the oscillation in Gauge 5 due to A, which is in fair agreement with the CFD results shown in Fig. 11. A significant difference exists between nominal/high- and low-pressure ratios. The big fluctuation sweeping the crown of the blade is no longer present at low-pressure ratio, due to a less intense TE shock coming from the vane. The reduction of the amplitude of the oscillations affects the whole profile.

Figure 10 shows the unsteady Nusselt distribution at three different blade heights for nominal pressure ratio. The amplitude of

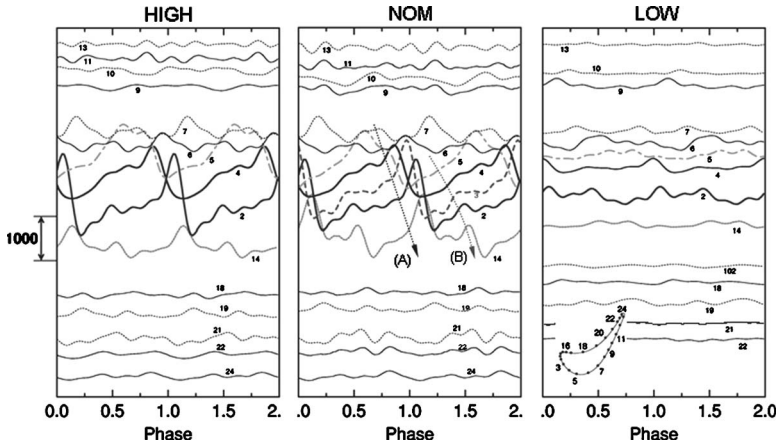

Fig. 9 Effect of the pressure ratio on the unsteady heat transfer

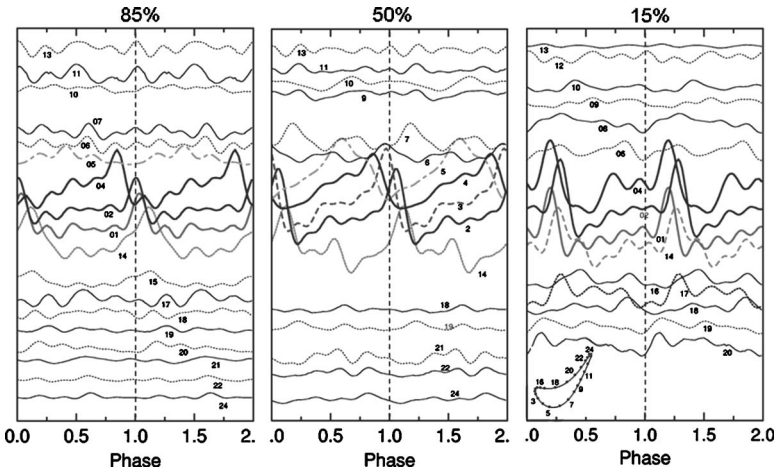

Fig. 10 Effect of the blade height at *nominal* pressure ratio

the oscillations increases from the tip to the hub. At the hub front suction side, the amplitude of the oscillations encountered is up to two times higher than those at the tip. The flow at the hub pressure side appears to be more distorted than at mid- and tip sections. The Mach number at the hub is higher than that at the tip due to radial equilibrium; consequently, stronger shocks take place at the hub region. These shocks produce higher oscillations in the heat flux. Depending on the blade height, the TE left-running shock hits the rotor blade at different times as it traverses one stator pitch: first the tip, then the midsection, and finally the hub. This delay is clearly identified on the measurements (Fig. 10) and is due to two different effects.

Due to the radial equilibrium, the shocks are stronger and more oblique at the hub than at the tip. The increase of this angle delays the impact of the shock on the rotor blade close to the hub region.

The rotor blade cross section changes from the hub to the tip, as depicted in Fig. 12. The tip section, in dark in the figure, traverses the vane pitch before the hub section, increasing even more the phase delay produced by the different inclination of the shocks.

At 15% span, the phase delay existing in between the signals in the crown is smaller than at 85%. The gauges are closer in space at 15%; also, the shape of the profile is different as well as the shock characteristics. Therefore, the way in which the shock sweeps both cross sections is different. Comparing the distributions at 85% and 50%, one can see that Gauge 5 is apparently hidden from the shock at 85% or the shock strength is lower in that position.

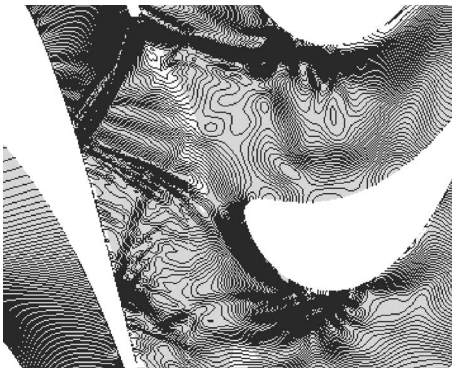

Fig. 11 Shock schematic, fluctuations in Gauges 14 and 5 in phase

Conclusions

Detailed aerodynamic and convective heat transfer measurements have been obtained on a highly loaded turbine stage at different pressure ratios. The measurements have been performed at three different heights in the rotor blade and at midspan in the NGV. Quasi-3D CFD computations have been performed to shed light on the shock interactions across the stage.

The time-averaged Nusselt number on the NGV is closely related to the measured Mach number distribution. The impingement location of the right-running shock in the neighboring stator vane is well captured both in the experiments and the CFD. A small separation bubble occurs due to the shock impingement, leading to a turbulent boundary layer and enhanced heat transfer levels. The variation of the stage pressure ratio implies a change in the relative inlet conditions. As a consequence, the rotor blade suction side time-averaged heat transfer increases with higher pressure ratios.

In general, the higher the pressure ratio, the higher the unsteady heat-load across the stage. However, an increase of the stage loading from nominal to high does not influence the unsteady heat transfer. This implies that further increases in the stage loading coefficient will marginally affect the stage unsteady vane-rotor interaction. The NGV unsteady heat load is confined to the rear suction side, which is directly exposed to the highly unsteady interstage flow field. Two reflected shocks have been identified sweeping the NGV rear suction side, where the instantaneous heat transfer rates can double the time-averaged level. The unsteady heat transfer on the front of the rotor blade is mostly dictated by the impingement of the shock coming from the NGV. The strength

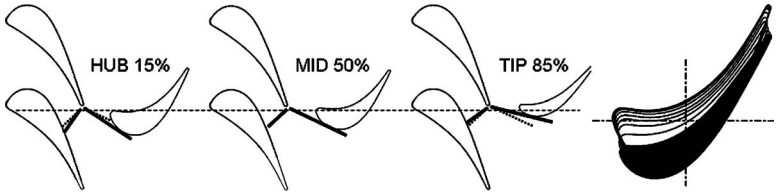

Fig. 12 Shock pattern comparison at three different blade heights

and inclination of the shocks depend not only on the pressure ratio but on the blade height. The fluctuations caused by the shock at 15% blade height are twice larger than those at 85%. The gathered data should be useful for the validation of unsteady 3D computations.

Acknowledgment

The authors would like to acknowledge Tolga Yasa for his assistance in the testing, Gabriele Valentini for the CFD support, and Giacomo Persico and Rémy Dénos for their preliminary work on this project. They would also like to acknowledge the financial support of the European Commission and Industrial Partners involved in TATEF2 "Turbine Aero-Thermal External Flows 2."

Nomenclature

C = chord (m)
h = height (m)
k_g = thermal conductivity (W/(m K))
M = Mach number
Nu = Nusselt number $\mathrm{Nu}=qC/k_g(T_g-T_w)$
P = pressure (bar)
q = heat flux ($\mathrm{W/m^2}$)
Re = Reynolds number $\rho VC/\mu$
S = curvilinear abscissa (m)
T = temperature (K)
t = time (s)
x = axial distance (m)

Subscripts

0 = total conditions
1 = stator inlet
2 = stator outlet, rotor inlet
3 = rotor outlet
r = relative conditions
ax = axial
le = leading edge

References

[1] Arts, T., and Lambert de Rouvroit, M., 1992, "Aero-Thermal Performance of a Two-Dimensional Highly Loaded Transonic Turbine Nozzle Guide Vane: A Test Case for Inviscid and Viscous Flow Computations," ASME J. Turbomach., **114**, pp. 147–154.
[2] Arts, T., Duboue, J. M., and Rollin, G., 1998, "Aero-Thermal Performance Measurements and Analysis of a Two-Dimensional High Turning Rotor Blade," ASME J. Turbomach., **120**(3), pp. 494–499.
[3] Popp, O., 1999, "Steady and Unsteady Heat Transfer in a Film Cooled Transonic Turbine Cascade," Doctoral Dissertation, Virginia Polytechnic Institute/Virginia State University, Blacksburg, VA.
[4] Giel, P. W., Van Fossen, G. J., Boyle, R. J., Thurman, D. R., and Civinskas, K. C., 1999, "Blade Heat Transfer Measurements and Predictions in a Transonic Turbine Cascade," ASME Paper No. 99-GT-125.
[5] Sieverding, C. H., and Arts, T., 1992, "The VKI Compression Tube Annular Cascade Facility CT3," ASME Paper No. 92-GT-336.
[6] Doorly, D. J., Oldfield, M. L. G., and Scrivener, C. T. J., 1985, "Wake Passing in a Turbine Rotor Cascade," AGARDograph No. 390.
[7] Doorly, D. J., and Oldfield, M. L. G., 1985, "Simulation of the Effects of Shock Wave Passing on a Turbine Rotor Blade," ASME Paper No. 85-GT-112.
[8] Ashworth, D. A., LaGraff, J. E., Schultz, D. L., and Grindrod, K. J., 1985, "Unsteady Aerodynamic and Heat Transfer Processes in a Transonic Turbine Stage," ASME J. Eng. Gas Turbines Power, **107**, pp. 1022–1030.
[9] Hilditch, M. A., and Ainsworth, R. W., 1990, "Unsteady Heat Transfer Measurements on a Rotating Gas Turbine Blade," ASME Paper No. 90-GT-175.
[10] Guenette, G. R., Epstein, A. H., Giles, M. B., Haimes, R., and Norton, R. J. G., 1989, "Fully Scaled Transonic Turbine Rotor Heat Transfer Measurements," ASME J. Turbomach., **111**, pp. 1–7.
[11] Dunn, G. M., 2001, "Convective Heat Transfer and Aerodynamics in Axial Flow Turbines," ASME J. Turbomach., **123**(4), pp. 637–686.
[12] Haldeman, C. W., Mathison, R. M., Dunn, G. M., Southworth, S., Harral, J. W., and Heitland, G., 2006, "Aerodyanmic and Heat Flux Measurements in a Single Stage Fully Cooled Turbine-Part I: Experimental Approach," ASME Paper No. GT2006–90966.
[13] Dunn, M. G., and Hauss, A., 1982, "Measurement of Heat Flux and Pressure in a Turbine Stage," ASME J. Eng. Power, **104**, pp. 215–223.
[14] Dunn, M. G., Rae, W. J., and Holt, J. L., 1984, "Measurement and Analysis of Heat Flux in a Turbine Stage: Part II-Discussion of Results and Comparison with Predictions," ASME J. Eng. Gas Turbines Power, **106**, pp. 234–240.
[15] Moss, R. W., Ainsworth, R. W., and Garside, T., 1998, "Effects of Rotation on Blade Surface Heat Transfer: An Experimental Investigation," ASME J. Turbomach., **120**, pp 530–540.
[16] Abhari, R. S., Guenette, G. R., Epstein, A. H., and Giles, M. B., 1992, "Comparison of Time-Resolved Turbine Rotor Blade Heat Transfer Measurements and Numerical Calculations," ASME J. Turbomach., **114**, pp. 818–826.
[17] Haldeman, C. W., Mathison, R. M., Dunn, G. M., Southworth, S., Harral, J. W., and Heitland, G., 2006, "Aerodyanmic and Heat Flux Measurements in a Single Stage Fully Cooled Turbine-Part II: Experimental Results," ASME Paper No. GT2006–90968.
[18] Dénos, R., Arts, T., Paniagua, G., Michelassi, V., and Martelli, F., 2001, "Investigation of the Unsteady Rotor Aerodynamics in a Transonic Turbine Stage," ASME J. Turbomach., **123**(1), pp. 81–89.
[19] Didier, F., Denos, R., and Arts, T., 2002, "Unsteady Rotor Heat Transfer in a Transonic Turbine Stage," ASME J. Turbomach., **124**, pp. 1–9.
[20] Haldeman, C. W., Dunn, M. G., MacArthur, C. D., and Murawski, C. G., 1992, "The USAF Advanced Turbine Aerothermal Research Rig (ATARR)," AGARDograph No. 527.
[21] Polanka, M. D., Hoying, D. A., Meininger, M., and MacArthur, C. D., 2002, "Turbine Tip and Shroud Heat Transfer and Loading Part A: Parameter Effects Including Reynolds Number, Pressure Ratio, and Gas to Metal Temperature Ratio," *ASME Paper* No. GT-2002-30186.
[22] Dénos, R., and Paniagua, G., 2005, "Rotor/Stator Interaction in Transonic HP Turbines," *VKI Lecture Series on Effects of Aerodynamic Unsteadiness in Axial Turbomachines*, Sint Genesius Rode, Paper No. VKI IS 2005–03.
[23] Sieverding, C. H., Arts, T., Dénos, R., and Martelli, F., 1996, "Investigation of the Flow Field Downstream of a Turbine Trailing Edge Cooled Nozzle Guide Vane," ASME J. Turbomach., **118**(2), pp. 291–300.
[24] Yasa, T., Paniagua, G., and Dénos, R., 2007, "Application of Hot-Wire Anemometry in a Blow-Down Turbine Facility," ASME J. Eng. Gas Turbines Power **129**(1), pp. 1–8.
[25] Schultz, D. L., and Jones, T. V., 1973, "Heat Transfer Measurements in Short Duration Facilities," AGARDograph No. 165.
[26] Billiard, N., Iliopoulou, V., Ferrara, F., and Denos, R., 2002, "Data Reduction and Thermal Product Calibration for Single and Multi-Layered Substrates Thin Film Gauges," *Proceedings of the 16th Symposium on Measuring Techniques in Transonic and Supersonic Flow in Cascades and Turbomachines*, Cambridge, Paper No. 6-2.
[27] Iliopoulou, V., Denos, R., Billiard, N., and Arts, T., 2004, "Time-Averaged and Time-Resolved Heat Flux Measurements on a Turbine Stator Blade Using Two-Layered Thin Film Gauges," ASME J. Turbomach., **126**(4), pp. 570–577.
[28] Adami, P., and Martelli, F., 2006, "Three-Dimensional Unsteady Investigation of HP Turbine Stages," J. Power and Energy, **220**(2), pp. 155–167.
[29] Martelli, F., Adami, P., and Belardini, E., 2002, "Unsteady Flow Simulation of a Turbine Stage," *Computational Fluid Dynamics*, Springer-Verlag, Berlin.
[30] Lowery, G. W., and Vachon, R. I., 1975, "The Effect of Turbulence on Heat Transfer from Heated Cylinders," Int. J. Heat Mass Transfer, **18**, pp. 1229–1242.
[31] Van Fossen, G. J., and Ching, C. Y., 1997, "Measurements of the Influence of Integral Length Scale on Stagnation Region Heat Transfer," Int. J. Rotating Mach., **3**(2), pp. 117–132.
[32] Solano, J. P., Paniagua, G., and Dénos, R., 2006, "2d Data Reduction Technique for Turbine Blade Heat Transfer Measurements Using Double-Layered Thin Film Gauges," *Proceedings of the 18th Symposium on Measuring Techniques in Transonic and Supersonic Flow in Cascades and Turbomachines*, Thessaloniki, Sept.
[33] Dénos, R., and Paniagua, G., 2005, "Effect of Vane-Rotor Interaction on the Unsteady Flowfield Downstream of a Transonic HP Turbine," J Power and Energy, Part A, **219**(6), pp. 431–442.

A Novel Antivortex Turbine Film-Cooling Hole Concept

James D. Heidmann
NASA Glenn Research Center,
Cleveland, OH 44135

Srinath Ekkad
Louisiana State University,
Baton Rouge, LA 70803

A novel turbine film-cooling hole shape has been conceived and designed at NASA Glenn Research Center. This "antivortex" design is unique in that it requires only easily machinable round holes, unlike shaped film-cooling holes and other advanced concepts. The hole design is intended to counteract the detrimental vorticity associated with standard circular cross-section film-cooling holes. This vorticity typically entrains hot freestream gas and is associated with jet separation from the turbine blade surface. The antivortex film-cooling hole concept has been modeled computationally for a single row of 30 deg angled holes on a flat surface using the 3D Navier–Stokes solver GLENN-HT. A blowing ratio of 1.0 and density ratios of 1.05 and 2.0 are studied. Both film effectiveness and heat transfer coefficient values are computed and compared to standard round hole cases for the same blowing rates. A net heat flux reduction is also determined using both the film effectiveness and heat transfer coefficient values to ascertain the overall effectiveness of the concept. An improvement in film effectiveness of about 0.2 and in net heat flux reduction of about 0.2 is demonstrated for the antivortex concept compared to the standard round hole for both blowing ratios. Detailed flow visualization shows that as expected, the design counteracts the detrimental vorticity of the round hole flow, allowing it to remain attached to the surface. [DOI: 10.1115/1.2777194]

Introduction

Film cooling is commonly used on high pressure turbine vanes and blades to enable increased turbine inlet temperatures for improved engine cycle performance. Relatively cool air is bled from the compressor to supply this film-cooling flow to the turbine. However, this compressor bleed represents a loss to the system and should be minimized. There has thus been a substantial effort to reduce the film-cooling flow rate required to provide the necessary cooling. Many new film-cooling hole shapes and concepts have been proposed in the literature to address this issue.

Goldstein [1] summarized early studies in the area of film cooling, primarily focusing on cooling flows issuing from slots. In a gas turbine engine, slots are typically not practical, so the flow must be introduced through discrete holes. Many published studies have discussed the physics and presented data for discrete hole film cooling in various geometries. Kercher [2,3] presents an exhaustive list of film-cooling references from the literature. The most basic film-cooling geometry consists of a row of round holes in a flat plate. There is a relatively large body of experimental data for 30–35 deg round holes with a pitch of 3*d* (Pedersen et al. [4], Foster and Lampard [5], Pietrzyk et al. [6], Pietrzyk et al. [7], and Sinha et al. [8]). This geometry allows for a study of jet lift-off behavior at various blowing ratios and is perhaps the most realistic simplified geometry for turbine film cooling. In addition, the computational study of Leylek and Zerkle [9] uses this geometry and gives an excellent description of the vortical flows associated with this geometry. The present study will use the data of Dhungel et al. [10] as the base line case, which consists of 30 deg round holes and a pitch of 3*d*.

A well-known and extensively studied property of the flow from a round film-cooling hole is the counter-rotating vortex pair that causes the cooling jet to separate from the surface at sufficiently high blowing ratio. This phenomenon is shown in Fig. 1. The counter-rotating vortex pair entrains the hot freestream gas and lifts the coolant away from the surface, drastically reducing its effectiveness. The counter-rotating vortex pair is described by Haven et al. [11]. Lemmon et al. [12] showed that this vorticity is caused by the bending of the jet by the freestream and not by viscous wall effects in the hole or plenum. For cases with varying density ratio, the momentum ratio is considered to be an even better predictor of jet lift-off than blowing ratio since higher density ratio jets will tend to remain attached to the surface at higher blowing ratios. The jet lift-off phenomenon typically occurs at momentum ratios above about 0.5. For very low momentum ratios such as 0.25, the circular cross-section hole produces lower vorticity levels and stays attached to the surface, providing excellent cooling. However, this momentum ratio is typically unachievable in an engine, as the available coolant pressure unavoidably produces higher coolant flow rates.

Shaped film-cooling holes have typically been used to combat the jet lift-off behavior. Bunker [13] provides an excellent overview of the shaped film-cooling hole literature. The primary effect of the hole shaping is to expand the exit area of the hole, thereby reducing jet velocity. However, shaped film-cooling holes can be expensive to manufacture and can be limited by flow and thermal barrier coating (TBC) limitations in their expansion angles and other parameters. Many other unique film-cooling designs have been proposed over the years to improve film-cooling effectiveness. Besides the typical shaped hole with spanwise and/or streamwise expanded exits, various exotic hole shapes have been proposed. Ideas such as struts within the holes (Shih et al. [14]), cusp-shaped holes (Papell [15]), triangular tabs at the hole exit (Zaman and Foss [16]), and trenched holes (Bunker [17]) have been proposed and studied. A common theme in these designs is the desire to offset the detrimental vorticity caused by the round hole jet. Many of the proposed designs are shown to be effective in this regard, but the majority of these ideas prove to be difficult to manufacture and/or produce unwanted features such as additional solid surfaces that must be cooled or additional sharp edges that are aerodynamic liabilities.

Another area of recent research has been in the area of pulsed film-cooling flows (e.g., Ekkad et al. [18]). The film-cooling flow is pulsed intentionally with the goal of producing an improvement in time-averaged cooling effectiveness. This concept is perhaps most effective for applications where a high blowing ratio would be present for the nonpulsed case. If such a film-cooling flow is

Contributed by the International Gas Turbine Institute of ASME for publication in the JOURNAL OF TURBOMACHINERY. Manuscript received June 7, 2007; final manuscript received June 18, 2007; published online May 6, 2008. Review conducted by David Wisler. Paper presented at the ASME Turbo Expo 2007: Land, Sea and Air (GT2007), Montreal, Quebec, Canada, May 14–17, 2007, Paper No. GT2007-27528.

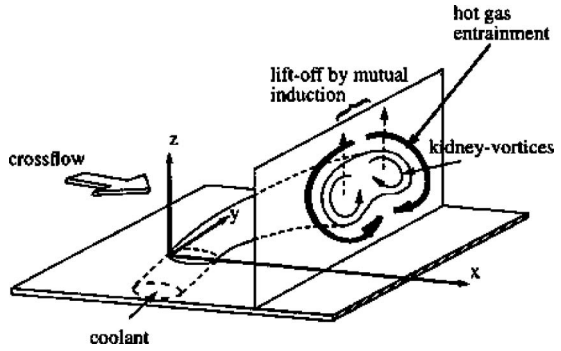

Fig. 1 Counter-rotating vortex pair and jet lift-off (from Haven et al. [11])

pulsed, it will reduce the effective blowing ratio and allow the coolant to remain closer to the surface than the steady, high blowing ratio jet. It is doubtful that pulsing an otherwise optimized film-cooling jet with a low to moderate blowing ratio would be beneficial. In the present study, a novel film-cooling concept is proposed using only round holes to provide high effectiveness attached film-cooling flows via a vortex cancellation effect.

Antivortex Film-Cooling Concept

The present study proposes a new film-cooling design concept, which has been conceived and developed at NASA Glenn Research Center. This "antivortex" film-cooling concept is designed to mitigate the effects of the counter-rotating vortex pair, which reduces the effectiveness of circular cross-section film-cooling holes at moderate to high blowing ratios. A preliminary design concept is shown in Figs. 2–4, and an improved design developed in the present study is shown in Figs. 5–7, although many parameters can be modified in an optimized design. The concept is applied in this study as a modification to a standard single row round film-cooling hole arrangement with the holes angled at 30 deg to the surface and a spanwise pitch of three hole diameters and is compared to the base line data of Dhungel et al. [10]. The holes are placed in a flat plate geometry, as shown in Fig. 8, which can be thought of as representing a turbine blade suction or pressure side film-cooling hole. In the antivortex design, two side holes are drilled which intersect with the main hole. These side holes are angled in the spanwise direction on either side of each main hole. Since each main hole has a side hole on both sides, the flow from the side holes of two adjacent main holes will interact with each other, producing a strong vortex. This vortex is opposite in sense

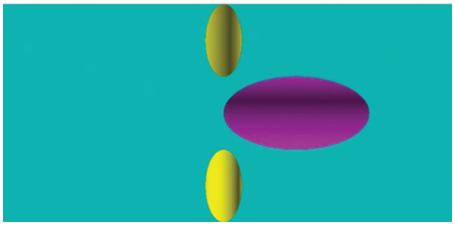

Fig. 2 Initial antivortex design (top view)

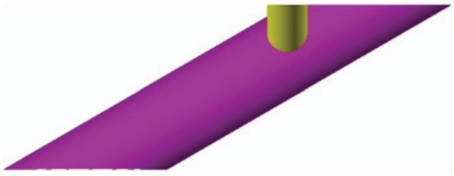

Fig. 3 Initial antivortex design (side view)

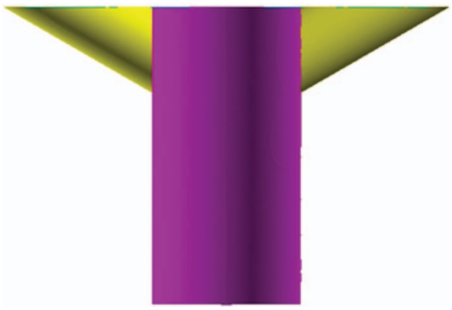

Fig. 4 Initial antivortex design (front view)

to the detrimental vorticity produced by the main hole and is intended to force the coolant flow from the main hole to remain attached to the surface. Another way to view this expected benefit is that the side holes produce a strong upwash, which must be balanced by a net downwash in the main hole jet centerline plane. There is an additional expected benefit from the side hole jet inclining away from the main jet in the spanwise direction, as this should draw the coolant from the bottom of the main jet away from the jet centerline, effectively flattening the coolant jet.

There are several expected advantages to the proposed antivortex film cooling concept. Shaped holes, while they have similar effects such as reduced adverse vorticity and enhanced jet spreading, are expensive to manufacture relative to round holes, which can be drilled quickly and inexpensively. Also, shaped holes do not actually cancel the adverse vorticity but merely reduce it because of their larger exit area and reduced jet exit velocity. Shaped holes can also perform more poorly than expected if the exit velocity profile is sharply peaked and not relatively uniform as expected in the design. It is anticipated that by optimizing the antivortex design, a beneficial vorticity can be produced which would not only oppose the detrimental vorticity but effectively cancel it, producing a strong flattening of the jet. Another comparison might be made to a two row staggered round film-cooling hole arrangement. In this staggered arrangement, the upstream row is designed to fill in the gaps in film cooling produced by the downstream row of holes. However, for sufficiently high blowing ratios, both rows will still lift off the surface, providing very low effectiveness. Although the upstream staggered row does produce a vortex which is opposite in sense to the adjacent hole in the downstream row, this vorticity is similar in magnitude to the downstream vortex and cannot effectively cancel it. Also, the hole inlet area is doubled by adding the upstream row which will double the coolant flow rate for a given plenum pressure. The antivortex design, since it incorporates side holes drilled into the main hole, does not increase the hole inlet area and therefore is expected to result in only a small increase in coolant flow rate for a given plenum pressure.

Two antivortex film-cooling hole designs were developed at NASA Glenn Research Center and analyzed in this study. The first concept specifies spanwise-angled side holes intersecting with the main hole very near the surface (Figs. 2–4). This was done to maximize the spanwise angle of the side hole, in hope that this would maximize the beneficial vorticity. However, it was found

Fig. 5 Modified antivortex design (top view)

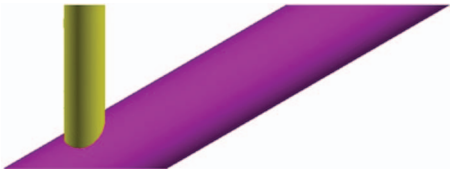

Fig. 6 Modified antivortex design (side view)

that the flow rate through these side holes was very low, and freestream gas actually entered the side holes at some locations. Therefore, very little beneficial vorticity was produced. This was due to the fact that the side hole intersected the main hole at a location of relatively low pressure, resulting in a very small pressure differential between the side hole entrance and exit. Because of this effect, it was decided to investigate a second design (shown in Figs. 5–7). This new design still has the side holes angled in the spanwise direction. However, they now intersect the main hole very close to the plenum wall. In fact, the side hole and main hole centerlines intersect at the plenum wall, but because the side holes are half the diameter of the main hole, the hole inlet area is unchanged. The side holes now have approximately the same pressure differential across them as the main hole, so a substantial amount of flow is expected through them. This was indeed borne out by the analysis. A necessary consequence of this design change is that the side holes now exit the plate upstream of the main holes. At first, this was thought to be a drawback. However, the analyses showed that this provided an opportunity for the beneficial vortex pair to develop and impact the main hole flow immediately upon its emergence from the hole. Another consequence of the design modification is that the spanwise angle of the side holes is not as large as in the initial design. However, this again may be favorable, as it increases the upwash velocity component for a given flow rate and may produce a stronger downwash at the main jet centerline.

One concern for this design is the limit on how small the side holes may be from either manufacturing or functional viewpoints. Bunker [13] has indicated that film-cooling holes may be laser drilled to a very small size, albeit with increasing relative geometrical errors. A greater concern may be the issue of plugging of the side holes from dust and particles in the cooling air. The present study considers side holes half the diameter of the

Fig. 7 Modified antivortex design (front view)

Fig. 8 Computational grid for baseline round hole case

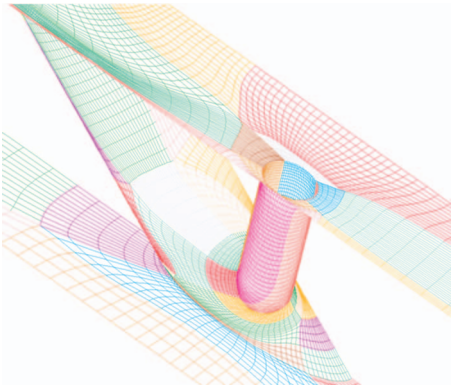

Fig. 9 Hole intersection grid close-up

standard-size main hole. However, if needed, the entire arrangement may be enlarged by a factor of 2 to keep the smallest hole size the same. In this case, the hole pitch-to-diameter ratio would need to be doubled (raw pitch increased by a factor of 4) to maintain the coolant hole inlet flow area and approximate coolant flow rate for a given plenum pressure.

Several variations on the NASA Glenn Research Center antivortex film-cooling hole concept have been studied experimentally by Dhungel et al. [10] at Louisiana State University (LSU) in conjunction with the present design/computational study. The experimental results corroborate the computational predictions that indicate a strong benefit to the antivortex cooling concept, especially at high blowing/momentum ratios. The LSU group has suggested some design modifications to the basic antivortex design, which show even better effectiveness. The fundamental difference in the LSU modifications is the angling of the secondary holes in the modified antivortex design toward the streamwise direction to place their exits closer to the main hole exit. Future work will focus on better understanding and optimizing the antivortex design parameters within the constraints of the actual turbine environment.

Computational Method

Multiblock structured computational grids were produced using GRIDPRO™ software for four geometries: the base line case with a single row of round holes at an angle of 30 deg to the flat plate surface and a pitch-to-hole diameter ratio of 3.0, the initial antivortex design with the side holes intersecting the main hole close to the plate surface (Figs. 2–4), a modified antivortex design (Figs. 5–7) with the side holes intersecting the main hole close to the plenum wall, and a flat plate grid with no holes to facilitate heat transfer coefficient comparisons. The computational domain and grid are shown in Figs. 8 and 9. Figure 9 highlights the grid quality near the hole intersection region for the antivortex geometry. All grids extended from the centerline plane of the main hole to the plane midway between two adjacent main holes. Symmetry boundary conditions were applied on both of these planes. This was done since the present study was performed with a steady computational fluid dyanmics (CFD) analysis in which no flow can cross these planes because of symmetry. However, future studies using unsteady Reynolds-averaged Navier–Stokes (RANS) or large eddy simulation (LES) tools will necessitate doubling the computational domain to include an entire hole pitch and using periodic boundary conditions to allow unsteady perturbations to cross these planes.

Inflow boundary conditions were prescribed at the freestream and plenum inlet planes. Standard total pressure and total temperature values were used at the freestream inlet with flow normal to the inlet plane. The freestream inlet is 19 hole diameters upstream of the main hole leading edge. The plenum inlet total pressure was adjusted to produce the desired blowing ratio. This typi-

cally produced a plenum pressure a few percent above the freestream value. It was observed that a slightly lower value of plenum pressure was required for the antivortex designs to produce the same blowing ratio as the base line case. A blowing ratio of 1.0 was considered in this study since it is high enough to capture the jet lift-off phenomenon and is representative of engine conditions. As is typically done, the blowing ratio is defined using the inlet area of the hole, so the various side hole geometries do not change the blowing ratio for a given mass flow rate. In other words, a given blowing ratio represents the same mass flow rate for all cases. Even higher blowing ratios ($M=2.0$ or above) are sometimes found in engine designs and the jet lift-off and expected benefit of the proposed hole design would be even stronger. The plenum inlet total temperature was set to either 0.95 or 0.5 times the freestream inlet total temperature. The 0.95 value was used to provide a temperature difference between the coolant and freestream for film effectiveness calculation while staying relatively close to a density ratio of 1.0 for comparison to existing data. The 0.5 value is considered representative of engine conditions. A turbulence intensity of 1.0% and a turbulence length scale of one hole diameter were specified at both inlets. The exit static pressure was set to 0.97 times the freestream inlet total pressure at the exit plane 30 hole diameters downstream of the main hole leading edge. This produced a Mach number of less than 0.3 in most of the flow domain. Although the large scale experiment of Dhungel et al. [10] has a lower Mach number and pressure ratio, the present conditions allow for more rapid numerical convergence while avoiding strong compressibility effects that would result from high subsonic conditions. The Reynolds number of the experiment is matched at 11,300 based on hole diameter and inlet conditions.

Two calculations were performed at each flow condition: an adiabatic wall case and a case with a small constant heat flux at the wall. This was done to allow independent determination of film effectiveness and heat transfer coefficient. More iterations are required to reach convergence for a constant wall heat flux boundary condition case than for a constant temperature wall boundary condition case. However, the constant heat flux condition better matches the companion experimental effort. For a turbulent flat plate flow, the heat transfer coefficient differs between the isothermal and constant heat flux conditions by a few percent. For the nonzero heat flux case, the heat flux was applied only on the wall outer surface—not on the plenum wall or hole pipe surfaces. This allowed the hole exit temperature profile to remain relatively unchanged and is analogous to an experiment where the heat flux is produced by a heater on the plate surface. In order to compute a net heat flux reduction (NHFR) for each case, the heat transfer coefficient must be compared to a base line case with no film cooling. For this reason, a flat plate case was run to determine the non-film-cooled heat transfer coefficient. No slip boundary conditions were employed at all walls.

A multiblock computational grid was developed using the GRIDPRO multiblock grid generator with approximately 2.5×10^6 computational cells for each case (the flat plate grid only required about 1.5×10^6 cells). An effort was made to maintain the grid point distribution and density between cases to facilitate comparison. Results were generated for the fine grid as well as for a coarse grid solution having half the number of computational cells in each direction or 1/8th overall (about 300,000 cells). This coarse grid solution was produced using the multigrid capability of the GLENN-HT code. Viscous clustering was employed at all solid walls with a y^+ value less than 1.0 at all locations. Stretching ratios less than 1.2 were used normal to the viscous walls. Each solution on the fine grid required approximately 2000 CPU hours to converge on the in-house NASA Glenn Turbine Linux cluster, "heat." This cluster consists of 48 nodes, each with two Intel Xeon processors. Cases were typically run with 30 processors. Convergence was considered achieved when both of the following criteria had been met: (1) reduction in all residuals of three orders of magnitude and (2) no observable change in surface temperature prediction for an additional 1000 iterations. The test cases are shown in Table 1.

Table 1 Calculation cases

Case	Density ratio	Blowing ratio	Momentum ratio	Geometry
1	1.05	1.0	0.95	Base line
2	1.05	1.0	0.95	Initial antivortex
3	1.05	1.0	0.95	Modified antivortex
4	2.0	1.0	0.5	Base line
5	2.0	1.0	0.5	Initial antivortex
6	2.0	1.0	0.5	Modified antivortex

The simulations in this study were performed using a multiblock computer code called GLENN-HT, previously known as TRAF3D.MB (Steinthorsson et al. [19]), which is based on a single block code designed by Arnone et al. [20]. This code is a general-purpose flow solver designed for simulations of flows in complicated geometries. The code solves the full compressible RANS equations using a multistage Runge–Kutta-based multigrid method. It uses the finite volume method to discretize the equations. The code uses central differencing together with artificial dissipation to discretize the convective terms. The overall accuracy of the code is second order. The present version of the code (Rigby et al. [21] and Ameri et al. [22]) employs the k-ω turbulence model developed by Wilcox [23,24], with subsequent modifications by Menter [25] as implemented by Chima [26]. The k-ω turbulence model is desirable because it does not require specification of distance to the wall. Such a specification is difficult for complex geometries requiring multiblock grids, such as considered in the present study. Accurate heat transfer predictions are possible with the code because the model integrates to the walls and no wall functions are used. Rather, the computational grid is generated to be sufficiently fine near walls to produce a y^+ value of less than 1.0 at the first grid point away from the wall. For heat transfer, a constant value of 0.9 for turbulent Prandtl number Pr_t is used. A constant value of $\mathrm{Pr}=0.72$ is used. Laminar viscosity is a function of temperature through a 0.7 power law (Schlichting, [27]) and c_p is taken to be a constant.

Results

Film effectiveness for a low Mach number flow may be defined as

$$\eta = (T_{\mathrm{in}} - T_{\mathrm{aw}})/(T_{\mathrm{in}} - T_c) \tag{1}$$

The heat transfer coefficient is defined as

$$h = q''/(T_w - t_{\mathrm{aw}}) \tag{2}$$

As described by Sen et al. [28], a NHFR parameter may be defined, which accounts for the contributions of both film effectiveness and heat transfer coefficient to the reduction in heat flux from the base line case of no film-cooling holes. NHFR is defined as

$$\mathrm{NHFR} = 1 - (h/h_o)(1 - \eta\theta) \tag{3}$$

where θ is a dimensionless temperature defined as

$$\theta = (T_{\mathrm{in}} - T_c)/(T_{\mathrm{in}} - T_w) \tag{4}$$

and h_o is the heat transfer coefficient in the absence of cooling holes. To solve for the NHFR, a value must be specified for θ. Typically, a value of 1.6 is used to represent engine-relevant conditions for a cooled turbine. For a coolant temperature half that of the freestream value, this represents a metal temperature of 0.6875 times the freestream value.

As a check on the grid sensitivity of the study, all calculations were carried out for both the fine grid ($\sim2.5\times10^6$ cells) and one level of multigrid coarsening ($\sim$300,000 cells). There are notice-

Table 2 Plenum pressures for $M=1.0$

Case	Density ratio	Plenum pressure ratio	Geometry
1	1.05	1.0392	Base line
2	1.05	1.0326	Initial antivortex
3	1.05	1.0106	Modified antivortex
4	2.0	1.0091	Base line
5	2.0	1.0060	Initial antivortex
6	2.0	0.9954	Modified antivortex

able but relatively small (typically less than 10%) differences between the respective coarse and fine grid results for the most stringent quantities of surface film effectiveness and heat transfer coefficient. This indicates that the fine grid is approaching grid independence. Due to the long calculation times for the fine grid cases and the extensive test matrix, the grid was not refined further in this study. All results in the following discussion are for the fine grid cases.

Table 2 gives the plenum pressure ratio required to yield $M=1.0$ for all cases. It can be seen that there is a moderate variation but not as large as would result from, for example, adding a second staggered row of holes while attempting to maintain the same coolant flow rate. This relative insensitivity in plenum pressure ratio is due to the hole throat or metering area remaining constant for all cases. The initial antivortex cases require only a slightly lower plenum pressure, while the modified design draws more flow from the plenum and requires a still lower pressure. This reflects the higher discharge coefficient for the antivortex design. However, since the antivortex design is anticipated to perform even better at higher blowing ratios (as is reflected in the data of Dhungel et al., [10]), this should not pose a problem in the application of the concept.

Figures 10–13 show the total temperature for various cases on a plane normal to the surface at $x/d=7$ (seven hole diameters from the hole leading edge or five hole diameters from the hole trailing edge). This streamwise location is representative of the region where film cooling jet lift-off is expected to occur for the base line case at moderate to high momentum ratio. Figures 10 and 11 are for the base line and modified antivortex cases, respectively, at DR=1.05. Figures 12 and 13 are for the base line and modified antivortex cases, respectively, at DR=2.0. The calculation domain extends from the hole centerline to the midpitch plane—the results are mirrored about the hole centerline for display purposes. It is apparent that the modified antivortex design produces the intended effect, as the coolant jet remains attached to the surface. The higher density ratio base line jet, as expected, remains closer to the surface by virtue of its lower momentum ratio, but for both density ratios, the antivortex cooling air remains much closer to the surface. This will be reflected in the surface film effectiveness values to follow. Another feature of the antivortex design is the entrainment of the coolant from the upstream secondary jets by the main coolant jet. Intuition might suggest that the upstream secondary coolant is "wasted" since it is immediately forced away from the surface by the jet interaction. However, it is seen that the

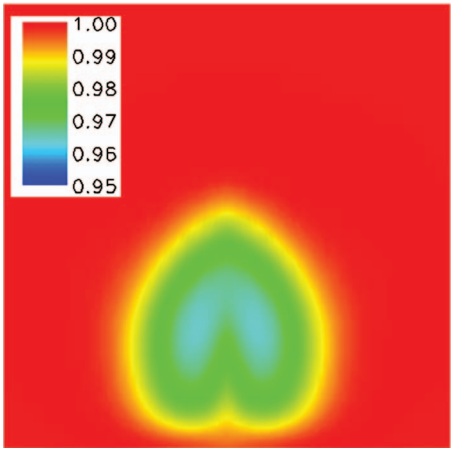

Fig. 10 Stagnation temperature (T/T_{in}), $x/d=7$ (Case 1)

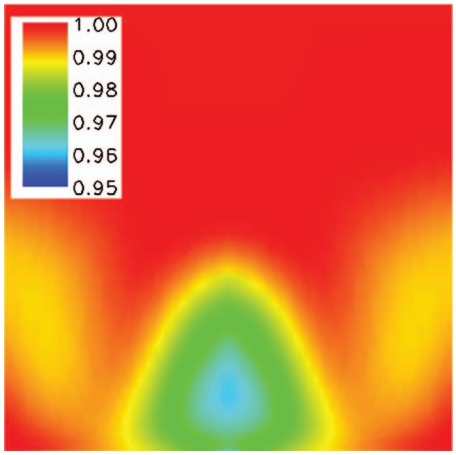

Fig. 11 Stagnation temperature (T/T_{in}), $xd=7$ (Case 3)

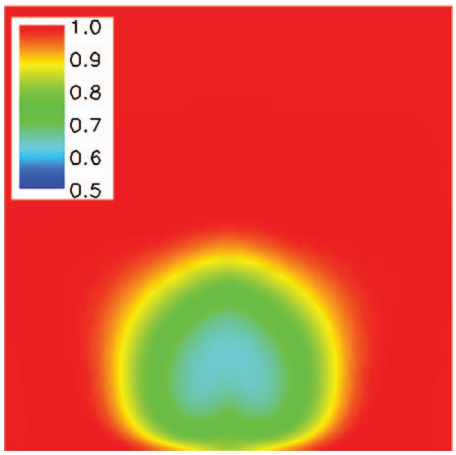

Fig. 12 Stagnation temperature (T/T_{in}), $x/d=7$ (Case 4)

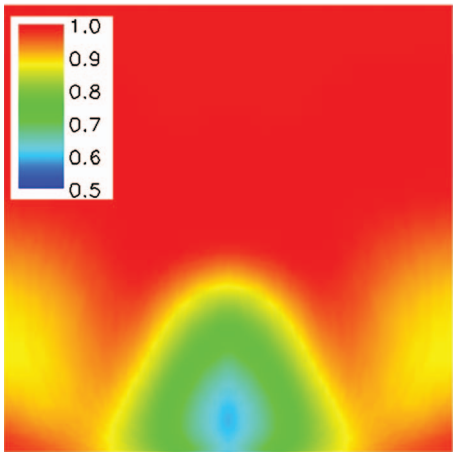

Fig. 13 Stagnation temperature (T/T_{in}), $x/d=7$ (Case 6)

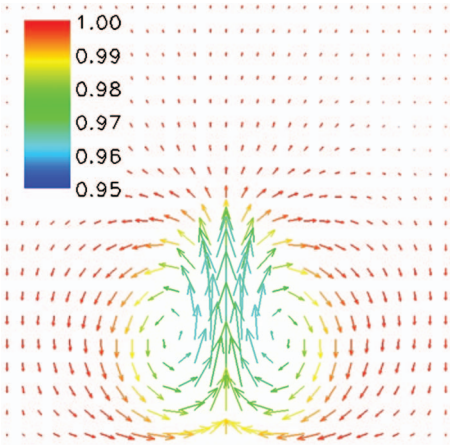

Fig. 14 Secondary flow vectors colored by temperature (T/T_{in}), $x/d=7$ (Case 1)

countervorticity of the secondary jets not only forces the main coolant jet downward toward the surface but also allows the coolant from the upstream holes to be entrained by the main jet. This contributes to the lower temperatures near the wall compared to the base line case, where the jet vorticity entrains hot freestream gas instead.

Figures 14 and 15 show secondary flow vectors at $x/d=7$ for the base line and modified antivortex cases, respectively, at DR $=1.05$. The vectors are colored by total temperature. It can be seen that the presence of the antivortex jets reduces the size and strength of the detrimental counter-rotating vortex pair of the main jet. In addition, as previously indicated, the fluid that is entrained by the main jet is much cooler for the antivortex case, owing to the presence of the upstream coolant injection.

It is illustrative to consider the streamwise evolution of the vorticity field for the various cases. Figure 16 presents the area-averaged streamwise (x-component) vorticity for the three geometries at DR$=1.05$. The vorticity is only averaged over the computational domain, not the entire mirrored region, since we only want to consider half of the vortex pair. (An average over the entire mirrored region would of course produce zero vorticity due to symmetry.) For all cases, the vorticity is zero as expected until the hole region is reached. For the base line case, a strong streamwise vorticity is produced at the hole, which convects downstream and dissipates somewhat. At $x/d=30$, the vorticity has diminished to less than half of its hole exit value. The initial antivortex design

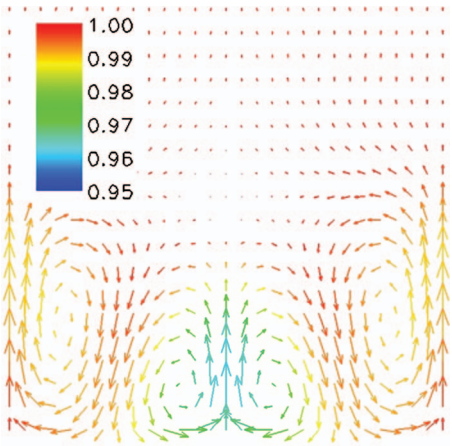

Fig. 15 Secondary flow vectors colored by temperature (T/T_{in}), $x/d=7$ (Case 3)

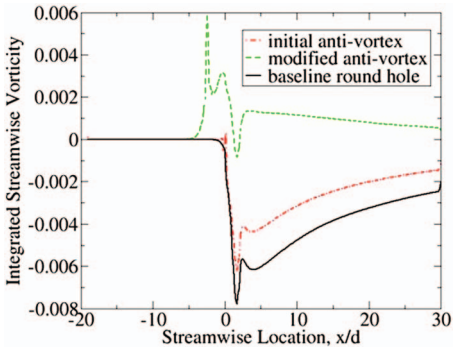

Fig. 16 Area-averaged streamwise vorticity

diminishes the main hole vorticity, but this effect is small due to the low flow rate through the side holes. The reduction in vorticity is about 25% and persists to $x/d=30$. The modified antivortex design, on the other hand, produces a large upstream vorticity at the secondary hole exit, which is opposite in sense to the main hole. This "preconditions" the flow for the emergence of the main jet. Interestingly, although the vorticity produced by the antivortex holes is of lower magnitude than that produced by the main hole in the base line case, the downstream vorticity for the modified antivortex case is in the same sense as the antivortex. This is because of the lower flow rate and associated vorticity in the main hole jet since some of the flow has been bled away to the secondary holes. (Recall that the total flow rate is held constant.) In fact, the positive downstream vorticity indicates that the modified antivortex design may be slightly too aggressive, as intuition argues that a zero downstream vorticity might be optimum.

Table 3 shows the relative flow splits between the main hole and secondary holes for each case. By definition, all the flow goes through the main hole for Cases 1 and 4. It is surprising how little net flow goes through the side holes in the initial design, yet as will be seen there is still a positive effect on film effectiveness. For the modified antivortex design, about two-thirds of the flow goes through the main hole. This correlates directly to the area ratio of the holes and makes sense since the holes branch from a location close to the plenum and have about the same pressure ratio across them.

Figure 17 shows the predicted film effectiveness on the surface for the various cases, again with the results mirrored about the hole centerline for display purposes. Both Figs. 17 and 18 have been compressed by a factor of 2 in the streamwise (x) direction for presentation purposes. The modified antivortex cases (3 and 6) not only exhibit a much higher film effectiveness but also show the effects of the jet "flattening" previously noted in Figs. 11 and 13. The jet footprint is broader than for the base line and initial designs. Cases 1 and 2 seem to indicate jet lift-off and reattachment, while cases 3–6 exhibit a more monotonic decay in film effectiveness. This is a consequence of the higher momentum ratio for Cases 1–3 (DR$=1.05$), except that for case 3, the antivortex flow keeps the jet attached.

Table 3 Main/secondary hole flow allocation

Case	Density ratio	Percentage of total flow through main hole	Geometry
1	1.05	100%	Base line
2	1.05	98.0%	Initial antivortex
3	1.05	64.2%	Modified antivortex
4	2.0	100%	Base line
5	2.0	96.0%	Initial antivortex
6	2.0	66.8%	Modified antivortex

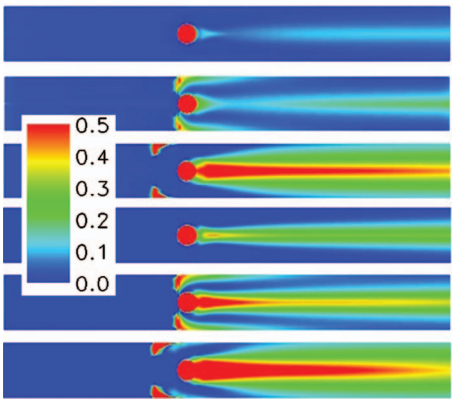

Fig. 17 Film effectiveness η (Cases 1–6)

Figure 18 shows the predicted heat transfer coefficient values on the surface for all cases. The values are normalized by the non-film-cooled flat plate heat transfer. For all cases, there is a characteristic v-shaped region of enhanced heat transfer downstream of the main hole due to jet/freestream interaction on each side of the jet. Somewhat surprisingly, there is not a large enhancement downstream of the secondary holes in the modified design. For Cases 1–3 (DR=1.05), the character of the heat transfer enhancement is similar, although somewhat higher in magnitude for the modified design of Case 3. This trend is more pronounced for Cases 4–6 (DR=2.0), with the antivortex designs producing a larger enhancement in heat transfer compared to the base line case (4).

Figure 19 is a plot of spanwise-averaged film effectiveness values downstream of the main hole for all cases. Note that $x=0$ is at the main hole leading edge. For both density ratios, the initial antivortex and modified antivortex designs provide higher film effectiveness than the base line case, with the modified design performing best for both density ratios. The modified design increases film effectiveness by about 0.2 over a wide range of streamwise locations for both density ratios. The initial design similarly provides an improvement in film effectiveness over the base line case, but the benefit is somewhat more pronounced for the higher density ratio. This might be a consequence of the doubling of net flow rate through the secondary holes for Case 5 versus Case 2 (Table 3). Considering these trends and Fig. 16, it is observed that the increase in film effectiveness is proportional to the percentage of offset vorticity in Fig. 16. The initial design offsets about 25% of the detrimental vorticity and provides about 0.05 benefit in film effectiveness, while the corresponding values for the modified design are about 100% and 0.2 benefit. So,

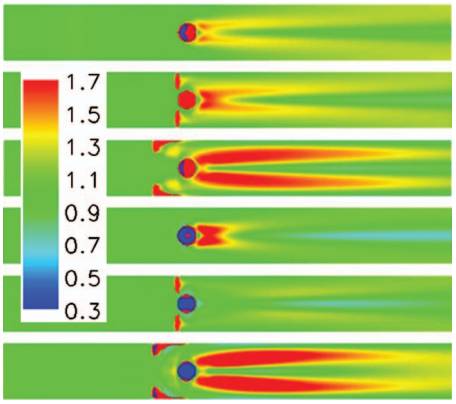

Fig. 18 Heat transfer coefficient h/h_o (Cases 1–6)

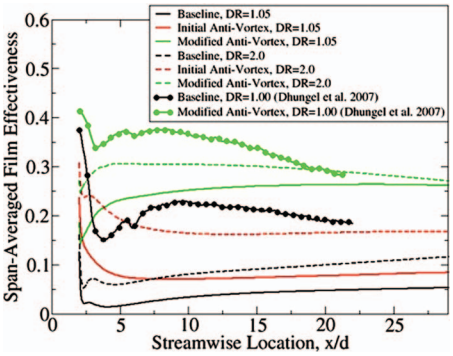

Fig. 19 Span-averaged film effectiveness

$$\eta_{\text{antivortex}} - \eta_{\text{base line}} = C(1 - \Omega_{\text{antivortex}}/\Omega_{\text{base line}}) \tag{5}$$

where for the present case $C=0.2$ and Ω represents integrated streamwise vorticity values downstream of the hole. Now, C is bounded by the maximum possible improvement of 1.0 for a jet, which is fully separated from the surface. However, comparing a row of round holes to a slot, the holes do not initially cover the entire span as they exit the hole. If we convert round holes to rectangular holes having the same exit area and streamwise extent, their effective width may be considered to be $\pi d/4$ or $0.785d$. Accounting for the pitch of $3d$ yields an effective spanwise coverage of $\pi/12$ or 0.262 of the pitch for this case. Thus, if the coolant were to issue through the effective rectangular holes and provide an effectiveness of 1.0 directly behind the holes, an increase in span-averaged effectiveness of 0.262 is the most that could be gained compared to a fully detached jet. Since the base line case does not have zero effectiveness, the available improvement of $(1-\eta_{\text{base line}})$ must also be considered. Applying these modifications to Eq. (5) and generalizing for variable hole pitch yield

$$\eta_{\text{antivortex}} - \eta_{\text{base line}} = (\pi/4)(1 - \Omega_{\text{antivortex}}/\Omega_{\text{base line}}) \times (1 - \eta_{\text{base line}})/(p/d) \tag{6}$$

as an estimate of the improvement afforded by the antivortex design or perhaps more generally for other film-cooling concepts, which modify the freestream vorticity field. The primary uncertainties in this estimate are the vorticity values. These might be estimated from computational studies such as in the present work or even from basic information such as hole angles and velocities.

Figure 19 also shows the experimental data of Dhungel et al. [10] for the base line and modified antivortex cases at DR=1.0. It can be seen that the computational predictions for these cases are much lower than for the data, although the benefit of the antivortex design is similar, with the experimental data also indicating an average improvement in effectiveness of nearly 0.2. The difficulty in predicting film effectiveness values is not entirely unexpected and should not invalidate the antivortex concept. It is known that steady RANS codes have difficulty predicting film effectiveness for high momentum ratio flows due to their inability to capture the additional mixing due to the strong freestream/jet interaction. It was shown in earlier work by Kapadia et al. [29] that a LES or detached eddy simulation (DES) could provide much better predictions of film effectiveness for such flows. However, the steady RANS code should be able to adequately predict the gross vorticity field, which is the basis for the antivortex concept benefit. The results of Dhungel et al. [10] indeed bear this improvement out.

Figure 20 is a plot of spanwise-averaged heat transfer coefficient values downstream of the main hole. The values are normalized by the non-film-cooled case heat transfer. The base line case spanwise-averaged heat transfer coefficient data of Dhungel et al. [10] are much better predicted by the analysis than was the effectiveness. However, the experimental data for the modified antivor-

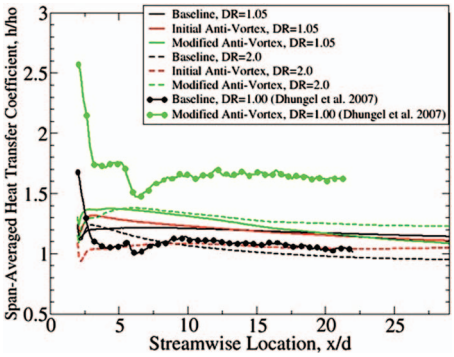

Fig. 20 Span-averaged heat transfer coefficient

tex design are higher than the predictions. This is likely due to an inability of the turbulence model to capture the highly three-dimensional and perhaps unsteady flow field near the wall and the associated heat transfer. It is surprising that the data of Dhungel et al. [10] show such a large increase in heat transfer coefficient for all seven shaped and antivortex cases examined. It would be insightful to examine field measurements of velocity, temperature, and turbulence intensity for these geometries to help understand these differences. Interestingly, the predicted base line and initial antivortex design at DR=2.0 show small regions of reduced heat transfer coefficient compared to the non-film-cooled case, perhaps due to the jet velocity being half of the freestream value. However, the modified antivortex design increases heat transfer for both density ratios and is higher than the initial design.

Table 4 gives area-averaged values of film effectiveness, heat transfer coefficient ratio, and NHFR for all cases. The NHFR is influenced by both the film effectiveness and the heat transfer coefficient, as indicated by Eq. (3). The averaging is done over the entire spanwise width and from $x=2$ (the main hole trailing edge) to $x=30$ (the end of the computational domain). The film effectiveness and heat transfer coefficient trends are reflective of the span-averaged results already described. The net heat flux shows a progressive increase in cooling performance from the base line to initial antivortex to modified antivortex design for both density ratios. The NHFR is driven primarily by the film effectiveness, although the benefit of the modified antivortex case for DR=2.0 (Case 6) is mitigated somewhat by its significantly higher h/h_o. The base line and initial antivortex DR=1.05 cases actually increase the heat flux because of their low effectiveness and enhanced heat transfer. The data of Dhungel et al. [10] indicate a NHFR of approximately 0.13 for their modified antivortex case with DR=1.0. While still quite beneficial, this represents about a 45% reduction from the predicted value of 0.235 and is a result of the much higher values of heat transfer coefficient in the data.

Summary and Conclusions

A novel "antivortex" film-cooling design concept has been conceived and designed at NASA Glenn Research Center. This concept has been shown computationally to dramatically improve film-cooling performance for a blowing ratio of 1.0 on a flat plate model versus the standard round hole. An improvement in area-averaged film effectiveness of about 0.2 and in NHFR of about 0.2 is predicted for the modified antivortex design versus the base line round hole for density ratios of 1.0 and 2.0. The concept is also easily manufactured due to the use of only round holes. A benefit has been shown relative to a standard single row of round holes at 30 deg angle of inclination and pitch-to-diameter ratio of 3.0. This concept could thus be added as a retrofit process to existing round hole geometries on turbine blades and vanes, as the total mass flow rate through the new hole is relatively insensitive to the addition of the side holes.

Additional work must be done to study the influence of the various geometrical parameters on the performance of the antivortex film-cooling concept. This study represents a first attempt at investigating those parameters, and some recommendations are described, but obviously the optimum configuration will depend on the application. One possible permutation would be to study the feasibility of increasing the pitch-to-diameter ratio of the main holes. This would reduce the total coolant flow rate for a given plenum pressure while maintaining or improving cooling effectiveness. This would be of great benefit to the engine cycle performance. Another design modification to consider would be increasing the size of the side holes to be the same as the main holes. This would simplify manufacturing and ease concerns about drilling very small holes. This was not done in the present study, partly due to the desire to limit the amount of coolant through the side holes but also due to the size constraints arising from the use of the small $p/d=3.0$. If p/d were increased, larger side holes could be employed. There are also indications that a larger percentage of coolant flowing through the side holes would not be a "loss" of coolant as was initially thought. Since the side hole flow was entrained by the main hole vorticity and brought back to the surface in the present study, it may not be detrimental to allow more flow to exit the side holes.

Future work will also include a broader range of blowing ratios and the inclusion of unsteady and increased freestream turbulence effects, as it is known that for high blowing ratios, these effects can be important. For example, at high blowing ratios, an increased level of unsteady mixing can actually increase the film effectiveness by causing cold fluid to migrate back to the surface relative to the steady detached jet. It remains to be seen if the antivortex concept is as beneficial under those conditions, which are more representative of the engine.

Table 4 Area-averaged quantities ($2 \leq x/d \leq 30$)

Case	η	h/h_o	NHFR
1	0.040	1.181	–0.120
2	0.081	1.187	–0.059
3	0.252	1.225	0.235
4	0.091	1.033	0.085
5	0.173	1.053	0.209
6	0.292	1.280	0.282

Nomenclature

c_p = specific heat
d = film-cooling hole diameter
DR = density ratio $=\rho_c/\rho_{\text{in}}$
h = heat transfer coefficient $=q''/(T_w-T_{\text{aw}})$
I = momentum ratio $=(\rho V^2)_c/(\rho V^2)_{\text{in}}$
k = turbulence kinetic energy
M = blowing ratio $=(\rho V)_c/(\rho V)_{\text{in}}$
NHFR = net heat flux reduction $=1-(h/h_o)(1-\eta\theta)$
p = film-cooling hole spanwise pitch
Pr = Prandtl number
Pr_t = turbulent Prandtl number
q'' = heat flux at wall
R = gas constant for air
Re = Reynolds number
T = temperature
x = streamwise distance from hole leading edge
y = transverse coordinate from hole centerline
y^+ = dimensionless grid spacing
z = normal coordinate from wall
η = film effectiveness $=(T_{\text{in}}-T_{\text{aw}})/(T_{\text{in}}-T_c)$
ρ = density
θ = dimensionless temperature $=(T_{\text{in}}-T_c)/(T_{\text{in}}-T_w)$
Ω = area-averaged streamwise vorticity

ω = dissipation per unit turbulence kinetic energy

Subscripts

aw = adiabatic wall conditions
c = coolant conditions
in = freestream inlet conditions
o = no injection conditions

References

[1] Goldstein, R. J., 1971, Adv. Heat Transfer, **7**, pp. 321–379.
[2] Kercher, D. M., 1998, "A Film-Cooling CFD Bibliography: 1971–1996," Int. J. Rotating Mach., **4**(1), pp. 61–72.
[3] Kercher, D. M., 2000, "Turbine Airfoil Leading Edge Film Cooling Bibliography: 1972–1998," Int. J. Rotating Mach., **6**(5), pp. 313–319.
[4] Pedersen, D. R., Eckert, E. R. G., and Goldstein, R. J., 1977, "Film Cooling With Large Density Differences Between the Mainstream and the Secondary Fluid Measured by the Heat-Mass Transfer Analogy," ASME J. Heat Transfer, **99**, pp. 620–627.
[5] Foster, N. W., and Lampard, D., 1980, "The Flow and Film Cooling Effectiveness Following Injection Through a Row of Holes," ASME J. Eng. Power, **102**, pp. 584–588.
[6] Pietrzyk, J. R., Bogard, D. G., and Crawford, M. E., 1989, "Hydrodynamic Measurements of Jets in Crossflow for Gas Turbine Film Cooling Applications," ASME J. Turbomach., **111**, pp. 139–145.
[7] Pietrzyk, J. R., Bogard, D. G., and Crawford, M. E., 1990, "Effects of Density Ratio on the Hydrodynamics of Film Cooling," ASME J. Turbomach., **112**, pp. 437–443.
[8] Sinha, A. K., Bogard, D. G., and Crawford, M. E., 1991, "Film-Cooling Effectiveness Downstream of a Single Row of Holes With Variable Density Ratio," ASME J. Turbomach., **113**, pp. 442–449.
[9] Leylek, J. H., and Zerkle, R. D., 1994, "Discrete-Jet Film Cooling: A Comparison of Computational Results With Experiments," ASME J. Turbomach., **116**, pp. 358–368.
[10] Dhungel, S., Phillips, A., Ekkad, S. V., and Heidmann, J. D., 2007, "Experimental Investigation of a Novel Anti-Vortex Film Cooling Hole Design," ASME Paper No. GT2007–27419.
[11] Haven, B. A., Yamagata, D. K., Kurosaka, M., Yamawaki, S., and Maya, T., 1997, "Anti-Kidney Pair of Vortices in Shaped Holes and Their Influence on Film Cooling Effectiveness," ASME Paper No. 97-GT-45.
[12] Lemmon, C. A., Kohli, A., and Thole, K. A., 1999, "Formation of Counter-Rotating Vortices in Film-Cooling Flows," ASME Paper No. 99-GT-161.
[13] Bunker, R. S., 2005, "A Review of Shaped Hole Turbine Film-Cooling Technology," ASME J. Heat Transfer, **127**, pp. 441–453.
[14] Shih, T. I.-P., Lin, Y.-L., Chyu, M. K., and Gogineni, S., 1999, "Computations of Film Cooling From Holes With Struts," ASME Paper No. 99-GT-282.
[15] Papell, S. S., 1984, "Vortex Generating Flow Passage Design for Increased Film-Cooling Effectiveness and Surface Coverage," Presented at the 22nd National Heat Transfer Conference, Niagara Falls, N.Y., 5–8 Aug. 1984.
[16] Zaman, K. B. M. Q., and Foss, J. K., 1997, "The Effects of Vortex Generators on a Jet in Crossflow," Phys. Fluids, **9**, pp. 106–114.
[17] Bunker, R. S., 2002, "Film Cooling Effectiveness Due to Discrete Holes Within a Transverse Surface Slot," ASME Paper No. GT-2002-30178.
[18] Ekkad, S. V., Ou, S., and Rivir, R. B., 2006, "Effect of Jet Pulsation and Duty Cycle on Film Cooling From a Single Jet on a Leading Edge Model," ASME J. Turbomach., **128**, pp. 564–571.
[19] Steinthorsson, E., Liou, M.-S., and Povinelli, L. A., 1993, "Development of an Explicit Multiblock/Multigrid Flow Solver for Viscous Flows in Complex Geometries," AIAA Paper No. 93-2380.
[20] Arnone, A., Liou, M.-S., and Povinelli, L. A., 1991, "Multigrid Calculation of Three-Dimensional Viscous Cascade Flows," AIAA Paper No. 91-3238.
[21] Rigby, D. L., Ameri, A. A., and Steinthorsson, E., 1997, "Numerical Prediction of Heat Transfer in a Channel With Ribs and Bleed," ASME Paper No. 97-GT-431.
[22] Ameri, A. A., Steinthorsson, E., and Rigby, D. L., 1997, "Effect of Squealer Tip on Rotor Heat Transfer and Efficiency," ASME Paper No. 97-GT-128.
[23] Wilcox, D. C., 1994, *Turbulence Modeling for CFD*, DCW Industries, LaCanada.
[24] Wilcox, D. C., 1994, "Simulation of Transition With a Two-Equation Turbulence Model," AIAA J., **32**(2), pp. 247–255.
[25] Menter, F. R., 1993, "Zonal Two-Equation k-ω Turbulence Models for Aerodynamic Flows," AIAA Paper No. 93-2906.
[26] Chima, R. V., 1996, "A k-ω Turbulence Model for Quasi-Three-Dimensional Turbomachinery Flows," NASA Paper No. TM-107051.
[27] Schlichting, H., 1979, *Boundary Layer Theory*, 7th ed., McGraw-Hill, New York, pp. 312–313.
[28] Sen, B., Schmidt, D. L., and Bogard, D. G., 1996, "Film Cooling With Compound Angle Holes: Heat Transfer," ASME J. Turbomach., **118**, pp. 800–806.
[29] Kapadia, S., Roy, S., and Heidmann, J., 2004, "First Hybrid Turbulence Modeling for Turbine Blade Cooling" J. Thermophys. Heat Transfer, **18**(1), pp. 154–156.

Heat/Mass Transfer Characteristics in Angled Ribbed Channels With Various Bleed Ratios and Rotation Numbers

Kyung Min Kim
Suk Hwan Park
Yun Heung Jeon
Dong Hyun Lee
Hyung Hee Cho
e-mail: hhcho@yonsei.ac.kr

Department of Mechanical Engineering,
Yonsei University,
Seoul 120-749, Korea

The present study investigates the effects of secondary flow due to angled rib turbulators on the heat/mass transfer in the square channels with channel rotation and bleed flow. The angle of attack of the angled ribs was 45 deg. The bleed holes were located between the rib turbulators on either the leading or trailing surface. The tests were conducted under the conditions corresponding to various bleed ratios (BR = 0.0, 0.2, and 0.4) and rotation numbers (Ro = 0.0, 0.2, and 0.4) at Re = 10,000. The results suggest that the heat/mass transfer characteristics were influenced by the Coriolis force, the decrement of the main flow rate, and the secondary flow. In the 90 deg angled ribbed channel, the heat/mass transfer reduced on the leading surface with an increment in the rotation number, but it increased on the trailing surface. However, it decreased on both surfaces in the 45 deg angled ribbed channel. As the bleed ratio increased, the Sherwood number ratios decreased on both the bleeding and nonbleeding surfaces for the 45 deg angled ribs but increased on the bleeding surface for the 90 deg angled ribs.
[DOI: 10.1115/1.2777196]

Introduction

In the development of high performance gas turbine engines, designing an effective cooling system is crucial. Therefore, the turbine inlet temperature has been increased steadily to improve the thermal efficiency of the turbine engines: however, this resulted in high heat loads on the turbine blades. To protect the blade materials from damage due to heating beyond the maximum allowable temperature, various cooling techniques have been employed. Among these techniques, internal passage cooling is used for cooling the inner turbulated surface; this was achieved using cooling air generated by a compressor. Film cooling is performed to protect the blade surfaces in contact with hot gases by using cooling air ejected through the holes on the blade surface after cooling internal passages. The bleed flow, flow structures, and heat transfer generated by the cooling air in the internal passage show differences. Moreover, when the turbine blades rotate, the Coriolis force causes greater variations in the flow structures; hence, it becomes necessary to understand how those parameters affect the cooling performance.

To promote heat transfer and cooling performance in the internal cooling passages, various cooling techniques (rib turbulator, pin fin, dimple, etc.) have been studied. Among these techniques, the technique of using repeated rib turbulators has been actively investigated since the early 1970s. Moreover, after Han et al. [1] reported that the repeated 45 deg angled ribs performed better than repeated 90 deg angled rib in a parallel-plate channel, many researchers [2–6] have studied the effects of various rib conditions such as rib height, rib angle of attack, rib-to-rib pitch, rib shape, and rib arrangement on the heat transfer and the flow structures using many measurement techniques.

In a practical cooling passage with rotor blades, the heat transfer distributions are significantly affected by rotational forces (Coriolis and rotating buoyancy forces), which produce secondary flow and force heavier cooling fluid to flow away from the center of rotation. The rotational effects on heat transfer have been experimentally reported by many researchers [7–10]. They explained that these force deflect the coolant fluid toward the trailing surface, in the case of outward flow, and toward the leading surface, in the case of inward flow. Thus, heat transfer discrepancy between the leading and trailing surfaces results.

In most modern turbine blades, the cooling passages have rib turbulators for heat transfer enhancement and ejection holes for film cooling. Bleed holes are formed on the blade surface and they have significant effects on the heat transfer in the cooling passage. Therefore, studying the effects of bleed flow is essential. Many researchers [11–14] measured the local heat transfer coefficients in stationary channels with bleed holes, and reported that the bleed flow on the surface yields higher heat transfer around the holes; further, they have lower friction factor than that under no bleed condition. They also reported that placing the bleed holes after the ribs widened the regions of high heat transfer because the recirculation flow behind the ribs was eliminated.

However, most of the studies on the heat transfer characteristics in the internal passages with bleed holes were conduced under stationary conditions. Therefore, to understand the cooling system of them, it is necessary to study the heat transfer characteristics under rotating conditions. Regarding this, Kim et al. [15] and Jeon et al. [16] have studied the effects of bleed flow on the detailed heat/mass transfer distributions in smooth and 90 deg angled ribbed channels under various rotating conditions. In the present study, to experimentally obtain the effects of an additional secondary flow, we measured the local heat/mass transfer distributions in rotating channels with 45 deg angled rib turbulators and various bleed flows; we then compared them with the data of the 90 deg angled ribbed cases.

Experimental Apparatus

Rotating Facility. A schematic view of the experimental apparatus is shown in Fig. 1. The test rig was comprised of a blowing system, a rotating system, and a measuring system. First, in the

Contributed by the International Gas Turbine Institute of ASME for publication in the JOURNAL OF TURBOMACHINERY. Manuscript received June 7, 2007; final manuscript received June 19, 2007; published online May 6, 2008. Review conducted by David Wisler. Paper presented at the ASME Turbo Expo 2007: Land, Sea and Air (GT2007), 2007, Montreal, Quebec, Canada, May 14–17, 2007, Paper No. GT2007-27166.

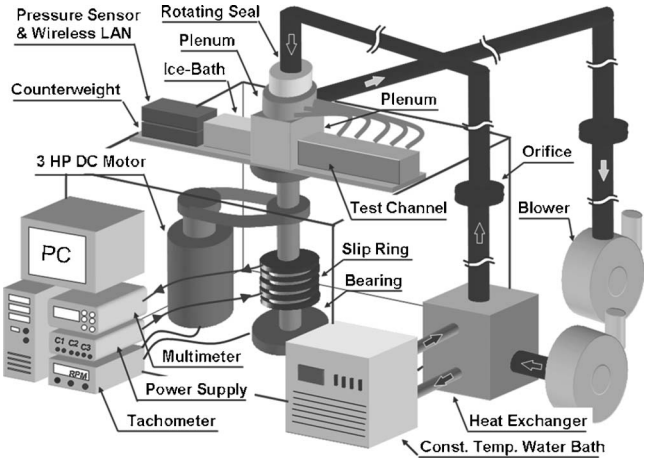

Fig. 1 Experimental apparatus

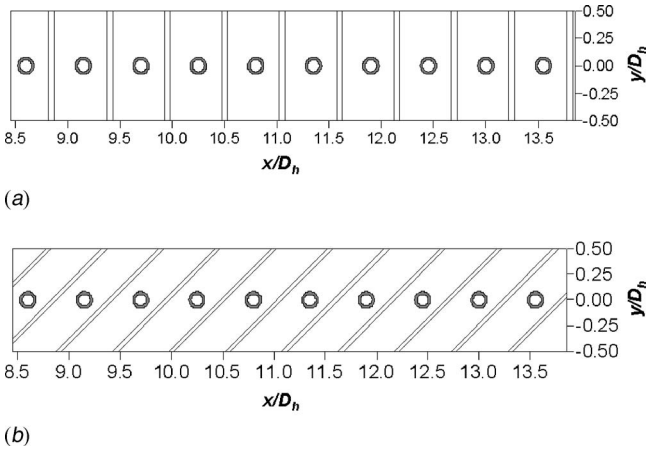

Fig. 3 Coordinate system of the test section with bleed holes: (*a*) 90 deg angled ribbed channel and (*b*) 45 deg angled ribbed channel

case of the blowing system, one blower supplied room air into the test section and another blower supplied the bleed flow through the test section. These blowers were controlled using frequency inverters. Air temperature was regulated during the experiment using a heat exchanger. The blowing and bleeding flows were measured by orifice flow meters. The Reynolds number (Re), which is based on the hydraulic diameter and the ratio of the bleed flow to the main flow (bleed ratio, BR), was monitored, and it was observed to be constant during the tests. The maximum difference in the bleed flow through each bleed hole was verified to be within 3% for all the cases by differential pressure tests. A magnetic rotating seal and a rib seal were equipped in order to prevent any leakage through the rotating parts. A 3 hp (2.24 kW) dc motor connected with to a V-belt drove the rotating shaft, whose rotation speed was measured by an optical tachometer. Rotation numbers remained 0.0, 0.2, and 0.4 during the tests. The maximum rotation number (Ro=0.4) corresponded to 400 rpm approximately. Lastly, for a measuring system (an Agilent data logger and a low pressure differential sensor by GE Druck) interfaced to a computer via slip rings and wireless LAN equipment, electrical output signals were recorded from the test sections. For accurate measurements of the naphthalene surface temperature, J-type thermocouples were embedded in the test plate because the vapor pressure of naphthalene is sensitive to temperature, and varies by about 10% change per °C. The temperature of the bulk air was also obtained by the thermocouples installed in the channel inlets and outlets.

Test Section. Figure 2 shows the geometry of the test channel with 90 deg rib turbulators and Fig. 3 shows the coordinate system of the test section. As shown in Table 1, the test channel had a hydraulic diameter (D_h) of 40.0. Further, its streamwise coordinate ranges from $x/D_h=8.45$ to $x/D_h=13.8$. The square rib turbulators were installed on both leading and trailing surfaces of the test channel and their array were inlined. The rib height-to-hydraulic diameter ratio (e/D_h) was 0.055 and the rib-to-rib pitch (p/e) was 10.0 times that of the rib height. Each bleed hole was located at the center of the rib turbulators on either leading or trailing surfaces; there were 20 holes each having a diameter (d) of 4.5 mm. The ratio of the hole spacing to the diameter (p_h/d) was 4.9. The ratio of the maximum rotating radius to the hydraulic diameter (R/D_h) was 14.5. The coordinate systems of the test sections are shown in Figs. 3(a) and 3(b). The streamwise, lateral, and vertical directions corresponded to the x, y, and z axes, respectively. The test section was covered with naphthalene from $x/D_h=8.45$ to $x/D_h=13.8$ and had ten bleed holes. The lateral domain ranged from $y/D_h=-0.5$ to $y/D_h=0.5$.

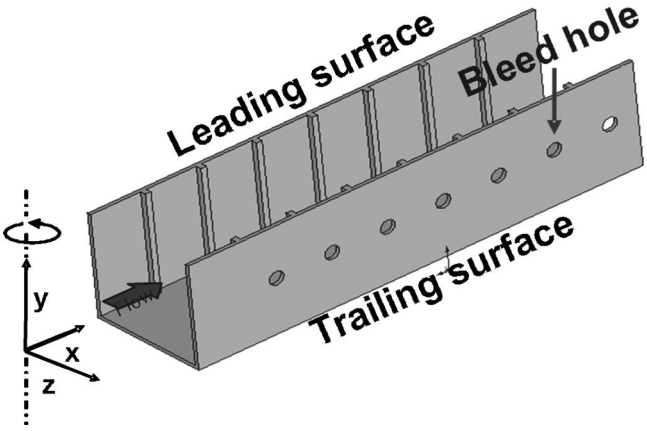

Fig. 2 Geometry of the test channel with 90 deg angled ribs

To measure the pressure drop across the channel, pressure tests were conducted by using an electronic pressure sensor. Eight pressure taps were drilled at $z/D_h=0.0$ on one of the sidewalls, with a spacing and a diameter of 66 mm and 0.8 mm, respectively.

Procedure and Data Reduction

A naphthalene sublimation method was employed to obtain detailed heat/mass transfer coefficients using the analogy between heat and mass transfer. The surfaces of the test section were cast with naphthalene to simulate heating condition of a cooling passage in a gas turbine blade. Naphthalene surfaces where mass transfer occurred correspond to a uniform wall temperature

Table 1 Test section configurations

Hydraulic diameter (D_h)	40.0 mm
Passage height (H)	40.0 mm
Passage width (W)	40.0 mm
Max. rotating radius (R)	580 mm
Test section length	552 mm
Naph. coated length	214 mm
Bleed hole diameter (d)	4.5 mm
Rim thickness of hole	1.0 mm
Hole-to-hole pitch (p_h)	22.0 mm
Rib height (e)	2.2 mm
Rib-to-rib pitch (p)	22.0 mm
Attack angle of rib (α)	45 deg or 90 deg

boundary condition of heat transfer experiments. The local naphthalene sublimation depth was measured to attain mass transfer coefficients on each position using a liner variable differential transformer LBB-375TA-020 and an automated positioning table. It is expressed as

$$h_m = \frac{\dot{m}}{\rho_{v,w} - \rho_{v,b}} = \frac{\rho_s(\Delta z/\Delta t)}{\rho_{v,w} - \rho_{v,b}} \tag{1}$$

where $\dot{m}$ is the local mass transfer rate of naphthalene per unit area, and $\rho_{v,w}$ and $\rho_{v,b}$ are the vapor density at the naphthalene surface and the bulk vapor density of naphthalene, respectively. From the local mass transfer coefficient, the Sherwood number is calculated as

$$\mathrm{Sh} = h_m D_h / D_{\mathrm{naph}} \tag{2}$$

where D_{naph} is the diffusion coefficient of naphthalene in air. The properties of naphthalene suggested by Ambrose et al. [17] and Goldstein and Cho [18] are used in the present study. The uncertainty in the Sherwood number is estimated to be within $\pm 8.0\%$ at a 95% confidence level using the uncertainty estimation method of Kline and McClintock [19]. The Nusselt numbers can be obtained from the Sherwood numbers by the correlation $\mathrm{Nu}/\mathrm{Sh} = (\mathrm{Pr}/\mathrm{Sc})^{0.4}$, which is for turbulent flows.

The mass transfer results are presented as the Sherwood number ratios $\mathrm{Sh}/\mathrm{Sh}_0$ to estimate the heat/mass transfer augmentation effectively, where Sh_0 is the Sherwood number for a fully developed turbulent flow in a stationary smooth circular tube correlated by McAdams [20] and converted to mass transfer parameters as

$$\mathrm{Sh}_0 = 0.023\mathrm{Re}^{0.8}\mathrm{Sc}^{0.4} \tag{3}$$

The averaged Sherwood numbers, such as $\overline{\mathrm{Sh}}_p$, $\overline{\mathrm{Sh}}_R$, and $\bar{\bar{\mathrm{Sh}}}_R$ are calculated by the integration of the local Sherwood numbers weighted by constant area (between rib turbulators and from $x/D_h = 10.5$ to 13.25).

The average pressure drop is obtained from the slope calculated by a linear curve fitting of the local pressure difference data in the middle region of the channel ($\Delta P/\Delta L$) where the static pressure decreases linearly. The friction factor is calculated with the average pressure drop as

$$f = \Delta P/[4(\Delta L/D_h)(1/2)\rho u_b^2] \tag{4}$$

The uncertainty of the friction factor is within 4.4%. The friction loss results are presented as the friction factor ratios f/f_0, where f_0 represents the friction factor for a fully developed turbulent flow in a stationary smooth circular tube. The empirical equation that closely fits the Kármán–Nikuradse equation proposed by Petukhov [21] is employed as $f_0 = 2(2.236 \ln \mathrm{Re} - 4.639)^{-2}$.

The thermal performance η obtained by considering both the heat/mass transfer augmentation and the friction loss increment is presented based on the constant pumping power condition and it is expressed as the following equation:

$$\eta = (\bar{\bar{\mathrm{Sh}}}_R/\mathrm{Sh}_0)/(f/f_0)^{1/3} \tag{5}$$

The detailed experimental procedure and data reduction are described in Kim et al. [15] and Jeon et al. [16].

Results and Discussion

Heat/Mass Transfer Characteristics

Cases With 90 deg Angled Rib Turbulators. Figure 4 shows the local Sherwood number ratio distributions in the channel with transverse ribs and bleed flow. The contours in this figure are presented in the range of $11.5 \leq x/D_h \leq 13.0$ due to the periodic patterns in the fully developed region.

When the rotation number was 0.0 (Fig. 4(*a*); stationary case), the high heat/mass transfer coefficients appeared in an inter-rib region on the nonbleeding surface due to the transverse ribs. The peak appeared at the upstream of the middle of the inter-rib region

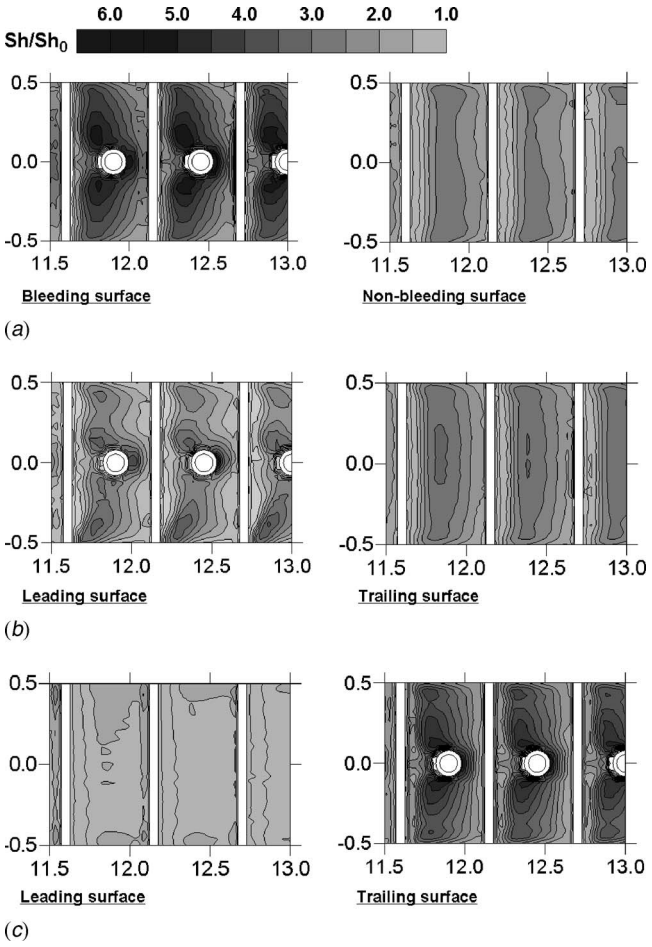

Fig. 4 The local $\mathrm{Sh}/\mathrm{Sh}_0$ distributions in the 90 deg angled ribbed channel with bleed flow (BR=0.4): (*a*) Ro=0.0, (*b*) Ro=0.4 (bleeding on the leading surface), and (*c*) Ro=0.4 (bleeding on the trailing surface)

due to the reattachment of the flows passing over the ribs. The lateral distributions were uniform except the corner of the passage. In these corner regions, the heat/mass transfer decreased due to weakened reattachment as a result of the redevelopment of flows caused by the wall friction. This is a typical pattern of the heat/mass transfer distributions on ribbed surfaces with flow separation and reattachment, and this pattern agreed well with the results of the previous studies such as Kukreja et al. [2], Aliaga et al. [3], and Acharya et al. [4]. On the bleeding surface with bleed holes, the heat/mass transfer was higher than that on the nonbleeding surface because the reattachment became strong around the holes due to the effect of the tripping flow, which impinges around the bleed holes due to the drawing flow by suction and augments the heat/mass transfer on the vicinity of them.

When the passage rotates (Figs. 4(*b*) and 4(*c*); Ro=0.4), in general, the heat/mass transfer decreases on the leading surface but increases on the trailing surface [7–11]. In other words, for the leading surface on the middle region except for the corners of the passage and the regions around the holes, the reattachment became weak due to the Coriolis force acting on the trailing surface. On the corner regions, a high heat/mass transfer appeared due to the impingement of the secondary flow returning from the trailing surface due to the Coriolis force. In the overall trailing surface region, the heat/mass transfer increased because the separated flow by the rib turbulators was reattached strongly by the Coriolis force

For cases with bleed flow on the leading surface (Fig. 4(*b*)), the heat/mass transfer decreased in the middle region of the leading

surface due to the Coriolis force acting on the trailing surface. The Sherwood number ratios around the holes were high due to the tripping flow, although the values were lower than those at Ro =0.0. For the entire trailing surface region, the heat/mass transfer without rotation and bleed flow was augmented by the Coriolis force. When bleed flow occurred on the trailing surface (Fig. 4(*c*)), the heat/mass transfer patterns were similar to those of Ro =0.0 for both the bleeding and nonbleeding surfaces. The heat/mass transfer on the nonbleeding (or leading) surface had a lower value. However, on the bleeding (or trailing) surface, the Sherwood number ratios were locally augmented in the corner region and almost identical to those in the middle region.

The pitch-averaged Sherwood number ratios obtained from the local experimental data among all the rib turbulators except those on the rib surface are shown in Fig. 5. The figure presents the averaged heat/mass transfer along the streamwise direction in the whole measured region at each rotation and bleed ratio.

In the stationary case (Fig. 5(*a*)), the fully developed values at BR=0.0 were enhanced greater than in the fully developed values (Sh_0) for a stationary smooth circular tube by approximately 2.7. In the case of BR=0.2, the heat/mass transfer on the leading (or bleeding) surface was increased by the effect of the tripping flow that occurs around the bleed holes due to the suction drawing flow, in contrast, the effect on the trailing (or nonbleeding) surface decreased by the reduction of the main flow. Further, the averaged values on both the surfaces decreased as the flow proceeded because of the continuous bleeding. As the bleed ratio increased, the heat/mass transfer coefficients on the leading surface gradually increased but those on the trailing surface decreased.

In the case of rotation with bleeding on the leading surface (Fig. 5(*b*)), the Coriolis force augmented the heat/mass transfer on the trailing surface onto which the coolant flow was deflected but deteriorated that on the leading surface. However, as the bleed ratio increased, the discrepancy between the heat/mass transfer coefficients of the leading and the trailing surfaces decreased due to the tripping flow effect. This was because the heat/mass transfer is enhanced on the bleeding surface but was reduced on the nonbleeding surface. In the case of rotation with bleeding on the trailing surface (Fig. 5(*c*)), the difference in heat transfer between the surfaces increased to more than that for BR=0.0 with an increment in the bleed ratio. In particular, the averaged coefficients on the nonbleeding (or leading) surface considerably reduced due to the reduction of the main flow and the deflection toward the trailing surface. However, the heat/mass transfer on the bleeding (or trailing) surface was almost identical because the main secondary flow moved toward the trailing surface.

Figure 6 shows the regional averaged Sherwood number ratios obtained from the local data between $x/D_h=10.5$ and 13.25 except for those on the rib surface. The averaged values taken from the fully developed five pitch regions at each rotation number and bleed ratio. The present data are compared to averaged heat transfer data obtained by Ekkad et al. [14,22] on the bleed surface in the first pass of the stationary channel with 90 deg ribs. Although the averaged values of the present study were higher than data by Ekkad et al. [14,22] due to different experimental conditions as introduced in Table 2, the values by bleed flow were enhanced. In the case of bleeding on the leading surface (Fig. 6(*a*)), as the rotation numbers increased, the heat/mass transfer on the leading surface gradually decreased; however, that on the trailing surface increased gradually. In the case of the bleed flow, for any rotation numbers, the values on the leading (or bleeding) surface were enhanced by the tripping flow. However, those on the trailing (or nonbleeding) surface were reduced by the reduction of the main flow. For bleeding on the trailing surface (Fig. 6(*b*)), as the rotation number and bleed ratios increased, the heat/mass transfer on the leading surface decreased whereas that on the trailing surface increased. In other words, the channel rotation and tripping flow caused a large difference in the average values between the leading and trailing surfaces.

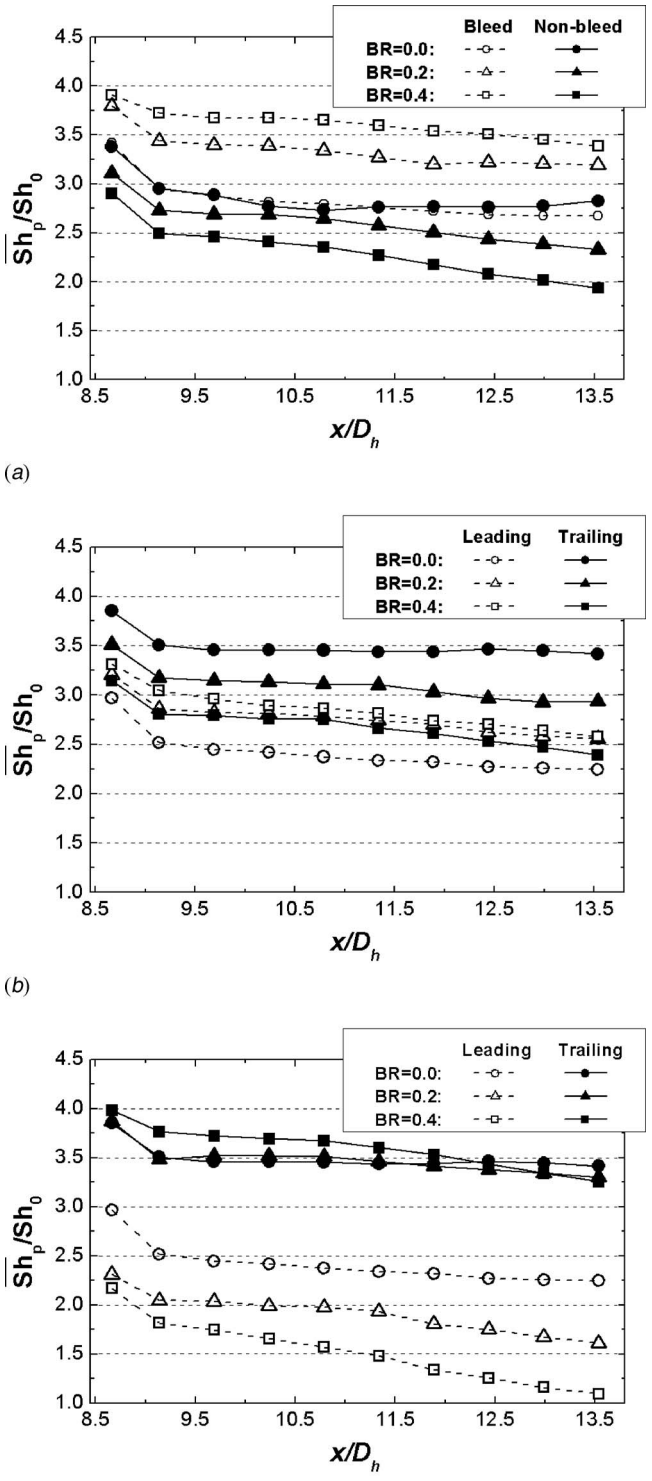

Fig. 5 Pitch averaged Sh/Sh_0 distributions in the 90 deg angled ribbed channel: (*a*) Ro=0.0, (*b*) Ro=0.4 (bleeding on the leading surface), and (*c*) Ro=0.4 (bleeding on the trailing surface)

Cases With 45 deg Angled Rib Turbulators. In this section, to investigate the secondary flow induced by angled rib turbulators, the experimental data for the 90 deg angled ribbed channels were used for comparison. Figure 7 shows the local Sherwood number ratio distributions in the channels with the 45 deg angled ribs and

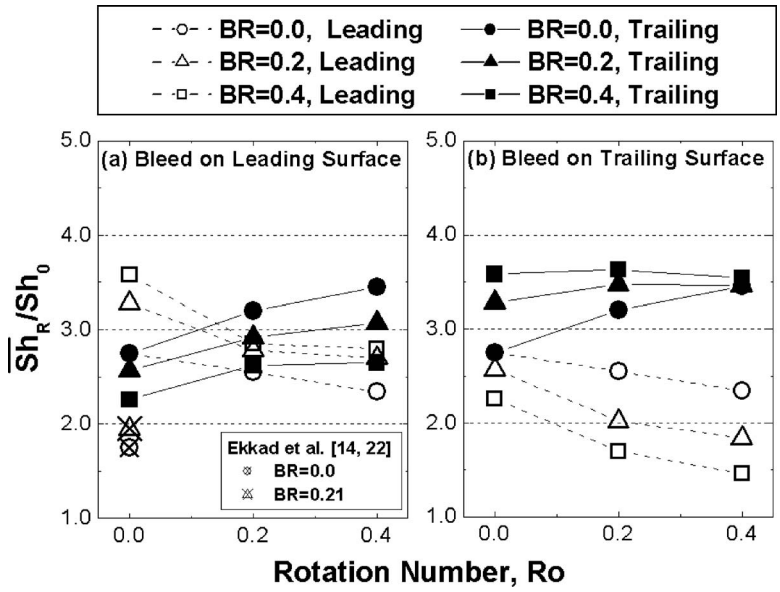

Fig. 6 Regional averaged Sh/Sh_0 ($10.5 \leq x/D_h \leq 13.25$) for all the tests in the 90 deg ribbed channel

bleed flow. The contours in this figure are presented in the range of $11.5 \leq x/D_h \leq 13.0$ due to the periodic patterns in the fully developed region.

In the stationary case (Fig. 7(*a*); Ro=0.0), high Sherwood number ratios were observed in the downward region ($-0.5 \leq y/D_h \leq -0.2$) of the secondary flow induced by the angled rib turbulators. These secondary flows moved along the angled ribs near the ribbed walls and then moved upwards near the one of the sidewall at $y/D_h=0.5$. In the results, downward flows were induced near the opposite side wall, $y/D_h=-0.5$. The secondary flows were induced near the opposite ribbed wall as well, which resulted in the creation of counter-rotating secondary flow cell pairs. Further, the high heat/mass transfer regions around the holes in the bleeding (or leading) surface appeared to be larger than those on the nonbleeding (or trailing) surface because the secondary flows strongly reattached due to the effect of the tripping flow.

Although the passage was rotated, the heat/mass transfer patterns were similar to those in the stationary case. This is because an additional vortex was not generated by the Coriolis force. In other words, a pair of vortices in the 90 deg ribbed channels was generated. In the 45 deg ribbed channels, although the channel rotation deflected the flow by acting on the one surface, the vortex flow was not caused. Thus, the low heat transfer regions appear on the entire opposite surface region. For cases with the bleed flow on the leading surface (Fig. 7(*b*)), the heat/mass transfer decreased in the middle region of the leading surface, but was large around the holes. On the trailing surface, the heat/mass transfer was augmented by the rotation, and the low heat transfer regions ranged

Table 2 Experimental conditions for data validation

	Present study	Ekkad et al. [14,22]
Experiment	Mass transfer	Heat transfer
D_h	40.0 mm	50.8 mm
W/H	1.0	1.0
e/D_h	0.055	0.125
p/e	10.0	10.0
α	45 deg, 90 deg	60 deg, 90 deg
d	4.5 mm	6.3 mm
Re	10,000	12,000
BR	0.0, 0.2, 0.4	0.0, 0.21

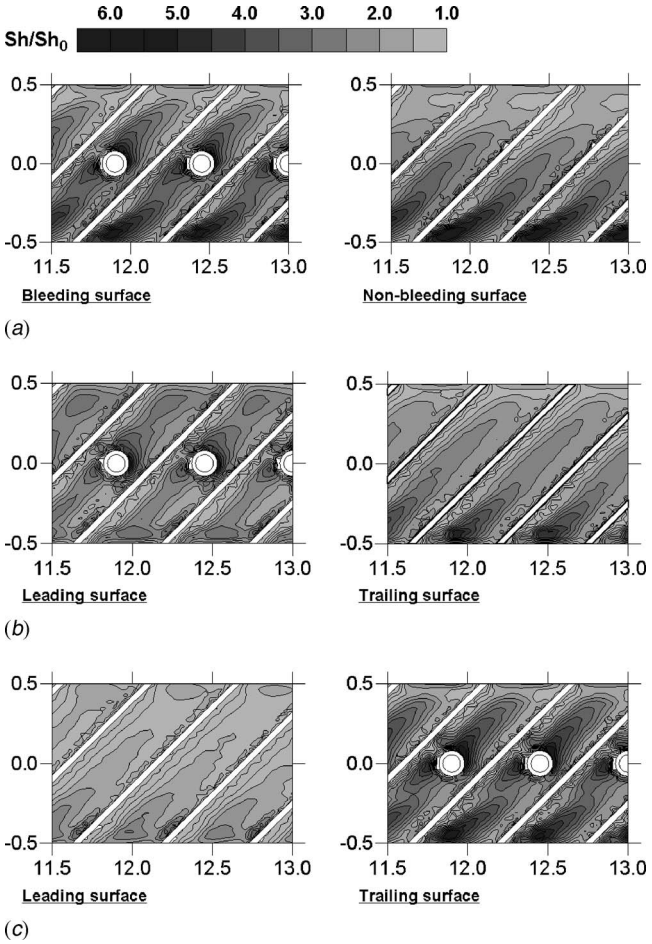

Fig. 7 The local Sh/Sh_0 distributions in the 45 deg angled ribbed channel with bleed flow (BR=0.4): (*a*) Ro=0.0, (*b*) Ro =0.4 (bleeding on the leading surface), and (*c*) Ro=0.4 (bleeding on the trailing surface)

from $y/D_h=0.0$ to 0.5, as shown in Fig. 7(*a*); further, these became narrower, as shown in Fig. 7(*b*). However, because of the decrement in the main flow rate, the Sherwood number ratios were lower than those of Ro=0.0. In the case of bleeding on the trailing surface (Fig. 7(*c*)), due to the bleed flow and Coriolis force, although the low heat/mass transfer regions appeared on the leading surface, the high regions were observed on the trailing surface.

Figure 8 shows the pitch-averaged Sherwood number ratios obtained from the local experimental data among the rib turbulators except for those on the rib surface. The figure presents the averaged heat/mass transfer along the streamwise direction in the whole measured region at each rotation and bleed ratio.

In a stationary channel with the 45 deg angled ribs (Fig. 8(*a*)), the fully developed values of BR=0.0 were higher than the fully developed values in the 90 deg angled ribbed channel (Fig. 5(*a*)) by approximately 18%. In cases with the bleed flow (BR=0.2 and 0.4), the heat/mass transfer in the upstream part ($8.5 \leqslant x/D_h \leqslant 9.5$) of the leading (or bleeding) surface was similar to the case of BR=0.0. In the downstream part ($11.5 \leqslant x/D_h \leqslant 13.5$) of the leading surface, the values were lower than those at BR=0.0. This was because the main flow rate reduced regularly as the flow continued. However, the values on the leading surface were not enhanced by the tripping flow in contrast to the 90 deg angled ribbed cases because of the angled rib-induced secondary flow. However, on the trailing surface, due to the reduction of the main flow, the Sherwood number ratios decreased gradually as the bleed ratios increased.

In the rotating channel with nonbleeding and 45 deg angled ribbed surfaces, the disparity of the heat/mass transfer between the leading and trailing surfaces was smaller than that in the 90 deg angled ribbed rotating channels. In other words, the increase in the rate of the heat/mass transfer on the trailing surface was less than that in the 90 deg angled ribbed cases. This is because the secondary flow induced by the angled rib turbulators was strong. In the case of bleeding on the leading surface (Fig. 8(*b*)), the heat/mass transfer was augmented in the upstream part ($8.5 \leqslant x/D_h \leqslant 9.5$) of the leading surface, but reduced in the downstream part ($11.5 \leqslant x/D_h \leqslant 13.5$) of the leading surface. Similar to the 90 deg angled ribbed channels, as the bleed ratios increased, the heat/mass transfer coefficients on the trailing surfaces were decreased by the reduction of the main flow. In the case of bleeding on the trailing surface (Fig. 8(*c*)), with an increment in the bleed ratio, the heat/mass transfer difference between the leading and trailing surfaces was more increased than that of BR=0.0. This phenomenon was similar to that in the 90 deg ribbed cases.

Figure 9 shows the regional averaged Sherwood number ratios obtained from the local data between $x/D_h=10.5$ and 13.25 except for those on the rib surface. The averaged values taken from the fully developed five pitch regions at each rotation number and bleed ratio. The present data are also compared to averaged heat transfer data obtained by Ekkad et al. [14,22] on the bleed surface in the first pass of the stationary channel with 45 deg ribs. Unlike the 90 deg ribbed case, the averaged values of the present study were higher than data by Ekkad et al. [14,22] and were reduced by bleed flow. For all the tests with angled ribs, with an increment in the rotation number, the decreasing rate of the heat/mass transfer on the leading and trailing surfaces was identical. As the bleed ratio increased, the averaged Sherwood number ratios reduced at a fixed rate. This was because the heat/mass transfer on the ribbed walls is significantly affected by the Coriolis force and main flow rate.

Figure 10 shows the mean Sherwood number ratios of both the leading and trailing surfaces at tested rotation number and bleed ratios. In the stationary cases, the mean values of the 45 deg angled ribbed cases were higher than those of the 90 deg angled ribbed cases because of the strong secondary flow induced by the angled ribs. Except for the 90 deg angled ribbed cases without the bleed flow, as the rotation number increased, the values decreased because of the Coriolis force that disturbed the reattachment of the main flow and the bleeding that reduced the flow rate. For the 90 deg angled ribbed cases without bleed flow, the values increased since the rotation-induced secondary flow enhanced the heat/mass transfer. In particular, in the channel with the 45 deg

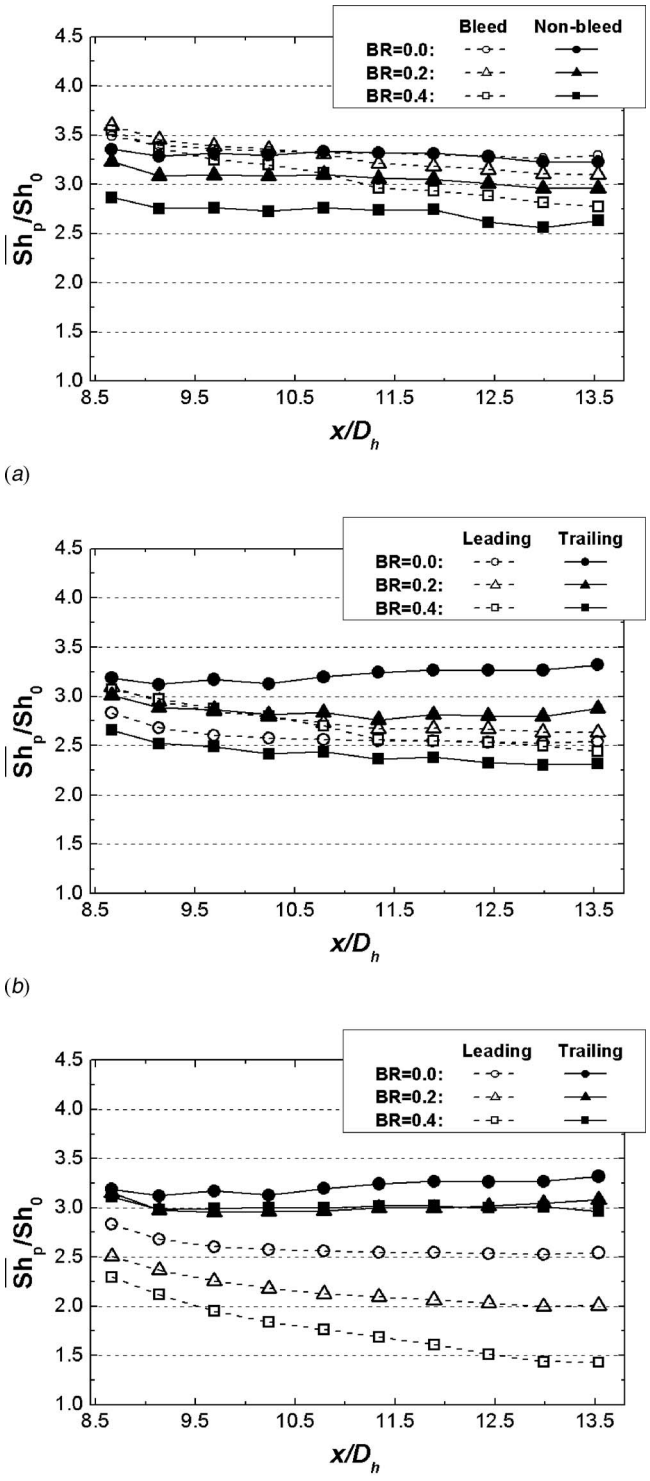

Fig. 8 Pitch averaged Sh/Sh_0 distributions in the 45 deg angled ribbed channel: (*a*) Ro=0.0, (*b*) Ro=0.4 (bleeding on the leading surface), and (*c*) Ro=0.4 (bleeding on the trailing surface)

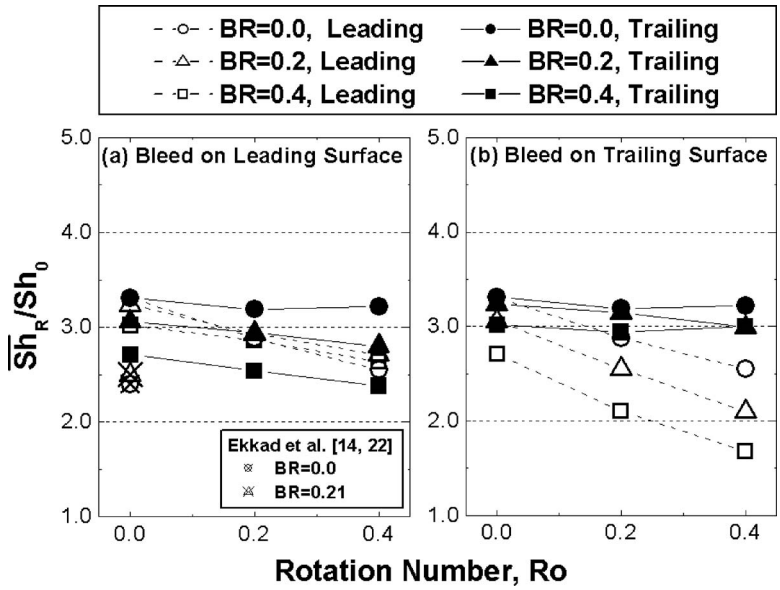

Fig. 9 Regional averaged Sh/Sh_0 ($10.5 \leq x/D_h \leq 13.25$) for all the tests in the 45 deg ribbed channel

angled rib turbulators, for the bleeding on the trailing surface, the higher rotation number or higher bleed ratios decreased the mean values.

Friction Loss and Performance. Figure 11 shows the friction loss results in the form of the friction factor ratios. As the rotation number increased, the friction factors gradually increased in only the 90 deg angled ribbed cases without bleed flow, but decreased in the other cases. This is because the turbulence intensity is strengthened to a greater extent by the rotation-induced secondary flow in cases with transverse ribs and nonbleeding surfaces. However, in cases with bleeding flow and angled ribs, the main flow rate was reduced and the angled rib-induced secondary flow was disturbed by deflection of the core flow. In the case of the bleed flow, the friction factor ratios decreased in all the tested cases. The declination resulted from the reduction of the internal flow due to the bleed flow and reduction in the area (of the bleed holes) where the flow contacted.

Figure 12 shows the thermal performance in the two ribbed channels. The thermal performance with both angled ribs and bleed flow was the highest for all the rotation numbers. This is because the heat/mass transfer was significantly enhanced by the angled rib turbulators and the friction factor decreased with the bleed flow. As the rotation number increased, the thermal performance for all the cases was almost identical even though the heat/mass transfers and the pressure drops were different for each channel.

Conclusions

In the present study, the heat/mass transfer characteristics in rotating angled ribbed channels with the bleed flow were experimentally investigated and compared with the 90 deg angled ribbed cases. The results are summarized as follows.

1. For cases without the bleed flow, the Sherwood number ratios were enhanced by approximately 2.7 and 3.3 times more than Sh_0 due to the transverse and angled ribs, respectively.

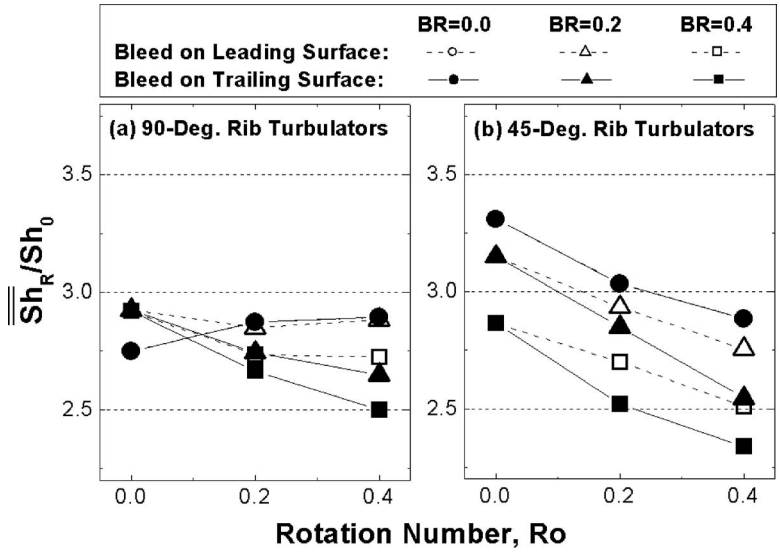

Fig. 10 Mean Sh/Sh_0 of the leading and trailing surfaces

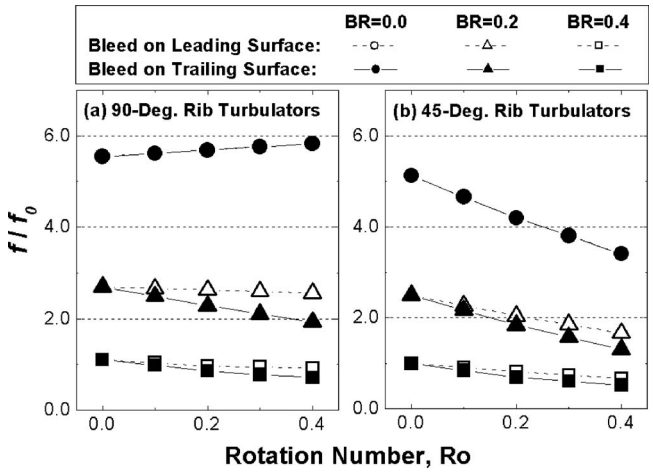

Fig. 11 Friction factor ratios at various rotation numbers

The heat/mass transfer in the 90 deg angled ribbed cases was augmented by the rotation-induced secondary flow; however, it was still almost identical to the 45 deg angled ribbed cases because the angled rib-induced secondary flow was strong.

2. For the cases with the transverse ribs and bleed flow, the Sherwood number ratios on the bleeding surfaces increased with the bleed ratios, but were decreased as the flow direction proceeded. Due to the rotation-induced secondary flow, high values were observed near both the walls while low values were observed in the middle region of the leading surface.
3. For the cases of the 45 deg angled ribs and bleed flow, the heat/mass transfer on the bleeding surface decreased due to the strong rib-induced secondary flow although the bleed ratios increased in contrast with the 90 deg angled ribbed cases. Further, due to the rotation-induced secondary flow, local heat/mass transfer distributions did not appear although the discrepancy between both the surfaces was shown by the deflection of the core flow.
4. The friction factor ratios increased with the rotation number only in cases with the transverse ribs and nonbleeding surfaces due to high turbulence intensity by the Coriolis force. The friction factor ratios decreased in the other cases as the flow rates and flow deflection by the Coriolis force decreased. However, the thermal performance was almost identical for all the rotation number.
5. At the maximum rotation number and bleed ratio under the tested conditions, the 90 deg rib turbulators have a cooling advantage in terms of higher heat transfer; however, the 45 deg rib turbulators have a high performance at the same coolant flow rate. Therefore, the design of the internal cooling passage should be considered with the thermal load, the operating conditions, etc.

Acknowledgment

This work was supported partially by the Korea Energy Management Corporation, through the Energy Technology Development Program.

Nomenclature

- BR = ratio of bleed flow rate to main flow rate
- d = bleed hole diameter
- D_h = hydraulic diameter
- D_{naph} = mass diffusion coefficient of naphthalene vapor in air ($\text{m}^2\ \text{s}^{-1}$)
- e = rib height
- f = friction factor, Eq. (4)
- f_0 = friction factor of a fully developed turbulent flow in a stationary smooth pipe
- h = heat transfer coefficient ($\text{W m}^{-2}\ \text{K}^{-1}$)
- h_m = mass transfer coefficient (m s^{-1})
- H = passage height
- k = thermal conductivity of coolant ($\text{W m}^{-1}\ \text{K}^{-1}$)
- $\dot{m}$ = local naphthalene mass transfer rate per unit area ($\text{kg m}^{-2}\ \text{s}^{-1}$)
- Nu = Nusselt number, hD_h/k
- p = rib-to-rib pitch
- p_h = hole to hole pitch
- Pr = Prandtl number, $\mu C_p/k$
- R = maximum radius of rotating arm
- Re = Reynolds number, $D_h u_b/\nu$
- Ro = rotation number, $D_h\Omega/u_b$
- Sc = Schmidt number, ν/D_{naph}
- Sh = Sherwood number, $h_m D_h/D_{\text{naph}}$

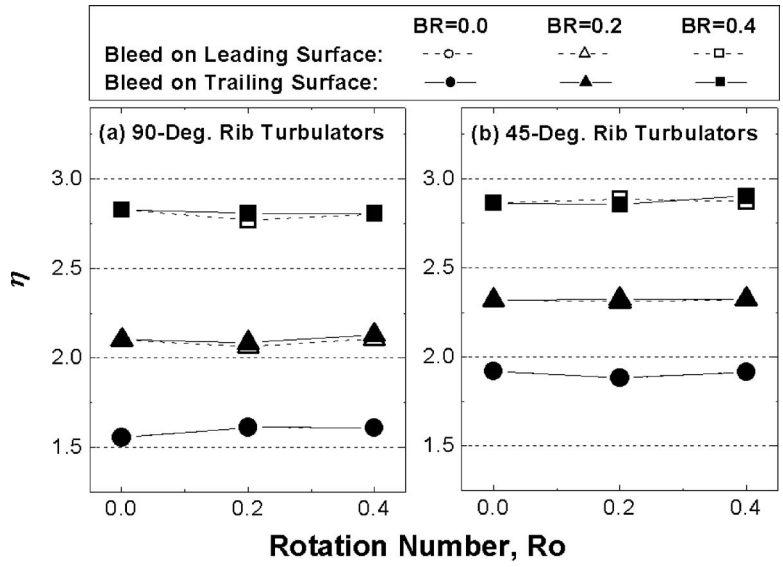

Fig. 12 Thermal performance for all tests

Sh_0 = Sherwood number of a fully developed turbulent flow in a stationary smooth pipe, Eq. (3)

$\overline{\mathrm{Sh}_0}$ = pitch averaged Sherwood number, $\int_{x_1}^{x_2}\int_{-W/2}^{W/2}\mathrm{Sh}\, dydx / \int_{x_1}^{x_2}\int_{-W/2}^{W/2} dydx$

$\overline{\mathrm{Sh}_R}$ = Sherwood number averaged over several pitches

$\bar{\overline{\mathrm{Sh}}}_R$ = mean $\overline{\mathrm{Sh}}_R$ of both the leading and trailing surfaces

u_b = passage averaged bulk velocity (m s^{-1})

W = passage width

x = coordinate and distance in the streamwise direction

y = coordinate and distance in the lateral direction

z = coordinate and distance in the vertical direction

α = attack angle of rib turbulator

Δt = runtime

Δz = sublimation depth of naphthalene surface

μ = dynamic viscosity (kg m^{-1} s^{-1})

ν = kinematic viscosity (m^2 s^{-1})

η = thermal performance, Eq. (5)

ρ_s = density of solid naphthalene (kg m^{-3})

$\rho_{v,b}$ = bulk vapor density of naphthalene (kg m^{-3})

$\rho_{v,w}$ = vapor density of naphthalene on the surface (kg m^{-3})

Ω = angular velocity (rad s^{-1})

References

[1] Han, J. C., Glicksman, L. R., and Rohsenow, W. M., 1978, "An Investigation of Heat Transfer and Friction for Rib-Roughened Surfaces," Int. J. Heat Mass Transfer, **21**, pp. 1143–1156.

[2] Kukreja, R. T., Lau, S. C., and McMillin, R. D., 1993, "Local Heat/Mass Transfer Distribution in a Square Channel With Full and V-Shaped Ribs," Int. J. Heat Mass Transfer, **36**, pp. 2013–2020.

[3] Agliga, D. A., 1994, "Convective Heat Transfer Distributions Over Plates With Square Ribs From Infrared Thermography Measurements," Int. J. Heat Mass Transfer, **36**(3), pp. 363–374.

[4] Acharya, S., Myrum, T., Qiu, X., and Sinha, S., 1997, "Developing and Periodically Developed Flow, Temperature and Heat Transfer in a Ribbed Duct," Int. J. Heat Mass Transfer, **40**, pp. 461–479.

[5] Astarita, T., Cardon, G., and Carlomagno, G. M., 1998, "Average Heat Transfer Measurements Near a Sharp 180 Degree Turn Channel for Different Aspect Ratios," *IMechE Conference Trans.: In Optical Methods and Data Processing in Heat and Fluid Flow*, London, pp. 137–146.

[6] Metzger, D. E., and Vedula, R. P., 1987, "Heat Transfer in Triangular Channels With Angled Roughness Ribs on Two Walls," Exp. Heat Transfer, **1**(1), pp. 31–44.

[7] Yang, W.-J., Zhang, N., and Chiou, J., 1992, "Local Heat Transfer in a Rotating Serpentine Flow Passage," ASME J. Heat Transfer, **114**, pp. 354–361.

[8] Iacovides, H., Jackson, D. C., Kelemenis, G., Launder, B. E., and Yuan, Y. M., 1999, "Experiments on Local Heat Transfer in a Rotating Square-Ended U-bend," Int. J. Heat Fluid Flow, **20**, pp. 302–310.

[9] Dutta, S., and Han, J. C., 1996, "Local Heat Transfer in Rotating Smooth and Ribbed Two-Pass Square Channels With Three Channel Orientations," ASME J. Heat Transfer, **118**, pp. 578–576.

[10] Murata, A., and Mochizuki, S., 1999, "Effect of Cross-sectional Aspect Ratio on Turbulent Heat Transfer in an Orthogonally Rotating Rectangular Smooth Duct," Int. J. Heat Mass Transfer, **42**, pp. 3803–3814.

[11] Taslim, M. E., Li, T., and Spring, S. D., 1995, "Experimental Study of the Effects of Bleed Holes on Heat Transfer and Pressure Drop in Trapezoidal Passages With Tapered Turbulators," ASME J. Turbomach., **117**, pp. 281–289.

[12] Shen, J. R., Wang, Z., Ireland, P. T., Jones, T. V., and Byerley, A. R., 1996, "Heat Transfer Enhancement Within a Turbine Blade Cooling Passage Using Ribs and Combinations of Ribs With Film Cooling Holes," ASME J. Turbomach., **118**, pp. 428–434.

[13] Thurman, D., and Poinastte, P., 2001, "Experimental Heat Transfer and Bulk Air Temperature Measurements for a Multipass Internal Cooling Model With Ribs and Bleed," ASME J. Turbomach., **123**, pp. 90–96.

[14] Ekkad, S. V., Huang, Y., and Han, J. C., 1998, "Detailed Heat Transfer Distributions in Two-Pass Square Channels With Rib Turbulators and Bleed Holes," Int. J. Heat Mass Transfer, **41**, pp. 3781–3791.

[15] Kim, K. M., Kim, S. I., Jeon, Y. H., Lee, D. H., and Cho, H. H., 2007, "Detailed Heat/Mass Transfer Distributions in a Rotating Smooth Channel With Bleed Flow," ASME J. Heat Transfer, **129**(11), pp. 1538–1545.

[16] Jeon, Y. H., Park, S. H., Kim, K. M., Lee, D. H., and Cho, H. H., 2007, "Effects of Bleed Flow on Heat/Mass Transfer in a Rotating Rib-Roughened Channel," ASME J. Turbomach., **129**(3), pp. 636–642.

[17] Ambrose, D., Lawrenson, I. J., and Sparke, C. H. S., 1975, "The Vapor Pressure of Naphthalene," J. Chem. Thermodyn., **7**, pp. 1173–1176.

[18] Goldstein, R. J., and Cho, H. H., 1995, "A Review of Mass Transfer Measurements Using Naphthalene Sublimation," Exp. Therm. Fluid Sci., **10**, pp. 416–434.

[19] Kline, S. J., and McClintock, F. A., 1953, "Describing Uncertainty in Single-Sample Experiments," Mech. Eng. (Am. Soc. Mech. Eng.), **75**, pp. 3–8.

[20] McAdams, W. H., 1942, *Heat Transmission*, 2nd ed., McGraw-Hill, New York.

[21] Petukhov, B. S., 1970, *Advances in Heat Transfer*, Vol. 6, Academic, New York, Vol. 6, pp. 503–504.

[22] Ekkad, S. V., and Han, J. C., 1997, "Detailed Heat Transfer Distributions in Two-Pass Square Channels With Rib Turbulators," Int. J. Heat Mass Transfer, **40**, pp. 2525–2537.

O. Schennach

R. Pecnik

Institute for Thermal Turbomachinery and
Machine Dynamics,
Graz University of Technology,
Graz 8010, Austria

B. Paradiso

Laboratorio di Fluidodinamica delle Macchine,
Dipartimento di Energetica,
Politecnico di Milano,
20133 Milano, Italy

E. Göttlich

A. Marn

J. Woisetschläger

e-mail: jakob.woisetschlaeger@tugraz.at

Institute for Thermal Turbomachinery and
Machine Dynamics,
Graz University of Technology,
Graz 8010, Austria

The Effect of Vane Clocking on the Unsteady Flow Field in a One-and-a-Half Stage Transonic Turbine

The current paper presents the results of numerical and experimental clocking investigations performed in a high-pressure transonic turbine with a downstream vane row. The objective was a detailed analysis of shock and wake interactions in such a 1.5-stage machine while clocking the vanes. Therefore, a transient 3D Navier–Stokes calculation was done for two clocking positions, and the three-dimensional results are compared with laser-Doppler-velocimetry measurements at midspan. Additionally, the second vane was equipped with fast response pressure transducers to record the instantaneous surface pressure for 20 different clocking positions at midspan. [DOI: 10.1115/1.2777199]

Introduction

To meet the objective of reduced costs and more compactness of turbomachinery, it is advantageous to reduce the number of stages resulting in high-pressure (HP) ratios and transonic conditions for these stages. To keep the efficiency at a high level, a detailed understanding of the unsteady flow is necessary.

The flow unsteadiness in turbomachinery is highly related to the vane-rotor motion and the wake-wake interaction. Additionally, in HP low-aspect-ratio turbines the secondary flows, strong potential fields and trailing edge shocks must be taken into account. These effects cause a time-varying, nonuniform flow field downstream of the stage affecting the performance and boundary layer of the next vane row [1–3].

Hummel [4] performed a two-dimensional numerical simulation of a single stage HP turbine and provided a guideline for positioning a second vane in order to minimize the effect of the trailing edge shock strength onto the second vane.

The basic idea of clocking (also known as indexing) is to improve the overall efficiency by varying the circumferential and/or the axial position of adjacent vanes or blades. The most common method is to rotate the nozzle ring with respect to a downstream vane row, while the largest efficiency increase is achieved with equal blade counts. It is well known that a maximum of efficiency is achieved when the first vane's wake impinges the leading edge of the second vane.

Much research work has been performed to investigate the influence of clocking in subsonic turbines. Experimental results reported by Huber et al. [5] for a two-stage turbine showed a 0.8% efficiency variation at midspan due to clocking of the second stage vane. Time accurate numerical studies by Arnone et al. [6] in a three-stage low-pressure (LP) turbine showed a 0.7% efficiency variation due to clocking. Furthermore, different investigated Reynolds numbers showed no major difference in the results. Reinmöller et al. [7] investigated the influence of clocking on the flow field between rotor and second vane as well as downstream the second vane using hot wire probes and pneumatic probes supported by numerical simulations. The authors found 1% relative efficiency variation at midspan.

Recent research work focuses on clocking effects in transonic turbines. Billiard et al. [8] focused on the heat transfer measurements on the second vane in a 1.5-stage HP turbine. It was found that clocking changes the mean levels of the heat transfer as well as the intensity and the trajectory of the fluctuations. Gadea et al. [9] investigated the influence of clocking on the time resolved pressure field of a second vane tested in a 1.5-stage HP turbine. It was shown that the optimum clocking position (CP) for aerodynamics is not the optimum for minimum unsteady forces. Haldeman et al. [10] performed aerodynamic measurements in 1.5-stage HP turbine indicating an overall efficiency increase of about 2%–3% using a variety of independent methods.

The current paper focuses on the propagation of shock waves and their interactions at midspan of a highly loaded low-aspect-ratio transonic turbine stage with respect to different CPs. An unsteady three-dimensional Navier–Stokes calculation was used to discuss the interaction mechanism in detail. Two circumferential measurement lines (gained with laser-Doppler velocimetry (LDV)) are used to validate the prediction. Furthermore, fast response surface-pressure measurements on the second vane were performed in order to get a better insight into the clocking phenomena. The experimental investigations were performed under engine representative conditions in a continuously running cold-flow test facility of the Institute.

Contributed by the International Gas Turbine Institute of ASME for publication in the JOURNAL OF TURBOMACHINERY. Manuscript received June 8, 2007; final manuscript received June 20, 2007; published online May 7, 2008. Review conducted by David Wisler. Paper presented at the ASME Turbo Expo 2007: Land, Sea and Air (GT2007), Montreal, Quebec, Canada, May 14–17, 2007. Paper No. GT2007-27848.

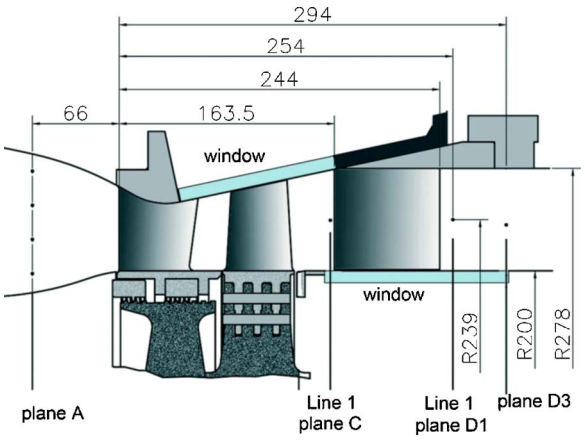

Fig. 1 Meridional flow path with LDV measurement positions in planes *C* and *D*1. In planes *A* and *D*3, probes were placed (measurement positions indicated by dots).

Experimental Facility and Instrumentation

Test Facility. The transonic test turbine at the Institute for Thermal Turbomachinery and Machine Dynamics is a continuously operating cold-flow open-circuit facility that allows the testing of turbine stages with a diameter of up to 800 mm in full flow similarity (corrected speed and pressure ratio). The turbine is driven by pressurized air, which is delivered by a separate 3 MW compressor station. A brake compressor delivers additional air mixed to the flow from the compressor station and increases the overall mass flow. The air temperature in the mixing chamber (turbine stage inlet) can be adjusted by coolers between 40°C to 185°C. The maximum shaft speed of the test rig is limited to 11,550 rpm. Depending on the stage characteristic, a maximum coupling power of 2.8 MW at a total mass flow of 22 kg/s can be reached. Detailed information on the design and construction of the facility can be found in Ref. [11] on the operation in Ref. [12].

Turbine Stage Tested. The meridional section of the turbine stage is given in Fig. 1. To provide access for all types of optical measurements, the hub contour is cylindrical while the shroud contour is conical in the rotor section. The second vane has a simple cylindrical contour and is designed as a LP vane to prevent condensation. Downstream of the second vane row, a deswirler takes out the circumferential velocity and reduces flow velocity and therefore exhaust losses (not shown in Fig. 1).

The optical access is realized with two glass windows upstream and downstream of the second vane row. The gaps between rotor blade tip and casing as well as the clearance of the second vane to the hub are 1 mm.

To allow a rotor-phase-resolved analysis of the measured velocities, a reference signal provided by the monitoring system of the turbine was used to trigger the data sampling (uncertainty: blade pitch/300, a phase delay depending on speed was accounted for). Some important operating conditions for this investigation and the geometrical data of the stage are given in Table 1.

Laser-Doppler Velocimetry. The velocity measurement in the flow field was performed by a two-component LDV system. The measurements were performed for two different CPs upstream of the second vane row and for ten different CPs downstream of the second vane row.

The discussion of the LDV data in this paper focuses onto CP1 and CP6. Figure 2 shows the investigated CPs as well as the LDV measurement locations upstream and downstream of the second vane row. To validate the computational fluid dynamics (CFD) prediction, a measurement line 3 mm upstream of the leading edge and a measurement line 10 mm downstream the trailing edge are used. Each circumferential line consists of 20 measurement positions and covers one vane pitch. A more detailed description of the optical setup and the measurement uncertainty is given in Ref. [13].

Table 1 Stage geometrical data and operating conditions

Number of nozzle guide vanes	24
Number of rotor blades	36
Number of second guide vanes	24
Nozzle chord (midspan) (mm)	78.9
Nozzle axial chord (midspan) (mm)	56.1
Geometric turning angle nozzle (deg)	70
Nozzle aspect ratio (exit height/chord)	0.70
Blade chord (midspan) (mm)	55.9
Blade axial chord (midspan) (mm)	46.8
Geometric turning angle blade (deg)	107
Blade aspect ratio (exit height/chord)	1.24
Second vane chord (midspan) (mm)	88.3
Second vane axial chord (midspan) (mm)	80.1
Geometric turning angle second vane (deg)	53
Second vane aspect ratio (exit height/chord)	0.88
Rotor tip clearance/span (%)	1.4
Second vane hub clearance/span (%)	1.3
First vane-blade spacing (% nozzle axial chord (midspan))	47
Blade–second-vane spacing (% blade axial chord (midspan))	73
Pressure ratio p_{tA}/p_C	3.30
Pressure ratio p_{tA}/p_{D3}	4.27
Rotational speed (rpm)	10,600
Inlet total temperature T_{tA} (K)	413
Reynolds number nozzle guide vane exit	2.57×10^6
Reynolds number rotor blade exit	1.69×10^6
Isentropic first vane exit Mach number	1.13
Blade outlet Mach number, midspan	0.51
Relative blade outlet Mach number, midspan	0.87
Second vane outlet Mach number	0.69
Loading factor $\Delta h/u^2$	1.51

Surface-Pressure Instrumentation. The instantaneous surface pressure on the second stator was measured with three fast response pressure transducers Entran EPIH-213-3,5B, which were embedded underneath a small tap of 0.8 mm diameter and 0.2 mm

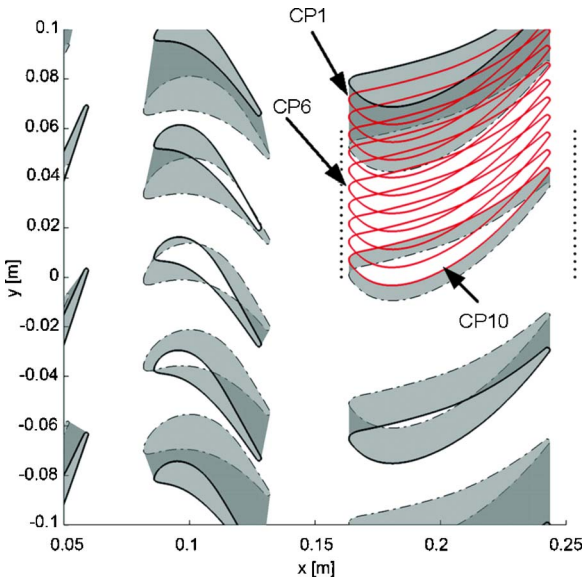

Fig. 2 LDV measurement positions at midspan together with the CP investigated (CP1–CP10)

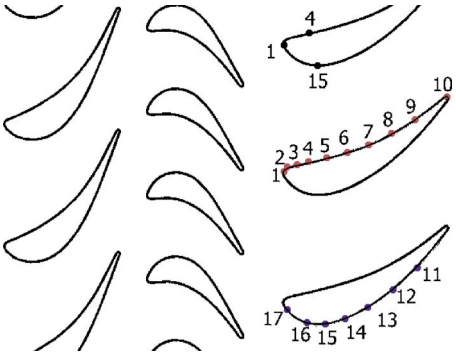

Fig. 3 Static pressure taps at midspan; additionally, measurement locations 1, 4, and 15 were equipped with fast response pressure transducers

depth. The amplified sensor signals and the trigger signal provided by the shaft monitoring system were fed to a National Instrument 4551 dynamic signal analyzer board (16 bit resolution, intern antialiasing filter). With a blade passing frequency of 6.4 kHz and a sample frequency of 204.8 kHz, the average number of samples acquired per rotor blade passages is 32. The instantaneous pressure was ensemble averaged over 535 rotor revolutions (20 evaluation windows sections within 10 deg blade pitch) [14].

The steady static pressure taps were connected to a PSI intelligent pressure transducer with an accuracy of 0.05% full scale (FS) (FS: 2.1 bars; sensor 1, 2, and 17: FS 0.35 bar). The locations of the pressure taps as well as of the fast response pressure transducers are shown in Fig. 3.

Unsteady Three-Dimensional Navier–Stokes Simulation

The computations were performed using the in-house Navier-Stokes code LINARS, developed at Graz University of Technology [15,16].

The compressible Reynolds/Favre-averaged Navier–Stokes (RANS) equations are solved in conservative form by means of a fully-implicit time-marching finite-volume method on structured curvilinear grids in multiblock alignment. The inviscid (Euler) fluxes are discretized with the upwind flux-difference splitting method of Roe [17]. In order to achieve a high order of spatial accuracy, a total variation diminishing (TVD) scheme with third-order interpolation was applied to get the state vector at each cell interface. The viscid flux vector at the cell interfaces is constructed with a second-order accurate central-differencing scheme using Green's theorem. To obtain a linear set of the time dependent Navier–Stokes equations, a second-order accurate Newton–Raphson procedure is applied for the discretization in time. At the left-hand side of the equation system, the inviscid fluxes are treated with first-order accuracy and the viscid fluxes with a thin-layer approximation to obtain a block-tridiagonal matrix for each grid index line. This linear equation set is solved by the alternating direction implicit (ADI) scheme. To cope with unequal pitch ratios, the code uses phase-lagged boundary conditions by means of a direct store technique at geometrical periodic boundaries, and hence, only one passage each blade row was simulated with a total of $\sim 2 \times 10^6$ cells. In this work, one blade passing period was calculated with 480 time steps for the rotor and 320 time steps for both stator passages. Furthermore, to save computational time and memory, pressure gradient wall functions based on the law-of-the-wall formulation by Spalding were used [18]. The turbulence was calculated using the one equation turbulence model of Spalart and Allmaras [19].

The geometrical details of the turbine stage containing the fillets and the rotor tip clearance were modeled as well (see Fig. 4). The clearance of the second vane to the hub was not modeled. In Fig. 7, the visualization was done with an in-house postprocessing tool, where the instantaneous flow field was discussed by means of the magnitude of the pressure gradient and the radial vorticity.

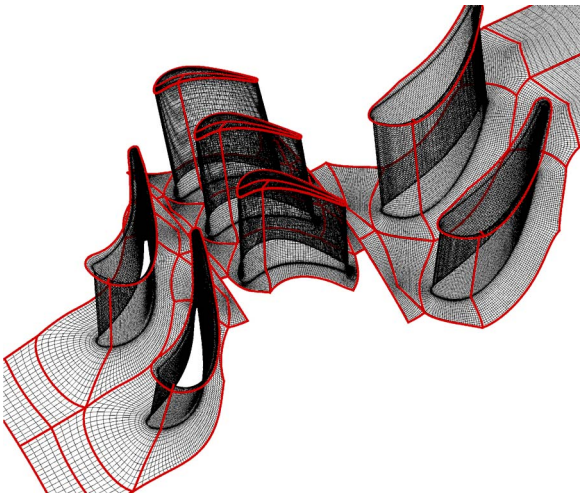

Fig. 4 Computational grid. The picture shows the surface mesh of the computational grid used for CFD. The fillets between blade-hub and blade–outer-casing and the rotor blade clearance are meshed to match the geometrical details of the test turbine facility.

Results and Discussion

Validation of the Numerical Scheme. The LDV-measurement line 1 in plane *C* and the LDV-measurement line 1 in plane *D*1 (see Fig. 1) were used to validate the CFD predictions. Figure 5 presents the time-averaged velocity and the instantaneous data in terms of maximum-minimum envelopes at measurement line 1 (close to the second vane leading edge) for both CPs.

The wake from the nozzle guide vane impinges the second vane's leading edge for CP6. Therefore, close to the leading edge, a 23% decrease of the time-averaged velocity is predicted, while with LDV, only 6% decrease was observed.

At CP6, the passing of the first vane wake segments causes lower velocity fluctuations (maximum and minimum envelope) close to the leading edge compared to CP1. This difference is much more pronounced in the prediction.

The use of the Spalart–Allmaras turbulence model results in lower wake mixing effects, and thus, lower wake velocities are predicted compared to LDV. This is visible by the minimum velocity envelopes at the leading edge for both CPs, provoked by the time-periodic rotor wake passing.

Furthermore, it can be seen that the largest deviations between CFD and LDV occur where the first vane wake influences the flow field, for CP1 at vane pitch 1.2 and for CP6 at vane pitch 0.7.

The time-averaged velocity magnitude and the velocity envelopes downstream of the second vane are shown in Fig. 6. The prediction and the measurement indicate a significant decrease of the velocity in the second vane wake for CP6. In contrast to Fig. 5, the numerical simulation shows higher velocities in the wake. It is believed that the hub leakage flow (not modeled in the CFD calculation) and a periodic boundary layer separation (not captured in the CFD) cause this difference. This could also explain the large fluctuations in the second vane wake observed in the measurements. The overall agreement between prediction and measurement is satisfactory.

Vane-Rotor-Vane Interaction Mechanism. The HP ratio of the investigated turbine stage caused a pronounced shock system, especially at the nozzle guide vane outlet. Considerable insight into the flow field can be obtained by numerical simulation. Figure 7(*a*) presents contour plots of the radial vorticity and isolines

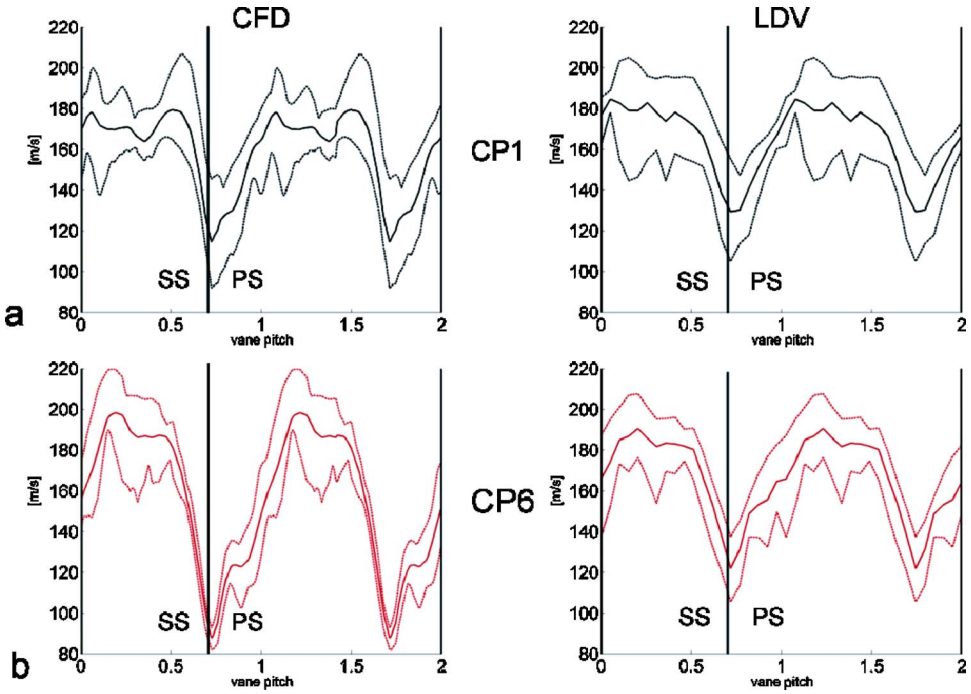

Fig. 5 Comparison of CFD (left) and LDV (right): Time-averaged and maximum-minimum envelope of the velocity magnitude for (*a*) CP1 and (*b*) CP6 (optimum CP); plane *C*, line 1, 3 mm upstream the second vane

of the pressure gradient for CP1 at midspan. Eight frames are shown corresponding to one blade passing period τ. Please note the vane to blade ratio of 2:3 and the related spatial periodicity (e.g., Fig. 7, $t/\tau=0$ and $t/\tau=0.5$; flow similarity for neighboring vanes).

At $t/\tau=0.5$, the suction side trailing edge shock of the nozzle guide vane "24" impinges at the suction side of rotor blade "1". At $t/\tau=0.625$, the reflected shock "A" moves upstream, and at $t/\tau=0.875$, the shock wave reaches the pressure side of blade "2" and is reflected again toward the blade suction side (marked with "B").

The reflected shock A propagates upstream ($t/\tau=0$ to $t/\tau=0.5$)

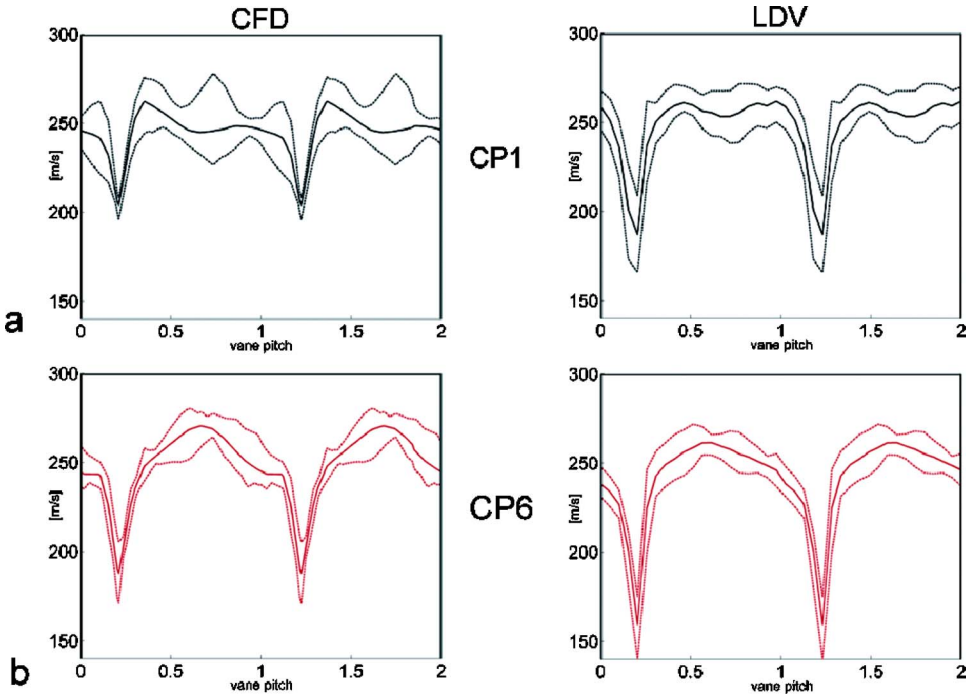

Fig. 6 Comparison of CFD (left) and LDV (right): Time-averaged velocity magnitude and maximum-minimum envelope of the velocity magnitude for (*a*) CP1 and (*b*) CP6; plane *D*, line 1, 10 mm downstream of the second vane

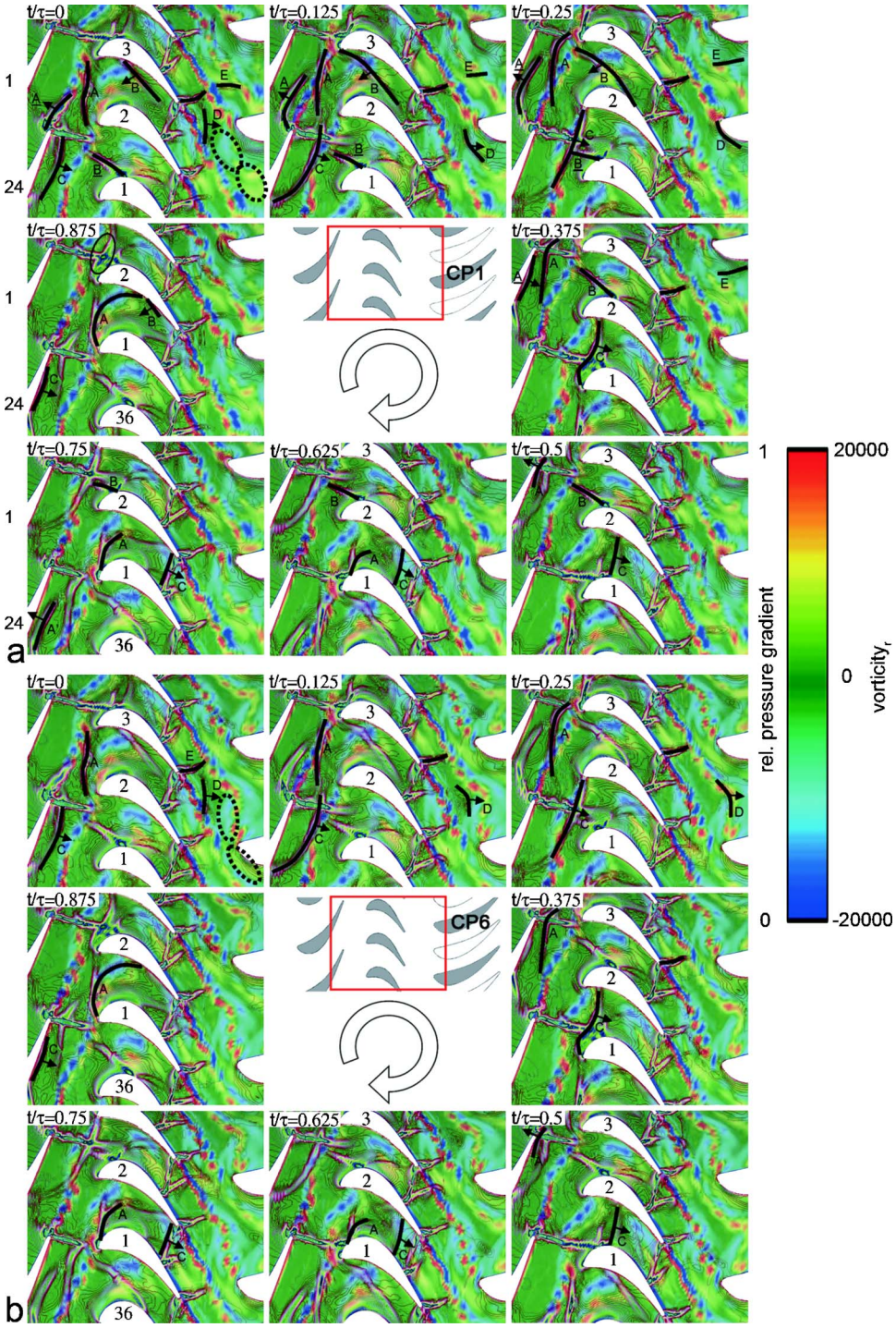

Fig. 7 Contour plot of radial vorticity and isolines of pressure gradient magnitude for (*a*) CP1 and (*b*) CP6 obtained by CFD

and interferes destructively with a previously shock wave "A" at approximately $t/\tau=0.5$. Hence, a part of the reflected shock A impinges weakly on the suction side of the nozzle guide vane 1 at $t/\tau=0.5$ and enforces a vortex separation. From then on, the vortex shedding is undisturbed until the next reflected shock wave triggers again. This shock wave induced phase locking phenomenon was explained in detail by Göttlich et al. [20].

The other part of shock wave A impinges more strongly at the suction side of the nozzle guide vane 2 (not shown in Fig. 7(*a*), or rather at vane 24 at $t/\tau=0.75$) and is reflected again ($t/\tau=0.875$, marked with "C"). The shock wave C propagates downstream ($t/\tau=0$ to $t/\tau=0.25$) and interacts first with the shock wave "B" at $t/\tau=0.375$ and interacts afterward with the trailing edge shocks at approximately $t/\tau=0.75$. The resulting weak shock wave marked with "D" propagates downstream and impinges the leading edge of the second vane for CP1 ($t/\tau=0.25$).

A modulation of the rotor's trailing edge shocks with respect to the circumferential position is clearly visible in Fig. 7. At axial positions where the rotor wakes and the suction side trailing edge shocks "E" interact, a shock weakening is observed. Hummel [4] explained this by a splitting of the shocks due to shock modula-

tions induced by the vane wake in the relative frame of reference. There, the author suggested positioning a second vane at this axial distance to reduce the impact of the shocks onto the leading edge. Since Hummel [4] investigated a single stage turbine, the influence of a second vane onto the shock strength was not discussed. In this work, the second vane was positioned at the appropriate position where rotor trailing edge shocks and rotor wakes interact.

For CP1, the suction side trailing edge shock E impinges at the suction side of the second vane and sweeps toward the leading edge of the second vane.

Furthermore, in Fig. 7, vorticity contour plots are used to identify the nozzle guide vane wakes as well as the rotor wakes. The nozzle guide vane vortex street is chopped by the rotor and is then convected through the rotor passage (details of wake-blade interactions are given by Hodson and Dawes [21]). The counter-rotating nozzle wakes modulate the strength of the shedding rotor vortices [4,20]. At CP1, these interfering wake segments convect between two vanes of the second vane row, whereas at CP6, the first vane wakes impinge onto the leading edge of the second vane (see Figs. 7(*a*) and 7(*b*), $t/\tau=0$, wake segments are marked by circles).

Effect of Clocking on the Shock Wave Propagation. The flow field of the optimum, CP6, is given in Fig. 7(*b*). The interaction of the induced static pressure field of the second vane with the total pressure field at rotor exit has a minor effect on the trailing edge shocks close to the rotor exit.

Miller et al. [22] performed time resolved rotor surface-pressure measurements in a transonic turbine stage. The authors found that the influence of a second vane only affects the rear part of the blade suction side. Therefore, upstream of the pressure side trailing edge shock, the instantaneous flow field is identical for both CPs.

At CP6, the rotor's suction side trailing edge shock close to the second vane is diminished as a result of the favorable interaction of the total pressure field at rotor exit and the potential field of the second vane. Therefore, at CP6, the boundary layer of the second vane is less disturbed by shocks compared to CP1. Furthermore, as previously discussed for CP1, the weak pressure wave D propagates through the midchannel of the second vanes.

Second Vane Surface-Pressure Measurements. Surface-pressure measurements were conducted at midspan for 20 different CPs for steady pressure taps as well as for the fast response pressure instrumentation. Figure 8 presents the steady surface-pressure distribution for CP1 and CP6. A high acceleration on the suction side up to position 15 (see Fig. 3), followed by a velocity decrease toward the trailing edge, is observed.

Note that clocking mainly affects the region close to the leading edge up to 15% axial chord; from then on, clocking does not affect the pressure distribution. At the measurement location close to the stagnation point (position 1), a decrease in surface pressure of ~3.4% is observed for the optimum, CP6.

For three positions at midspan, unsteady pressure fluctuations were recorded by surface-pressure transducers for 20 CPs (Fig. 9, half steps for the ten CPs shown in Fig. 2). Different CPs were investigated by rotating the first vane row, while the second vane row remained at a fixed position. Therefore, circumferential flow nonuniformities originating from the turbine inlet have no influence on the pressure data.

Figure 9 presents time-space plots of the periodic component of the ensemble-averaged pressure (ensemble-averaged pressure minus time mean) for sensor locations 1, 4, and 15. In Fig. 9, time is given in terms of blade passing period; along the ordinate, the different CPs can be found. The pressure data in Figs. 9 and 10 is normalized by the maximum pressure fluctuation for CP8 at the stagnation point.

The time signal for each CP was shifted so that the rotor phase is related to the first vane position. In this diagram, effects from the bypassing rotor blades appear as diagonal structures, whereas

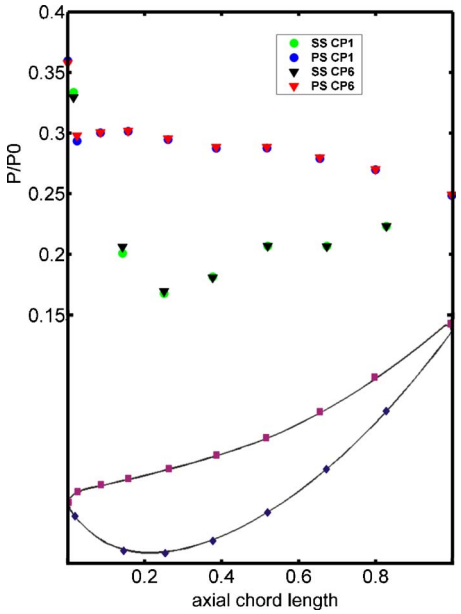

Fig. 8 Steady surface-pressure distribution for CP1 and CP6 at midspan

effects from the first stator are horizontal.

These results are supported by the efficiency recordings at midspan for the CPs presented by Schennach et al. [13]. On the left side of Fig. 9, the relative total-to-total efficiency (based on the area averaged stagnation values in planes *A* and *D*3, see Fig. 1) is used to quantify the clocking effect close to midspan. Traversing was performed by rotating both vane rows and consists of 40 measurement positions over one vane pitch.

The relative efficiency shows a broad maximum from CP4 to CP6 and corresponds to the CPs with the lowest pressure fluctuations at the stagnation point. From CP8 to CP5, the pressure fluctuation amplitude decreases by roughly 84%. For the optimum, CP6, a pressure fluctuation amplitude decrease of 38% is found compared to CP1.

These experimental findings also support the numerical simulations. Note that close to CP6, the chopped first stator wake segments impinge in the vicinity of the second vane leading edge resulting in lower pressure fluctuations due the fact that these vortex segments transport low-speed fluid material.

This observation was also confirmed by the LDV measurements 3 mm upstream of the leading edge for CP1 and CP6. From CP1 to CP6, the maximum envelope of the velocity close to the leading edge decreases about 11%, whereas the minimum envelope remains nearly constant, see Fig. 5.

The time-space plots of the pressure side and the suction side pressure recordings show less surface-pressure fluctuations, which are mainly caused by the negative jet effect of the rotor wakes. This effect is provoked by the rotor wake passing and introduces two regions of secondary circulations transporting fluid material from the pressure to the suction side of the second vane. This results in periodic changes of the surface pressure, while the rotor wakes convect with the main flow [21].

At the optimum, CP6, a pressure amplitude increase of 96% on the suction side transducer is observed compared to CP1. This is in good agreement with Gadea et al. [9]. They found experimentally that the optimum CP for aerodynamics is not the optimum for minimum unsteady forces. On the other hand, the pressure side transducer gives 16% lower pressure fluctuations at CP6 compared to CP1. Note that at the pressure side transducer, only smooth pressure variations are found at all CPs, indicating less shock activity. However, this is not the case for the suction side

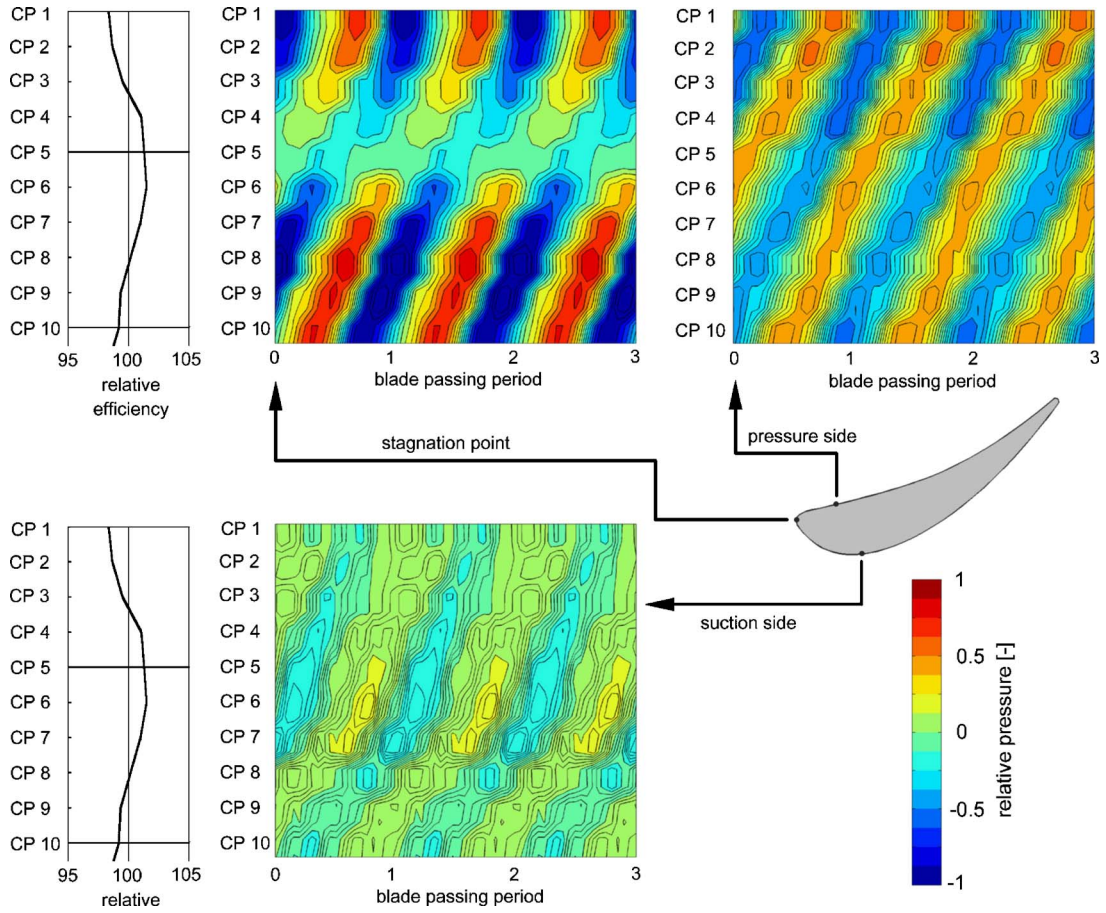

Fig. 9 Second vane pressure fluctuations at three different measurement locations at midspan for different CPs. These fluctuations are compared to the relative efficiency at midspan. Time is given in terms of blade passing period.

transducer.

The pressure fluctuations for CP1 and CP6 at the suction side transducer are shown in Fig. 10. At the optimum, CP6, the pressure fluctuation is smoother than at CP1. This observation is confirmed by the CFD prediction, where at CP1, the trailing edge shocks sweep toward the leading edge of the second stator (see Fig. 7(*a*)). On the other side, at CP6, less shock activity was found in the prediction (see Fig. 7(*b*)).

However, the CFD predicts pressure fluctuations on the suction side sensor location with a 44% lower amplitude for CP6 compared to CP1. On the other hand, at the pressure side and stagnation point sensor location, a fluctuation amplitude decrease of 45% and, respectively, of 56% were predicted for CP6 compared to CP1 and are in good agreement with the experiment.

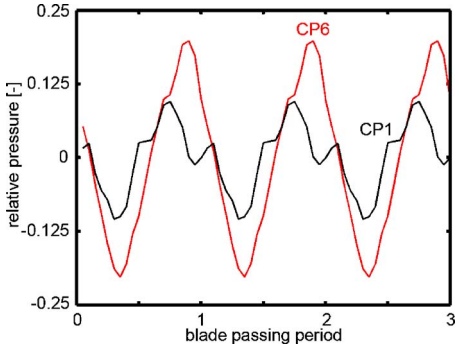

Fig. 10 Pressure fluctuations on the suction side transducer for CP1 and CP6

The investigations in this paper focused on the midspan. Due to the low-aspect-ratio turbine, the three-dimensional effects have a major influence on the clocking phenomena. Please note that due to the simple design of the second vane, the optimum CP changes over the span. Future work is necessary to understand the influence of the secondary flows on the clocking effect.

Conclusions

In the presented paper, vane clocking in a 1.5-stage transonic turbine was investigated using an unsteady three-dimensional Navier-Stokes simulation and fast response pressure transducers at the second vane surface. Two selected CPs were discussed in detail, with special focus on the midspan. The CFD prediction was compared with LDV results at midspan and showed good overall agreement.

A detailed discussion of the shock interaction mechanism with respect to clocking was given. It was found that clocking has a minor influence on the trailing edge shocks close to the rotor exit. While in LP turbines the dominant clocking mechanism is the wake-blade interaction, in transonic turbines, shock waves must be taken into account.

In the optimum CP (CP6), a decreased time-averaged velocity close to the leading edge of the second vane was observed. Additionally, a pressure fluctuation amplitude decrease by roughly 38% at the leading edge was found in the experiment compared to CP1, whereas the CFD predicted a 56% decrease in amplitude at

the same position. Furthermore, decreased shock strength close to the leading edge of the second vane was found in the prediction for the optimum CP.

Acknowledgment

This work was made possible by the Austrian Science Fund (FWF) within Grant No. P16521-N07, "Experimental Investigation of the Stator-Rotor-Stator Interaction in a Transonic Turbine." A visiting scientist grant from the Politecnico di Milano, Italy for one of the authors (B.P.) and the support of Dr. H. P. Pirker in the operation of the compressor station are also gratefully acknowledged.

Nomenclature

Latin

p = absolute pressure (bar)
t = time (s)

Greek

τ = rotor blade passing period (s)

Subscripts

A = first vane row inlet
C = rotor outlet
$D1$, $D3$ = second vane row outlet
rel = relative
t = total

References

[1] Miller, R. J., Moss, R. W., Ainsworth, R. W., and Horwood, C. K., 2003, "Time-Resolved Vane-Rotor Interaction in a High-Pressure Turbine Stage," ASME J. Turbomach., **125**(1), pp. 1–13.
[2] Tiedemann, M., and Kost, F., 2001, "Some Aspects of Wake-Wake Interactions Regarding Turbine Stator Clocking," ASME J. Turbomach., **123**(3), pp. 526–533.
[3] König, S., Heidecke, A., Stoffel, B., Fiala, A., and Engel, K., 2004, "Clocking Effects in a 1.5-Stage Axial Turbine—Boundary Layer Behaviour at Midspan," ASME Paper No. GT2004-54055.
[4] Hummel, F., 2002, "Wake-Wake Interaction and Its Potential for Clocking in a Transonic High-Pressure Turbine," ASME J. Turbomach., **124**(1), pp. 69–76.
[5] Huber, F. W., Johnson, P. D., Sharma, O. P., Staubach, J. B., and Gaddis, S. W., 1996, "Performance Improvement Through Indexing of Turbine Airfoils: Part 1-Experimental Investigation," ASME J. Turbomach., **118**(4), pp. 630–635.
[6] Arnone, A., Marconcini, M., Pacciani, R., Schipani, C., and Spano, E., 2002, "Numerical Investigation of Airfoil Clocking in a Three-Stage Low-Pressure Turbine," ASME J. Turbomach., **124**(1), pp. 61–68.
[7] Reinmöller, U., Stephan, B., Schmidt, S., and Niehuis, R., 2002, "Clocking Effects in a 1.5 Stage Axial Turbine-Steady and Unsteady Experimental Investigations Supported by Numerical Simulations," ASME J. Turbomach., **124**(1), pp. 52–60.
[8] Billiard, N., Paniagua, G., and Dénos, R., 2005, "Effect of Clocking on the Heat Transfer Distribution of a Second Stator Tested in a One and a Half Stage HP Turbine," ASME Paper No. GT2005-68462.
[9] Gadea, J., Dénos, R., Paniagua, G., Billiard, N., and Sieverding, C. H., 2004, "Effect of Clocking on the Second Stator Pressure Field of a One and a Half Stage Transonic Turbine," ASME Paper No. GT2004-53463.
[10] Haldeman, C. W., Dunn, M. G., Barter, J. W., Green, B. R., and Bergholz, R. F., 2004, "Experimental Investigation of Vane Clocking in a One and $\frac{1}{2}$ Stage High Pressure Turbine," ASME Paper No. GT2004-53477.
[11] Erhard, J., and Gehrer, A., 2000, "Design and Construction of a Transonic Test Turbine Facility," ASME Paper No. GT2000-480.
[12] Neumayer, F., Kulhanek, G., Pirker, H. P., Jericha, H., Seyr, A., and Sanz, W., 2001, "Operational Behavior of a Complex Transonic Test Turbine Facility," ASME Paper No. GT2001-489.
[13] Schennach, O., Woisetschläger, J., Fuchs, A., Göttlich, E., Marn, A., and Pecnik, R., 2006, "Experimental Investigations of Clocking in a One-and-a-Half-Stage Transonic Turbine Using Laser Doppler Velocimetry and a Fast Response Aerodynamic Pressure Probe," ASME J. Turbomach., **129**(2), pp. 372–381.
[14] Glas, W., Forstner, M., Kuhn, K., and Jaberg, H., 2000, "Smoothing and Statistical Evaluation of LDV Data of Turbulent Flows in Reciprocating Machinery," Exp. Fluids, **29**, pp. 411–417.
[15] Pecnik, R., Pieringer, P., and Sanz, W., 2005, "Numerical Investigation of the Secondary Flow of a Transonic Turbine Stage Using Various Turbulence Closures," *Proceedings of ASME Turbo Expo 2005*, Reno-Tahoe, NV, June 6–9, Paper No. GT2005-68754.
[16] Pecnik, R., and Sanz, W., 2006, "Application of the Turbulent Potential Model to Heat Transfer Predictions on a Turbine Guide Vane," *Proceedings of ASME Turbo Expo 2006*, May 8–11, Barcelona, Spain.
[17] Roe, P. L., 1981, "Approximate Riemann Solvers, Parameter Vectors and Differencing Scheme," J. Comput. Phys., **43**, pp. 357–372.
[18] Pieringer, P., and Sanz, W., 2005, "A Pressure Gradient Sensitive Wall Function for the Prediction of Turbulent Flow in Thermal Turbomachinery," *Proceedings of ASME Turbo Expo 2005*, Reno-Tahoe, NV, June 6–9, Paper No. GT2005-68471.
[19] Spalart, P. R., and Allmaras, S. R., 1994, "A One Equation Turbulence Model for Aerodynamic Flows," Rech. Aerosp., **1**, pp. 5–21.
[20] Göttlich, E., Woisetschläger, J., Pieringer, P., Hampel, B., and Heitmeir, F., 2005, "Investigation of Vortex Shedding and Wake-Wake Interaction in a Transonic Turbine Stage Using Laser-Doppler-Velocimetrie and Particle-Image-Velocimetrie," ASME J. Turbomach., **128**(1), pp. 178–187.
[21] Hodson, H. P., and Dawes, W. N., 1998, "On the Interpretation of Measured Profile Losses in Unsteady Wake-Turbine Blade Interaction Studies," ASME J. Turbomach., **120**(2), pp. 276–284.
[22] Miller, R. J., Moss, R. W., Ainsworth, R. W., and Harvey, N. W., 2003, "Wake, Shock, and Potential Field Interactions in a 1.5 Stage Turbine-Part I: Vane-Rotor and Rotor-Vane Interaction," ASME J. Turbomach., **125**(1), pp. 33–39.

Heat Transfer and Friction Factor in a Square Channel With One, Two, or Four Inclined Ribbed Walls

Soo Whan Ahn

Ho Keun Kang

School of Mechanical and Aerospace Engineering,
Gyeongsang National University,
Tongyong, Gyeongnam 650-160, Korea;
Institute of Marine Industry,
Gyeongsang National University,
Tongyong, Gyeongnam 650-160, Korea

Sung Taek Bae
Department of Mechanical System Engineering,
Graduate School,
Gyeongsang National University,
Tongyong, Gyeongnam 650-160, Korea

Dae Hee Lee
School of Mechanical and Automotive Engineering,
Inje University,
607 Obang-Dong,
Gimhae, Gyeongnam 621-749, Korea

An experimental study was carried out to investigate the heat transfer and friction characteristics of a fully developed turbulent air flow in a square channel with 45 deg inclined ribs on one, two, or four walls. Either two opposite walls or all four walls in the channel were heated. Tests were performed for Reynolds numbers (Re) ranging from 7600 to 24,900, the pitch to rib height ratio (P/e) of 8.0, the rib height to channel hydraulic diameter ratio (e/D_h) of 0.0667, and the channel aspect ratio of 1.0. The results show that the local Nusselt number and friction factor increase with the number of ribbed walls. With one ribbed wall, the Nusselt numbers on the ribbed side (B) were 50% and 63% greater than those on the adjacent smooth sides (L/R) and the opposite smooth side (T), respectively. The Nusselt numbers, when the two opposite walls of a four-wall ribbed channel are heated, are found to be 1.49–1.52 times greater than those obtained when all four walls are heated. [DOI: 10.1115/1.2775488]

Keywords: square channel, ribbed walls, Nusselt number, friction factor, 45 deg inclined ribs, number of heated walls

1 Introduction

Surface ribs can break up the viscous sublayer of a flow and promote local wall turbulence, which, in turn, enhances the heat transfer from the rib-roughened heated wall. In addition, a rib-roughened wall provides a greater surface area for heat transfer compared to a plain wall. When cooling gas turbine airfoils, rib turbulators are usually cast on two opposite sides of the cooling channel since the heat transfer takes place from both the inner walls of the pressure and suction sides of the blade. In some applications for electronic equipment, heat exchangers, and nuclear reactors, however, rib turbulators are mounted on one, two, three, or all four sides of the cooling channel.

Han et al. [1] and Han and Park [2] provided state-of-the-art reviews of turbine blade cooling and analyses of the heat transfer and friction characteristics in channels with two opposite ribbed walls. The effects of Reynolds number and rib geometry (rib height, rib spacing, rib angle of attack, and rib configuration) on the heat transfer and pressure drop in the fully developed region of uniformly heated square channels with two opposite ribbed walls have been investigated by Han et al. [1]. Further studies of the combined effects of rib geometry and channel aspect ratio on the local values of the heat transfer and pressure drop have also been reported by Han and Park [2]. These results show that angled ribs provide better heat transfer performance than transverse ribs and that lower aspect ratio channels perform better than higher aspect ratio channels.

Chandra et al. [3] did an experimental study of wall heat transfer and friction characteristics of fully developed turbulent air flow in a rectangular channel with transverse ribs on one, two, and four walls. Tests were performed for Reynolds numbers ranging from 10,000 to 80,000. The pitch to rib height ratio (P/e) was kept at 8. They reported that the heat transfer coefficient and friction factor values were enhanced with the increase in the number of transverse ribbed walls.

One objective of this study was to determine the effects of the number of inclined ribbed walls and the number of heated walls on the wall friction and heat transfer coefficients in a square channel. In the past, the majority of investigations have considered turbine blade cooling in channels with transverse ribbed walls. However, there is a need to examine the effects of varying the number of inclined ribbed walls and heated walls in rectangular channels on the heat exchanger systems. This study extends the existing knowledge base by providing experimental data for square channels with one, two, and four inclined ribbed walls. The square channel was heated on either two or four walls and was roughened with ribs inclined at 45 deg. Tests were performed for Reynolds numbers (Re) ranging from 7600 to 24,900, the pitch to rib height ratio (P/e) of 8.0, and the rib height to channel hydraulic diameter ratio (e/D_h) of 0.0667. The results of this investigation can be used in various applications, such as turbine blade internal cooling systems, electronic equipment, heat exchangers, and nuclear reactors.

2 Experimental Apparatus and Procedure

A 195-W blower delivered laboratory air through an 8.16-cm-diameter flexible tube at room temperature. The air then passed through an orifice to measure flow rates through a long straight square channel with a hydraulic diameter of $D_h=3.0$ cm and length of $L_h=90$ cm, and finally through the heated square test channel with $D_h=3.0$ cm and $L=180$ cm. Two aluminum plates of 90 cm were used on each wall.

The test channel is shown in Fig. 1. It was constructed of four 0.5-cm-thick aluminum plates having a cross section of 3.0×3.0 cm^2. Sharp-edged square aluminum ribs with a height of $e=0.2$ cm ($e/D_h=0.067$) and an equal spacing of $P=1.6$ cm ($P/e=8$) were glued with silicone adhesive onto the channel walls. The ribs were positioned with an inclination angle of 45 deg. To minimize the conduction heat loss to the ambient, the backside surfaces of the aluminum plates were well insulated using a 50-mm-thick pine wood ($k=0.112$ W/m °C) with a 0.8-mm-thick fiber gasket between the aluminum plate and the woven heater. Four thermocouples attached to the backside of the ribbed wall measured the outer wall temperatures and determined the conduction heat loss through the pine wood to the ambient, which turned out to be only 1.1% of the total power input. The radiation heat loss was also evaluated using a diffuse gray-surface

Contributed by the Turbomachinery Division of ASME for publication in the JOURNAL OF TURBOMACHINERY. Manuscript received July 6, 2006; final manuscript received February 13, 2007; published online May 2, 2008. Review conducted by Ronald S. Bunker.

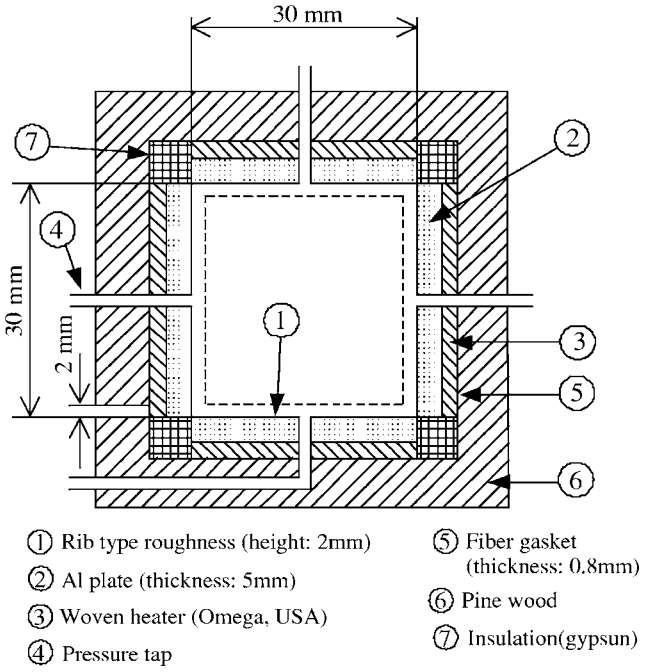

Fig. 1 Details of the test section

network [4] and was less than 0.9% of the total power input. It was because the surfaces of the aluminum plates and ribs were highly polished to minimize emissivity, and the heated-wall-to-unheated-wall temperature difference was between 11°C and 41°C only.

The channel walls were heated individually with electric woven heaters that were embedded and placed flat between the aluminum and pine wood plates to ensure good thermal contact. A transformer controlled the heaters independently so that a constant heat flux thermal boundary condition was created on the channel walls. Thermocouples embedded on the walls were used to measure the rib spanwise surface temperature at one downstream location in the test section to examine the temperature uniformity along the rib surface. Wall temperatures along the axial direction of the four channel walls were measured using 40 copper constantan thermocouples. The temperature of the air entering and leaving the test channel was also recorded.

Ten temperature positions, which were transversed vertically, were used to measure bulk mean air temperature entering the test channel and leaving the test channel. All of the thermocouples used in the experiment were carefully calibrated to an accuracy of ±0.15°C. Five pressure taps were installed along the axial centerline of the walls to determine the pressure drop. A micromanometer was used to measure the pressure differential over the specified channel length. The Reynolds numbers based on the channel hydraulic diameter (D_h) ranged from 7600 to 24,900. An 8.16-cm-diameter pipe, equipped with an orifice plate, was used to measure the mass flow rate. The air bulk velocity in the test section was obtained from the measurements in the smooth tube before the test section.

The power supplied to the heaters was adjusted such that the wall temperatures at a particular cross-sectional location were nearly the same while monitoring four different wall temperatures in the channel. Over the range of test conditions, the difference between the wall temperature at the end of the channel and the exit air temperature was around 15°C and the room temperature was kept between 24°C and 26°C.

3 Data Reduction

The friction factor for a fully developed flow in a square channel can be defined in terms of the dimensionless channel length (normalized by the hydraulic diameter D_h), pressure drop, and air velocity as follows:

$$f = \Delta p/[4(L/D_h)(\rho u_b^2/2)] \tag{1}$$

The semiempirical correlations developed by Han and Park [2] for ribbed channels are based on the assumption that the friction factor and rib-side heat transfer coefficient in a channel with two smooth and two ribbed walls can be calculated from geometrically similar channels with four smooth walls and four ribbed walls. The values for the four-sided smooth and ribbed wall cases are weighted proportionally to the areas of the smooth and ribbed walls. Therefore, the average ribbed channel friction factor f_{ra} is the weighted average of the four-sided smooth channel friction factor f_{sm} and the four-sided ribbed channel friction factor f_{rs}. If the total wall area of the channel is C, the smooth wall area of the channel is C_{sm}, and the ribbed wall area of the channel is C_{rs}, then the average friction factor for a ribbed channel can be expressed as follows:

$$f_{ra} = f_{sm}(C_{sm}/C) + f_{rs}(C_{rs}/C) \tag{2}$$

The average ribbed channel friction factor was normalized by the friction factor for a fully developed turbulent flow in a smooth circular channel (with the channel diameter replaced by the hydraulic diameter of the square channel), as proposed by Blasius for $\mathrm{Re} < 50{,}000$,

$$f_{ra}/f_{ss} = f_{ra}/(0.079\ \mathrm{Re}^{-0.25}) \tag{3}$$

The heat transfer coefficient was calculated from the net heat transfer rate per unit surface area exposed to the cooling air ($\dot{Q}$), the wall temperature (T_w), and the bulk mean air temperature (T_b),

$$h = \dot{Q}/[A(T_w - T_b)] \tag{4}$$

where A is the total heat transfer area of the smooth walls (i.e., excluding the surface area of the ribs). The heat transfer rate ($\dot{Q}$) was defined as

$$\dot{Q} = \dot{m}C_p(T_{b2} - T_{b1}) \tag{5}$$

The Nusselt number was defined using the area-averaged heat transfer coefficient and the hydraulic diameter D_h for the square channel,

$$\mathrm{Nu} = hD_h/k \tag{6}$$

The Nusselt number for fully developed turbulent flow in a smooth channel has been correlated by Sieder and Tate [5],

$$\mathrm{Nu}_{ss} = 0.027\ \mathrm{Re}^{0.8}\ \mathrm{Pr}^{1/3}(\mu/\mu_w)^{0.14} \tag{7}$$

The average Stanton number of the ribbed wall, St_{ra}, was determined from the average Nusselt number of the ribbed wall, Nu_{ra},

$$\mathrm{St}_{ra} = \mathrm{Nu}_{ra}/(\mathrm{Re\ Pr}) \tag{8}$$

The experimental uncertainties were estimated using the procedure outlined by Kline and McClintock [6]. The maximum uncertainty in the heat transfer rate ($\dot{Q}$) was estimated to be ±6.2%, resulting in the maximum uncertainty of the convection heat transfer coefficient (h) of ±8.9% at Re=19,100. It was also found that the uncertainties for the Reynolds number and friction factor were ±5.9% and ±9.7%, respectively.

4 Results and Discussion

The friction factor and heat transfer coefficient for a smooth channel were determined before performing tests in channels with ribbed walls. It was confirmed that there was a good agreement between the empirical correlation by Sieder and Tate [5] and our results.

Figures 2–4 show the Nusselt number distributions in square channels with ribbed walls as a function of the dimensionless axial location, x/D_h, for one, two, and four walls with 45 deg inclined ribs. The exact rib locations on the channel walls are shown in the square boxes. The letters B, L, R, and T represent the bottom, left, right, and top walls, respectively.

Figure 2 shows the streamwise Nusselt number distributions for the test section with ribs on the bottom wall. In general, the Nusselt number decreased monotonically from its maximum value at the beginning of the test section with increasing axial distance, eventually reaching a constant value at $L/D_h \cong 36$, where the flow was fully developed for the given Reynolds number. The results also showed that for all cases, the local Nusselt numbers on both the ribbed and smooth walls increased with the Reynolds number. Hu and Shen [7] reported similar results in their study of square channel walls with 45 deg inclined discrete ribs.

Figure 2 indicates that the Nusselt numbers on the ribbed bottom walls, Nu_{rs} (B), were 1.9–2.5 times greater than the fully developed Nusselt numbers on a smooth wall correlated by Sieder and Tate [5] for Reynolds numbers ranging from 7600 to 24,900. However, the Nusselt numbers on the ribbed side (B) were 50% and 63% greater than those on the adjacent smooth sides (L/R) and the opposite smooth side (T), respectively. The higher Nusselt numbers on the ribbed wall (B) were due to the increased level of turbulence generated by the ribs, which broke up the growth of the thermal boundary layer.

Figure 3 shows the streamwise Nusselt number distributions in the channel with ribs on two opposite sides (T/B) of the wall. The Nusselt numbers on the ribbed walls (T/B) were greater than those on the smooth walls (L/R), consistent with the behavior observed in Fig. 2. Figure 4 shows the local Nusselt numbers in the channel with ribs on all four walls and indicates the largest heat transfer enhancement of the three cases. This additional heat transfer enhancement is due to the larger increase in turbulence intensity resulting from a more active mixing of the flow caused by the additional ribs.

The fully developed Nusselt numbers in a rib-roughened channel normalized by the fully developed Nusselt numbers in a smooth channel from the Sieder and Tate correlation, Nu_{ra}/Nu_{ss}, are presented in Fig. 5 for four Reynolds numbers ranging from 7600 to 24,900. Three rib orientations and two wall heating conditions were selected to investigate the effect of the number of ribbed walls and the thermal wall boundary conditions on the heat transfer characteristics of the channel. Nusselt number distributions were obtained for ribs on one wall, two opposite walls, and all four walls with heating applied to both two opposite walls and all four walls.

It is evident from Fig. 5 that a higher heat transfer rate was experienced with each additional ribbed wall due to more active mixing of the separated flow caused by the ribs. Values of Nu_{ra}/Nu_{ss} with heating applied to two opposite walls were 1.49–1.52 times greater than those obtained with heating applied to all four walls at the same Reynolds number. This occurred because the colder fluid from the two unheated walls moved toward the two heated walls, resulting in higher heat transfer coefficients; such behavior was more marked with ribbed walls on one side or two opposite sides rather than on all four sides.

Figure 5 includes the experimental data of El-Husayni et al. [8], in which the test section was an area between a pair of ribs at the channel length to hydraulic diameter ratio (L/D_h) of 9.53 and the rib height to hydraulic diameter ratio (e/D_h) of 0.24. The differences in Nu_{ra}/Nu_{ss} between two opposite wall heated cases and four wall heated cases in the present work were much greater than those for El-Husayni et al. [8]. It is mainly because the average Nusselt numbers in the present work were measured farther downstream in the range of x/D_h=36–61 and at the lower rib height to hydraulic diameter ratio (e/D_h) of 0.0667. Therefore, it can be

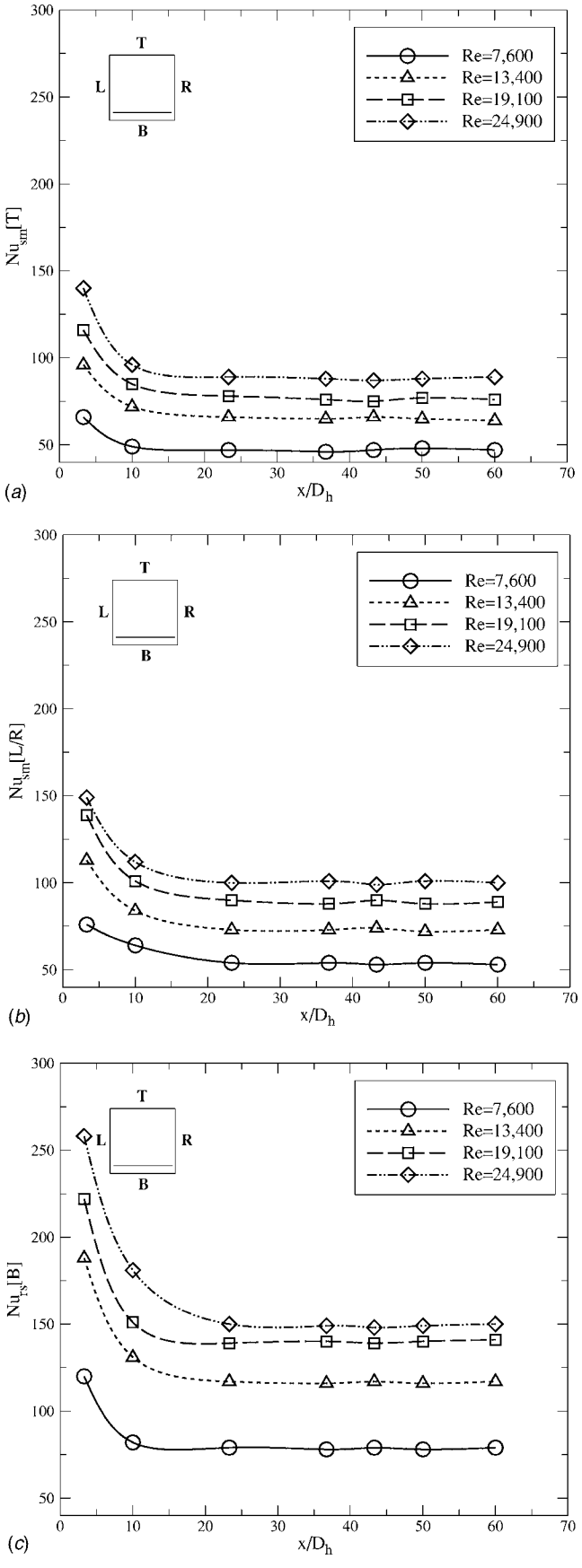

Fig. 2 Local Nusselt number distributions in a channel with a ribbed bottom wall

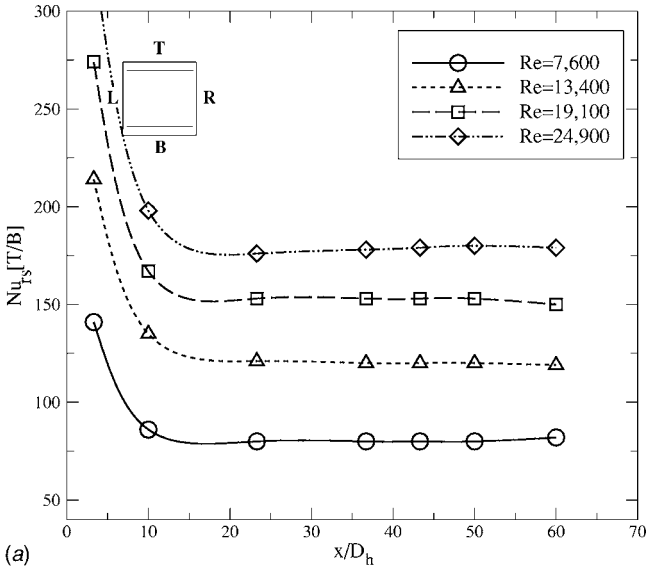

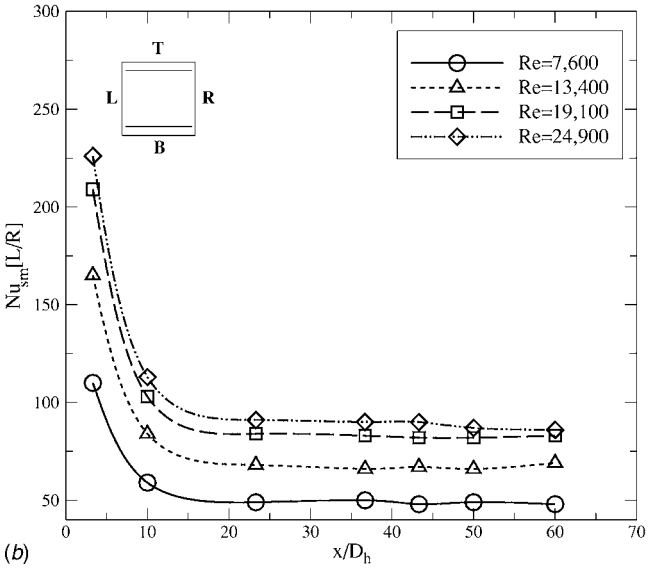

Fig. 3 Local Nusselt number distributions in a channel with two opposite ribbed walls

inferred that the colder fluid from the two unheated walls hardly moved toward the two heated walls in the case of El-Husayni et al. [8].

Figure 6 compares the heat transfer performance between the three ribbed wall cases and a smooth wall at four Reynolds numbers. The heat transfer performance factor $[(St_{ra}/St_{ss})/(f_{ra}/f_{ss})^{1/3}]$ was evaluated for the same surface area and pumping power. In general, the results show that the heat transfer performance factor gradually decreased with increasing Reynolds number. Values of the heat transfer performance factor with one ribbed wall, two opposite ribbed walls, and four ribbed walls were in the ranges of 1.32–1.93, 1.25–1.57, and 1.18–1.49, respectively. The best heat transfer performance occurred with one ribbed wall, which had a maximum of 93% greater heat transfer performance factor than the smooth wall at Re=7600.

5 Conclusion

The effects of the number of ribbed walls on the distribution of the heat transfer coefficients and friction factors in a square channel were investigated for four Reynolds numbers ranging from 7600 to 24,900. The following conclusions were drawn.

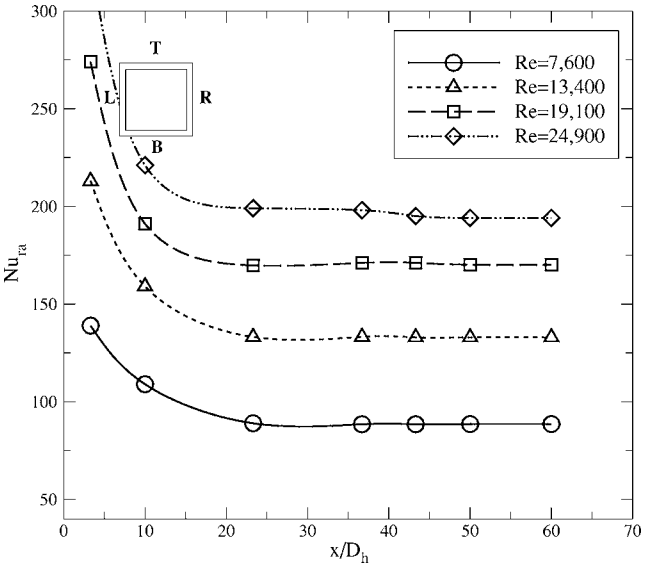

Fig. 4 Local Nusselt number distributions in a channel with four ribbed walls

(1) With one ribbed wall, the Nusselt numbers on the ribbed side (B) were 50% and 63% greater than those on the adjacent smooth sides (L/R) and the opposite smooth side (T), respectively.
(2) When two opposite walls of a four-wall ribbed channel were heated, the ratio of the fully developed Nusselt number to that measured in a smooth channel (Nu_{ra}/Nu_{ss}) was 1.49–1.52 times greater than those obtained when all four walls were heated at the same Reynolds number.
(3) The average friction factor increased with the number of ribbed walls. The maximum friction factor obtained with ribs on all four walls was nearly 9.0 times greater than that measured in a smooth channel at Re=24,900.
(4) The best heat transfer performance occurred with one ribbed wall, which had a maximum of 93% greater heat transfer performance factor than the smooth wall at Re =7600.

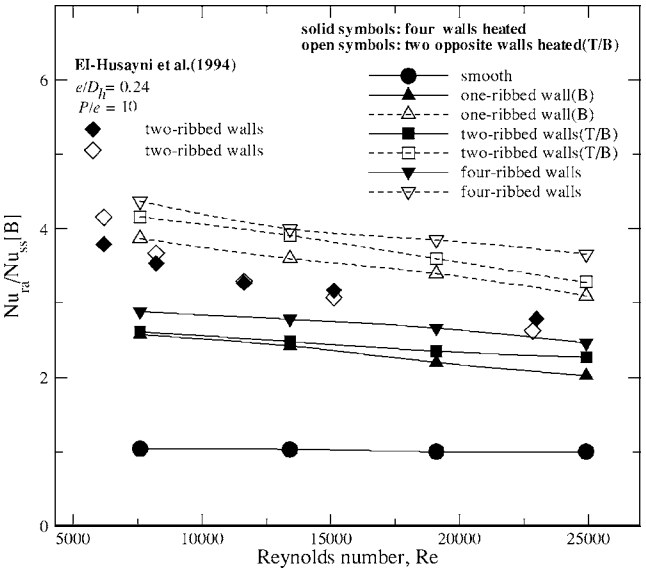

Fig. 5 Nusselt number variation for different ribbed wall conditions and Reynolds numbers

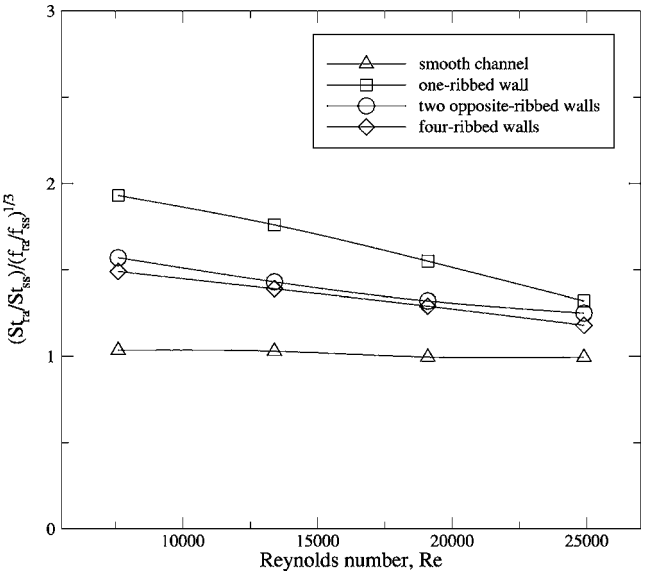

Fig. 6 Comparison of the heat transfer performance under a constant pumping power for different ribbed wall conditions

Acknowledgment

This work was supported by the Korea Research Foundation and New University for Regional Innovation projects.

Nomenclature

A = heat transfer area, m^2
h = area-averaged heat transfer coefficient, $W/m^2\,°C$
k = thermal conductivity of air, W/m °C
L = test section length, m
L_h = hydrodynamic entrance length, m
$\dot{m}$ = mass flow rate, kg/s
Δp = pressure drop, N/m^2
u = mean air velocity, m/s
x = distance from the entrance of the heated test section, m
α = attack angle, deg

Subscripts

1 = entrance
2 = exit
b = bulk
ra = average value of the ribbed channel
rs = ribbed wall
sm = smooth wall
ss = empirical correlation for smooth channel

References

[1] Han, J. C., Park, J. S., and Lei, C. K., 1985, "Heat Transfer Enhancement in Channels With Turbulence Promoters," ASME J. Eng. Gas Turbines Power, **107**, pp. 629–635.
[2] Han, J. C., and Park, J. S., 1988, "Developing Heat Transfer in Rectangular Channels With Rib Turbulators," Int. J. Heat Mass Transfer, **31**, pp. 183–195.
[3] Chandra, P. R., Niland, M. E., and Han, J. C., 1997, "Turbulent Flow Heat Transfer and Friction in a Rectangular Channel With Varying Numbers of Ribbed Walls," ASME J. Turbomach., **119**, pp. 374–380.
[4] Micheal, F. M., 2003, *Radiative Heat Transfer*, Academic, New York, pp. 162–189.
[5] Sieder, E. N., and Tate, C. E., 1936, "Heat Transfer and Pressure Drop of Liquids in Tubes," Ind. Eng. Chem., **28**, pp. 1429–1453.
[6] Kline, S. J., and McClintock, F. A., 1953, "Describing Uncertainties in Single Sample Experiments," Mech. Eng. (Am. Soc. Mech. Eng.), **75**, pp. 3–8.
[7] Hu, Z. J., and Shen, J., 1996, "Heat Transfer Enhancement in a Converging Passage With Discrete Ribs," Int. J. Heat Mass Transfer, **39**, pp. 1719–1727.
[8] El-Husayni, H. A., Taslim, M. E., and Kercher, D. M., 1994, "Experimental Heat Transfer Investigation of Stationary and Orthogonally Rotating Asymmetric and Symmetric Heated Smooth and Turbulated Channels," ASME J. Turbomach., **116**, pp. 124–132.